UNIVERSITEIT VAN PRETORIA
UNIVERSITY OF PRETORIA
YUNIBESITHI YA PRETORIA

HEAT TRANSFER AUGMENTATION IN A RECTANGULAR CHANNEL BY THE USE OF POROUS SINUSOIDAL SCREEN INSERTS.

by

Andrew Michael Torr

Presented in partial fulfilment of the requirements for the degree of

Master of Engineering

in the Department of Mechanical and Aeronautical Engineering

University of Pretoria

January 2019

Supervisor: Dr. G. I. Mahmood

Co-supervisor: Prof. J. P. Meyer

Abstract

HEAT TRANSFER AUGMENTATION IN A RECTANGULAR CHANNEL BY THE USE OF POROUS SINUSOIDAL SCREEN INSERTS.

Author:	A. M. Torr
Supervisor:	Dr. G. I. Mahmood
Co-supervisor:	Prof. J. P. Meyer
Department:	Mechanical and Aeronautical Engineering
Degree:	Master of Engineering (Mechanical Engineering)

Most regions in Southern Africa, South Africa in particular receives an abundancy of solar energy when compared to other regions across the globe. The most economical way to harness this energy is to design and implement economical heat exchangers with air as the working fluid. The performance of heat exchangers can be enhanced by implementing passive techniques such as coated or roughened surfaces, extended surfaces, displaced insert devices, flow swirl devices and coiled tubes among others. The addition of inserts in heat exchangers can increase the overall efficiency of the heat exchanger by increasing the convective heat transfer at the wall by generating local turbulence and mixing. The porous insert aims to the increase the rate of heat transfer by either increasing the convective heat transfer coefficient, the heat transfer area or both. The porous inserts act in such a way to repeatedly grow and destroy thin boundary layers on the surface providing a higher heat transfer coefficient. The porous inserts are lightweight, increase the structural integrity of the heat exchanger walls and can be retrofitted to the heat exchanger. By measuring the effects on the convection heat transfer rate, pressure drop, and turbulence caused by a wavy screen insert in a rectangular channel with air as the working fluid will help determine the thermal performance of the wavy screen insert. By independently investigating the effects of geometrical properties of the wavy screen insert, such as the porosity and periodicity of the insert, the size and shape of the insert can be determined to increase the thermal performance and reduce the size of the compact heat exchanger. This research aims to increase the thermal effectiveness of the heat exchanger channels while minimizing the increase in pressure penalty in the same channels. Increased thermal effectiveness directly affects the convection heat transfer, compact size, initial cost of the heat exchanger and how a small pressure penalty affects the operating cost of the heat exchanger. This research aims to investigate the effects of porosity and periodicity of the sinusoidal screen insert in a rectangular channel on the convection heat transfer rate and pressure drop across the channel to improve the thermal performance of the heat exchanger employed in solar panels, energy recovery systems, electronic chips, and machine components. To investigate the thermal performance of sinusoidal screen inserts in flat plate heat exchangers an experimental test facility is constructed which is capable of replicating the conditions of the heat exchanger. Six inserts are fabricated with varying wavelength and porosity. The height or amplitude of the sinusoidal waveform remains constant at 14 mm for all the inserts. The wavelength, λ is investigated at 12 mm, 16 mm and 20 mm. The effects of the porosity of the insert, ζ is investigated for at 48 % and 68 % porosity. The inserts are placed inside a 203 x 14 mm rectangular test section and wall temperature and pressure measurements along the test section are recorded over a range of $400 < Re < 35\ 000$. The study shows that the use of sinusoidal inserts in flat plate heat exchangers can increase the thermal performance over the range of $400 \leq Re \leq 3000$. Above $Re = 3000$ the increased pressure penalty decreases the performance of the heat exchanger.

Acknowledgements

I like to would acknowledge the following for their guidance and support:

- Dr. G. I. Mahmood and Prof. J. P. Meyer for their guidance, support, patience and in-depth knowledge in this field of study.
- C. Govender and D. Keetse for their assistance with the construction of the test facility.
- Mr D. Torr and Mrs. C. Torr for your unwavering moral support.

I would like to acknowledge the following for their financial aid and for making the research possible:

- NRF.
- University of Pretoria.
- Mr. D. Torr.
- Mr. C. Coetzee on behalf of Resonant Solutions.

Finally, to all the teachers, tutors, lectures and researchers in the engineering environment who have paved the way for this undertaking. Your contributions and services are most gratefully acknowledged.

Table of Contents

List of Figures

Appendix A

Appendix B

Appendix C

Appendix D

Appendix E

Appendix F

List of Tables

Appendix A

Appendix B

Appendix G

Appendix H

Nomenclature

A	Area	m^2
C_p	Specific heat capacity	J/kgK
D	Diameter	m
d	Orifice diameter	m
g	Gravitational acceleration	m/s^2
H	Channel height	m
H_f	Fluid Pressure Head	m
h	Heat transfer coefficient	W/m^2K
I	Current	A
k	Thermal conductivity	W/mK
L	Length	m
$\dot{m}$	Mass flow rate	kg/s
P	Perimeter	m
P_w	Pumping power	W
p	Pressure	Pa
Q	Discharge	m^3/s
$\dot{Q}$	Heat	W
$\dot{q}$	Heat flux	W/m^2
r	Radius	m
T	Temperature	K or °C
x	Distance	m
V	Voltage	V
$\overline{V}$	Mean velocity	m/s

Dimensionless Parameters

C	Discharge coefficient
f	Fanning or skin-friction factor
I_P	Performance index
Nu	Nusselt number
ΔP^*	Normalized pressure
Pr	Prandtl number
Re	Reynolds number
x^*	Normalized distance

Greek Letters

α	Thermal diffusivity	m^2/s
α^*	Aspect ratio	-
β	Beta ratio	-
ε	Expansion coefficient	-
ζ	Porosity	%
λ	Wavelength	m
μ	Dynamic viscosity	m^2/s
ν	Kinematic viscosity	kg/ms^2
ρ	Density	kg/m^3
τ	Wall shear stress	kg/ms^2

Subscripts

a	air
amb	ambient
avg	average
c	cross-section
conv	convective
h	hydraulic
ht	heat transfer
hy	hydrodynamic
I	insulation
l	loss
m	mean
p	pesrpex
w	wall
T	total
th	thermal
x	distance
0	smooth channel/baseline/reference

1 Introduction

1.1 Background

Most regions in Southern Africa, South Africa in particular receives an abundancy of solar energy when compared to other regions across the globe. The majority of this energy is untapped due to inadequate or expensive equipment not suited for the African environment and economy. The most economical way to harness this energy is to design and implement economical heat exchangers with air as the working fluid.

As solar energy is only available for less than half a day, the methods used to recover the energy need to be efficient. Enhancement methods fall under two categories, namely passive and active techniques. Passive techniques include coated or roughened surfaces, extended surfaces, displaced insert devices, flow swirl devices and coiled tubes among others. The porous insert aims to increase the rate of heat transfer by either increasing the convective heat transfer coefficient, the heat transfer area or both.

The addition of inserts in heat exchangers can increase the overall efficiency of the heat exchanger with an increased system pressure penalty. An enhanced heat transfer surface has a modified surface geometry that provides a higher heat transfer value per unit surface area when compared to that of a plain surface. The enhancement ratio is the ratio of the heat transfer from the enhanced surface to that of a plain or smooth surface [1].

The heat transfer coefficient on the gas side of a liquid-to-gas heat exchanger is much smaller than that on the liquid-side and therefore gas-side fins are implemented to increase the heat transfer on the gas-side. Plain fins are ‘old technology’ and enhanced surface geometries such as wavy fins give higher performance than plain fins [1]. The enhanced surface geometries act in such a way to turbulate and repeatedly grow and destroy thin boundary layers on the surface providing a higher heat transfer coefficient. Application of fins to heat exchanges can be beneficial if the fins can dominate the thermal resistance. The fins can have the effect to reduce or increase the heat transfer coefficient of the heat exchanger. Fin enhancements are either machined as part of the heat exchanger wall or are physically bonded to the wall. The material of construction of the fins is similar to that of the heat exchanger wall and can add a significant increase to the mass and cost of the heat exchanger [1].

Enhanced or extended surfaces are used to lower the thermal resistance on the gas-side of heat exchangers if the heat transfer coefficient is typically 5 – 20 % of that of the liquid-side. Specially configured extended surfaces may increase the heat transfer coefficient by 50 - 150 % times that of the plain surface and as a result the size of the heat exchanger can be drastically reduced. Due to the low density of gases and small hydraulic diameter the Reynolds numbers are typically in the range of $500 < Re_{Dh} < 1500$. Transitioning the flow into the turbulent regime by increasing the Reynolds number will increase the performance of the heat exchanger however the fan power normally limits the operation to lower Reynolds numbers. The performance of the enhanced surface is determined by parameters such as wave pitch, the corrugation angle and the channel spacing. The performance will also be affected by whether the wave geometry has sharp or smooth corners [1].

An alternative enhancement technique to fins and extended surfaces is presented in the form of wavy porous inserts. The wavy porous insert acts to enhance the thermal performance of the heat exchanger by increasing the turbulence in the gas-side flow passages. The pores of the insert promote local turbulence in small scales to enhance mixing and increase the convective heat transfer coefficient at the surface of the wall. The insert is not bonded to the heat exchanger wall and only makes line contact with the surface of the wall. As the insert is not bonded to the wall it is not necessary to conduct heat from the base surface to the insert allowing for a wide range of affordable materials of construction for the inserts. The inserts can easily be fitted to new and existing heat exchangers for maintenance or replacement.

When compared to solid metal, metal mesh, wire brush and twisted tape inserts the wavy porous insert is lighter and expected to produce a reduced pressure drop penalty due to the porous nature of the insert. In comparison the wavy porous insert is smaller, lighter and increases the structural integrity of the heat exchanger passages allowing for a more compact, light-weight and economical heat exchanger. The thermal performance i.e. the increase in heat transfer with pressure penalty is thus expected to be superior in the channel with the wavy screen inserts compared to the other heat transfer enhancers employed in the heat exchangers. The technological importance of the research is significant in cooling and heating channels in electronics, solar panels, flat plate heat exchangers, condensers and evaporators.

By measuring the effects on the convection heat transfer rate, pressure drop, and turbulence caused by a wavy screen insert in a rectangular channel with air as the working fluid will help determine the thermal performance of the wavy screen insert. By independently investigating the effects of geometrical properties of the wavy screen insert, such as the porosity and periodicity of the insert, the size and shape of the insert can be determined to increase the thermal performance and reduce the size of the compact heat exchanger.

1.2 Problem Statement

Current enhancement techniques result in high pressure losses, are dependent on the conductivity of the material used and are machined or bonded to the wall of the heat exchanger and cannot be replaced or retrofitted to existing heat exchangers. By independently investigating the physical properties of a wavy porous insert, such as the porosity, size and periodicity of the insert, the best size and shape of the insert can be determined for increasing the effectiveness, size, weight and thermal performance of the heat exchanger.

1.3 Aim

This research aims to increase the thermal performance of the heat exchanger channels by enhancing the convective heat transfer while minimizing the increase in pressure penalty in the same channels. Increased thermal effectiveness directly affects the convection heat transfer, compact size, initial cost and operating cost of the heat exchanger. This research aims to investigate the effects of porosity and periodicity of the sinusoidal screen insert in a rectangular channel on the convection heat transfer rate and pressure drop across the channel. The results can be employed to design thermally improved heating and cooling channels in solar panels, energy recovery systems, electronic chips, and machine condensers and evaporators.

1.4 Scope of Work

The aim of the research is to increase the thermal effectiveness of the heat exchanger channels while minimizing the increase in pressure penalty in the same channel. An environment in which the research can be investigated is constructed. The research is conducted in rectangular channels where two sides or one side of the channel can be heated. This scenario is common in heat exchanger applications. In order to evaluate the performance of the inserts the pressure drop across the insert and convective heat transfer coefficient at the heated walls of the channel are to be determined.

Previous works show that wavy inserts offer the greatest heat transfer enhancement in the transitional flow regime however heat exchangers in industrial applications operate at a wide range of flow rates. Therefore, the performance of the inserts is evaluated in the laminar, transition and turbulent flow regimes. The research aims to investigate the effects of porosity and periodicity of the sinusoidal screen insert. The thermal performance of multiple (six) inserts with varying wavelengths and porosities is investigated. The height (amplitude) of sinusoidal insert remains constant. The scope of work is thus summarized as:

- The construction of an experimental setup capable of replicating the conditions inside a flat walled plate heat exchanger.
- The fabrication of six sinusoidal screen inserts of varying porosity and wavelength.
- Investigation of the pressure drop across the inserts.
- Investigation of the heat transfer coefficient at the heated walls of the rectangular channel for both a one wall and a two wall heating boundary condition.
- The thermal performance estimations of the sinusoidal inserts over the range of $400 < Re < 35\ 000$.

2 Literature Study

2.1 Introduction

This chapter addresses key fundamental concepts which are essential to understanding internal convective heat transfer and pressure drop in heat exchangers. This chapter discusses the flow regimes and entry lengths typical of internal forced convection in ducts. Previous work and literature pertaining to the flow regime and the use of inserts in heat transfer augmentation is also discussed.

2.2 Non-dimensional Parameters

Reynolds Number

Early researchers in fluid flow observed that the transition of flow from the laminar to the turbulent flow regimes was dependent on a variety of factors including the geometry, flow velocity, surface roughness, type of fluid and the temperature amongst other factors. In acknowledgement of Osborn Reynolds' work in fluid flow this ratio is termed as the Reynolds number and is given by [2]:

$$Re = \frac{inertia\ forces}{Viscous\ forces} = \frac{\rho VD}{\mu} \tag{2.1}$$

Low Reynolds numbers indicate a slow, viscous creeping type of flow where the inertia forces are negligible. High Reynolds numbers indicates a time-mean varying flow with superimposed strong random high frequency fluctuations governed by the inertia forces [3].

Friction Factor

By solving the mass and momentum equations the wall shear stress (at $r = r_w$) for fully developed flow in a circular tube (Hagen-Poiseullie flow) can be expressed [4]:

$$\tau_w = \frac{r_w}{2}\left(-\frac{dP}{dx}\right) \tag{2.2}$$

The wall shear stress can also be express in terms of a non-dimensional friction coefficient and the dynamic pressure which is commonly used in fluid flow applications [4]:

$$\tau_r = f\frac{\rho\bar{V}^2}{2} \tag{2.3}$$

Solving Eq. 2.2 and 2.3 for the friction factor yields:

$$f = \frac{(r_0/2)(-dP/dx)}{0.5\rho\bar{V}^2} = \frac{(D_0/4)(-dP/dx)}{0.5\rho\bar{V}^2} \tag{2.4}$$

f is known as the Fanning or skin-friction factor. The pressure drop per meter in the test section with an insert present is the combination of the wall shear stress and the profile losses due to the blockage of the insert. For rectangular ducts if D_h if substituted for D in Eq. 2.4 the equation is found to still be valid [4]. D_h is known as the hydraulic diameter and is calculated by the equation:

$$D_h = \frac{4\ x\ flow\ area}{perimeter} = \frac{4A_c}{P} \tag{2.5}$$

Eq 2.4 becomes:

$$f = \frac{(D_h/4)(-dP/dx)}{0.5\rho\bar{V}^2} \tag{2.6}$$

Nusselt Number

The Nusselt number or dimensionless convection heat transfer coefficient is the ratio of the convective heat transfer coefficient to the thermal conductivity of a fluid and is given by the equation [2]:

$$Nu = \frac{\dot{q}_{conv}}{\dot{q}_{cond}} = \frac{hD}{k} \tag{2.7}$$

Prandtl Number

In 1904 Ludwig Prandtl introduced the concept of boundary layers and made significant contributions to boundary layer theory. The Prandtl number relates the relative thickness of the velocity to thermal boundary layer. The Prandtl number is defined as [2]:

$$Pr = \frac{Molecular\ diffusivity\ of momentum}{Molecular\ diffusivity\ of\ heat} = \frac{v}{\alpha} = \frac{\mu c_p}{k} \tag{2.8}$$

Liquids with low Prandtl numbers such as liquid metals will dissipate heat much more quickly than liquids with high Prandtl numbers such as oils relative to dissipation of momentum.

Heat Transfer Factor

It is possible to establish a relationship between the friction due to surface shear and heat transfer by substituting Nu ∝ $Pr^{1/3}$ into Colburn's statement of the Reynolds analogy. The resulting factor is termed the heat transfer factor [1]:

$$StPr^{2/3} \equiv j = f/2 \tag{2.9}$$

Performance Index

The performance index of the insert can be determined by comparing the gain in heat transfer to the increase in pressure loss along the channel test section between a smooth and an enhanced channel. The thermal performance can be quantified by taking the ratio of Nusselt number increase to the friction factor increase compared to the smooth channel to illustrate the enhancement in the heat transfer per unit enhancement in the pumping power. The design objectives for turbulence inserts for heat exchangers should be threefold, [5,6] namely when compared to the smooth channel the insert should:

- Reduce heat transfer area for equal pumping power and heat transfer rate.
- Enhance the heat transfer rate for equal heat transfer are and pumping power.
- Reduce the pumping power for equal heat transfer area and rate.

The performance indices are calculated by the following equations:

$$I_{p1} = \frac{Nu/Nu_0}{f/f_0} \tag{2.10}$$

$$I_{p2} = \frac{Nu/Nu_0}{(f/f_0)^{1/3}} \qquad 2.11$$

Once the performance index has be determined the design of the insert can be evaluated to the design objectives listed above. For example, for a value of $(Nu/Nu_0)/(f/f_0)^{1/3} = 0.9$ at a specific Reynolds number the performance of the channel with the insert is estimated to:

- Require an increase in the heat transfer area of $(1 - 0.9^{1.5})$ or 15 % to achieve the same heat transfer for equal pumping power as that in the smooth channel.
- Require an increase in the heat transfer rate of (1 - 0.9) or 10 % to achieve the same heat transfer area for equal pumping power as that in the smooth channel.
- Require an increase in the pumping power of $(1 - 0.9^{3.0})$ or 27 % to achieve the same heat transfer rate and heat transfer area as that in the smooth channel.

Hence for Eq. 2.11 above the performance index should be greater than one for the insert to be deemed advantageous as described by [5,6].

2.3 Entry Lengths

The hydrodynamic and thermal entry lengths are defined as the duct length required for the centreline velocity and temperature to reach 99 % of the fully developed values. Shah and London [7] present numerous findings for the hydrodynamic entry length in the laminar flow regime in rectangular channels however only Han [8] and McComas [9] present data which can be interpolated for a rectangular channel with an aspect ratio of 0.069 which is the aspect ratio considered in this study. The data presented by [8] is low due the rapid flow development in the duct while the data presented [9] is low due to an unrealistic assumption of an inviscid core made near the entrance of the duct [7]. Kays and Crawford [4] provide an estimate for the developing length in an axisymmetric circular tube which results in an entry length larger than that suggested by [8] and [9]. For laminar flow White [3] suggests a commonly accepted correlation of $L_{hy}/D = 0.06Re_D$. The hydrodynamic entry lengths are shown in Table 2.1.

Table 2.1: Hydrodynamic entry lengths in the laminar flow regime for a rectangular channel with $\alpha^* = 0.069$

Re	L_{hy} [m]			
	Han [8]	McComas [9]	Kays-Crawford [4]	White [3]
400	0.178	0.082	0.524	0.629
600	0.266	0.123	0.786	0.943
1000	0.444	0.205	1.310	1.572
1400	0.622	0.286	1.834	2.200
2000	0.888	0.409	2.620	3.143

The thermal entrance length, L_{th} in a channel with a rectangular cross-section for hydrodynamically developed and thermally developing flow with a constant heat flux boundary condition and a Prandtl number of 0.7 is investigated by [7] and is shown in Table 2.2. The data is interpolated for a channel with an aspect ratio of 0.069. Comparison of Table 2.1 and Table 2.2 shows that the thermal entrance length is less than the hydrodynamic entrance length proposed by [9] and [8]. From the definition of the Prandtl number, for fluids with a Prandtl number of less than 1 the thermal entrance length is expected to less than the hydrodynamic entrance length.

In the turbulent flow regime the hydrodynamic entry length in a circular tube can be calculated using the following equation developed by Latzko [4]:

$$(x/D)_{entry} = 0.623Re^{0.25} \tag{2.12}$$

It is noted that the hydrodynamic developing length is much shorter in the turbulent flow regime, approximately 10D [2], than in the laminar flow regime where 100D is typical [4]. The developing lengths based on the channel hydraulic diameter and Reynolds number range applicable to the research in this paper are shown in Table 2.3 [3,4].

Table 2.2: Thermal entry lengths in the laminar flow regime for a rectangular channel with $\alpha^* = 0.069$

Re	L_{th} [m]
	Shah-London [7]
400	0.015
600	0.022
1000	0.037
1400	0.051
2000	0.073

Table 2.3: Hydrodynamic entry lengths in the turbulent flow regime for a rectangular channel with $\alpha^* = 0.069$

Re	L_{hy} [m]		
	Kays-Crawford [4]	Anselmet [3]	White [3]
10000	0.163	0.419	0.535
15000	0.181	0.464	0.572
20000	0.194	0.498	0.600
25000	0.205	0.527	0.623
30000	0.215	0.552	0.642
35000	0.223	0.573	0.659

Infinite series solutions for the thermal entry length in the turbulent flow regime show that there is little dependence of the thermal entry length on the Reynolds number for fluids with a Prandtl number equal to 0.7 [4]. The infinite series solutions show that for Reynolds numbers 50 000 < Re < 200 000 the local Nusselt number is within 2 % of the converged value between 20 < x/D < 25 and is shown in Figure 2.1.

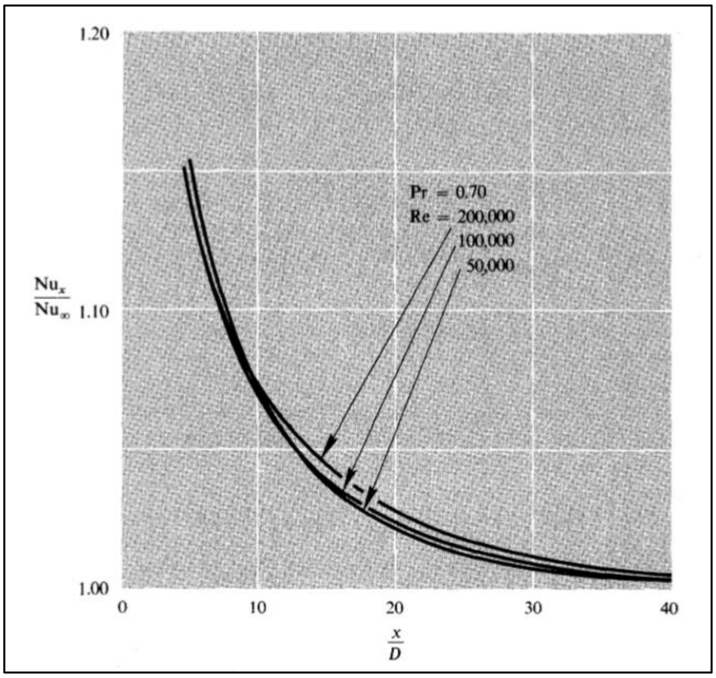

Figure 2.1: Nusselt numbers in the thermal-entry length of a circular tube, for constant heat rate: influence of Re at Pr = 0.7 [4]

2.4 Flow Regimes

2.4.1 Laminar Flow

In the laminar flow regime the heat transfer coefficient can be easily influenced by secondary flows caused by buoyancy forces. This is typically of flows with a weak driving force. This section will only deal with internal forced convection.

2.4.1.1 Friction Factor Correlations

Extensive work was done by Shah and London [7] on internal forced convection in ducts. Shah and London tabulated friction factor data for fully developed flow in rectangular channels with varying aspect ratios. The data can be can be approximated by the following equation [7]:

$$fRe = 24[1 - 1.3553\alpha^{*} + 1.9467\alpha^{*2} - 1.7012\alpha^{*3} + 0.9564\alpha^{*4} - 0.2537\alpha^{*5}] \tag{2.13}$$

Where α^* is the ratio of the long side of the duct to the short side. For circular pipes with Hagen-Poiseullie flow the friction factor can be solved from first principles [2]:

$$f = \frac{16}{Re} \tag{2.14}$$

Using similar principles, the Fanning friction factor between parallel plate is determined to be:

$$f = \frac{24}{Re} \tag{2.15}$$

2.4.1.2 Heat Transfer Correlations

The Nusselt number is dependent on the thermal boundary conditions i.e. a constant temperature or a uniform constant heat flux boundary. For fully developed (hydrodynamic and thermal) flow in a rectangular channel subject to a constant uniform heat flux at the wall the Nusselt number determined by Shah and London [7] is independent of the Reynolds number and only influenced by the aspect ratio of the channel. An analytical expression with a 0.03% accuracy was developed by [7] and is given by:

$$Nu = 8.235[1 - 2.0421\alpha^{*} + 3.0853\alpha^{*2} - 2.4765\alpha^{*3} + 1.0578\alpha^{*4} - 0.1861\alpha^{*5}] \tag{2.16}$$

Where α^{*} is the ratio of the long side of the duct to the short side. This equation is applicable to a channel in which all four sides of the channel are heated. Shah and London [7] also provide tabulated data for channels where one or more heated walls are heated.

2.4.2 Transitional Flow

The friction factors and thermal properties of liquids are difficult to predict in the transitional regime as the flow behaviour is highly dependent on the geometry, flow velocity, surface roughness, type of fluid and the temperature amongst other factors. Extensive research has been done by Meyer [10] in the field of transition flow in circular pipes. The transitional regime has been identified to contain two sub-categories, the transitional region and the low-Reynolds-number-end region. In the low-Reynolds-number-end region the flow approaches turbulent flow but has not reached fully turbulent flow. Current correlations tend to over predict the Nusselt number in this region [11].

2.4.3 Turbulent Flow

In the turbulent flow regime the flow pattern rapidly changing and the inertial forces are dominant. The flow fluctuates around a mean value. Numerous research has been done in the turbulent flow regime and hence the friction factors and Nusselt numbers are predictable.

2.4.3.1 Friction Factor Correlations

The friction factor in smooth tubes can be determined by the first Petukhov equation [2]:

$$4f = (0.790 lnRe - 1.64)^{-2} \tag{2.17}$$

The skin-friction factor can also be determined by iterative or goal seek methods from the Classical Karman-Nikuradse equation [4]:

$$\frac{1}{\sqrt{f/2}} = 2.46 \ln\left(Re\sqrt{f/2}\right) + 0.30 \tag{2.18}$$

This equation can be cumbersome and awkward to use. The following empirical equation closely fits the Karman-Nikuradse equation over the range 30 000 < Re < 10 000 000 [4]:

$$\frac{f}{2} = 0.023Re^{-0.2} \tag{2.19}$$

2.4.3.2 Heat Transfer Correlations

Multiple correlations and experimental data are available for the Nusselt number in circular tubes in the turbulent flow regime. Equations 2.20, 2.21 and 2.22 below are not sensitive to the thermal boundary condition and can be used for both a constant temperature and a constant heat flux condition [2]. The equation of Gnielinski is valid for the range 3 000 < Re < 5 000 000:

$$Nu = \frac{\left(\frac{f}{2}\right)(Re - 1000)Pr}{1 + 12.7\left(\frac{f}{2}\right)^{0.5}\left(Pr^{2/3} - 1\right)} \tag{2.20}$$

The second Petukhov equation is valid for the range 100 000 < Re < 5 000 000:

$$Nu = \frac{\left(\frac{f}{2}\right)RePr}{1.07 + 12.7\left(\frac{f}{2}\right)^{0.5}\left(Pr^{2/3} - 1\right)} \tag{2.21}$$

The Nusselt number is related to the friction factor through the Chilton-Colburn analogy [2]:

$$Nu = 0.125\left(\frac{f}{4}\right)RePr^{1/3} \tag{2.22}$$

Kays and Crawford [4] do not provide a correlation but do provide tabulated data in the turbulent flow regime for parallel plates with one side insulated and one side heated with a uniform constant heat flux.

2.5 Previous Works

Gee, D. L. and Webb. R. L. [5]

Gee and Webb investigated forced convection heat transfer in helically rib-roughed tubes. The authors also investigated the effect of the helix angle on the heat transfer augmentation. Friction factor and heat transfer characteristics were obtained for helix angle of 30°, 49° and 70°. The authors concluded that a particular roughness will not significantly increase the efficiency of the heat exchanger if it is operated over a wide Reynolds number range. Therefore a certain roughness factor only offers thermal enhancement over a certain Reynolds number range. The studied showed that the helix rib-roughened tubes offered greater heat transfer than the transverse rib-roughened counter-parts. The preferred helix angle was determined to be 49°.

Jeng, T., Tzeng, S. and Tang, F. [12]

The study experimentally investigated the fluid flow and heat transfer characteristics of a porous heat sink located in a rectangular channel. The heat sink measures 60 x 60 x 24 mm. The Reynolds numbers and the bypass area (the open area between the heat sink and the channel) are the variables in the study. The results showed that increasing the bypass area increased the flow around the heat sink. This was confirmed by flow visualization imagery. The average heat transfer enhancement, (Nu/Nu_0) increases with the Reynolds number for both the heat sinks for a bypass ratio less than 1.6. The greatest (Nu/Nu_0) enhancement was achieved at lower Reynolds numbers with a bypass ratio greater than 1.6

Heidary, H. and Kermani, M. J. [13]

The authors conducted a numerical study on the heat transfer and flow field in a wavy channel linked to a porous gas diffusion layer. The study has applications to be used as membranes in proton exchange in fuel cells. The study considers heat transfer from the wall to the free flow. A wide range of sinusoidal periods, 0 - 10 (dimensionless) and wave amplitudes, 0 - 0.3 (dimensionless) were simulated over a Reynolds number range of $100 < Re < 1000$. It was observed that a wavy wall can significantly enhance the heat transfer between the wall and the flow. The largest amplitude and number of wave periods results in the largest increase in the Nusselt number. The simulations show excellent agreement with literature with heat transfer enhancement up to 100 % depending on the duct size and sinusoidal period and amplitude.

Mahmood, G. I., Simonson, C. J. and Besant, R. W. [14]

The authors conducted research on the thermal performance of a screen insert in a 5 mm rectangular channel normal to the flow direction. The insert was tested over a range of $1380 < Re < 3800$. Friction factor and heat transfer measurements were obtained for both a one wall and a two wall heating boundary condition. The results indicated that both the Nusselt number ratio (Nu/Nu_0) and the friction factor ratio (f/f_0) increased with the Reynolds number. The results show that the performance index $(Nu/Nu_0)/(f/f_0)^{1/3}$ was only greater than 1.0 for $Re > 2500$. For the insert to provide beneficial heat transfer the performance index must be larger than 1.0.

Cramer, L., Mahmood, G. I., and Meyer, J. P. [15]

The authors researched the thermohydraulic performance of porous inserts with varying porosity and wave period in a 5 mm wide rectangular channel. The results show a strong dependence of the friction factor and Nusselt number on the Reynolds number. The investigation shows that the porosity and wave period significantly influence the friction factor and friction factor ratio. The results show that the use of the inserts is viable in heat exchanger applications.

Kahalerras, H. and Targui, N. [16]

The authors conducted a numerical study of the heat transfer enhancement in a double pipe heat exchanger by using porous fins. The fins are attached to the outer surface of the inner pipe which are in contact with the cold fluid. The height of the porous fins is non-dimensionalized by the hydraulic diameter for an annulus pipe and range between 0 - 1. The spacing of the fins range between 0 - 39 m. The study is limited to the same fluid flowing at the same flow rate through both pipe ducts. The study shows the implementations of the fins can significantly alter the flow patterns depending on the height and the porosity of the fins. The net energy gain is dependent on the fin thermal conductivity, this is typically for fin enhancement applications and increase rapidly at high Darcy numbers. The optimal fin spacing resulting in the highest heat transfer rate is dependent on the fin permeability. The performance of the heat exchanger was found to increase at most by 10 %.

Pavel, B. I. and Mohamad, A. A. [17]

A numerical and experimental study was conducted on the heat transfer enhancement for gas heat exchangers fitted with porous media. The research is conducted in a circular pipe subject to a uniform heat flux thermal boundary condition. The porosity of the insert ranged from 97 - 99%. From the experiments it was concluded that it is possible to achieve enhanced heat transfer rates by the use of the porous medium however the enhancement comes with a pressure penalty cost. The heat transfer enhancement was greatest for inserts with the same diameter as the duct and a smaller porosity.

Suri, A. R. S., Kumar, A. and Maithani, R. [18]

The authors conducted an experimental investigation on the heat transfer and fluid flow behaviour in multiple square perforated twisted tapes with square wing inserts in a heat exchanger tube. The performance of each insert was based on a performance factor equivalent to $(Nu/Nu_0)/(f/f_0)^{1/3}$. The performance factor was determined to be as large as 4 in the Reynolds number range of 25 000 < Re < 30 000. The increase in the Nusselt number and friction factor when compared to the baseline increased by factors of approximately 6 and 8 respectively.

Webb, R, L. and Kim, N. [1]

The authors present subject matter on the design of high-performance heat exchange devices. The research shows that enhanced surfaces and geometries promote much higher rates of heat transfer when compared to the plain or smooth surfaces. Design information and data is presented for heat transfer research in areas such as integral-fin and micro-fin tubes, complex plate-fin geometries and micro channels for single phase and multiphase flow.

Bekele, A., Mishra, M. and Dutta, S. [19]

The authors provide experimental data on solar air heaters enhanced with surface mounted obstacles. The delta shaped obstacles are mounted on the absorber surface of a duct with a 6:1 ratio. Friction factor and heat transfer data are obtained for relative obstacle heights ranging from 0.25 to 0.75, relative obstacle longitudinal pitch ranging from 1.5 to 5.5, relative transverse pitch ranging from 1 to 2.3 and an incidence angle ranging from 30° to 60°. The flow rate is varied between 2100 < Re < 30000. The thermal performance of the enhanced channel is compared to a wide variety alternative enhancement technique. The thermo-hydraulic performance of the channel is improved up to a factor of 3.89 when compared to the smooth channel configuration.

Bekele, A., Mishra, M. and Dutta, S. [20]

The authors provide experimental data on solar air heaters enhanced with surface mounted obstacles. The delta shaped obstacles are mounted on the absorber surface of a duct with a 6:1 ratio. Friction factor and heat transfer data are obtained for relative obstacle heights ranging from 0.5 to 0.75, relative obstacle longitudinal pitch ranging from 1.5 to 5.5. The relative transverse pitch and angle of attack remain constant at 2.3 and 90° respectively. The flow rate is varied between 3400 < Re < 328000. The thermo-hydraulic performance of the channel is improved up to a factor of 3.6 when compared to the smooth channel configuration. The study is further investigated with a numerical analysis using FLUENT^{TM} software.

2.6 Conclusion

Multiple methods of heat transfer enhancement in heat exchangers has been researched. The research is moving away from the use of fins and pins on the walls of the heat exchanger and towards the implementation of inserts in the channels. The inserts offer a larger heat transfer enhancement area without introducing a width-wise temperature gradient at the heated wall as the insert and the wall are independent from each other. The primary set back of the insert is the added pressure drop penalty hence research has been done on porous materials in an attempt to alleviate the pressure penalty. A large portion of the research is numerically based and relies heavily theoretical calculations and previously published literature. Of the experimentally based research the majority is conducted in circular tubes or concentric annuli. Although research has been conducted in smooth rectangular channels very little is known about the flow behaviour and heat transfer characteristics in the transitional flow regime. Furthermore, there are less publications with regards to the heat transfer enhancement is rectangular channels which not only makes this study relevant but also important in establishing a database of experimental results and insight into the heat transfer augmentation in rectangular channels employing porous inserts.

3 Experimental Setup and Procedure

3.1 Introduction

This chapter shows the experimental setup, instrumentation, experimental procedure and the data reduction for the research conducted on the inserts. The materials of construction and the properties of such materials where necessary are given. The sampling rate and acquisition of the data from the test section is highlighted. This chapter shows the geometry of the sinusoidal porous inserts and describes the methods used to manufacture the inserts.

3.2 Experimental Setup

3.2.1 Overview

The experiments are performed in an open-circuit low speed atmospheric wind-tunnel as shown in Figure 3.1. The air flow in the tunnel is generated by a centrifugal fan. The wind-tunnel setup consists primarily of rectangular and circular ducting. The flow enters the inlet 2-D contraction and is directed into a rectangular channel inlet section which is set to a height of 14 mm. The inlet section is 2.0 m long to settle and develop the flow before it enters the test section. From the inlet section the flow travels into the test section which has same cross-section and aspect ratio (14 mm : 203 mm) as the inlet section. The test section is used to house the inserts and measurement instrumentations. The walls of the test section are removable so that the walls with appropriate instrumentations and fittings can replace the present walls to allow for the pressure drop or heat transfer measurements. All the measurements are thus obtained in one wind tunnel employing the same test section. The flow moves out of the test section through an outlet section having the same cross-section as the test section and then into an outlet plenum. The lengths of the test section and outlet section are indicated in Figure 3.1. The flow is extracted out of the plenum by the fan via two circular pipes with inner diameters of 100 mm and 57 mm. The pipes can be opened or closed by ball valves. The pipes are metered with ISO standard orifice plate and flange assemblies. The mass flow rate of the air through the circular pipes is determined from the pressure drop across the orifice plates. The fan speed is controlled with a variable speed drive (VSD) to control the air flow rate in the wind tunnel. The walls of the wind-tunnel are constructed with 12 mm thick commercial grade acrylic plates. The experimental setup is supported on a commercial grade steel frame fabricated from 41 x 41 mm lip channels.

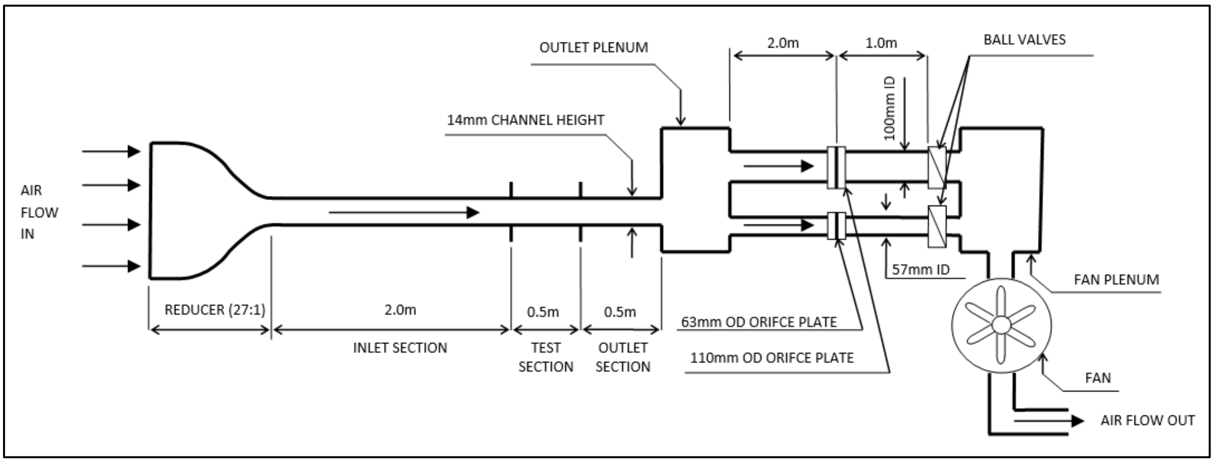

Figure 3.1:Plan view of experimental setup

3.2.2 Inlet Section

3.2.2.1 General Assembly

The inlet section consists of a 0.5 m long 2-D contraction with a 27:1 inlet to outlet ratio and four 0.5 m long rectangular channel modules. The channel heights are adjustable as indicated in Figure 3.2. The inlet contraction ensures the smooth entry and acceleration of ambient air and the development of the hydraulic boundary layer leading into the inlet section as well as assists in reducing the pressure drop at the inlet. The inlet contraction in covered with plastic mesh to prevent the ingress of particulates into the channel. The inlet contraction and modules are assembled from 12 mm thick clear acrylic plastic parts. The individual acrylic parts are fabricated on CNC milling machines to the desired surface finishes and tolerances. The free 203 mm wall is adjustable via slotted bolt connections to allow for a channel height ranging from 5 mm to 30 mm. The inlet section assembly is shown in Figure 3.2. The adjustable height also ensures that all the inlet section modules have the same cross-section when assembled.

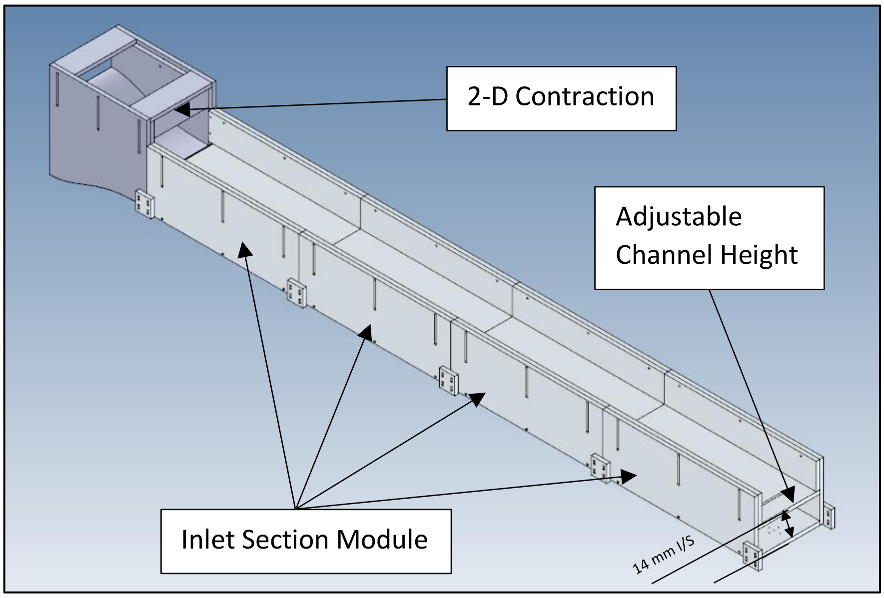

Figure 3.2: Inlet section assembly

3.2.2.2 Instrumentation

The inlet contraction is fitted with a single thermocouple to record the temperature of the ambient air entering the channel. The fixed endwall upstream of the test section is drilled to accommodate pressure taps as shown in Figure 3.3. The pressure taps allow for measurement of the upstream static wall pressure before the flow enters the test section. The friction factor estimated from the upstream pressure measurements confirm the fully developed laminar flow at inlet of the test section.

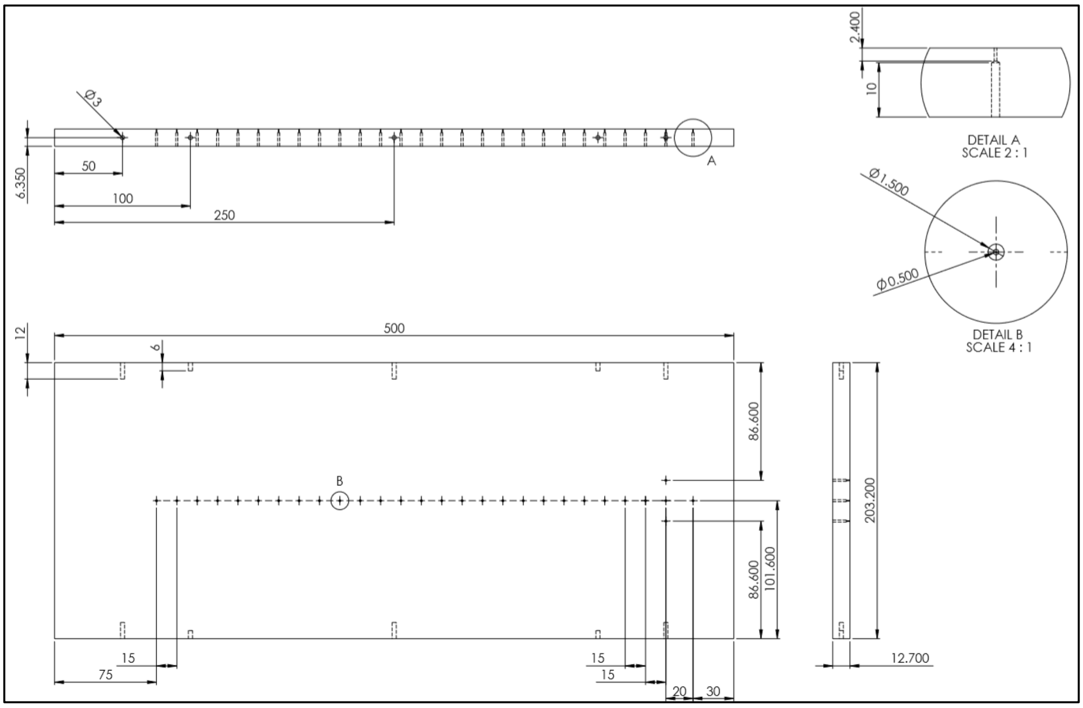

Figure 3.3: Inlet section endwall pressure tap detail.

3.2.3 Pressure Drop Test Section

3.2.3.1 General Assembly

The test section used for the pressure drop and friction measurements consists of a modified endwall. The modifications include two rows of thirty pressure tap as shown in Figure 3.4. Brass tubes 20 mm long with a 1.5 mm outer diameter are fitted in the pressure tap holes and are sealed all around with silicon sealant. PVC medical tubing of 1.5 mm inner diameter is used to connect the free open end of the brass tubes to the inlet side of a manual multiport scanivalve. The multiport-side plate of the scanivalve is connected to all the pressure taps. The output-side plate of the scanivalve has one single port. PVC tubing of 5 mm inner diameter connects the outlet port to the low-pressure end of the differential pressure transducer. The high-pressure end of the differential pressure transducer is left open to the ambient air. The details of the manual scanivalve are provided by Arnachellan [21].

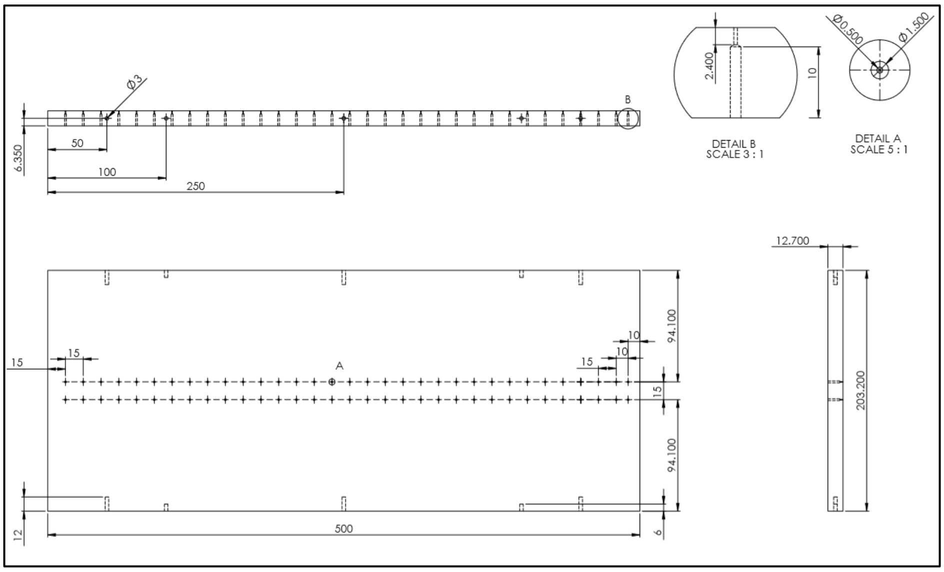

Figure 3.4: Pressure drop test section endwall

3.2.3.2 Instrumentation

The scanivalve connecting the pressure taps to the differential pressure transducer allows for individual isolation and measurement of a specific pressure tap without having to disconnect and reconnect pressure tubing. The outlet-side plate of scanivalve consists of a rotating dial with a single port. To scan a pressure port in the test section, the dial is manually rotated about its axis to align and connect the outlet port with the inlet port of the multiport side which is connected to the desired pressure tap. Only one pressure tap at a time can be connected for measurements to the transducer when the outlet dial is rotated and properly positioned.

The static wall pressure is measured using four differential pressure transducers with a varying measurement range. The appropriate pressure transducer is selected depending on the magnitude of the wall static pressure. The differential pressure transducers are listed in Table 3.1. Transducer PX164-010D5V (a) is used to measure the static pressure on the test section while transducer PX164-010D5V (b) is used to measure the pressure drop across the orifice plates. The transducers are powered by a D.C. power supply unit at the manufacturer specified excitation voltage.

The voltage output terminals of the differential transducers are connected to the National Instrument™ Data acquisition (NiDaq) system. The NiDaq is connected to the research station desktop computer. The analogue signal from the pressure ports are converted to voltage signals by the transducers and are then digitized by the NiDaq system. The digitized signals are time averaged and recorded to .txt files via control scripts written in an in-house Labview™ program. The voltage readings from the pressure transducers are sampled at 200 Hz for 10 sec before time-averaging.

The differential pressure transducers are calibrated using a Setra MicroCal calibration unit. The details of the calibration procedure are given in Appendix A.2. The average voltage recorded at each channel of the NiDaq system is converted to the pressure unit of Pa after applying the appropriate calibration curves. The uncertainties involved the pressure measurement are summarized in Section 4.2 and discussed at length in Appendix B.

Table 3.1: Differential pressure transducers

Differential Pressure Transducer	Pressure Range	
	In. H2O	Pa
PX2650-05D5V	0.5	124.4
PX2650-2D5V	2	497.7
PX164-005D5V	5	1244.2
PX164-010D5V (a)	10	2488.4
PX164-010D5V (b)	10	2488.4

3.2.4 Heat Transfer Test Section

3.2.4.1 General Assembly

The heat transfer test section consists of two modified endwalls shown in Figure 3.5. The modifications include the replacement of the two 203 mm endwalls with endwalls with a reduced thickness of 6 mm. On the flow side of the endwalls Kapton encapsulated electric-heating strips are attached. The reduce thickness of the endwall reduces the heat transfer in the axial direction. One of the heated endwalls is drilled through with 1 mm holes to allow for insertion of the thermocouples to measure the temperature of the surface of the heating strip. Figure 3.5 shows the locations of the thermocouples on the endwall. The entire heat transfer test section (all walls) is covered with two layers of 25 mm thick SPX 33 insulation material. SPX 33 is a closed cell, cross-linked expanded polyethylene foam with a nominal density of 32 kg/m^3 and a thermal conductivity of 0.037 W/m.K.

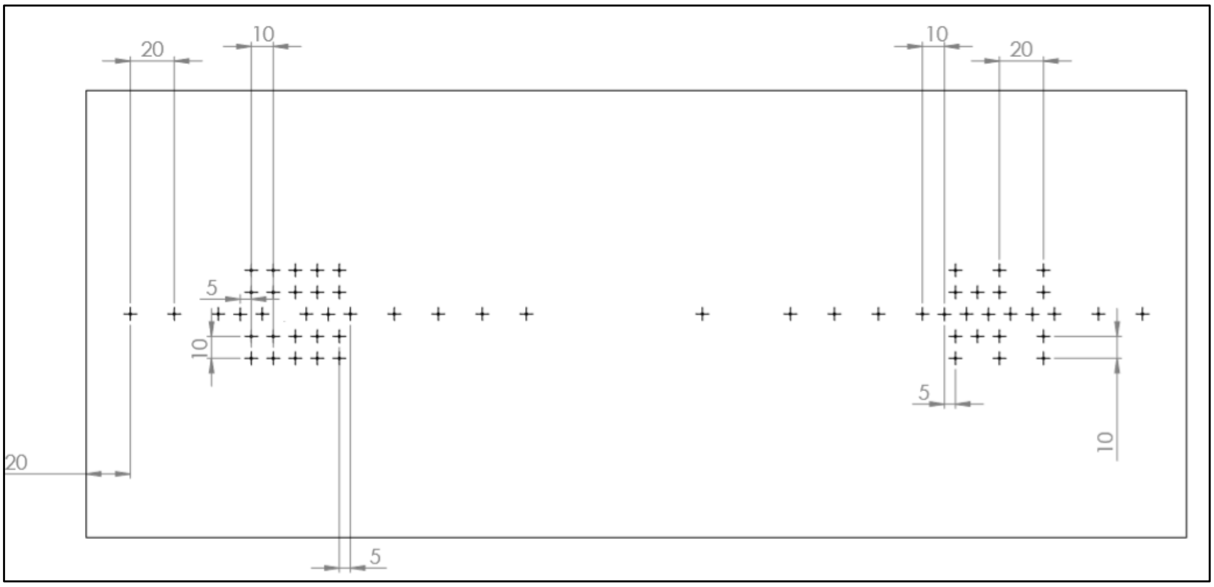

Figure 3.5: Heat transfer test section thermocouple locations.

3.2.4.2 Instrumentation

The thermocouples are all cut from spools of Omega^{TM} duplex insulated copper-constantan ANSI Type TT-T-30 thermocouple wires with an accuracy of 0.1 °C. The thermocouples are spot welded and calibrated before being mounted to the test section. Details of the calibration procedure is shown in Appendix A.3. A total of 64 T-type thermocouples are mounted in the test section endwall in the way shown in Figure 3.6. The thermocouple tip is covered in a conductive thermal paste before being inserted into the test section endwall. The tips of the thermocouples are placed adjacent to the heater surface. An additional 10 thermocouples are used to determine the thermal conduction losses through the insulation layers. 5 thermocouples are placed on the outer surface of the acrylic plate endwall and the remaining 5 thermocouples are place between the two layers of insulation. The spatial locations of the insulation thermocouples across the first insulation layer in Fig. 3.6 correspond to the same axial and lateral positions. An increment of 0.1 m axially relative to the start of the test section is employed to place the thermocouples on both sides of the insulation. Figure 3.6. (b) shows the two wall heating endwall heater arrangement. For the one wall heating case the top wall is replaced will a smooth insulated wall endwall without a heater. The one wall heating configuration can simulate a solar air heater with the bottom heated wall acting as the solar absorber.

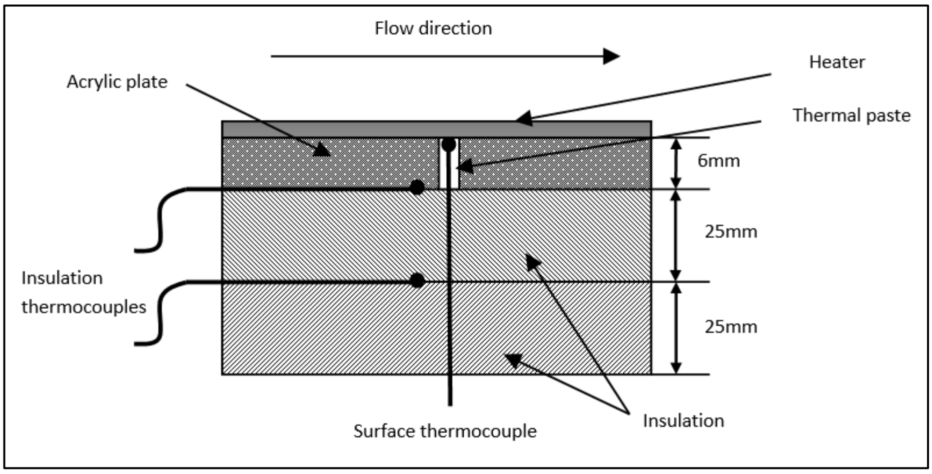

(a)

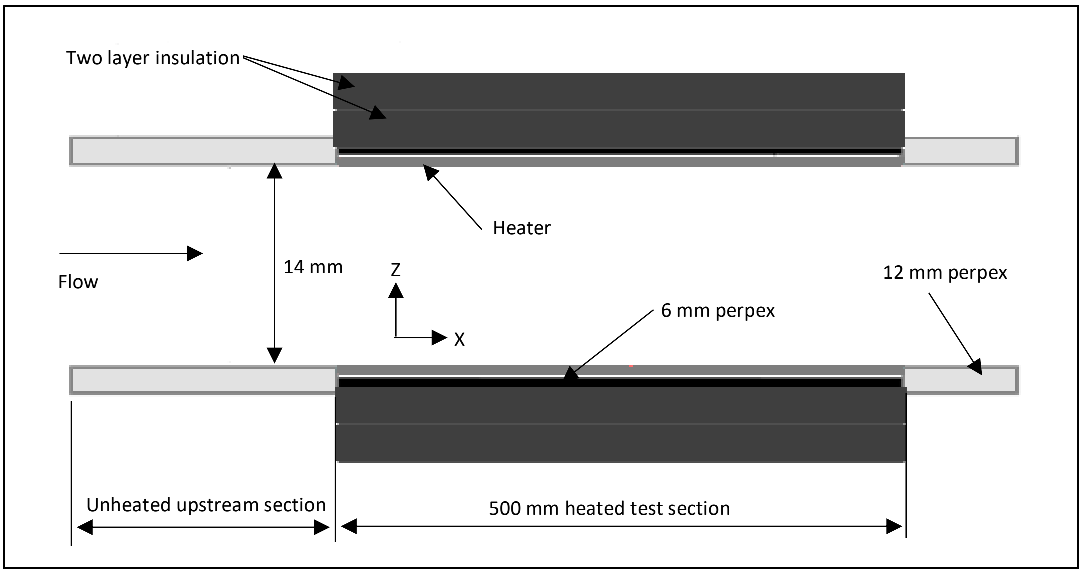

(b)

Figure 3.6: (a) Elevation view of a typical thermocouple location in test section and (b) test section wall heater arrangement

The free ends of the thermocouples are connected to the National Instrument^{TM} Data acquisition (NiDaq) thermocouple modules. The NiDaq is connected to the research station desktop computer. The analogue voltage signals from each of the thermocouples are digitized by the NI data logger at a sampling rate of 2 kHz for 2 sec. The data are then time-averaged and recorded to .txt files via control scripts written in an in-house Labview^{TM} program. The time-averaged data are then converted to the °C unit after applying the appropriate calibration curves for the corresponding thermocouples. The uncertainties associated with the temperature measurements are summarized in Section 4.2 and discussed at length in Appendix B.

The commercially sourced endwall heater strip consists of etched foil element encapsulated between two layers of polyamide film known as Kapton^{TM}. The heaters have adhesive surfaces on the back and are attached directly to the test section walls. Two heater strips of dimensions 10 x 8 inch are employed to cover each endwall. All the heaters are then connected in series electrically to have the same current flow and provide the same heating power. For the one wall heat transfer measurements one of the endwalls remains unheated. For the two-wall heat transfer boundary condition both the endwalls are heated. All the heat transfer measurements are obtained with no heating of the air flow upstream of the test section.

The heaters used in the heat transfer experiments are powered by a 240 volt A.C. variac power supply unit. The voltage and current applied to the heaters are monitored by a UNI-T UT33A and a UNI-T UT60A multi-meter. The voltage and current readings are recorded at the start and end of each experimental run.

3.2.5 Outlet Section and Downstream Equipment.

3.2.5.1 General Assembly

The outlet section of Figure 3.1 consists of a smooth channel with an adapter flange at the end of the section to allow for the attachment of the outlet plenum. The inside dimensions of the outlet plenum measures approximately 500 x 500 x 200 mm resulting in a volume of 0.05 m^3. The outlet plenum allows for the settling of flow and serves as a buffer zone between the pipe sections and test section. As a result a more uniform suction flow is drawn through the outlet section and hence through the test section.

A 110 mm OD and a 63 mm OD pipe connect the outlet plenum to the fan plenum. The pipes also house the flanged orifice plates which are designed based on the standard ISO 5167-1980 [22]. A straight distance of 20 diameters is allowed for upstream of the orifice plates and a straight length of 10 diameters is allowed for downstream of the plates. The diameter ratio of orifice hole to pipe (β) is 0.51 in the 110 mm pipe and 0.21 in the 63 mm pipe. The pipes are fitted with ball valves to open or close the flow through the pipes as needed. The fan plenum serves as a connection between the fan and the pipes. The fan outlet exhausts the air away from the research station.

3.2.5.2 Instrumentation

The orifice plates are manufactured in-house on lathes at the University of Pretoria from commercial grade steel plate. The diameters and eccentricity of the orifice is checked using vernier callipers with an accuracy 0.2 mm. The 110 mm and 63 mm orifice plate have an orifice diameter of 51 mm and 12 mm respectively. The orifice plates are manufactured according to ISO standards [22]. The orifice plates are mounted between two flat faced flanges with a rubber O-ring on either side of the plate to provide an air-tight seal. The orifice plates provide a cheap, effective and reliable method of determining the flow rate through the pipes. As mentioned in Section 3.2.3.2 the pressure drop across the orifice plate is measured at distances 1D upstream and 0.5D downstream. The excitation, sampling rates and data control for this differential pressure transducer are the same as those of the differential pressure transducers in Section 3.2.3.2. The uncertainties associated with the orifice plates and the flow rate are summarized in Section 4.2 and discussed at length in Appendix B.

The centrifugal fan is powered by a 1.5 kW three phase electric motor. The motor is control via a VSD which is located sufficiently far from the instrumentation behind a concrete wall so that the electromagnetic waves produced by the VSD do not interfere with the instrumentation. The VSD is adjusted until the pressure drop across the orifice plate corresponds to the required flow rate. The flow rate in the pipe is then used to estimate the Reynolds number in the channel as the measurements are obtained at steady-states.

3.3 Insert Characteristics

The inserts are fabricated from grade 304 stainless steel wire-mesh purchased from Merco Industries (Pty) Ltd, Roodepoort, South Africa. Two stainless steel mesh types are considered, namely a 16 strand per inch and a 27.91 strand per inch mesh. Both meshes have a wire diameter of 0.28 mm. The 16 strand per inch mesh has an aperture of approximately 1.31 mm before any distortions and hence, has a porosity of 68%. The 27.91 strand per inch mesh has an aperture of approximately 0.63 mm before any distortions and therefore, has a porosity of 48%. The apertures in both meshes are square in geometry.

Six different sinusoidal (wavy) inserts are fabricated from the mesh for testing, three from each porosity with a varying wavelength. All the sinusoidal insets have a peak to peak height of 14 mm. The porosity of the insert is denoted with the Greek symbol ζ and the wavelength of the insert is denoted by the Greek symbol λ in this thesis. The inserts are labelled as shown in Table 3.2. A schematic of the insert cross section is shown Figure 3.7 (b). The value of H is fixed at 14 mm in the figure. Duplicate inserts are fabricated for inserts 2.1 and 2.2 to evaluate the sensitivity of the results on the manufacture methods.

Table 3.2: Insert nomenclature

Insert	Porosity, ζ [%]	Wavelength, λ [mm]
1.1	68	20
1.2	48	20
2.1	68	16
2.2	48	16
3.1	68	12
3.2	48	12

(a)

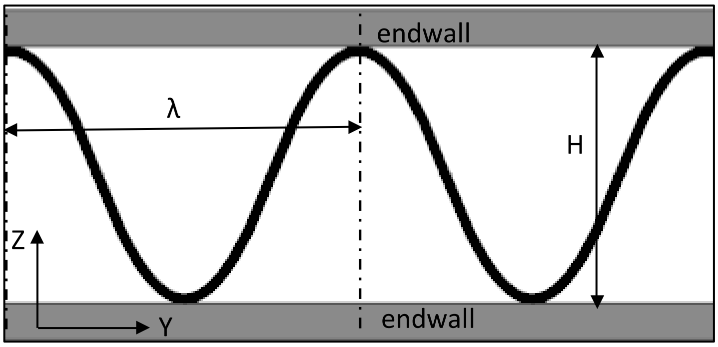

(b)

Figure 3.7: (a) actual insert and (b) schematic of insert sinusoidal waveform in the YZ plane

The inserts are fabricated by pre-forming the sinusoidal shapes of the insert as closely as possible by hand and then forming the inserts to the required profile in a fly press with a custom jig. The jig consists of a top and bottom welded 20 mm plates and sliding angle iron assemblies. The top and bottom assemblies hold ten 10 mm steel plates each which are plasma cut to the upper and lower profiles of the required inserts. The jig is shown in Figure 3.8.

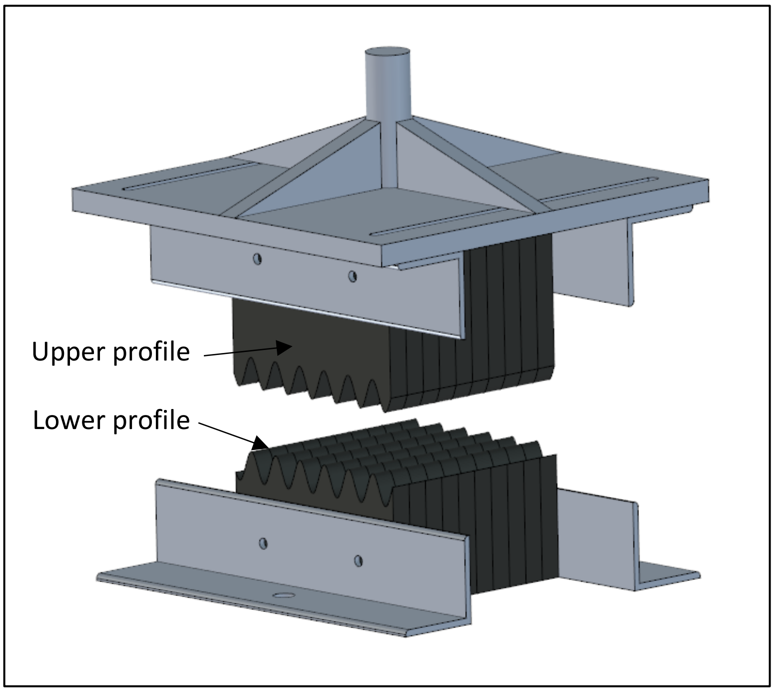

Figure 3.8: Insert forming jig

3.4 Experimental Procedure

The entire length of the channel is set to a height of 14 mm section by section by measuring each corner of the sections with a vernier calliper. Once each section is measured to be at the appropriate height the section modules are tightened in position with bolts and butterfly nuts. The sections are bolted together and sealed on the inside and outside of the joins with silicon sealant. The required insert is placed inside the test section and the channel height is set to 14 mm following the same procedure. The VSD is turned on to power the fan and set to high speed so that the testing apparatus can be inspected for air leaks. Once the apparatus has been cleared from any leakage the test work is started.

For the friction factor measurements, the endwall with the pressure taps is installed in the test section. The appropriate differential pressure transducer is connected to the scanivalve. The ball valves are opened or closed for the required flow rate. The VSD is set to the correct speed for the required pressure drop at the orifice plate to obtain the desired flow rate and Reynolds number. Once the flow thought the test section has reached a steady-state the ambient temperature and pressure in the laboratory are recorded. The steady-state is confirmed when the ΔP across the orifice does not change more than by ±1% over 10 minutes. The scanivalve is used to select the first pressure tap and two pressure readings are recorded. After the output voltages from the differential pressure transducer have been logged the scanivalve is rotated to select the next pressure tap. The stepping of the scanivalve continues until measurements have been recorded at all the pressure taps. The output .txt file is saved to the computer.

The procedures for the pressure measurements are the same for baseline smooth channel (no insert in test section) and with an insert. A new insert is placed in the test section by removing the seals and movable endwall and then replacing the endwall and the seals.

For the heat transfer experiments, the heat transfers endwalls with the heating strips and thermocouples are installed in the test section. The separation between the endwalls is adjusted to account for the thickness of the heaters into the flow area. The insulation material is secured all around the test and outlet sections. The required number of heating stirps are connected to the multi-meters and the power supply depending on whether a one wall or two wall heating boundary condition is required. The multi-meters measuring the voltage and current are connected in parallel and series respectively across the heating strips. The VSD is set to produce the required mass flow rate through the test section in a similar manner to the friction factor measurements.

Power is supplied to the heating strips to produce a temperature difference of 10 - 15 °C between the free flow mean temperature and the heated wall temperatures. The electrical power supplied to the heaters is limited so that the surface temperature does not exceed 60 °C to avoid damage to the experimental apparatus. The test section is allowed to reach a steady-state before measurements are recorded. The test section is deemed to be at a quasi steady-state if the temperature recorded by the thermocouples changes by 0.1 °C or less over a 10 minute interval. Once a steady-state has been reached the ambient pressure and temperature in the laboratory are recorded. The temperatures are recorded via the NiDaq and Ladview^{TM} program for a further 10 minutes. The temperatures at all 80 thermocouples are recorded almost instantaneous by the NiDaq and Labview^{TM} program for the given sampling period. The procedures for the heat transfer measurements are also the same for the baseline smooth channel (no insert in test section) and with an insert.

As the mass flow rate or Reynolds number in the channel is changed, the power input level to the endwall heaters has to be adjusted to maintain a ΔT of 10 - 15 °C between the bulk-mean temperature of air flow and wall temperatures. The average convective heat-flux input to the flow is thus different for different Reynolds numbers employed in the channel. To confirm the convective heat transfer coefficient is independent of the input heat flux, temperature measurements are obtained at different heat flux levels with the insert at a given Reynolds number. The heat transfer coefficients at the endwalls are found to be within ±2% for different heat flux levels at the given Reynolds number [23]. Such variations fall within the uncertainty bounds. The procedure to place or replace an insert into the test section is the same as that for the pressure drop measurements.

3.5 Data Reduction

The calculation of the Fanning friction factor and Nusselt number require certain flow related parameters be calculated beforehand. The Reynolds number in the test section is calculated as:

$$Re = \frac{\dot{m} D_h}{\mu A_c} \quad 3.1$$

The viscosity is interpolated at the bulk average temperature of the channel flow from tables given by [2]. The mass flow rate is determined from the pressure difference recorded across the orifice plate. The mass flow rate is given by [22]:

$$\dot{m} = \frac{C \varepsilon d^2}{\sqrt{(1-\beta^4)}} \sqrt{2 \Delta p \rho} \quad 3.2$$

The values for the discharge coefficient, C and expansion coefficient, ε are calculated by an iterative program developed by [14] taking into account the increased temperature of the fluid during the heat transfer experiments. The quantity β in Eq. 3.2 is the diameter ratio of the orifice hole *d*, to the pipe internal diameter. Δp in Eq. 3.2 is the pressure drop across the orifice plate measured at the 1D and 0.5D pressure taps and ρ is the density of the air at the bulk mean temperature. The flow is considered incompressible as the pressure drop across the test section for all the test conditions is less than 2750 Pa. The expansion coefficient can be estimated as $\varepsilon \approx 1.0$ due to the incompressible flow and the discharge coefficient ranges from *C* = 0.59 to 0.62 for the Reynolds number range tested i.e. $400 < Re < 35000$.

D_h in Eq. 3.1 is the hydraulic diameter of the test section and is calculated by [4]:

$$D_h = \frac{4A_c}{P} \quad 3.3$$

A_c in Eq. 3.1 and Eq. 3.3 is the cross-sectional area of the channel and P is the wetted perimeter.

The mean channel velocity is calculated from the mass flow rate by:

$$\bar{V} = \frac{\dot{m}}{\rho A_c} \quad 3.4$$

The pressure drop along the length of the channel, (p_0-p_x) is calculated from the measured static wall pressures. P_0 is the reference static wall pressure and is taken at first pressure tap near the inlet of the test section. The pressure drop is normalized by the dynamic pressure to obtain the non-dimensional pressure Δp*.

$$\Delta p^* = \frac{p_0 - p_x}{0.5 \rho \bar{V}^2} \quad 3.5$$

The Fanning or skin friction factor is calculated from the pressure drop per meter along the test section in the fully developed flow region, the hydraulic diameter and the test section dynamic pressure by the equation:

$$f = \frac{(\Delta p / \Delta x)(D_h/4)}{0.5 \rho \bar{V}^2} \quad 3.6$$

The pressure drop per meter, ($\Delta p/\Delta x$) in Eq. 3.6 is obtained from the linear slope of $\Delta p = (p_0\text{-}p_x)$ data distribution along the test section length, x. The fully developed flow region with the screen insert is considered at the location where the slope of ($\Delta p/\Delta x$) becomes almost constant.

The bulk mean temperature at any position in the channel can be calculated using the following equation:

$$T_{m,x} = \mathrm{T_{amb}} + \frac{\sum Q_{conv,x}}{\dot{m}C_p} \qquad 3.7$$

T_{amb} in Eq. 3.7 is the inlet temperature of the air measured at the inlet contraction. The specific heat capacity C_p is relatively constant over the temperature range observed at the test section and is interpolated at the bulk mean temperature from the data presented by [2]. $Q_{conv,x}$ is the convective power at the point of consideration along the test section (from x = 0 to x) and is calculated by subtracting the conduction power losses from the power supplied to the heating strips:

$$\sum \dot{Q}_{conv,x} = \sum \dot{Q}_{T,x} - \sum \dot{Q}_{l,x} \qquad 3.8$$

The cumulative total energy supplied up to the point of consideration is calculated using the electrical power equation assuming that the power is distributed uniformly along the length of heater strip and no power losses in the connection wires:

$$\sum \dot{Q}_{T,x} = \frac{x}{L} VI \qquad 3.9$$

L is the length of the test section, V is voltage across the heating strips in volts and I is the current through the heating strips in amps. The heat losses through the insulated sides of the test section is calculated using Fourier's law [2] based on one-dimensional conduction and the temperatures recorded at the thermocouple locations across the insulation layer. As stated in Section 3.2.4.2, five thermocouples are placed on each side of the first layer of insulation. Most of the heater power is assumed to be convected into the flow as the heater is placed on the flow side of the endwall. The conduction heat is assumed to flow normal to the endwall surface due to the small thickness of the endwall. The conduction heat loss rate at each thermocouple position (i=1 to 5) is calculated as:

$$\dot{q}_{l,i} = \frac{k_I\left(T_{p,i} - T_{I,i}\right)}{x_{I,i}} \qquad 3.10$$

In Eq. 3.10, T_p is the temperature of the Perspex endwall plate (insulation side), T_I is the temperature at the interface between the two insulation layers, x_I is the thickness of an insulation layer and k_I is the thermal conductivity of the insulation material. The total conductional losses through the insulation layers of one endwall is then estimated by numerically integrating the linear distribution of $\dot{q}_{l,i}$ vs. x_I:

$$\dot{Q}_{l,x} = \int_0^L \left(\dot{q}_{l,i}\, W\right) dx \qquad 3.11$$

where W is the width of the endwall. The axial conduction losses along the length of the channel are considered to be negligible [14]. The estimation of convection power to the flow in Eq. 3.8 also neglects any radiation losses to the surroundings as the temperature difference between the surroundings of test facility and heated endwall is less than 30 °C.

With the convective power known it is possible to determine the local Nusselt number, Nu_x at each thermocouple position:

$$Nu_x = \frac{\dot{Q}_{conv} D_h}{A_{ht} k_a (T_{w,x} - T_{m,x})} \tag{3.12}$$

In Eq. 3.12, k_a is the thermal conductivity of the air interpolated at the bulk mean temperature from data presented by [2]. $T_{w,x}$ is the temperature at the endwall thermocouple location under consideration. Note, Nu_x in Eq. 3.12 is estimated based on the average convective heat flux, $(\dot{Q}_{conv,x})/A_{ht}$. The average Nusselt number can be calculated as the average of the local Nusselt numbers in the hydrodynamic and thermally fully developed region ($x/L \geq 0.6$):

$$Nu_{avg} = \left[\frac{\sum_i^n Nu_{x,i}}{n}\right] \tag{3.13}$$

The performance index in the channel with the insert is then calculated from the following two equations by considering the ratio of the heat transfer enhancement to the increased pressure drop [5,6] all relative to the smooth channel heat transfer and pressure drop:

$$I_{P1} = \left(\frac{Nu}{Nu_0}\right) / \left(\frac{f}{f_0}\right) \tag{3.14}$$

$$I_{P2} = \left(\frac{Nu}{Nu_0}\right) / \left(\frac{f}{f_0}\right)^{\frac{1}{3}} \tag{3.15}$$

3.6 Conclusion

The experimental setup and test procedures are described in this chapter. The experimental setup consists primarily of a rectangular cross-section wind tunnel and circular ducts connected to a fan controlled by a VSD. The speed of the fan is varied to produce air flow through the test section providing a Reynolds number ranging from 400 < Re < 35 000. The experimental setup is designed so that the height of the rectangular channel can be adjusted. The mass flow rate of air through the test section is measured using orifice plates in the circular ducts. The inlet length before the test section is sufficiently long to allow the flow to become hydrodynamically fully developed before entering the test section. The test section is sufficiently long the allow the flow to become thermally fully developed towards the end of the test section for all test conditions.

The porous sinusoidal inserts are fabricated in-house at the University of Pretoria from common industrial wire-mesh. The manufacturing methods of the inserts allow for a wide variety of sinusoidal waveforms to be fabricated at a minimal cost.

The data reduction shows that the number and positions of the pressure taps and thermocouples provide numerous measurements at key locations in order to gain a comprehensive understanding of the pressure drop and heat transfer characteristic along the test section. All measurements are recorded at steady state conditions. The test section is insulated to minimize thermal losses. The raw data are stored in the laboratory computer for traceability and safekeeping.

4 Validation and Uncertainty

4.1 Introduction

This chapter shows the uncertainties associated with the experimental instrumentation, experimental smooth channel friction factors and Nusselt numbers. The details of uncertainty analysis and sample calculations are shown in Appendix B. This chapter serves to validate the results obtained from the baseline test section by comparing the results obtained for the baseline tests without the addition of inserts against published theoretical and experimental correlations for smooth rectangular ducts. The measured results in the smooth channel are also used as a baseline for comparisons with the results obtained in the test section with the sinusoidal inserts.

4.2 Uncertainty

The uncertainty analyses suggested by [24,25] are conducted to calculate the uncertainties associated with the measured parameters and computed parameters. The uncertainties in the computed parameters are calculated via the propagation of errors technique. The bias errors in the instrumentation are obtained from the manufacturer specifications or from the offset readings when no tests are conducted. The precision errors are calculated by multiplying the standard deviations of the measured data set with the Student's t-variable known from the statistical analysis. The resultant uncertainty in a parameter is calculated as the root square sum of the precision and bias errors. The uncertainties in the instruments used throughout the course of the research are shown in Table 4.1. The accuracy specified in each instrument is accounted as the bias error. Measurements are also repeated multiple times for some test conditions to check for the repeatability of the results. All the repeated test cases show the results fall within the uncertainty bounds of the data.

The uncertainty associated with measured dimensions is shown in Table 4.2 below. The uncertainty in the dimension is determined by the greater of the manufacturing tolerance used to fabricate the part or by the accuracy of the instrument used to measure the dimension.

The uncertainties associated with the friction factor related parameters i.e. the test section pressure drop, mass flow rate, average channel velocity, Reynolds number, Fanning friction factor and friction factor ratio are shown in Figure 4.1 (a). The uncertainties in the friction factor in the laminar regime (up to Re = 2000) range from 7 - 8 %. The high uncertainties in low Re are caused by the measurement uncertainties in the small ΔP in the channel and across the orifice plate. From Re = 3000 onwards the uncertainty in the friction factor remains relatively constant at 5 %. The uncertainty in the Reynolds number is calculated to range from 3 - 4 % for the Reynolds numbers tested. The uncertainty in the pressure data is reduced by subtracting the zero offset of the transducer reading when there is no flow in the channel from the transducer reading during the actual test with air flowing in the channel.

The uncertainties in the two wall and one wall heat transfer related parameters are shown in Figure 4.1 (b) and Figure 4.1 (c), respectively. For the two wall heating case the uncertainty in the local Nusselt number at Re = 400 is approximately 8.3 % and decreases rapidly with the increase in the Reynolds number to reach a steady value of approximately 4.5 % at Re = 7500. For the one wall heating case the local Nusselt number uncertainty remains fairly constant at 4 %.

Table 4.1: Uncertainty in instrumentation

Instrument	Range	Accuracy
Temperature		
T -type Thermocouple	< 260 °C	0.1 °C
NI 9213	-40 °C - 70 °C	0.02 °C
PT 100	10 °C - 70 °C	0.1 °C
Kestrel 4200	-29 °C - 60 °C	0.5 °C
Pressure Transducers		
Setra MicroCal	> 249 Pa	0.12% full scale range
	< 249 Pa	0.1% full scale range
PX2650-05D5V	0 Pa - 124 Pa	2.88 %
PX2650-2D5V	0 Pa < 498 Pa	2.03 %
PX164-005D5V	0 Pa < 1244 Pa	0.95 %
PX164-010D5V	0 Pa < 2488 Pa	0.99 %
Kestrel 4200	30 kPa - 110 kPa	0.1 kPa
Electrical Power		
UNI-T UT33A	0 V - 400V AC	1.2% full scale range
UNI-T UT60A	0 A - 4 A	2.5% full scale range
Orifice Plates		
Discharge Coefficient	< 2000 Re	0.81%
	2000 Re - 10000 Re	1.10%
	> 10000 Re	0.60%
Expansion Coefficient	< 35000 Re	0.40%

Table 4.2: Uncertainty in physical dimensions

Parameter	Dimension	Accuracy	
100 mm ID Pipe	100 mm	0.2 mm	0.20%
57 mm ID Pipe	57 mm	0.2 mm	0.40%
2'' Orifice Plate Diameter	12 mm	0.2 mm	0.40%
4'' Orifice Plate Diameter	51 mm	0.2 mm	1.60%
2'' Orifice Plate Beta Ratio	0.21	0.004	1.70%
4'' Orifice Plate Beta Ratio	0.51	0.002	0.40%
Test Section Width	203.2 mm	0.5 mm	0.10%
Test Section Height	14 mm	0.26 mm	1.86%
Test Section Length	485 mm		
Hydraulic Diameter	26.2 mm	0.46 mm	1.75%
Test Section Cross Sectional Area	2844.8 mm^2	53.8 mm^2	1.89%
Ambient Temperature (typical)	296.4 K	0.51 K	0.17%
Ambient Pressure (typical)	870.24 kPa	0.1 kPa	0.10%
Air Density (typical)	1.02 kg/m^3	0.0013 kg/m^3	0.13%
Heat Transfer Area (Two Wall Heating)	196910 mm^2	632.5 mm^2	0.32%
Heat Transfer Area (One Wall Heating)	98455 mm^2	316.3 mm^2	0.32%

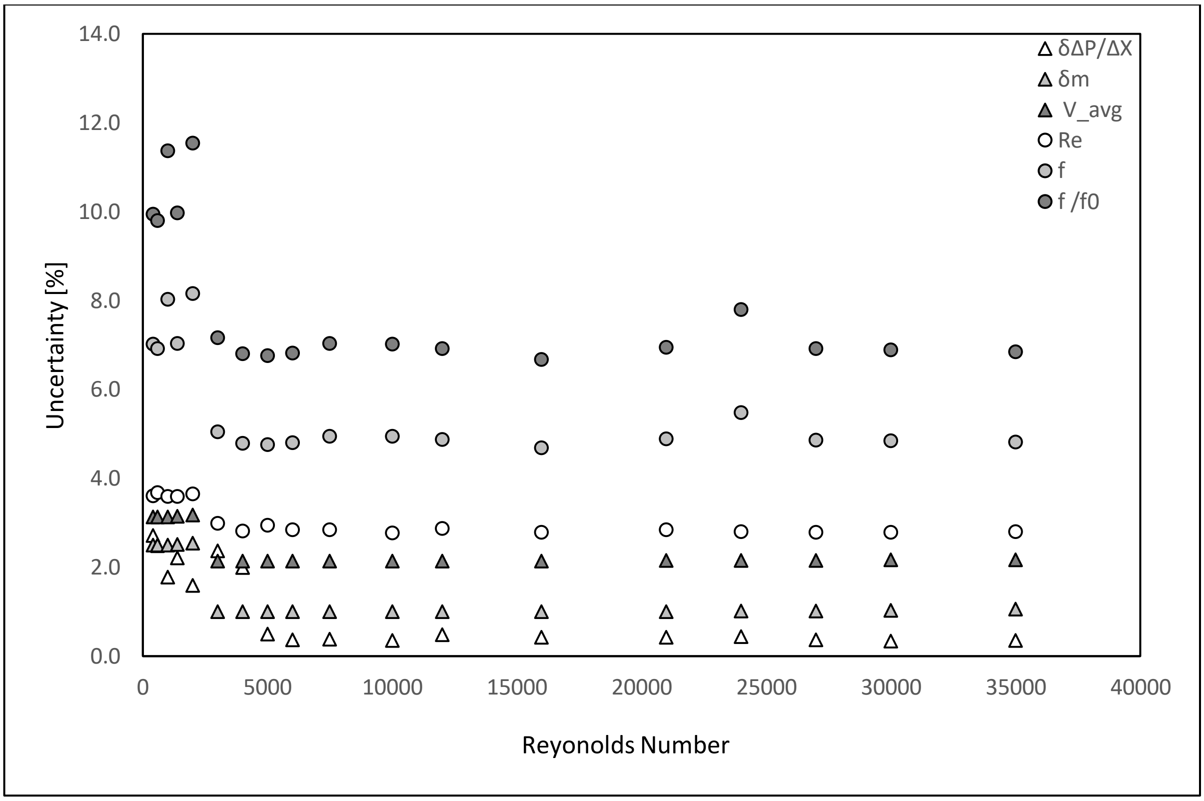
Uncertainty [%]
14.0
12.0
10.0
8.0
6.0
4.0
2.0
0.0
0
5000
10000
15000
20000
25000
30000
35000
40000
Reyonolds Number
δΔP/ΔX
δm
V_avg
Re
f
f /f0

(a)

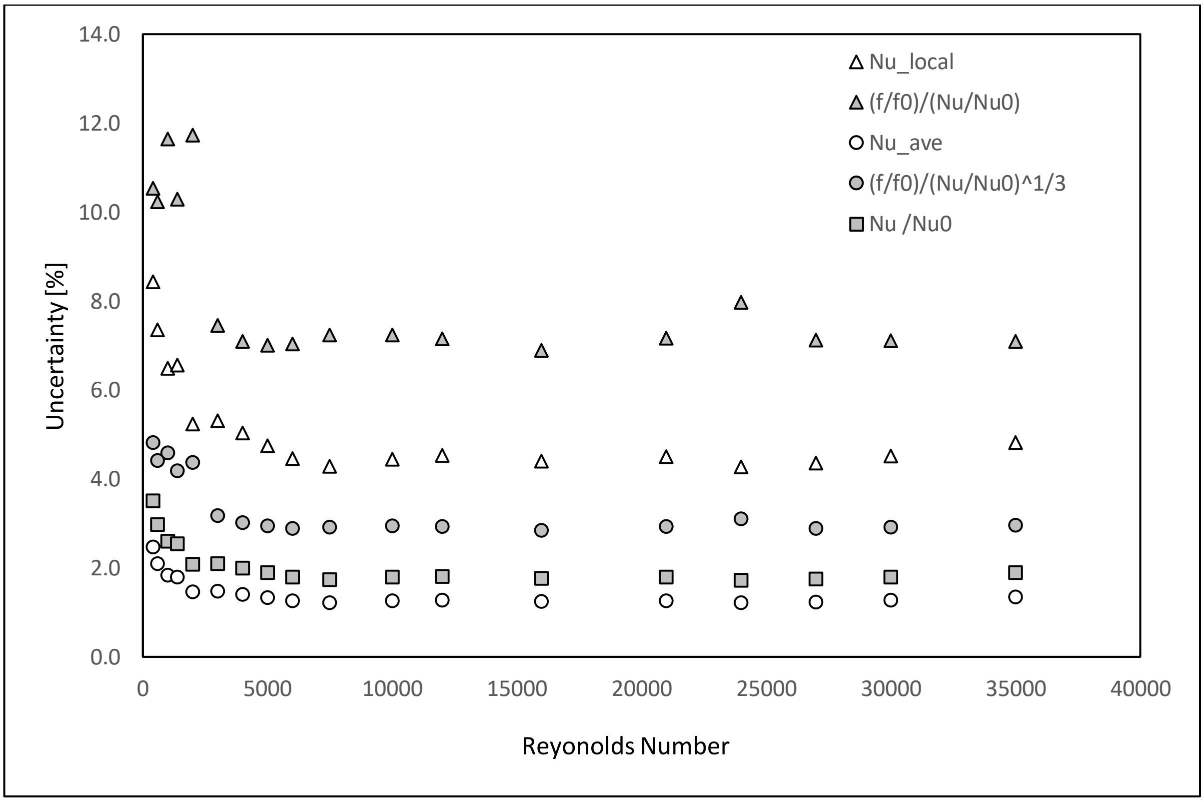
Uncertainty [%]
14.0
12.0
10.0
8.0
6.0
4.0
2.0
0.0
0
5000
10000
15000
20000
25000
30000
35000
40000
Reyonolds Number
Nu_local
(f/f0)/(Nu/Nu0)
Nu_ave
(f/f0)/(Nu/Nu0)^1/3
Nu /Nu0

(b)

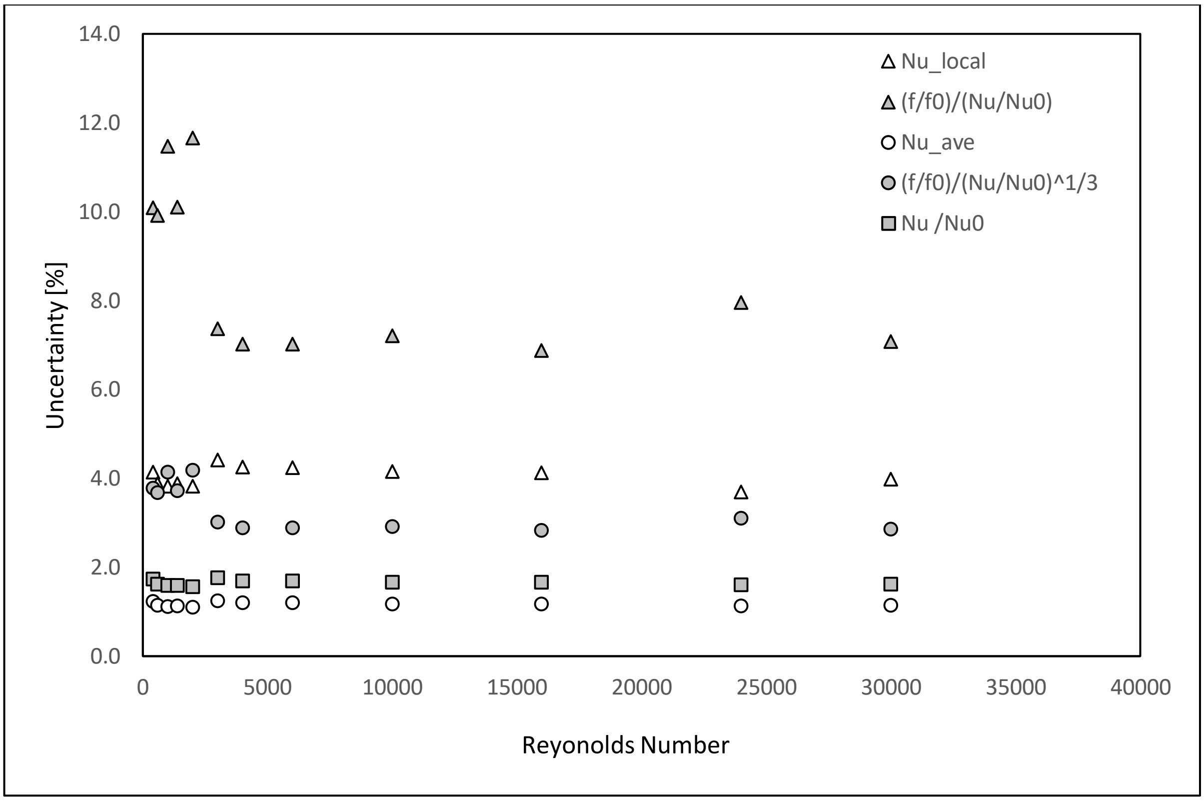

(c)

Figure 4.1: Uncertainty in (a) friction factor, (b) two wall heat transfer and (c) one wall heat transfer related parameters

4.3 Pressure Drop (Baseline Smooth Channel)

The static pressure is measured at 25 points along the test section wall without any insert. The pressure recorded at each pressure tap is shown along with the pressure gradient in Appendix C. The static wall pressure difference is normalized relative to the dynamic pressure by Eq. 3.5. The pressure tap location is normalized relative to the length of the test section as given by Eq. 4.1:

$$x^* = \frac{x}{L} \tag{4.1}$$

Figure 4.2 shows a decreasing normalized Δp* with increasing Reynolds number. Figure 4.2 (a) shows fluctuations in Δp* for Re < 1000. The fluctuations occur as the flow pulsates due the VSD's inability to maintain low rotational speed of the fan. The low air flow rate and flow speed in the channel at low Re is very sensitive to the fan rotational speed. Figure 4.2 (b) shows fluctuations in Δp* for 3000 < Re < 6000. The fluctuations occur as the flow pulsates and turbulent "slugs" propagate through the channel which is typical of transitional flow [26]. The gradients of the normalized Δp* distributions along x* are fairly constant for the Reynolds number range 7500 < Re < 35000.

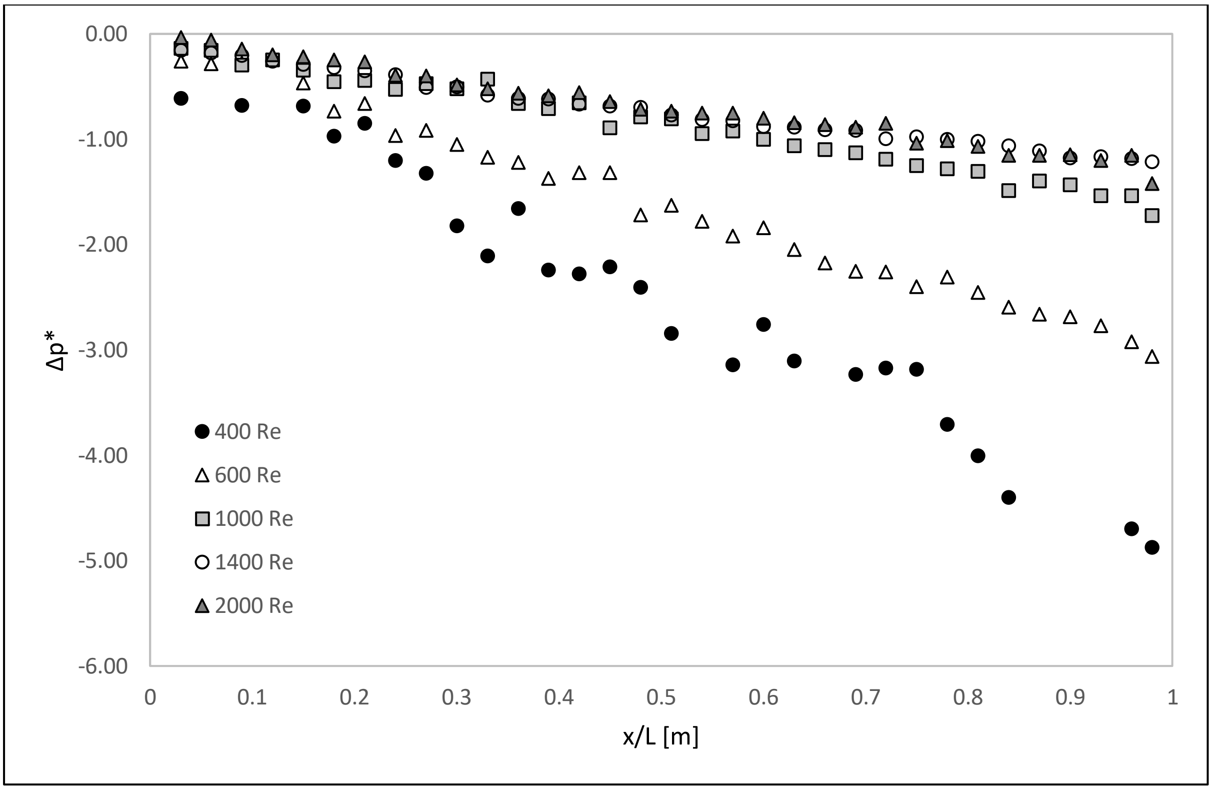
0.00
-1.00
-2.00
-3.00
-4.00
-5.00
-6.00
Δp*
0
0.1
0.2
0.3
0.4
0.5
0.6
0.7
0.8
0.9
1
x/L [m]
● 400 Re
△ 600 Re
▨ 1000 Re
○ 1400 Re
▲ 2000 Re

(a)

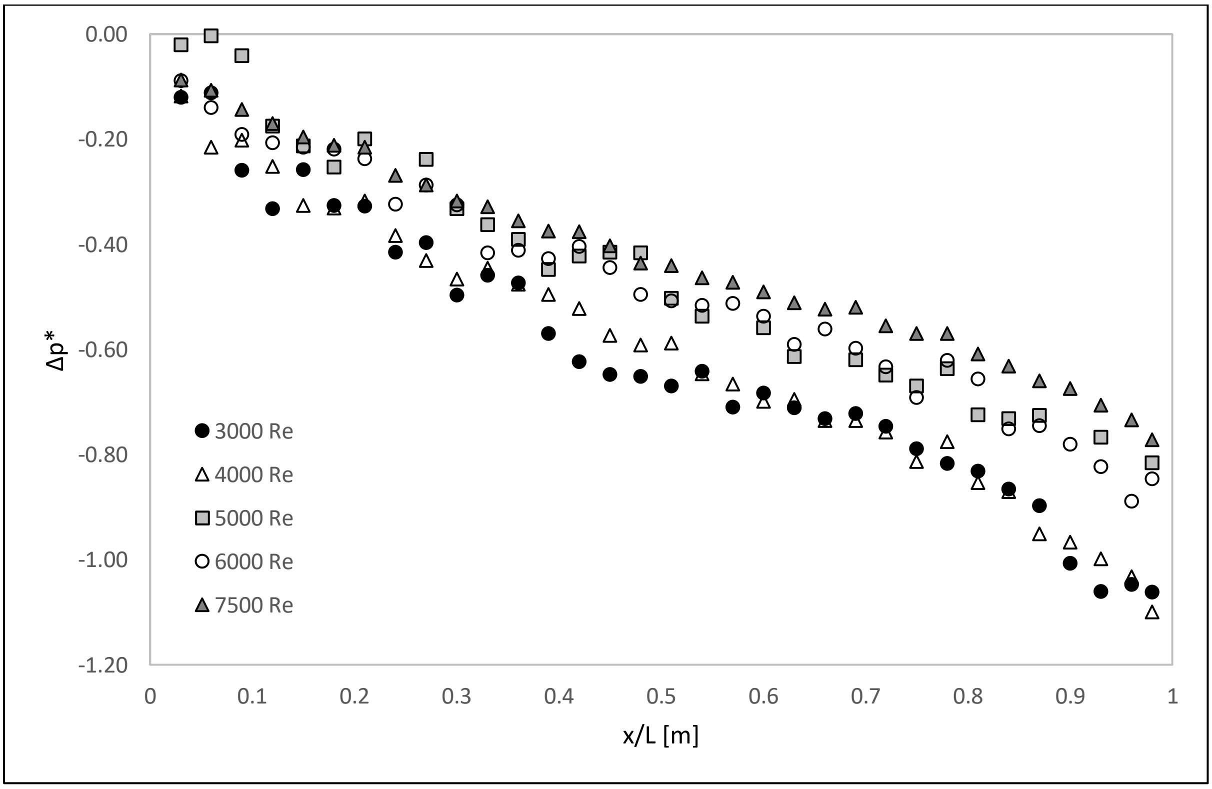
0.00
-0.20
-0.40
-0.60
-0.80
-1.00
-1.20
Δp*
0
0.1
0.2
0.3
0.4
0.5
0.6
0.7
0.8
0.9
1
x/L [m]
● 3000 Re
△ 4000 Re
▨ 5000 Re
○ 6000 Re
▲ 7500 Re

(b)

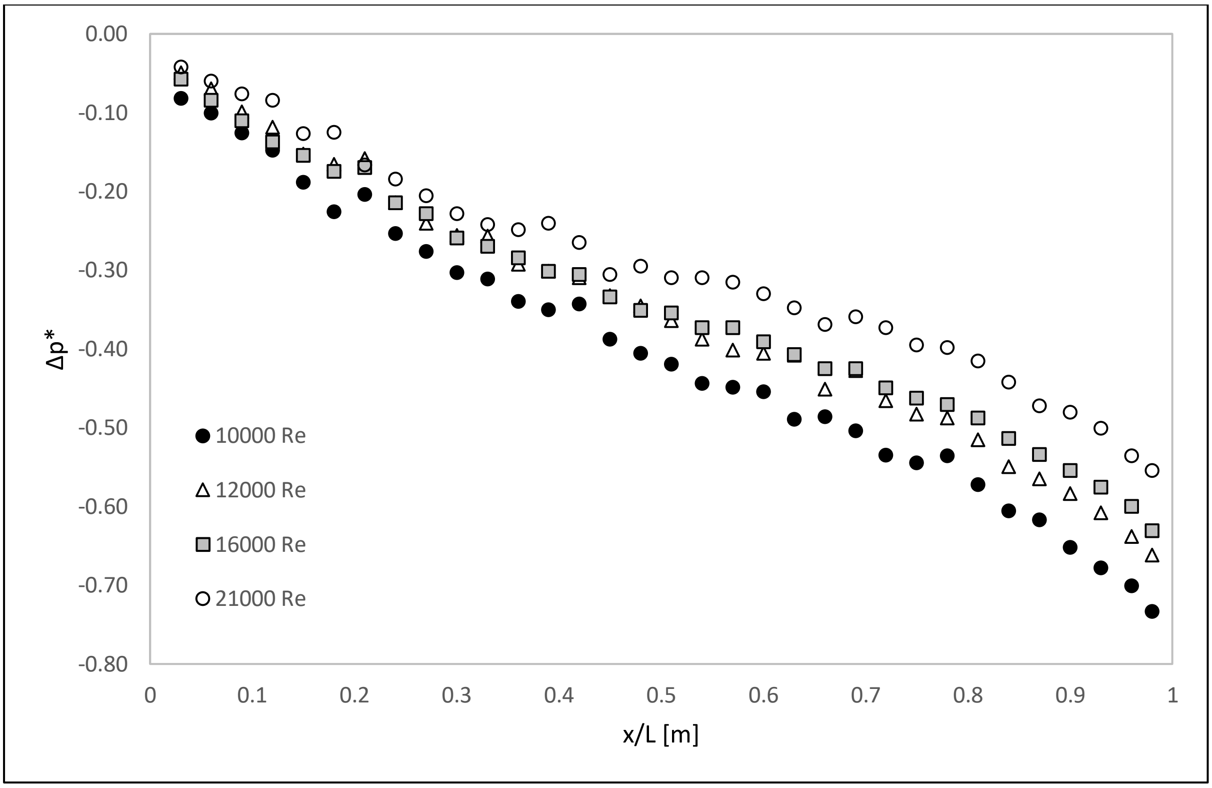

(c)

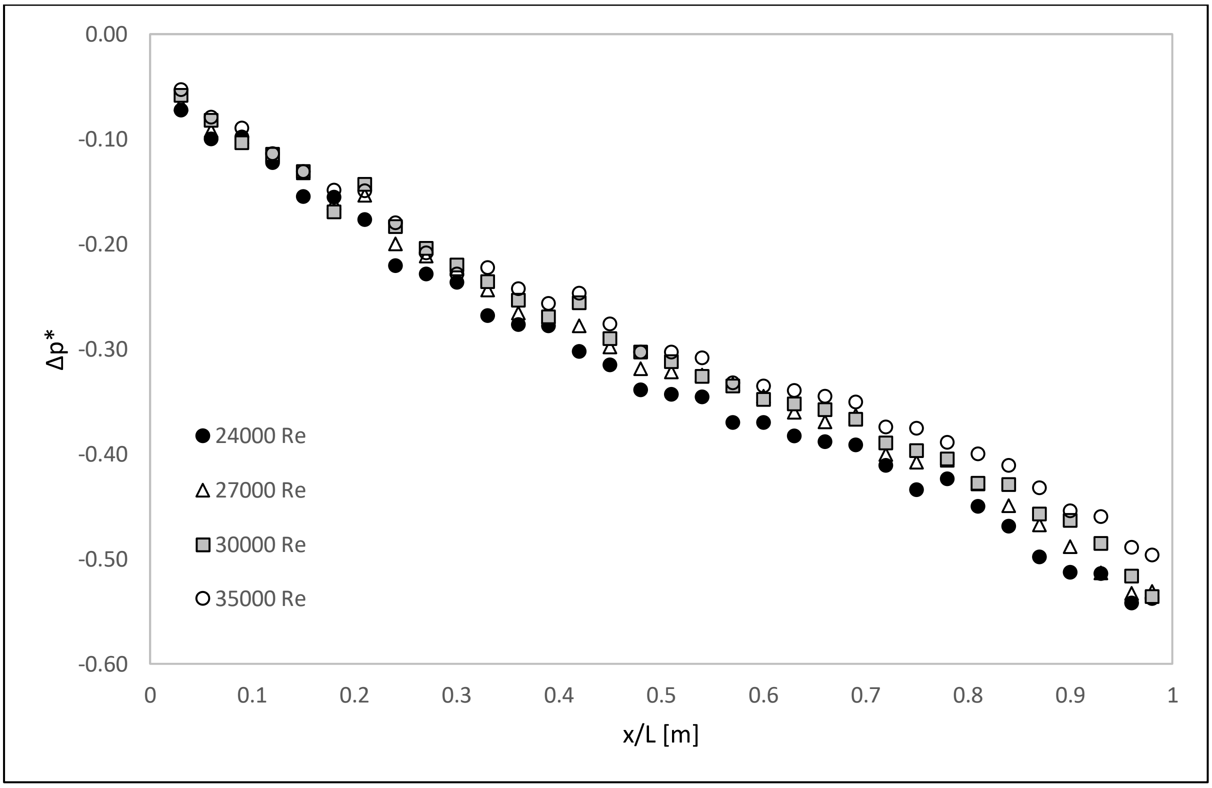

(d)

Figure 4.2: Normalized baseline pressure for (a) 400 < Re < 2000, (b) 3000 < Re < 7500, (c) 10000 < Re < 21000 and (d) 24000 < Re < 35000

4.4 Friction Factor

Figure 4.3 below shows the experimental baseline Fanning friction factors plotted against the Reynolds number as well as calculated uncertainty bars in the friction factor values. In the laminar regime (Re < 2000) the experimental data are compared with Eq. 2.13 of [7]. Over the range 400 < Re < 2000 the experimental data is calculated to deviate from Eq. 2.13 by a maximum value of 3.9 %.

In the transitional regime (2000 < Re < 10000) published experimental and theoretical correlations could not be obtained. In the turbulent regime (Re > 10000) the experimental friction factor is compared to Eq. 2.18 of Karman and Nikuradse. Over the 10000 < Re < 35000 the experimental data are calculated to deviate from Eq. 2.18 by a maximum value of 5.7 %.

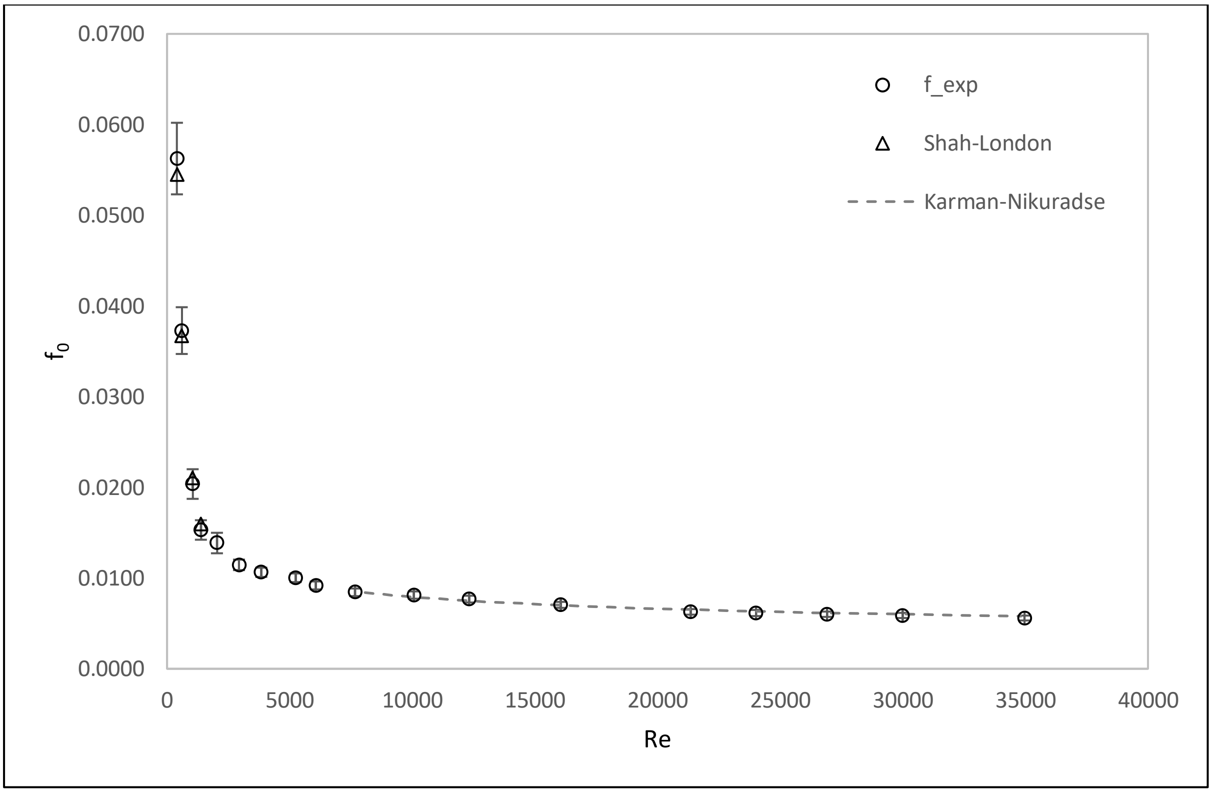

Figure 4.3: Baseline experimental and theoretical Fanning friction factors

4.5 Nusselt Numbers - Two Wall Heat Transfer

4.5.1 Local Nusselt Numbers

The experimental local Nusselt numbers for the two wall heating boundary condition are shown in Figure 4.4. As the entry length section is unheated the x/L = 0 of the test section marks the start of the thermal boundary condition. The local Nusselt number is observed to decrease as x/L increases as the temperature profile develops in the test section until an almost steady value is reached towards the end of the test section where the temperature profile is assumed to be fully developed. The local Nu_0 value in the fully developed region at any given Re in Figure 4.4 (a) to (d) changes by 7% at a maximum. The thermal developing length where the Nu_0 varies significantly is observed to decrease with the increase in Reynolds number. For 400 < Re < 2000 (Figure 4.4 (a)) the local Nusselt numbers reach a steady value at approximately x/L = 0.6. For 3000 < Re < 7500 (Figure 4.4 (b)) the local Nusselt numbers reach a steady value at approximately x/L = 0.44. For 10000 < Re < 21000 (Figure 4.4 (c)) the local Nusselt numbers reach a steady value at approximately x/L = 0.28. For 24000 < Re <35000 (Figure 4.4 (d)) the local Nusselt numbers reach a steady value at approximately x/L = 0.44. For 0.6 < x/L < 1 and the flow is said to be thermally fully developed.

At the last thermal couple location, x/L = 0.96 the Nusselt numbers in some of the experiments is measured to be higher than those in the neighbouring upstream measurement points. This irregularity can be attributed to the separation of heater from the endwall because of the high temperature.

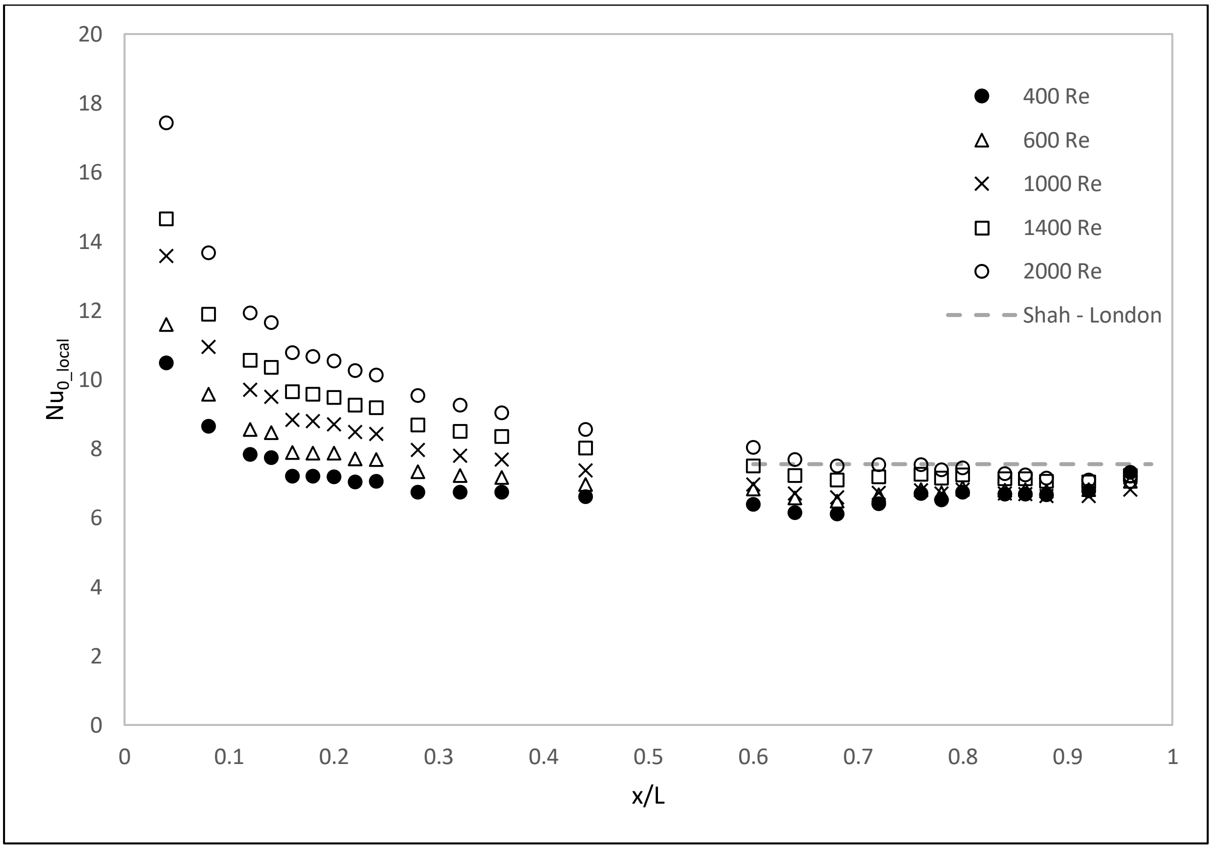

(a)

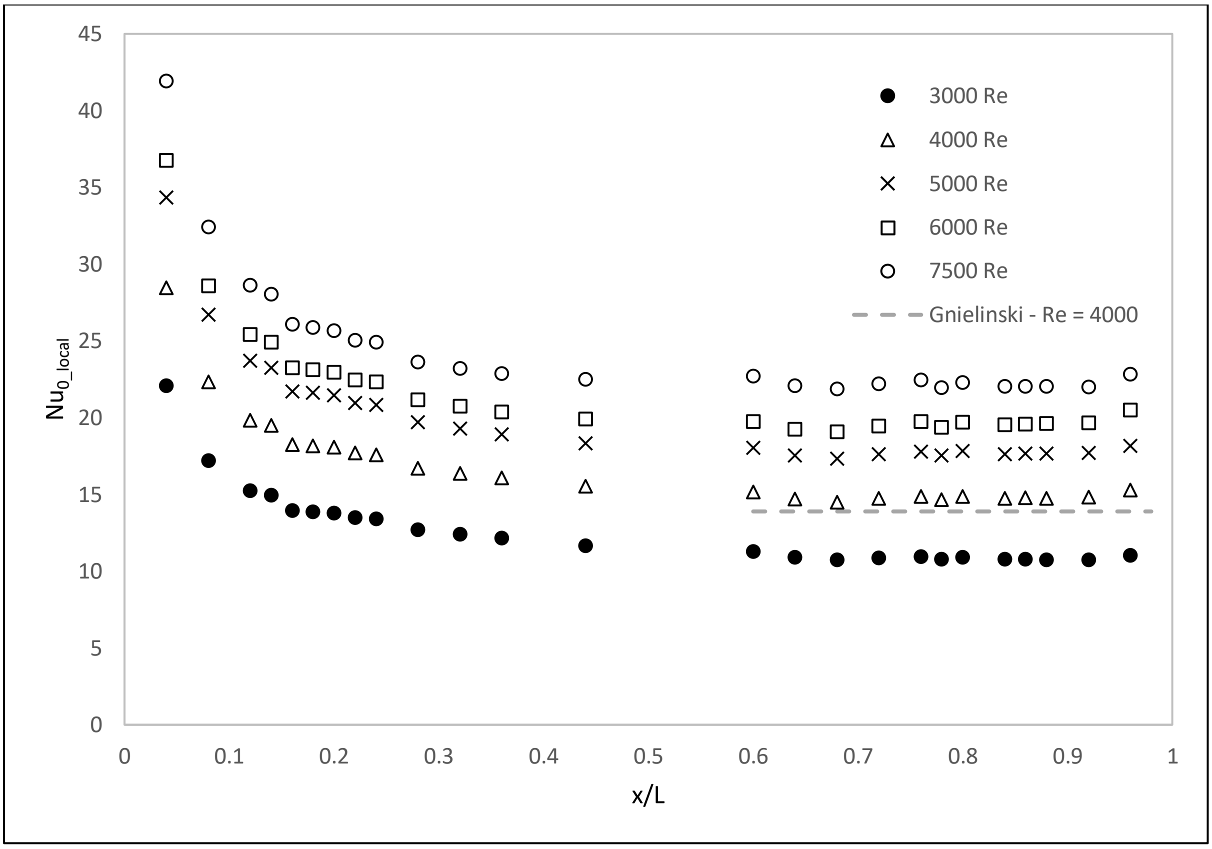
Nu_{0_local}
x/L
0
5
10
15
20
25
30
35
40
45
0
0.1
0.2
0.3
0.4
0.5
0.6
0.7
0.8
0.9
1
● 3000 Re
Δ 4000 Re
× 5000 Re
□ 6000 Re
○ 7500 Re
Gnielinski - Re = 4000

(b)

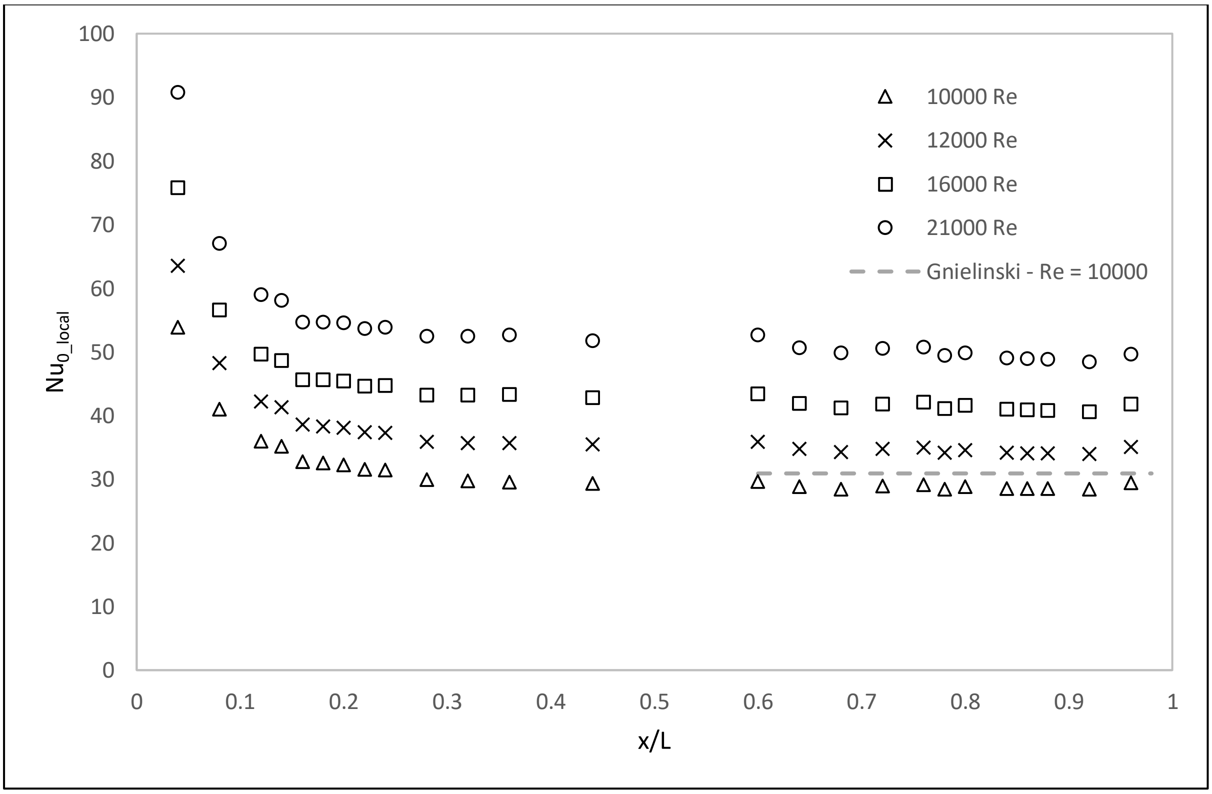
Nu_{0_local}
x/L
0
10
20
30
40
50
60
70
80
90
100
0
0.1
0.2
0.3
0.4
0.5
0.6
0.7
0.8
0.9
1
Δ 10000 Re
× 12000 Re
□ 16000 Re
○ 21000 Re
Gnielinski - Re = 10000

(c)

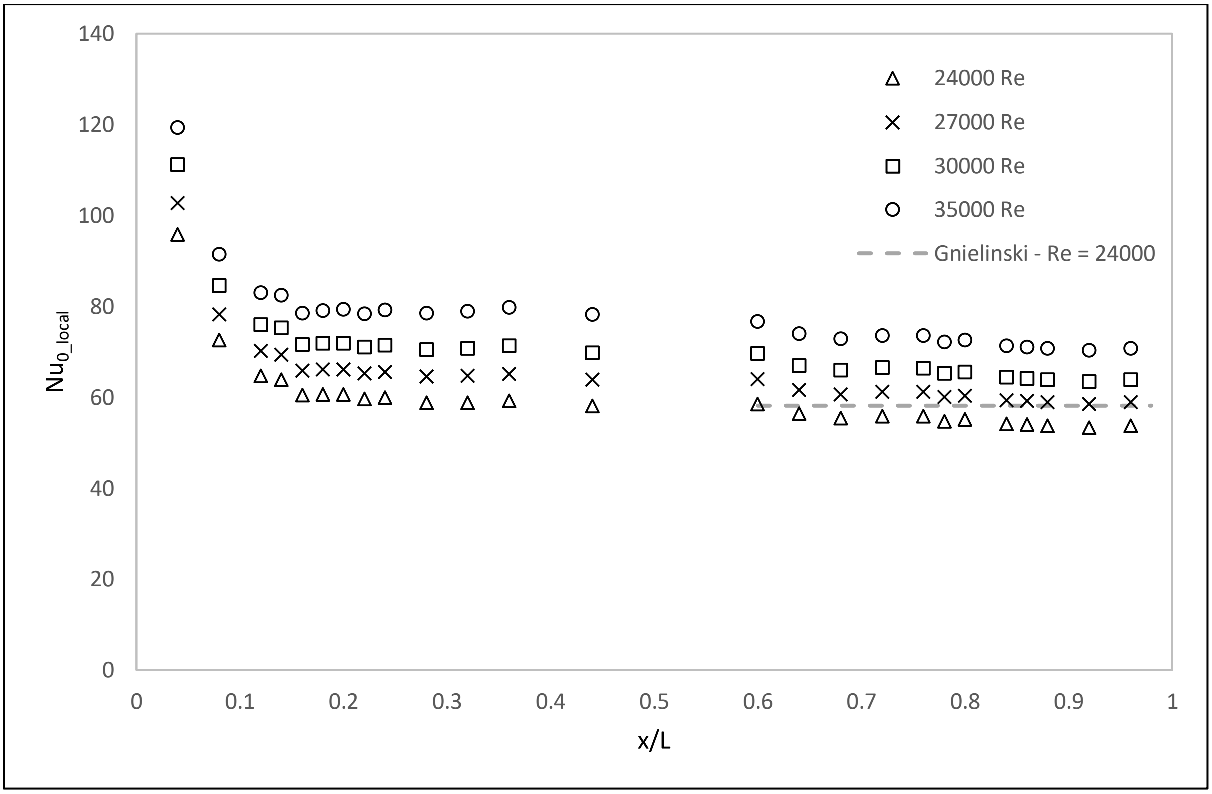

(d)

Figure 4.4: Two wall heating baseline local Nusselt numbers for (a) 400 < Re < 2000, (b) 3000 < Re < 7500, (c) 10000 < Re < 21000 and (d) 24000 < Re < 35000

4.5.2 Average Nusselt Numbers

The local Nusselt numbers, Nu_{0_local} between 0.6 < x/L < 0.92 at a Reynolds number presented in Section 4.5.1 are arithmetically averaged to produce the average Nusselt number, Nu_{0_avg} and are shown in Figure 4.5. The average Nusselt number between 400 < Re < 2000 is observed to remain almost constant at approximately 6.5 in Figure 4.5(a). From Re = 3000 the average Nusselt number increases with the Reynolds number to reach a maximum value of 73.5 at Re = 35123 suggesting that the flow has transitioned out of the laminar regime for Re > 2000.

In the laminar flow regime the experimental result in Figure 4.5 (a) is compared with Eq. 2.13 of Shah and London [7] for a rectangular channel with the same boundary conditions. The experimental Nusselt number is calculated to deviate from the analytical data of Shah and London [7] by a maximum value of 9 % at Re = 400. In the turbulent flow regime (Re ≥ 10000) the experimental data are compared with Eq. 2.20 of Gnielinski [2]. The equation presented by Gnielinski [2] is derived for constant peripheral heat flux applied to a circular tube. A comparison between the analytical data of Gnielinski [2] and the experimental results can still be drawn as 94% of the test section perimeter is uniformly heated for the two wall heating boundary condition experiments. The experimental average Nusselt number is calculated to deviate for the analytical data of Gnielinski [2] by a maximum value of 10 % at Re = 10000

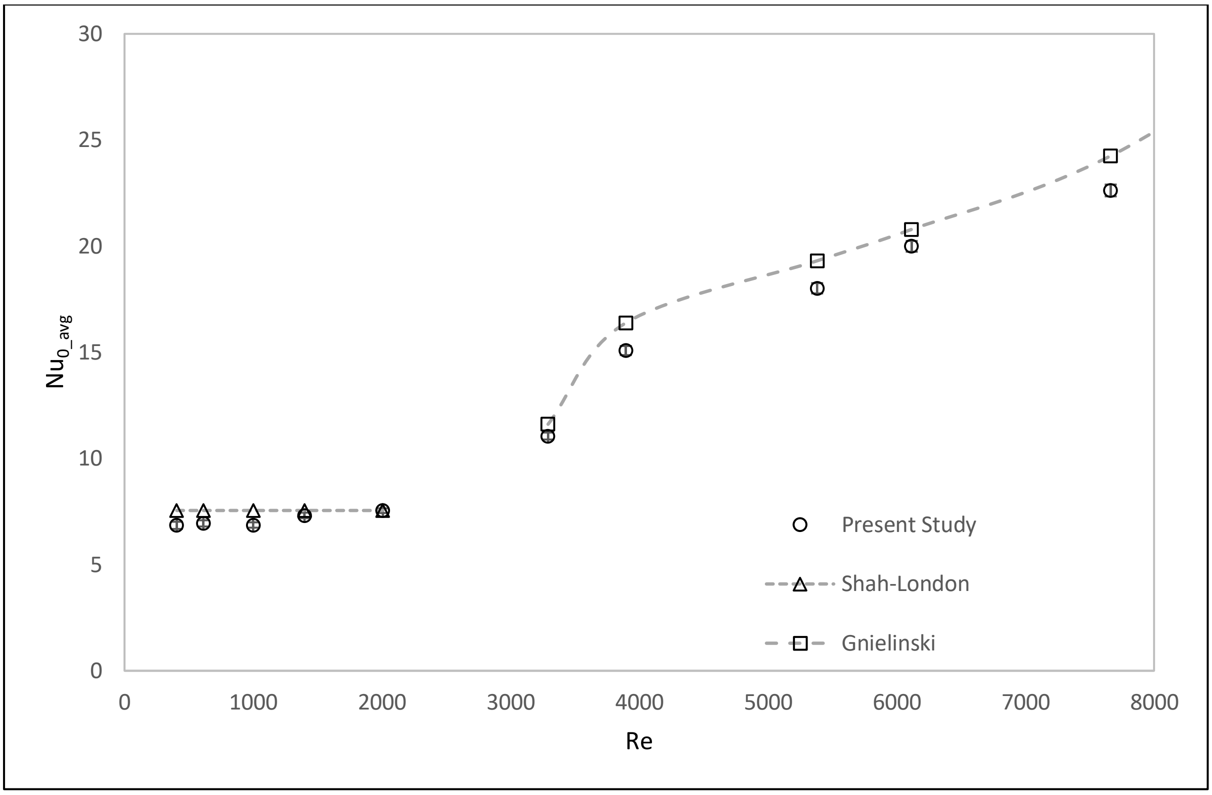

(a)

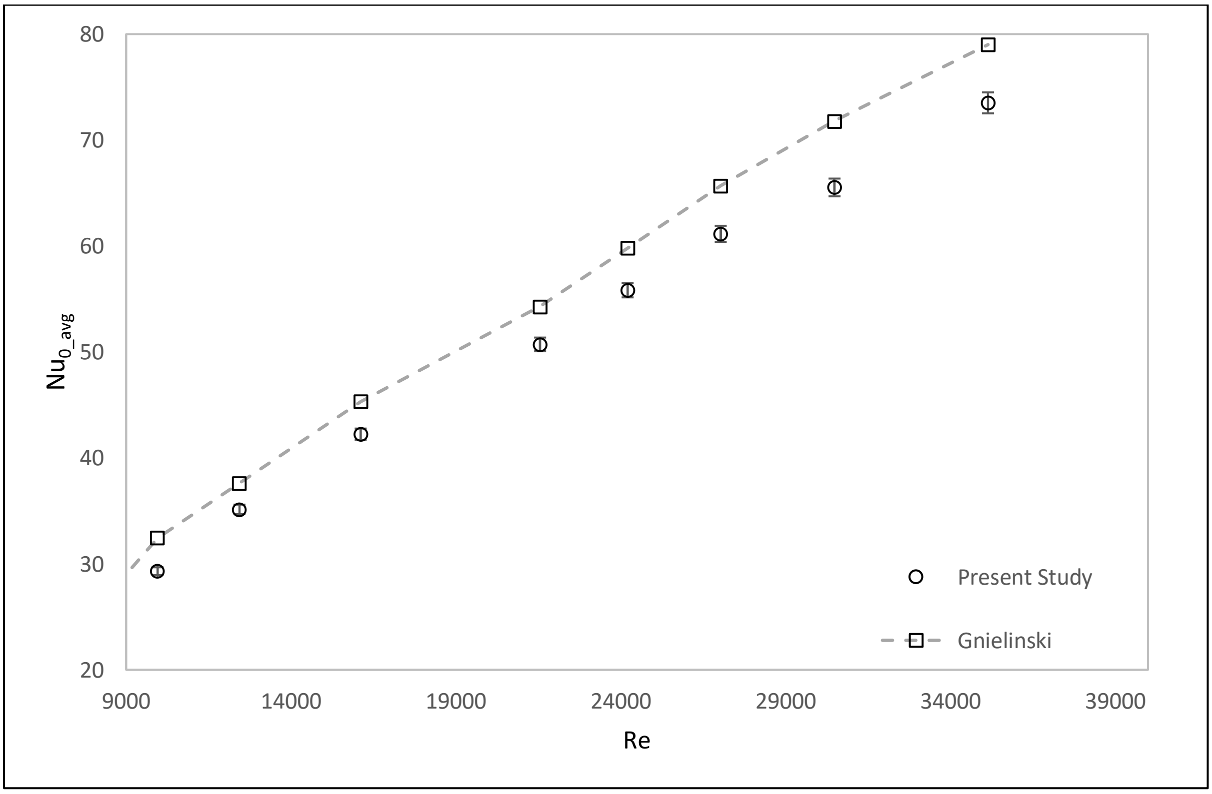

(b)

Figure 4.5: Two wall heating average Nusselt numbers for (a) 400 < Re < 7500 and (b) 10000 < Re < 35000

4.6 Nusselt Numbers - One Wall Heat Transfer

4.6.1 Local Nusselt Numbers

The experimental local Nusselt numbers, Nu_{0_local} for the one wall heating boundary condition are shown in Figure 4.6. Similar to the two wall heating boundary condition, the local Nusselt number is observed to decrease as x/L increases along test section up to the point where the temperature profile becomes fully thermally developed. The Nu_{0_local} values reach a steady value at x/L for any Re in Figure 4.6 (a) and (b) in the fully thermally developed region which is identified by a Nu_{0_local} variation of less than 5 % along x/L. The thermal developing length is observed to decrease with the increase in Reynolds number. For 400 < Re < 2000 (Figure 4.6 (a)) the local Nusselt numbers reach a steady value at approximately x/L = 0.6. For 3000 < Re < 30000 (Figure 4.6 (b)) the local Nusselt numbers reach a steady value at approximately x/L = 0.44. For 0.6 < x/L < 1 and the flow is said to be thermally fully developed.

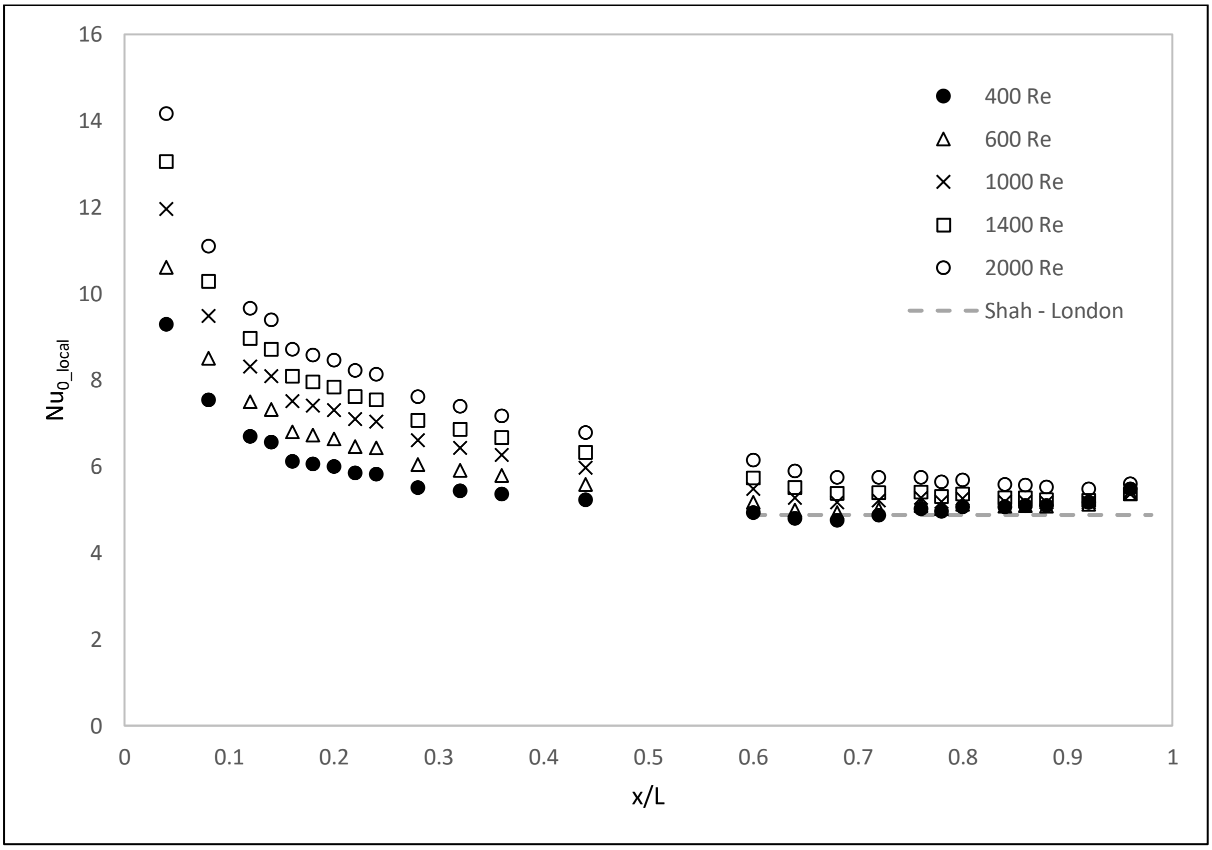

(a)

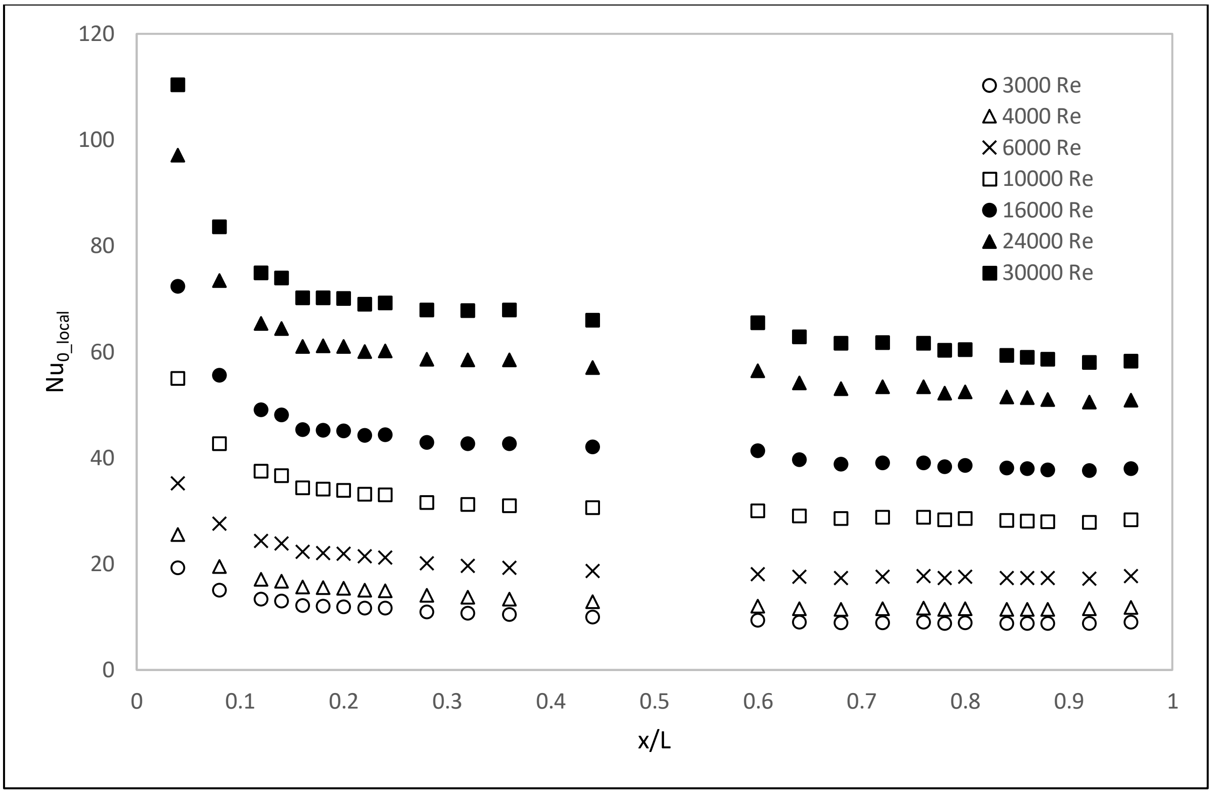

(b)

Figure 4.6: One wall heating baseline local Nusselt numbers for (a) 400 < Re < 2000 and (b) 3000 < Re < 30000

4.6.2 Average Nusselt Numbers

The local Nusselt numbers, Nu_{0_local} between 0.6 < x/L < 0.92 presented in Section 4.6.1 are arithmetically averaged to produce the average Nusselt numbers, Nu_{0_avg} shown in Figure 4.7. The average Nusselt numbers between 400 < Re < 2000 are observed to remain relatively constant at approximately 5.2 in Figure 4.7 (a). From Re = 3000 the Nu_{0_ave} increases with the Reynolds number to reach a maximum value of 61.3 at Re = 30112.

In the laminar flow regime (Re ≤ 2000) in Figure 4.7 (a), experimental results are compared with Eq. 2.13 of Shah and London [7] for a rectangular channel with the same boundary conditions. The experimental Nusselt number is calculated to deviate from the analytical data of Shah and London [7] by a maximum value of 10 % at Re = 1400. In the turbulent flow regime (Re ≥ 10000), the experimental data are compared with tabulated data of Kays and Crawford [4]. The equation presented by Kays and Crawford [4] is derived for parallel plate with one wall heated and the other wall insulated. The experimental average Nusselt numbers is calculated to deviate from the analytical data of Kays and Crawford [4] by a maximum value of 7 % at Re = 16000.

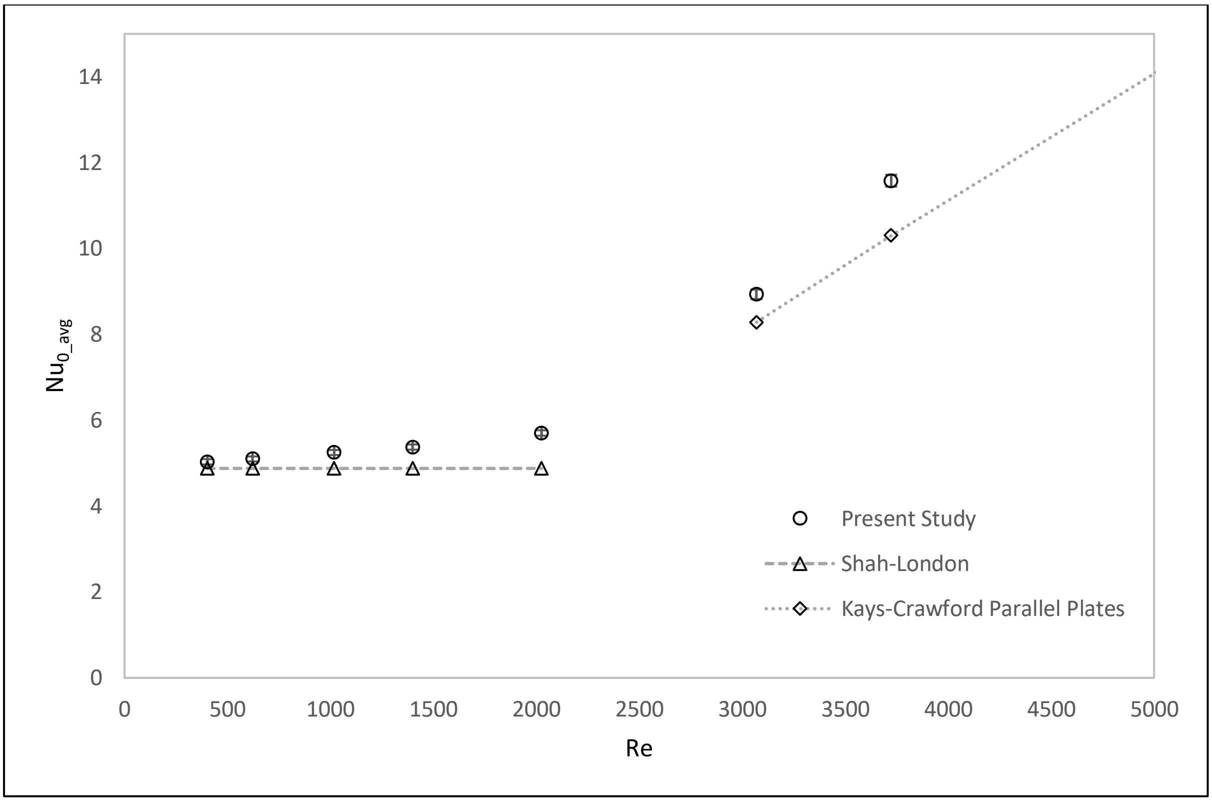

(a)

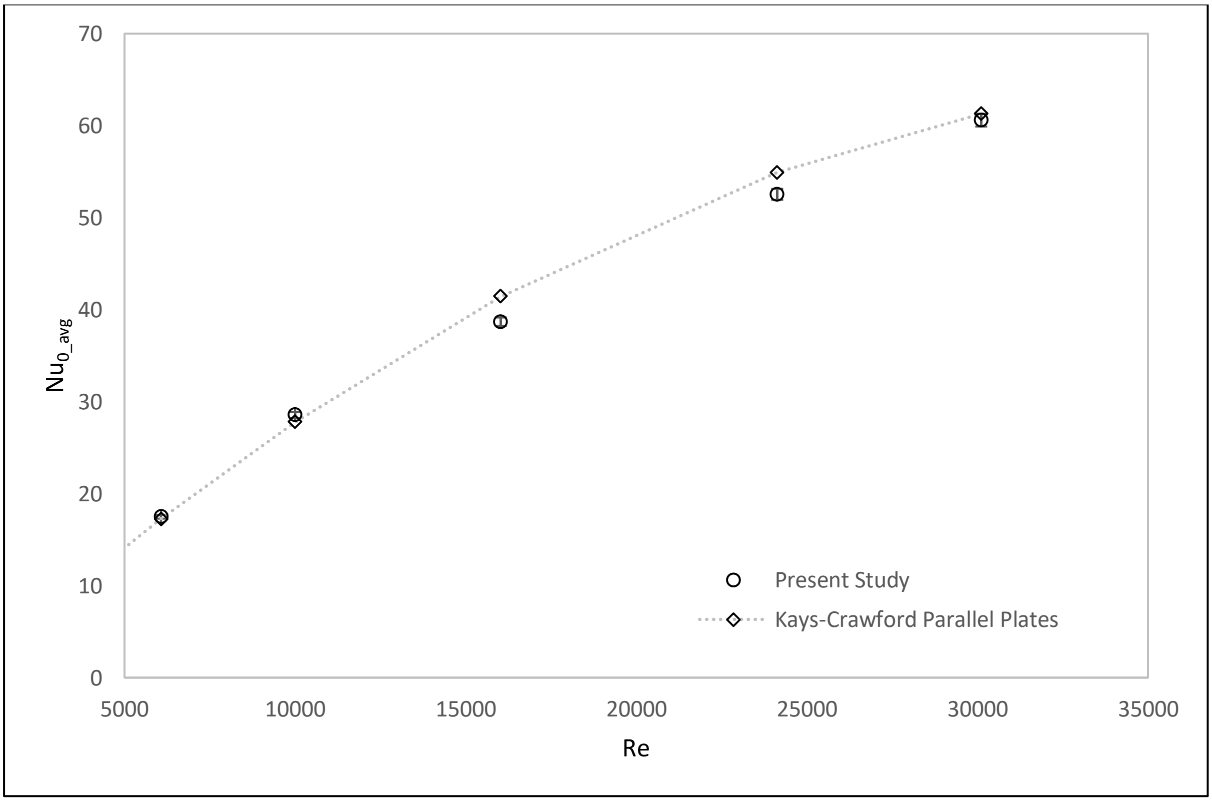

(b)

Figure 4.7: One wall heating average Nusselt numbers for (a) 400 < Re < 4000 and (b) 6000 < Re < 30000

4.7 Repeatability of Results

To evaluate the quality and the effects of small defects and imperfections in the inserts produced by the manufacturing methods, duplicate inserts with a wavelength of 16 mm are manufactured. The duplicate inserts are manufactured and tested under the identical conditions as their counterparts. The friction factors, f obtained for the duplicate set of inserts with ζ = 68 % are shown in Figure 4.8 (a) while that for the set of inserts with ζ = 48 % are shown in Figure 4.8 (b). The comparisons between the primary insert and duplicate insert are presented at Re = 400, 1000, 5000, 7500, 12000, 24000 and 35000.

The friction factors, f obtained for the duplicate sets of inserts with ζ = 68 % differ by 5 % or less. For inserts with ζ = 48 % the friction factors, f differs by 2 % or less with the exception of the result obtained at Re = 3000 where the friction factor differs by 6 %. From the friction factor results in Figure 4.8 (a) and (b), it can be seen that the change or sensitivity in the friction factors due to the skewness, undulations or imperfections resulting from the manufacturing of the inserts are minimal and can be ignored.

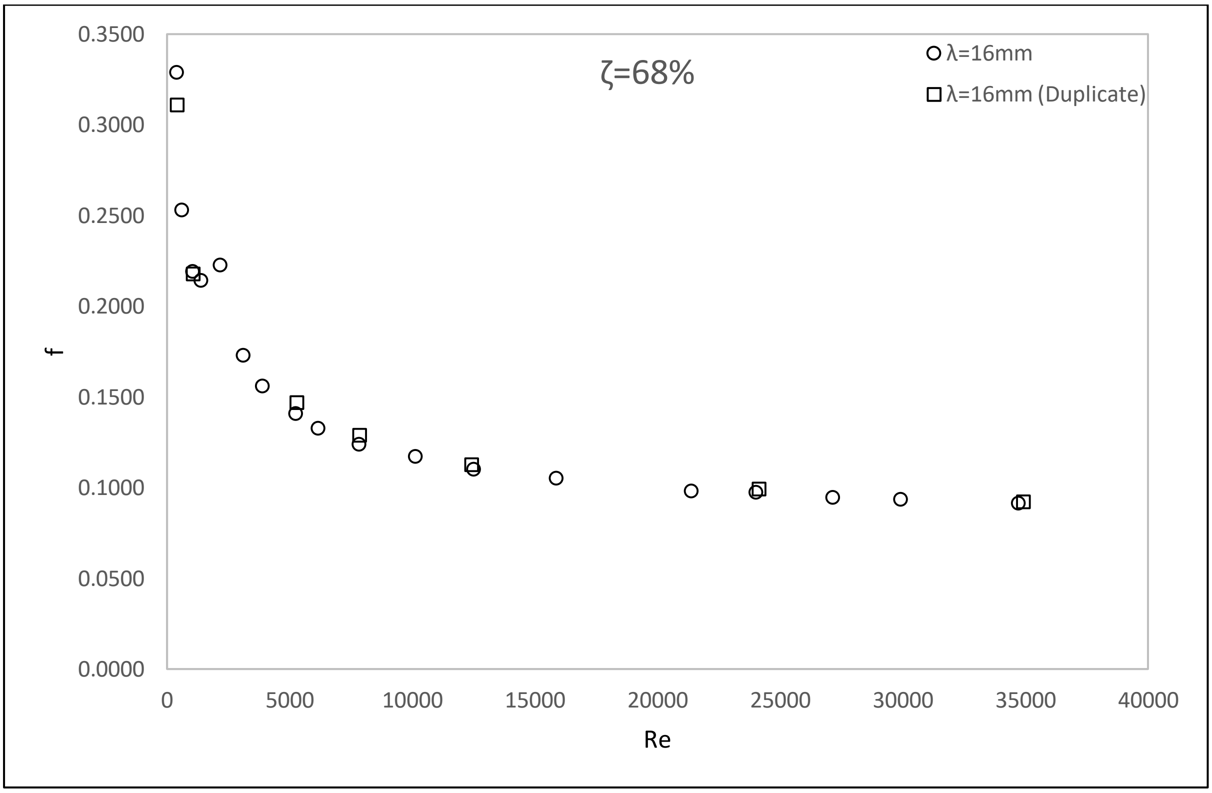

(a)

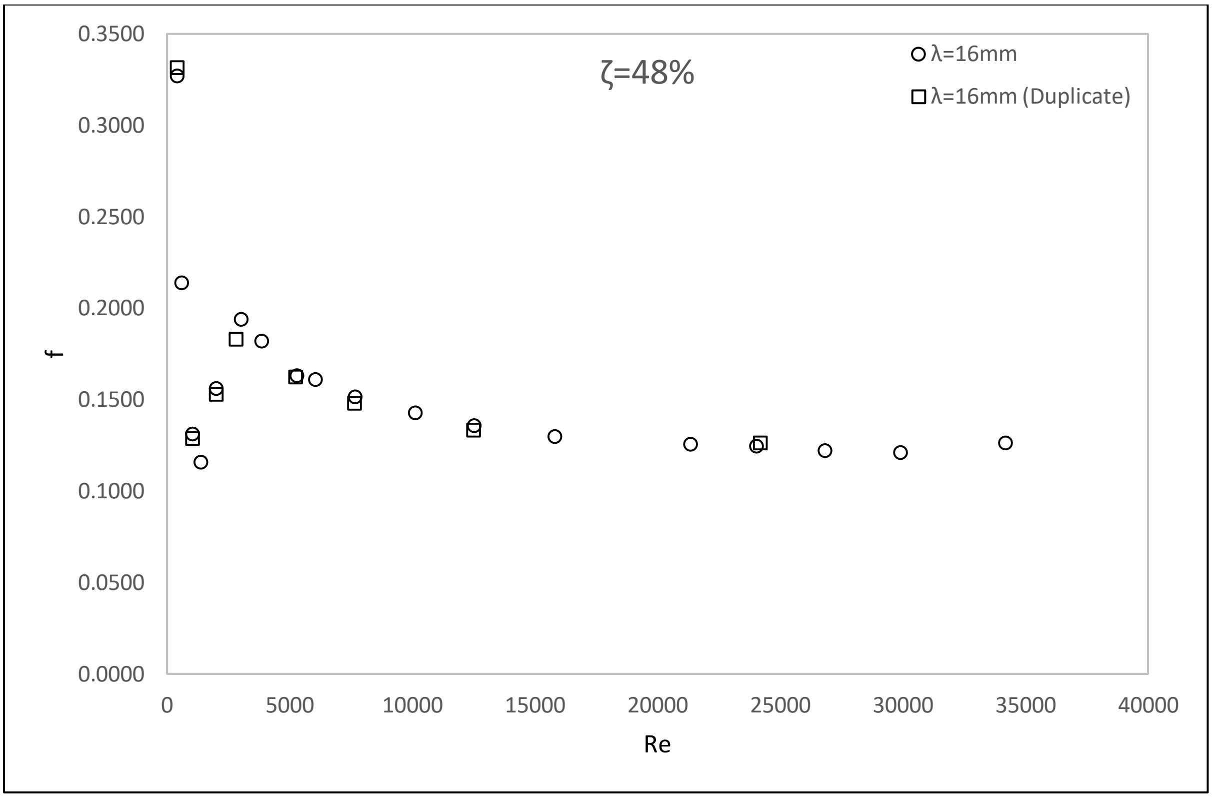

(b)

Figure 4.8: Influence of insert manufacture on fiction factor for (a) 68 % porosity and (b) 48 % porosity

The repeatability of the Nusselt numbers obtained for the one wall and two wall heating boundary condition is evaluated using the primary insert 2.1 with a wavelength of 16 mm and a porosity of 68%. The aim of repeating the experiments under the same flow rates and heat flux is to determine if the results obtained from the test section are accurate and true.

The average Nusselt numbers obtained from two sets of independent tests are shown in Figure 4.9 (a) and (b) for a two wall and one wall heat transfer boundary condition, respectively. The repeated tests are compared at Re = 400, 600, 1000, 1400 2000, 3000, 4000, 6000, 10000, 16000, 24000 and 30000. The average Nusselt number, Nu_{avg} with the two wall heating boundary condition differ by 6 % or less while that of the one wall heating boundary condition differ by 9 % or less for the repeated cases which is within the uncertainty bounds of the experiments. The change in the local Nusselt number with varying heat flux for both the two wall heating and one wall heating boundary condition are analysed by Cramer [23] at the same research station. The results obtained in [23] show that the experimental Nusselt number result is not sensitive to the applied heat flux.

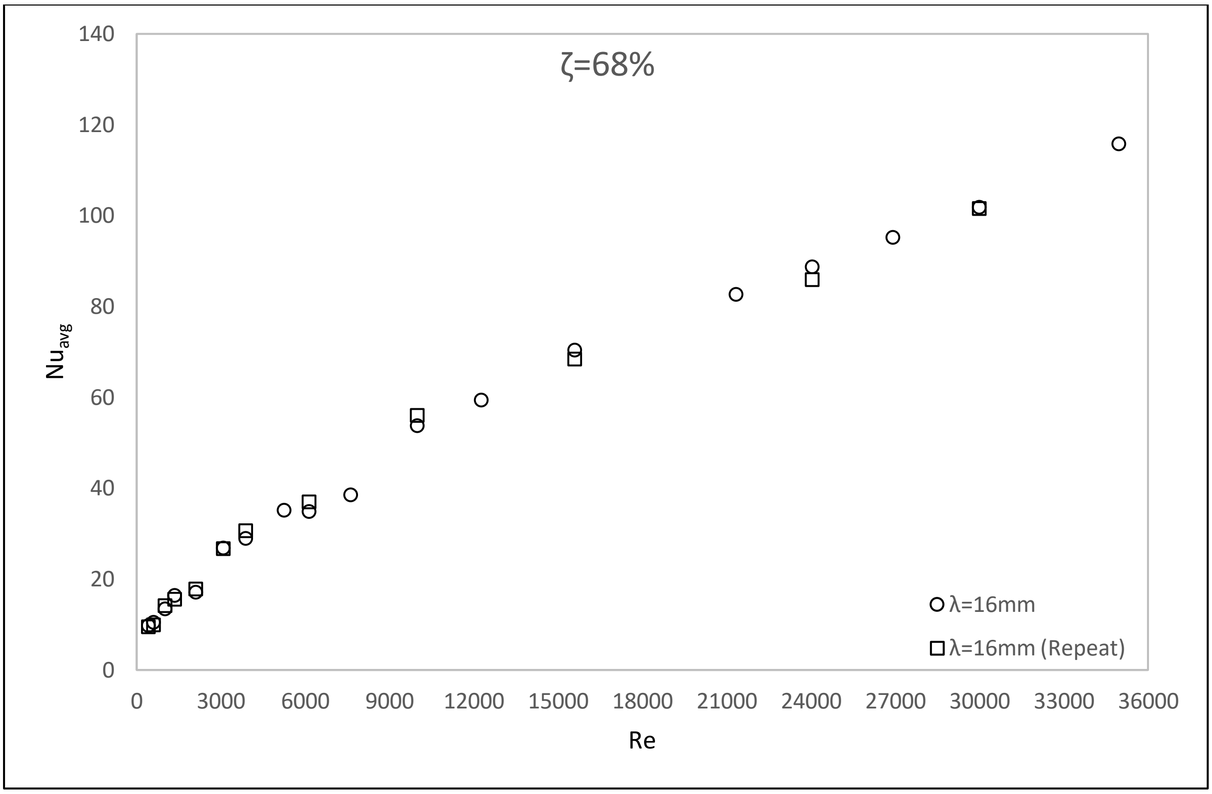

(a)

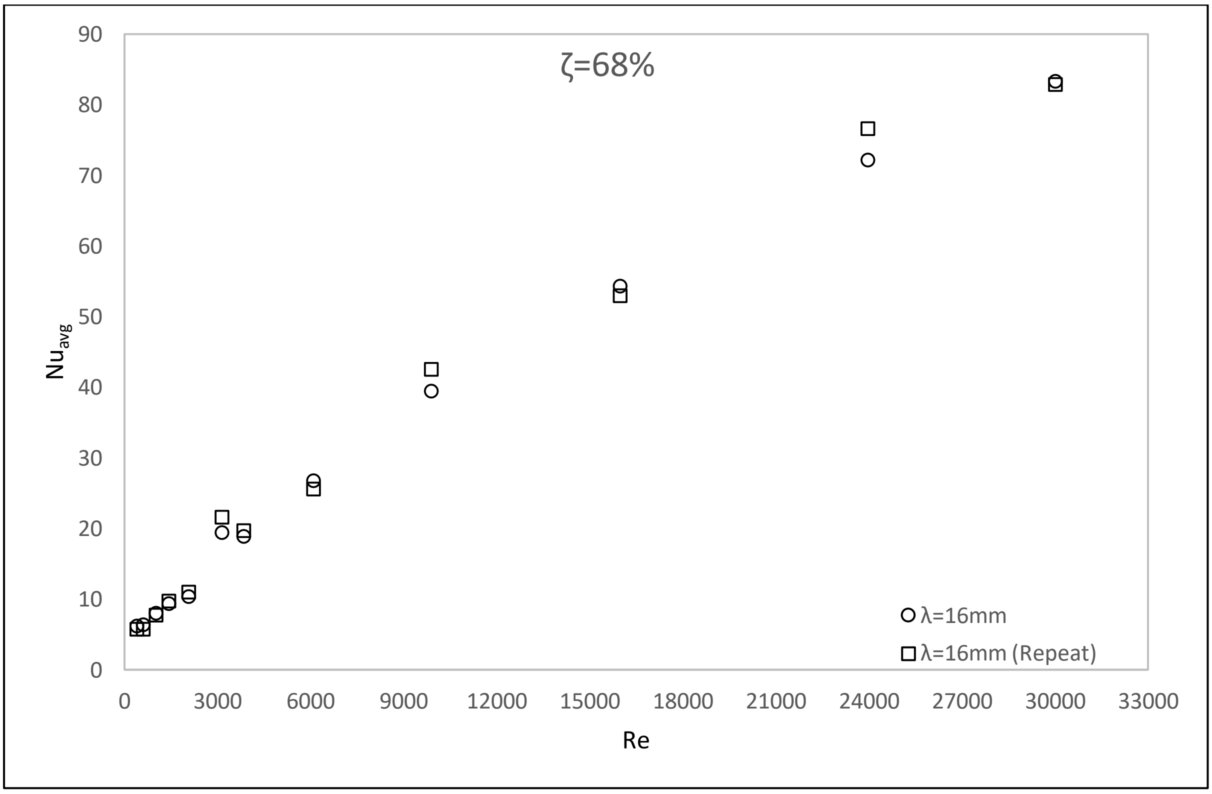

(b)

Figure 4.9: Repeatability of average Nusselt number for (a) two wall heating boundary condition and (b) one wall heating boundary condition

4.8 Conclusion

The theoretical entry lengths presented in Section 2.3 suggest the flow may not be fully developed at the start of the test section. The pressure drop plots in Section 4.3 show a constant gradient over the length of the test section indicating hydrodynamically fully developed flow at the start of the test section.

The friction factors obtained in Section 4.4 show a maximum deviation from the data presented by Shah and London [7] of 3.9 % in the laminar regime. In the turbulent regime the experimental friction factor deviates by a maximum value of 5.7 % from the analytical friction factors presented by Karman and Nikuradse [4]. The experimental pressure drop and friction factor data obtained from the research station are hence deemed accurate within the experimental error margins.

The local Nusselt numbers presented in Section 4.5 and 4.6 show a decreasing Nusselt number along the length of the test section as the flow becomes thermally developed. In the laminar flow regime, the experimental average Nusselt numbers for the one wall and two wall heat transfer boundary condition are compared to the analytical data derived by Shah and London [7] for flow in rectangular channels with the same boundary conditions. For the one wall heat transfer scenario the experimental average Nusselt number is calculated to deviate from the analytical data presented by Shah and London [7] by a maximum of 10 %. For the two wall heating boundary condition the experimental data deviates by a maximum of 9 % from that presented by Shah and London [7].

In the turbulent flow regime for the two wall heating boundary condition the experimental average Nusselt number is compared to analytical data presented by Gnielinski [2] for a constant peripheral heating boundary condition. This comparison is fair as during the experimental two wall heating boundary condition 94 % of the channel perimeter is heated uniformly. The experimental average Nusselt number differs from data presented by Gnielinski [2] by a maximum of 10 % over the range $3000 < Re < 35000$. For the one wall heating experiments the average Nusselt number is compared to extrapolated data presented by Kays and Crawford [4] for parallel plates of the same boundary condition. The data is calculated to deviate from that suggested by Kays and Crawford [4] by a maximum of 7 % over the range $10000 < Re < 30000$. The experimentally determined local and average Nusselt numbers are hence deemed accurate within the experimental error margins.

The comparison between the fiction factors obtained from duplicate inserts tests show that the methods used to manufacture the inserts do not influence the turbulence on a significant level. The friction factors obtained for the duplicate set of inserts with $\zeta = 68$ % differ by 5 % or less. For inserts with $\zeta = 48$ % the friction factors differ by 2 % or less with the exception of the result obtained at $Re = 3000$ where the friction factor differs by 6 %. As the duplicate inserts produce similar friction factors it is reasonable to assume that the duplicate insert will produce similar Nusselt numbers due to analogous turbulence characteristics of the inserts

Independent tests conducted at the same Reynolds number with both one wall and two wall heated boundary conditions show that the experimentally obtain Nusselt numbers are repeatable and constant for a given flow rate. Tests conducted at similar flow rates with a two wall heating boundary condition differ by 6 % or less while that of the one wall heating boundary condition differ by 9 % or less which are in the uncertainty bounds of the experiment. Research conducted by Cramer [23] shows increasing or decreasing the heat flux at the heated wall does not influence the local and average Nusselt numbers obtained from the test section.

5 Results

5.1 Introduction

This chapter shows the results obtained from the test section for the pressure drop, Fanning friction factor, local and average Nusselt numbers for a two wall and a one wall heating boundary condition and the performance index for a two wall and a one wall heating boundary condition.

5.2 Pressure Drop

Figure 5.1 and Figure 5.2 below show the normalized pressure drop, Δp* along the test section (x/L) with inserts 1.1 and 1.2, respectively. The normalized pressure drop is calculated according to Eq. 3.5. Figure 5.3 and Figure 5.4 in Section 5.2.2 show the normalized pressure plots, Δp* vs. x/L for the inserts 2.1 and 2.2. Figure 5.5 and Figure 5.6 in Section 5.2.3 show the normalized pressure plots, Δp* vs. x/L for the inserts 3.1 and 3.2. A higher negative value for Δp^* indicates a larger pressure drop over the channel test section. The normalized pressure drop plots for Re > 10000 for all the inserts can be found in Appendix C.

5.2.1 Inserts 1.1 and 1.2

Analyses of Figure 5.1 and Figure 5.2 show a decrease in the normalized pressure drop distributions with the increase in the Reynolds number. Figure 5.1 (a) and (b) show fluctuating Δp* for Re ≤ 3000 as the velocity and mass flow rate requirements inside the channel are very low at Re ≤ 3000. The corresponding fan speed to provide the low mass flow rate at low Re is much lower than the recommended speed. Consequently, the frequency input to the fan motor from the variable speed drive and fan speed fluctuate about the required rate. The mass flow rate and pressure in the channel thus vary about the mean values to create wavy fluctuations in the Δp* data at Re ≤ 3000. The slope of Δp* along x/L also decreases as the Re increases in Figures 5.1 (a) and (b) and 5.2 (a) and (b). The hydrodynamic developing length is analysed is Section 5.2.4.

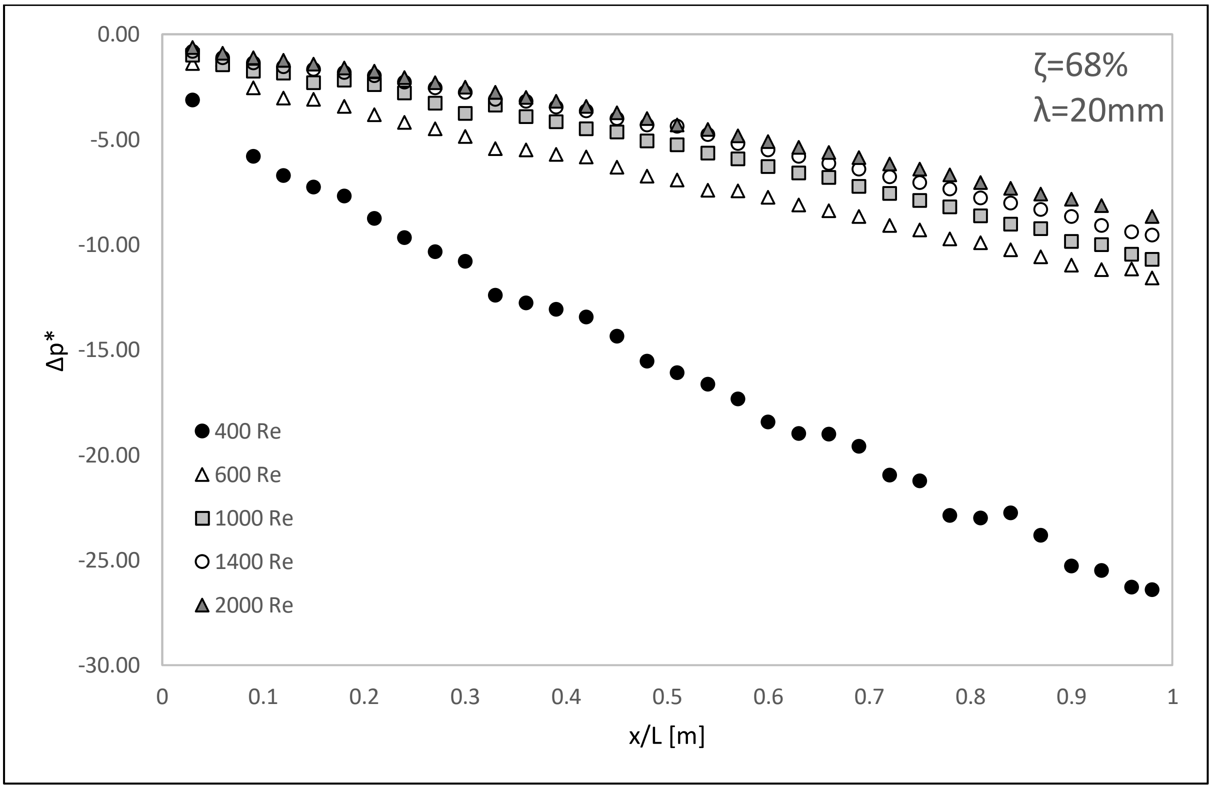

(a)

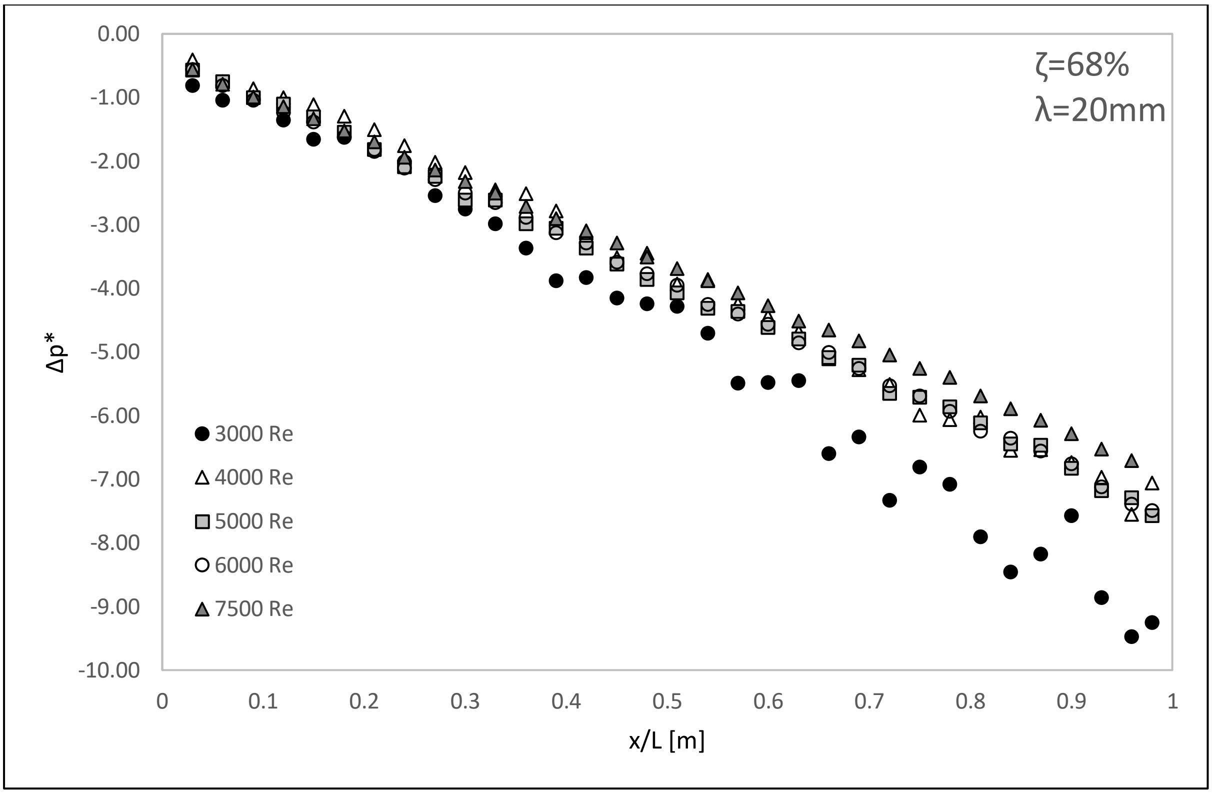

(b)

Figure 5.1: Test section normalized pressure drop with insert 1.1 (ζ = 68%, λ = 20 mm) for Reynolds number range (a) 400 < Re < 2000 and (b) 3000 < Re < 7500

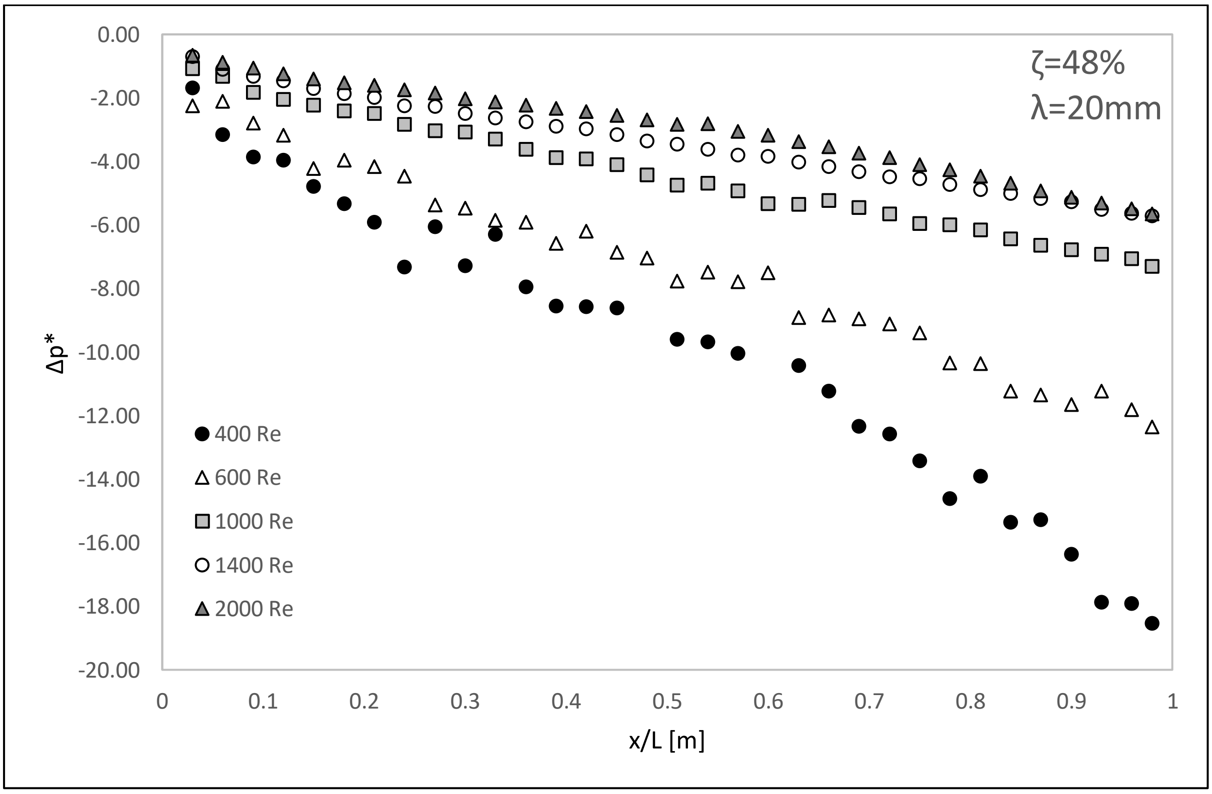

(a)

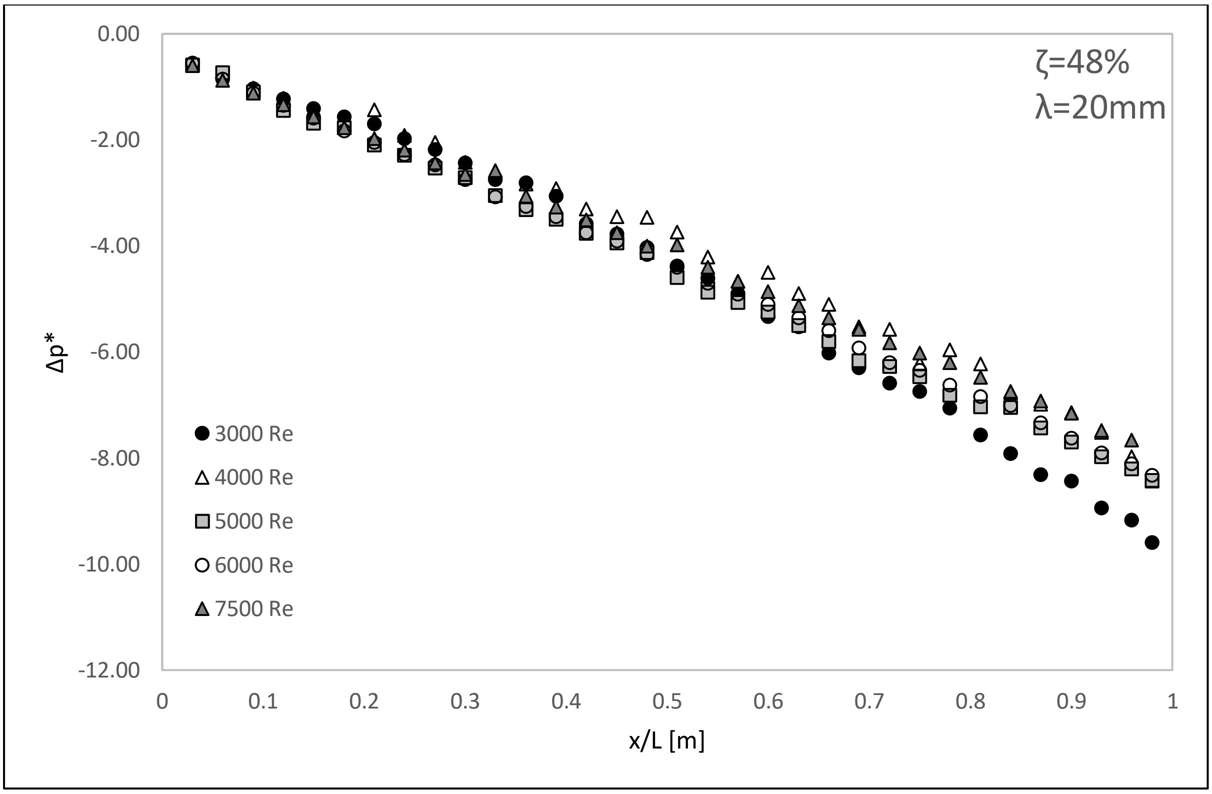

(b)

Figure 5.2: Test section normalized pressure drop with insert 1.2 (ζ =48%, λ = 20 mm) for Reynolds number range (a) 400 < Re < 2000 and (b) 3000 < Re < 7500

5.2.2 Inserts 2.1 and 2.2

Analyses of Figure 5.3 and Figure 5.4 show a decrease in the normalized Δp* distribution with the increase in the Reynolds number. The slope of the Δp* vs. x/L also decreases as the Re increases. Figure 5.3 (a) and (b) show fluctuating Δp* along x/L at Re ≤ 4000 which is explained in Section 5.2.1. The hydrodynamic developing length is analysed is Section 5.2.4.

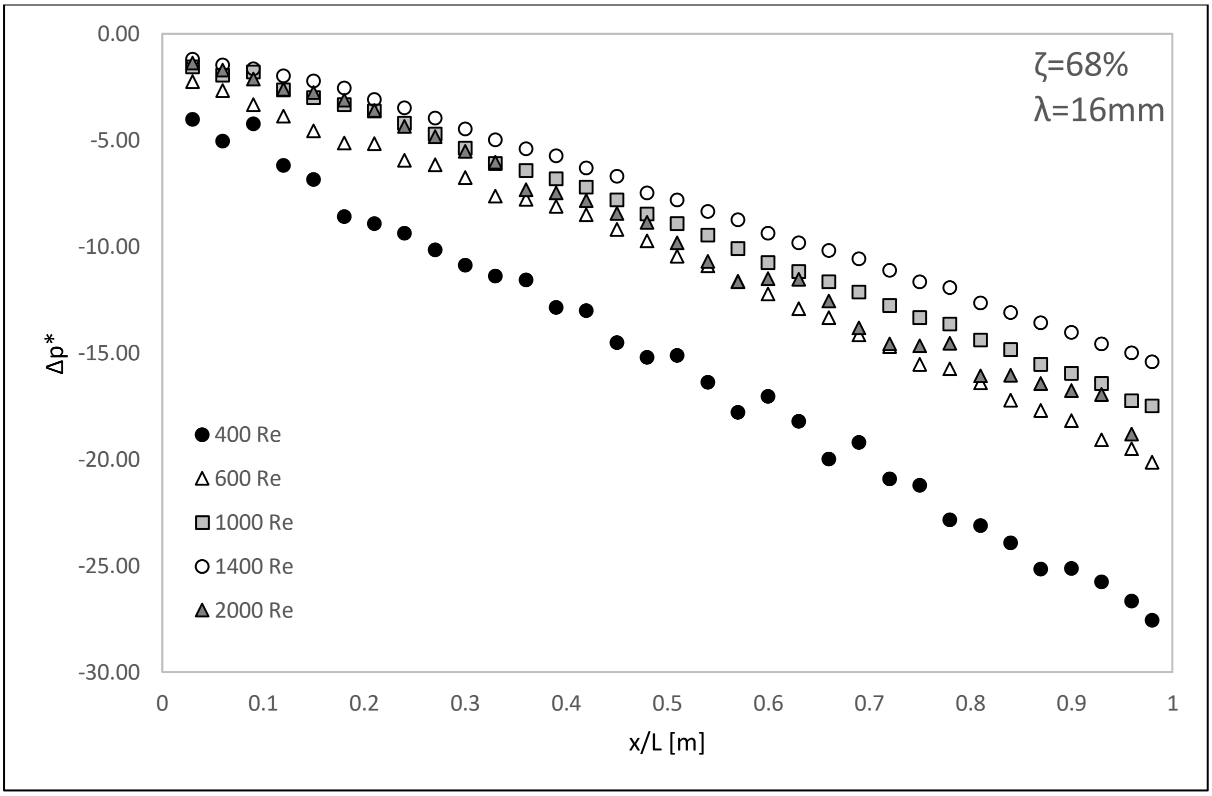

(a)

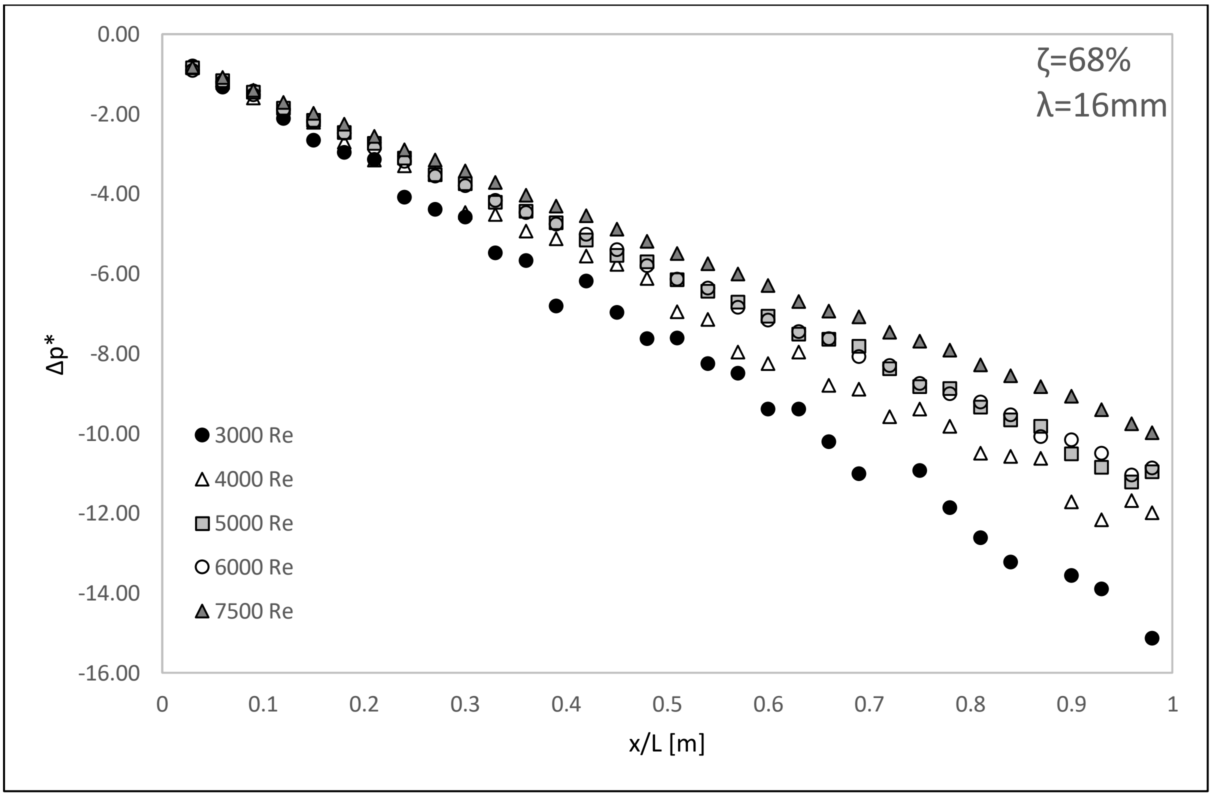

(b)

Figure 5.3: Test section normalized pressure drop with insert 2.1 (ζ = 68%, λ= 16 mm) for Reynolds number range (a) 400 < Re < 2000 and (b) 3000 < Re < 7500

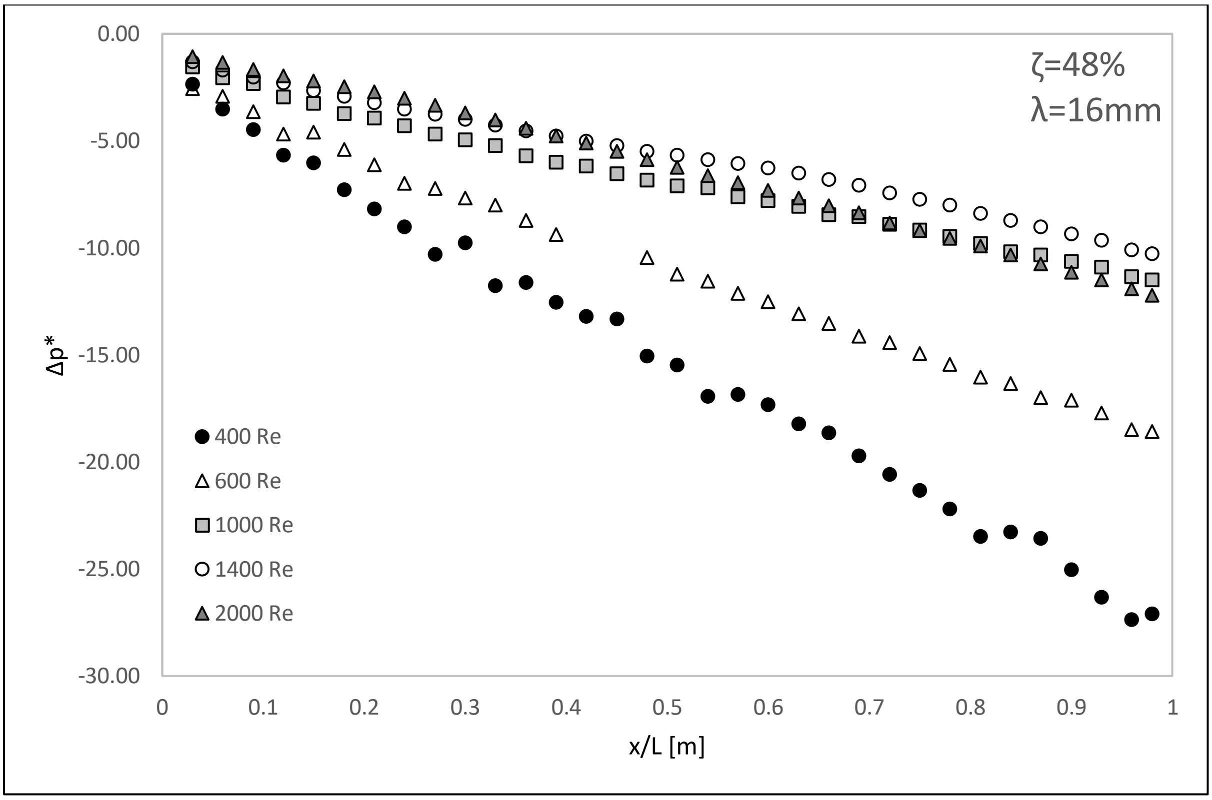

(a)

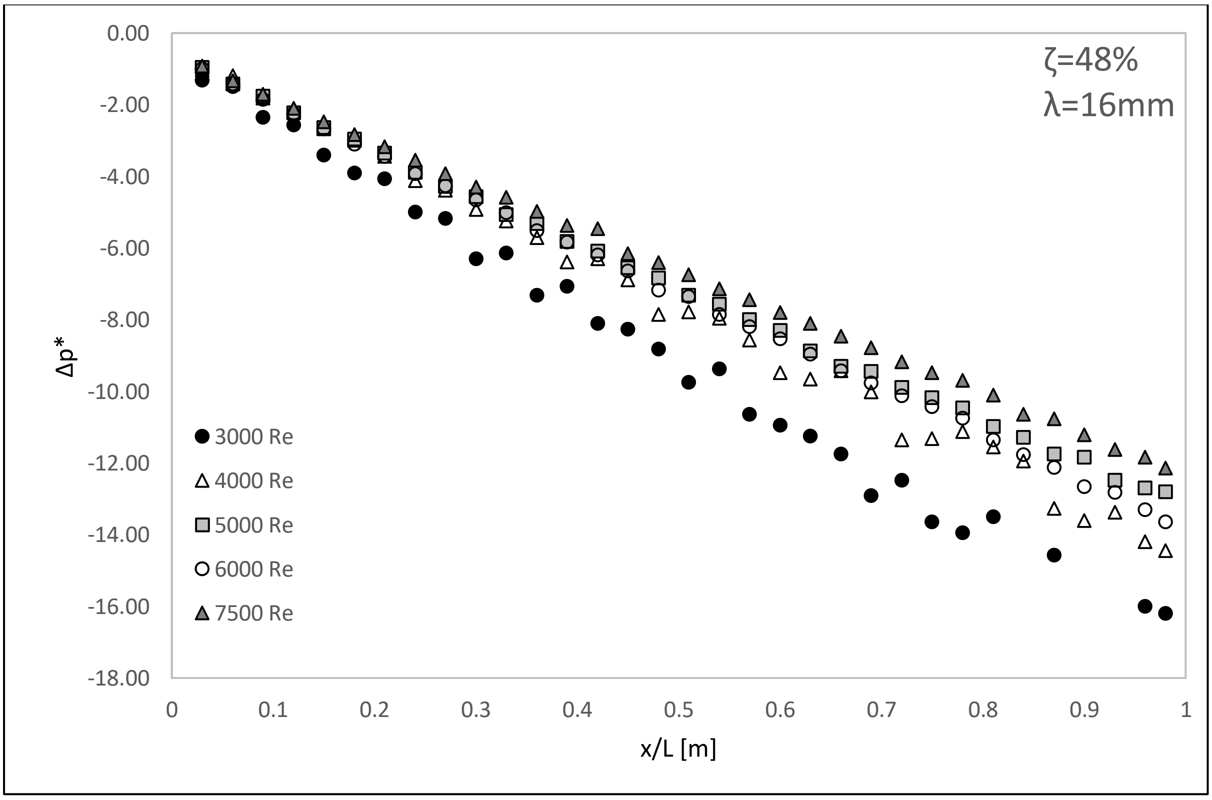

(b)

Figure 5.4: Test section normalized pressure drop with insert 2.2 (ζ = 48%, λ= 16 mm) for Reynolds number range (a) 400 < Re < 2000 and (b) 3000 < Re < 7500

5.2.3 Inserts 3.1 and 3.2

Analyses of Figure 5.5 and Figure 5.6 show a decrease in the Δp* magnitudes as well as in the slope of Δp* along x/L with the increase in the Reynolds number. Figure 5.5 (a) and (b) show fluctuating Δp* magnitudes for Re ≤ 4000 which is explained in Section 5.2.1. The hydrodynamic developing length is analysed is Section 5.2.4.

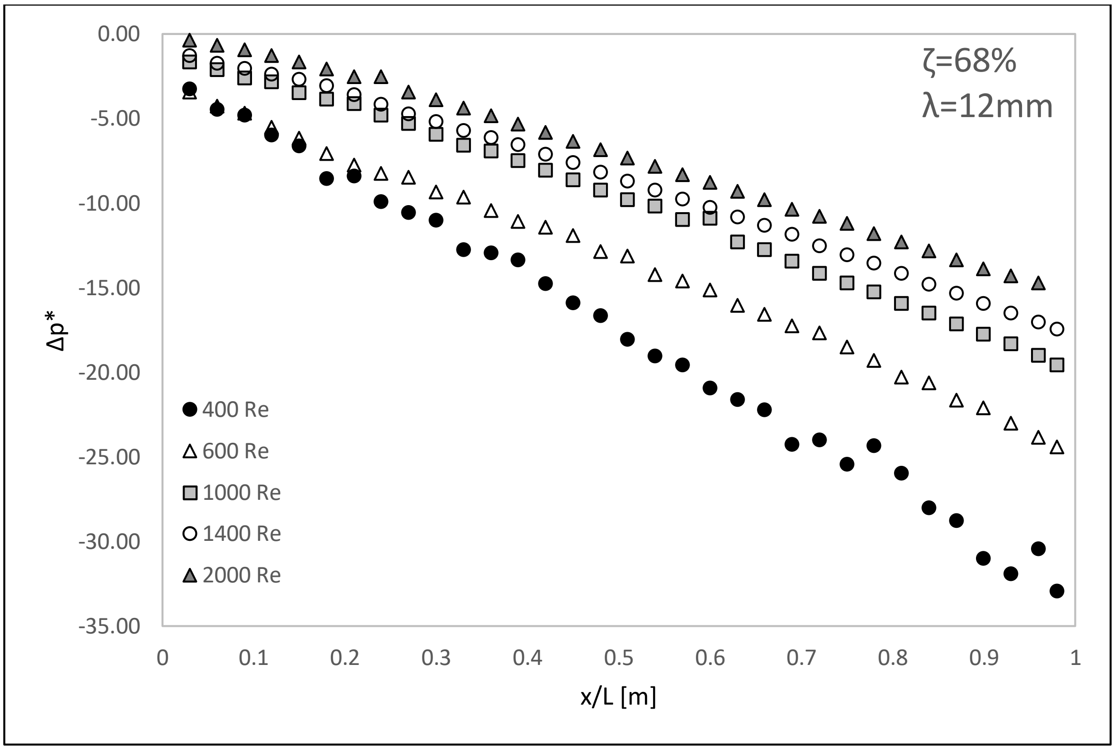

(a)

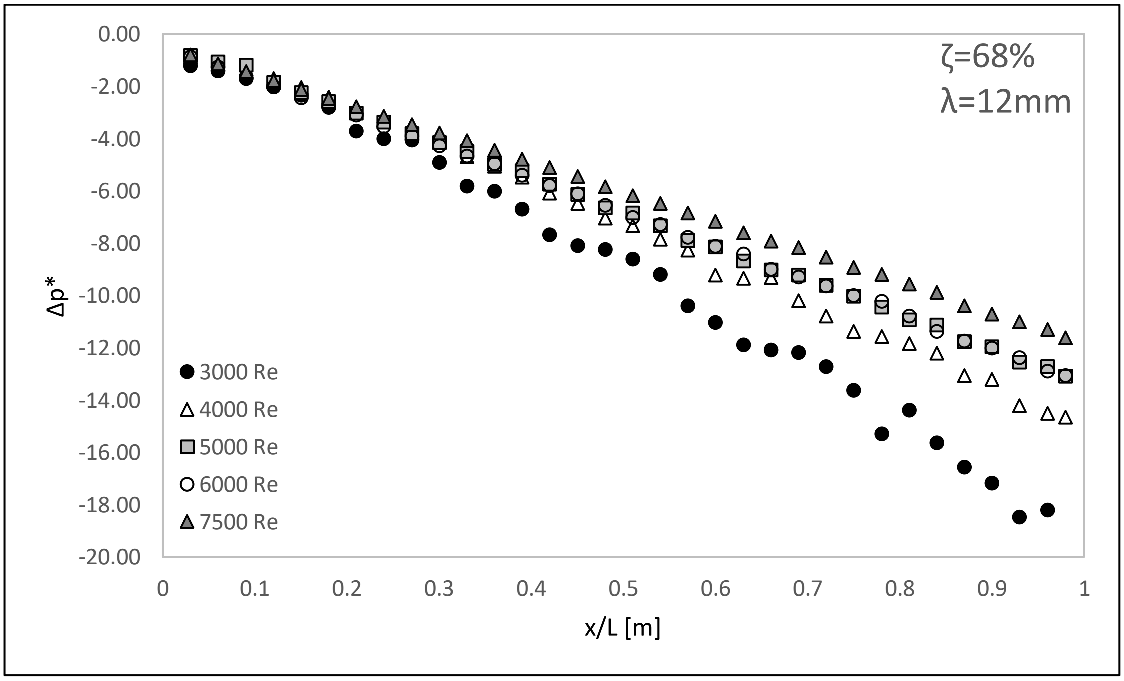

(b)

Figure 5.5: Test section normalized pressure drop with insert 3.1 (ζ = 68%, λ = 12 mm) for Reynolds number range (a) 400 < Re < 2000 and (b) 3000 < Re < 7500

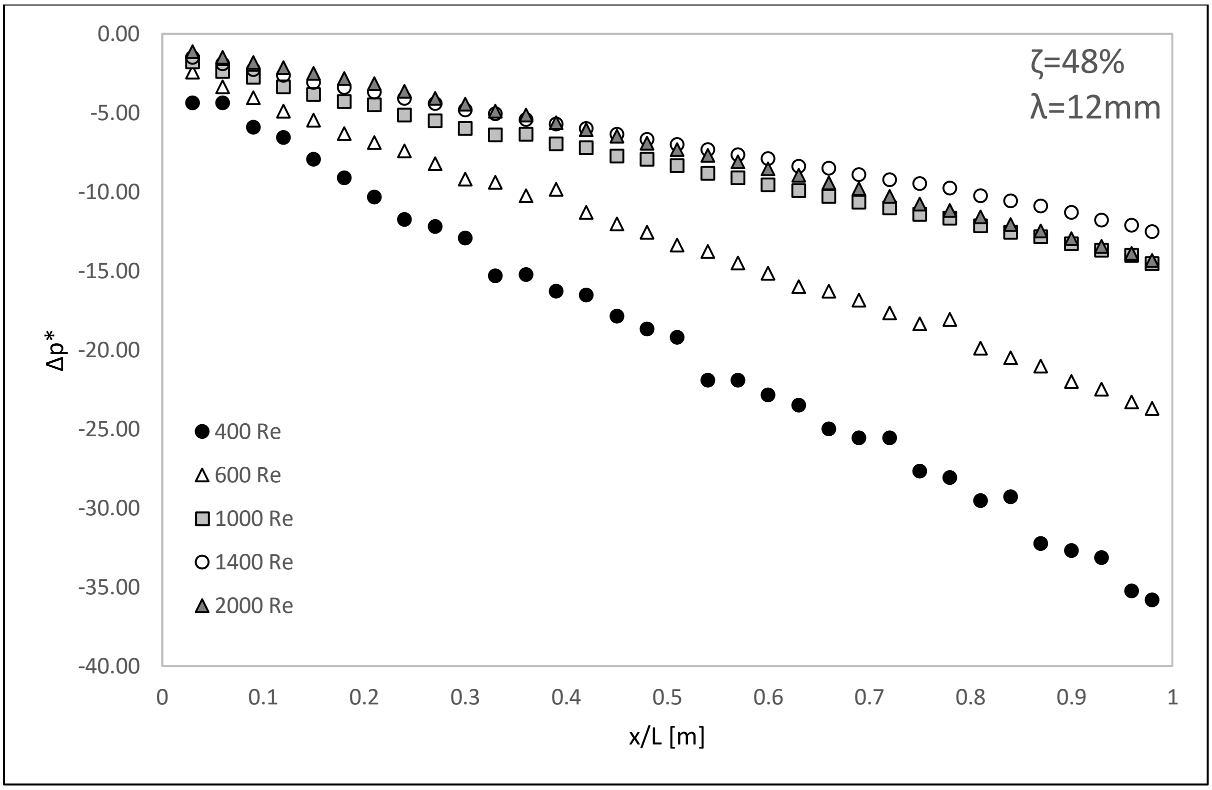

(a)

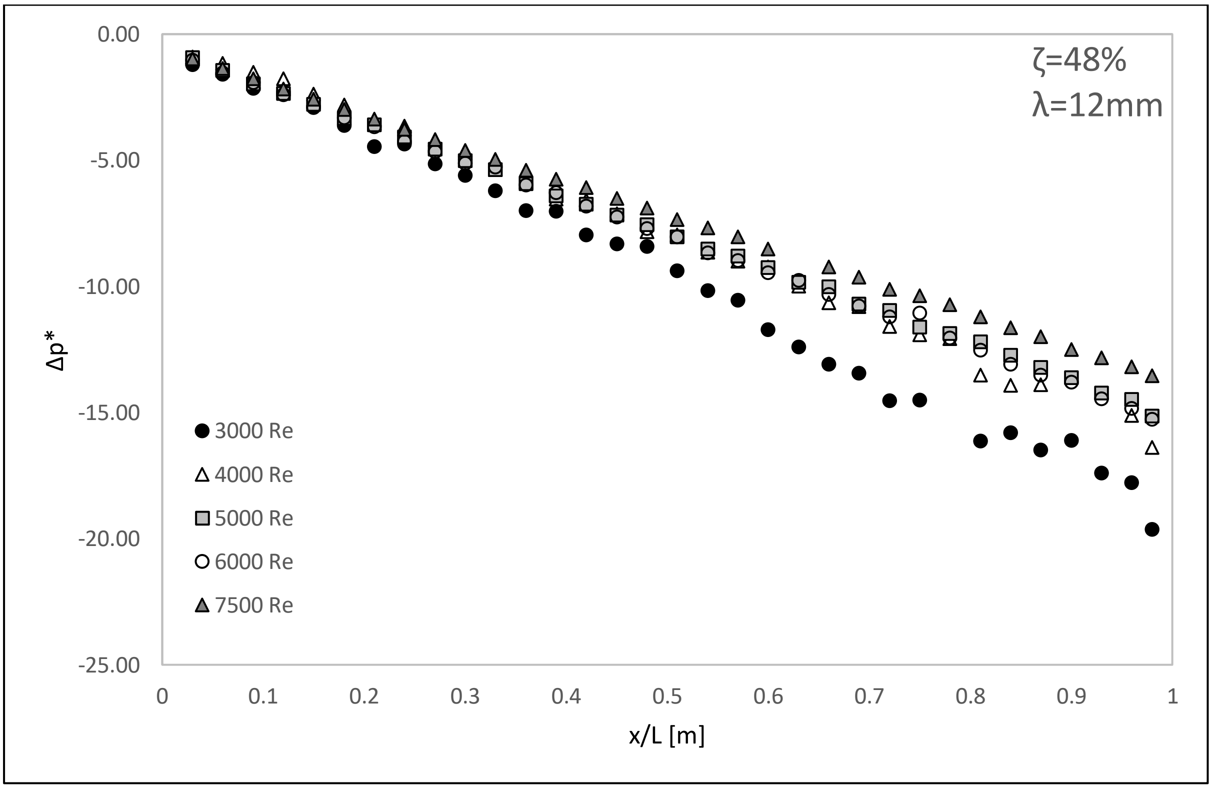

(b)

Figure 5.6: Test section normalized pressure drop with insert 3.2 (ζ = 48%, λ = 12 mm) for Reynolds number range (a) 400 < Re < 2000 and (b) 3000 < Re < 7500

5.2.4 Hydrodynamic Entry Length

For all the inserts tested the Δp* distribution along x/L decreases in magnitudes as well as in slope as the Reynolds number increases. Also, the normalized pressure drop, Δp* in the channel at a given Re with an insert is observed to be always higher than that of the corresponding base line pressure drop shown in Section 4.3 which is expected.

The developing length of the velocity profile between 2000 < Re < 4000 Re is calculated graphically from the normalized pressure drop plots. Figure 5.7 shows the normalized pressure plot for insert 2.2 at Re = 2000. A line of best fit from the regression analysis is plotted for the points between 0.2 < x/L < 1.0. The correlation coefficient, R^2 for the straight-line fit is 0.9995. The start of the fully developed turbulent velocity profile in the channel with a screen insert is determined as the point where the gradient of Δp* along x/L becomes constant. For Figure 5.7 below the start of fully developed flow is determined at x/L = 0.2. The beginning of the fully developed flow for each insert is shown in Table 5.1 for 1400 < x/L < 4000. The results show that for all the inserts tested the start location of the fully developed turbulent velocity profile moves downstream from the test section inlet with the increase in the Reynolds number as the insert properties (ζ, λ) remain constant. For a porous insert tested in a 5 mm rectangular channel Mahmood et al. [14] show that the developing length, x/L of the velocity profile is 0.31 and 0.34 from the inlet (x/L = 0) at Reynolds numbers of 1670 and 3120, respectively.

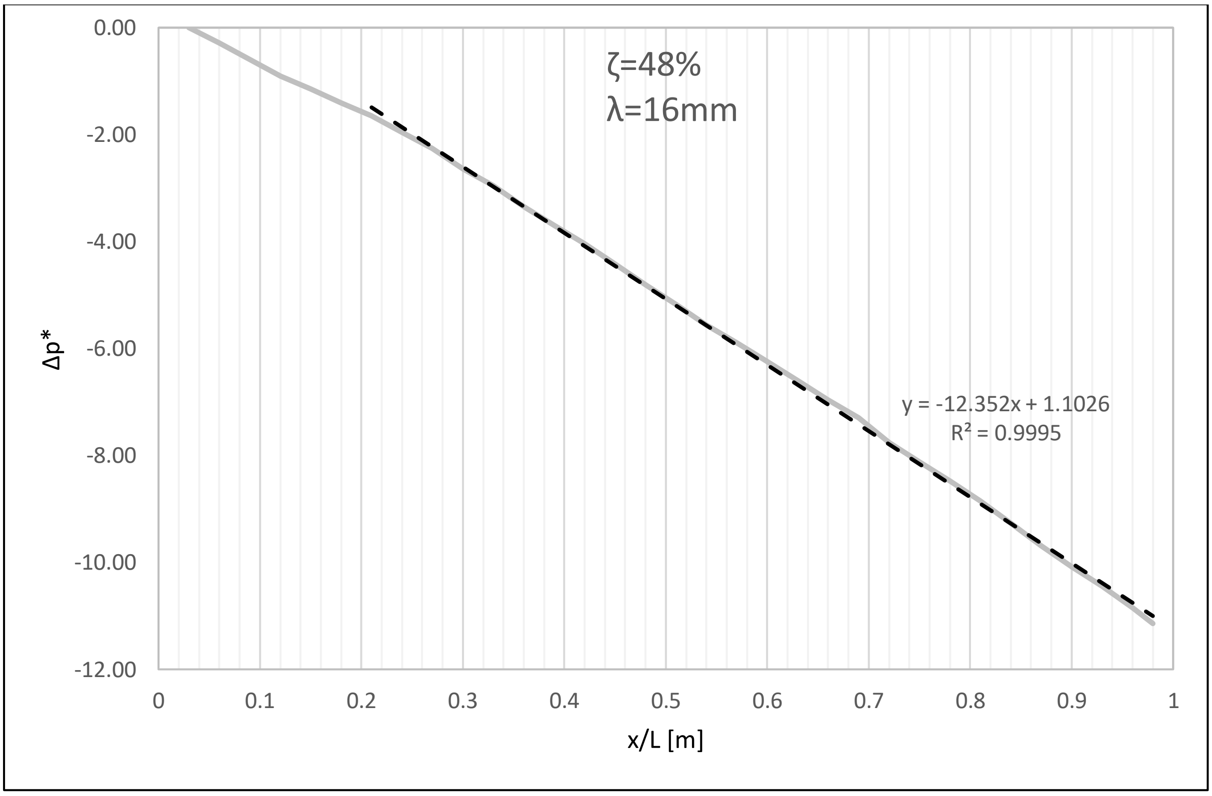

Figure 5.7: Test section normalized pressure drop with insert 2.2 (ζ = 48 %, λ= 16 mm) at Re = 2000

Table 5.1: Hydrodynamic developing lengths for 2000 < x/L < 4000

Re	**x/L**					
	ζ=68%			**ζ=48%**		
	λ=20mm	**λ=16mm**	**λ=12mm**	**λ=20mm**	**λ=16mm**	**λ=12mm**
1400	0.18	0.18	0.20	0.15	0.15	0.16
2000	0.2	0.18	0.20	0.20	0.20	0.20
3000	0.24	0.21	0.22	0.20	0.22	0.24
4000	0.24	0.24	0.25	0.22	0.25	0.27

5.3 Friction Factor

The Fanning friction factor, f with the insert is calculated from Eq. 3.6 using the gradient of the line of best fit for the Δp* vs. x/L data in the fully developed region. The friction factor ratio is calculated by dividing the friction factor, f obtained with an insert present in test section by the friction factor, f_0 obtained from the smooth channel in Section 4.4.

5.3.1 Inserts 1.1, 2.1 and 3.1 (Effects of Wavelength, λ at ζ = 68%)

The Fanning friction factors, f and friction factor ratios, f/f_0 for the inserts with 68 % porosity (λ = 20, 16, 12 mm) are shown in Figure 5.8 and Figure 5.9, respectively, as the Re varies. The results in Figure 5.8 show that the insert with the shortest wavelength, λ = 12 mm produces the highest friction factors generally followed by the insert with a wavelength λ = 16 mm. The insert with λ = 20 mm produces the lowest friction factors at all the Re tested. The difference in the friction factors between insert λ = 20 mm and λ = 16 mm is approximately twice as large as that between inserts λ = 16 mm and λ = 12 mm suggesting a non-linear relationship between the wavelength of the insert and the friction factor. The f value increases as the λ decreases because the flow blockage increases as the side-walls of the wave form are closer together for a shorter wavelength.

For the three inserts tested the f values in Figure 5.8 in general decrease with the increase in the Reynolds numbers. For the insert with λ = 12 mm the friction factor decreases rapidly between 400 < Re < 2000 then increases to a local maximum at Re = 3000. From 3000 < Re < 35000 the friction factor decreases with increasing Reynolds number. The friction factor-Reynolds number relationship for the insert with λ = 16 mm is similar in nature that of the insert with λ = 12 mm. For λ = 12 mm and 16 mm the friction factor decreases rapidly between 400 < Re < 1400 then increases to a local maximum at Re = 2100. From 2100 < Re < 35000 the friction factor then decreases with increasing Reynolds number. For the insert with λ = 20 mm the friction factor decreases with increasing Reynolds number except at Re = 1400 and at Re = 3000 where the friction factor increases to the local maximums.

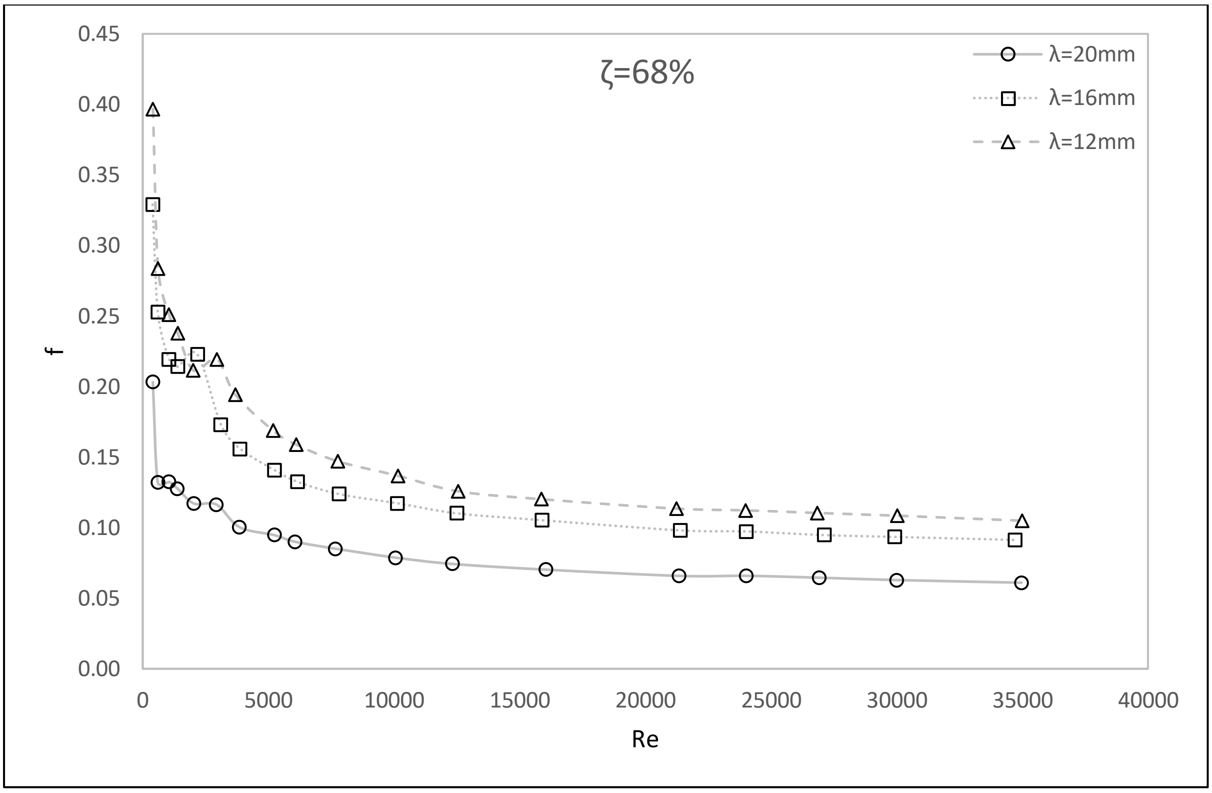

Figure 5.8: Fanning friction factor, f vs. Re for inserts with 68 % porosity

The friction factor results (f) in Figure 5.8 are divided by the smooth channel experimental fiction factor (f_0) at the corresponding Reynolds number. As the experimental smooth channel friction factors closely match those of the analytical data as shown in Section 4.4, the ratio f/f_0 remains about the same when dividing by either the experimental or analytical baseline. In the absence of analytical smooth channel data in the transitional flow regime, the f with an insert is divided by the experimental f_0. The ratio f/f_0 presented in Figure 5.9 uses both (f, f_0) from the experiments to maintain consistency. The results of Figure 5.9 are important as they estimate the increase in fluid pumping power through the channel when an insert is employed at a given mass flow rate and then compares the increase in pumping power between different inserts at the same mass flow rate. For example, the pumping power, $\dot{m}(\Delta p)/\rho$ through the channel with the insert (ζ = 68 %, λ = 16 mm) is 14.7 times that of the smooth channel at Re = 7800 in Figure 5.9.

The results in Figure 5.9 show that the insert with the shortest wavelength, λ = 12 mm produces the highest friction factor ratio followed by the insert with a wavelength λ = 16 mm. The insert with λ = 20 mm produces the lowest friction factor ratio. The friction factor ratios for the inserts tested show an increasing relationship with the increase in the Reynolds number. The insert with λ = 12mm shows a sharp increase in the friction factor ratio between 400 < Re < 1400 from where the friction factor ratio dips to a local minimum at Re = 2000. The friction factor ratio then increases rapidly up to Re = 3000 and decreases to a second local minimum at Re = 5000 from where ratio f/f_0 increases up to Re = 7500 then decrease to a third local minimum at Re = 12500. Between 12500 < Re < 35000 the friction factor ratio increases with the increase in the Reynolds number. This distribution of f/f_0 as the Re increases for the inserts with λ = 16 mm and λ = 20 mm is similar to that for λ = 12 mm as indicated in Figure 5.9.

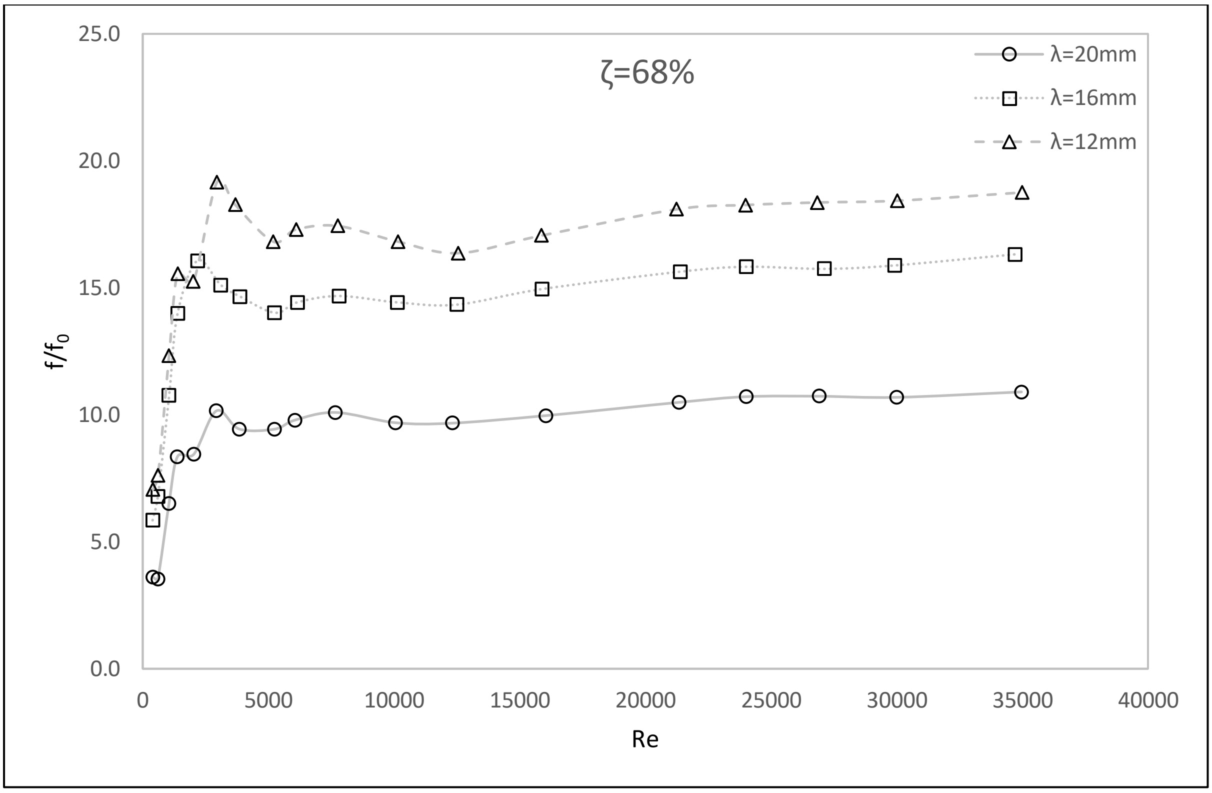

Figure 5.9: Friction factor ratios, f/f_0 vs. Re for inserts with 68 % porosity

5.3.2 Inserts 1.2, 2.2 and 3.2 (Effects of Wavelength, λ at ζ = 48%)

The friction factor-Reynolds number (f-Re) relationships for the inserts with ζ = 48 % in Figure 5.10 are similar to those of ζ = 68 %. The insert with wavelength λ = 12 mm produces the highest friction factor followed by the insert with a wavelength λ = 16 mm; the insert with λ = 20 mm produces the lowest friction factor values in Figure 5.10. For the insert with λ = 12 mm the friction factor decreases rapidly between 400 < Re < 1400 and then increases to a local maximum at Re = 3000. From 3000 < Re < 35000 the friction factor decreases with increasing Reynolds number. The friction factor for insert with λ = 16 mm decreases rapidly between 400 < Re < 1400 and then increases to a local maximum at Re = 3000. From 3000 < Re < 35000 the friction factor decreases with increasing Reynolds number. For insert with λ = 20 mm, the friction factor distribution as the Re increases follows the same trend as for the insert with wavelength λ = 16 mm.

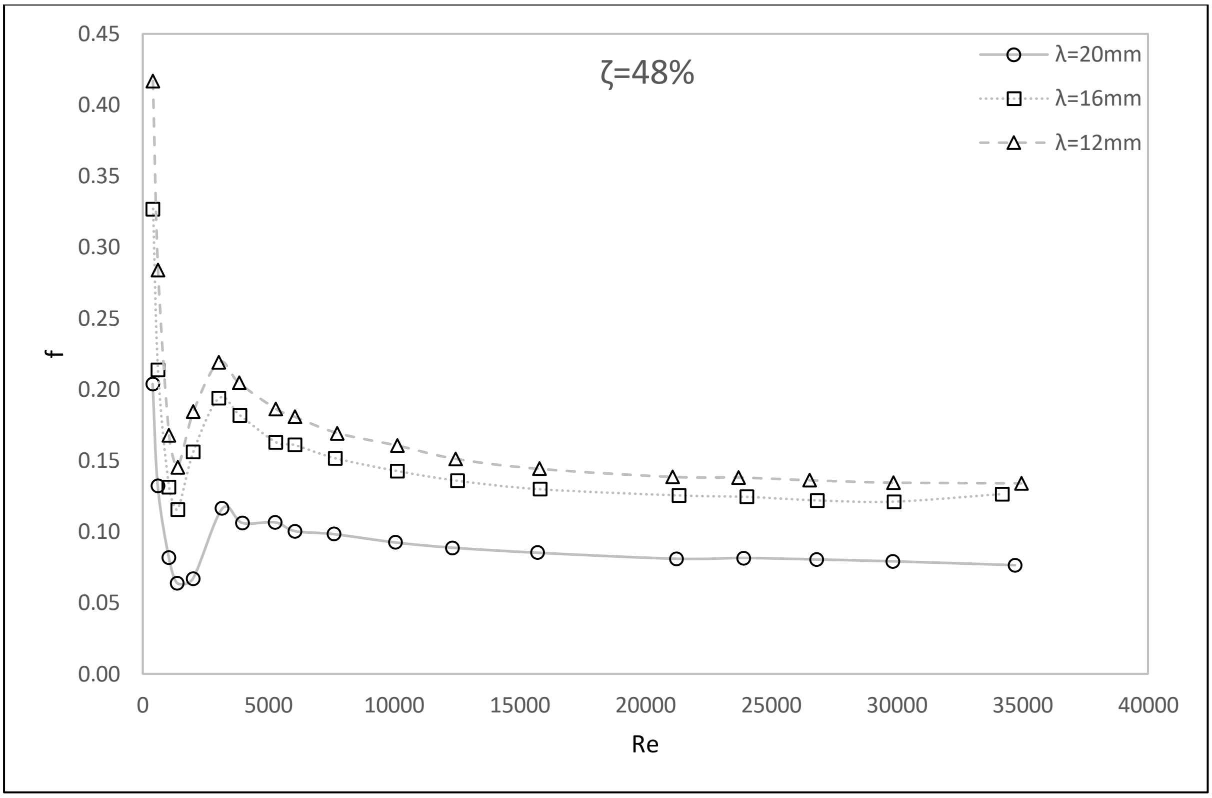

Figure 5.10: Fanning friction factors, f vs. Re for inserts with 48 % porosity

In Figure 5.11, the ratio f/f_0 for the inserts with $\zeta = 48$ % are obtained from the experimental f and f_0. The friction factor ratios in the figure are compared as the λ and Re vary. The results in Figure 5.11 show that the insert with the shortest wavelength, λ = 12 mm produces the highest friction factor ratio followed by the insert with a wavelength λ = 16 mm; the insert with λ = 20 mm produces the lowest friction factor ratio. The friction factor ratios, f/f_0 for the inserts tested in Figure 5.11 show an increasing relationship with the increase in the Reynolds number. The insert with λ = 12 mm shows a sharp increase in the friction factor ratio between $400 < Re < 3000$ from where the friction factor ratio dips to a local minimum at Re = 5300. The friction factor ratio then increases rapidly up to Re = 7500 and decreases to a second local minimum at Re = 12500. Between $12500 < Re < 35000$ the friction factor ratio increases with the increase in the Reynolds number. The increasing-decreasing relationship is similar in nature for the insert with wavelength λ = 16 mm and λ = 20 mm.

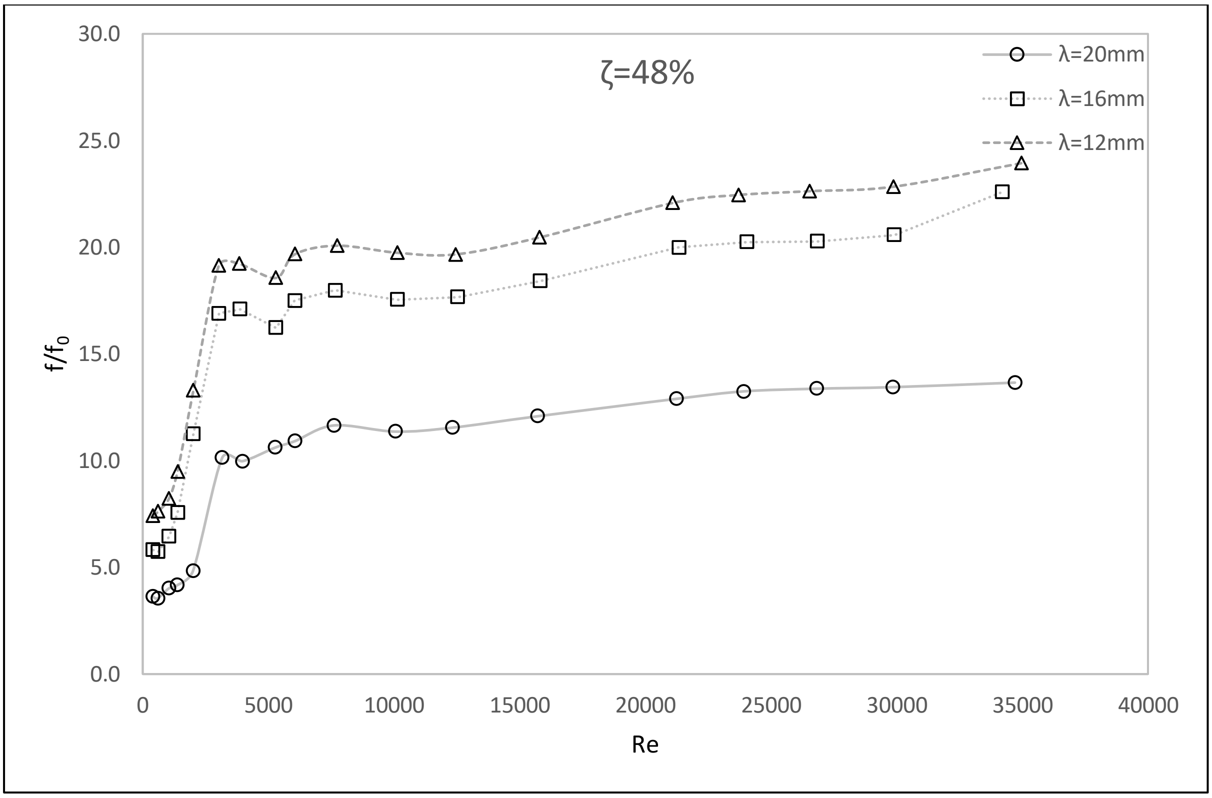

Figure 5.11: Friction factor ratios, f/f₀ vs. Re for inserts with 48 % porosity

The results of Figure 5.8 and Figure 5.10 show an inverse relationship between the porosity of the insert and the friction factor. The higher the porosity of the insert the lower the measured friction factor when the wavelength, λ and flow, Re remain the same for the inserts. This is to be expected. As the open area of the insert decreases the flow obstruction and form drag in the channel increases. Plots of f and f/f_0 vs. Re for constant wavelength, λ are given in Figure C. 70 and Figure C. 71 in Appendix C.

The increase in the friction factor, f between 2000 < Re < 3000 is greater for inserts with ζ = 48 % than that with ζ = 68 % when the insert λ value is unchanged. The inserts with ζ = 68 % and ζ = 48 % both show a rapid increase in the friction factor in the laminar flow regime (Re < 2000) followed by a drop in the friction factor at approximately Re = 5000. The inserts with ζ = 68 % show a decrease in the friction factor at Re = 2000 whereas the inserts with ζ = 48 % do not. The inserts with ζ = 68 % and ζ = 48 % both show a small decrease in the friction factor for wavelengths λ = 12 mm and λ = 16 mm between 10000 < Re < 12000. This decrease between 10000 < Re < 12000 is less prominent for λ = 20 mm. The friction factor ratio is always greater than zero indicating an increase in required fan power when any of the inserts are employed.

The friction factor ratio f/f_0 as dependent upon (Re, λ, ζ) can be expressed as mathematical correlations in the form of a power equation which is a function of the Reynolds number, porosity and wavelength. The equation is given as:

$$\frac{f}{f_0} = \zeta^A \left(\frac{H}{|\lambda - EH|}\right)^B CRe^{D\zeta^F} \qquad 5.1$$

Where A, B, C, D, E and F are constants, H is the height of the channel in meters and ζ and λ are the porosity ranging between 0 and 1 and wavelength in meters of the insert respectively. The correlations are calculated for three Re ranges, $400 \leq Re \leq 2000$, $3000 \leq Re \leq 7500$ and $10000 \leq Re \leq 35000$. The constant values for each respective Re range are given in Table 5.2.

Table 5.2: Friction factor ratio correlations

	Re Range		
Constant	$400 \leq Re \leq 2000$	$3000 \leq Re \leq 7500$	$10000 \leq Re \leq 35000$
A	3	0,2	0,41
B	-0,5	-0,5	-0,44
C	0,06	2,65	2,3
D	0,9	0,09	0,1
E	0,98	0,98	0,98
F	1,8	0	0

The analytical and experimental friction factor ratios, f/f_0 are shown in Figure 5.12. For $400 \leq Re \leq 2000$, 60 % of the f/f_0 values determined using the correlation are within 10 % of the experimental value, 77 % are within 15 % of the experimental value and 13 % of the analytically determined values deviate by 20 % or more from the experimental values. The maximum deviation of the analytical f/f_0 from the experimental f/f_0 is 28 % for the insert with $\xi = 0.68$ and $\lambda = 12$ mm at $Re = 600$.

For $3000 \leq Re \leq 7500$, 90 % of the analytical f/f_0 deviate from the experimental values by 10 % or less. The maximum deviation of the analytical f/f_0 from the experimental f/f_0 is 14 % for the insert with $\xi = 0.68$ and $\lambda = 20$ mm at $Re = 3000$. Figure 5.12 (a) shows the inability of the correlation to capture the peak in the f/f_0 at $Re = 3000$.

For $10000 \leq Re \leq 35000$, 98 % of the analytical f/f_0 deviate from the experimental values by 10 % or less. The maximum deviation of the analytical f/f_0 from the experimental f/f_0 is 13 % for the insert with $\xi = 0.48$ and $\lambda = 16$ mm at $Re = 3000$.

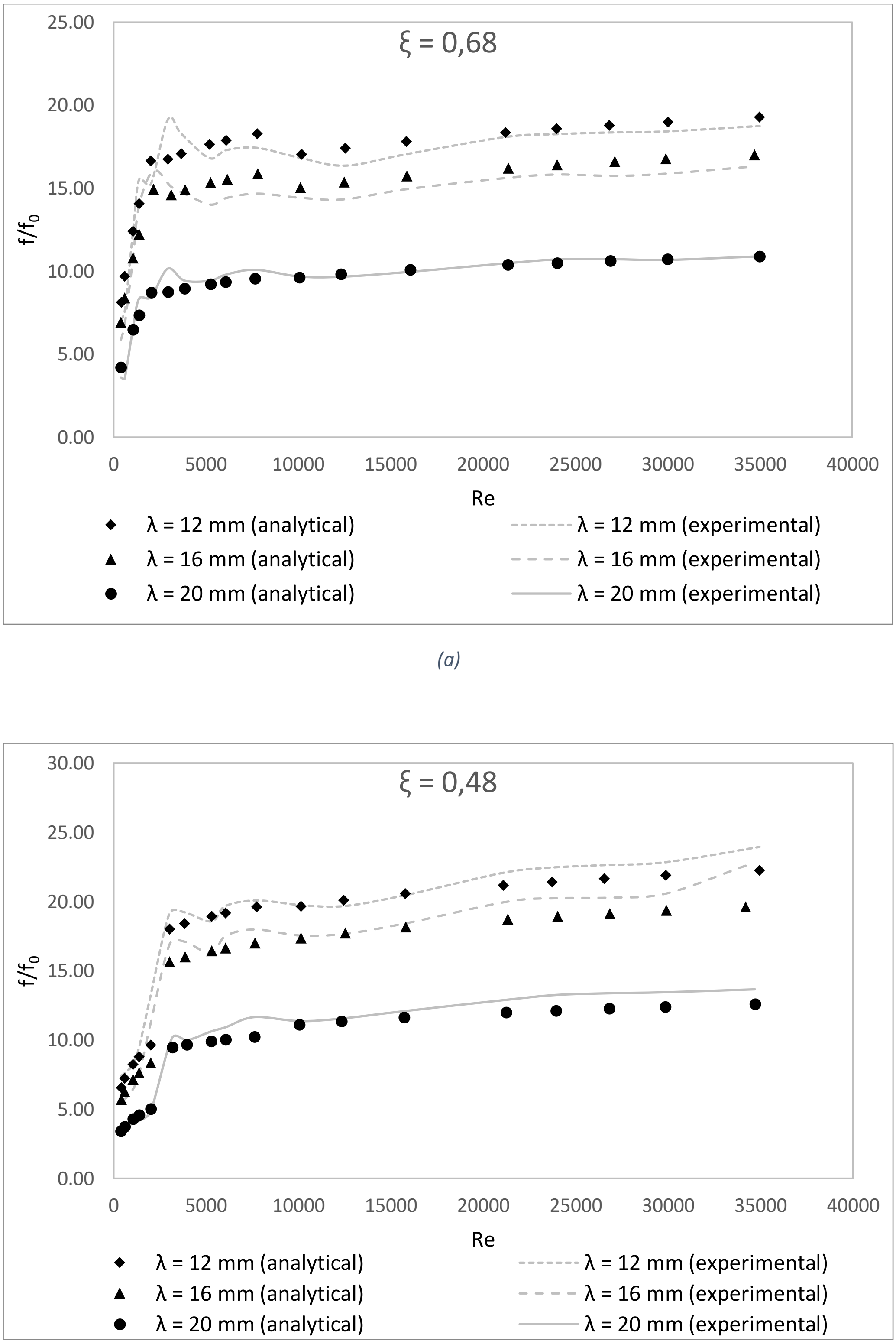

(a)

(b)

Figure 5.12: Friction factor ratio, f/f₀ correlations vs. Re for (a) ξ = 0.68 and (b) ξ = 0.48

5.4 Local Nusselt Number - Two Wall Heat Transfer

During the heat transfer measurements, the input heat flux at the heated wall is increased with the Reynolds number to maintain a reasonable temperature difference between the walls and the air. The difference in temperature between the wall and air, ($T_{w,x} - T_{m,x}$) is maintained at approximately 10 °C. The heat flux is controlled so that the wall temperature does not exceed 60 °C to avoid excessive thermal stresses and melting of the plastic components of the test sections.

The local Nusselt number is calculated at 25 locations along the test section centreline at Y/W = 0.5. Temperature measurements are not recorded between 0.22 < x/L < 0.3 as thermocouples are not installed in this region. The local Nusselt number plots for the two wall heating with the inserts are shown in Figure 5.13 to Figure 5.18.

5.4.1 Inserts 1.1 and 1.2

The local Nusselt numbers, Nu_{local} for the inserts with a wavelength of λ = 20 mm (ζ = 68%, 48%) are shown in Figure 5.13 and Figure 5.14 for 400 < Re < 10000. Plots for Re > 10000 can be found in Appendix D. The local Nusselt number plots are divided into subplots to clearly show the effects of inlet Re in laminar, transition and turbulent flow regimes on the Nu_{local}. Figure 5.13 and Figure 5.14 shown an increase in the local Nusselt number with the increase in the Reynolds number due to the increase in the velocity and mass flow rate.

The local Nusselt number, Nu_{local} in all the plots of Figure 5.13 and Figure 5.14 is observed to decrease as x/L increases and the temperature profile develops until an asymptotic constant value is measured towards the downstream half (x/L > 0.5) of the test section where the temperature profile is said to be fully developed. The thermal developing length in the upstream half of the test section, where the Nu_{local} changes significantly as x/L increases, is observed to decrease with the increase in Reynolds number for both inserts with ζ = 68 % and ζ = 48 %. Also note the dip in the Nu_{local} distributions at location x/L = 0.15 for Re > 1000 in Figure 5.13 (ζ = 68 %) and for Re > 1400 in Figure 5.14 (ζ = 48 %). The dip in the Nu_{local} is the clear indication of the approximate start location of the thermal boundary layer transition. Downstream of the location of the Nu_{local} dip, the Nusselt number increases because of the transition. For 400 < Re < 35000 the local Nusselt numbers, Nu_{local} reach an approximate constant value near x/L = 0.6. For 0.6 < x/ L< 1 the flow is said to be thermally fully developed. The distributions of Nu_{local} with the inserts in the upstream developing section of the channel are important for applications such as HVAC compact heat exchangers, electronic cooling, and fuel cell cooling that employ smaller lengths of heat transfer channel.

Comparisons between Figure 5.13 and Figure 5.14 show that the local Nusselt number for insert with ζ = 68 % is approximately equal, in general, to that for insert with ζ = 48 % over the range 400 < Re < 2000. However, at Re = 1000 and Re = 1400 the local Nusselt numbers for the insert with ζ = 68 % are 20 % and 30 % higher, respectively, than the ζ = 48 % porosity insert. Over the range 3000 < Re < 21000 the local Nusselt number for insert with ζ = 48 % is approximately 4 % to 8 % larger than that of the insert with ζ = 68 %. For the range 24000 < Re < 35000 the Nu_{local} values are similar for the two inserts.

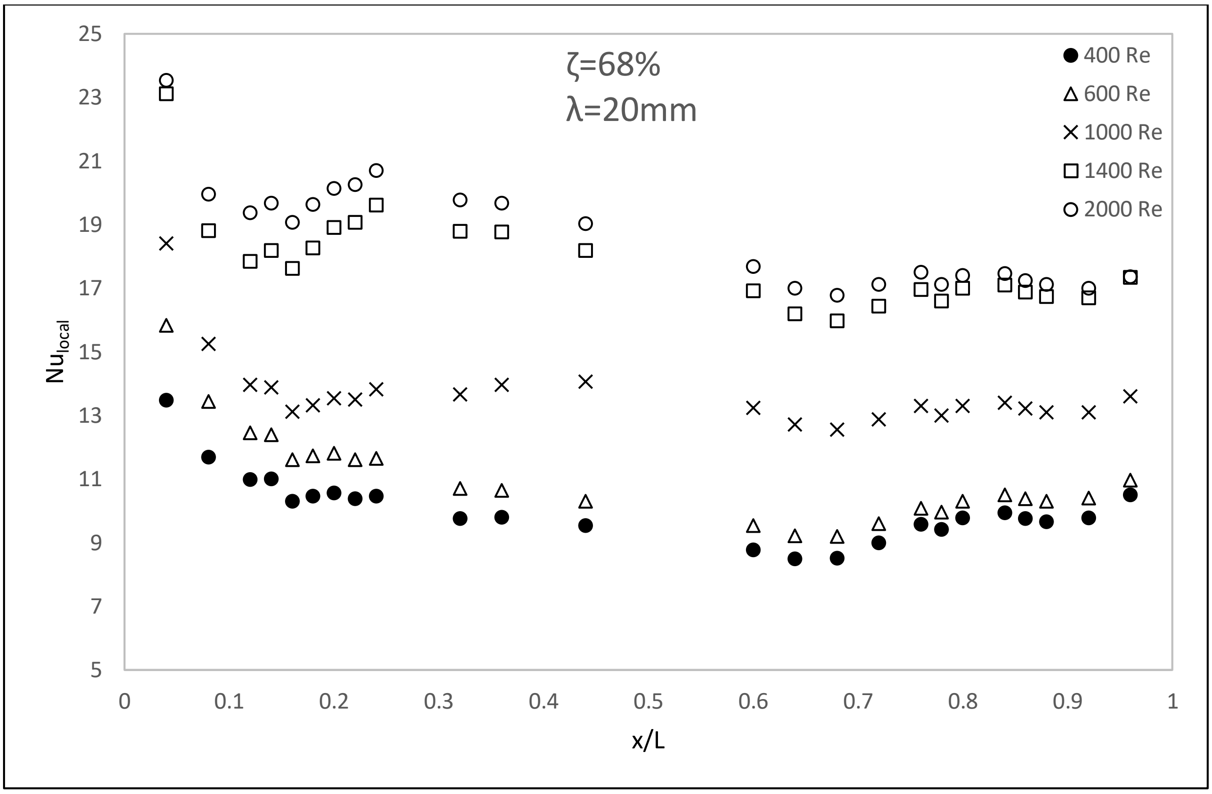

(a)

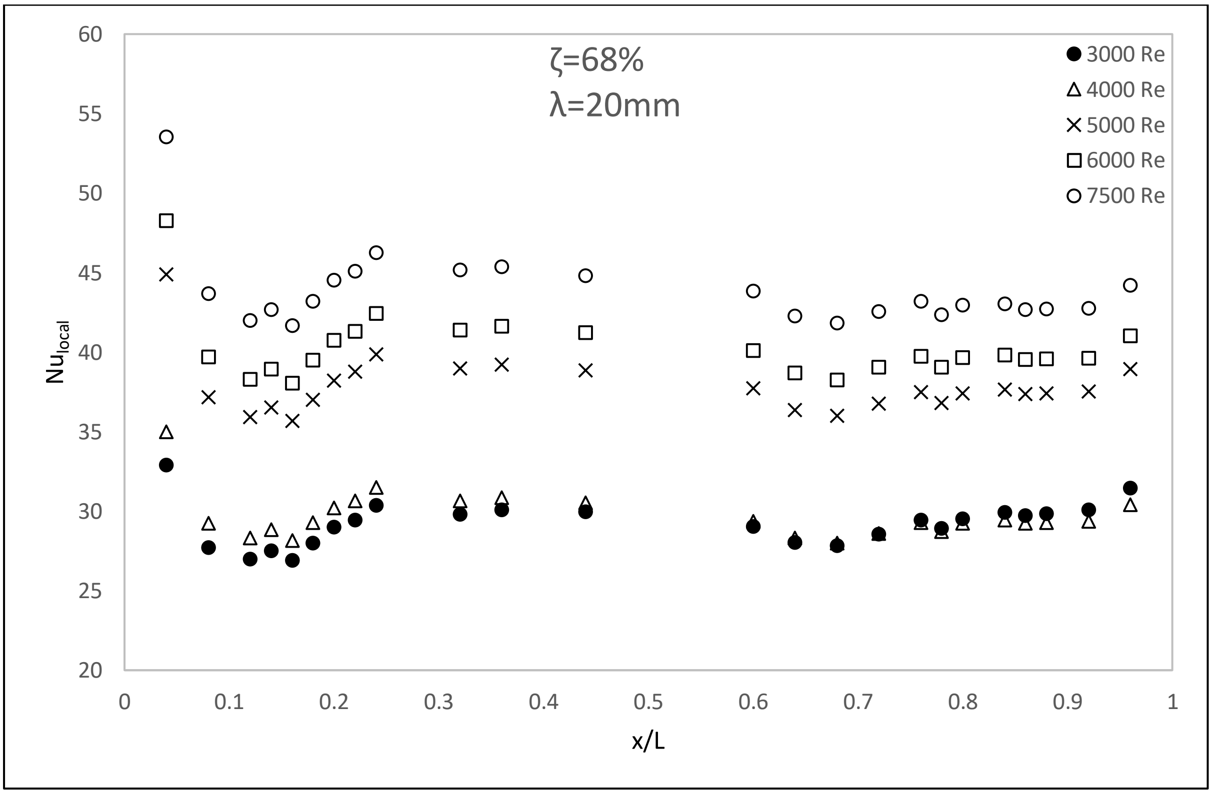

(b)

Figure 5.13: Insert 1.1 (ζ = 68%, λ = 20 mm) test section centreline local Nusselt number with two walls heated for Reynolds number range: (a) 400 < Re < 2000 and (b) 3000 < Re < 7500

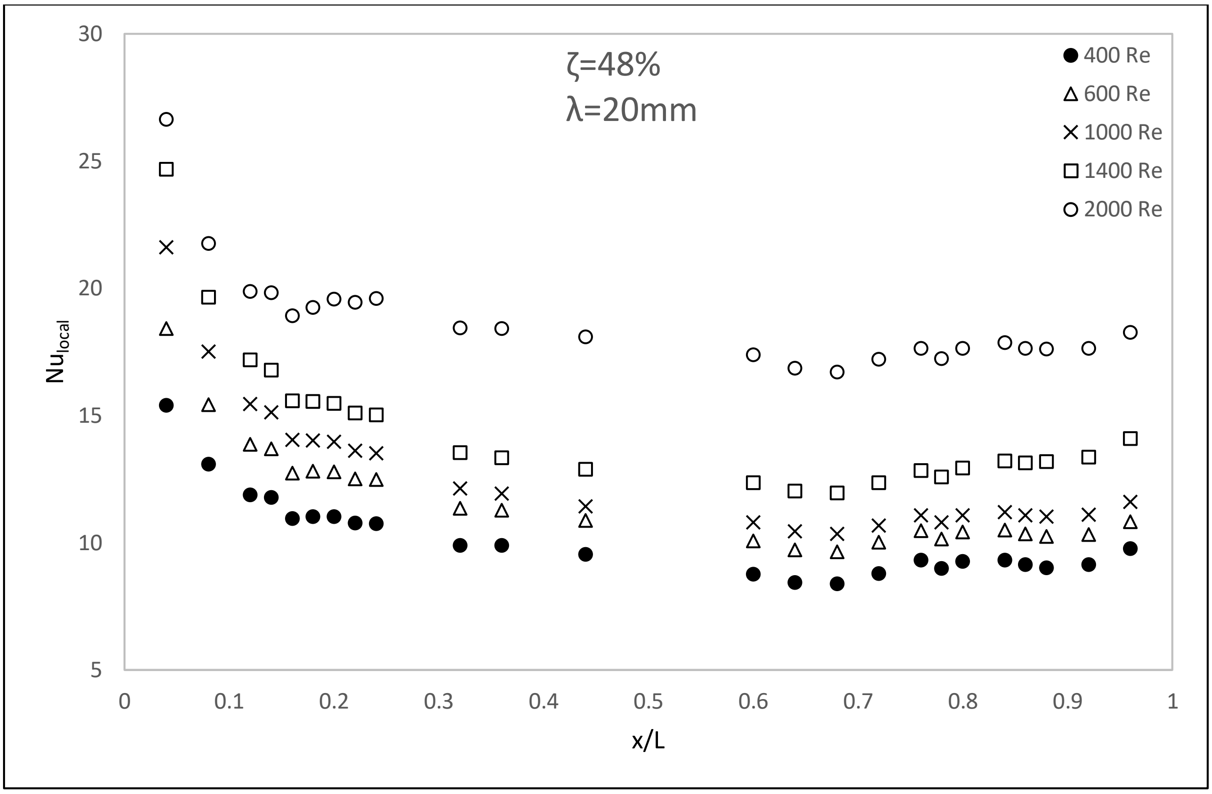

(a)

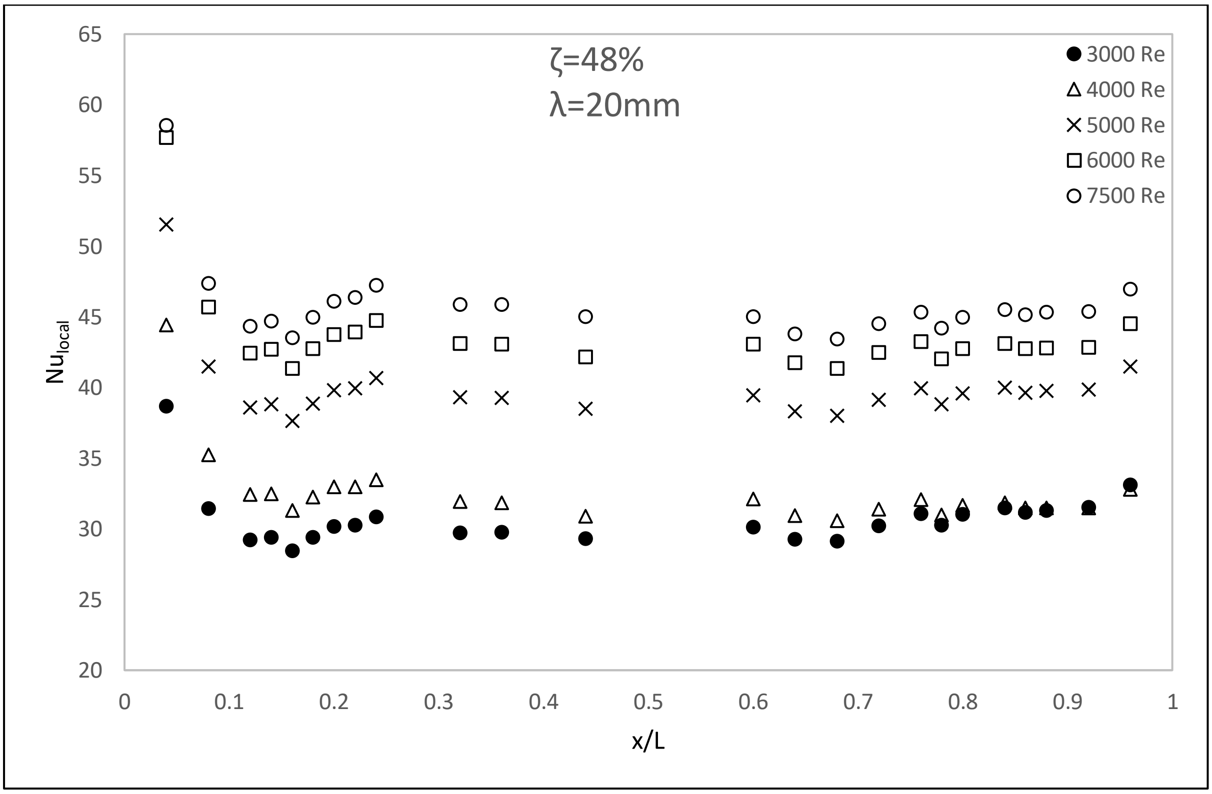

(b)

Figure 5.14: Insert 1.2 (ζ = 48%, λ = 20 mm) test section centreline local Nusselt number with two walls heated for Reynolds number range: (a) 400 <Re < 2000 and (b) 3000 < Re < 7500

5.4.2 Inserts 2.1 and 2.2

The local Nusselt numbers, Nu_{local} for the inserts with a wavelength of λ = 16 mm (ζ = 68 %, 48 %) are shown in Figure 5.15 and Figure 5.16. The local Nusselt number plots are divided into subplots to clearly show the effects of inlet Re in the laminar, transition and turbulent flow regimes on Nu_{local}. Figure 5.15 and Figure 5.16 shows an increase in the local Nusselt number with the increase in the Reynolds number similar to Section 5.4.1.

The local Nusselt number is observed decrease as x/L increases and the temperature profile develops until an asymptotic constant value is measured towards the downstream half (x/L > 0.5) of the test section where the temperature profile is said to be fully developed. As with Section 5.4.1 the dip in the Nu_{local} demarcating the start of the transition is observed for Re > 1000 in Figure 5.15 and Re > 2000 in Figure 5.16. For 400 < Re < 35000 the local Nusselt numbers reach a steady value at approximately x/L = 0.6. For 0.6 < x/L < 1 the flow is said to be thermally fully developed.

Comparison between Figure 5.15 and Figure 5.16 shows that the local Nusselt number for inserts with ζ = 68 % is approximately equal to that for insert with ζ = 48 % over the range 400 < Re < 2000 except at Re = 1000 where the local Nusselt numbers for the inserts with ζ = 68 % is 11 % higher than the lower porosity insert. Over the range 3000 < Re < 35000 the local Nusselt number for insert with ζ = 48 % is approximately 5 - 12 % larger than that for insert with ζ = 68 %.

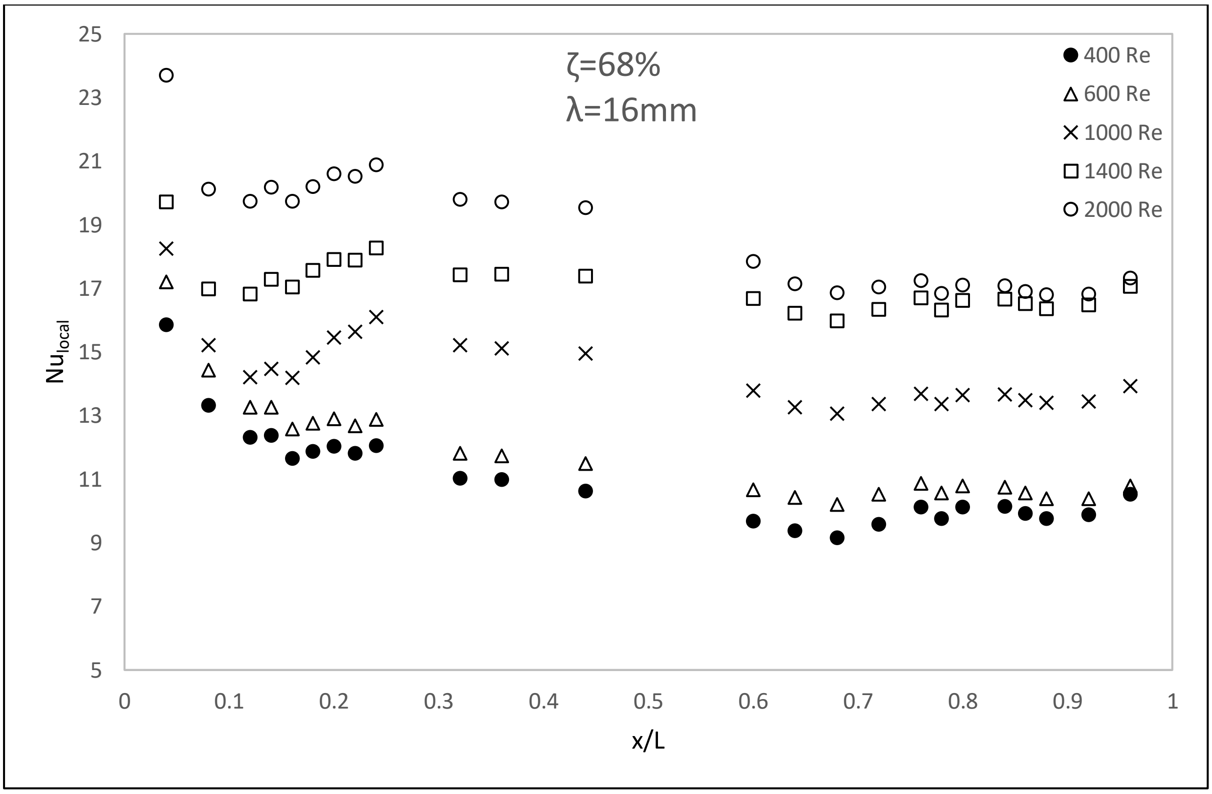

(a)

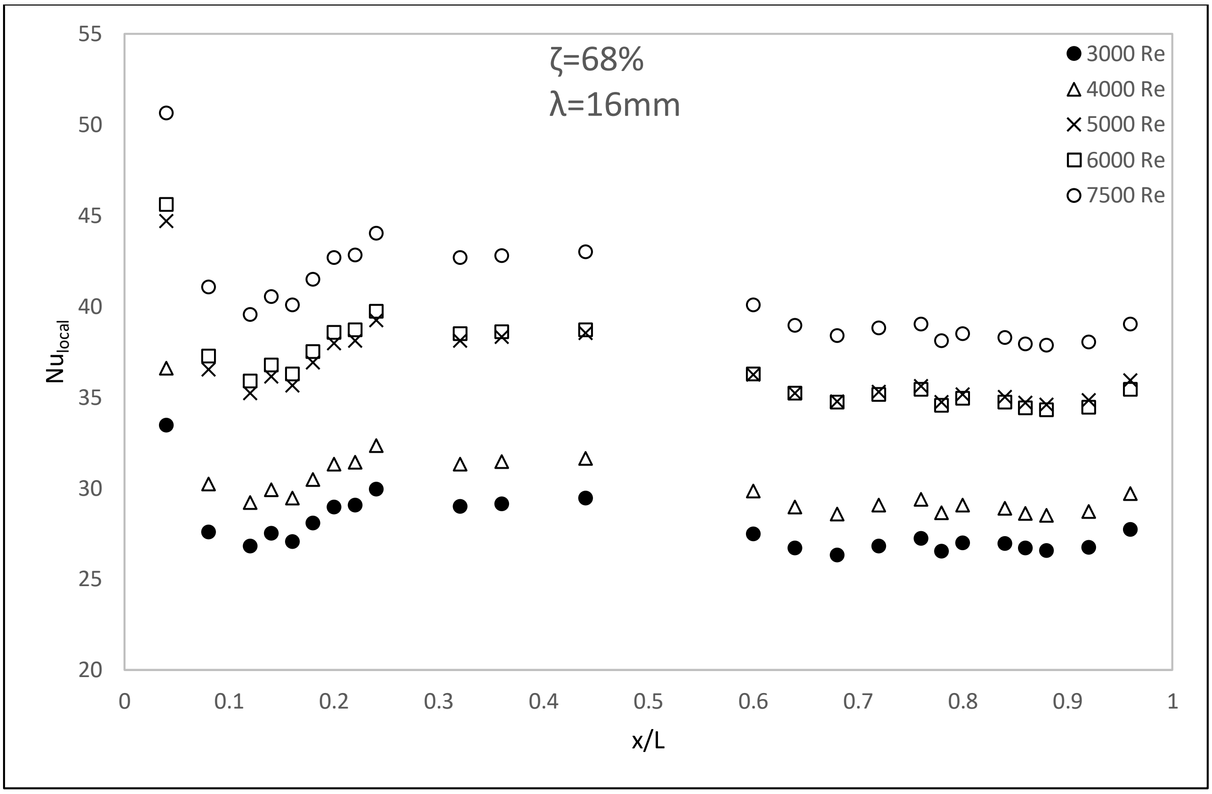

(b)

Figure 5.15: Insert 2.1 (ζ = 68%, λ = 16 mm) test section centreline local Nusselt number with two walls heated for Reynolds number range: (a) 400 < R e< 2000 and (b) 3000 < Re < 7500

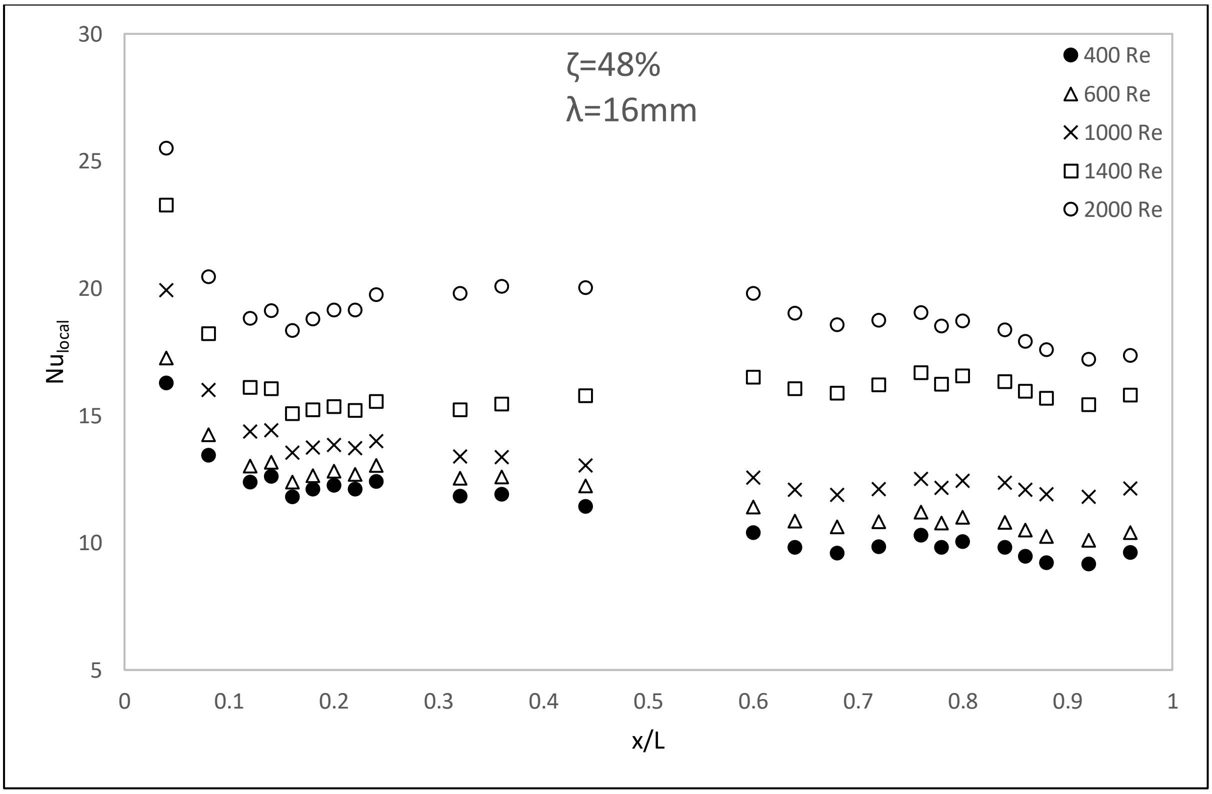

(a)

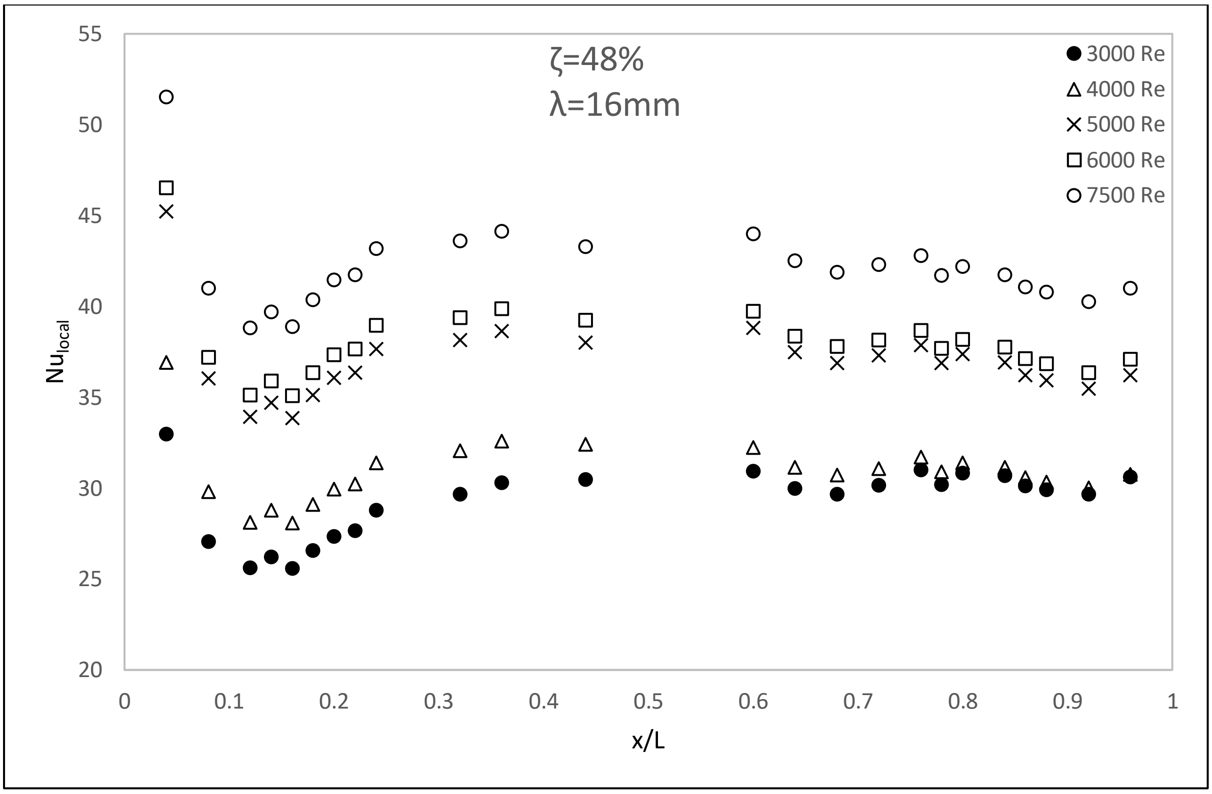

(b)

Figure 5.16: Insert 2.2 (ζ = 48%, λ = 16 mm) test section centreline local Nusselt number with two walls heated for Reynolds number range: (a) 400 < Re < 2000 and (b) 3000 < Re < 7500

5.4.3 Inserts 3.1 and 3.2

The local Nusselt numbers, Nu_{local} along the test section for the inserts with a wavelength of λ = 12 mm (ζ = 68 %, 48 %) are shown in Figure 5.17 and Figure 5.18 below. The local Nusselt number plots are divided into subplots to clearly show the effects of laminar, transition and turbulent flow regimes of the inlet Reynolds number. Figure 5.17 and Figure 5.18 shows an increase in the local Nusselt number with the increase in the Reynolds number due to the flow velocity and mass flow rate with Re.

The local Nusselt number, Nu_{local} is observed to decrease as x/L increases and the temperature profile develops until an asymptotic constant value is measured towards the downstream half (x/L > 0.5) of the test section where the temperature profile is said to be fully developed. As with Section 5.4.1 and 5.4.2 the dip in the Nu_{local} demarcating the start of the transition is observed for Re > 1000 in Figure 5.17 and Re > 1000 in Figure 5.18. For 400 < Re < 35000 the local Nusselt numbers reach a steady value at approximately x/L = 0.6. For 0.6 < x/L < 1 the flow is said to be thermally fully developed.

Comparison between Figure 5.17 and Figure 5.18 shows that the local Nusselt number for inserts with ζ = 48 % is always higher than that for inserts with ζ = 68 % over the range 400 < Re < 35000 with the most notable difference being 16 % and 17 % at Re = 400 and Re = 600 respectively.

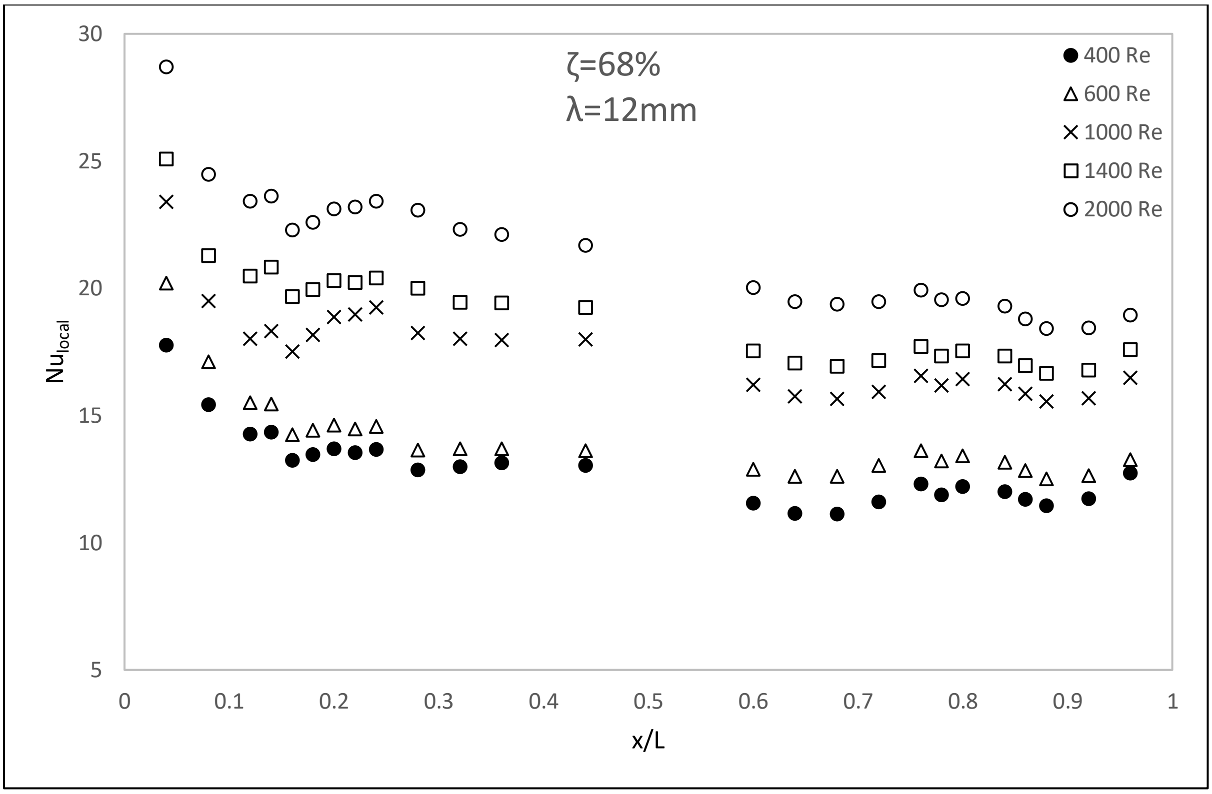

(a)

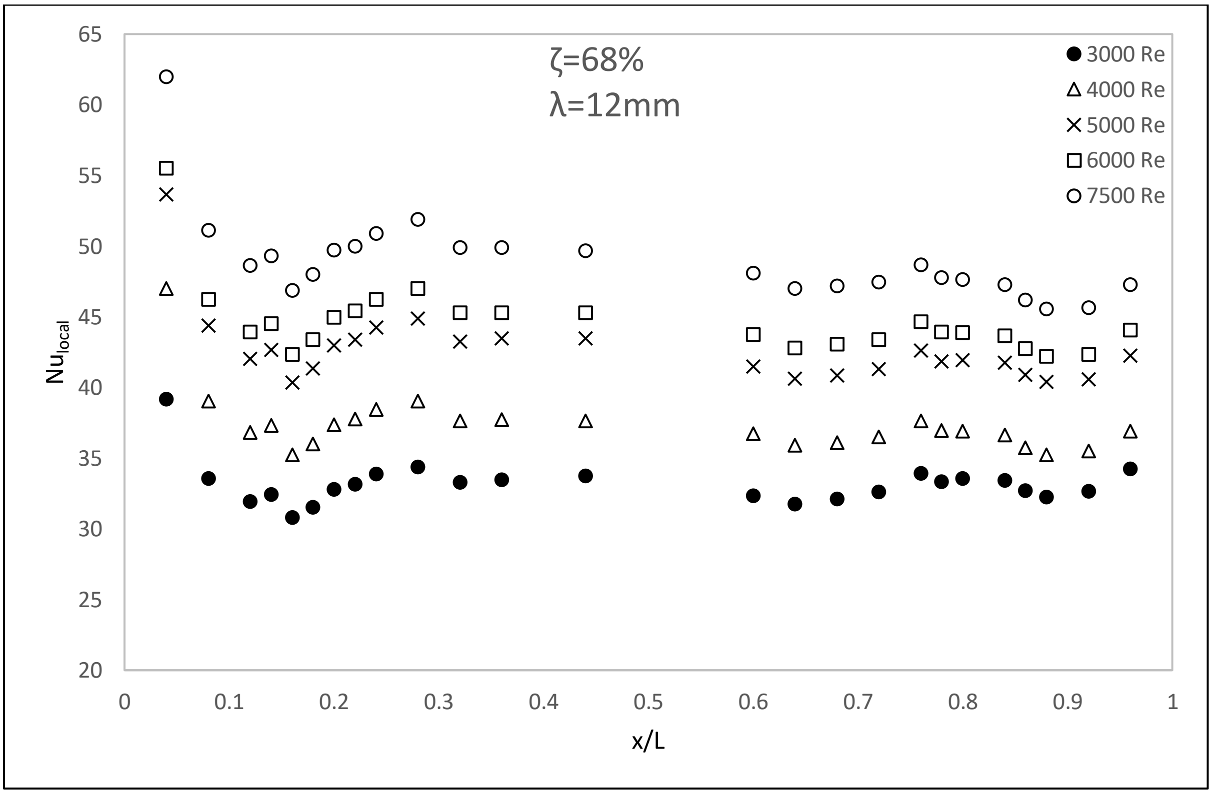

(b)

Figure 5.17: Insert 3.1 (ζ = 68%, λ = 12 mm) test section centreline local Nusselt number with two walls heated for Reynolds number range: (a) 400 < Re < 2000 and (b) 3000 < Re < 7500

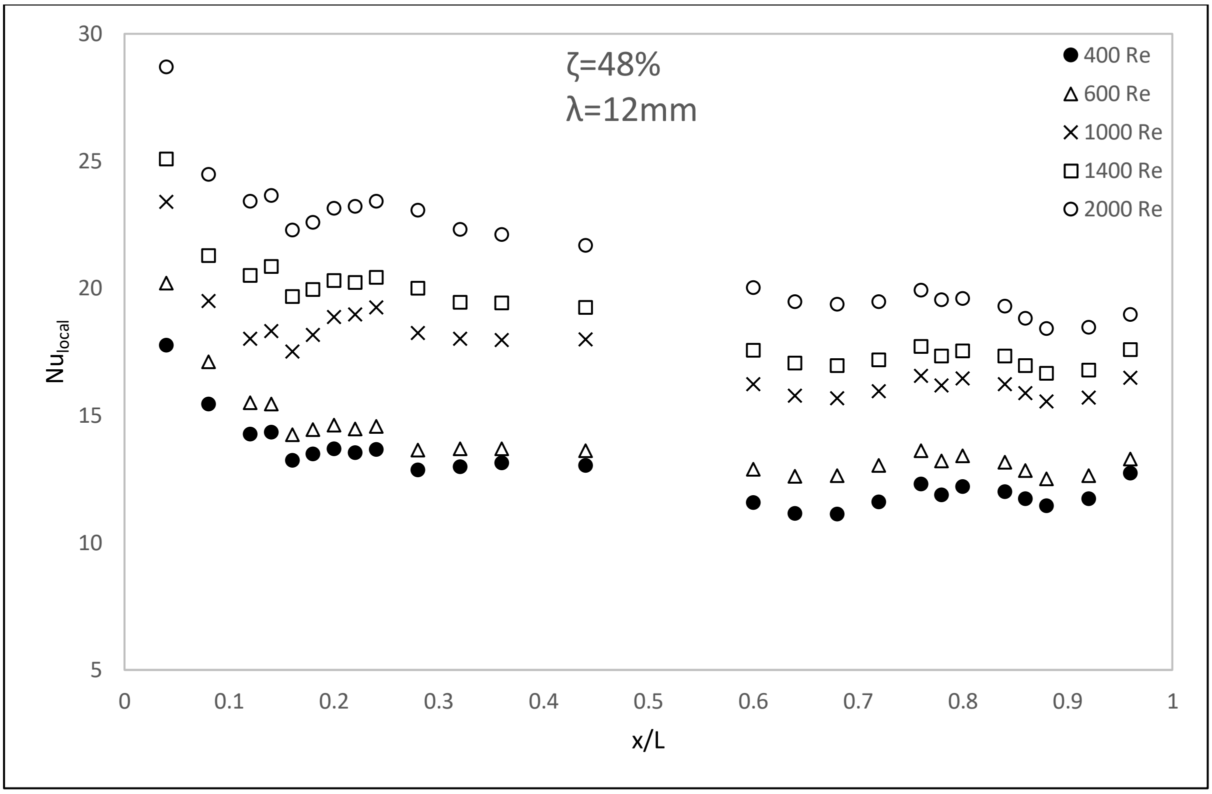

(a)

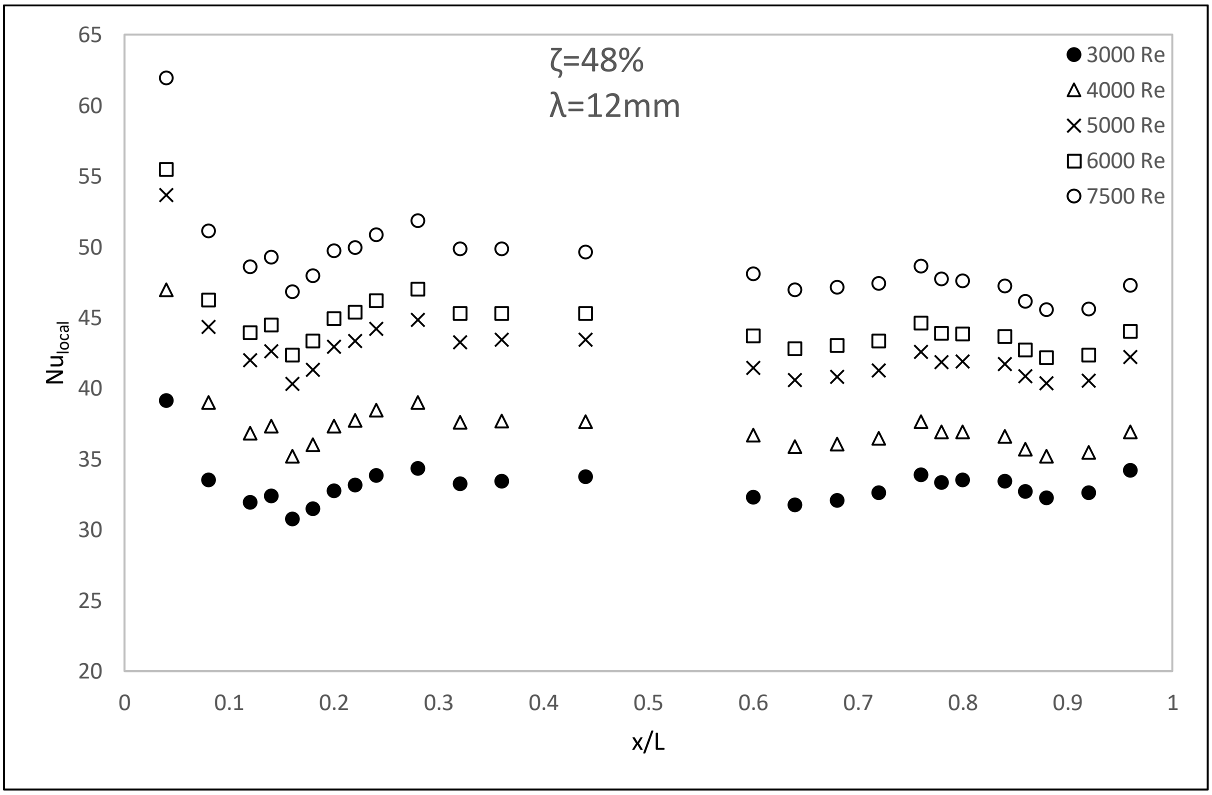

(b)

Figure 5.18: Insert 3.2 (ζ = 48%, λ = 12 mm) test section centreline local Nusselt number with two walls heated for Reynolds number range: (a) 400 < Re < 2000 and (b) 3000 < Re < 7500

5.5 Local Nusselt Number - One Wall Heat Transfer

The Nusselt number is calculated from the wall temperatures measured at the thermocouple locations show in Figure 3.5. Only one wall is electrically heated as described in Section 3.4. The heat flux on the heated wall increases with the Reynolds number to maintain a reasonable temperature difference between the walls and the air. The difference in temperature between the heated wall and free stream, ($T_{w,x} – T_{m,x}$) is maintained at approximately 15 °C. The heat flux is controlled so that the wall temperature does not exceed 60 °C to avoid excessive thermal stresses and melting of the plastic components of the test sections.

The local Nusselt number is calculated at 25 locations on the test section centreline at regular intervals over the range $0 < x/L < 1$. The local Nusselt number plots for the one wall heating experiments are shown in Figure 5.19 to Figure 5.24. There will be no comparisons in the local and average Nusselt numbers between the two wall heating and one wall heating case as the thermal boundary layers as well as the intended applications of two cases are different.

5.5.1 Inserts 1.1 and 1.2

The local Nusselt numbers, Nu_{local} along the test section for the inserts with a wavelength of $\lambda = 20$ mm (ζ = 68%, 48%) is shown in Figure 5.19 and Figure 5.20 below. The local Nusselt number plots are divided into subplots to clearly show the effects of laminar, transition and turbulent flow regimes of inlet flow Re. Figure 5.19 and Figure 5.20 show an increase in the local Nusselt number with the increase in the Reynolds number due to the increase in the velocity and mass flow rate with the Re.

As with the two wall heating experiments the flow is observed to be thermally developed at $x/L = 0.6$ in Figure 5.19 and Figure 5.20 for all the Reynolds numbers tested with one wall heating. As previously stated in Section 5.4.1 some Nu_{local} data in the distributions in Figure 5.19 and Figure 5.20 are missing where no thermocouples in the heated endwall are present.

Comparisons between Figure 5.19 and Figure 5.20 show that the local Nusselt number for insert with $\zeta = 68$ % is approximately equal to that for insert with $\zeta = 48$ % over the range $400 < Re < 2000$ except at Re = 1000 and Re = 1400 where the local Nusselt numbers for the insert with $\zeta = 68$ % is 14 % and 20 % higher, respectively, than the lower porosity insert ($\zeta = 48$ %). Over the range $3000 < Re < 10000$ the local Nusselt number for insert with $\zeta = 48$ % is approximately 10 % to 16 % larger than that for insert with $\zeta = 68$ %. For the range $16000 < Re < 30000$ the Nusselt numbers, Nu_{Local} are similar for the two inserts. Also note that the dip in Nu_{local} distribution in both Figure 5.19 and Figure 5.20 identifying the start of the transition of the thermal boundary layer to turbulent appears at $x/L \approx 0.15$ for $Re \geq 1400$ with the one wall heating.

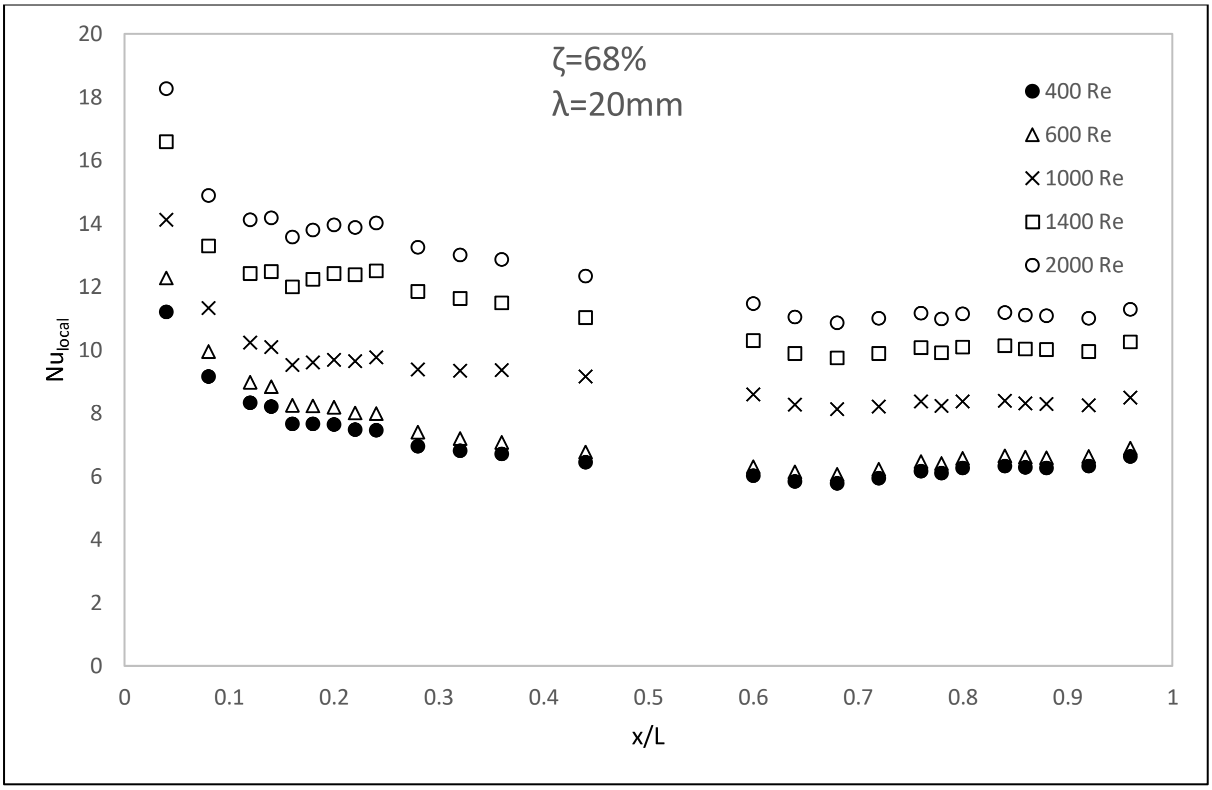

(a)

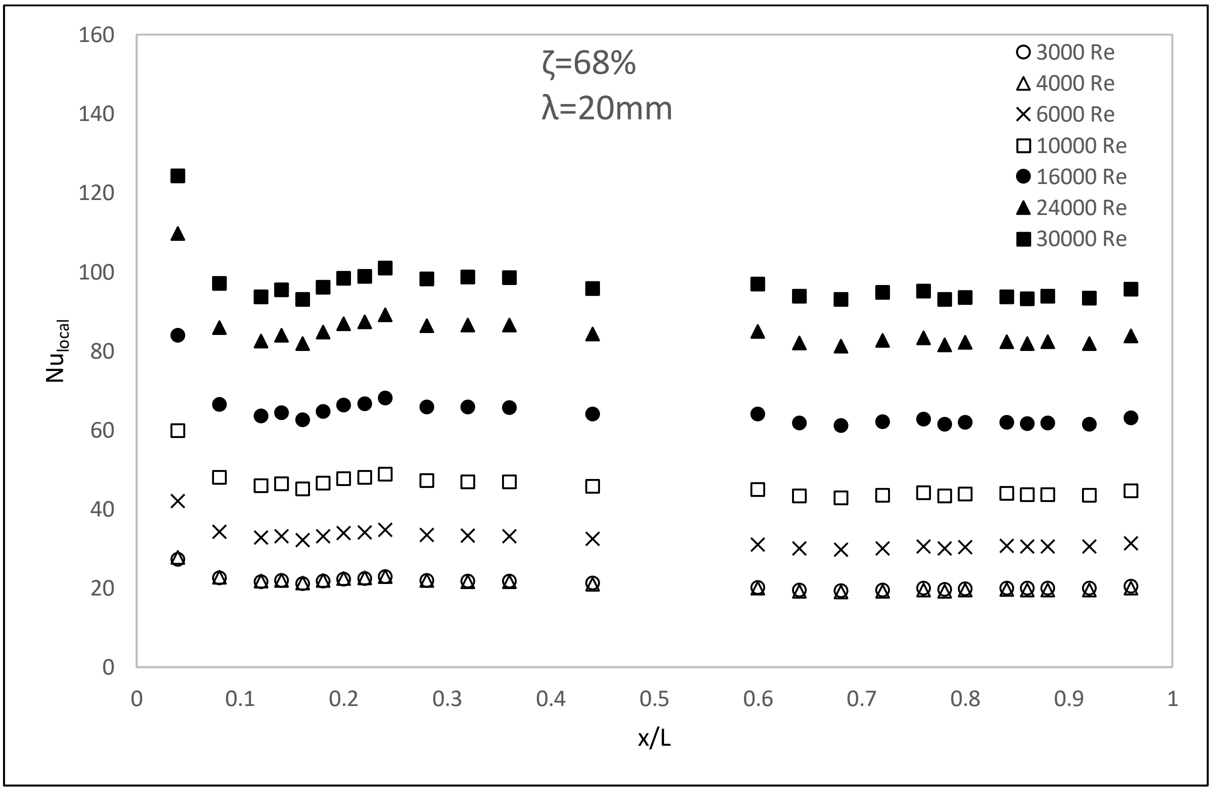

(b)

Figure 5.19: Insert 1.1 (ζ = 68%, λ = 20 mm) test section centreline local Nusselt number with one wall heated for Reynolds number range: (a) 400 < Re < 2000 and (b) 3000 < Re < 30000

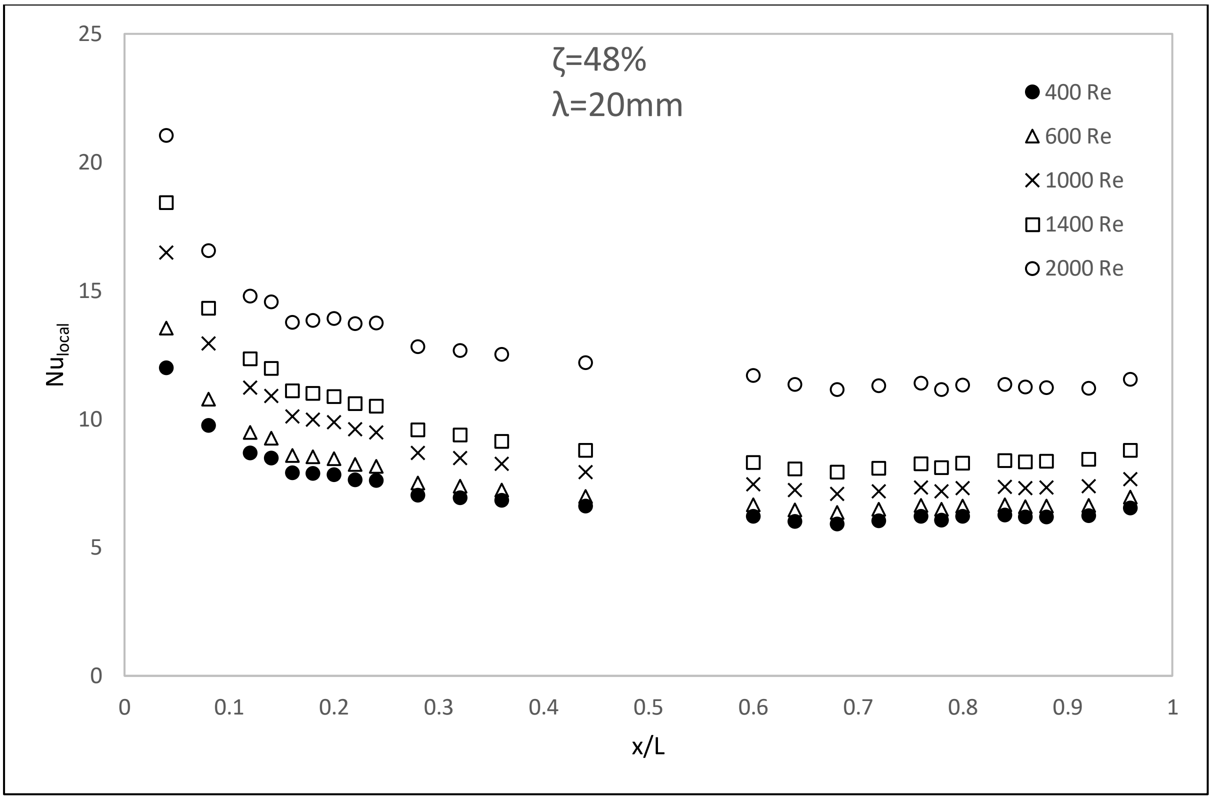

(a)

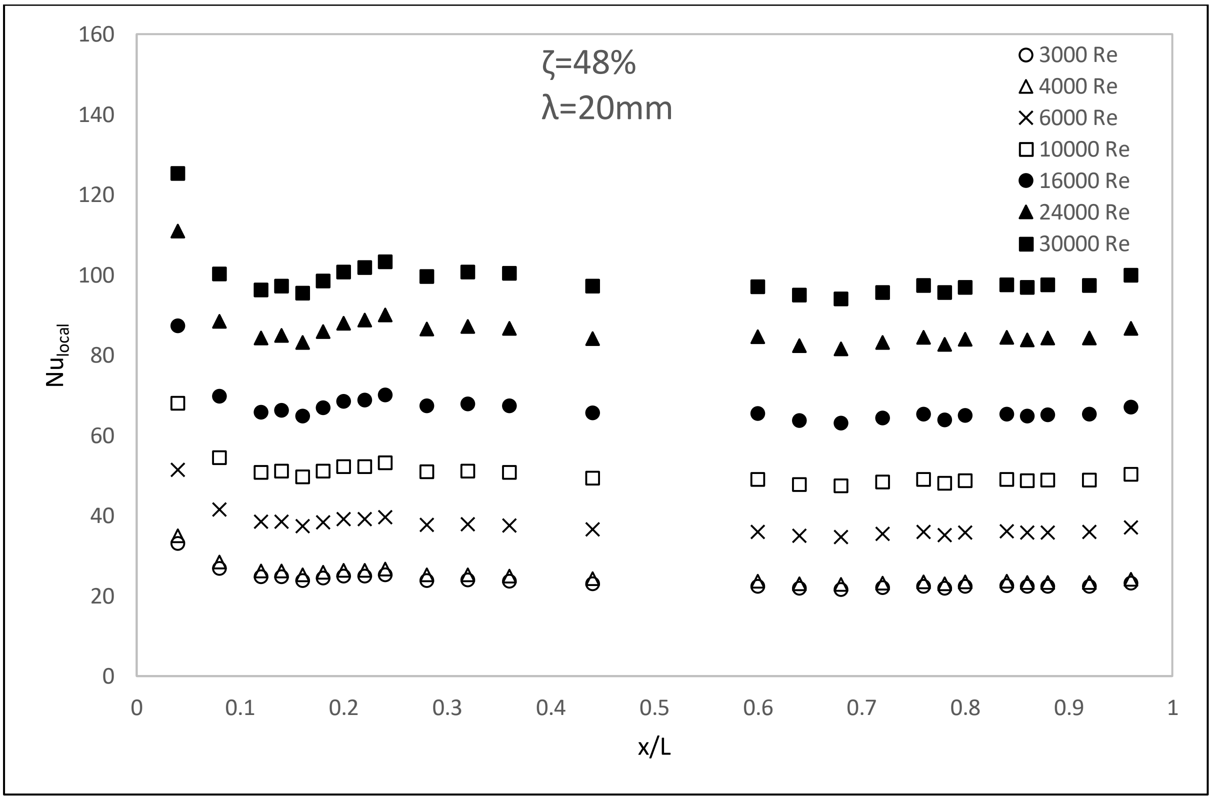

(b)

Figure 5.20: Insert 1.2 (ζ = 48%, λ = 20 mm) test section centreline local Nusselt number with one wall heated for Reynolds number range: (a) 400 < Re < 2000 and (b) 3000 < Re < 30000

5.5.2 Inserts 2.1 and 2.2

The local Nusselt numbers, Nu_{local} along the test section for the inserts with a wavelength of λ = 16 mm (ζ = 68%, 48%) is shown in Figure 5.21 and Figure 5.22. The local Nusselt number plots are divided into subplots to clearly show the effects of laminar, transition and turbulent flow regimes of inlet flow Re. Figure 5.21 and Figure 5.22 show an increase in the local Nusselt number with the increase in the Reynolds number due to the increase in the velocity and mass flow rate with the Re. The flow is observed to be thermally developed at x/L = 0.6 in Figure 5.21 and Figure 5.22 for all the Reynolds numbers tested with one wall heating.

Comparison between Figure 5.21 and Figure 5.22 shows that the local Nusselt number for the insert with ζ = 48 % is always higher than that for insert with ζ = 68 % over the range 400 < Re < 30000 except at Re = 1000. The most notable difference in the local Nusselt numbers is calculated as 13 % and 17 % at Re = 16000 and Re = 24000 respectively. The dip in Nu_{local} distribution in both Figure 5.21 and Figure 5.22 identifying the start of the transition of the thermal boundary layer to turbulent appears at x/L ≈ 0.15 for Re ≥ 1400 with the one wall heating.

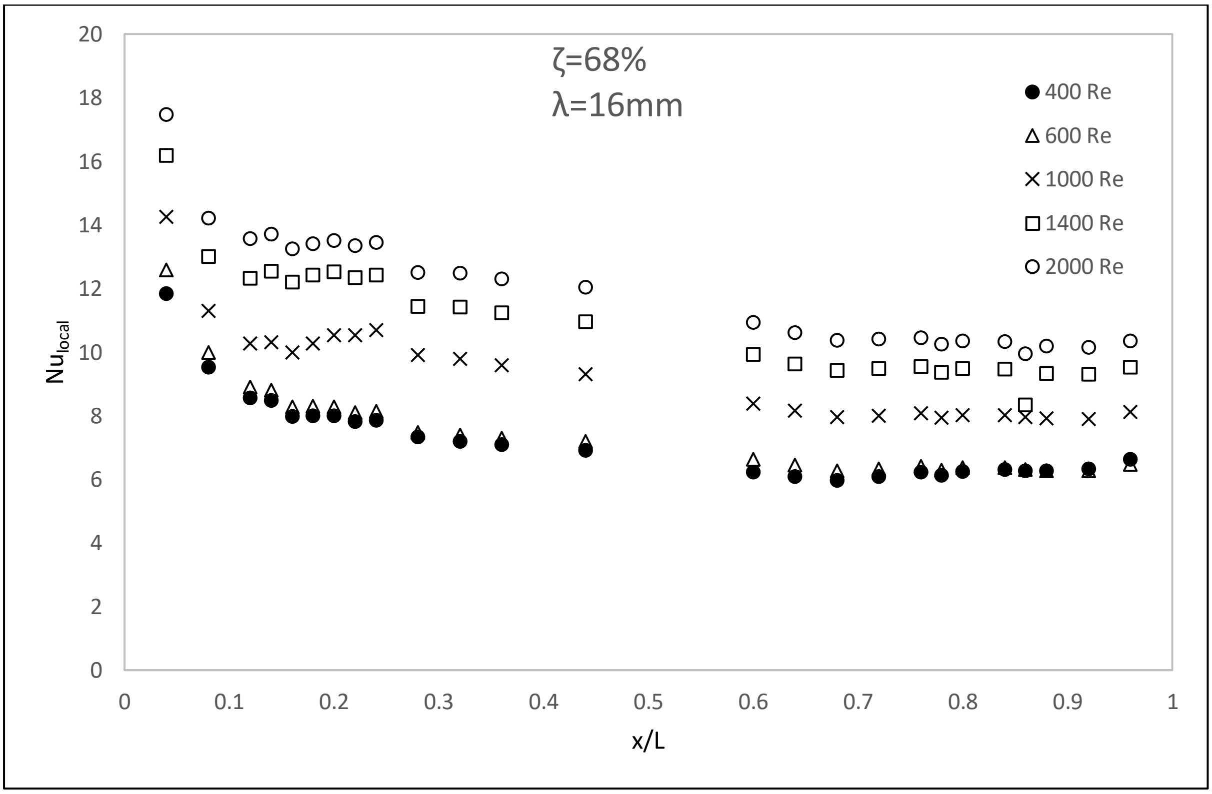

(a)

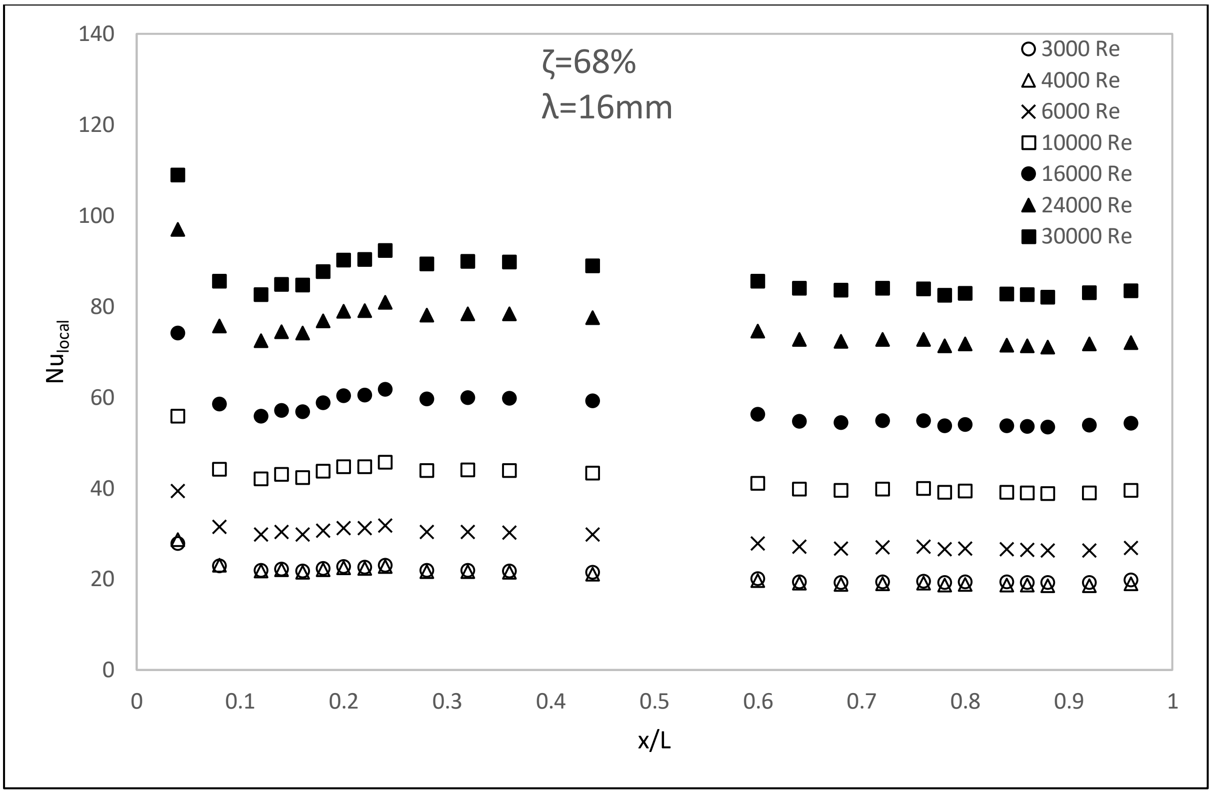

(b)

Figure 5.21: Insert 2.1 (ζ = 68%, λ = 16 mm) test section centreline local Nusselt number with one wall heated for Reynolds number range: (a) 400 < Re < 2000 and (b) 3000 < Re < 30000

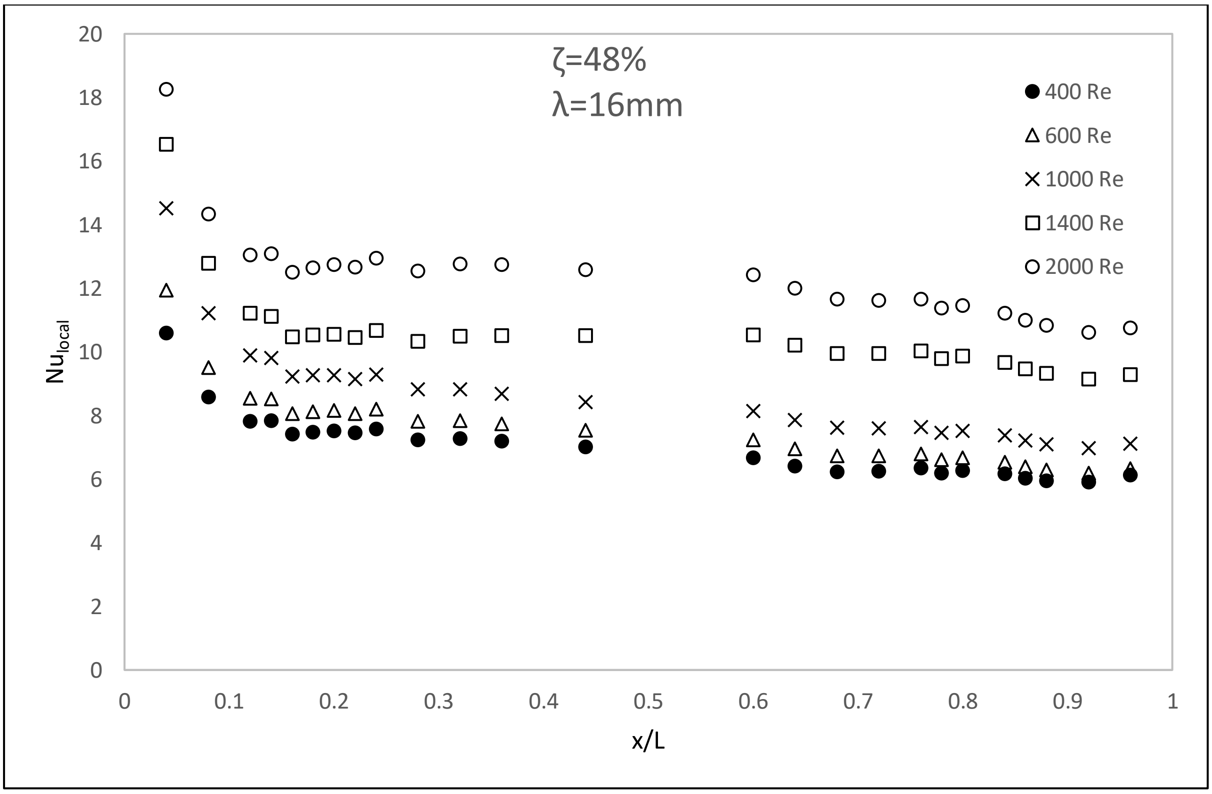

(a)

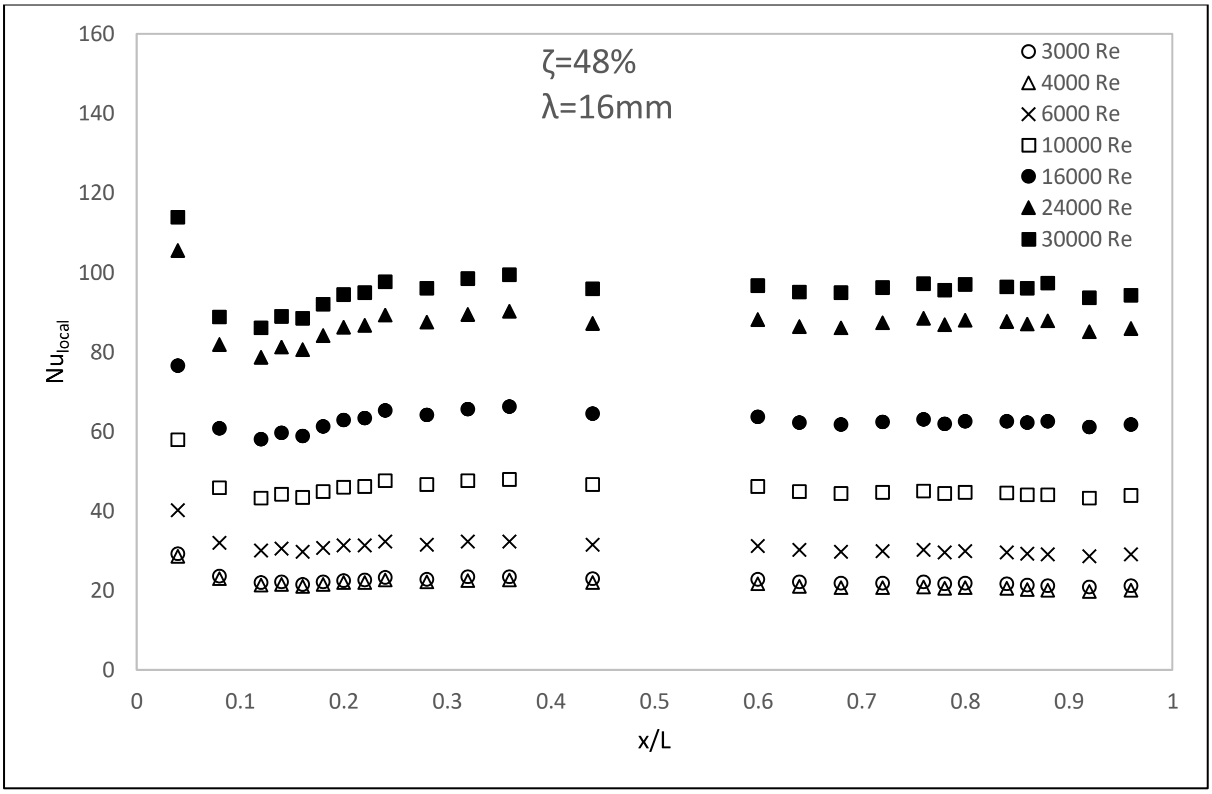

(b)

Figure 5.22: Insert 2.2 (ζ = 48%, λ = 16 mm) test section centreline local Nusselt number with one wall heated for Reynolds number range: (a) 400 < Re < 2000 and (b) 3000 < Re < 30000

5.5.3 Inserts 3.1 and 3.2

The local Nusselt numbers, Nu_{local} along the test section for the inserts with a wavelength of λ = 12 mm (ζ = 68%, 48%) is shown in Figure 5.23 and Figure 5.24 below. The local Nusselt number plots are divided into subplots to clearly show the effects of laminar, transition and turbulent flow regimes of inlet flow Re. Figure 5.23 and Figure 5.24 show an increase in the local Nusselt number with the increase in the Reynolds number due to the increase in the velocity and mass flow rate with the Re. The flow is observed to be thermally developed at x/L = 0.6 in Figure 5.23 and Figure 5.24 for all the Reynolds numbers tested with one wall heating.

Comparison between Figure 5.23 and Figure 5.24 shows that the local Nusselt number for insert with ζ = 48 % is always higher than that for insert with ζ = 68 % over the range 400 < Re < 30000. The difference in the local Nusselt numbers between the two inserts is small and ranges between 2 % and 5 % over the Reynolds number range tested. The dip in Nu_{local} distribution in Figure 5.23 identifies the start of the transition of thermal boundary layer to turbulent appears at x/L ≈ 0.15 for Re ≥ 1000 with the one wall heating.

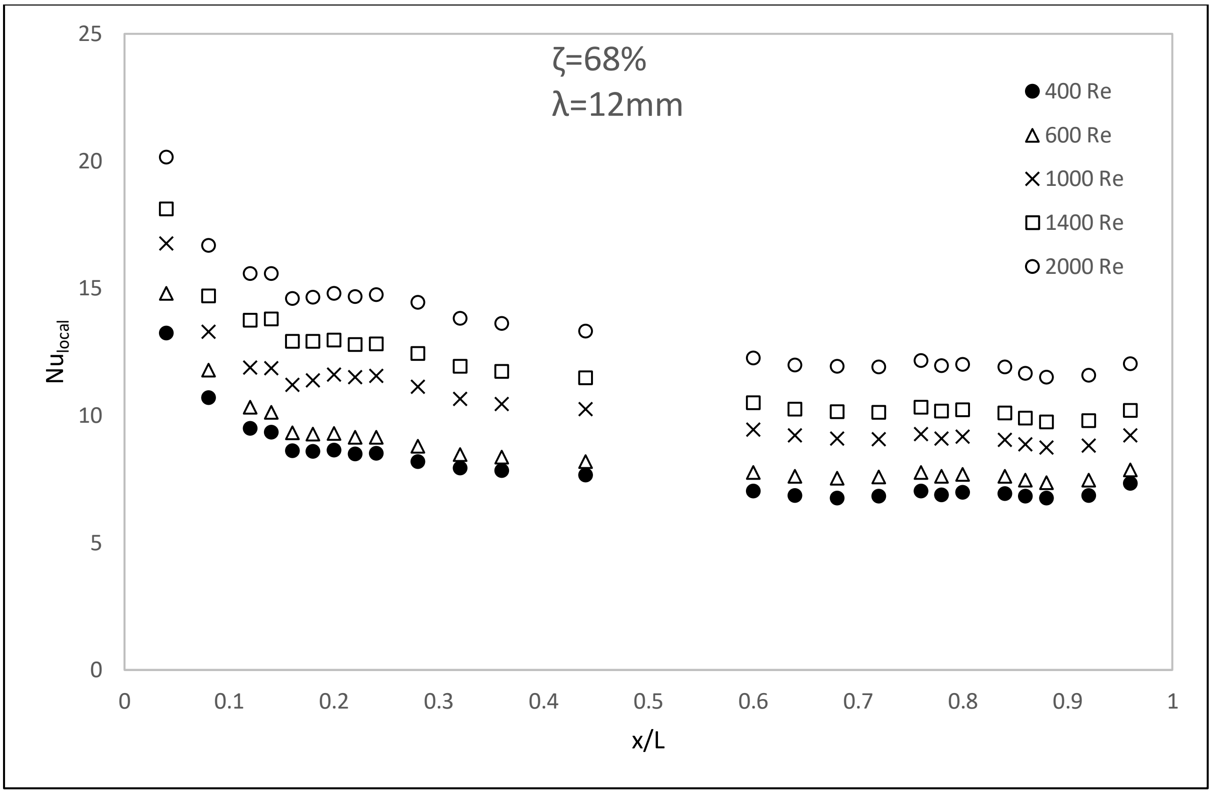

(a)

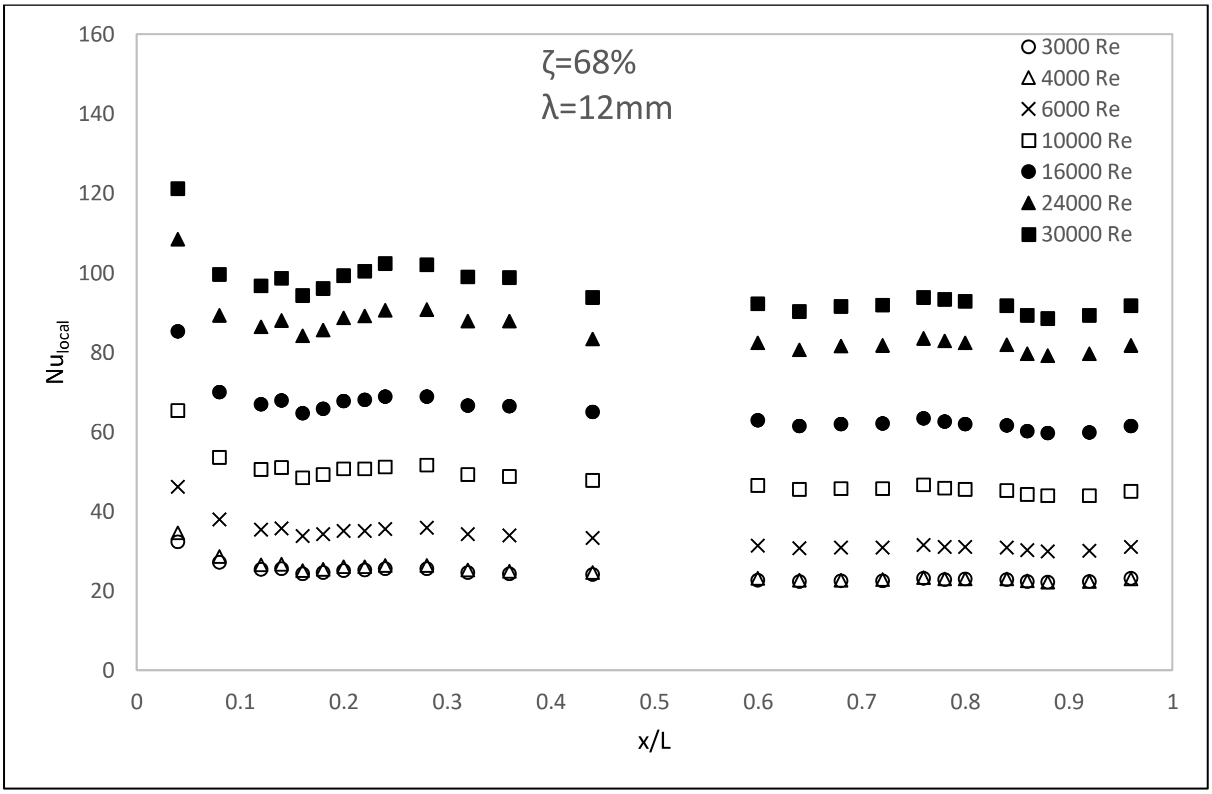

(b)

Figure 5.23: Insert 3.1 (ζ = 68%, λ = 12 mm) test section centreline local Nusselt number with one wall heated for Reynolds number range: (a) 400 < Re < 2000 and (b) 3000 < Re < 30000

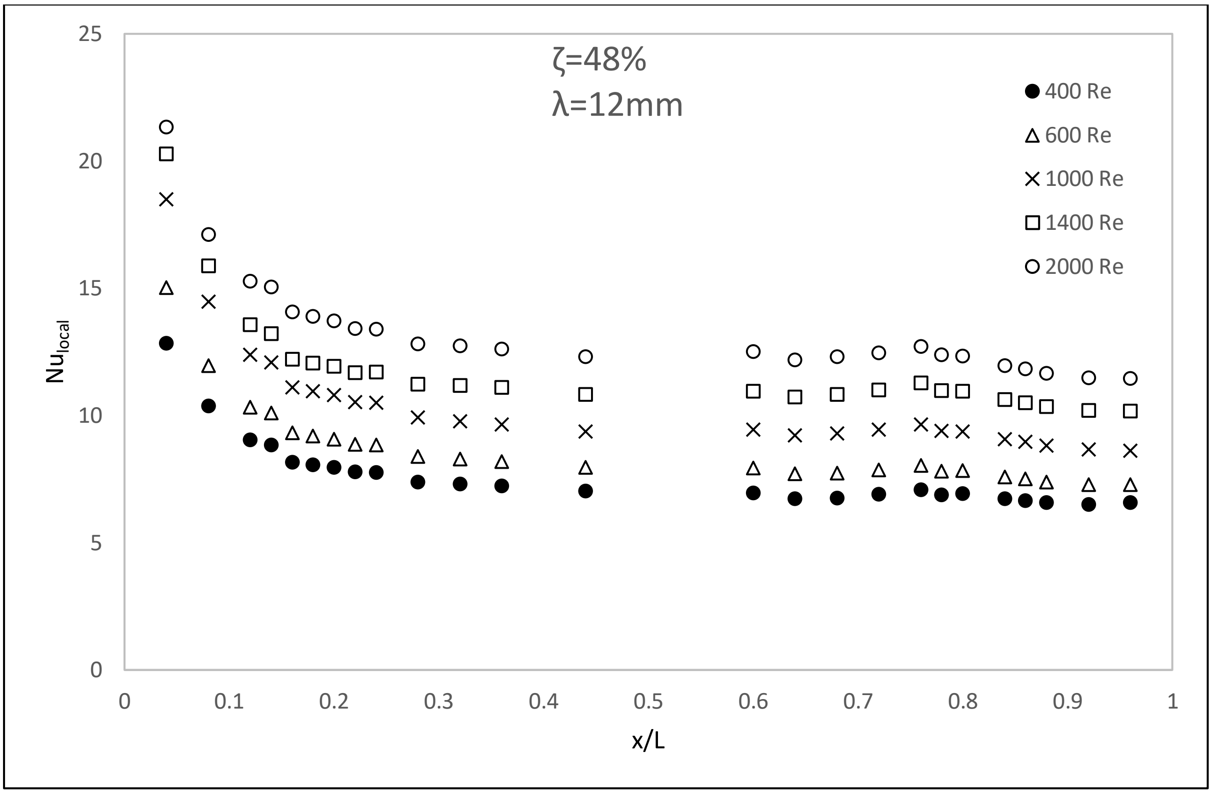

(a)

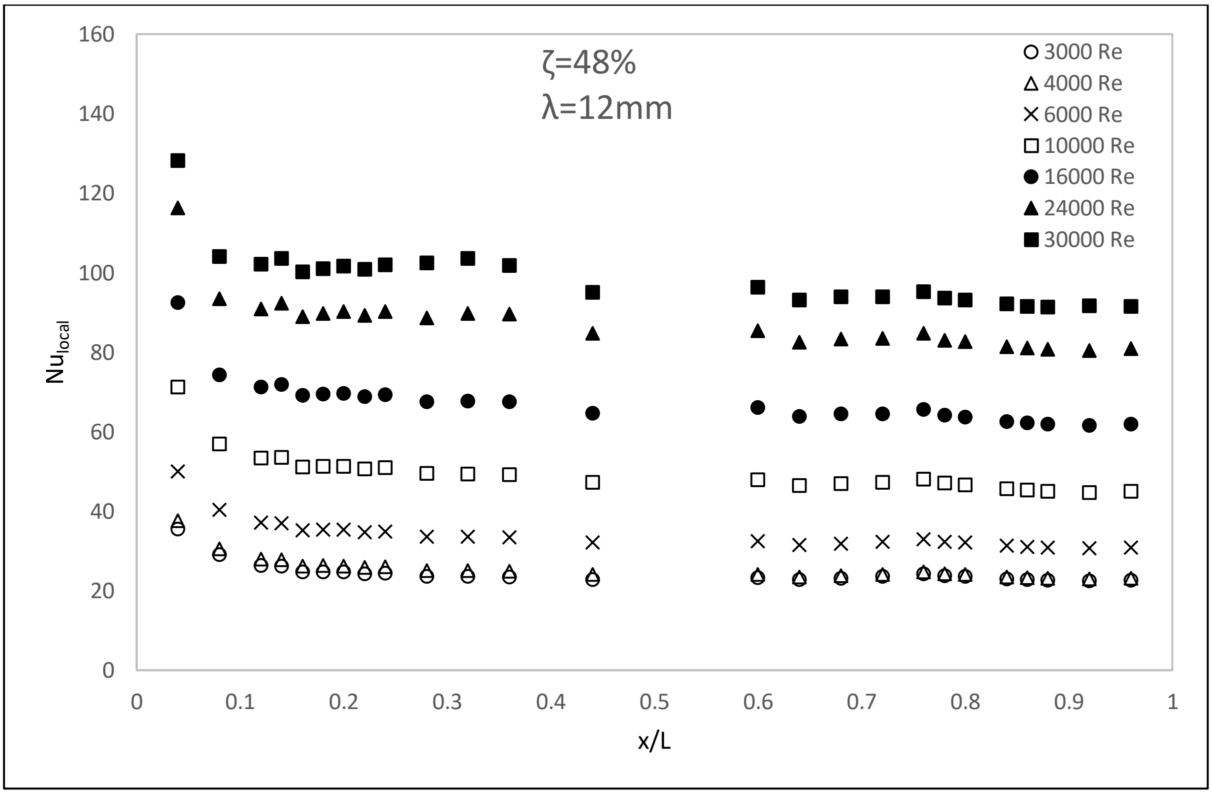

(b)

Figure 5.24: Insert 3.2 (ζ = 48%, λ = 12 mm) test section centreline local Nusselt number with one wall heated for Reynolds number range: (a) 400 < Re < 2000 and (b) 3000 < Re < 30000

5.6 Average Nusselt Numbers - Two Wall Heat Transfer

The average Nusselt number plots for the two wall heating scenario are shown in Figure 5.25 and Figure 5.27 for the inserts with ζ = 68 % and ζ = 48 %, respectively, as the Reynolds number varies. The average Nusselt number, Nu_{avg} is calculated by averaging the local Nusselt numbers, Nu_{local} in the thermally fully developed region between x/L = 0.6 and x/L = 0.92. The conductional losses through the test section insulation are accounted for in the local and average Nusselt number calculations as shown in Section 3.4. The conductional losses are found to be small and in the region of 1 W to 2.6 W (2.2 - 3.5 % of the total heat input) depending on the wall temperature of the test section. The axial conductional losses along the direction of flow in the test section is determined to be negligible [14].

The average Nusselt number ratios are shown in Figure 5.26 and Figure 5.28 as the Re varies. The Nusselt number ratio, Nu/Nu_0 is calculated by dividing the average Nusselt numbers of Figure 5.25 and Figure 5.27 by the experimental Nusselt numbers, Nu_0 in the smooth channel at the corresponding Re shown in Section 4.5. The data in of Figure 5.25 and Figure 5.27 are important as a value of Nu/Nu_0 greater than 1.0 is always desirable with the insert. The ratio $Nu/Nu_0 > 1.0$ indicates the enhancement of the convection heat transfer coefficient or the heat transfer rate in the channel when an insert is employed at a particular mass flow rate and at a particular wall-to-flow temperature difference, (T_w-T_m). For a given flow rate, heat load, and wall-to-flow temperature difference, the ratio $Nu/Nu_0 > 1.0$ may further imply that the heater surface area or heat exchanger size can be reduced as the insert is employed in the heat transfer channel. For example, using the value of $Nu/Nu_0 = 1.7$ at Re = 7600 for the insert (ζ = 68%, λ = 16 mm) of Figure 5.26 (a) the heat transfer surface area of the channel can be reduced by a factor of 0.41 or by 41% when the insert is employed in the channel at Re = 7600 and at the equivalent values for $(\dot{Q},\, T_w - T_m)$. The heat exchanger size or volume is thus reduced. The volume of heat exchanger per unit of heat load is an important design parameter for the heat exchanger.

5.6.1 Inserts 1.1, 2.1 and 3.1 (Effects of Wavelength, λ at ζ = 68%)

The average Nusselt numbers, Nu_{avg} for inserts with ζ = 68 % are shown in Figure 5.25 below. The average Nusselt number is observed to increase with the increase in the Reynolds number. Between 400 < Re < 1000 the average Nusselt number for inserts with λ = 20 mm and λ = 16 mm is of a similar value while those for the insert with λ = 12 mm is approximately 50 % larger. Between 2000 < Re < 3000 the average Nusselt numbers for all three inserts increase by 50 - 70 %. For 3000 < Re < 35000 the average Nusselt numbers for all three inserts increase linearly with the Re as the velocity and flow rate increases in the channel.

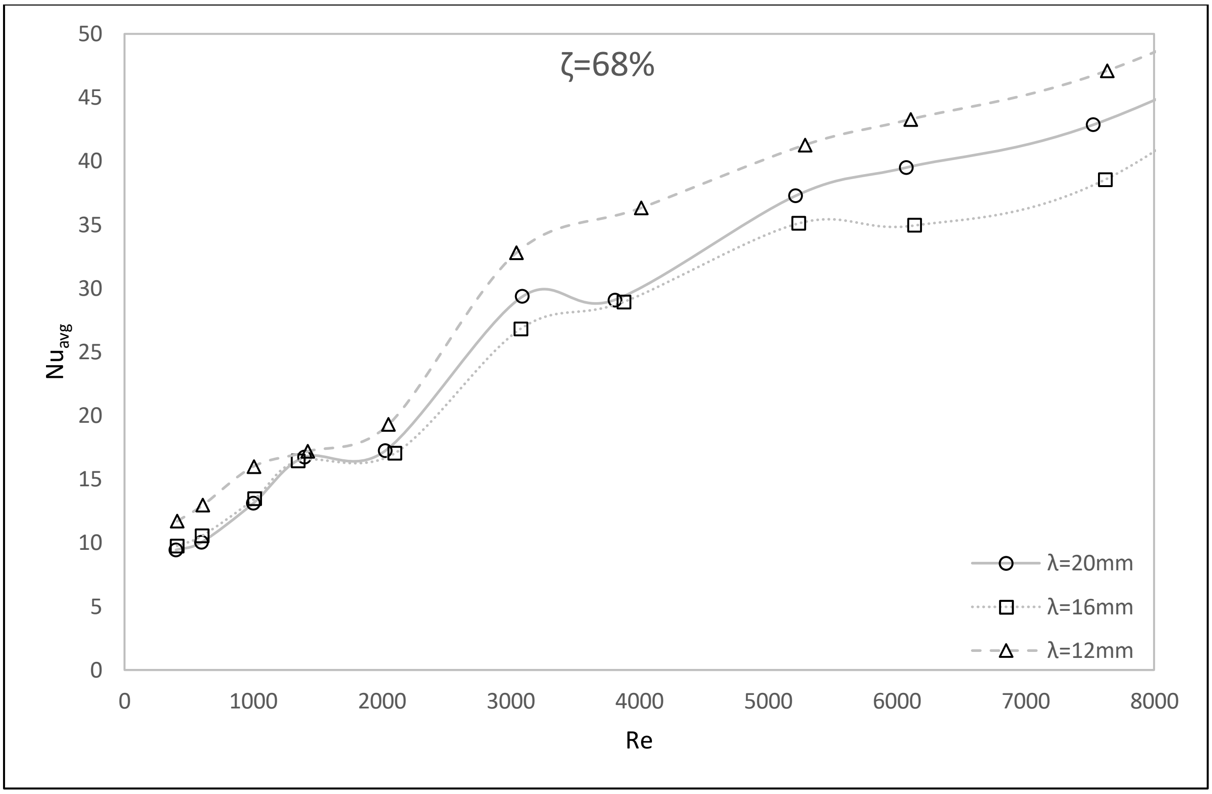

(a)

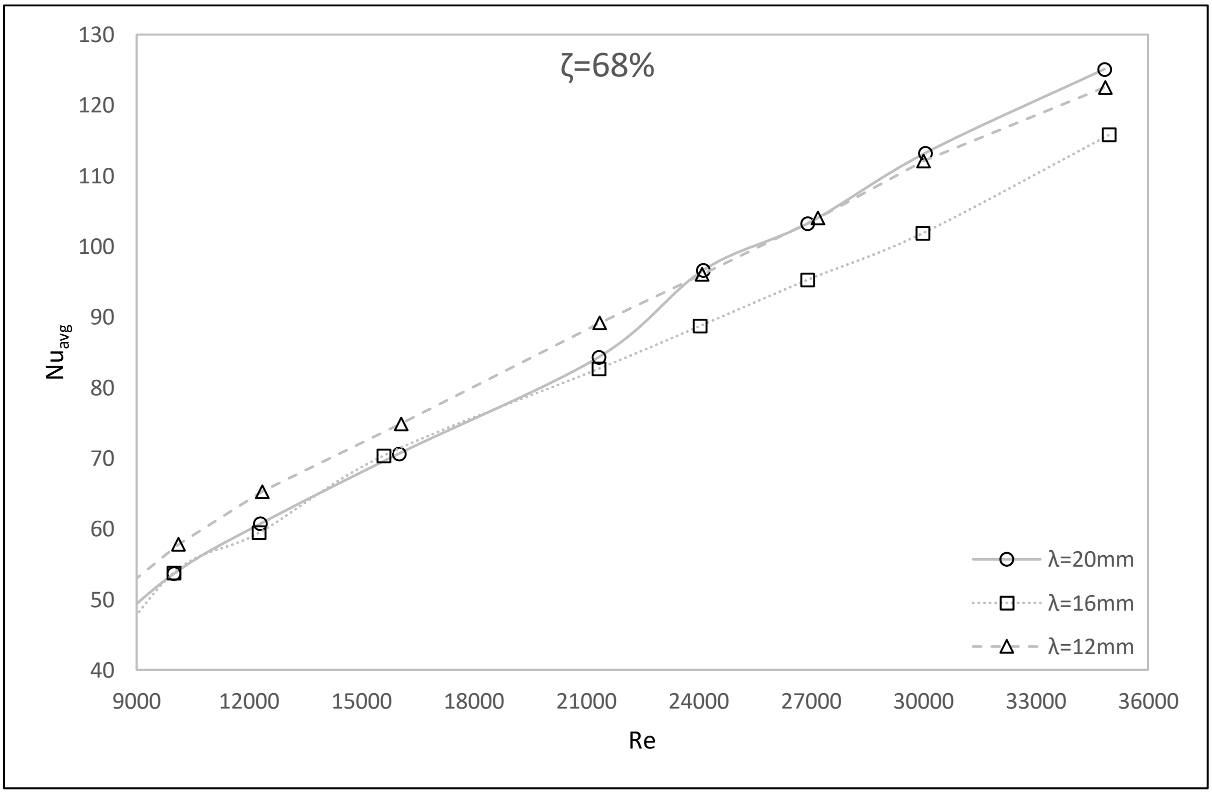

(b)

Figure 5.25: Average Nusselt numbers, Nu_{avg} for inserts with ζ = 68% with two walls heated for Reynolds number range: (a) 400 < Re < 7500 and (b) 10000 < Re < 35000

The Nu/Nu_0 distributions against the Re for the inserts with ζ = 68 % are shown in Figure 5.26. As the experimental smooth channel Nusselt numbers closely match those of the analytical data as shown in Section 4.5 there is little to no difference in dividing the insert data by the experimental or analytical smooth channel result. In the absence of analytical data in the transitional flow regime the insert data is divided by the experimental smooth channel average Nusselt number.

The Nusselt number ratio in Figure 5.26 is always larger than one as the local turbulence in the test section created by the insert enhances the local heat transfer coefficient and heat transfer rate. The Nusselt number ratio for all three inserts is observed to increase between 400 < Re < 3000 and then decrease as the Re increases further. Between 600 < Re < 1000 the Nusselt number ratio increases by approximately 30 % for three inserts. Between 2000 < Re < 3000 the Nusselt number increase by a further 15 % to reach a maximum value for all three inserts tested. The Nusselt number ratio is the largest for the insert with λ = 12 mm.

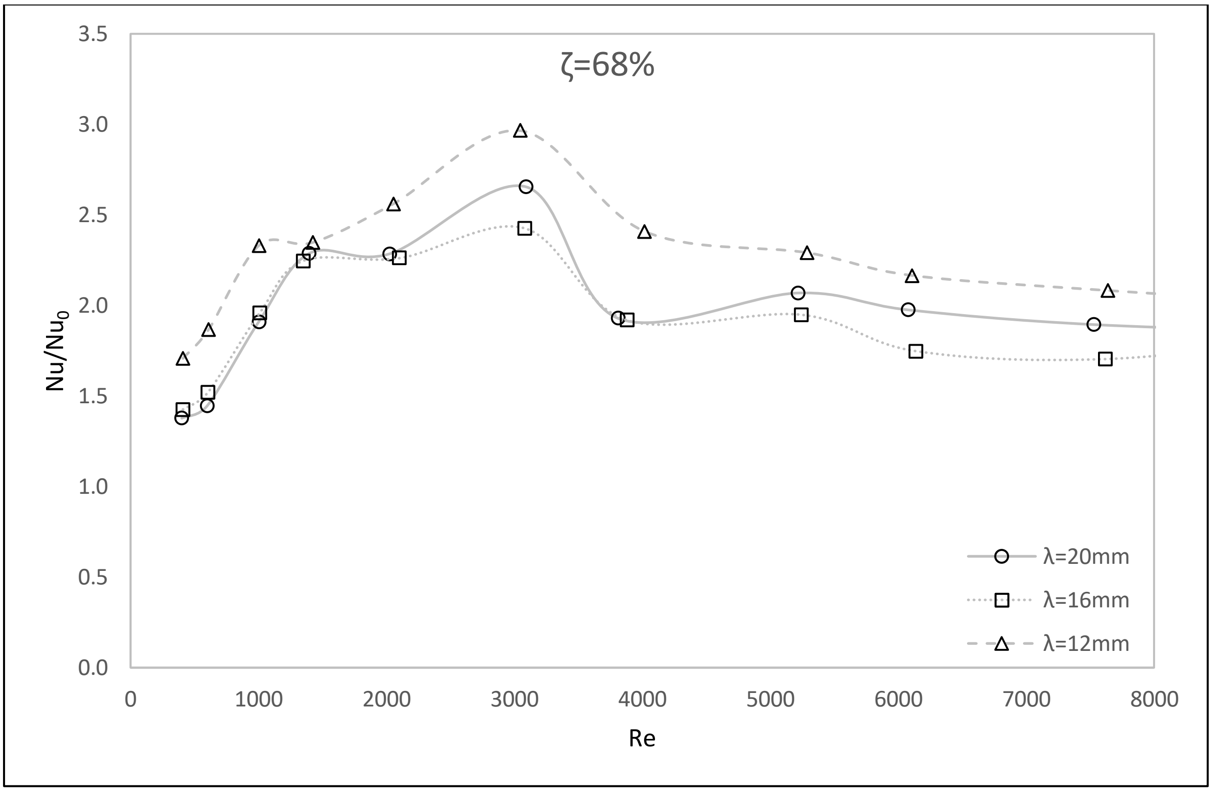

(a)

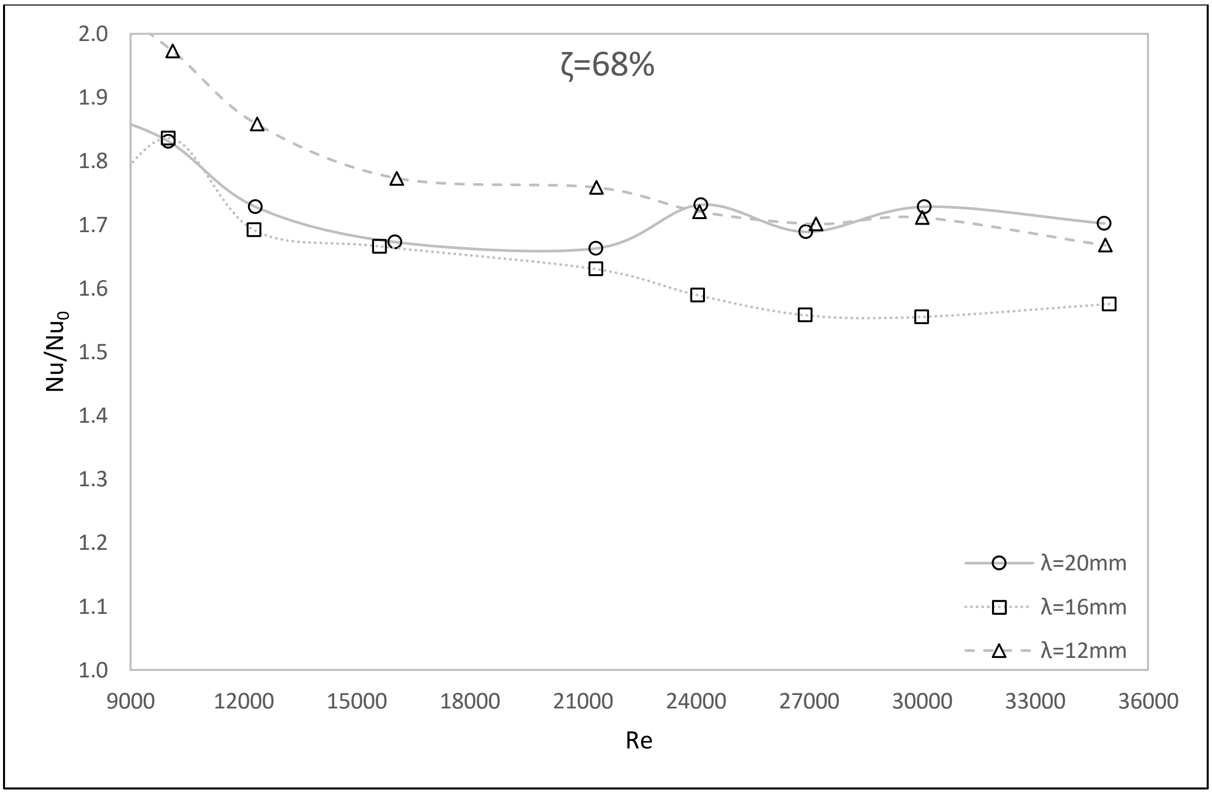

(b)

Figure 5.26: Average Nusselt number ratios, Nu/Nu_0 for inserts with ζ = 68 % with two walls heated for Reynolds number range: (a) 400 < Re < 7500 and (b) 10000 < Re < 35000

5.6.2 Inserts 1.2, 2.2 and 3.2 (Effects of Wavelength, λ at ζ = 48%)

The average Nusselt numbers for inserts with ζ = 48 % are shown in Figure 5.27. The average Nusselt number is observed to increase with the increase in the Reynolds number. Between 400 < Re < 2000 the average Nusselt numbers increases linearly. Between 2000 < Re < 3000 the average Nusselt numbers for all three inserts increase by approximately 75 %. For 4000 < Re < 35000 the average Nusselt numbers for all three inserts increase linearly as the velocity and flow rate increases in the channel with the Re. The average Nusselt number is greatest for insert with λ = 12 mm.

The average Nusselt number ratios for inserts with ζ = 48 % are shown in Figure 5.28. The Nusselt number ratio is always larger than one as the local turbulence in the test section created by the insert enhances the local heat transfer coefficient and heat transfer rate. The Nusselt number ratio for all three inserts is observed to increase between 400 < Re < 3000 to reach a maximum value and then decrease as the Re increases further. Unlike the inserts with ζ = 68 % the average Nusselt number ratio does not increase rapidly in the range of 400 < Re < 3000 and increases with a linear gradient with the exception of the insert with λ = 16 mm. For the insert with λ = 16 mm the Nusselt number ratio increases by 32 % between 1400 < Re < 2000 and by a further 18 % between 2000 < Re < 3000. The Nusselt number ratio is greatest for the insert with λ = 12 mm.

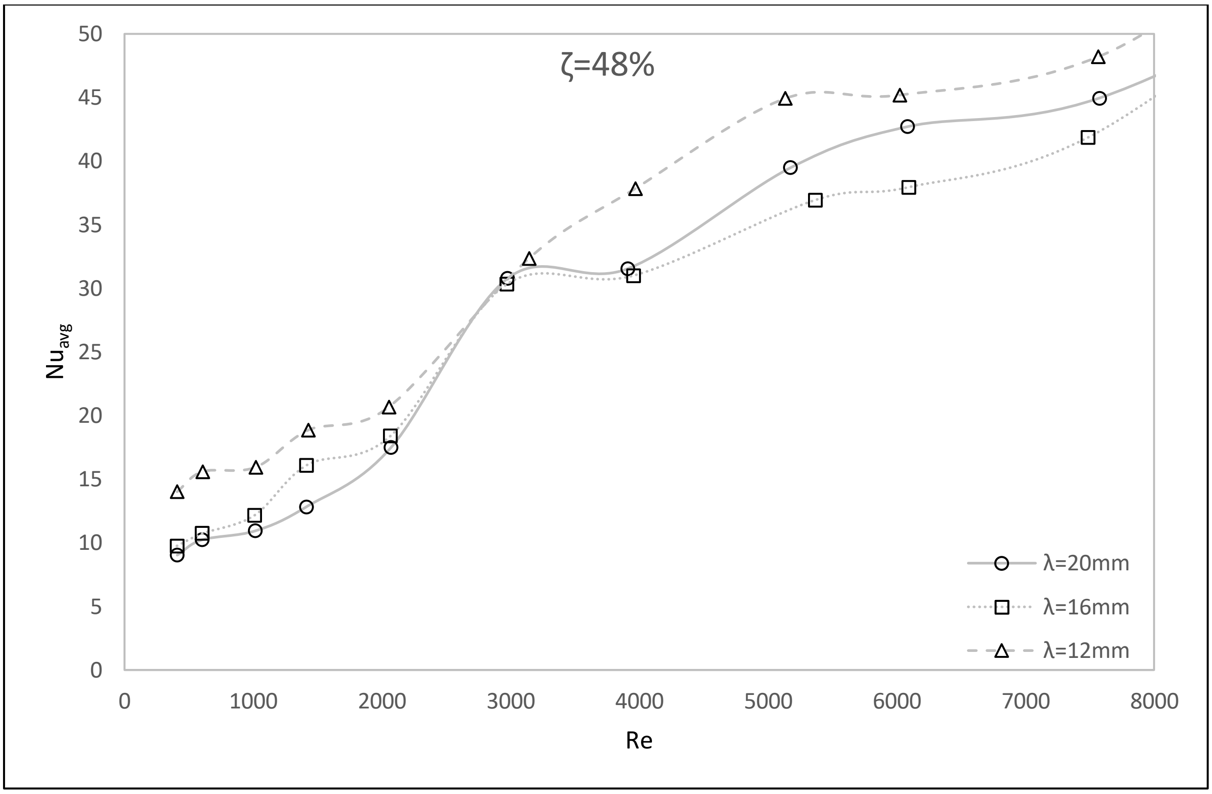

(a)

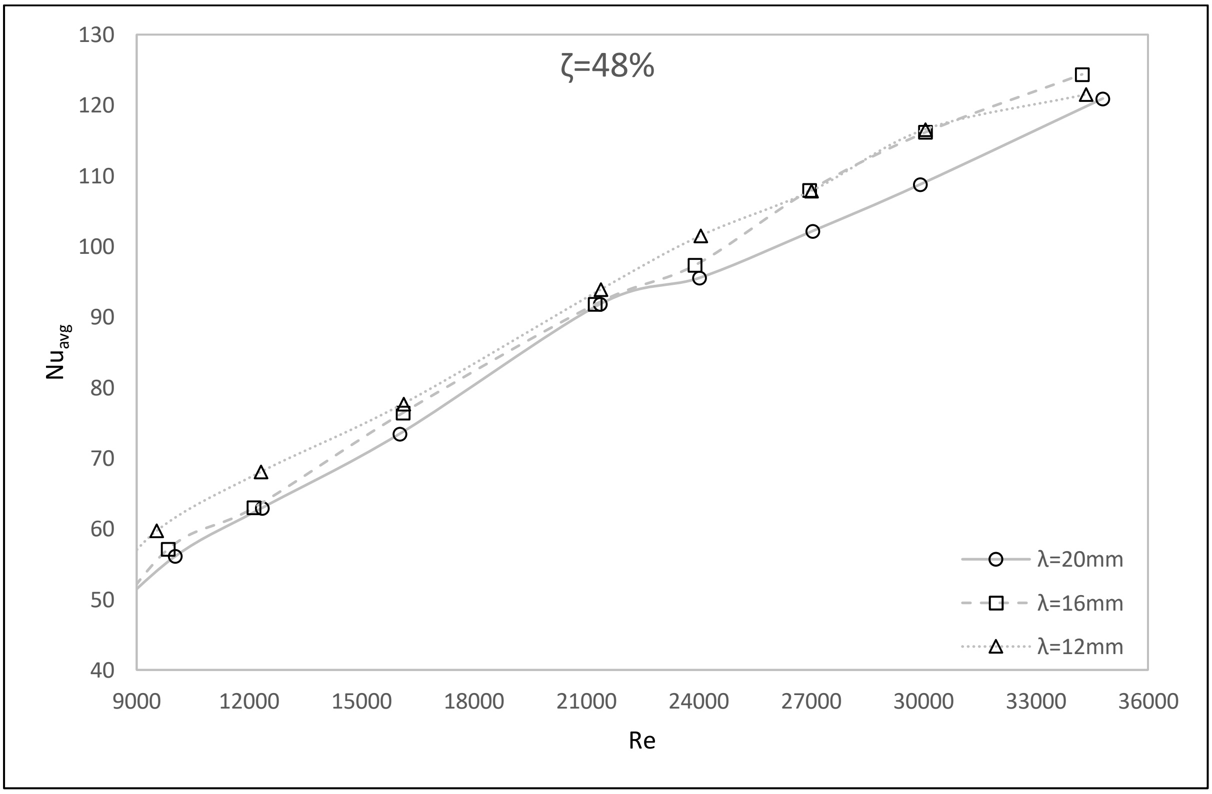

(b)

Figure 5.27: Average Nusselt numbers, Nu$_{avg}$ for inserts with ζ = 48 % with two walls heated for Reynolds number range: (a) 400 < Re< 7500 and (b) 10000 < Re < 35000

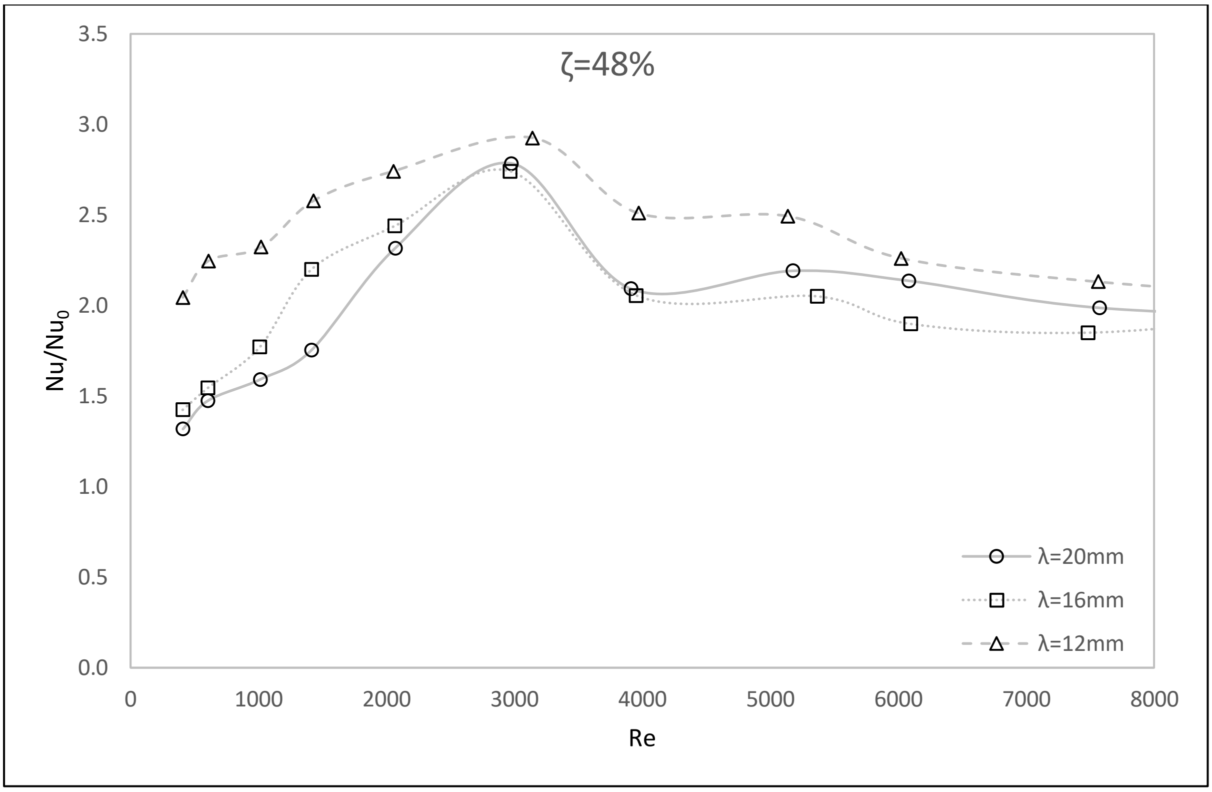

(a)

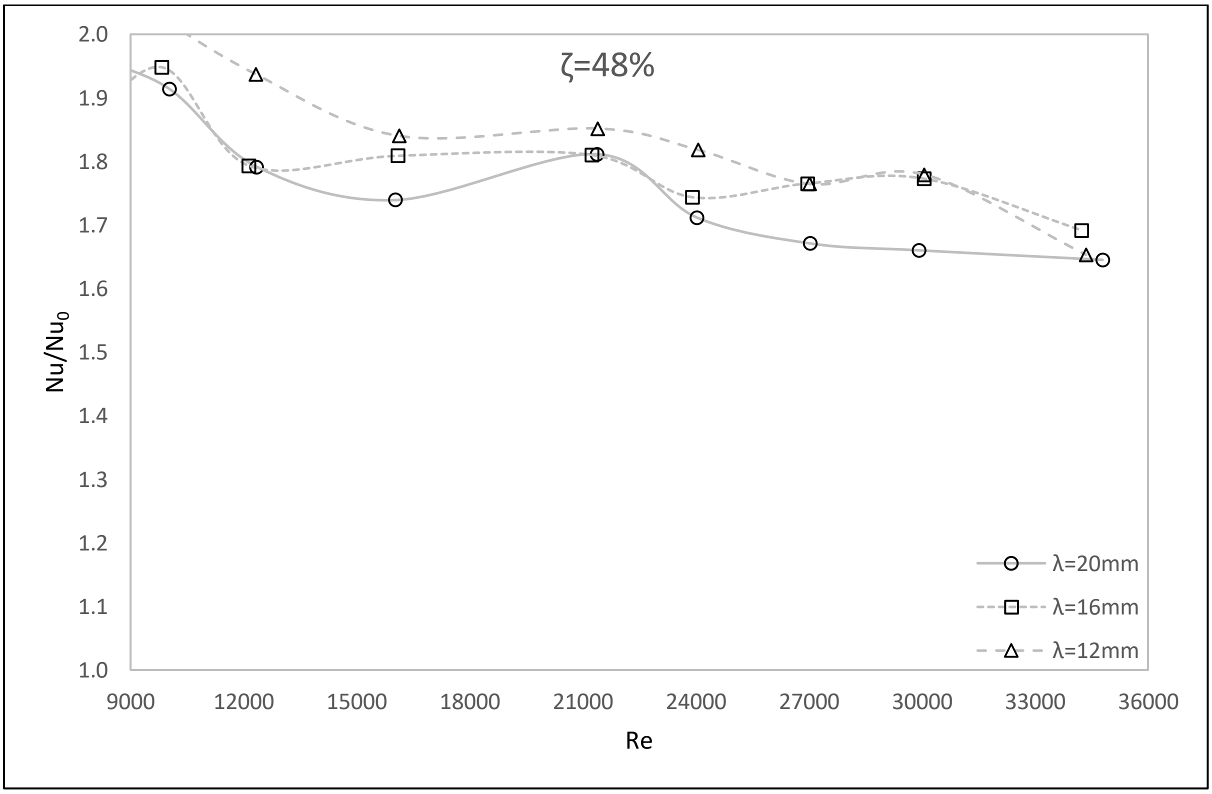

(b)

Figure 5.28: Average Nusselt number ratios, Nu/Nu₀ for inserts with ζ=48% with two walls heated for Reynolds number range: (a) 400 < Re < 7500 and (b) 10000 < Re < 35000

The Nusselt number ratio is always greater than zero indicating an increase in the heat transfer rate when any of the inserts are employed. Plots of Nu_{avg} and Nu/Nu_0 vs. Re for constant wavelength, λ are given in Figure D. 70 and Figure D. 71 in Appendix D. The inserts with ζ = 48 % have a larger Nu_{avg} and Nu/Nu_0 than the inserts with ζ = 68 % (up to 10 %) for the majority of the Reynolds numbers tested. The Nu_{avg} and Nu/Nu_0 results in Figure D. 70 and Figure D. 71 show in inverse relationship between the Nusselt number and the porosity of the insert.

The experimental Nusselt number ratio can be expressed as mathematical correlations in the form of a power equation which is a function of the Reynolds number, porosity and wavelength of the insert. The equation is given as:

$$Nu/Nu_0 = \zeta^A \left(\frac{H}{\lambda}\right)^B CRe^D \tag{5.2}$$

Where A, B, C and D are constants, H is the height of the channel in meters and ζ and λ are the porosity ranging between 0 and 1 and wavelength in meters of the insert respectively. The correlations are calculated for three Re ranges, 400 ≤ Re ≤ 3000, 4000 ≤ Re ≤ 7500 and 10000 ≤ Re ≤ 35000. The constant values for each respective Re range are given in Table 5.3.

Table 5.3: Two wall heating average Nusselt number correlations

	Re Range		
Constant	400 ≤ Re ≤ 3000	4000 ≤ Re ≤ 7500	10000 ≤ Re ≤ 35000
A	-0,06	-0,2	0,05
B	-0,6	-0,31	-0,14
C	0,24	7,55	4,41
D	0,31	-0,16	-0,089

The analytical and experimental Nusselt number ratios, Nu/Nu_0 are shown in Figure 5.29. For 400 ≤ Re ≤ 3000, 75 % of the Nu/Nu_0 values determined using the correlation are within 10 % of the experimental value and 97 % are within 15 % of the experimental value. The maximum deviation of the analytical Nu/Nu_0 from the experimental Nu/Nu_0 is 18 % for the insert with ξ = 0.68 and λ = 20 mm at Re = 1400.

For 4000 ≤ Re ≤ 7500, 92 % of the analytical Nu/Nu_0 deviate from the experimental values by 10 % or less. The maximum deviation of the analytical Nu/Nu_0 from the experimental Nu/Nu_0 is 11 % for the insert with ξ = 0.68 and λ = 16 mm at Re = 6000. For 10000 ≤ Re ≤ 35000, 100 % of the analytical Nu/Nu_0 deviate from the experimental values by 10 % or less. The maximum deviation of the analytical Nu/Nu_0 from the experimental Nu/Nu_0 is 10 % for the insert with ξ = 0.68 and λ = 16 mm at Re = 27000.

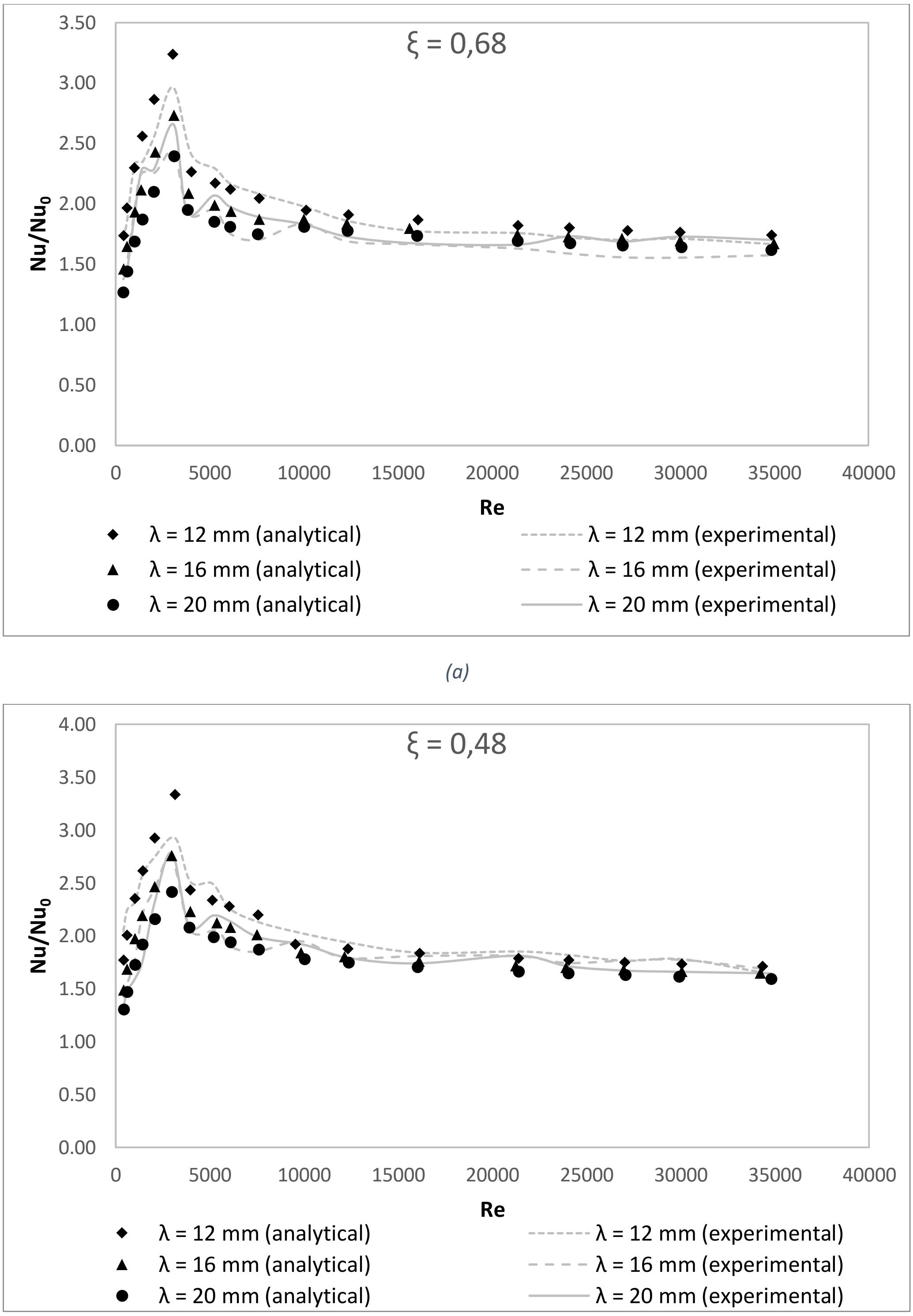

(a)

(b)

Figure 5.29: Nusselt number ratio, Nu/Nu$_0$ correlations vs. Re for (a) ξ = 0.68 and (b) ξ = 0.48

5.7 Average Nusselt Numbers - One Wall Heat Transfer

The average Nusselt number plots for the one wall heating scenario are shown in Figure 5.30 and Figure 5.32 for the inserts with ζ = 68 % and ζ = 48 % respectively. The average Nusselt number is calculated by averaging of the local Nusselt numbers in the thermally fully developed region between x/L = 0.6 and x/L = 0.92. The conductional losses through the test section insulation are accounted for in the local and average Nusselt number calculations as shown in Section 3.4. As with the two wall heating experiments the conductional losses are found be small and in the region of 2 W to 3.2 W (1.8 - 3.1 % of the total heat input) depending on the wall temperature of the test section. The axial conductional losses along the direction of flow in the test section is determined to be negligible [14].

The average Nusselt number ratios are shown in Figure 5.31 and Figure 5.33 as the Re varies. The Nusselt number ratio is calculated by dividing the average Nusselt numbers of Figure 5.30 and Figure 5.32 by the experimental Nusselt number in the smooth channel at the corresponding Re shown in Section 4.6.

5.7.1 Inserts 1.1, 2.1 and 3.1 (Effects of Wavelength, λ at ζ = 68%)

The average Nusselt numbers for inserts with ζ = 68 % are shown in Figure 5.30 below. The average Nusselt number is observed to increase with the increase in the Reynolds numbers as with the two wall heating experiments. Between 400 < Re < 2000 the average Nusselt numbers for the three inserts follow a linear trend as the Reynolds number increases. Between 2000 < Re < 3000 the average Nusselt numbers for all three inserts increase by approximately 90 %. For 4000 < Re < 30000 the average Nusselt numbers for all three inserts increase linearly.

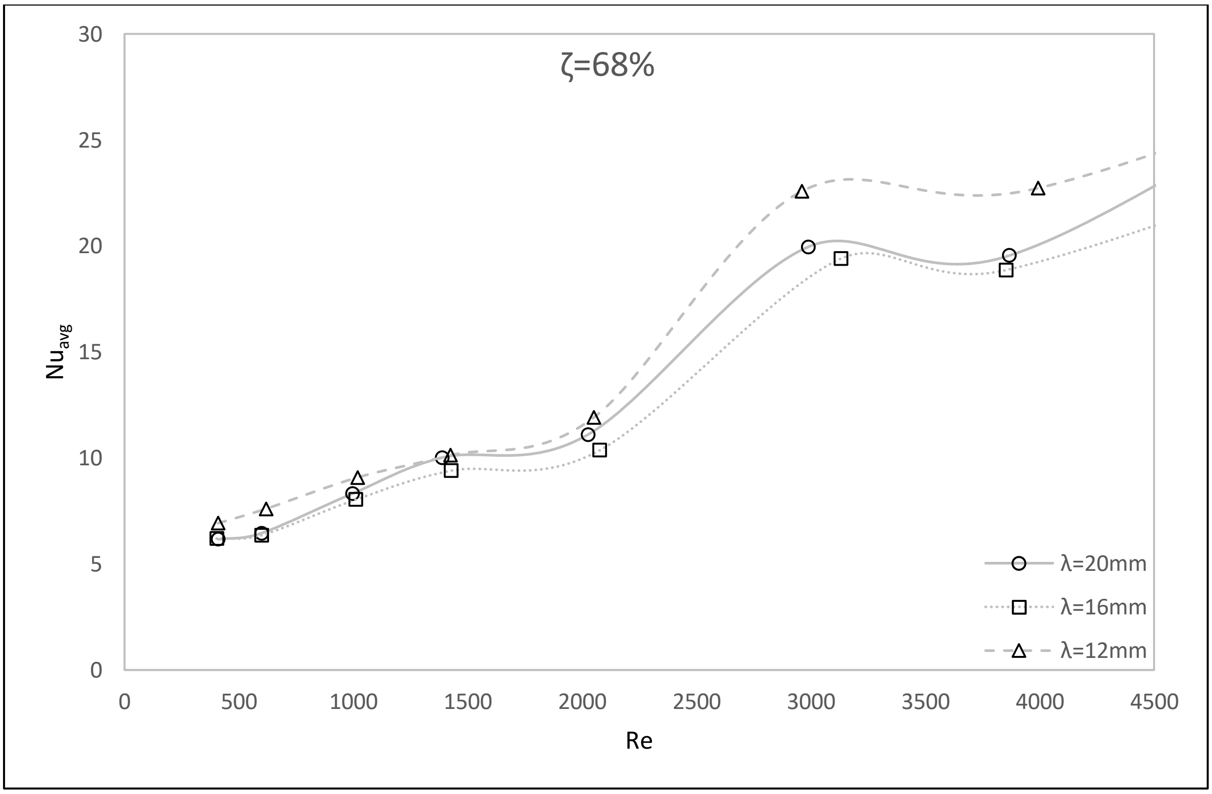

(a)

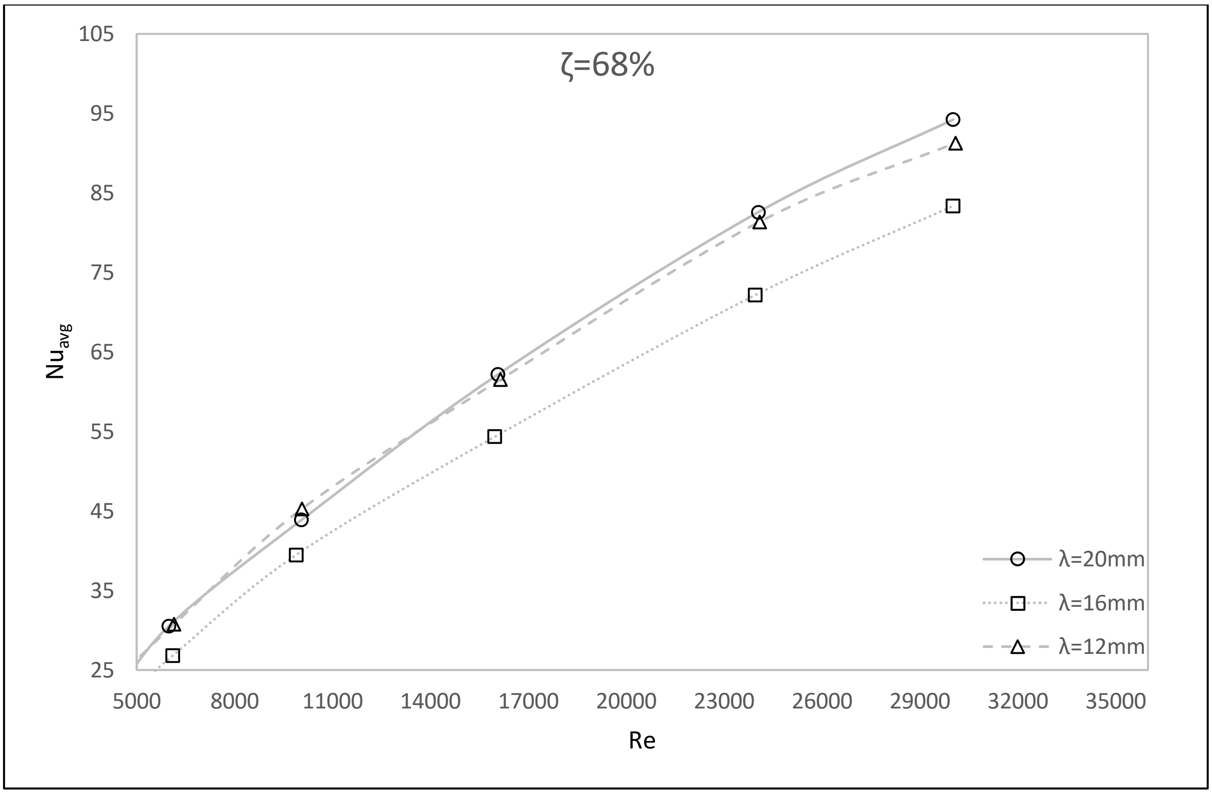

(b)

Figure 5.30: Average Nusselt numbers, Nu$_{avg}$ for inserts with ζ = 68% with one wall heated for Reynolds number range: (a) 400 < Re < 4000 and (b) 5000 < Re < 30000

The Nu/Nu$_0$ distributions against the Re for the inserts with ζ = 68 % are shown in Figure 5.31. The Nusselt number ratio is calculated to always be larger than one as with the two wall heating scenario. The Nusselt number ratio is for all three inserts increases between 400 < Re < 3000 from where the Nusselt number ratio decreases for increasing Re. Between 600 < Re < 1000 the Nusselt number ratio increases by approximately 20 %. Between 2000 < Re < 3000 the Nusselt number ratios increase by a further 30 % to reach a maximum value for all three inserts tested.

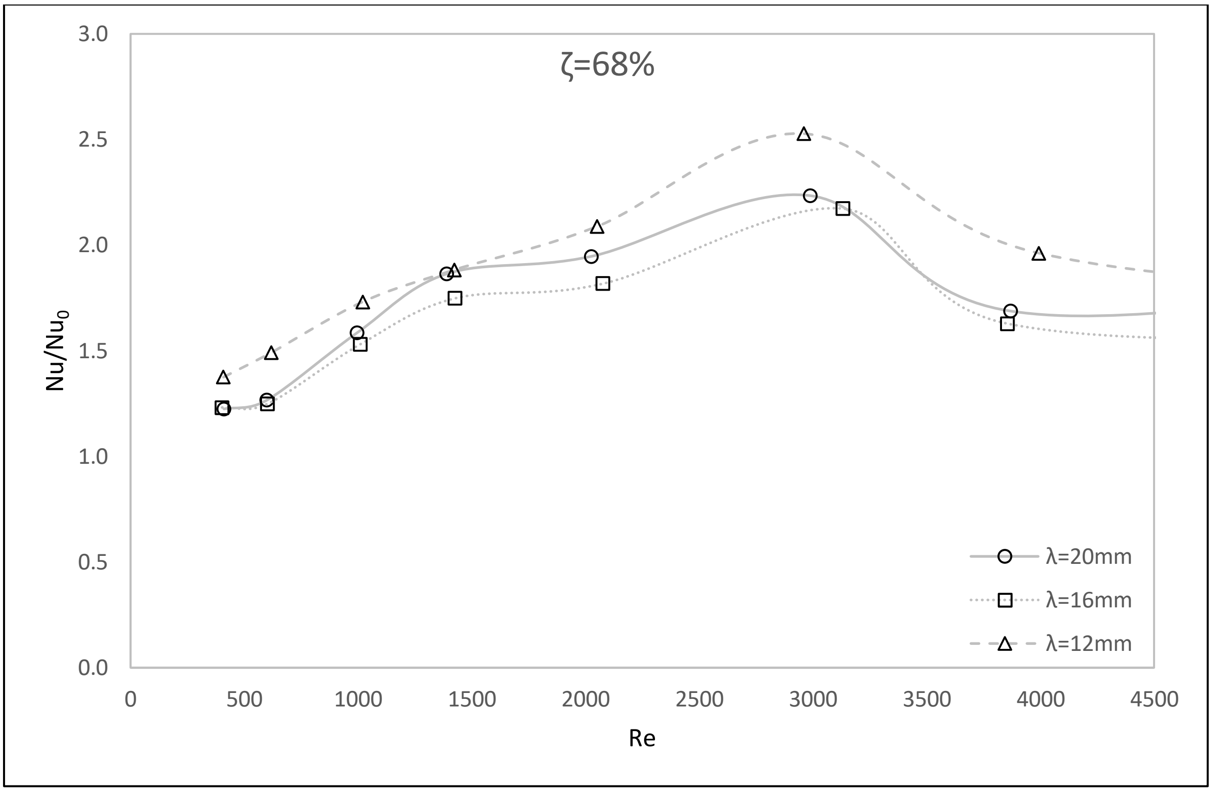

(a)

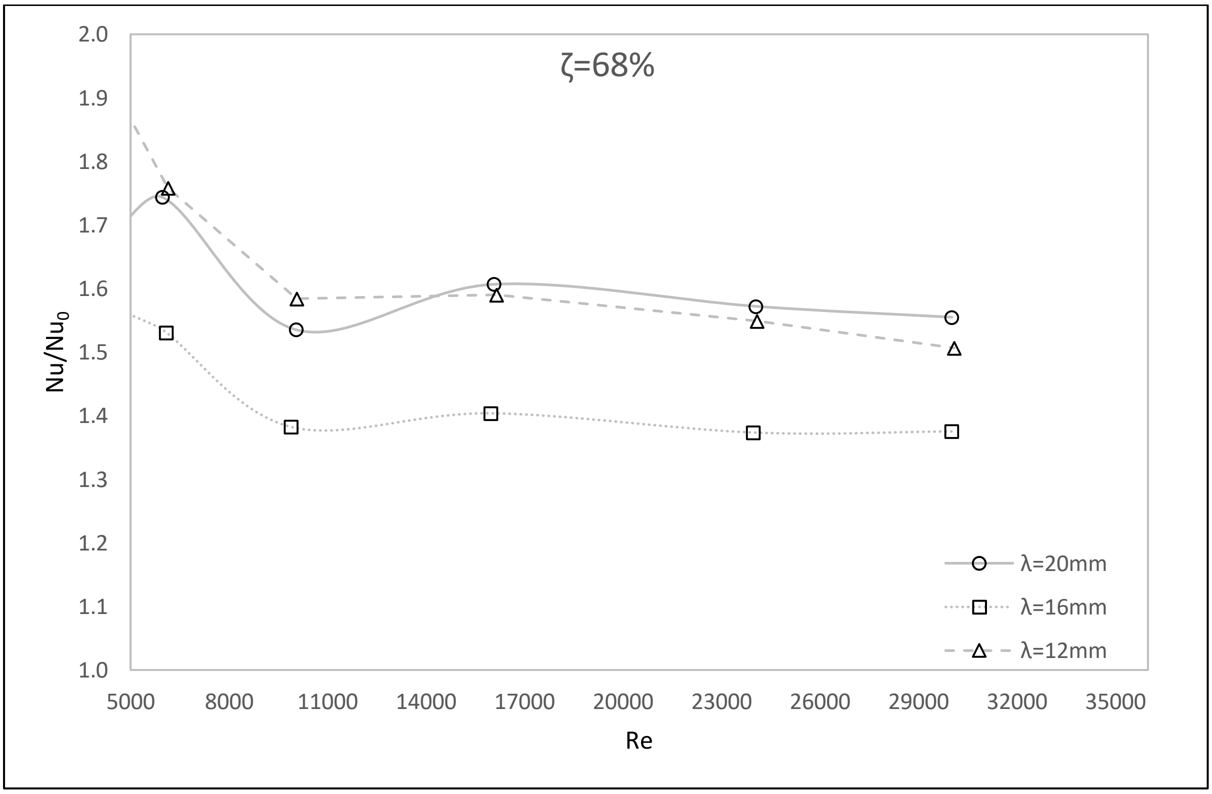

(b)

Figure 5.31: Average Nusselt number ratios, Nu/Nu_0 for inserts with ζ=68% with one wall heated for Reynolds number range: (a) 400 < Re < 4000 and (b) 5000 < Re < 30000

5.7.2 Inserts 1.2, 2.2 and 3.2 (Effects of Wavelength, λ at ζ = 48%)

The average Nusselt numbers for inserts with ζ = 48 % are shown in Figure 5.32 below. The average Nusselt number increases with the increase in the Reynolds numbers as with the two wall heating experiments. Between 400 < Re < 2000 the average Nusselt numbers for the three inserts follow a linear trend as the Reynolds number increases. Between 2000 < Re < 3000 the average Nusselt number for all three inserts increases by approximately 90 %. For 4000 < Re < 30000 the average Nusselt numbers for all three inserts increases linearly.

The average Nusselt number results are divided by the smooth channel experimental average Nusselt number at the corresponding Reynolds number and are shown in Figure 5.33. The Nusselt number ratio is always larger than one as with the two wall heating scenario. The Nusselt number ratio for all three inserts is observed to increase between 400 < Re < 3000 from where the Nusselt number ratio decreases. Between 600 < Re < 1000 the Nusselt number ratio increases by approximately 20 %. Between 2000 < Re < 3000 the Nusselt number increases by a further 30 % to reach a maximum value for all three inserts tested.

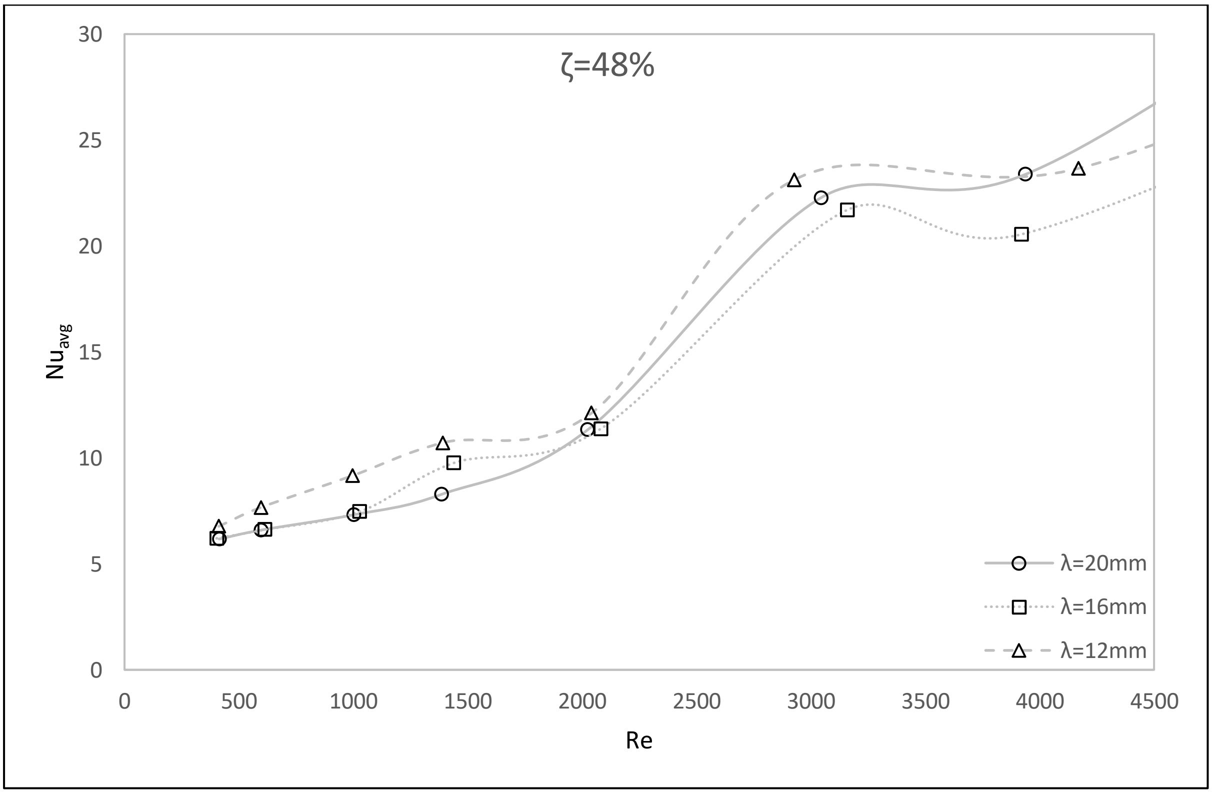

(a)

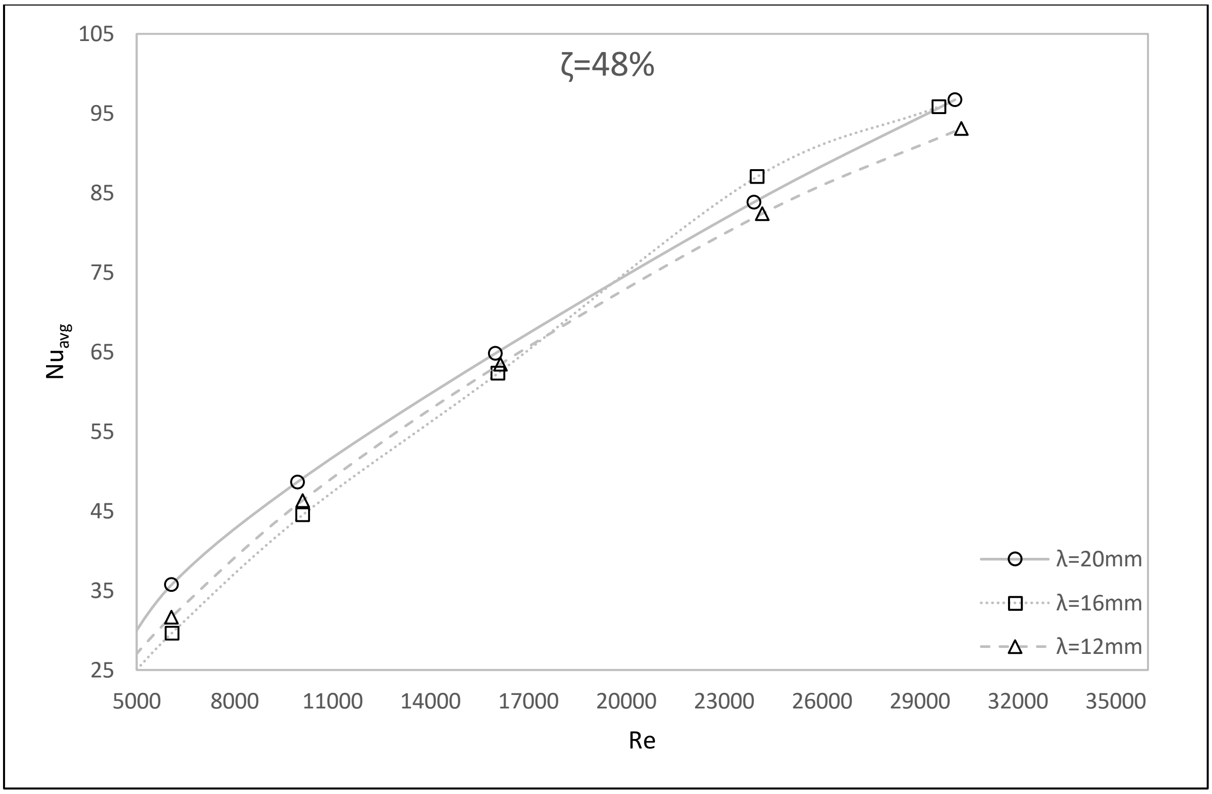

(b)

Figure 5.32: Average Nusselt numbers, Nu_{avg} for inserts with ζ=48% with one wall heated for Reynolds number range: (a) 400 < Re < 4000 and (b) 5000 < Re < 30000

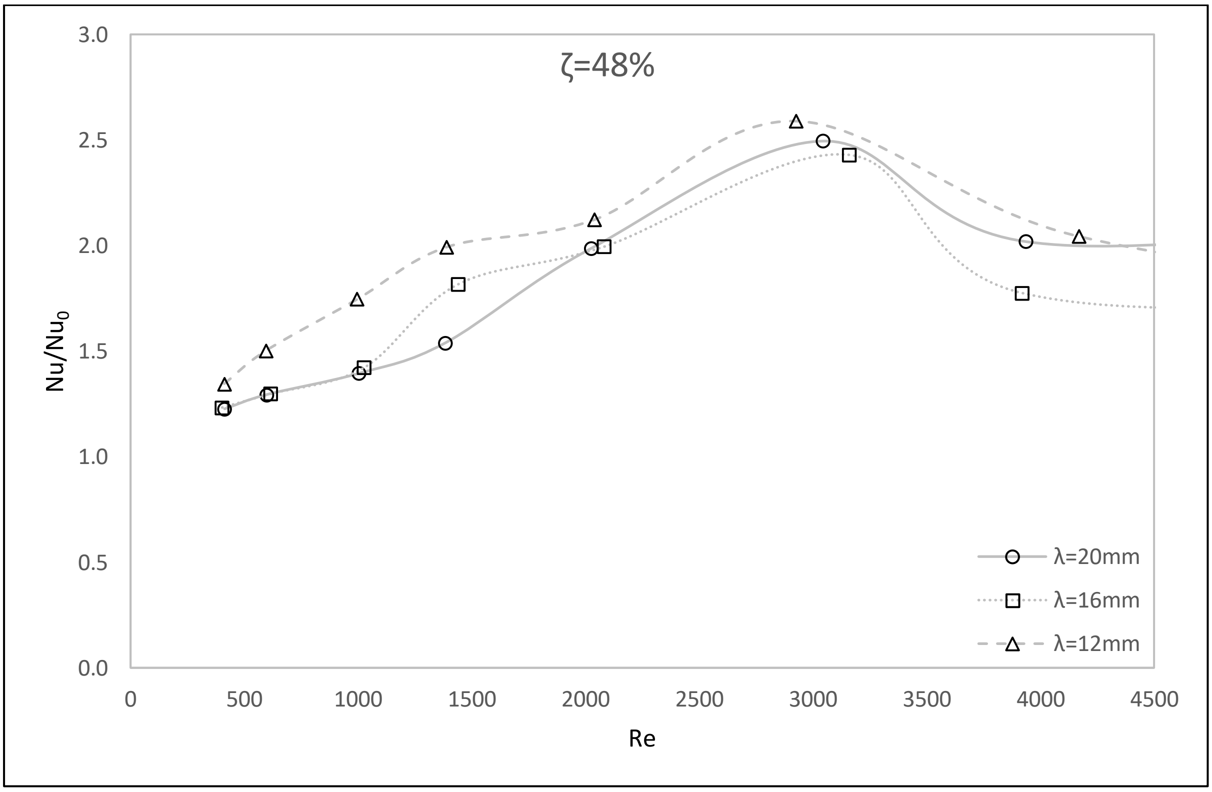

(a)

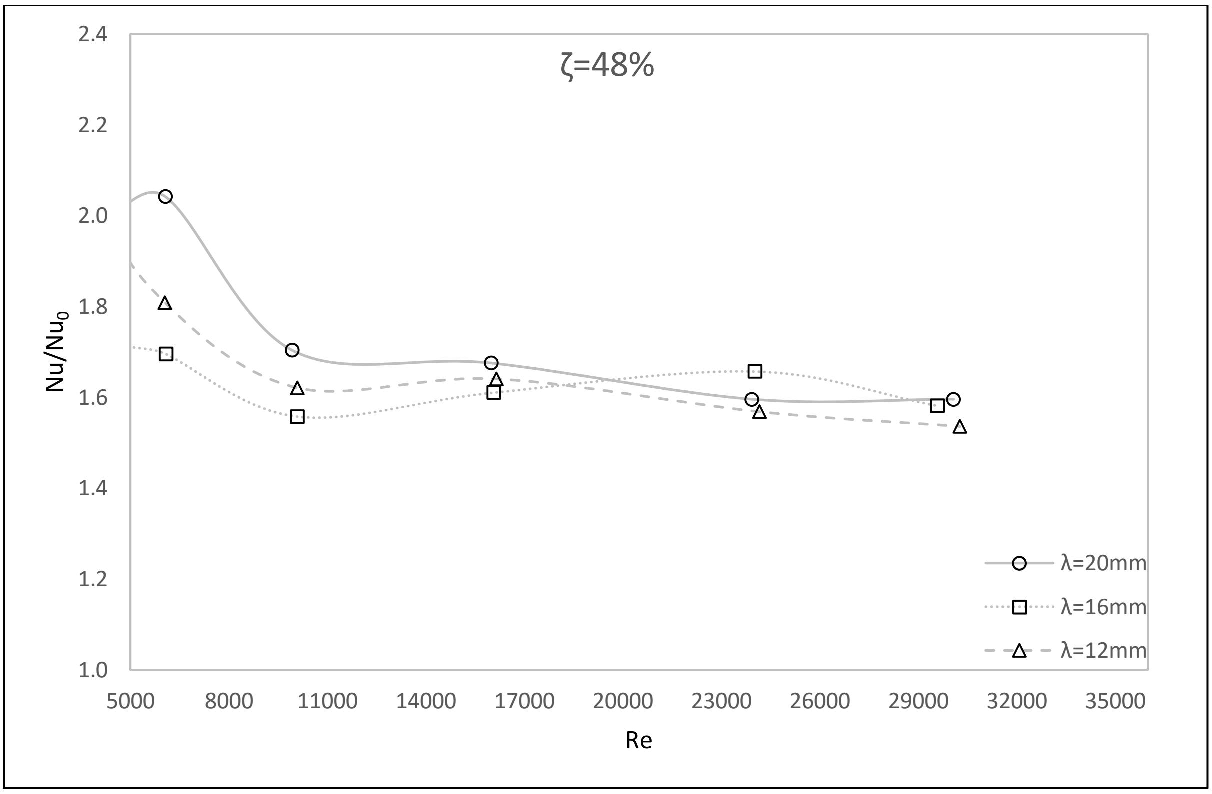

(b)

Figure 5.33: Average Nusselt number ratios, Nu/Nu₀ for inserts with ζ=48% with one wall heated for Reynolds number range: (a) 400 < Re < 4000 and (b) 5000 < Re < 30000

The Nusselt number ratio is always greater than one indicating an increase in the heat transfer rate when any of the inserts are employed. Plots of Nu_{avg} and Nu/Nu_0 vs. Re for constant wavelength, λ are given in Figure E. 43 and Figure E. 44 in Appendix E. The inserts with ζ = 48 % have a larger Nu_{avg} and Nu/Nu_0 than the inserts with ζ = 68 % (up to 23 %) for the majority of the Reynolds numbers tested. The largest differences between the Nu/Nu_0 occur over the range 3000 < Re < 4000. The Nu_{avg} and Nu/Nu_0 results in Figure E. 43 and Figure E. 44 show in inverse relationship between the Nusselt number and the porosity of the insert.

As shown in Section 5.6 the experimental average Nusselt number can be expressed as mathematical correlations in the form of a power equation which is a function of the Reynolds number, porosity and wavelength of the insert. The constants to be used in Eqn. 5.2 are given in Table 5.4 below.

Table 5.4: One wall heating average Nusselt number correlations

	Re Range		
Constant	400 ≤ Re ≤ 3000	4000 ≤ Re ≤ 7500	10000 ≤ Re ≤ 35000
A	0,01	-0,15	0,05
B	-0,16	-0,15	-0,16
C	0,19	7,9	3,07
D	0,31	-0,18	-0,0637

The analytical and experimental Nusselt number ratios, Nu/Nu_0 are shown in Figure 5.34. For $400 \leq Re \leq 3000$, 92 % of the Nu/Nu_0 values determined using the correlation are within 10 % of the experimental value. The maximum deviation of the analytical Nu/Nu_0 from the experimental Nu/Nu_0 is 14 % for the insert with $\xi = 0.48$ and $\lambda = 20$ mm at $Re = 3000$.

For $4000 \leq Re \leq 7500$, 78 % of the analytical Nu/Nu_0 deviate from the experimental values by 10 % or less. The maximum deviation of the analytical Nu/Nu_0 from the experimental Nu/Nu_0 is 15 % for the insert with $\xi = 0.48$ and $\lambda = 20$ mm at $Re = 6000$. For $10000 \leq Re \leq 35000$, 83 % of the analytical Nu/Nu_0 deviate from the experimental values by 10 % or less. The maximum deviation of the analytical Nu/Nu_0 from the experimental Nu/Nu_0 is 13 % for the insert with $\xi = 0.68$ and $\lambda = 16$ mm at $Re = 16000$.

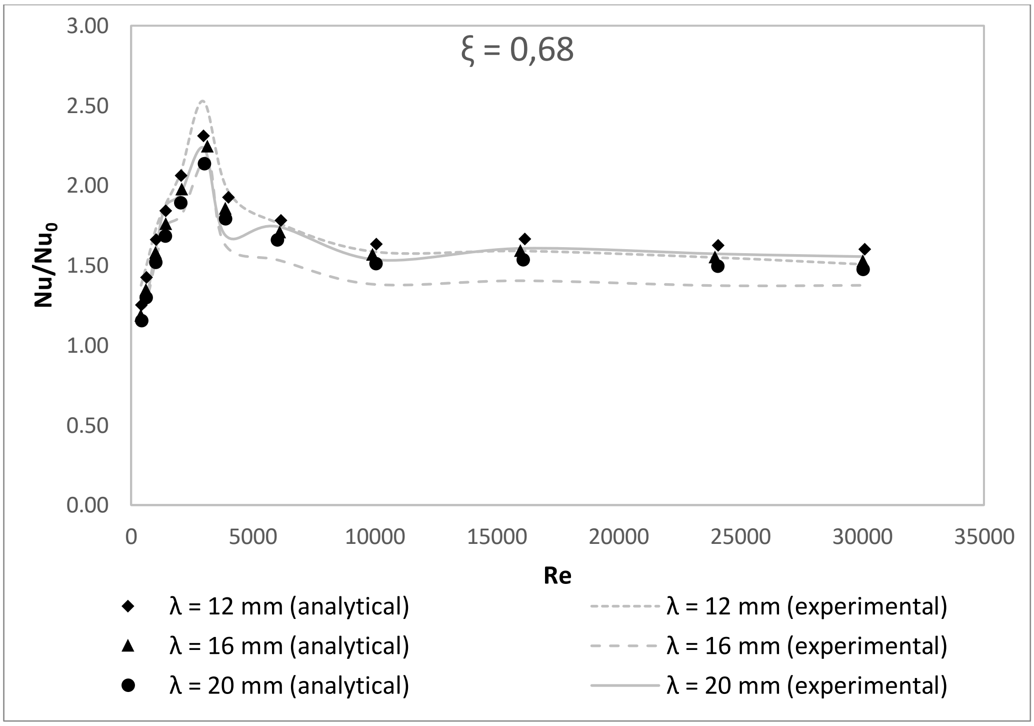

(a)

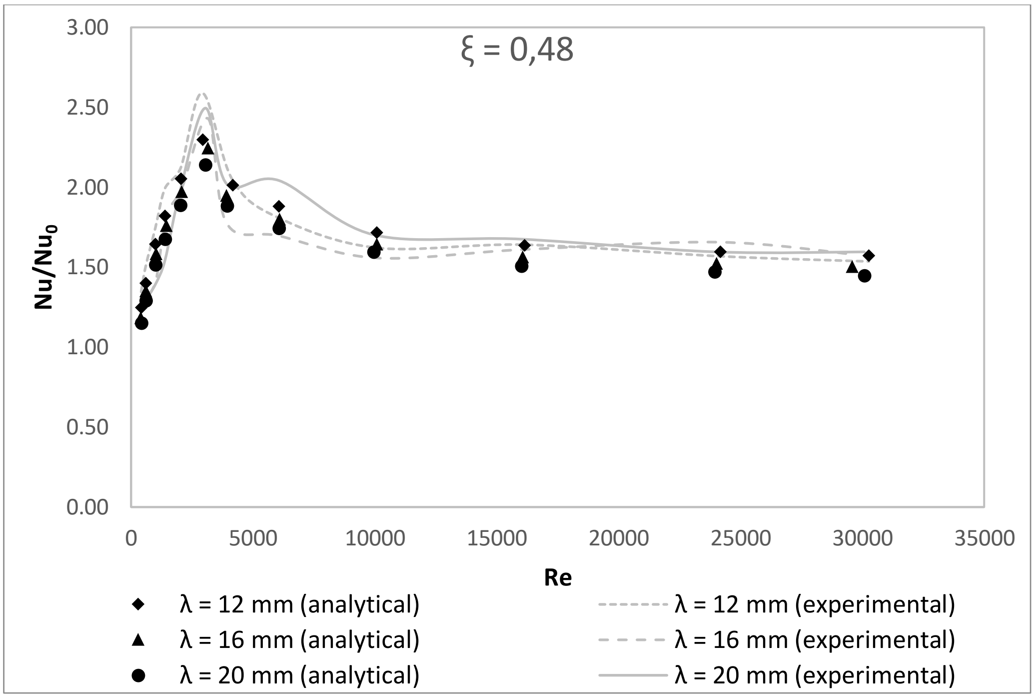

(b)

Figure 5.34: Nusselt number ratio, Nu/Nu_0 correlations vs. Re for (a): ξ = 0.68 and (b) ξ = 0.48

5.8 Performance Index - Two Wall Heat Transfer

The performance of each insert is evaluated by analysing the increase in the Nusselt number to the increase in the friction factor compared to the smooth channel case. The average Nusselt number is considered for each calculation.

5.8.1 Inserts 1.1, 2.1 and 3.1 (Effects of Wavelength, λ at ζ = 68%)

The performance index, $(Nu/Nu_0)/(f/f_0)$ for the inserts with ζ = 68 % for two wall heating boundary condition is shown in Figure 5.35. The $(Nu/Nu_0)/(f/f_0)$ index shows a general decrease with the increase in the Reynolds numbers. The insert with λ = 12 mm shows an increase in the index at Re = 2000 and Re = 5000 while the insert with λ = 16 mm shows an increase in the index at Re = 3000 and again at Re = 5000. The insert with λ = 20 mm shows an increase in the performance index at Re = 1000 and Re = 5000. Inserts with λ = 16 mm and λ = 12mm are analysed to have a similar $(Nu/Nu_0)/(f/f_0)$ index while the insert with λ = 20 mm has an index that is approximately 50 - 60 % larger.

The performance index, $(Nu/Nu_0)/(f/f_0)^{1/3}$ for the inserts with ζ = 68 % with a two wall heating boundary condition is shown in Figure 5.36. The $(Nu/Nu_0)/(f/f_0)^{1/3}$ index increases with the increase in the Reynolds number between 400 < Re < 3000 from where the index is seen to decrease with the increase in the Reynolds number. As with the $(Nu/Nu_0)/(f/f_0)$ index, the $(Nu/Nu_0)/(f/f_0)^{1/3}$ index is greatest for the insert with λ = 20 mm however the effects of the wavelength on this index is not as pronounced. The $(Nu/Nu_0)/(f/f_0)^{1/3}$ index is greater than 1 between 1000 < Re < 3000 for the insert with λ = 20 mm, between 2000 < Re < 3000 for the insert with λ = 12 mm and reaches a maximum value of 0.98 at Re = 3000 for the insert with λ = 16 mm.

The performance index, $(Nu/Nu_0)/(f/f_0)^{1/3}$ can be used to evaluate the three design objectives of the heat exchanger according to parameters set out by [5,6] which are explained in Section 2.2. For example, $(Nu/Nu_0)/(f/f_0)^{1/3} = 0.85$ at Re = 2200 for two heated walls, can be interpreted in terms of the three design objectives as follows:

- Increase screen channel heat transfer area by ($1 - 0.85^{1.5}$) or 22% when pumping power and heat transfer rate are the same in the screen channel and baseline channel [5,6].
- Decrease screen channel heat transfer rate by (1 - 0.85) or 15% when pumping power and heat transfer area are equal in the screen channel and baseline channel [5,6].
- Increase screen channel pumping power by ($1 - 0.85^{3.0}$) or 39% when heat transfer rate and heat transfer area are the same in the screen channel and baseline channel [5,6].

The performance index, $(Nu/Nu_0)/(f/f_0)^{1/3}$ is summarized in Table 5.5. The optimal operating point of each insert is determined by the $(Nu/Nu_0)/(f/f_0)^{1/3}$ index as shown above. The optimal operating point for each insert is given in Table 5.6 in Section 5.10.

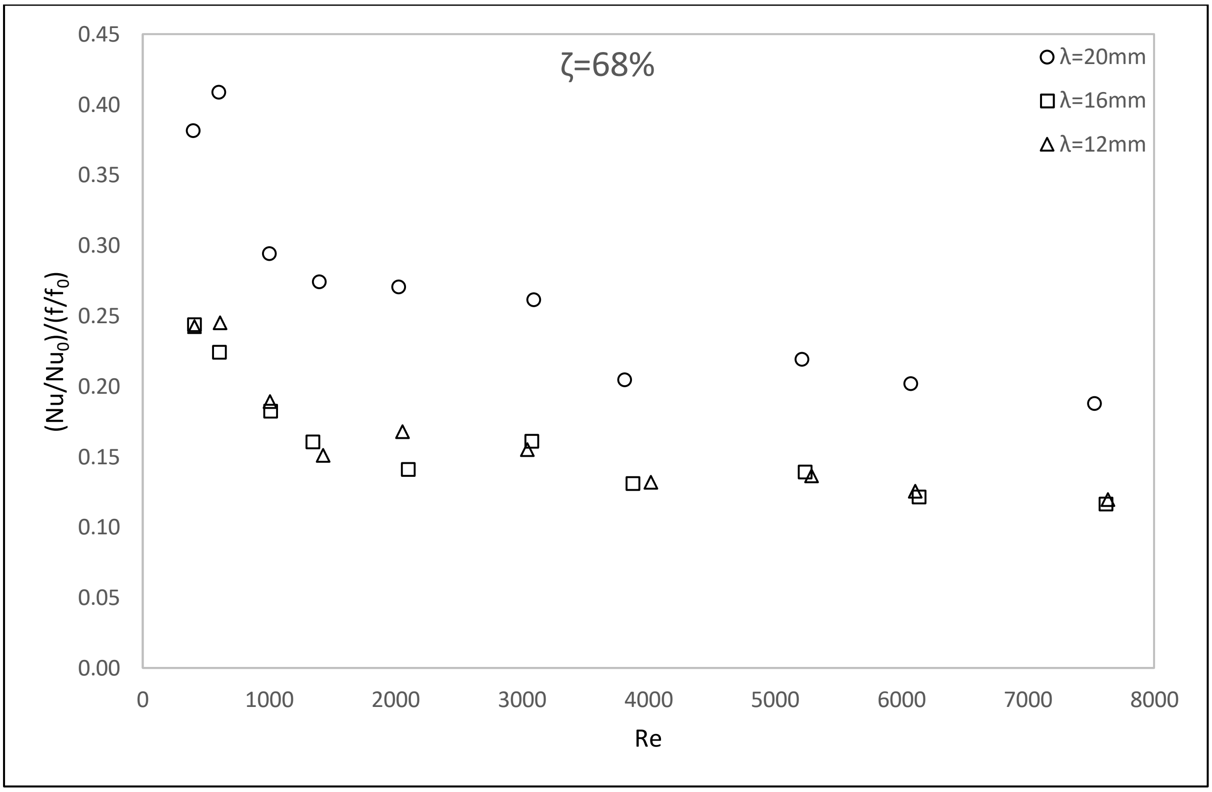

(a)

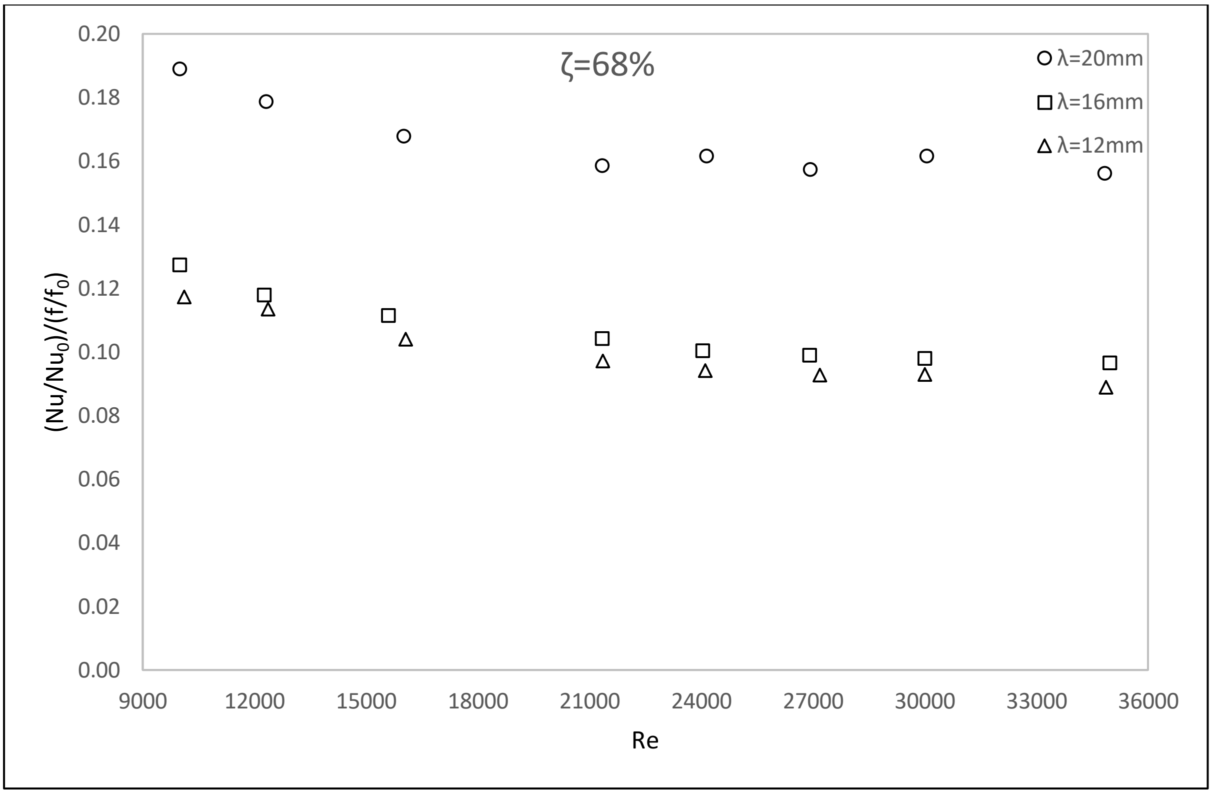

(b)

Figure 5.35: Performance index, $(Nu/Nu_0)/(f/f_0)$ for inserts with ζ = 68% with two walls heated for (a) 400 < Re < 7500 and (b) 10000 < Re < 35000

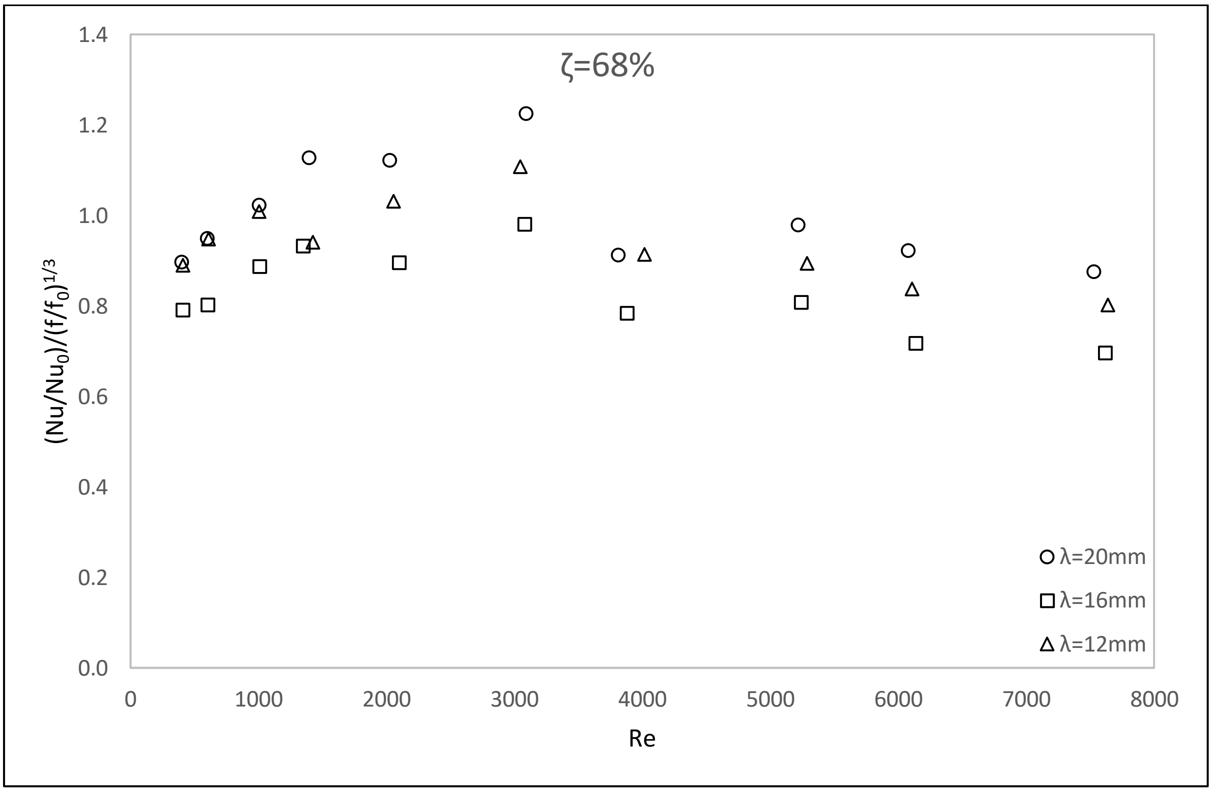

(a)

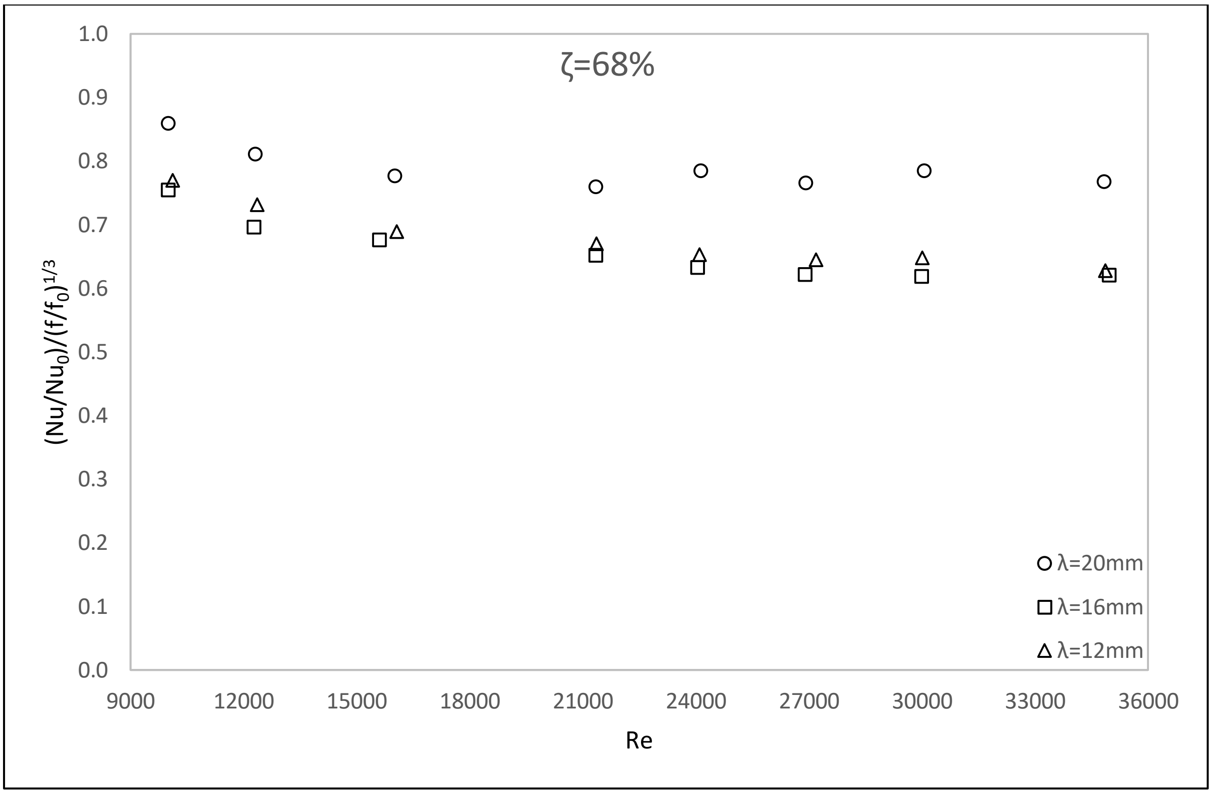

(b)

Figure 5.36: Performance index, $(Nu/Nu_0)/(f/f_0)^{1/3}$ for inserts with ζ = 68% with two walls heated for (a) 400 < Re < 7500 and (b) 10000 < Re < 35000

5.8.2 Inserts 1.2, 2.2 and 3.2 (Effects of Wavelength, λ at ζ = 48%)

The performance index, $(Nu/Nu_0)/(f/f_0)$ for the inserts with ζ = 48 % with a two wall heating boundary condition is shown in Figure 5.37. With the exception of the insert with λ = 12 mm the $(Nu/Nu_0)/(f/f_0)$ index increases with the increase in the Reynolds numbers between 400 < Re < 2000 then decreases with the increase in Reynolds Number. Inserts with λ = 16 mm and λ = 12 mm show similar $(Nu/Nu_0)/(f/f_0)$ index while the insert with λ = 20 mm had an index that is approximately 60 - 70 % larger.

The performance index, $(Nu/Nu_0)/(f/f_0)^{1/3}$ for the inserts with ζ = 48 % with a two wall heating boundary condition is shown in Figure 5.38. The $(Nu/Nu_0)/(f/f_0)^{1/3}$ index increases with the increase in the Reynolds number between 400 < Re < 2000 from where the index decreases with the increase in the Reynolds number. The $(Nu/Nu_0)/(f/f_0)^{1/3}$ index is greatest for the insert with λ = 20 mm for Re > 2000 however for Re < 2000 the index is greatest for the insert with λ = 12 mm. The $(Nu/Nu_0)/(f/f_0)^{1/3}$ index is greater than 1 between 1000 < Re < 3000 for the insert with λ = 20 mm, between 1400 < Re < 3000 for the insert with λ = 12 mm and between 400 < Re < 3000 for the insert with λ = 16 mm. The performance index, $(Nu/Nu_0)/(f/f_0)^{1/3}$ can be used to evaluate the three design objectives of the heat exchanger as shown in Section 5.8.1. The performance index, $(Nu/Nu_0)/(f/f_0)^{1/3}$ is summarized in Table 5.5. The optimal operating point for each insert is given in Table 5.6 in Section 5.10.

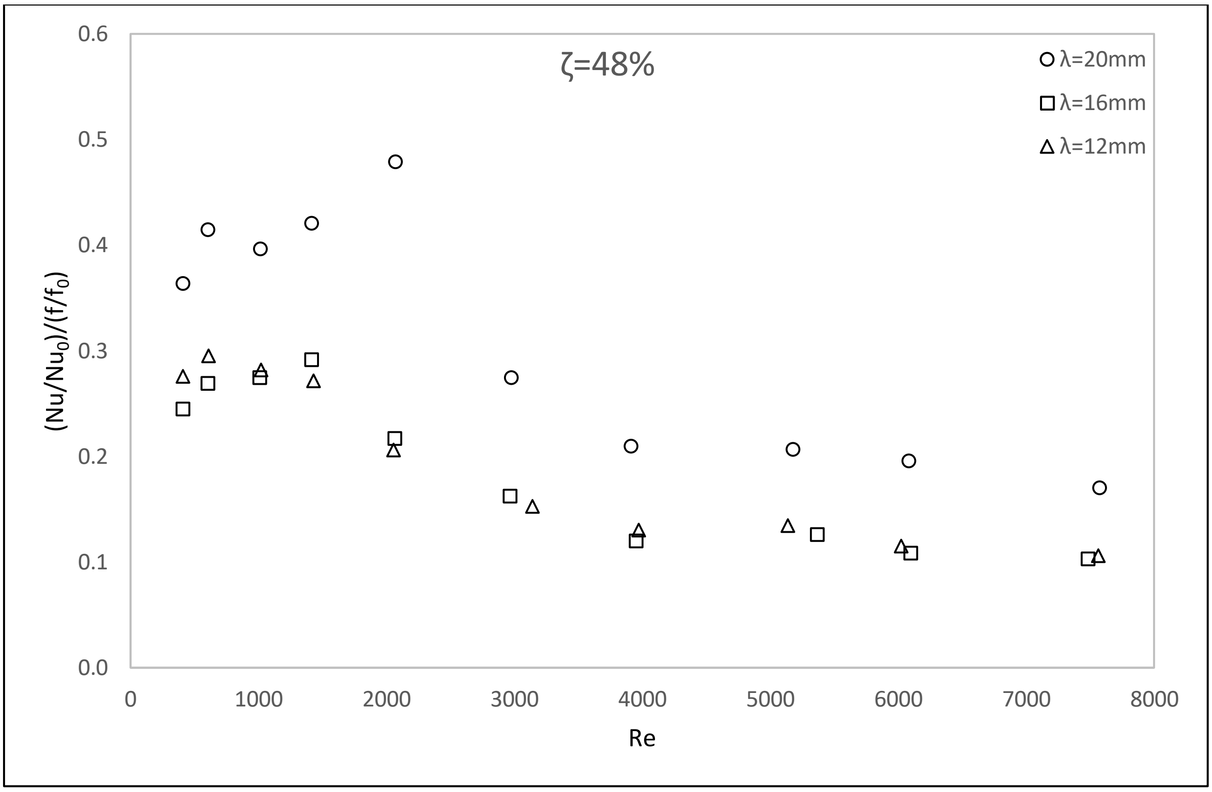

(a)

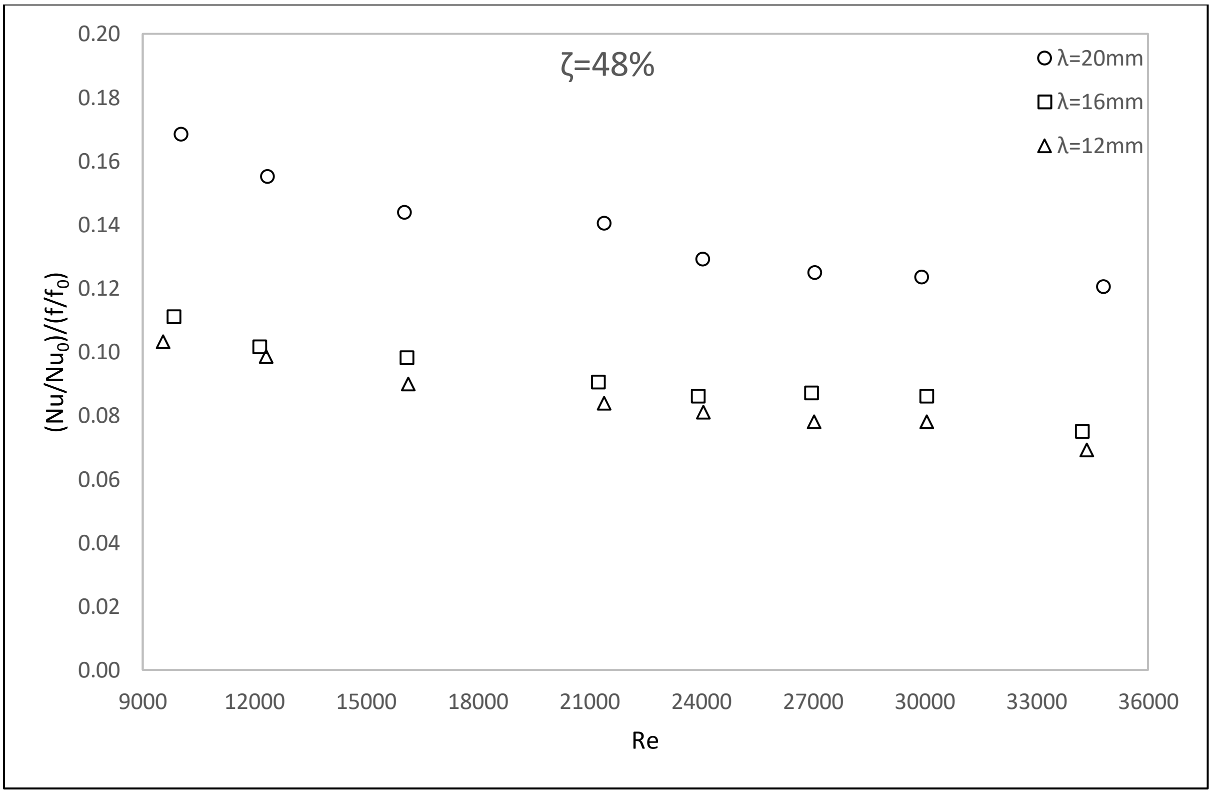

(b)

Figure 5.37: Performance index, $(Nu/Nu_0)/(f/f_0)$ for inserts with ζ = 48 % with two walls heated for (a) 400 < Re < 7500 and (b) 10000 < Re < 35000

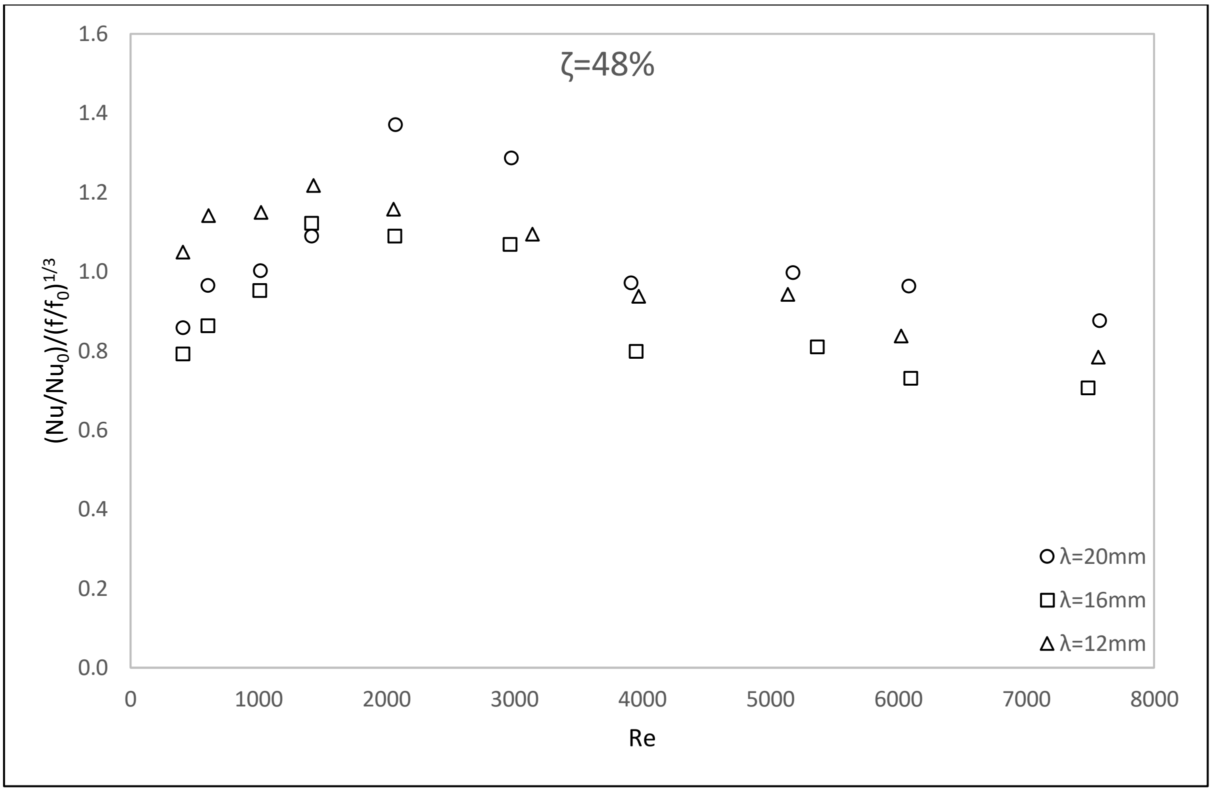

(a)

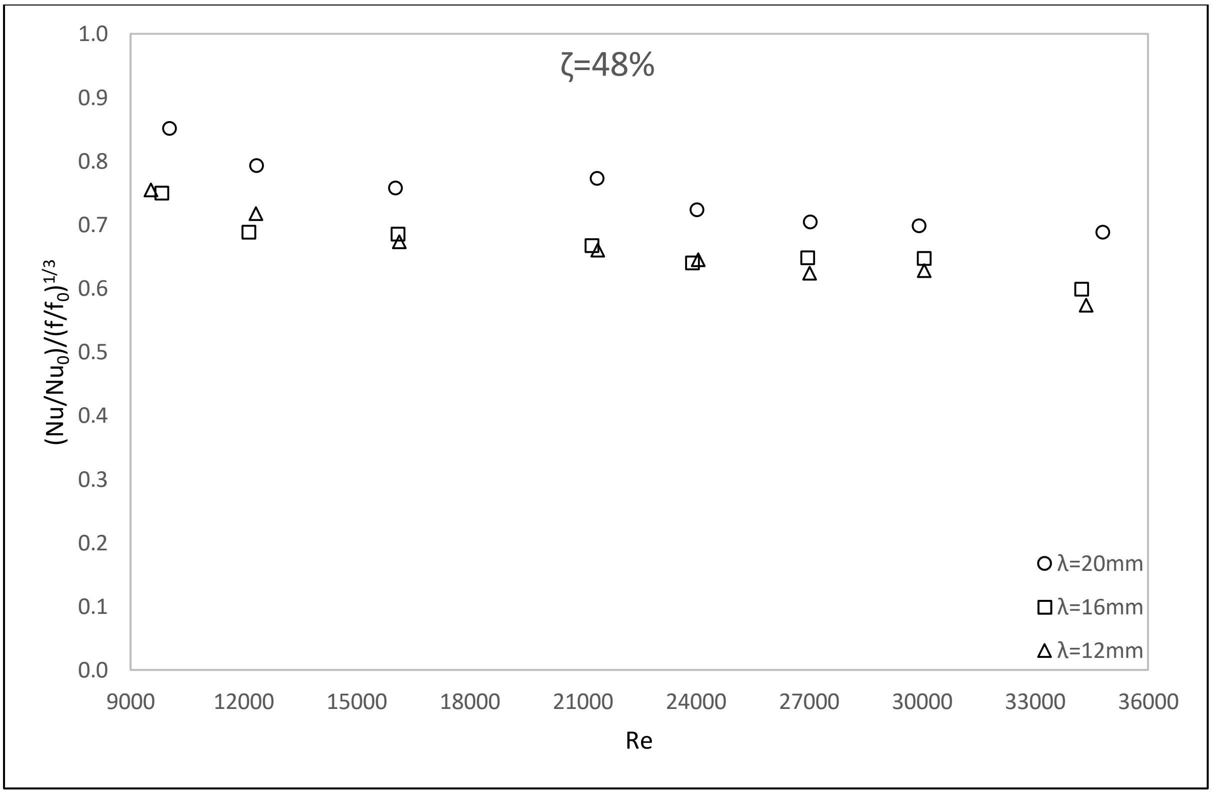

(b)

Figure 5.38: Performance index, $(Nu/Nu_0)/(f/f_0)^{1/3}$ for inserts with $\zeta = 48\%$ with two walls heated for (a) $400 < Re < 7500$ and (b) $10000 < Re < 35000$

Plots of $(Nu/Nu_0)/(f/f_0)^{1/3}$ vs. Re for constant wavelength, λ are given in Figure D. 72 in Appendix D. Between 400 < Re < 3000 the performance index for the inserts with ζ = 48 % is approximately 5 - 30 % larger than that for the inserts with ζ = 68 %. For Re > 4000 the porosity of the insert has little to no influence on the performance index with the expectation of the inserts with λ = 20 mm. Between 24000 < Re < 35000 for the inserts with λ = 20 mm the performance index with insert ζ = 68 % is 10 % larger than the insert with ζ = 48 %.

5.9 Performance Index - One Wall Heat Transfer

5.9.1 Inserts 1.1, 2.1 and 3.1 (Effects of Wavelength, λ at ζ = 68%)

The performance index, $(Nu/Nu_0)/(f/f_0)$ for the inserts with ζ = 68 % with a one wall heating boundary condition is shown in Figure 5.39. The $(Nu/Nu_0)/(f/f_0)$ index shows a general decrease with the increase in the Reynolds numbers as with the two wall heat transfer case. The insert with λ = 12 mm shows an increase in the index at Re = 600 and Re = 2000 while the insert with λ = 16 mm shows and increase in the index at Re = 3000. The insert with λ = 20 mm shows an increase in the performance index at Re = 2000. Inserts with λ = 16 mm and λ = 12 mm show similar $(Nu/Nu_0)/(f/f_0)$ index while the insert with λ = 20 mm has an index that is approximately 70 - 80 % larger.

The performance index, $(Nu/Nu_0)/(f/f_0)^{1/3}$ for the inserts with ζ = 68 % with a one wall heating boundary condition is shown in Figure 5.40. The $(Nu/Nu_0)/(f/f_0)^{1/3}$ index increases with the increase in the Reynolds number between 400 < Re < 3000 from where the index is seen to decrease with the increase in the Reynolds number. As with the two wall heat transfer boundary condition, the $(Nu/Nu_0)/(f/f_0)^{1/3}$ index is greatest for the insert with λ = 20 mm. The $(Nu/Nu_0)/(f/f_0)^{1/3}$ index is only greater than 1 at Re = 3000 for the insert with λ = 20 mm. For inserts with λ = 16 mm and λ = 12 mm the index reaches a maximum value of 0.88 and 0.94 respectively at Re = 3000. The performance index, $(Nu/Nu_0)/(f/f_0)^{1/3}$ can be used to evaluate the three design objectives of the heat exchanger as shown in Section 5.8.1. The performance index, $(Nu/Nu_0)/(f/f_0)^{1/3}$ is summarized in Table 5.5. The optimal operating point for each insert is given in Table 5.6 in Section 5.10.

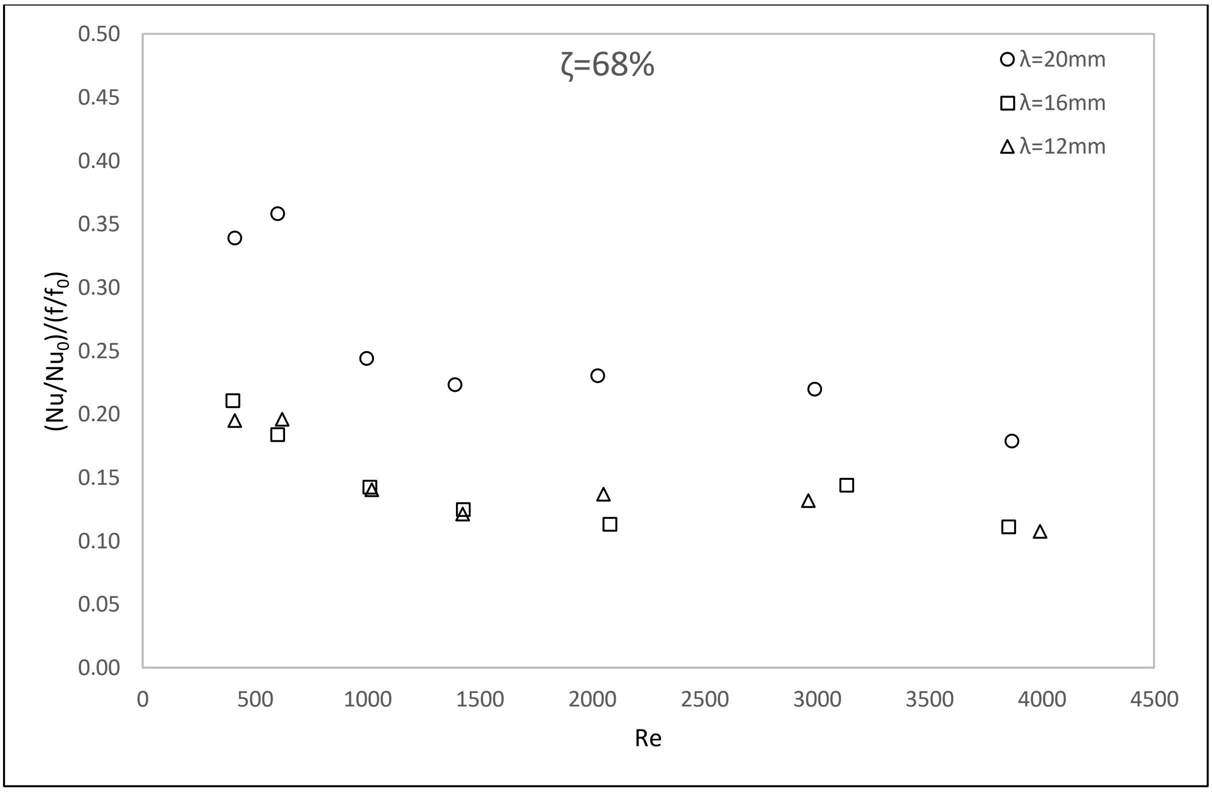

(a)

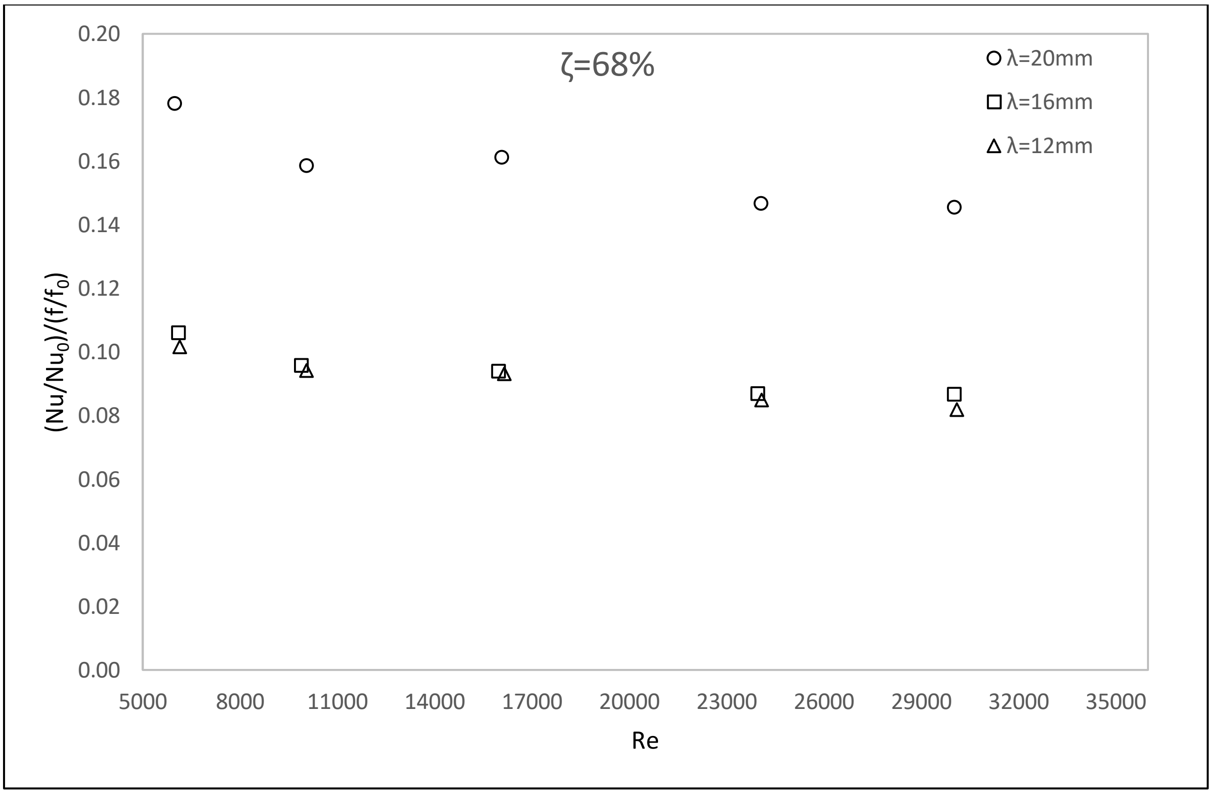

(b)

Figure 5.39: Performance index, $(Nu/Nu_0)/(f/f_0)$ for inserts with $\zeta = 68$ % with one wall heated for (a) $400 < Re < 4000$ and (b) $5000 < Re < 30000$

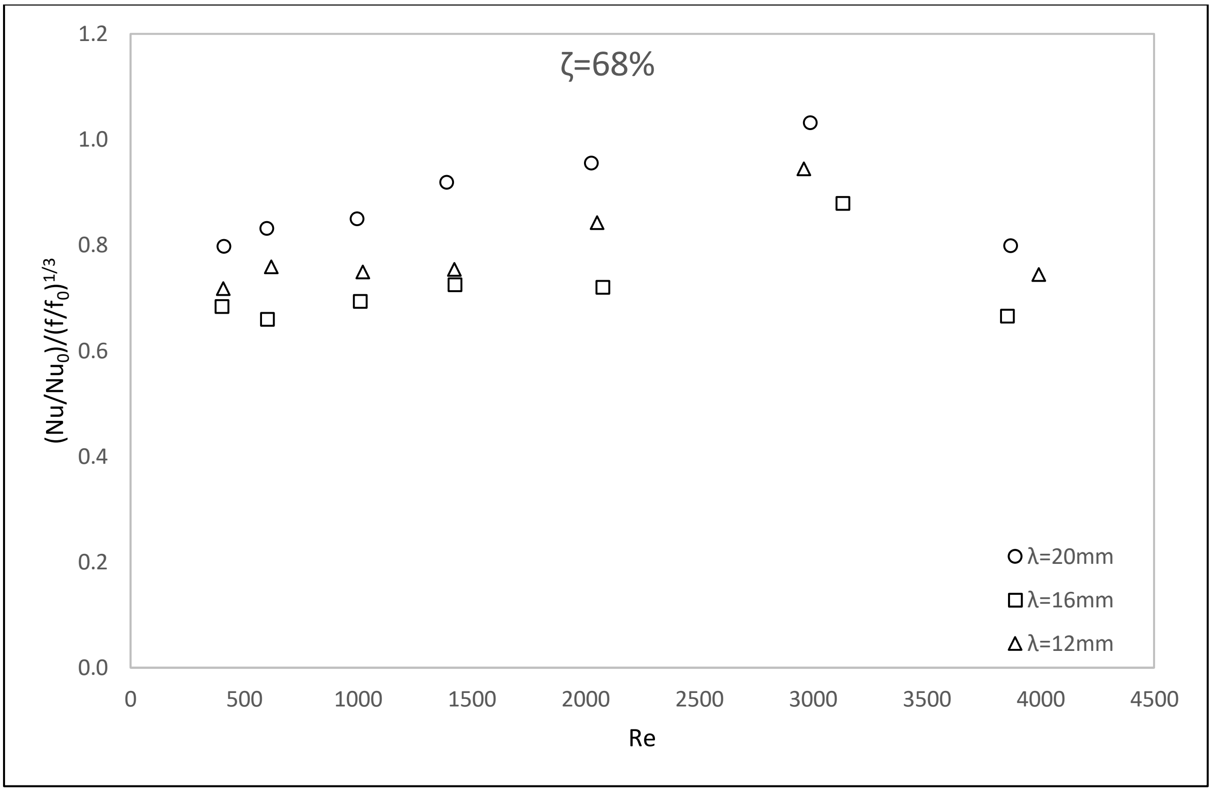

(a)

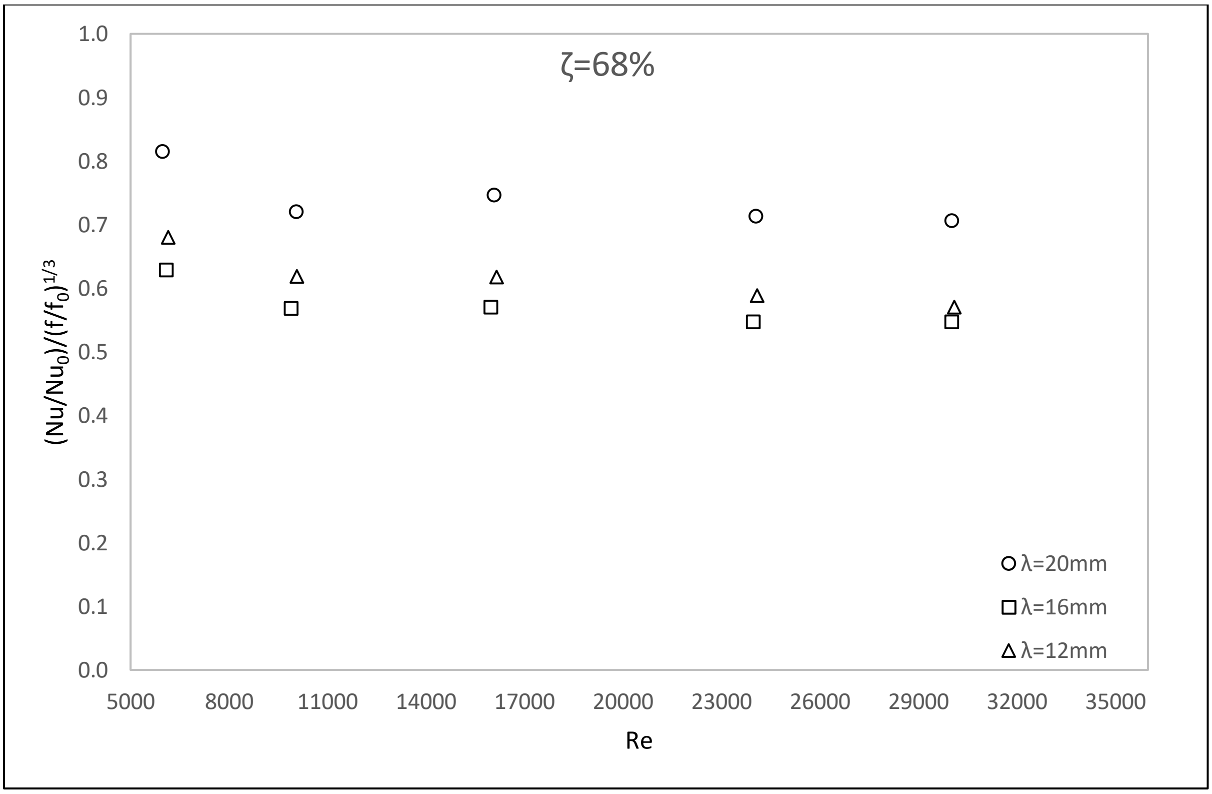

(b)

Figure 5.40: Performance index, $(Nu/Nu_0)/(f/f_0)^{1/3}$ for inserts with ζ = 68 % with one wall heated for (a) 400 < Re < 4000 and (b) 5000 < Re < 30000

5.9.2 Inserts 1.2, 2.2 and 3.2 (Effects of Wavelength, λ at ζ = 48%)

The performance index, $(Nu/Nu_0)/(f/f_0)$ for the inserts with ζ = 48 % with a one wall heating boundary condition is shown in Figure 5.41. The $(Nu/Nu_0)/(f/f_0)$ index increases with the increase in the Reynolds numbers between 400 < Re < 1400 then decreases with the increase in Reynolds Number. The inserts with λ = 12 mm and λ = 16 mm reach a maximum value at Re = 1400 while the insert with λ = 20 mm reaches a maximum value at 2000 Re. Inserts with λ = 16 mm and λ = 12 mm show similar $(Nu/Nu_0)/(f/f_0)$ index while the insert with λ = 20 mm has an index that is approximately 50 - 100 % larger over the Reynolds number range tested.

The performance index, $(Nu/Nu_0)/(f/f_0)^{1/3}$ for the inserts with ζ = 48 % with a one wall heating boundary condition is shown in Figure 5.42. The $(Nu/Nu_0)/(f/f_0)^{1/3}$ index increases with the increase in the Reynolds number between 400 < Re < 2000 from where the index decreases with the increase in the Reynolds number. The $(Nu/Nu_0)/(f/f_0)^{1/3}$ index is greatest for the insert with λ = 20 mm. The $(Nu/Nu_0)/(f/f_0)^{1/3}$ index is only greater than 1 between 2000 < Re < 3000 for the insert with λ = 20 mm. For inserts with λ = 16 mm and λ = 12 mm the index reaches a maximum value of 0.95 and 0.97 respectively at Re = 3000. The performance index, $(Nu/Nu_0)/(f/f_0)^{1/3}$ can be used to evaluate the three design objectives of the heat exchanger as shown in Section 5.8.1. The performance index, $(Nu/Nu_0)/(f/f_0)^{1/3}$ is summarized in Table 5.5. The optimal operating point for each insert is given in Table 5.6 in Section 5.10.

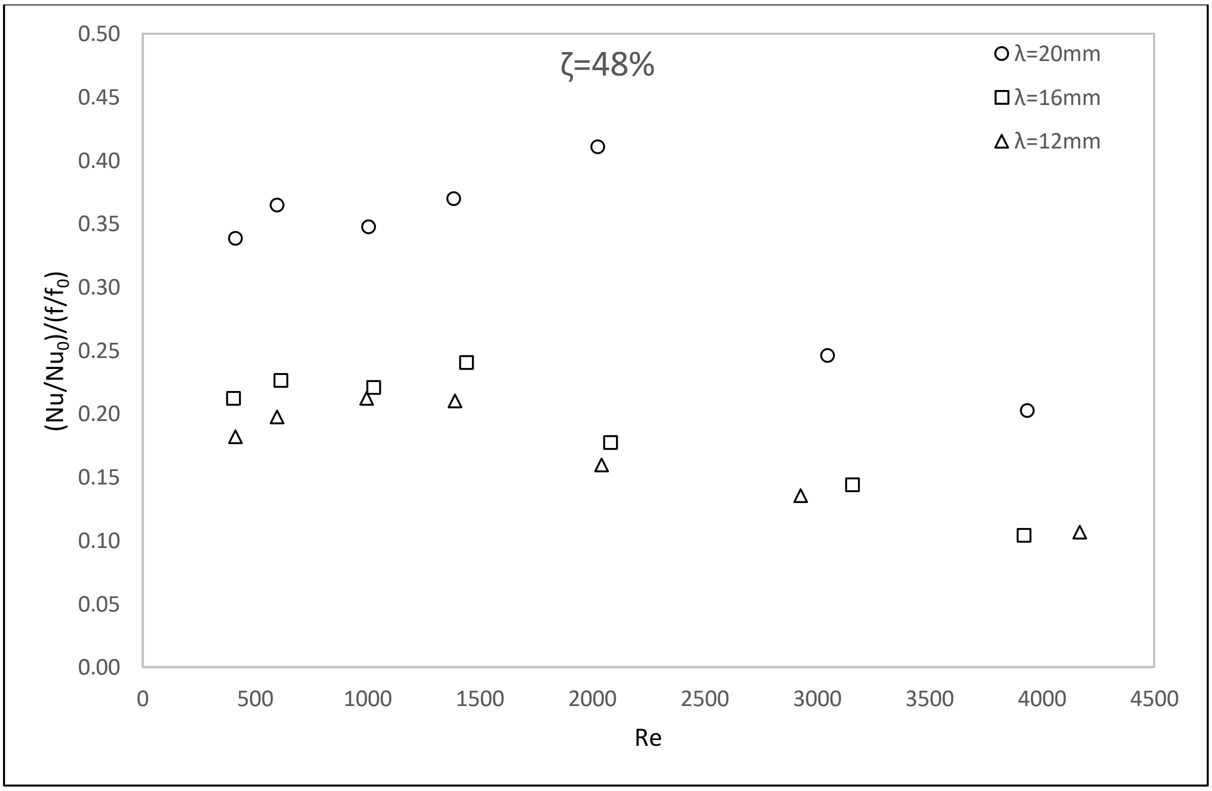

(a)

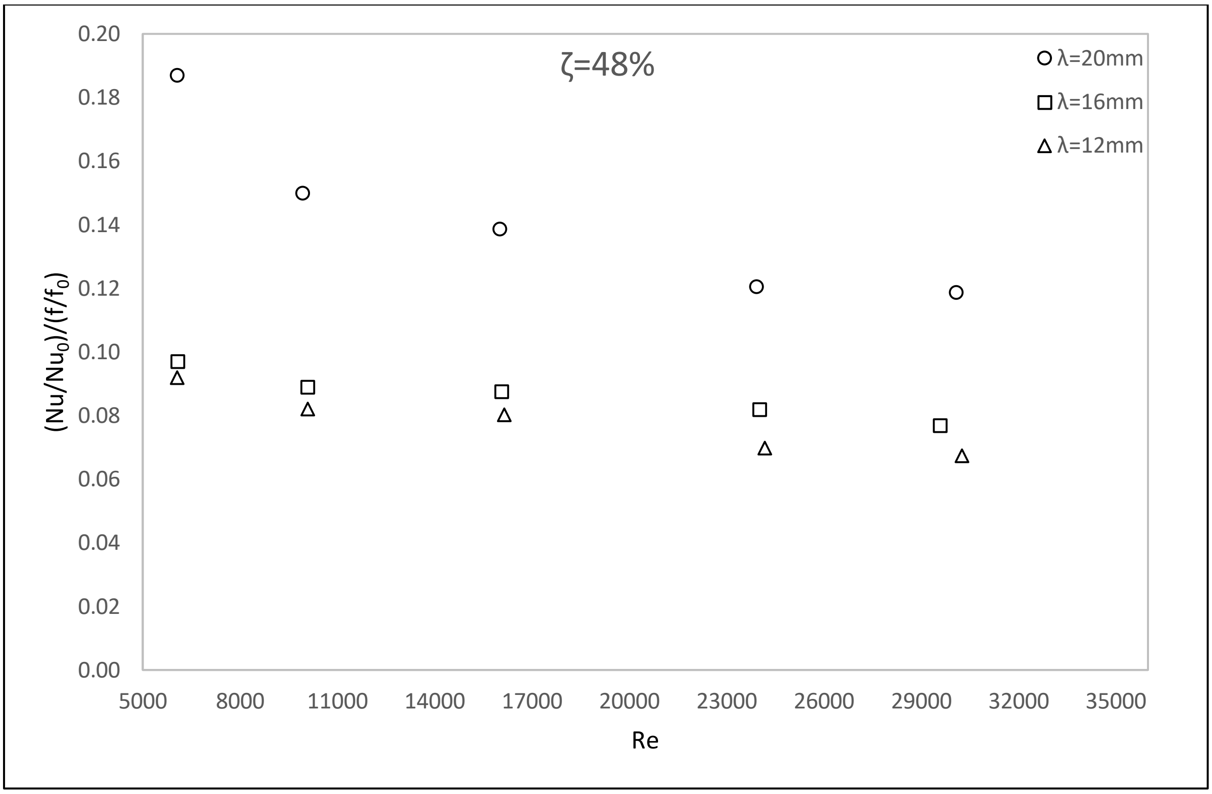

(b)

Figure 5.41: Performance index, $(Nu/Nu_0)/(f/f_0)$ for inserts with ζ = 48 % with one wall heated for (a) 400 < Re < 4000 and (b) 5000 < Re < 30000

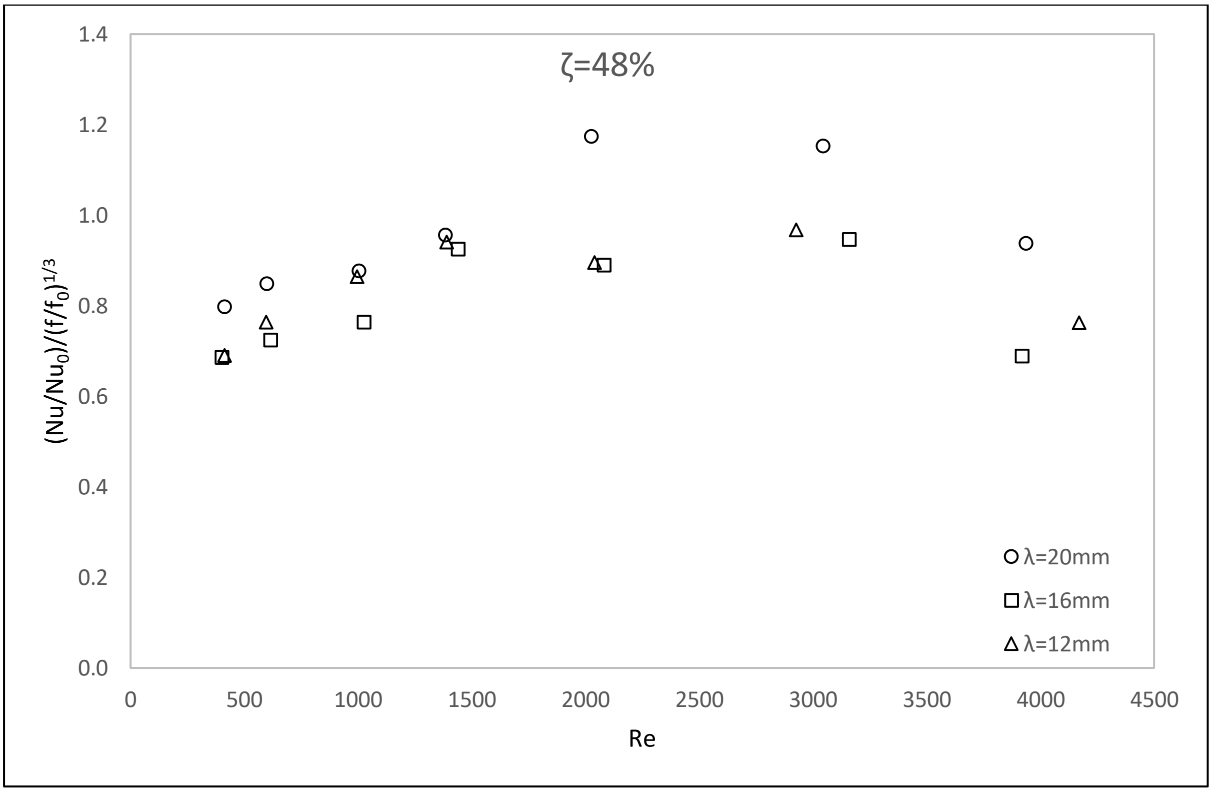

(a)

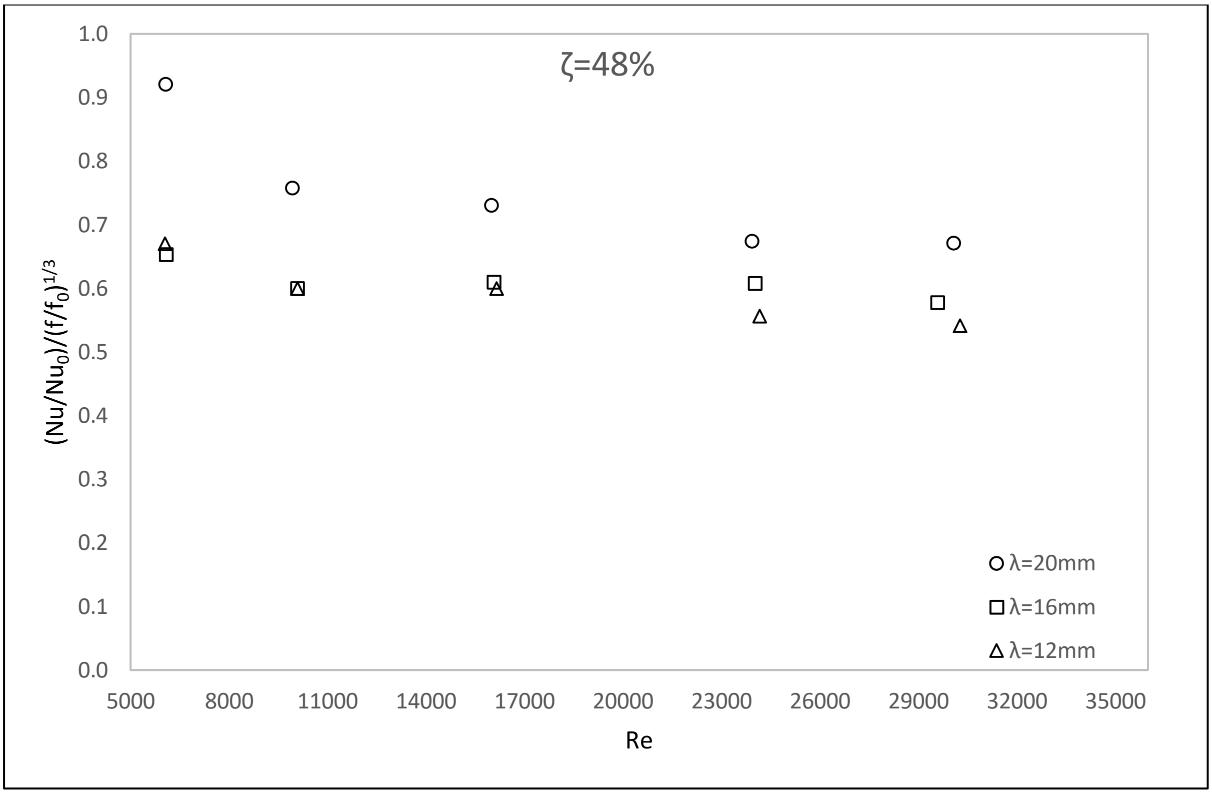

(b)

Figure 5.42: Performance index, $(Nu/Nu_0)/(f/f_0)^{1/3}$ for inserts with ζ = 48 % with one wall heated for (a) 400 < Re < 4000 and (b) 5000 < Re < 30000

Plots of $(Nu/Nu_0)/(f/f_0)^{1/3}$ vs. Re for constant wavelength, λ are given in Figure E.45 in Appendix E. Between 400 < Re < 3000 the performance index for the inserts with ζ = 48 % is approximately 5 - 25 % larger than that for the inserts with ζ = 68 %. For Re > 4000 the porosity of the insert has variable effects on the performance index. For inserts with λ = 12 mm, the performance index with ζ = 68 % is greater than that with ζ = 48 % while for inserts with λ = 16 mm the performance index with ζ = 68 % is less than that with ζ = 48 %. For inserts with λ = 20 mm the performance index with ζ = 48 % is greater than with ζ = 68 % up to Re = 10000.

5.10 Conclusion

For all the inserts tested the normalized pressure drop decreases as the Reynolds number increases. The normalized pressure drop in the channel with an insert is observed to always be higher than that of the baseline pressure drop at the corresponding Re. The hydrodynamic developing length of the inserts is analysed to range between 0.08 m and 0.14 m between 1400 < Re < 4000. The developing length equates to $3 < D_h < 6$.

The results shown that the insert with the shortest wavelength, λ = 12 mm produces the highest friction factor followed by the insert with a wavelength λ = 16 mm and the insert with λ = 20 mm producers the lowest friction factor. The friction factor increases with the decrease in the wavelength of the insert. The relationship between the friction factor and the wavelength is observed to be non-linear. The increase in the friction factor between λ = 20 mm and λ = 16 mm is significantly larger than the increase in the friction factor between λ = 16 mm and λ = 12 mm. This relationship was prevalent for both insert porosities investigated.

Generally the friction factor increases with the decrease in porosity. This is to be expected, as the open area of the insert decreases the flow obstruction and form drag in the channel increases. The results show that the friction factors between $1000 < Re < 2000$ for the inserts with $\zeta = 48$ % decrease to local minimums which are lower than that of the inserts with $\zeta = 68$ %. The decrease in the fiction factor over this Reynolds number range is observed for all three wavelengths analysed. The results show an inverse relationship between the friction factor and the porosity of the insert.

The friction factor results with an insert are divided by the smooth channel experimental fiction factor at the corresponding Reynolds numbers. The friction factor ratios for the inserts tested show an increasing relationship with the increase in the Reynolds number. The results shown that the insert with the shortest wavelength, $\lambda = 12$ mm produces the highest friction factor ratio followed by the insert with a wavelength $\lambda = 16$ mm and the insert with $\lambda = 20$ mm producers the lowest friction factor ratio. All six inserts show a decrease in the friction factor ratio at $Re = 5000$ while only the inserts with $\zeta = 68$ % show a decrease in the friction factor ratio at $Re = 2000$. The friction factor ratio is always greater than zero indicating an increase in required fan power.

The friction factor ratio, f/f_0 for the inserts with ($\lambda = 12$ mm, $\zeta = 68$ %) and ($\lambda = 12$ mm, $\zeta = 48$ %) compare well with similar inserts ($\lambda = 12$ mm, $\zeta = 68$ %) and ($\lambda = 12$ mm, $\zeta = 48$ %) tested by Cramer [21]. For the inserts $\lambda = 12$ mm and $\zeta = 68$ % between $400 < Re < 10\,000$ the f/f_0 obtained differ by 4 % on average while that of the inserts with $\lambda = 12$ mm and $\zeta = 48$ % differ by 2 % on average. Cramer [21] obtained f/f_0 data for inserts with $\lambda = 22$ mm and $\zeta = 48$ % and 68 %. This data determined by Cramer [21] is of similar values (2 % to 4 % deviation) when compared to the f/f_0 data for both porosity inserts ($\zeta = 48$ % and 68 %) with $\lambda = 20$ mm. The friction factor data collected by Cramer [21] also shows inverse relationships between f/f_0 and the porosity of the insert and between f/f_0 and the wavelength, λ.

Figure 5.13 to Figure 5.24 show an increase in the local Nusselt number with the increase in the Reynolds number due to the increase in the velocity and mass flow rate. This was observed for both the two wall and one wall heating boundary conditions. The local Nusselt number is observed to decrease as x/L increases as the temperature profile develops until an asymptotic constant value is measured towards the downstream half ($x/L > 0.5$) of the test section where the temperature profile is said to be fully developed. The thermal developing length is observed to decrease with the increase in Reynolds number for both inserts with $\zeta = 68$ % and $\zeta = 48$ %. For $400 < Re < 35000$ the local Nusselt numbers reach a steady value at approximately $x/L = 0.6$. For $0.6 < x/L < 1$ and the flow is said to be thermally fully developed. The results show a dip in the Nu_{local} distributions at approximately $x/L = 0.15$ for $Re > 1000$. The dip in the Nu_{local} is an indication of the start location of the thermal boundary layer transition. The axial conductional losses along the direction of flow in the test section is determined to be negligible [14].

The average Nusselt number is calculated by taking the average of the local Nusselt numbers in the thermally fully developed region between $x/L = 0.6$ and $x/L = 0.92$. The average Nusselt number increases with the increase in the Reynolds number. For the two wall heating boundary condition, between $2000 < Re < 3000$ the average Nusselt number for all six inserts increased by 50 - 75 %. Over the same Reynolds number range the average Nusselt number increased by 90 % for the one wall heat transfer boundary condition. The average Nusselt number for the two wall heating boundary condition is observed to be larger that of the one wall heating boundary condition at the corresponding Reynolds numbers.

For the majority of the Reynolds numbers tested, the insert with λ = 12 mm produced the highest Nusselt number followed by the insert with λ = 20 mm. The insert with λ = 16 mm produced the lowest Nusselt number. The inserts with ζ = 48 % produce a higher Nusselt number than the inserts with ζ = 68 % however the difference is marginal. The results suggest an inverse relationship between the porosity and the Nusselt number.

The average Nusselt number results are divided by the smooth channel experimental average Nusselt number at the corresponding Reynolds numbers. The Nusselt number ratio is calculated to always be larger than one as the additional local turbulence in the test section created by the insert enhances the heat transfer rate. The Nusselt number ratio for all six inserts is observed to increase from Re = 400 to a maximum value at Re = 3000 from where the Nusselt number ratio decreases.

In general, the inserts with λ = 12 mm produce the highest Nusselt number ratio and the inserts with λ = 16 mm produce the lowest. The insert with λ = 20 mm produces a Nusselt number ratio which fluctuates between that of λ = 12 mm and λ = 16 mm. The Nusselt number ratio is larger for the two wall heating boundary condition than the one wall heating boundary condition. For the majority of the heat transfer experiments conducted the Nusselt number ratio for inserts with ζ = 48 % is larger than that of the inserts with ζ = 68 %.

For the one wall heating boundary condition the Nu/Nu_0 is on average 4 % lower than the Nu/Nu_0 obtained by Cramer [21] for the inserts with λ = 12 mm and ζ = 68 %. The Nu/Nu_0 for the insert with λ = 12 mm and ζ = 48 % is 3 % lower on average compare to that obtained by Cramer [19] for a similar insert. For the insert with λ = 22 mm and ζ = 48 % the Nu/Nu_0 data determined by Cramer [21] is up to 16 % lower than that of the insert with λ = 20 mm and ζ = 48 % between 1000 < Re < 10 000 with the most notable difference at Re = 4200. For a two wall heating boundary condition Nu/Nu_0 for the insert λ = 20 mm and ζ = 48 % is on average 7 % higher than the Nu/Nu_0 obtained by Cramer [21] for the insert with λ = 22 mm and ζ = 48 % for 400 < Re < 10 000. For the same Reynolds number range the Nu/Nu_0 values for the insert with λ = 20 mm and ζ = 68 % are 3 % higher on average than the insert (λ = 22 mm, ζ = 68 %) evaluated by Cramer [21]. For the inserts with λ = 12 mm and ζ = 68 %, the Nu/Nu_0 evaluated in this paper is on average 5 % higher than obtained by Cramer [21] except at Re = 10 000.

The performance index, $(Nu/Nu_0)/(f/f_0)^{1/3}$ is the greatest between 1400 < Re < 3000 for the six inserts tested. The performance index is observed to be larger for the two wall heating boundary condition than the one wall heating boundary condition. From Figure 5.35 to Figure 5.42 it is difficult to draw comparisons between the performance index, porosity and wavelength and therefore the $(Nu/Nu_0)/(f/f_0)^{1/3}$ index is tabulated in Table 5.5. From Table 5.5 it can be seen the performance index is higher for the insets with ζ = 48 % than with ζ = 68 %. For both porosities the inserts with a wavelength of λ = 20 mm produced the highest performance index followed by the inserts with λ = 12 mm. The performance of each insert compared to the smooth channel result at the recorded optimal Reynolds number is evaluated to the design criteria set by [5,6] and is listed in Table 5.6. The insert with ζ = 48 % and λ = 20 mm offers the greatest enhancement to the heat transfer in a 14 mm channel for both the two wall and one wall heat transfer boundary condition.

Table 5.5: $(Nu/Nu_0)/(f/f_0)^{1/3}$ performance index summary

Re	**Two Wall Heating Boundary Condition**						**One Wall Heating Boundary Condition**					
	ζ=68%			**ζ=48%**			**ζ=68%**			**ζ=48%**		
	λ			**λ**			**λ**			**λ**		
	20mm	**16mm**	**12mm**	**20mm**	**16mm**	**12mm**	**20mm**	**16mm**	**12mm**	**20mm**	**16mm**	**12mm**
400	0,90	0,79	0,89	0,86	0,79	**1,05**	0,80	0,68	0,72	0,80	0,69	0,69
600	0,95	0,80	0,95	0,97	0,86	**1,14**	0,83	0,66	0,76	0,85	0,72	0,76
1000	**1,02**	0,89	**1,01**	**1,00**	0,95	**1,15**	0,85	0,69	0,75	0,88	0,76	0,86
1400	**1,13**	0,93	0,94	**1,09**	**1,12**	**1,22**	0,92	0,73	0,75	0,96	0,93	0,94
2000	**1,12**	0,90	**1,03**	**1,37**	**1,09**	**1,16**	0,96	0,72	0,84	**1,17**	0,89	0,90
3000	**1,23**	0,98	**1,11**	**1,29**	**1,07**	**1,09**	**1,03**	0,88	0,94	**1,15**	0,95	0,97
4000	0,91	0,78	0,91	0,97	0,80	0,94	0,80	0,67	0,75	0,94	0,69	0,76
5000	0,98	0,81	0,89	1,00	0,81	0,94	-	-	-	-	-	-
6000	0,92	0,72	0,84	0,96	0,73	0,84	0,81	0,63	0,68	0,92	0,65	0,67
7500	0,88	0,70	0,80	0,88	0,71	0,78	-	-	-	-	-	-
10000	0,86	0,75	0,77	0,85	0,75	0,75	0,72	0,57	0,62	0,76	0,60	0,60
12000	0,81	0,70	0,73	0,79	0,69	0,72	-	-	-	-	-	-
16000	0,78	0,68	0,69	0,76	0,68	0,67	0,75	0,57	0,62	0,73	0,61	0,60
21000	0,76	0,65	0,67	0,77	0,67	0,66	-	-	-	-	-	-
24000	0,79	0,63	0,65	0,72	0,64	0,64	0,71	0,55	0,59	0,67	0,61	0,56
27000	0,77	0,62	0,64	0,70	0,65	0,62	-	-	-	-	-	-
30000	0,78	0,62	0,65	0,70	0,65	0,63	0,71	0,55	0,57	0,67	0,58	0,54
35000	0,77	0,62	0,63	0,69	0,60	0,57	-	-	-	-	-	-

Table 5.6: Insert design criteria

Insert	**Optimal Re**	**Heat Transfer Area Increase**	**Heat Transfer Rate Increase**	**Pumping Power Decrease**
Two Wall Heating Boundary Condition				
ζ=68%, λ=20mm	3000	36%	23%	84%
ζ=68%, λ=16mm	3000	-3%	-2%	-5%
ζ=68%, λ=12mm	3000	17%	11%	36%
ζ=48%, λ=20mm	2000	60%	37%	157%
ζ=48%, λ=16mm	1400	19%	12%	41%
ζ=48%, λ=12mm	1400	34%	22%	81%
One Wall Heating Boundary Condition				
ζ=68%, λ=20mm	3000	5%	3%	10%
ζ=68%, λ=16mm	3000	-18%	-12%	-32%
ζ=68%, λ=12mm	3000	-8%	-6%	-16%
ζ=48%, λ=20mm	2000	27%	17%	62%
ζ=48%, λ=16mm	3000	-8%	-5%	-15%
ζ=48%, λ=12mm	3000	-5%	-3%	-9%

6 Case Study: Tobacco Barn Solar Enhancement

6.1 Introduction

The thermal performance of the inserts can be further evaluated by applying the experimental results to an industrial process. In this theoretical study the inserts are placed on the roof of a tobacco drying shed in an attempt to utilize solar radiation to aid in the heating of the air used to dry the tobacco leaves. The boiler system of the tobacco barn can be modified so that a portion of the ambient air is pulled through the inserts which line the roof. This portion of air will then be heated via solar radiation before entering the barn hence decreasing the amount fuel of consumed by the boiler. The study will evaluate the performance of the inserts based on the potential capital savings in kilograms of coal.

6.2 Application in the Tobacco Drying Industry

The information shown in the section is based on historical data for the drying of Virginia tobacco provided by Brown Engineering [27]. Conventional tobacco drying barns use either coal fired or LPG boilers to increase the temperature of the air inside the barn during the tobacco drying process. This case study is focused on a tobacco drying tunnel which is 41 m long, 15 m wide and 4 m in height. The tobacco leaves are placed on a conveyor rail and are slowly moved along the length of the tunnel. The geometry of the tunnel is shown in Figure 6.1. The 203 x 14 mm rectangular channels used to house the inserts are installed on the entire surface of the roof as shown in Figure 6.2. The top surface of the channel which is exposed to the sun is painted black and covered with double glazed glass panels to minimize thermal losses.

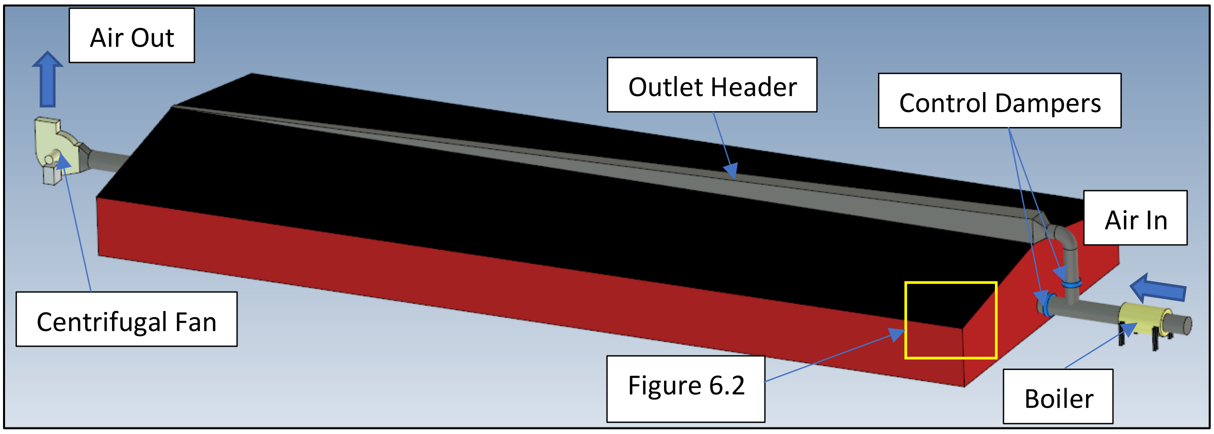

Figure 6.1: Tobacco drying tunnel

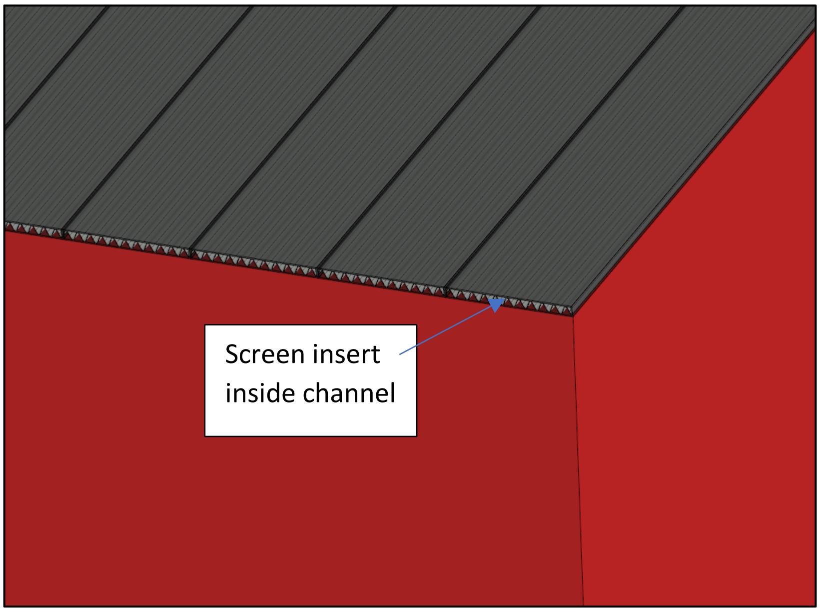

Figure 6.2: Drying tunnel roof detail

The temperature of the air inside the tunnel is controlled depending on the drying stage. At the start of the drying process the temperature inside the tunnel is controlled at approximately 38 °C. The temperature is increased in increments over a period of one week to a high of approximately 70 °C. Averaging the temperature over a one week drying time results in an average temperature of 55 °C. For the drying tunnel shown in Figure 6.1 the required flow rate is 20 000 cfm or 9.43 m^3/s. The energy required to heat the air is calculated as:

$$\dot{Q}_{req} = \dot{m}c_p(T_e - T_i) \tag{6.1}$$

$$\dot{Q}_{req} = 9.43x1007x(55 - 25) = 285\ kW$$

Recent solar mapping conducted by Meyer, [28] shows that most regions in southern Africa receive approximately 2400 kWhr/m^2 direct normal irradiance on average annually. This coverts to an average of 274 W/m^2 which will have relevance later on in this chapter. Historical data collected from the tobacco farmers in Zimbabwe indicate an average boiler coal consumption of 0.6 kg of coal burnt per 1 kg of dry tobacco leaves. The tunnel shown in Figure 6.1 has the capacity to dry 470 000 leaves or 16.45 t of dried tobacco in a 7-day period. Assuming a coal energy density of 30 000 kJ/kg the actual power consumption of the boiler is calculated as:

$$\dot{Q}_{act} = coal\ burnt * energy\ density/time \tag{6.2}$$

$$\dot{Q}_{act} = 0.6x16450x\frac{30000}{604800} = 490\ kW$$

The efficiency of the air heating process via the boiler is calculated by the ratio of the power required to heat the air to the actual power used as 58 %.

Insert 1.2 with λ = 20 mm and ζ = 48 % is selected for this case study as this insert has the highest performance index for the one wall heating boundary condition. For the tunnel shown in Figure 6.1 the heat transfer area on the roof is calculated as 624 m^2. The length of the tunnel allows for 197 channels to be placed on each side of the roof. Running the insert through the entire length of each channel results in a total insert length of approximately 3000 m. The pressure drop per meter for insert 1.2 was experimentally determined to be 10.03 Pa/m at Re = 2000.

The control damper on the roof duct line is adjusted so that the flow through the channels is at a Reynolds number of Re = 2000. At this Reynolds number the performance index for insert 1.2 is a maximum. This Reynolds number corresponds to a mass flow rate of 1.58 kg/s. At Re = 2000 the convective heat transfer coefficient is calculated from the experimentally determined Nusselt number as 11.3 W/m^{2}K. Assuming that a 10 °C temperature difference can be maintained between the bulk mean temperature of the air and the top surface temperature of the channel, the power added to the air via the solar radiation is calculated as:

$$\dot{Q_{sol}} = hA_{ht}(T_s - T_m) \tag{6.3}$$

$$\dot{Q_{sol}} = 11.3x624x10 = 70.2\ kW$$

Assuming that this auxiliary solar system will be operational for 8 hours a day and using the same coal energy density of 30 000 kJ/kg, a total of 810 kg of coal can be saved each day. The net head for a centrifugal pump is calculated by the difference in the pressure across the insert [3]:

$$H_f = \frac{\Delta P}{\rho g} \tag{6.4}$$

And the power delivered to the fluid is calculated as:

$$P_w = \rho g Q H_f \tag{6.5}$$

The additional pumping power required to move the air through the total length of channel is calculated by the discharge multiplied by the net pressure head:

$$P_w = Q\Delta P \tag{6.6}$$

$$P_w = 1.582x10.3x3000 = 47.6\ kW$$

Working this power value back to a coal mass assuming an 8 hour operating time results in an additional energy cost of 320 kg of coal. The net saving in energy over a six-month drying season is 20.8 tons of coal. Based on the price of coal and a USD to ZAR exchange rate as of the May 2018 this saving in energy is calculated R27 183.

The calculations above are based on maintaining a 10 °C temperature difference between the bulk mean temperature of the air and the top surface temperature of the channel. In order to maintain this temperature difference a heat flux of 112.4 W/m^2 needs to be applied to the top surface of the channel. This is well below the 274 W/m^2 specified by Meyer [28] suggesting that the scenario is plausible. If a heat flux of 274 W/m^2 is applied to the top surface of the channel the resulting temperature difference would be 24 °C and the outlet temperature of the air from the channels would be 130 °C. An outlet temperature as high as 130 °C would be difficult to achieve as radiational losses back to the environment would start to become significant. However, if a temperature difference of 24 °C could be maintained the capital savings over a six-month period could be as high as R54 500.

Figure 6.3 shows the plots of the potential savings in coal usage and Rand as a function of the temperature difference. Figure 6.3 clearly shows that energy saved in the solar system is directly proportional to the sustainable temperature difference between the bulk mean temperature of the air and top surface temperature of the channel. The plot also shows that should the temperature difference drop below 3 °C the process would no longer be financially viable due to the increased pressure drop of the system.

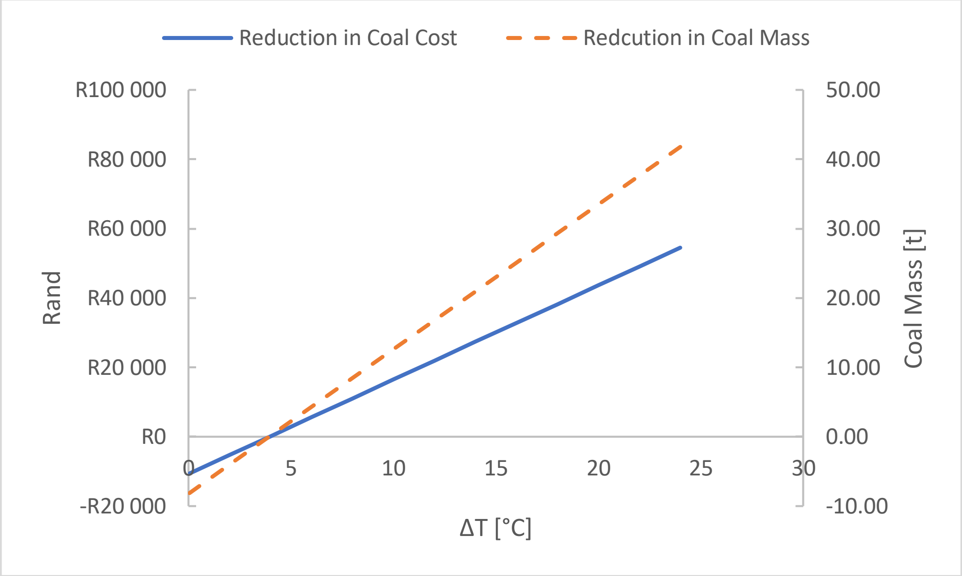

Figure 6.3: Capital savings as a function of channel temperature difference

Calculations show that for Reynolds numbers greater than Re = 2000 the system as shown in Figure 6.1 will not be viable as the pressure drop per meter over the insert increases rapidly. The pumping power required to overcome the additional pressure drop outweighs the power that can be collected from the roof channels via solar radiation. Figure 6.4 shows the savings that can be achieved for the system running at Reynolds numbers of Re = 400, 1000 and 2000. The plots show that the total energy saved is potentially greatest at the lowest Reynolds number. This is due to the insert having the lowest pressure drop per meter at the given air flow velocity. However, it should be noted that the difference between the bulk mean temperature of the air and the top surface of the channel needs to increase as the Reynolds number decreases to be able to supplement the same amount of power. With Re = 400 and a heat flux of 274 W/m^2 the temperature difference between the air and the top surface of the channel would be approximately 45 °C. The outlet temperature of the air from the channel would theoretically be in excess of 540 °C. Thermal losses would prevent such a scenario from being plausible.

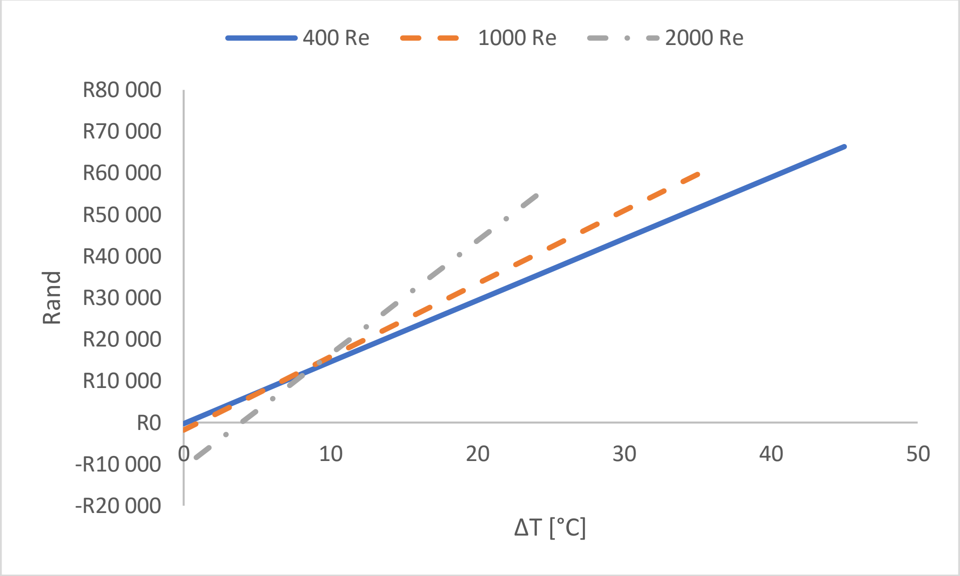

Figure 6.4: Capital savings as a function of Reynolds number

The insert considered by Mahmood et al. [14] in a 5 mm high channel is considered in the case study. The performance index of the insert is greatest at a Reynolds number of Re = 3100. The 260 Pa/m pressure drop accompanying the insert is too large to be considered practical in this application. The required pumping power at this Reynolds number would be approximately 1.8 MW. The initial cost of the fan alone would not be financially feasible for this application. The same conclusion can be drawn for the 5 mm inserts studied by Cramer [23]. The 14 mm inserts studied by Cramer [23] leads to plausible scenarios when applied to the tunnel as shown in Figure 6.1. For the 14 mm inserts studied by Cramer [23] the highest performance index was achieved with Insert 1.1 at 1000 Re in a one wall heating application. The calculations show a potential savings of almost R62 000 per season is obtainable for a temperature difference between the air and the top surface of the channel of 18 °C. A comparison of the insert studied by Cramer and Insert 1.2 of this study is shown in Figure 6.5.

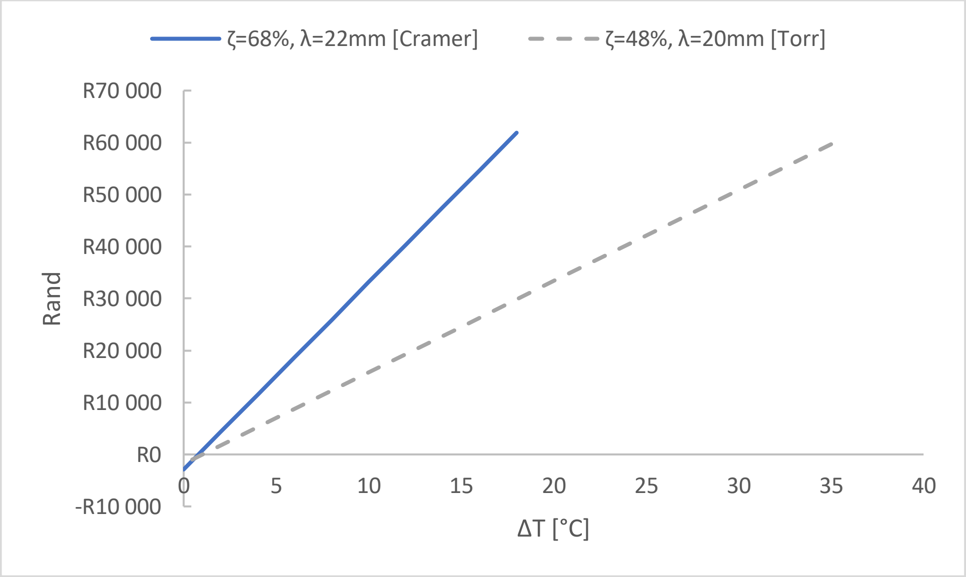

Figure 6.5: Comparison of inserts studied by Cramer and Torr at Re = 1000

6.3 Conclusion

The case study shows that insert 1.2 (48 % porosity with a wavelength of 20 mm) can be implemented in a cost-effective manner to a tobacco drying system in order to reduce operating costs by harnessing solar energy. The study shows that up to R60 000 per drying tunnel per season can be saved in coal expenditure depending on the operating conditions of the system. Calculations show that running the system at low Reynolds numbers does not result in a cost-effective system. The study shows that there is an optimal operating point where the pressure drop per meter of insert is low, the temperature difference between the mean temperature of the fluid and the channel heated surface as well as the outlet temperature of the fluid is plausible and the solar heat flux is equal to or below measured data.

The case study was extended to multiple inserts whose performance index as set by [5,6] is greater than one. The study shows that not all inserts can be implemented in such system as the pressure drop per meter of insert renders the insert financially unsuitable. These inserts need to be short in length and the operating temperatures need to be high in order for the insert to be effective. The smaller 5 mm inserts could still have applications in smaller plate heat exchangers.

7 Summary, Conclusion and Recommendations

7.1 Summary

To investigate the thermal performance of sinusoidal screen inserts in flat plate heat exchangers an experimental test facility is constructed which is capability of replicating the conditions of a heat exchanger. The test facility is primarily composed of rectangular and circular ducting. The inlet, outlet and test sections are fabricated from acrylic plate and designed to allow for an adjustable channel height. The test facility allows for the measurement of the pressure drop across the insert as well has the convective heat transfer coefficient at the heated walls of the rectangular channel for both a one wall and a two wall heat transfer boundary condition.

Six inserts are fabricated with varying wavelength and porosity. The height or amplitude of the sinusoidal waveform remains constant at 14 mm for all the inserts. The wavelength, λ is investigated at 12 mm, 16 mm and 20 mm. The effects of the porosity of the insert, ζ is investigated at 48 % and 68 % porosity. The inserts are placed inside the 14 mm rectangular test sections and temperature and pressure measurements are recorded and validated over a range of 400 Re to 35 000 Re. The smooth channel case is investigated to serve as a comparative baseline result. The inserts are not attached to the test section side walls and only make line contact along the peaks of the sinusoidal waveform. As a result, there is no thermal conduction between the heated wall and the insert due to the zero area contact points.

The Fanning friction factor for the insert is calculated by measuring the static wall pressures at 30 locations along the centreline of the test section. The friction factor is determined for each of the 6 inserts (as well as the smooth channel) at 18 different Reynolds numbers ranging from 400 < Re < 35 000 amounting to 3 780 pressure measurements. The average and local Nusselt numbers are determined by measuring the temperature at 25 locations along the centreline of the heated walls. For the two wall heating boundary condition the Nusselt number is calculated at 18 Reynolds numbers ranging from 400 < Re < 35 000. For the one wall heating boundary condition the Nusselt number is calculated at 12 Reynolds numbers ranging from 400 < Re < 30 000. In total 6 300 temperature measurements are recorded. The test section is insulated for the heat transfer experiments to minimize heat losses. The losses through the insulation on the broad side of the channel are calculated to range from 1 W to 3.2 W (1.8 – 3.5 %) depending on the surface temperature of the heated wall.

The friction factors and average Nusselt numbers for the smooth channel are validated against analytical and experimental data published in literature. The experimental data obtained from the test section agrees with that in the publish literature. An uncertainly analysis is performed on the measurement and data reduction techniques. The uncertainty in the friction factor range from 8.1 % at low Reynolds numbers to 4.7 % at high Reynolds number. The uncertainty in the local and average Nusselt numbers ranges from 8.4 - 4.3 % and 2.5 - 1.2 % respectively with the highest uncertainty at low Reynolds numbers.

The performance of each insert is evaluated by taking a ratio of the increase in the Nusselt number compared to the smooth channel to the increase in the pressure penalty compared to the smooth channel. The performance index evaluates the enhanced heat exchanger (test section with an insert) against the baseline heat exchanger (smooth channel) according to three basic enhancement design criteria [5,6], namely the increase in heat transfer area for the same pumping power and heat transfer rate, the increase in the heat transfer rate for the same heat transfer area and pumping power and the decrease in pumping power for the same heat transfer rate and area.

7.2 Conclusion

The smooth channel validation shows that the experimental test facility is capable of replicating the conditions experienced in flat plate heat exchangers. The smooth channel friction factors show a maximum deviation from the data presented by Shah and London [7] of 3.9 % in the laminar regime (Re < 2000). In the turbulent flow regime (Re > 10 000) the experimental friction factor deviates by a maximum value of 5.7 % from the analytical friction factors presented by Karman and Nikuradse [4]. In the laminar flow regime the one wall heat transfer boundary condition experimental smooth channel average Nusselt number is calculated to deviate from the analytical data of [7] by a maximum of 10 %. For the two wall heating boundary condition the experimental data deviated by a maximum of 9 %. In the turbulent flow regime for the two wall heating boundary condition the experimental smooth channel average Nusselt number is compared to analytical data presented by Gnielinski [2] for a constant peripheral heating boundary condition. The experimental average Nusselt number differs from the analytical data by a maximum of 10 % over the range 3000 < Re < 35 000. For the one wall heating experiments the smooth channel average Nusselt number is compared to extrapolated data presented by Kays and Crawford for parallel plates of the same boundary condition [4]. The data is calculated to deviate from that suggested by Kays and Crawford by a maximum of 7 % over the range 10 000 < Re < 30 000.

The uncertainty analysis shows that instrumentation and data reduction methods result in reliable and accurate measurements. The uncertainty in the friction factor ranges from 8.1 % at low Reynolds numbers to 4.7 % at high Reynolds number. The uncertainty in the local and average Nusselt numbers ranges from 8.4 - 4.3 % and 2.5 - 1.2 % respectively with the highest uncertainty at low Reynolds numbers.

The mesh manufacture methods prove to be efficient and economical. The friction factors obtained for the duplicate set of inserts with ζ = 68 % differ by 5 % or less. For inserts with ζ = 48 % the friction factors differ by 2 % or less with the exception of the result obtained at Re = 3000 where the friction factor differs by 6 %. From the friction factor results obtained for the duplicate sets of inserts it is determined that changes in the friction factors between the various inserts tested are attributed to changes in the wavelength and porosity rather than skewness, undulations or imperfections resulting from the manufacture of the inserts. As the duplicate inserts produce similar friction factors it is reasonable to assume that the duplicate insert will produce similar Nusselt numbers due to analogous turbulence characteristics of the inserts

The theoretical developing lengths suggest by [3,4] are longer than the inlet section on the experimental setup for Reynolds numbers around Re = 2000. However the baseline wall static pressure measurements obtained from the test section show a constant gradient suggesting that the flow is hydrodynamically fully developed. If the flow velocity profile is not fully developed at the start of the test section, it is very close to being so, so close that the effects are not evident in the experimental data.

For all the inserts tested the normalized pressure drop decreases as the Reynolds number increases. The normalized pressure drop in the channel with an insert is observed to be always be higher than that of the corresponding base line pressure drop. The hydrodynamic developing length of the inserts is analysed to range between 0.08 m and 0.14 m between 1400 < Re < 4000.

The insert with the shortest wavelength, λ = 12 mm produces the highest friction factor followed by the insert with a wavelength λ = 16 mm and the insert with λ = 20 mm producers the lowest friction factor. The friction factor increases with the decrease in the wavelength on the insert. The relationship between the friction factor and the wavelength is observed to be nonlinear. The increase in the friction factor between λ = 20 mm and λ = 16 mm is significantly larger than the increase in the friction factor between λ = 16 mm and λ = 12 mm. This relationship was prevalent for both insert porosities investigated.

The friction factor increases with the decrease in porosity however this in not true for the entire Reynolds number range tested. The friction factors between $1000 < Re < 2000$ for the inserts with ζ = 48% decrease to local minimums which are lower than that of the inserts with ζ = 68%. The decrease in the fiction factor over this Reynolds number range is observed for all three wavelengths analysed. The results show an inverse relationship between the porosity of the insert and the friction factor.

The friction factor ratios for the inserts tested show an increasing relationship with the increase in the Reynolds number. The results shown that the insert with the shortest wavelength, λ = 12 mm produces the highest friction factor ratio followed by the insert with a wavelength λ = 16 mm and the insert with λ = 20 mm producers the lowest friction factor ratio. All six inserts show a decrease in the friction factor ratio at Re = 5000 while only the inserts with ζ = 68 % show a decrease in the friction factor ratio at Re = 2000.

The local Nusselt number increases with the increase in the Reynolds number due to the increase in the velocity and mass flow rate in the test section. This was observed for both the two wall and one wall heat transfer boundary conditions. The thermal developing length is observed to decrease with the increase in Reynolds number for both inserts with ζ = 68 % and ζ = 48 %. For $400 < Re < 35000$ the local Nusselt numbers reach a steady value at approximately $x/L = 0.6$.

The average Nusselt number is observed to increase with the increase in the Reynolds number. For the two wall heating boundary condition, between $2000 < Re < 3000$ the average Nusselt number for all six inserts increased by 50 - 75 % will over the same Reynolds number range the average Nusselt number increased by 90 % for the one wall heat transfer boundary condition. The average Nusselt number for the two wall heating boundary condition was observed to larger that of the one wall heating boundary condition at the corresponding Reynolds number.

The inserts with λ = 12 mm produce the highest Nusselt number ratio and the inserts with λ = 16 mm produce the lowest. The Nusselt number ratio for the insert with λ = 20 mm fluctuates between the two previously stated wavelengths. The Nusselt number ratio is larger for the two wall heating boundary condition than the one wall heating boundary condition. For the majority of the heat transfer experiments conducted the Nusselt number ratio for inserts with ζ = 48 % is larger than that of the inserts with ζ = 68 %. The results suggest an inverse relationship between the porosity of the insert and the Nusselt number.

The thermal losses through the insulation on the heated walls is calculated to small compared to the power supplied to the heaters. However due to the high uncertainties and low power supplied to the heaters at lower Reynolds numbers ($400 < Re < 6000$) the losses should still be considered in the calculations. The axial conductional losses along the direction of flow in the test section is determined to be negligible [14].

The performance index, $(Nu/Nu_0)/(f/f_0)^{1/3}$ is the greatest between $1400 < Re < 3000$ for all six inserts tested. The performance index is larger the two wall heating boundary condition than the one wall heating boundary condition. The performance index is higher for the insets with ζ = 48 % than ζ = 68 %. For both porosities the inserts with a wavelength of λ = 20 mm produced the highest performance index followed by the inserts with λ = 12 mm. The insert with ζ = 48 % and λ = 20 mm is determined to offer the greatest enhancement to the heat transfer in a 14 mm channel for both the two wall and one wall heat transfer boundary condition. The insert increases the effective heat transfer area 60 %, the heat transfer rate by 37 % or decrease the fluid pumping power by 157 %.

The performance index shows that the optimal flow rate for enhance heat transfer varies with the porosity and wavelength of the insert. This implies that while one insert may offer improved thermal performance in a heat exchanger at a specific flow rate, another may not. The optimal operating range is limited to a Reynolds number range of approximately 1000.

The case study shows that the 14 mm inserts can be implemented on the roof of tobacco drying barns as solar heat exchangers. The inserts provide a cost effective and clean energy source that can supplement the fossil fuels burnt in the boiler. Further research should be done with inserts with a larger amplitude. The increased amplitude will allow for a larger flow rate through the channel, decreased pressure drop and may result in the redundancy of the coal boiler during the day. The case study shows that although the 5mm inserts evaluated by [14,23] have a performance index greater than 1 and show enhanced thermal characteristics when evaluated to the design objectives stated by [5,6], the use of the inserts is not suited for applications with long channels due to the large pressure head need to pump the fluid through the insert. Such inserts would be better suited for short plate heat exchangers such as that on the collection tank of a solar water heaters where the fluid can be passed through the heat exchanger multiple times.

The study shows that that the use of sinusoidal inserts in flat plate heat exchanges can produce an increase in the thermal performance over the range of $400 < Re < 3000$. The inserts do not significantly increase the manufacture cost of the heat exchanger and add to the integrity of the channel structure with a minimal increase in the mass.

As stated in the problem statement "by independently investigating the physical properties of a wavy porous insert, such as the porosity, size and periodicity of the insert, the best size and shape of the insert can be determined for increasing the effectiveness, size, weight and thermal performance of the heat exchanger", the result show that he insert with $\zeta = 48$ % and $\lambda = 20$ mm is offers the greatest enhancement to the heat transfer in a 14 mm channel for both the two wall and one wall heat transfer boundary condition. The insert with $\zeta = 48$ % and $\lambda = 20$ mm can therefore be considered ideal for the test section dimensions and over the range $48 \leq \zeta \leq 68$ %, $12 \leq \lambda \leq 20$ mm and $400 \leq Re \leq 35\ 000$. As shown in the case study the best insert for heat transfer enhancement in a heat exchanger is dependent on the heat exchanger application. For example, the ideal insert to be used in electronic chip cooling channel will differ considerably to that used to supplement the boiler efficiency in the tobacco industry. The electronic chip cooling insert will have a small amplitude and wavelength as the cooling channels are typically short in length whereas the ideal insert to be used in a tobacco barn roof requires an insert with a large amplitude and wavelength to reduce the pressure drop along the channel as well as a larger pore diameter to avoid the accumulation of dust in the pores of the insert. It is therefore noted that the best sinusoidal insert for heat transfer augmentation in a rectangular channel is not only dependant on the wavelength, amplitude and porosity of the insert but also on the application in which the insert is employed.

7.3 Recommendations

The following outcomes are recommended with regards to the design of the experimental setup and areas of future study:

- The experimental setup is designed in a modular basis to accommodate the work space on the CNC machines. Assembly of modules can become cumbersome and time consuming however it in necessary to dissemble and assembly the module to replace inserts and perform maintenance. It is recommended that all non-essential components be further assembled and fixed together. This will allow for aligned of a single part when adjusting the channel height and assembling the channels. This will also reduce errors introduced by the ingress of air and by the misalignment between parts.
- The sampling rate of the wall static pressure measurements of the smooth at the high end of laminar regime and in the transitional regime should be adjusted to reduce the effects of the turbulent fluctuations in the channel.
- An additional section can be added to the inlet of the channel to increase the inlet length to 3.0 m. This will eliminate any dispute with regards to the hydrodynamic developing length of the low around Re = 2000.
- A single heating strip for the heated test section walls should be made on special request. The join between the two heating strips contributes to a discontinuity in the heat flux which contradicts the assumptions that a uniform heat flux is applied to the heated walls.
- The pressure drop per meter of insert significantly influence the thermal efficiency of the system. It is suggested that the insert be split into pieces and spaced equidistantly down the length of the test section. The staggering of the insert will reduce the total length of the insert and hence the form drag. It is expected that the heat transfer will be reduced but still enhanced in the empty space between inserts. Research can be done on the optimal distance of such spacings.
- The results shown an inverse relationship between the porosity of the insert and the friction factor. It is recommended that further research be done on inserts with a higher porosity as the friction factor is expected to further decrease.
- The results show that thermal enhancement of the inserts is poor in the turbulent flow regime due to the overwhelming pressure drop developed across the insert. It is recommended that the Reynolds number range be reduced to only cover the laminar and transitional flow regime (Re < 12 000). This will allow for the investigation of a wider range of inserts in the time allocated for test work.
- As the performance of the insert is dependent on the application and environment in which the heat exchanger is employed it is recommended that the field of study be narrowed down to one particular application or process.

References

[1] Webb, R. L., and Kim, N.-H., 2005, *Principles of Enhanced Heat Transfer*, 2nd ed., Taylor and Francis, Oxon, UK.

[2] Cengel, Y. A., and Ghajar, A. J., 2011, *Heat and Mass Transfer*, 4th ed., McGraw-Hill, New York.

[3] White, F. M., 2011, *Fluid Mechanics*, 7th ed., McGraw-Hill, Singapore.

[4] Kays, W. M., and Crawford, M. E., 1980, *Convective Heat and Mass Transfer*.

[5] Gee, D. L., and Webb, R. L., 1980, “Forced Convection Heat Transfer in Helical Ribbed Tubes,” International Journal of Heat and Mass Transfer, **23**(8), pp. 1127–1136.

[6] Webb, R. L., and Eckert, E. R. G., 1972, “Application of Rough Surfaces to Heat Exchanger Design,” International Journal of Heat and Mass Transfer, **15**(9), pp. 1647–1658.

[7] Shah, R. K., and London, A. L., 1978, *Laminar Flow Forced Convection in Ducts: A Source Book for Compact Heat Exchanger Analytica Data*.

[8] Han, L. S., 1960, “Hydrodynamic Entrance Lengths for Incompressible Laminar Flow in Rectangular Ducts,” Journal of Applied Mechanics, **27**, pp. 403–409.

[9] McComas, S. T., 1967, “Hydrodynamics Entrance Lengths for Ducts of Arbitrary Cross Section,” Journal of Basic Engineering, **89**, pp. 847–850.

[10] Meyer, J. P., 2014, “Heat Transfer in Tubes in the Transitional Flow Regime,” *15th International Heat Transfer Conference*, Kyoto, Japan.

[11] Everts, M., 2014, “Heat Transfer and Pressure Drop of Developing Flow in Smooth Tubes in the Transitional Flow Regime,” University of Pretoria.

[12] Jeng, T.-M., Tzeng, S.-C., and Tang, F.-Z., 2009, “Fluid Flow and Heat Transfer Charateristics of the Porous Metallic Heat Sink with a Conductive Cylinder Partially Filled in a Rectangular Channel,” International Journal of Heat and Mass Transfer, **53**, pp. 4216–4227.

[13] Heidary, H., and Kermani, M. J., 2011, “Enhancement of Heat Exchangers in a Wavy Channel Linked to a Porous Domain; a Possible Duct Geometry for Fuel Cells,” International Communications in HEat and Mass Transfer, **39**, pp. 112–120.

[14] Mahmood, G. I., Simonson, C. J., and Besant, R. W., 2014, “Experimental Pressure Drop and Heat Transfer in a Rectangular Channel With a Sinusoidal Porous Screen,” ASME Journal of Heat Transfer, **137**(4).

[15] Cramer, L., Mahmood, G. I., and Meyer, J. P., 2018, “Thermohydraulic Performance of a Channel Employing Wavy Porous Inserts,” Heat Transfer Research, **49**(18), pp. 1867–1883.

[16] Kahalerras, H., and Targui, N., 2008, “Numerical Analysis of Heat Transfer Enhancement in a Double Pipe Heat Exchangerwith Porous Fins,” International Journal of Numerical Methods for Heat & Fluid Flow, **18**(5), pp. 593–617.

[17] Pavel, B. I., and Mohamad, A. A., 2004, “An Experimental and Numerical Study on Heat Transfer Enhancement for Gas Heat Exchangers Fitted with Porous Media,” International Journal of Heat and Mass Transfer, **47**(23), pp. 4939–4952.

[18] Suri, A. R. S., Kumar, A., and Maithani, R., 2018, “Experimental Investigation of Heat Transfer and Fluid Flow Behaviour in Multiple Square Perforated Twisted Tape with Square Wing Inserts Heat Exchanger Tube,” Heat and Mass Transfer, **54**(6), pp. 1813–1826.

[19] Bekele, A., Mishra, M., and Dutta, S., 2014, “Performance Characteristics of Solar Air Heater with Surface Mounted Obstacles,” Energy Conversion and Management, **85**, pp. 603–611.

[20] Bekele, A., Mishra, M., and Dutta, S., 2013, “Heat Transfer Augmentation in Solar Air Heater Using Delta-Shaped Obstacles Mounted on the Absorber Plate,” International Journal of Sustainable Energy, **32**(1), pp. 53–69.

[21] Mahmood, G. I., and Arnachellan, K., 2018, “Effects of Upstream Endwall Film Cooling on a Vane Cascade Flowfield,” Journal of Propulsion and Power, **34**(2), pp. 460–468.

[22] ISO-5167, I. S., 1980, *Measurements of Fluid Flows by Means of Orifice Plates, Nozzles and Venturi Tubes Inserted in Circular Cross-Section Conduits Running Full*.

[23] Cramer, L., 2016, “Enhancement of the Thermal Performance of Solar Heat Exchanges with Porous Inserts,” University of Pretoria.

[24] Moffat, R. J., 1988, “Descibing the Uncertainty in Experimental Results,” Experimental Thermal and Fluid Science, **1**(3), pp. 3–17.

[25] Figliola, R. S., and Beasley, D. E., 2000, *Theory and Design for Mechanical Measurements*, 3rd ed., John Wiley & Sons, New York.

[26] White, F. M., 2006, “Viscous Fluid Flow,” *Viscous Fluid Flow*, McGraw-Hill, New York, pp. 96–205.

[27] Fraser-Mackenzie, J., 2018, *Engineering Consultant at Brown Engineering*, private communication, Harare.

[28] Meyer, R., 2015, *Accuarcy Enhanced Solar Maps of South Africa, Zambia and Malawi*, African Utility Week.

Appendix A: Calibration

A.1. Introduction

This appendix describes the calibration procedures for the various differential pressure transducers and thermocouples used throughout the course of the research. This appendix shows the calibration curves for the differential pressure transducers and lists the calibration curves for the thermocouples in tabular format.

A.2. Pressure Transducer Calibration

The differential pressure transducers are used to measure the pressure drop along the test section wall as well as the pressure drop across the orifice plates. Four pressure transducers are used individually to obtain the pressure drop along the test section. The appropriate differential pressure transducer is selected depending to the magnitude of the pressure drop along the test section. A single pressure transducer is used to measure the pressure drop across the orifice plate.

Each differential pressure transducer is calibrated using a Setra MicroCal advanced modular pressure calibrator. The differential pressure transducer is connected to the NI 9201 data acquisition module and an excitation voltage is applied across the transducer via a D.C. power supply. The differential pressure transducer is calibrated by plotting the output voltage from the differential pressure transducer against the applied pressure from the MicroCal.

The zero offset voltage is recorded before a pressure applied across the transducer. A total of six increasing pressures are applied and to each of the transducers until the pressure reaches the maximum range of the differential pressure transducer. A further three decreasing pressures are applied to the transducer to compensated for the linearity and hysteresis of the transducer. The calibration pressure is applied to the transducer and maintained until a steady voltage is achieved. Five sample pressures and voltages are recorded at each calibration point. The average values of the differential pressure transducer output voltage are plotted against the average values of the MicroCal applied pressure to obtain the calibration curve. The calibration curve for each transducer is shown in Figure A.1 below. The calibration curve is used to transform the recorded transducer output voltage to a differential pressure throughout the course of the experiments.

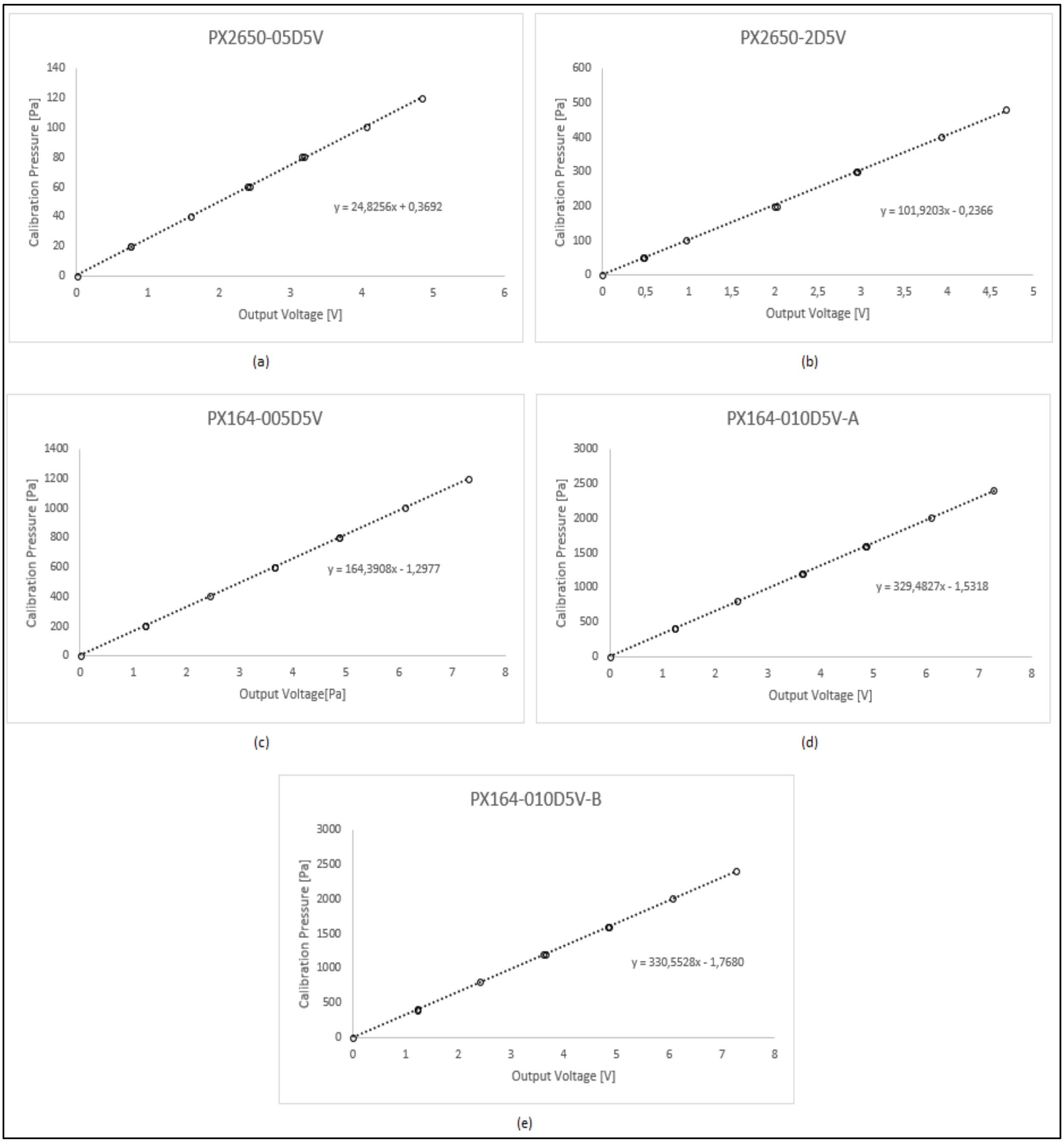

(a)

(b)

(c)

(d)

(e)

Figure A.1: Calibration Curves for (a) 0.5”, (b) 2”, (c) 5’’, (d) 10” channel and (e) 10” orifice plate differntial presssure transducers.

A.3. Thermocouple Calibration

80 thermocouples are used to measure the temperatures at various locations on the heated walls of the test section. One thermocouple was used to measure the temperature of the ingressed air at the inlet of the channel. 10 thermocouples were used to measure temperatures at various position in the insulation to determine the amount of heat lost from the heated walls.

The Omega Type T TT-T-30 thermocouple are cut to the appropriate length and spot welded at one end. The free ends of the thermocouples are attached to the NI 9213 data acquisition cards. The welded ends of the thermocouples along with a PT-100 thermocouple probe are inserted into the Lauder Eco RE 1225 thermal bath which has an accuracy of 0.03 °C.

The thermocouples are calibrated over 17 increments ranging from 20 - 60 °C. A minimum of 10 data points is collected at each temperature once the calibration unit has reached a steady state. The average values of the thermocouple temperature are plotted against the average values of the thermal bath temperature to obtain the calibration curve. The calibration curve for each thermocouple is shown in Table A.1 below. The calibration curve transforms the recorded thermocouple temperature to a calibrated temperature throughout the course of the experiments.

Table A.1: Thermocouple calibration curves

TC	a [°C/°C]	c [°C]	δT [°C]	TC	a [°C/°C]	c [°C]	δT [°C]	TC	a [°C/°C]	c [°C]	δT [°C]
1	1,00034	0,32	0,17	28	1,0003	0,58	0,17	55	1,0024	0,34	0,26
2	1,0019	0,39	0,23	29	1,0007	0,52	0,18	56	1,0018	0,52	0,22
3	1,0019	0,42	0,23	30	1,0008	0,58	0,18	57	1,0017	0,53	0,22
4	1,001	0,48	0,19	31	1,0013	0,53	0,20	58	1,0016	0,56	0,21
5	1,0015	0,48	0,21	32	1,0015	0,44	0,21	59	1,0008	0,59	0,18
6	1,0006	0,52	0,18	33	1,0018	0,35	0,22	60	1,0003	0,63	0,17
7	1,0011	0,52	0,19	34	1,0013	0,41	0,20	61	1,0003	0,62	0,17
8	1,0007	0,54	0,18	35	1,0017	0,41	0,22	62	1,0002	0,59	0,17
9	1,0001	0,57	0,17	36	1,0011	0,47	0,19	63	1,0002	0,59	0,17
10	1,0006	0,57	0,18	37	1,0007	0,50	0,18	64	1,0002	0,49	0,17
11	1,0009	0,60	0,18	38	1,0001	0,53	0,17	65	1,0002	-0,47	0,16
12	1,0009	0,63	0,18	39	0,9997	0,56	0,17	66	1,0004	-0,70	0,16
13	1,0006	0,64	0,18	40	1,0000	0,55	0,17	67	1,0025	-0,83	0,20
14	1,0011	0,62	0,19	41	1,0002	0,57	0,17	68	1,0017	-1,00	0,21
15	1,0011	0,58	0,19	42	0,9999	0,59	0,17	69	0,9998	-0,52	0,18
16	1,0006	0,49	0,18	43	1,0000	0,62	0,17	70	0,9995	-0,39	0,18
17	1,0024	0,29	0,26	44	1,0002	0,65	0,17	71	0,9993	-0,02	0,19
18	1,0021	0,34	0,24	45	1,0005	0,64	0,17	72	0,999	-0,02	0,20
19	1,0011	0,39	0,19	46	1,0006	0,62	0,18	73	0,9993	0,22	0,19
20	1,0007	0,43	0,18	47	1,0007	0,57	0,18	74	1,0006	-0,07	0,19
21	1,0004	0,44	0,17	48	1,0011	0,48	0,19	75	0,9998	-0,26	0,18
22	1,0003	0,47	0,17	49	1,0015	0,14	0,21	76	1,0001	-0,42	0,19
23	0,9999	0,43	0,17	50	1,0021	0,36	0,24	77	0,9943	0,15	0,17
24	0,9998	0,51	0,17	51	1,0024	0,31	0,26	78	0,9936	0,38	0,17
25	1,0004	0,51	0,17	52	1,0023	0,40	0,25	79	0,9952	0,66	0,17
26	1,0000	0,54	0,17	53	1,0024	0,44	0,25	80	0,9956	0,81	0,17
27	1,0007	0,55	0,18	54	1,0022	0,47	0,24	-	-	-	-

A.4. Conclusion

This appendix contains the calibrations procedures and results for the thermocouples and differential pressure transducers used in the course of the experimentation. The calibration process reduces the bias error and improves the accuracy of the measured pressures and temperatures. The thermocouples are calibrated using a thermal bath with an accuracy of 0.03 °C. The pressure transducers are calibrated with a high precision pressure calibration unit with a maximum error of 0.12% of the transducer full-scale range.

Appendix B: Uncertainty Analysis

B.1. Introduction

In order to quantify the accuracy for the experimental results an uncertainty analysis is conducted considering both the experimental procedure and the various instruments used. The analysis incorporates the errors involved with the collection of the raw data from the experimental through to the calculation of the end deliverables such as friction factors and Nusselt number ratios, efficiencies and performance factors. The measurement errors are subjected to the same mathematical procedures as the experimental data to give an accurate reflection of the propagation of the error throughout the experiment

B.2. Theory

The sources of errors involved in the experiment can be categorized as fixed or random depending on whether the type of error that is introduced is steady or fluctuating. The fixed or bias errors produce an experimental result which is continuously offset from the true value while the random or precision errors produce a result which varies around the true value, presumable with a zero mean [1]. The combination of the bias and precision errors can be calculated as:

$$\mathrm{\delta X_i} = \left(\mathrm{b_i^2} + \mathrm{p_i^2}\right)^{0.5} \tag{B.1}$$

Where X_i represent the error involved with a single measurement and δX_i represents the standard deviation in the measurement multiplied with the Student’s t-variable [1]. For an experimental procedure involving multiple measurements the result of the experiment is a function of multiple independent variables:

$$\mathrm{R} = \mathrm{R}(\mathrm{X_1}, \mathrm{X_2}, \mathrm{X_3}, \cdot\ \cdot\ \cdot, \mathrm{X_N}) \tag{B.2}$$

For an experiment involving a single measurement subject to an error, the effect of the error in the measurement on the result can be calculated as:

$$\delta R_{Xi} = \frac{\partial R}{\partial X_i} \delta X_i \tag{B.3}$$

The partial derivative of R with respect to X_i is the sensitivity coefficient for the result R with respect to the measurement X_i. For an experiment involving several independent measurements with associated independent errors the factors can be combined in root-sum-square method [1]:

$$\delta R = \left\{ \sum_{i=1}^{N} \left(\frac{\partial R}{\partial X} \delta X_i \right)^2 \right\}^{0.5} \tag{B.4}$$

The bias uncertainty in the thermocouple and differential pressure transducers is calculated by using a linear regression analysis. The precision uncertainty is calculated according to the manufacturer specifications. The overall uncertainty in the temperature and pressure measurements is calculated using the following equations [2]:

$$U_x = \left[\left(U_{cal,eqn}\right)^2 + (a_1 U_{xi})^2\right]^{0.5} \tag{B.5}$$

Where U_x is the uncertainty in the measured parameter and a_1 is the gradient for linear line of best fit obtained from the calibration procedure for the specified thermocouple or differential pressure transducer. $U_{cal,\ eqn}$ is the uncertainty introduced from the calibration procedure and is calculated as [2]:

$$U_{cal,eqn} = \left[(t_{v,95}\, S_{yx})^2 + (A_{cal})^2 + (a_1 U_x)^2\right]^{0.5} \tag{B.6}$$

A_{cal} is the accuracy of the calibration equipment and $t_{v,\ 95}$ is the students-t variable based on a 95% confidence interval. S_{yx} is the standard deviation based the deviation of each calibration data point form the linear line of best fit. S_{yx} was calculated as:

$$S_{yx} = \left[\frac{\sum_{i=1}^{N}(y_i - y_{ci})^2}{v}\right]^{0.5} \tag{B.7}$$

N is the number of data points used in the linear fit, y_{ci} is the measured parameter calculated using the equation of the line of best fit and *v* is the degree of freedom for the linear fit.

U_x is the precision uncertainty in the thermocouple or the differential pressure transducer and is calculated by:

$$U_x = \left[(t_{v,95}\, S_x)^2 + (A_{trans})\right]^{0.5} \tag{B.8}$$

S_x is the standard deviation of the recorded voltage for each calibration data point from the calibration linear line of best fit and is calculated by using the following equation:

$$S_x = \left[\left(\frac{1}{N-1}\right)\sum_{i=1}^{N}(x_i - \bar{x})^2\right]^{0.5} \tag{B.9}$$

N is the sample size of the measured voltage points, x_i is the recorded voltage value and $\bar{x}$ is the average of the measured voltage points calculated as:

$$\bar{x} = \sum_{i=1}^{N} x_i \tag{B.10}$$

B.3. Instruments

The uncertainty in the instruments is calculated considering the manufacturers specifications or the manufacture tolerances as well as the accuracy and uncertainty involved with the calibration process of the instruments. The precision uncertainty is calculated using the standard deviation of the calibration data sets while the bias uncertainty is calculated from the manufacturer specifications. All instruments are calibrated within a 95% confidence interval.

B.3.1. Pressure Transducers

All pressure transducers are calibrated as outlined in Section A.2. Each transducer is calibrated over ten pressure points set using the Setra MicroCal. The Setra MicroCal has an accuracy of 0.12% of the full-scale range for pressures below 250 Pa and 0.1% of the full-scale range for pressures above 250 Pa. The PX160 and PX2650 series differential pressure transducers have an accuracy of 1% of the full-scale range

Each calibration pressure point is the average of five sample pressures. The standard deviation in the recorded pressure is calculated via equation B.7. The standard deviation in the voltage reading is calculated via equation B.9 and B.10. The precision uncertainty is then calculated using equation B.6 and similarly the bias uncertainty is calculated via equation B.8. The total uncertainty in the measured pressures is calculated using equation B.5. The uncertainty in the differential pressure transducers range from 2.9 % at low Reynolds numbers to 1.1% at high Reynolds numbers. The uncertainty for the various differential pressure transducers is shown in Table B.1 below.

Table B.1: Differential pressure transducer uncertainties

Transducers	Range	Uncertainty	
PX2650-05D5V	0 Pa - 124 Pa	3,59 Pa	2,9%
PX2650-2D5V	0 Pa - 498 Pa	10,11 Pa	2,0%
PX164-005D5V	0 Pa - 1244 Pa	11,77 Pa	0,9%
PX164-010D5V	0 Pa - 2488 Pa	26,86 Pa	1,1%

B.3.2. Thermocouples

All eighty thermocouples are calibrated as outlined in Section A.3. Each thermocouple is calibrated using seventeen temperature points over a range of 20 °C to 60 °C against ta PT100 temperature probe inside a thermal bath. The PT100 temperature probe has an accuracy of 0.1 °C. The thermocouples are all cut from a spools of Omega duplex insulated copper constantan ANSI Type T TT-T-30 thermocouple wire with an accuracy of 0.1 °C.

Each calibration temperature point is the average of eleven sample temperatures. The standard deviation in the recorded temperature is calculated via equation B.7. The standard deviation in the voltage reading is calculated via equation B.9 and B.10. The precision uncertainty is then calculated using equation B. 6 and similarly the bias uncertainty was calculated via equation B.8. The total uncertainty in the measured pressures is calculated using equation B.5. The uncertainty in the thermocouples range from 1.6 °C to 2.6 °C with an average of 1.9 °C.

B.3.3. Orifice Plates

The orifice plates are manufactured in-house on lathes at the University of Pretoria from commercial steel plate. The diameters and eccentricity of the orifice is checked using vernier callipers with an accuracy 0.2 mm. The orifice plates are manufactured according to ISO standards [3]. The uncertainty in the discharge coefficient is calculated to range from 0.81 % at 400 Re to 0.6 % at 35 000 Re. The expansion coefficient is calculated to range from 0.02 % at 400 Re to 0.36 % at 35 000 Re [3].

B.3.4. Power Supply

The kapton heaters used in the heat transfer experiments are powered by a 240 volt A.C. variac power supply unit. The voltage and current applied across and to the heaters are monitored by a UNI-T UT33A and a UNI-T UT60A multi-meter. The voltage and current is observed to fluctuate over the course of the experiments. The voltage and current reading are recorded at the start of end each experimental run. The fluctuations in the voltage and current readings are used to determine the precision error in the applied power while the bias error is determined by accuracy and resolution of the digital multi-meters.

For the two wall heat transfer experiments the total error in the voltage is calculated to range from 0.82 V at low power levels to 3.069 V at high power levels. The total error in the current is calculated to range from 6.5 mA at low power levels to 24.5 mA at high power levels. For the one wall heat transfer experiments the total error in the voltage is calculated to range from 0.633 V at low power levels to 3.069 V at high power levels. The total error in the current is calculated to range from 10 mA at low power levels to 27.1 mA at high power levels. The uncertainty in the power supplied to the heaters for both the two wall and one wall heat transfer experiments is calculated to range from 2.79 - 2.77 % for the Reynolds numbers tested.

B.3.5. Physical Dimensions

The uncertainty in the dimensions of the test section is governed by the manufacture methods and assembly tolerances of the test section perspex plates. The test section components where manufactured by CNC milling machines. The uncertainty in the test section width and length is determined to be 0.5 mm. The uncertainty in the test section height was calculated from multiple measurement recorded by the use of a vernier calliper. Before each channel insert was tested the height of channel was measured at each corner of the test section to ensure that the test section and insert had been correctly assembled. The uncertainty in the channel height is calculated to be 0.26 mm.

The 2'' and 4'' PVC class 9 pipes are measured with Vernier callipers with an accuracy of 0.2mm. The 2'' and 4'' PVC pipes have a wall thickness of 3 mm and 5mm respectively.

B.4. Calculated Parameters

B.4.1. Channel Pressure Drop

The uncertainty in the channel pressure drop, $\Delta p/\Delta x$ is detonated by δb_1 and can be defined as the gradient of the line of best fit for the channel pressure versus distance plot. The uncertainty in the channel pressure drop, δb_1 is calculated as:

$$\delta b_1 = t_{v,95} S_{b1} \tag{B.11}$$

Where S_{b1} is determined as:

$$S_{b1} = S_{yx}\left[\frac{N}{N\sum_{i=1}^{N} x_i^2 - \left(\sum_{i=1}^{N} x\_i\right)^2}\right]^{0.5} \tag{B.12}$$

S_{yx} is determined via equation B.7.

B.4.2. Hydraulic Diameter

The uncertainty in the hydraulic diameter was calculated as follows:

$$D_h = \frac{4A}{P} = \frac{2wh}{w+h} \tag{B.13}$$

$$\delta D_h = \left[\left(\frac{\partial D_h}{\partial w}\delta w\right)^2 + \left(\frac{\partial D_h}{\partial h}\delta h\right)^2\right]^{0.5}$$

$$\delta D_h = \left[\left(\frac{2h^2}{(w+h)^2}\delta w\right)^2 + \left(\frac{2w^2}{(h+w)^2}\delta h\right)^2\right]^{0.5} \tag{B.14}$$

B.4.3. Density

The uncertainty in the density is calculated as follows:

$$\rho = \frac{p}{RT} \tag{B.15}$$

$$\delta\rho = \left[\left(\frac{\partial \rho}{\partial p}\delta p\right)^2 + \left(\frac{\partial \rho}{\partial T}\delta T\right)^2\right]^{0.5}$$

$$\delta\rho = \left[\left(\frac{1}{RT}\delta p\right)^2 + \left(\frac{-p}{RT^2}\delta T\right)^2\right]^{0.5} \tag{B.16}$$

B.4.4. Mass Flow Rate

The uncertainty in the mass flow rate is calculated according to [3]:

$$\frac{\delta\dot{m}}{\dot{m}} = \left[\left(\frac{\delta C}{C}\right)^2 + \left(\frac{\delta\varepsilon}{\varepsilon}\right)^2 + \left(\frac{2\beta}{1-\beta^4}\right)^2\left(\frac{\delta D}{D}\right)^2 + \left(\frac{2}{1-\beta^4}\right)^2\left(\frac{\delta d}{d}\right)^2 + \frac{1}{4}\left(\frac{\delta\Delta p}{\Delta p}\right)^2 + \frac{1}{4}\left(\frac{\delta\rho}{\rho}\right)^2\right]^{0.5} \tag{B.17}$$

B.4.5. Cross Sectional Area

The uncertainty in the cross-sectional area of the test channel is calculated as follows:

$$A_c = wh \tag{B.18}$$

$$\delta A_c = \left[\left(\frac{\partial A_c}{\partial w}\delta w\right)^2 + \left(\frac{\partial A_c}{\partial h}\delta h\right)^2\right]^{0.5}$$

$$\delta A_c = [(h\delta w)^2 + (w\delta h)^2]^{0.5} \tag{B.19}$$

B.4.6. Mean Channel Velocity

The uncertainty in the mean channel velocity is calculated as follows:

$$\overline{\mathrm{V}} = \frac{\dot{m}}{\rho A_c} \tag{B.20}$$

$$\delta\overline{\mathrm{V}} = \left[\left(\frac{\partial\overline{\mathrm{V}}}{\partial\dot{m}}\delta\dot{m}\right)^2 + \left(\frac{\partial\overline{\mathrm{V}}}{\partial\rho}\delta\rho\right)^2 + \left(\frac{\partial\overline{\mathrm{V}}}{\partial A_c}\delta A_c\right)^2\right]^{0.5}$$

$$\delta\overline{\mathrm{V}} = \left[\left(\frac{1}{\rho A_c}\delta\dot{m}\right)^2 + \left(\frac{-\dot{m}}{\rho^2 A_c}\delta\rho\right)^2 + \left(\frac{-\dot{m}}{\rho A_c^2}\delta A_c\right)^2\right]^{0.5} \tag{B.21}$$

B.4.7. Reynold Number

The uncertainty in the mean channel velocity is calculated as follows:

$$Re = \frac{\dot{m} D_h}{\mu A_c} \tag{B.22}$$

$$\delta\mathrm{Re} = \left[\left(\frac{\partial\mathrm{Re}}{\partial\dot{m}}\delta\dot{m}\right)^2 + \left(\frac{\partial\mathrm{Re}}{\partial D_h}\delta D_h\right)^2 + \left(\frac{\partial\mathrm{Re}}{\partial A_c}\delta A_c\right)^2\right]^{0.5}$$

$$\delta Re = \left[\left(\frac{D_h}{\mu A_c}\delta\dot{m}\right)^2 + \left(\frac{\dot{m}}{\mu A_c}\delta D_h\right)^2 + \left(\frac{\dot{m} D_h}{\mu A_c^2}\delta A_c\right)^2\right]^{0.5} \tag{B.23}$$

B.4.8. Fanning Friction Factor

The uncertainty in the friction factor is calculated as follows:

$$f = \frac{b_1(D_h/4)}{0.5\rho\overline{\mathrm{V}}^2} \tag{B.24}$$

$$\delta f = \left[\left(\frac{\partial f}{\partial b_1}\delta b_1\right)^2 + \left(\frac{\partial f}{\partial D_h}\delta D_h\right)^2 + \left(\frac{\partial f}{\partial\rho}\delta\rho\right)^2 + \left(\frac{\partial f}{\partial\overline{\mathrm{V}}}\delta\overline{\mathrm{V}}\right)^2\right]^{0.5}$$

$$\delta f = \left[\left(\frac{(D_h/4)}{0.5\rho\overline{\mathrm{V}}^2}\delta \mathrm{b}_1\right)^2 + \left(\frac{b_1}{0.5\rho\overline{\mathrm{V}}^2}\delta D_h\right)^2 + \left(\frac{b_1(D_h/4)}{0.5\rho^2\overline{\mathrm{V}}^2}\delta\rho\right)^2 + \left(-\frac{b_1(D_h/4)}{\rho\overline{\mathrm{V}}^3}\delta\overline{\mathrm{V}}\right)^2\right]^{0.5} \tag{B.25}$$

B.4.9. Friction Factor Ratio

The uncertainty in the friction factor ratio is calculated as follows:

$$R_f = \frac{f}{f_0} \tag{B.26}$$

$$\delta R_f = \left[\left(\frac{\partial R_f}{\partial f}\delta f\right)^2 + \left(\frac{\partial R_f}{\partial f_0}\delta f_0\right)^2\right]^{0.5}$$

$$\delta R_f = \left[\left(\tfrac{1}{f_0}\delta f\right)^2 + \left(\tfrac{f}{f_0^2}\delta f_0\right)^2\right]^{0.5} \qquad B.27$$

B.4.10. Electrical Power

The uncertainty in the electrical power is calculated as follows:

$$Q = VA \qquad B.28$$

$$\delta Q = \left[\left(\frac{\partial \mathrm{Q}}{\partial V}\delta V\right)^2 + \left(\frac{\partial \mathrm{Q}}{\partial \mathrm{A}}\delta \mathrm{A}\right)^2\right]^{0.5}$$

$$\delta Q = [(A\delta V)^2 + (V\delta A)^2]^{0.5} \qquad B.29$$

B.4.11. Heat Transfer Area

The uncertainty in the heat transfer area is calculated as follows:

$$A_{ht} = 2wl \qquad B.30$$

$$\delta A_{ht} = \left[\left(\frac{\partial A_{ht}}{\partial w}\delta w\right)^2 + \left(\frac{\partial A_{ht}}{\partial \mathrm{l}}\delta \mathrm{l}\right)^2\right]^{0.5}$$

$$\delta A_{ht} = [(2l\delta w)^2 + (2w\delta l)^2]^{0.5} \qquad B.31$$

B.4.12. Heat Flux

The uncertainty in the heat flux is calculated as follows:

$$q = \frac{Q}{A_{ht}} \qquad B.32$$

$$\delta q = \left[\left(\frac{\partial q}{\partial Q}\delta Q\right)^2 + \left(\frac{\partial q}{\partial \mathrm{A_{ht}}}\delta \mathrm{A_{ht}}\right)^2\right]^{0.5}$$

$$\delta q = \left[\left(\tfrac{1}{A_{ht}}\delta Q\right)^2 + \left(\tfrac{-Q}{A_{th}^2}\delta A_{th}\right)^2\right]^{0.5} \tag{B.33}$$

B.4.13. Bulk Mean Temperature

The uncertainty in the heat flux is calculated as follows:

$$T_{m,x} = \mathrm{T}_{\mathrm{amb}} + \frac{Q_{c,x}}{\dot{m}C_p} \tag{B.34}$$

$$\delta T_{m,x} = \left[\left(\frac{\partial T_{m,x}}{\partial T_{amb}}\delta T_{amb}\right)^2 + \left(\frac{\partial T_{m,x}}{\partial Q_{c,x}}\delta Q_{c,x}\right)^2 + \left(\frac{\partial T_{m,x}}{\partial \dot{m}}\delta \dot{m}\right)^2\right]^{0.5}$$

$$\delta T_{m,x} = \left[(\delta T_{amb})^2 + \left(\tfrac{1}{\dot{m}C_p}\delta Q_{c,x}\right)^2 + \left(\tfrac{-Q_{c,x}}{\dot{m}^2 C_p}\delta \dot{m}\right)^2\right]^{0.5} \tag{B.35}$$

B.4.14. Local Nusselt Number

The uncertainty in the local Nusselt number is calculated as follows:

$$Nu_x = \frac{Q_c D_h}{A_{ht}k(T_{w,x} - T_{m,x})} \tag{B.36}$$

$$\delta Nu_x = \left[\left(\frac{\partial Nu_x}{\partial Q_c}\delta Q_c\right)^2 + \left(\frac{\partial Nu_x}{\partial D_h}\delta D_h\right)^2 + \left(\frac{\partial Nu_x}{\partial A_{ht}}\delta A_{ht}\right)^2 + \left(\frac{\partial Nu_x}{\partial T_{w,x}}\delta T_{w,x}\right)^2 + \left(\frac{\partial Nu_x}{\partial T_{m,x}}\delta T_{m,x}\right)^2\right]^{0.5}$$

$$\begin{aligned}\delta Nu_x = \Bigg[&\left(\frac{D_h}{A_{ht}k(T_{w,x} - T_{m,x})}\delta Q_c\right)^2 + \left(\frac{Q_c}{A_{ht}k(T_{w,x} - T_{m,x})}\delta D_h\right)^2 \\ &+ \left(\frac{-Q_c D_h}{A_{ht}^2 k(T_{w,x} - T_{m,x})}\delta A_{ht}\right)^2 + \left(\frac{-Q_c D_h}{A_{ht}k\left(T_{w,x} - T_{m,x}\right)^2}\delta T_{w,x}\right)^2 \\ &+ \left(\frac{-Q_c D_h}{A_{ht}k\left(T_{w,x} - T_{m,x}\right)^2}\delta T_{m,x}\right)^2\Bigg]^{0.5}\end{aligned} \tag{B.37}$$

B.4.15. Average Nusselt Number

The average Nusselt number is taken as the average of the local Nusselt numbers at thermocouple locations 18 to 29. The uncertainty in the average Nusselt number is calculated as follows:

$$Nu_{avg} = \left[\frac{\sum_{i=18}^{29} Nu_{x,i}}{12}\right] \tag{B.38}$$

$$\delta Nu_{avg} = \left[\left(\frac{Nu_{avg}}{\partial Nu_{x,18}}\delta Nu_{x,18}\right)^2 + \left(\frac{Nu_{avg}}{\partial Nu_{x,19}}\delta Nu_{x,19}\right)^2 + \cdots + \left(\frac{Nu_{avg}}{\partial Nu_{x,29}}\delta Nu_{x,29}\right)^2\right]^{0.5}$$

$$\delta Nu_{avg} = \left[\left(\frac{\delta Nu_{x,18}}{12}\right)^2 + \left(\frac{\delta Nu_{x,19}}{12}\right)^2 + \cdots + \left(\frac{\delta Nu_{x,29}}{12}\right)^2\right]^{0.5} \tag{B.39}$$

B.4.16. Nusselt Number Ratio

The uncertainty in the Nusselt number ratio is calculated as follows:

$$R_{Nu} = \frac{Nu}{Nu_0} \tag{B.40}$$

$$\delta R_{Nu} = \left[\left(\frac{\partial R_{Nu}}{\partial Nu}\delta Nu\right)^2 + \left(\frac{\partial R_{Nu}}{\partial Nu_0}\delta Nu_0\right)^2\right]^{0.5}$$

$$\delta R_{Nu} = \left[\left(\frac{1}{Nu_0}\delta Nu\right)^2 + \left(\frac{Nu}{Nu_0^2}\delta Nu_0\right)^2\right]^{0.5} \tag{B.41}$$

B.4.17. Performance Index 1

The uncertainty in the first performance index is calculated as follows:

$$I_{P1} = \left(\frac{Nu}{Nu_0}\right) / \left(\frac{f}{f_0}\right) \tag{B.42}$$

$$\delta I_{P1} = \left[\left(\frac{\partial I_{P1}}{\partial R_{Nu}}\delta R_{Nu}\right)^2 + \left(\frac{\partial I_{P1}}{\partial R_f}\delta R_f\right)^2\right]^{0.5}$$

$$\delta I_{P1} = \left[\left(\frac{1}{R_f}\delta R_{Nu}\right)^2 + \left(\frac{R_{Nu}}{R_f^2}\delta R_f\right)^2\right]^{0.5} \tag{B.43}$$

B.4.18. Performance Index 2

The uncertainty in the second performance index is calculated as follows:

$$I_{P2} = \left(\frac{Nu}{Nu_0}\right) / \left(\frac{f}{f_0}\right)^{\frac{1}{3}} \tag{B.44}$$

$$\delta I_{P2} = \left[\left(\frac{\partial I_{P2}}{\partial R_{Nu}}\delta R_{Nu}\right)^2 + \left(\frac{\partial I_{P2}}{\partial R_f}\delta R_f\right)^2\right]^{0.5}$$

$$\delta I_{P2} = \left[\left(\frac{1}{R_f^{1/3}}\delta R_{Nu}\right)^2 + \left(-\frac{1}{3}\frac{R_{Nu}}{R_f^{4/3}}\delta R_f\right)^2\right]^{0.5} \qquad B.45$$

B.5. Sample Calculation

This section shows the typical calculations used in determining the friction factor, friction factor ratio, Nusselt number and Nusselt number ratio. The calculations are shown for mesh insert 2.1 at a Re = 400.

B.5.1. Test Section Pressure Drop

The pressure drop along the test section is determined from the gradient of the plot of the channel pressure versus distance. The gradient of the line of best fit is from the transducer calibration is determined to be 24.826 Pa/V. Using 0.5'' differential pressure transducer calibration data and equation B.7 S_{yx} is calculated as:

$$S_{yx} = \left[\frac{\sum_{i=1}^{N}(y_i - y_{ci})^2}{v}\right]^{0.5}$$

$$S_{yx} = [[(0-0)^2 + (20.3-18.3)^2 + (40.1-39.4)^2 + (60.2-60.1)^2 + (80.1-78.9)^2 + (100.2-100.4)^2 + (120.1-119.8)^2 + (80.0-78.0)^2 + (60.1-59.2)^2 + (20.2-18.4)^2]/(8)]^{0.5}$$

$$S_{yx} = \left[\frac{14.36}{8}\right]^{0.5} = 1.34\ Pa$$

Where v is calculated as:

$$v = N - (m+1) = 10 - 2$$

with m equal to 1 for a linear fit. From equation B.9 and the calibration data, S_x is calculated for each calibration dada point as:

$$S_{xi} = \left[\left(\frac{1}{N-1}\right)\sum_{i=1}^{N}(x_i - \bar{x})^2\right]^{0.5}$$

$$S_{x1} = \left[\left(\frac{1}{5-1}\right)[(0.744-0.752)^2 + (0.755-0.752)^2 + (0.767-0.752)^2 + (0.741-0.752)^2 + (0.751-0.752)^2]\right]^{0.5}$$

$$S_{x1} = 0.01$$

Similarly:

$$S_{x2} = 0.0053$$

$$S_{x3} = 0.005$$

$$S_{x4} = 0.0032$$

$$S_{x5} = 0.0053$$

$$S_{x6} = 0.0037$$

$$S_{x7} = 0.0046$$

$$S_{x8} = 0.0063$$

$$S_{x9} = 0.0045$$

$$S_x = \left[\left(\frac{1}{N-1}\right)\sum_{i=1}^{N} S_{xi}^2\right]^{0.5}$$

$$S_x = \left[\left(\frac{1}{9-1}\right)[0.01^2 + 0.0053^2 + 0.005^2 + 0.0032^2 + 0.0053^2 + 0.0037^2 + 0.0046^2 + 0.0063^2 + 0.0045^2\right]^{0.5}$$

$$S_x = 0.006\ V$$

From the manufacturer specifications the accuracy of the differential pressure transducer, A_{trans} is determined to be 0.149 Pa. The students t-distribution variable, $t_{9,95}$ is calculated as 2.306. Solving equation B.8 for U_x yields:

$$U_x = \left[(t_{v,95}\ S_x)^2 + (A_{trans})\right]^{0.5}$$

$$U_x = [(2.306 * 0.006)^2 + 0.05]^{0.5}$$

$$U_x = 0.052\ V$$

The uncertainty in the calibration equation is calculated from equation B.6 with the accuracy in the calibration transducer A_{cal} equal to 0.149 Pa.

$$U_{cal,eqn} = \left[(t_{v,95}\ S_{yx})^2 + (A_{cal})^2 + (a_1 U_x)^2\right]^{0.5}$$

$$U_{cal,eqn} = [(2.306 * 1.34)^2 + (0.149)^2 + (24.826 * 0.052)^2]^{0.5}$$

$$U_{cal,eqn} = 3.35\ Pa$$

The uncertainty in the measured pressure reading is then determined by equation B.5 to be:

$$U_p = \left[\left(U_{cal,eqn}\right)^2 + (a_1 U_{xi})^2\right]^{0.5}$$

$$U_p = [(3.35)^2 + (24.826 * 0.052)^2]^{0.5}$$

$$U_p = 3.59\ Pa$$

Figure B.1 shows the pressure drop along the channel for Mesh 2.1 at Re = 400. The gradient of the line of best fit was determined to be 1.9152 Pa/m. The uncertainty in the channel pressure drop is calculated in a similar manner as the differential pressure transducer. For the 30 pressure taps along the test section S_{yx} is calculated using equation B.7 to be 0.021 Pa. S_{b1} is calculated using equation B.12:

$$S_{b1} = S_{yx}\left[\frac{N}{N\sum_{i=1}^{N} x_i^2 - \left(\sum_{i=1}^{N} x\_i\right)^2}\right]^{0.5}$$

$$S_{b1} = 0.021\left[\frac{33}{33 * 168 - 5537}\right]^{0.5} = 0.025\ Pa/m$$

The uncertainty in the channel pressure drop is determined via equation B.11 as:

$$\delta b_1 = t_{v,95} S_{b1}$$

$$\delta b_1 = 2.04 * 0.025 = 0.052\ Pa/m$$

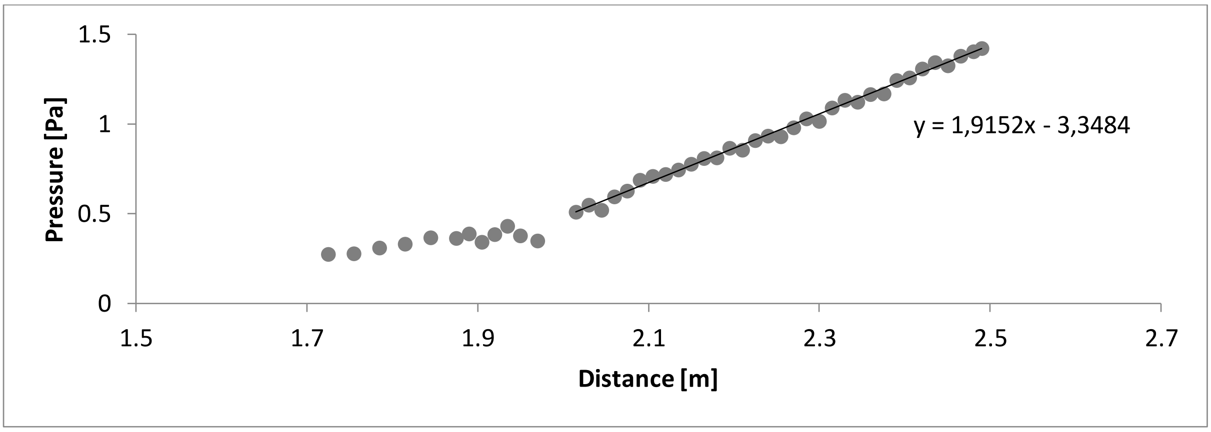

Figure B.1: Channel Pressure Drop for Mesh 2.1 at Re = 400

B.5.2. Reynolds Number

The uncertainty in the Reynolds number can be calculated once the uncertainty in the mass flow rate, hydraulic diameter, density and the channel cross sectional area are known. The uncertainty in the density of the air is calculated from equation B.16:

$$\delta\rho = \left[\left(\frac{1}{RT}\delta p\right)^2 + \left(\frac{-p}{RT^2}\delta T\right)^2\right]^{0.5}$$

$$\delta\rho = \left[\left(\frac{1}{287.058 * 296.44} * 100.5\right)^2 + \left(\frac{-87025.89}{287.058 * 296.44^2}0.17\right)^2\right]^{0.5}$$

$$\delta\rho = 0.00132\frac{kg}{m^3}$$

The uncertainty in the mass flow rate was calculated from equation B.17:

$$\frac{\delta\dot{m}}{\dot{m}} = \left[\left(\frac{\delta C}{C}\right)^2 + \left(\frac{\delta\varepsilon}{\varepsilon}\right)^2 + \left(\frac{2\beta}{1-\beta^4}\right)^2\left(\frac{\delta D}{D}\right)^2 + \left(\frac{2}{1-\beta^4}\right)^2\left(\frac{\delta d}{d}\right)^2 + \frac{1}{4}\left(\frac{\delta\Delta p}{\Delta p}\right)^2 + \frac{1}{4}\left(\frac{\delta\rho}{\rho}\right)^2\right]^{0.5}$$

$$\frac{\delta\dot{m}}{\dot{m}} = \left[(0.006)^2 + (0.0002)^2 + \left(\frac{2 * 0.21}{1 - 0.21^4}\right)^2 (0.0035)^2 + \left(\frac{2}{1 - 0.21^4}\right)^2 (0.017)^2 + \frac{1}{4}(0.0108)^2 + \frac{1}{4}(0.0013)^2\right]^{0.5}$$

$$\frac{\delta\dot{m}}{\dot{m}} = 0.0249$$

$$\delta\dot{m} = 2.01E^{-5}\ \frac{kg}{s}$$

The uncertainty in the hydraulic diameter is calculated from equation B.14:

$$\delta D_h = \left[\left(\frac{2h^2}{(w+h)^2}\delta w\right)^2 + \left(\frac{2w^2}{(h+w)^2}\delta h\right)^2\right]^{0.5}$$

$$\delta D_h = \left[\left(\frac{2 * 0.014^2}{(0.2032 + 0.014)^2} * 0.0005\right)^2 + \left(\frac{2 * 0.2032^2}{(0.014 + 0.2032)^2} * 0.000263\right)^2\right]^{0.5}$$

$$\delta D_h = 0.00046\ m$$

The uncertainty in the test section cross sectional area is determined from equation B.19:

$$\delta A_c = [(h\delta w)^2 + (w\delta h)^2]^{0.5}$$

$$\delta A_c = [(0.014 * 0.0005)^2 + (0.2032 * 0.000263)^2]^{0.5}$$

$$\delta A_c = 5.38E^{-5}\ m^2$$

With the preceding parameter the uncertainty in the Reynolds number is calculated from equation B.23:

$$\delta Re = \left[\left(\frac{0.0262}{0.0000185 * 0.00284} * 2.01e^{-5}\right)^2 + \left(\frac{0.00081}{0.0000185 * 0.00284} * 0.00046\right)^2 + \left(\frac{0.000841 * 0.0262}{0.0000185 * 0.00284^2} * 5.38E^{-5}\right)^2\right]^{0.5}$$

$$\delta Re = 14$$

B.5.3. Fanning Friction Factor

The uncertainty in the Fanning friction factor can be calculated once the uncertainty in the channel pressure drop, hydraulic diameter, density and the mean channel velocity have been determined. The uncertainty in the mean channel velocity is calculated from equation B.21:

$$\delta\overline{\mathrm{V}} = \left[\left(\frac{1}{\rho A_c}\delta\dot{m}\right)^2 + \left(\frac{-\dot{m}}{\rho^2 A_c}\delta\rho\right)^2 + \left(\frac{-\dot{m}}{\rho A_c^2}\delta A_c\right)^2\right]^{0.5}$$

$$\delta\overline{\mathrm{V}} = \left[\left(\frac{1}{1.01 * 0.00284} * 2.01E^{-5}\right)^2 + \left(\frac{0.00081}{1.01^2 * 0.00284} * 0.0013\right)^2 + \left(\frac{-0.00081}{1.01 * 0.00284^2} * 5.38E^{-5}\right)^2\right]^{0.5}$$

$$\delta\overline{\mathrm{V}} = 0.009\ \frac{\mathrm{m}}{\mathrm{s}}$$

The Fanning friction factor is calculated from equation B.25:

$$\delta f = \left[\left(\frac{(D_h/4)}{0.5\rho\overline{\mathrm{V}}^2}\delta \mathrm{b}_1\right)^2 + \left(\frac{b_1}{0.5\rho\overline{\mathrm{V}}^2}\delta D_h\right)^2 + \left(\frac{b_1(D_h/4)}{0.5\rho^2\overline{\mathrm{V}}^2}\delta\rho\right)^2 + \left(-\frac{b_1(D_h/4)}{\rho\overline{\mathrm{V}}^3}\delta\overline{\mathrm{V}}\right)^2\right]^{0.5}$$

$$\delta f = \left[\left(\frac{(0.0262/4)}{0.5 * 1.01 * 0.28^2} * 0.052\right)^2 + \left(\frac{1.92}{0.5 * 1.01 * 0.28^2} * 0.00046\right)^2 + \left(\frac{1.92 * (0.0262/4)}{0.5 * 1.01^2 * 0.28^2} * 0.00132\right)^2 + \left(-\frac{1.92 * (0.0262/4)}{1.01 * 0.28^3} * 0.009\right)^2\right]^{0.5}$$

$$\delta f = 0.0231$$

The friction factor for mesh 2.1 at a Re = 400 is calculated to be 0.326. The uncertainty in the friction factor is calculated as 7.0%.

The uncertainty in the friction factor ratio is determined from equation B.27:

$$\delta R_f = \left[\left(\frac{1}{f_0}\delta f\right)^2 + \left(\frac{f}{f_0^2}\delta f_0\right)^2\right]^{0.5}$$

$$\delta R_f = \left[\left(\frac{1}{0.0545} * 0.0231\right)^2 + \left(\frac{0.329}{0.0545^2} * 0.00383\right)^2\right]^{0.5}$$

$$\delta R_f = 0.6$$

The friction factor ratio for mesh 2.1 at a Re = 400 is calculated to be 6.0. The uncertainty in the friction factor is calculated as 9.9%.

B.5.4. Wall Surface Temperature

The uncertainty in the measured wall temperature is calculated using equations B.5 to B.10. Thermocouple 1 which is located at the start of the test section is used in the sample calculations. The gradient of the line of best fit is from the thermocouple calibration is determined to be 1.0002 °C/°C. Using the thermocouple calibration data and equation B.7 S_{yx} is was calculated as:

$$S_{yx} = \left[\frac{\sum_{i=1}^{N}(y_i - y_{ci})^2}{v}\right]^{0.5}$$

$$\begin{aligned} S_{yx} = [[&(19.424 - 19.428)^2 + (21.554 - 21.558)^2 + (23.569 - 23.573)^2 + (25.472 - 25.477)^2 \\ &+ (27.552 - 27.558)^2 + (29.582 - 29.587)^2 + (31.579 - 31.585)^2 \\ &+ (33.561 - 33.568)^2 + (35.558 - 35.565)^2 + (37.505 - 37.512)^2 \\ &+ (39.541 - 39.549)^2 + (42.501 - 42.510)^2 + (45.534 - 45.543)^2 \\ &+ (48.562 - 48.572)^2 + (51.591 - 51.601)^2 + (54.543 - 54.555)^2 \\ &+ (57.465 - 57.477)^2]/(11)]^{0.5} \end{aligned}$$

$$S_{yx} = \left[\frac{0.000986}{15}\right]^{0.5} = 0.0082\ °C$$

S_x is calculated for each calibration dada point as:

$$S_{xi} = \left[\left(\frac{1}{N-1}\right)\sum_{i=1}^{N}(x_i - \bar{x})^2\right]^{0.5}$$

$$S_{x1} = \left[\left(\frac{1}{12-1}\right)[(19.381-19.423)^2 + (19.404-19.423)^2 + (19.406-19.423)^2 + (19.436-19.423)^2 + (19.441-19.423)^2 + (19.427-19.423)^2 + (19.421-19.423)^2 + (19.425-19.423)^2 + (19.425-19.423)^2 + (19.443-19.423)^2 + (19.436-19.423)^2 + (19.442-19.423)^2]\right]^{0.5}$$

$$S_{x1} = 0.0186° \text{ C}$$

Similarly:

$$S_{x2} = 0.0101° \text{ C}$$

$$S_{x3} = 0.0126° \text{ C}$$

$$S_{x4} = 0.0207° \text{ C}$$

$$S_{x5} = 0.0181° \text{ C}$$

$$S_{x6} = 0.0140° \text{ C}$$

$$S_{x7} = 0.0243° \text{ C}$$

$$S_{x8} = 0.0204° \text{ C}$$

$$S_{x9} = 0.0186° \text{ C}$$

$$S_{x10} = 0.0158° \text{ C}$$

$$S_{x11} = 0.0173° \text{ C}$$

$$S_{x12} = 0.0145° \text{ C}$$

$$S_{x13} = 0.0143° \text{ C}$$

$$S_{x14} = 0.0140° \text{ C}$$

$$S_{x15} = 0.0193° \text{ C}$$

$$S_{x16} = 0.0139° \text{ C}$$

$$S_x = \left[\left(\frac{1}{N-1}\right)\sum_{i=1}^{N} S_{xi}^2\right]^{0.5}$$

$$S_x = \left[\left(\frac{1}{16-1}\right)[0.0186^2 + 0.0126^2 + 0.0207^2 + 0.0181^2 + 0.0140^2 + 0.0243^2 + 0.0204^2 + 0.0186^2 + 0.0158^2 + 0.0173^2 + 0.0145^2 + 0.0143^2 + 0.0140^2 + 0.0193^2 + 0.0139^2\right]^{0.5}$$

$$S_x = 0.0185 \text{ ° C}$$

From the manufacturer specifications the accuracy of the thermocouple, A_{thermo} is determined to be 0.1 °C. The students t-distribution variable, $t_{11,95}$ is calculated as 2.201. Solving equation B.8 for U_x yields:

$$U_x = \left[(t_{v,95}\, S_x)^2 + (A_{trans})\right]^{0.5}$$

$$U_x = [(2.201 * 0.0185)^2 + 0.1]^{0.5}$$

$$U_x = 0.108\,^\circ\mathrm{C}$$

The uncertainty in the calibration equation is calculated from equation B.6 with the accuracy in the thermal bath A_{cal} equal to 0.02 °C.

$$U_{cal,eqn} = \left[(t_{v,95}\, S_{yx})^2 + (A_{cal})^2 + (a_1 U_x)^2\right]^{0.5}$$

$$U_{cal,eqn} = [(2.131 * 0.082)^2 + (0.02)^2 + (1.0002 * 0.108)^2]^{0.5}$$

$$U_{cal,eqn} = 0.111\,^\circ\mathrm{C}$$

The uncertainty in the measured wall temperature is then determined by equation B.5 to be:

$$U_T = \left[\left(U_{cal,eqn}\right)^2 + (a_1 U_{xi})^2\right]^{0.5}$$

$$U_T = [(0.111)^2 + (1.0002 * 0.108)^2]^{0.5}$$

$$U_T = 0.155\,^\circ\mathrm{C}$$

B.5.5. Nusselt Number

The uncertainty in the heat flux, mass flow and the bulk mean temperature must be determined before the uncertainty in the Nusselt number can calculated. Sample calculations are shown for the two wall heat transfer experiment with mesh insert 2.1.

The accuracy in the voltage and current readings are determined from the multi-meter manufacturer specification to be 1.2 % and 2.5 % respectively. The random errors in the voltage and current readings are determined from 90 measurement samples to be 0.107 V and 0.00055 A. The uncertainty in the measured voltage for the power supplied to test section at a Re = 400 is calculated to be 0.820 V while that of the current reading is calculated to be 0.0065 A. The uncertainty in power is calculated via equation B.29:

$$\delta Q = [(A\delta V)^2 + (V\delta A)^2]^{0.5}$$

$$\delta Q = [(0.259 * 0.820)^2 + (67.7 * 0.0065)^2]^{0.5}$$

$$\delta Q = 0.49\ \mathrm{W}$$

The uncertainty in the heat transfer area is determined from equation B.31:

$$\delta A_{ht} = [(2l\delta w)^2 + (2w\delta l)^2]^{0.5}$$

$$\delta A_{ht} = [(2 * 0.5 * 0.005)^2 + (2 * 0.2032 * 0.001)^2]^{0.5}$$

$$\delta A_{ht} = 0.0006\ m^2$$

The uncertainty in the heat flux is then calculated form equation B.33:

$$\delta q = \left[\left(\frac{1}{A_{ht}}\delta Q\right)^2 + \left(\frac{-Q}{A_{th}^2}\delta A_{th}\right)^2\right]^{0.5}$$

$$\delta q = \left[\left(\frac{1}{0.2032} * 0.49\right)^2 + \left(\frac{-17.5}{0.2032^2} * 0.0006\right)^2\right]^{0.5}$$

$$\delta q = 2.42\ W/m^2$$

Thermocouple number 64 is used to record the ambient temperature at the inlet of the channel. The uncertainty in this thermocouple is calculated to be 0.17 °C. The uncertainty in the bulk mean temperature at the location of thermocouple 29 is determined using equation B.35:

$$\delta T_{m,29} = \left[(\delta T_{amb})^2 + \left(\frac{1}{\dot{m}C_p}\delta Q_{c,29}\right)^2 + \left(\frac{-Q_{c,29}}{\dot{m}^2 C_p}\delta\dot{m}\right)^2\right]^{0.5}$$

$$\delta T_{m,29} = \left[(0.17)^2 + \left(\frac{1}{0.000804 * 1007} * 0.285\right)^2 + \left(\frac{-10.2}{0.000804^2 * 1007} * 2.01E^{-5}\right)^2\right]^{0.5}$$

$$\delta T_{m,x} = 0.5\ K$$

Calculations are shown for the local Nusselt number at location of thermocouple number 29. The local Nusselt number is determined from equation B.37 to be:

$$\delta Nu_x = \left[\left(\frac{D_h}{A_{ht}k(T_{w,x} - T_{m,x})}\delta Q_c\right)^2 + \left(\frac{Q_c}{A_{ht}k(T_{w,x} - T_{m,x})}\delta D_h\right)^2 + \left(\frac{-Q_c D_h}{A_{ht}^2 k(T_{w,x} - T_{m,x})}\delta A_{ht}\right)^2 \right.$$
$$\left. + \left(\frac{-Q_c D_h}{A_{ht}k\left(T_{w,x} - T_{m,x}\right)^2}\delta T_{w,x}\right)^2 + \left(\frac{-Q_c D_h}{A_{ht}k\left(T_{w,x} - T_{m,x}\right)^2}\delta T_{m,x}\right)^2\right]^{0.5}$$

$$\delta Nu_x = \left[\left(\frac{0.0262}{0.102 * 0.0264 * (318.89 - 311.87)} * 0.20\right)^2 \right.$$
$$+ \left(\frac{7.1}{0.102 * 0.0264 * (318.89 - 311.87)} * 0.00046\right)^2$$
$$+ \left(\frac{-7.1 * 0.0262}{0.102^2 * 0.0264 * (318.89 - 311.87)} * 0.0006\right)^2$$
$$+ \left(\frac{-7.1 * 0.0262}{0.102 * 0.0264 * (318.89 - 311.87)^2} * 0.18\right)^2$$
$$\left. + \left(\frac{-7.1 * 0.0262}{0.102 * 0.0264 * (318.89 - 311.87)^2} * 0.5\right)^2\right]^{0.5}$$

$$\delta Nu_x = 0.82$$

The local Nusselt number at thermocouple location 29 is calculated to be 9.87 therefore the uncertainty in the local Nusselt number is evaluated at 8.3%.

The average Nusselt number is the average of the local Nusselt numbers measured at thermocouple location 18 through to 29. The uncertainty in the average Nusselt number is determined from equation B.39 as:

$$\delta Nu_{avg} \;\; = \left[\left(\frac{\delta Nu_{x,18}}{12}\right)^2 + \left(\frac{\delta Nu_{x,19}}{12}\right)^2 + \cdots + \left(\frac{\delta Nu_{x,29}}{12}\right)^2\right]^{0.5}$$

$$\delta Nu_{avg} \;\; = \left[\left(\frac{0.81}{11}\right)^2 + \left(\frac{0.74}{11}\right)^2 + \left(\frac{0.71}{11}\right)^2 + \left(\frac{0.77}{11}\right)^2 + \left(\frac{0.85}{11}\right)^2 + \left(\frac{0.80}{11}\right)^2 + \left(\frac{0.85}{11}\right)^2 + \left(\frac{0.85}{11}\right)^2 + \left(\frac{0.82}{11}\right)^2 + \left(\frac{0.80}{11}\right)^2 + \left(\frac{0.82}{11}\right)^2\right]^{0.5}$$

$$\delta Nu_{avg} \;\; = 0.24$$

The local Nusselt number at thermocouple location 25 is excluded from the calculation as the thermocouple reading was deemed to be erroneous for this experimental run. The average Nusselt number is calculated to be 9.76 resulting in an average Nusselt number uncertainty of 2.48 %.

The uncertainty in the Nusselt number ration is calculated from equation B.41:

$$\delta R_{Nu} = \left[\left(\frac{1}{Nu_0}\delta Nu\right)^2 + \left(\frac{Nu}{Nu_0^2}\delta Nu_0\right)^2\right]^{0.5}$$

$$\delta R_{Nu} = \left[\left(\frac{1}{7.6} * 0.24\right)^2 + \left(\frac{9.76}{7.6^2} * 0.19\right)^2\right]^{0.5}$$

$$\delta R_{Nu} = 0.045$$

B.5.6. Performance Index

The uncertainty in the first performance index is calculate via equation B.43 as:

$$\delta I_{P1} = \left[\left(\frac{1}{R_f}\delta R_{Nu}\right)^2 + \left(\frac{R_{Nu}}{R_f^2}\delta R_f\right)^2\right]^{0.5}$$

$$\delta I_{P1} = \left[\left(\frac{1}{6.04} * 0.045\right)^2 + \left(\frac{1.29}{6.04^2} * 0.60\right)^2\right]^{0.5}$$

$$\delta I_{P1} = 0.023$$

The first performance index is evaluated at 0.21 resulting in an uncertainty of 10.5%. The uncertainty in the second performance index is calculate via equation B.45 as:

$$\delta I_{P2} = \left[\left(\frac{1}{R_f^{1/3}}\delta R_{Nu}\right)^2 + \left(-\frac{1}{3}\frac{R_{Nu}}{R_f^{4/3}}\delta R_f\right)^2\right]^{0.5}$$

$$\delta I_{P2} = \left[\left(\frac{1}{6.04^{1/3}} * 0.045\right)^2 + \left(-\frac{1}{3} * \frac{1.29}{6.04^{\frac{4}{3}}} * 0.60\right)^2\right]^{0.5}$$

$$\delta I_{P2} = 0.0343$$

The first performance index is evaluated at 0.71 resulting in an uncertainty of 4.8%.

B.6. Conclusion

This appendix contains the theory and motivation behind the uncertainty analysis. Typical equations and sample calculations are provided for each step in the analysis. The analysis accounts for the errors involved in all the measured values and parameters as well the accuracy of the instruments used to record the parameters. The analysis shows the propagation of the errors through the mathematical operations used in determining calculated values.

The uncertainty in the differential pressure transducer reading varied from 1 - 3 % of the full-scale range. The uncertainty in the thermocouple readings varied from 0.16 - 0.26 °C. The uncertainty in the friction factor varied from 5 - 8 % while that of the average Nusselt number varied from 1 - 3%. The uncertainty in the performance index varied from 3 - 5 %

[1] Moffat, R. J., 1988, "*Describing the Uncertainty in Experimental Results,*" Experimental Thermal and Fluid Science, **1**(3), pp. 3–17.

[2] Figliola, R. S., and Beasley, D. E., 2000, *Theory and Design for Mechanical Measurements*, 3rd ed., John Wiley & Sons, New York, pp. 121–138.

[3] International Standards ISO, 5167, 1980, *Measurements of Fluid Flows by Means of Orifice Plates, Nozzles and Venturi Tubes Inserted in Circular Cross-Section Conduits Running Full*, pp. 346–351.

Appendix C: Pressure Drop Data

C.1. Introduction

This appendix includes the measured pressure data used in determining the pressure drop along the test section channel. Results are show for each experiment conducted throughout the course of the research. Note that certain data points have been excluded from the respective data sets. The measured pressure point was deemed to be erroneous either due a poor connection at the scanivalve sliding interface or due to damaged pressure tap tubing resulting from the disassembly and assembly of the test section.

C.2. Baseline

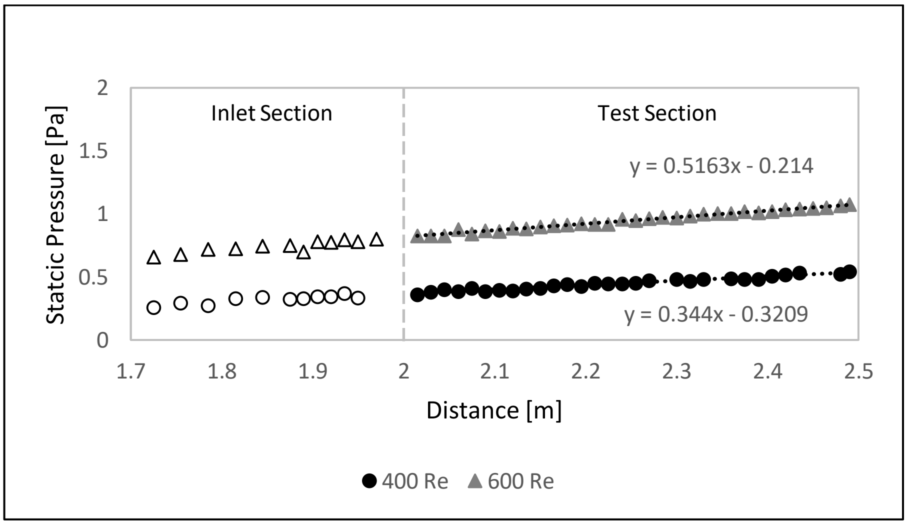

Figure C.1: Base Line Test Section Static Pressure at Re = 400 and Re = 600

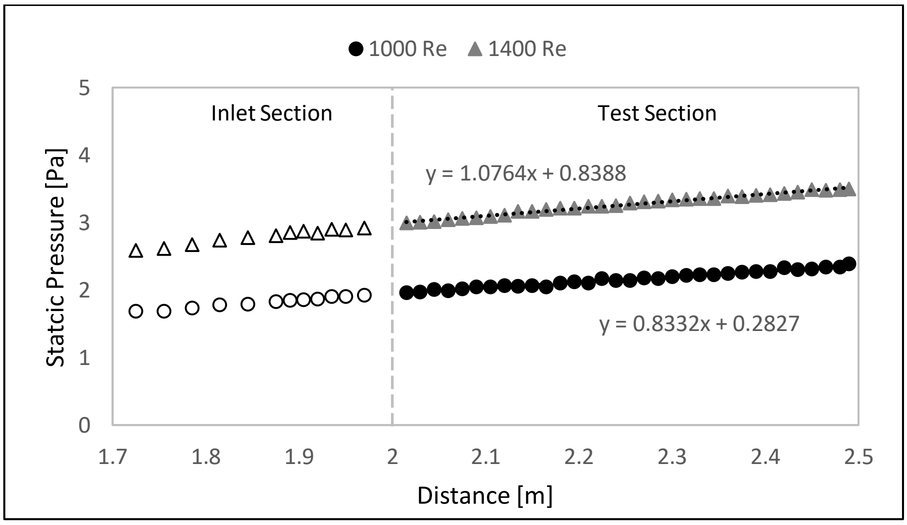

Figure C.2: Base Line Test Section Static Pressure at Re = 1000 and Re = 1400

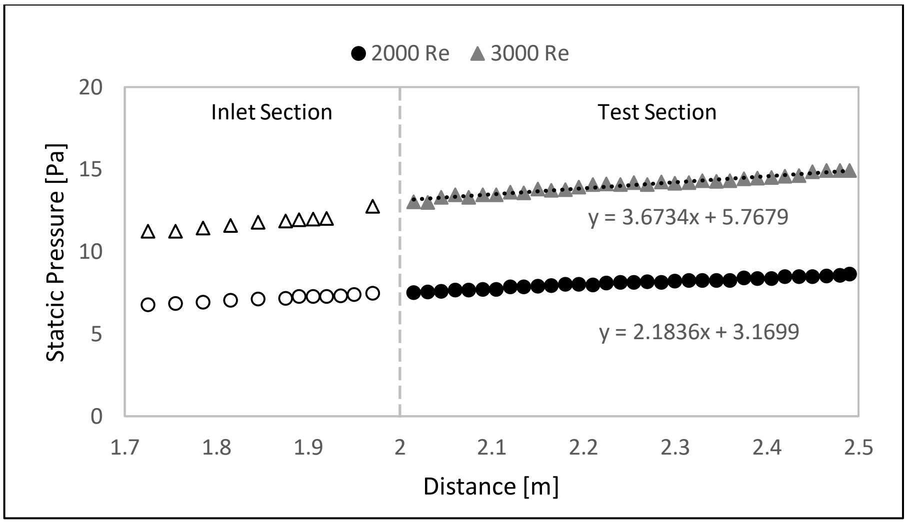

Figure C.3: Base Line Test Section Static Pressure at Re = 2000 and Re = 3000

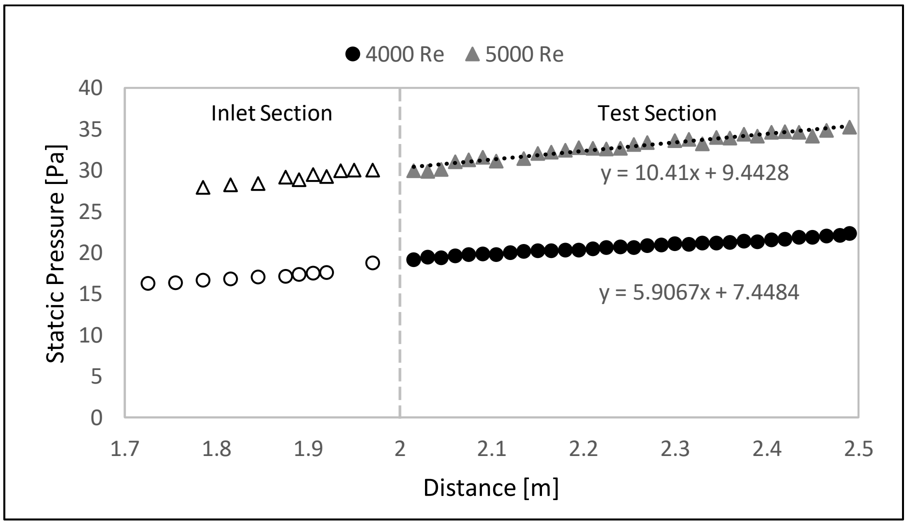

Figure C.4: Base Line Test Section Static Pressure at Re = 4000 and Re = 5000

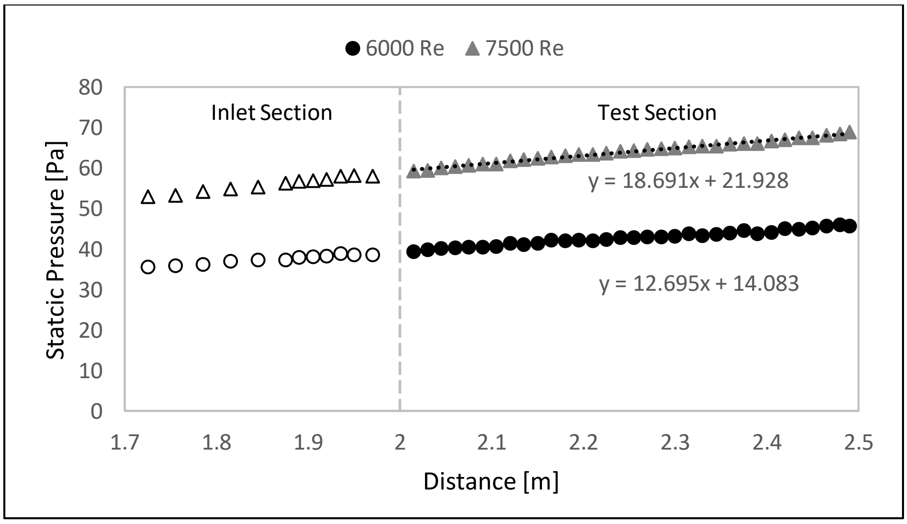

Figure C.5: Base Line Test Section Static Pressure at Re = 6000 and Re = 7500

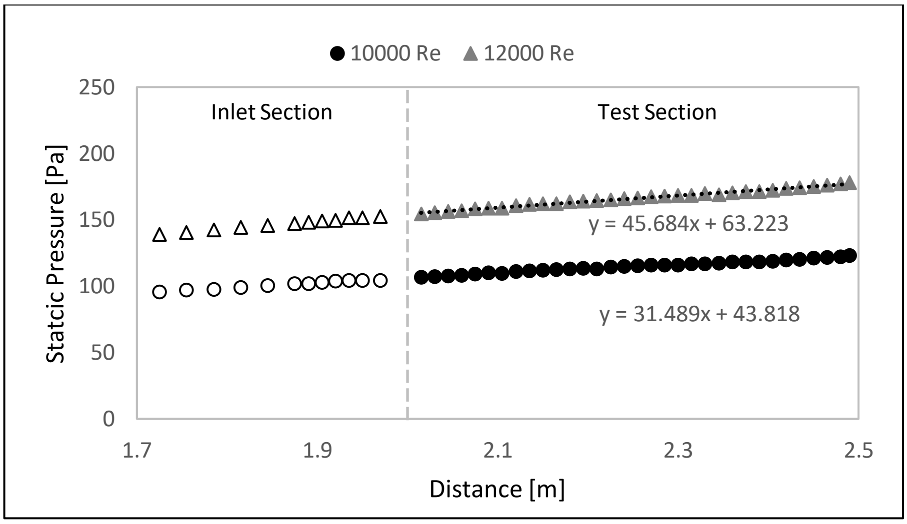

Figure C.6: Base Line Test Section Static Pressure at Re = 10000 and Re = 12000

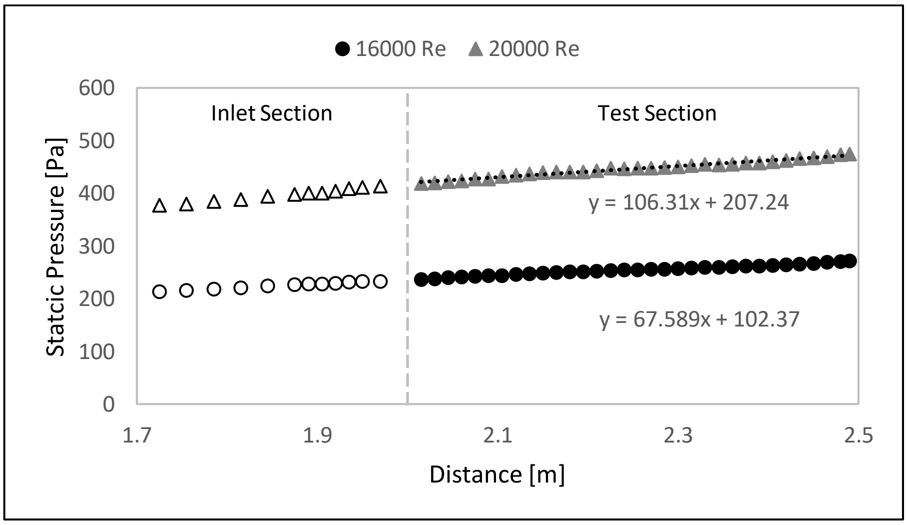

Figure C.7: Base Line Test Section Static Pressure at Re = 16000 and Re = 20000

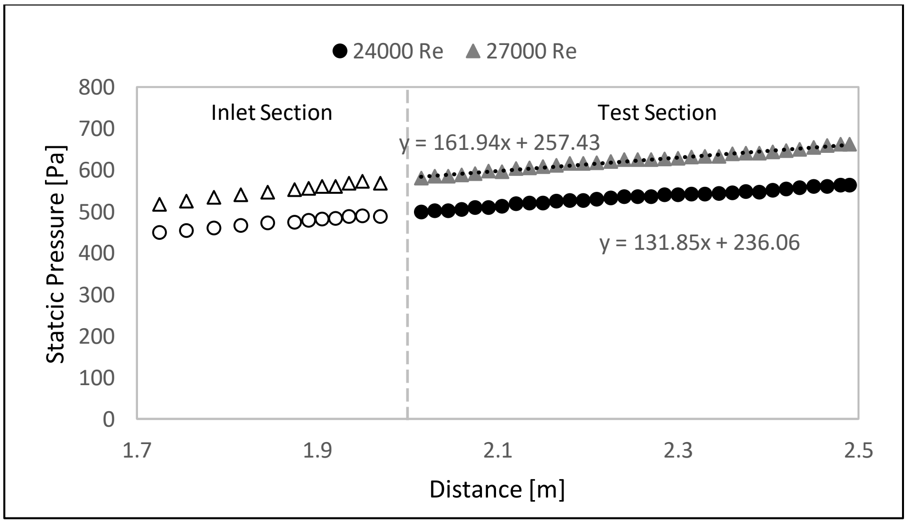

Figure C.8: Base Line Test Section Static Pressure at Re = 24000 and Re = 27000

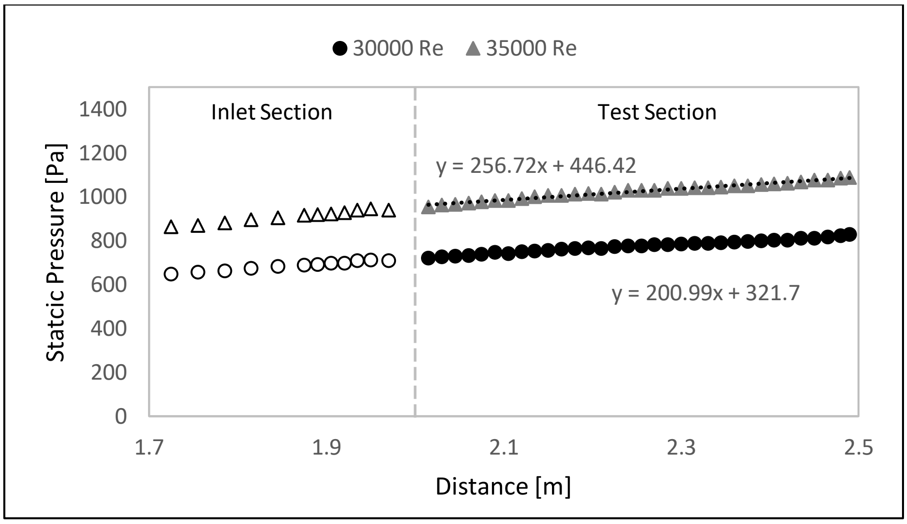

Figure C.9: Base Line Test Section Static Pressure at Re = 30000 and Re = 35000

C.3. Mesh 1.1 (λ = 20 mm, ξ = 68 %)

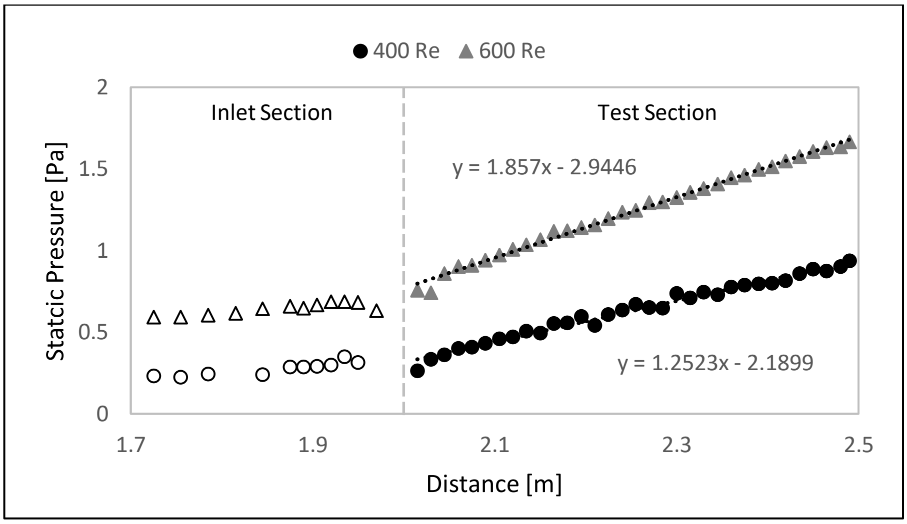

Figure C.10: Test Section Static Pressure for Insert 1.1 at Re = 400 and Re = 600

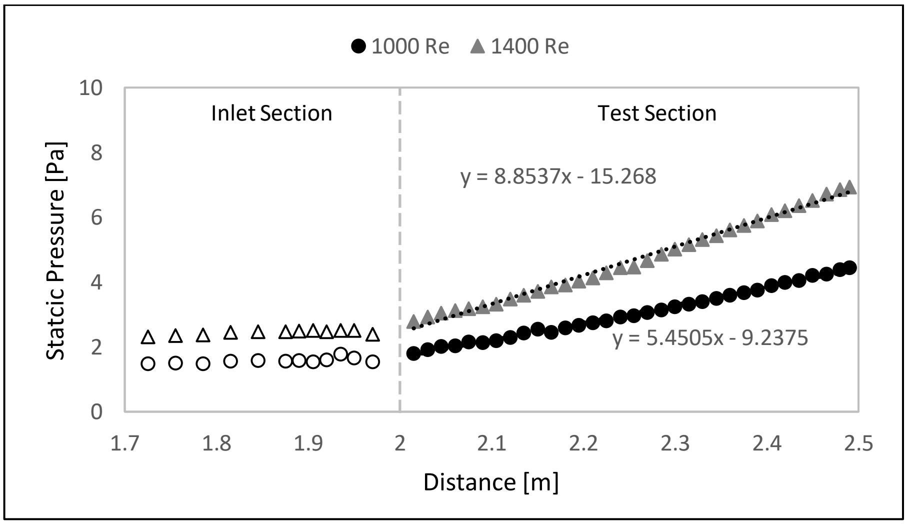

Figure C.11: Test Section Static Pressure for Insert 1.1 at Re = 1000 and Re = 1400

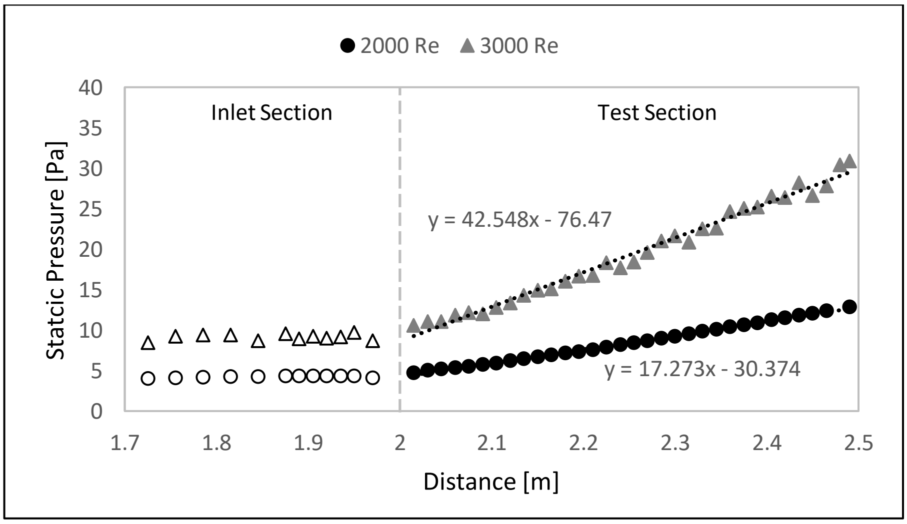

Figure C.12: Test Section Static Pressure for Insert 1.1 at Re = 2000 and Re = 3000

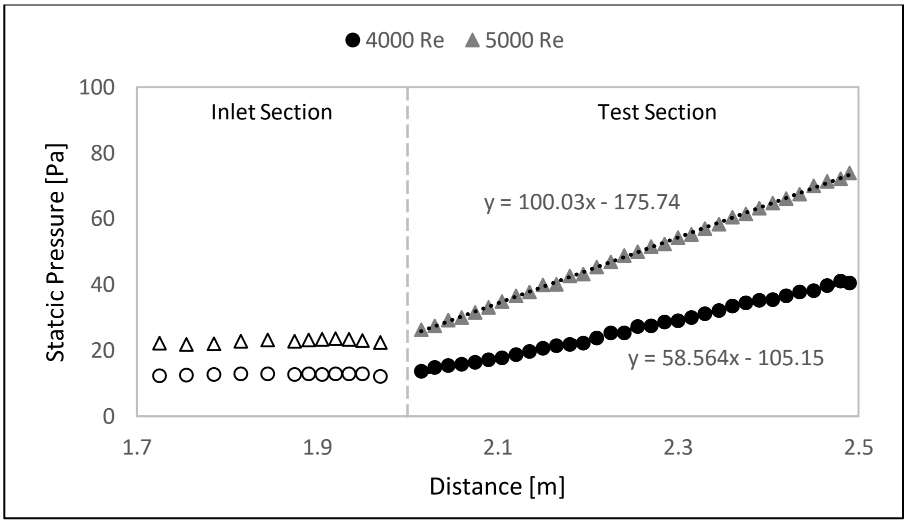

Figure C.13: Test Section Static Pressure for Insert 1.1 at Re = 4000 and Re = 5000

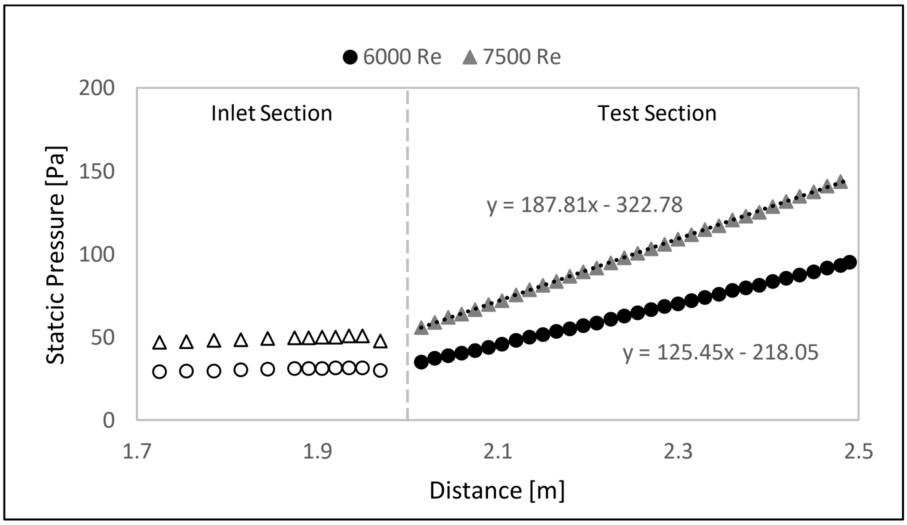

Figure C.14: Test Section Static Pressure for Insert 1.1 at Re = 6000 and Re = 7500

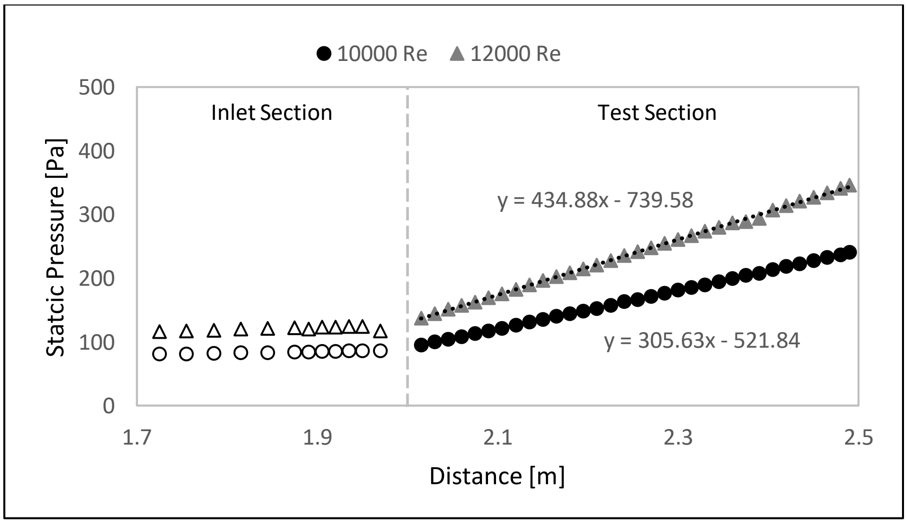

Figure C.15: Test Section Static Pressure for Insert 1.1 at Re = 10000 and Re = 12000

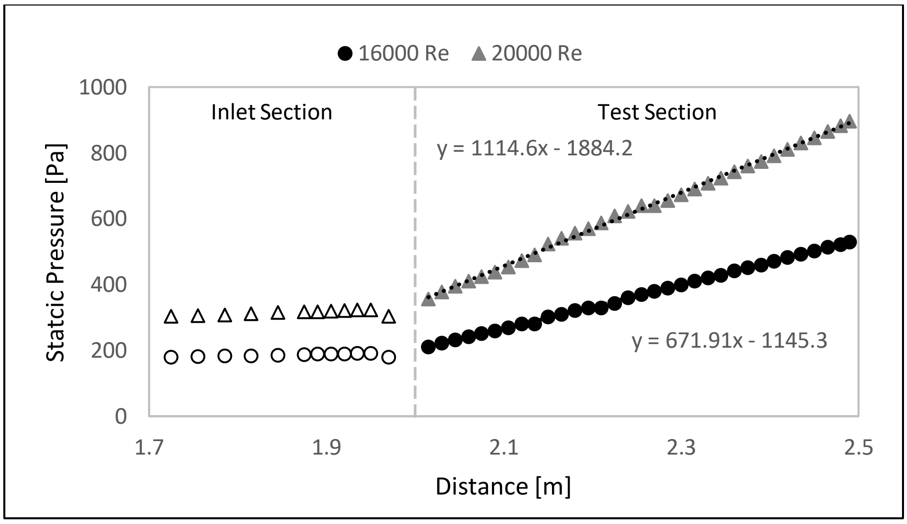

Figure C.16: Test Section Static Pressure for Insert 1.1 at Re = 16000 and Re = 20000

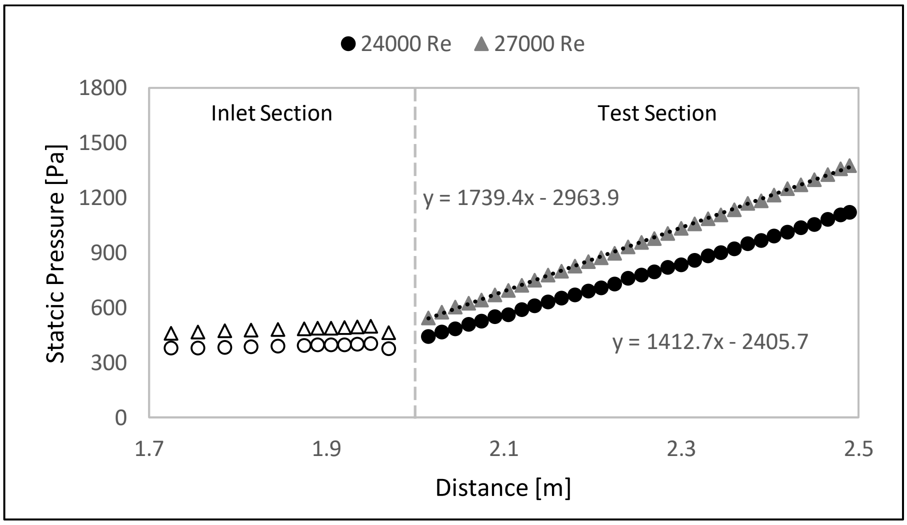

Figure C.17: Test Section Static Pressure for Insert 1.1 at Re = 24000 and Re = 27000

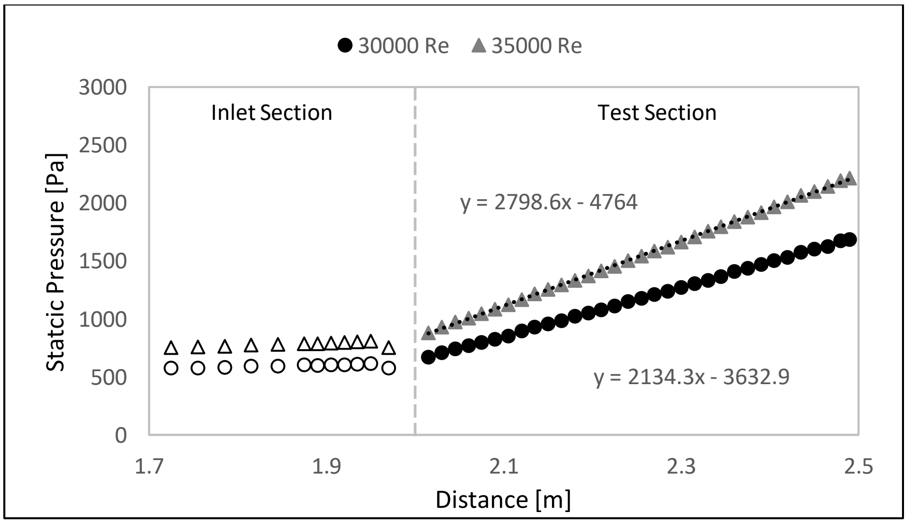

Figure C.18: Test Section Static Pressure for Insert 1.1 at Re = 30000 and Re = 35000

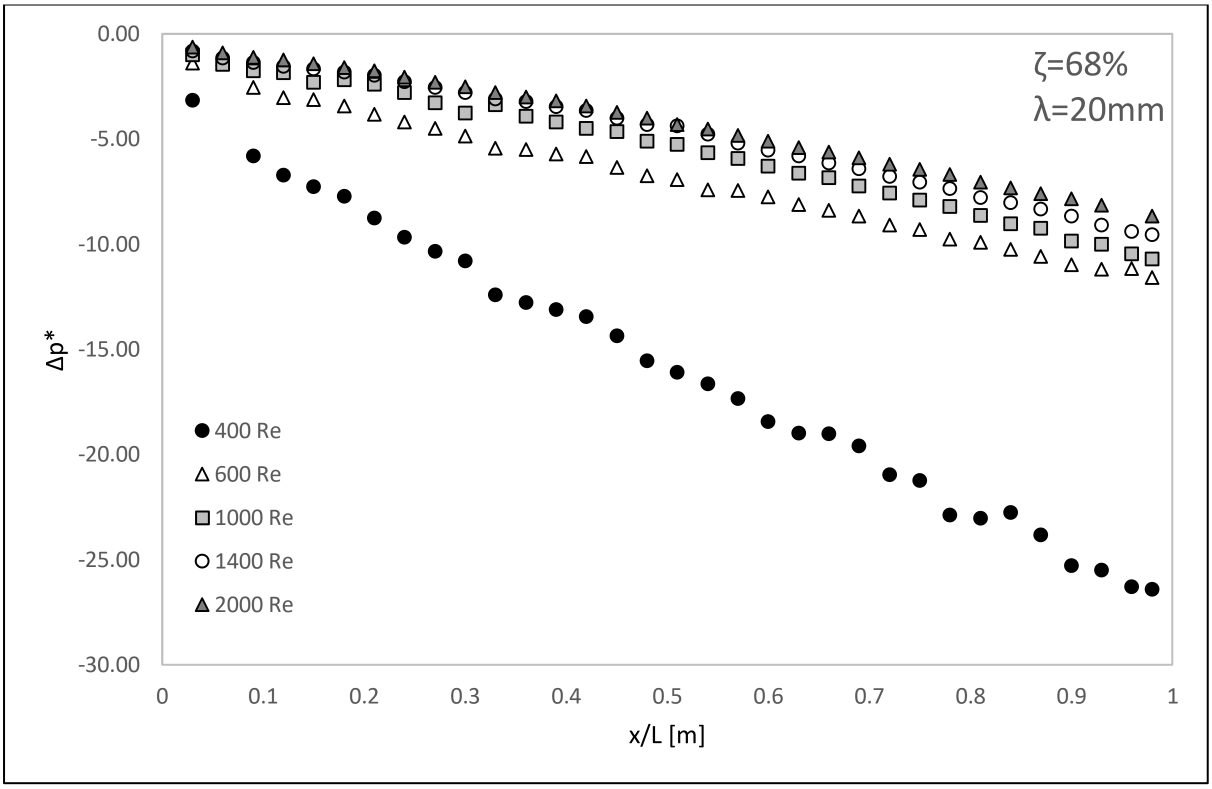
ζ=68%
λ=20mm
Δp*
0.00
-5.00
-10.00
-15.00
-20.00
-25.00
-30.00
0
0.1
0.2
0.3
0.4
0.5
0.6
0.7
0.8
0.9
1
x/L [m]
● 400 Re
△ 600 Re
▨ 1000 Re
○ 1400 Re
▲ 2000 Re

(a)

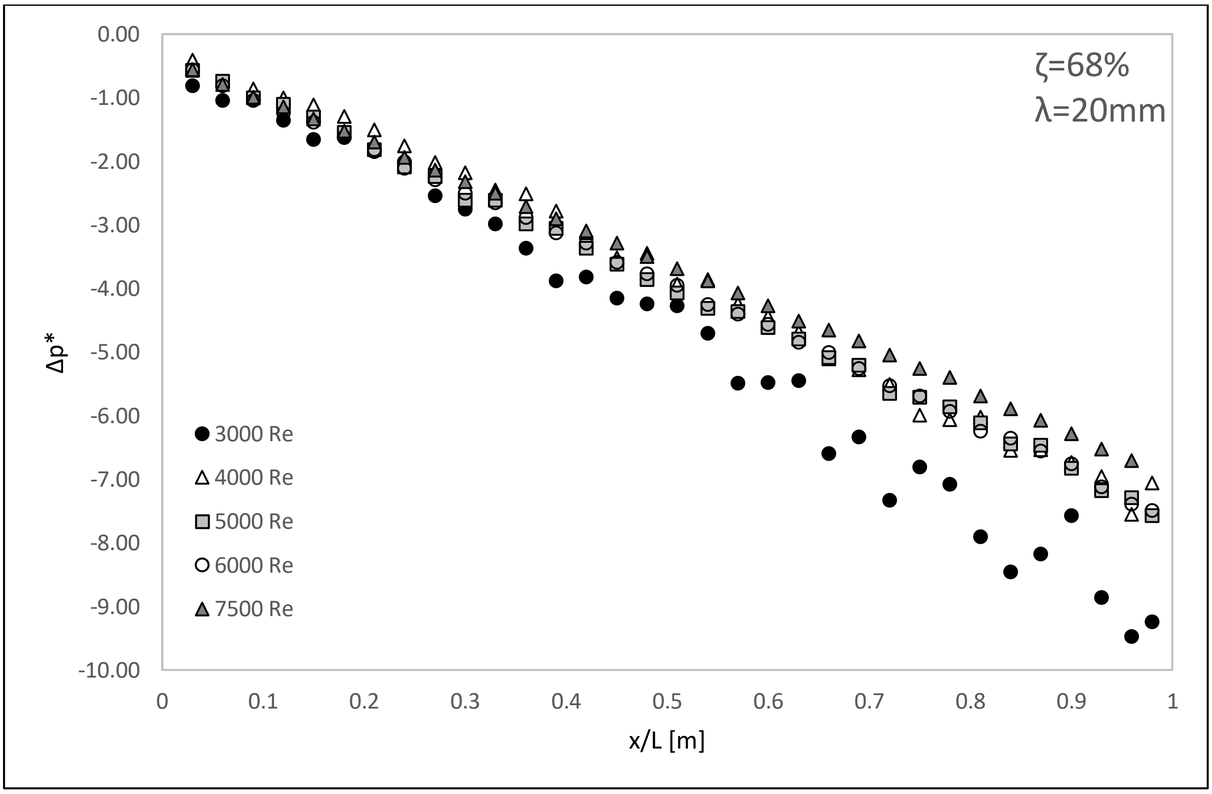
ζ=68%
λ=20mm
Δp*
0.00
-1.00
-2.00
-3.00
-4.00
-5.00
-6.00
-7.00
-8.00
-9.00
-10.00
0
0.1
0.2
0.3
0.4
0.5
0.6
0.7
0.8
0.9
1
x/L [m]
● 3000 Re
△ 4000 Re
▨ 5000 Re
○ 6000 Re
▲ 7500 Re

(b)

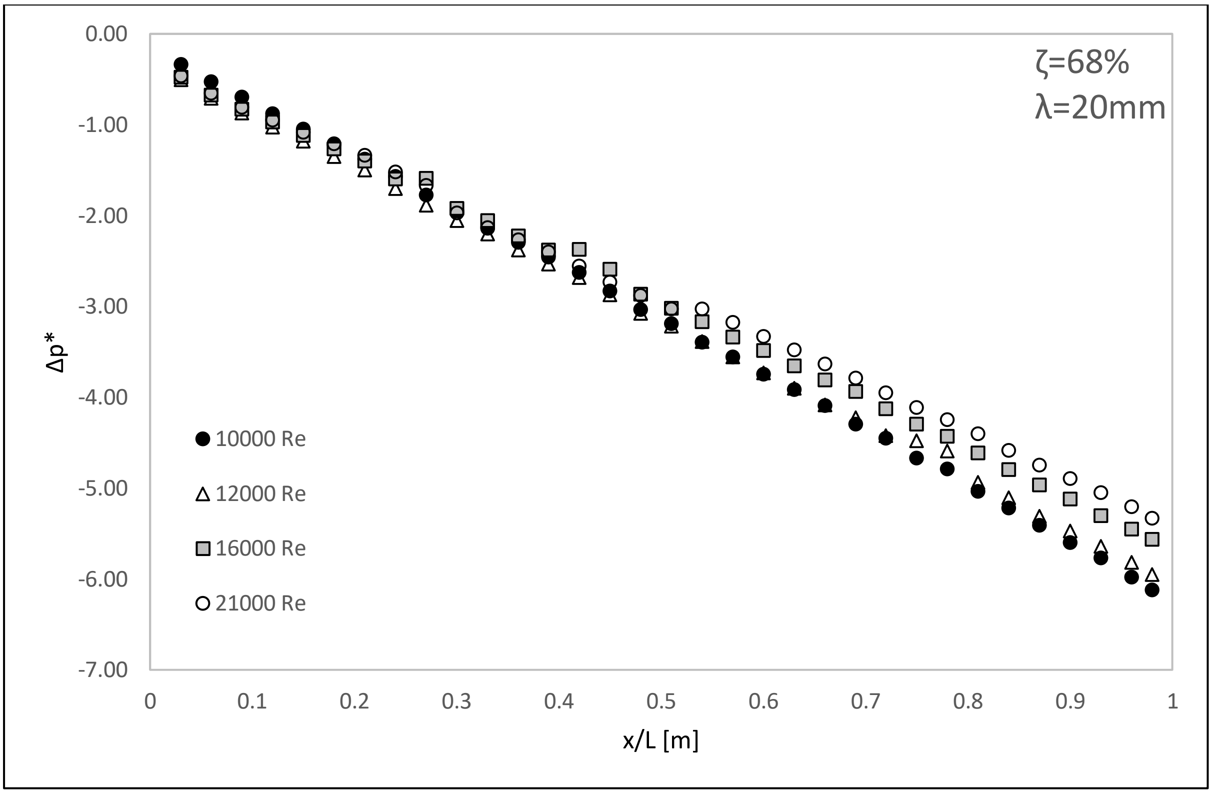

(c)

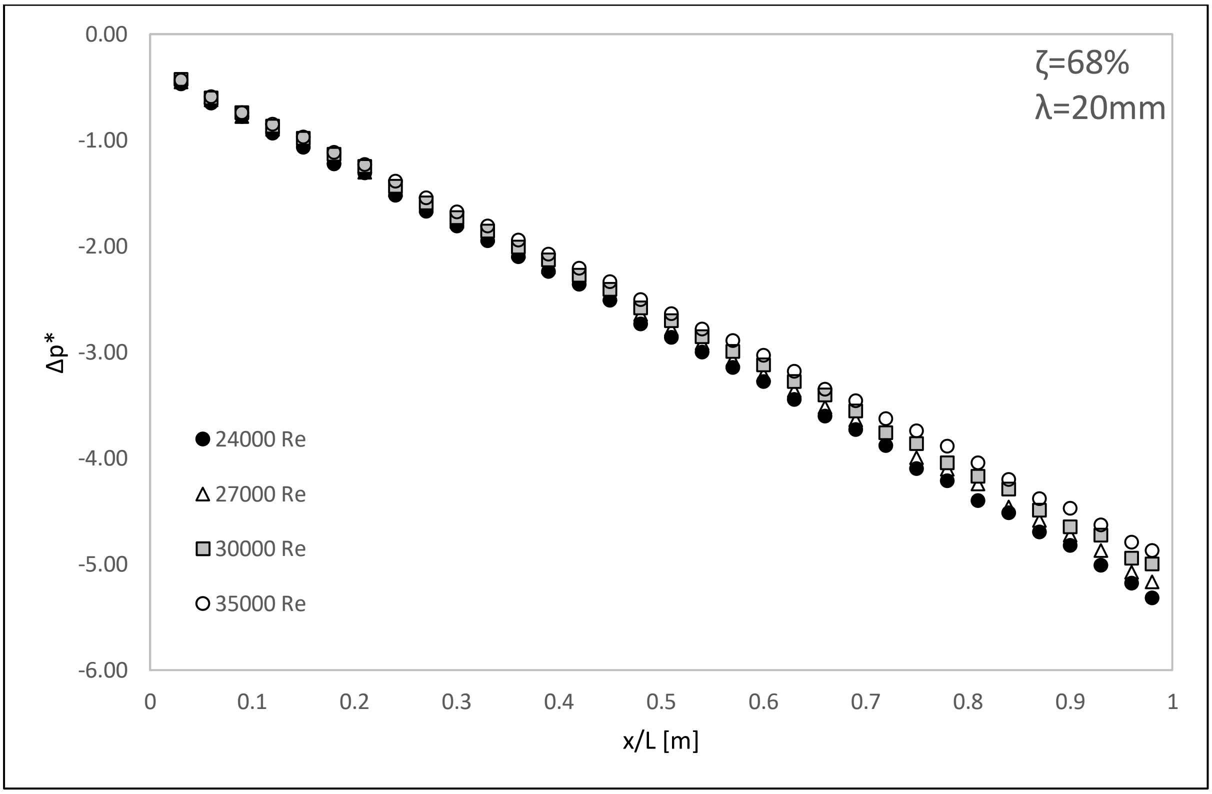

(d)

Figure C.19: Test section normalized pressure drop with insert 1.1 for Reynolds number range (a) 400 < Re < 2000, (b) 3000 < Re < 7500, (c) 10000 < Re < 21000 and (d) 24000 < Re < 35000

C.4. Mesh 1.2 (λ = 20 mm, ξ = 48 %)

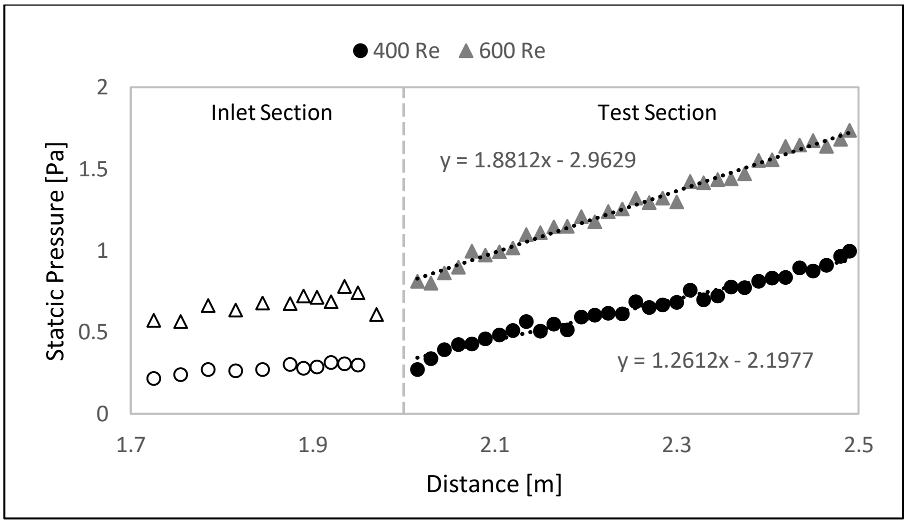

Figure C.20: Test Section Static Pressure for Insert 1.2 at Re = 400 and Re = 600

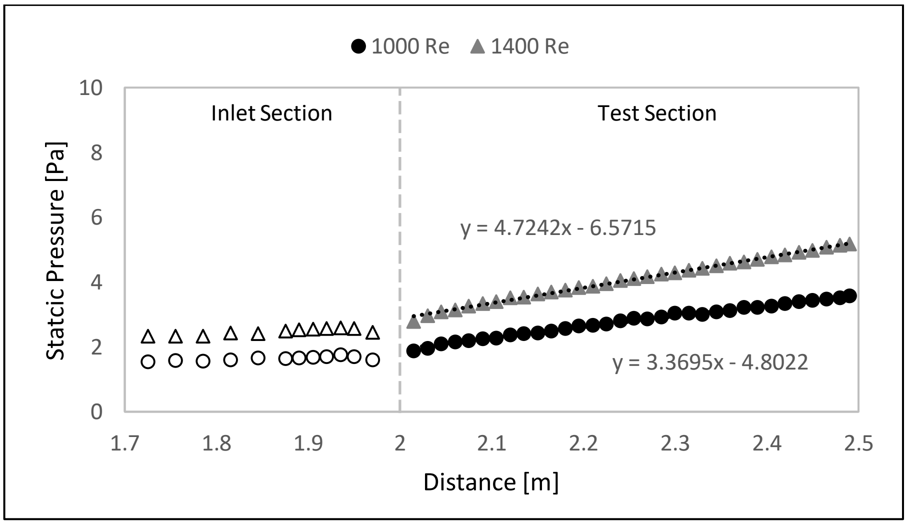

Figure C.21: Test Section Static Pressure for Insert 1.2 at Re = 1000 and Re = 1400

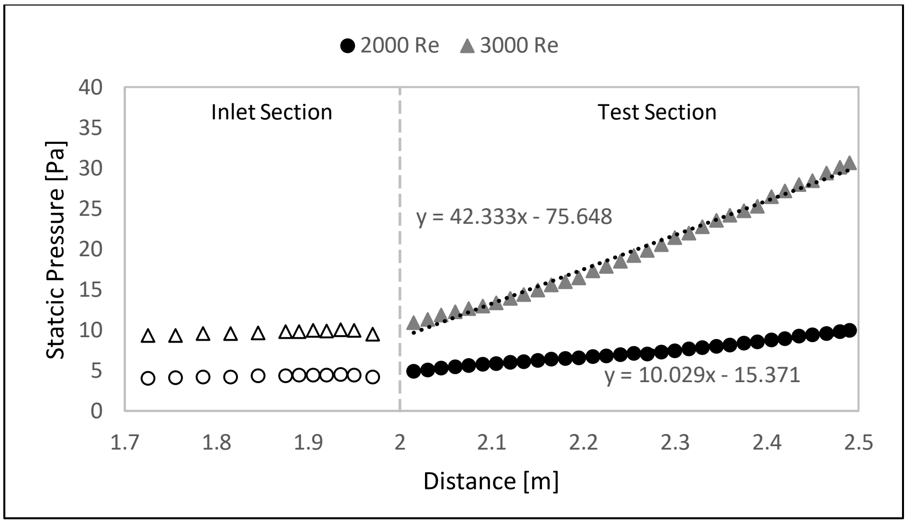

Figure C.22: Test Section Static Pressure for Insert 1.2 at Re = 2000 and Re = 3000

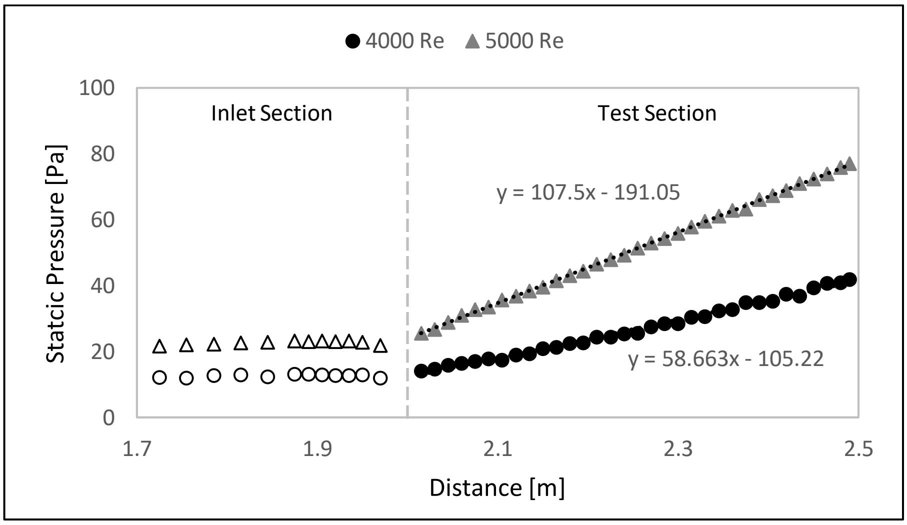

Figure C.23: Test Section Static Pressure for Insert 1.2 at Re = 4000 and Re = 5000

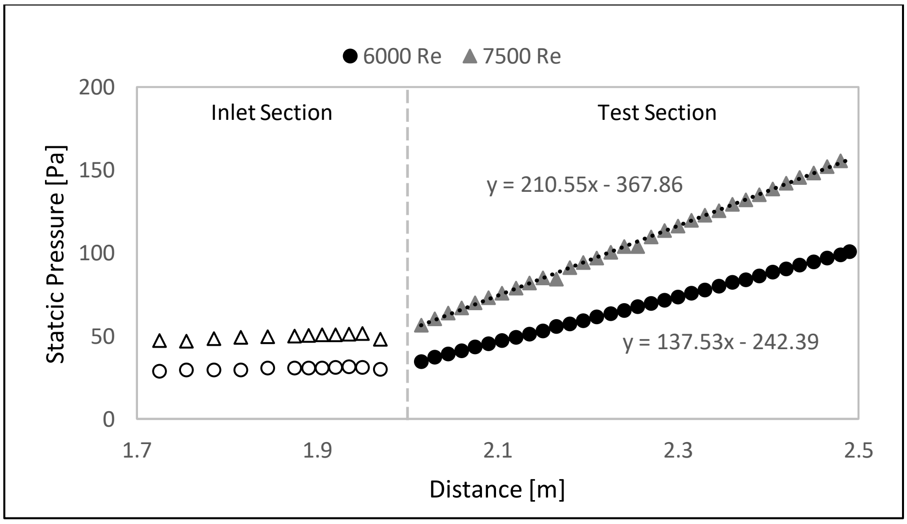

Figure C.24: Test Section Static Pressure for Insert 1.2 at Re = 6000 and Re = 7500

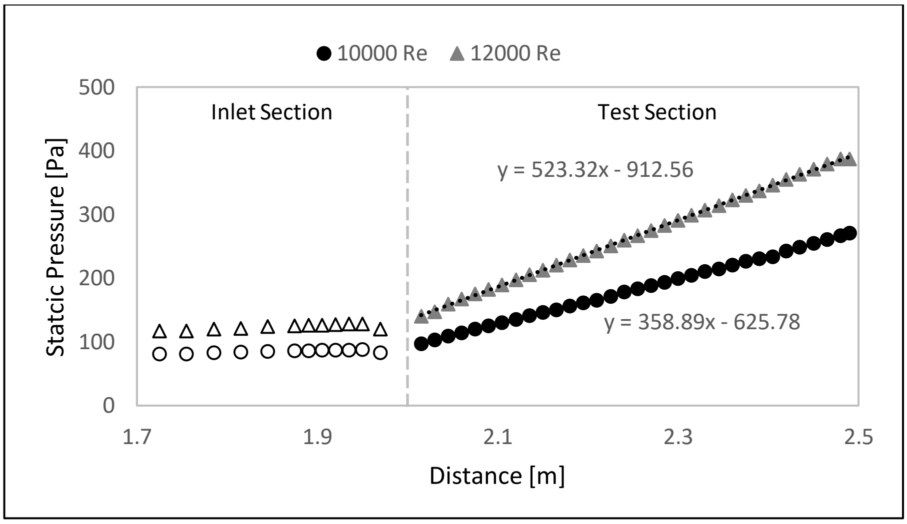

Figure C.25: Test Section Static Pressure for Insert 1.2 at Re = 10000 and Re = 12000

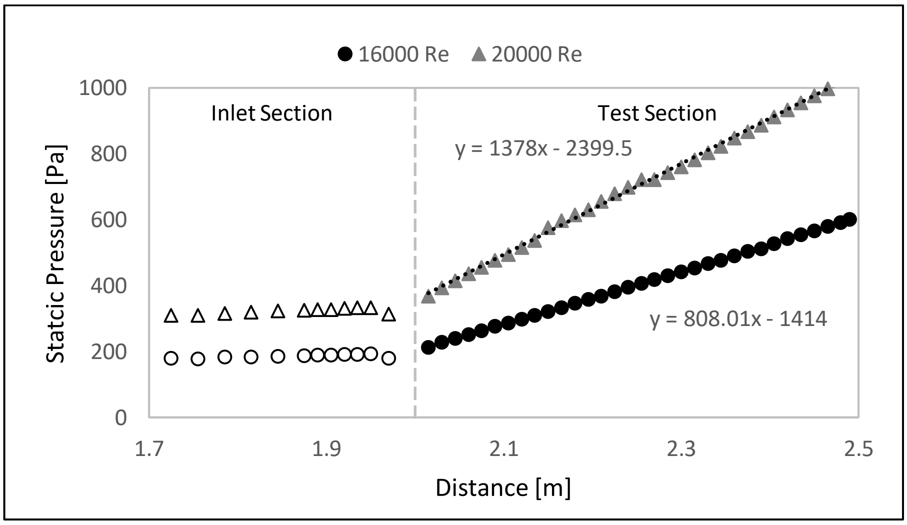

Figure C.26: Test Section Static Pressure for Insert 1.2 at Re = 16000 and Re = 20000

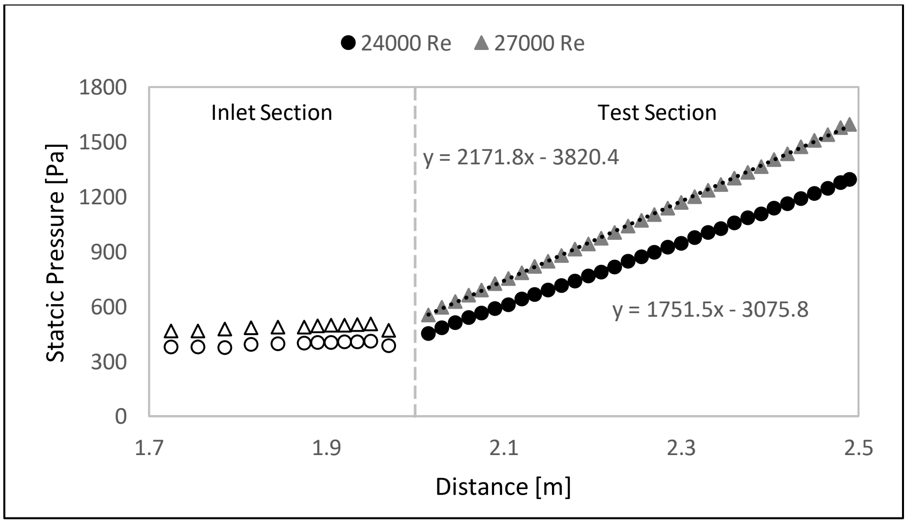

Figure C.27: Test Section Static Pressure for Insert 1.2 at Re = 24000 and Re = 27000

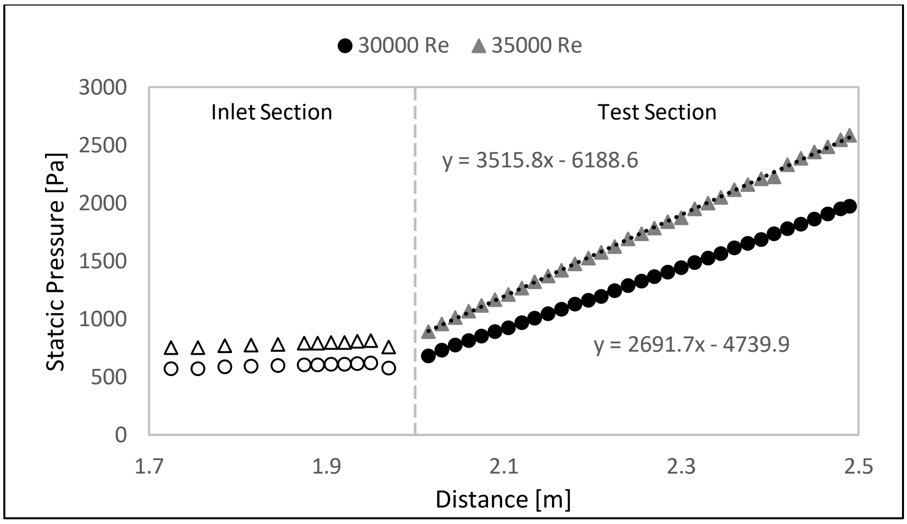

Figure C.28: Test Section Static Pressure for Insert 1.2 at Re = 30000 and Re = 35000

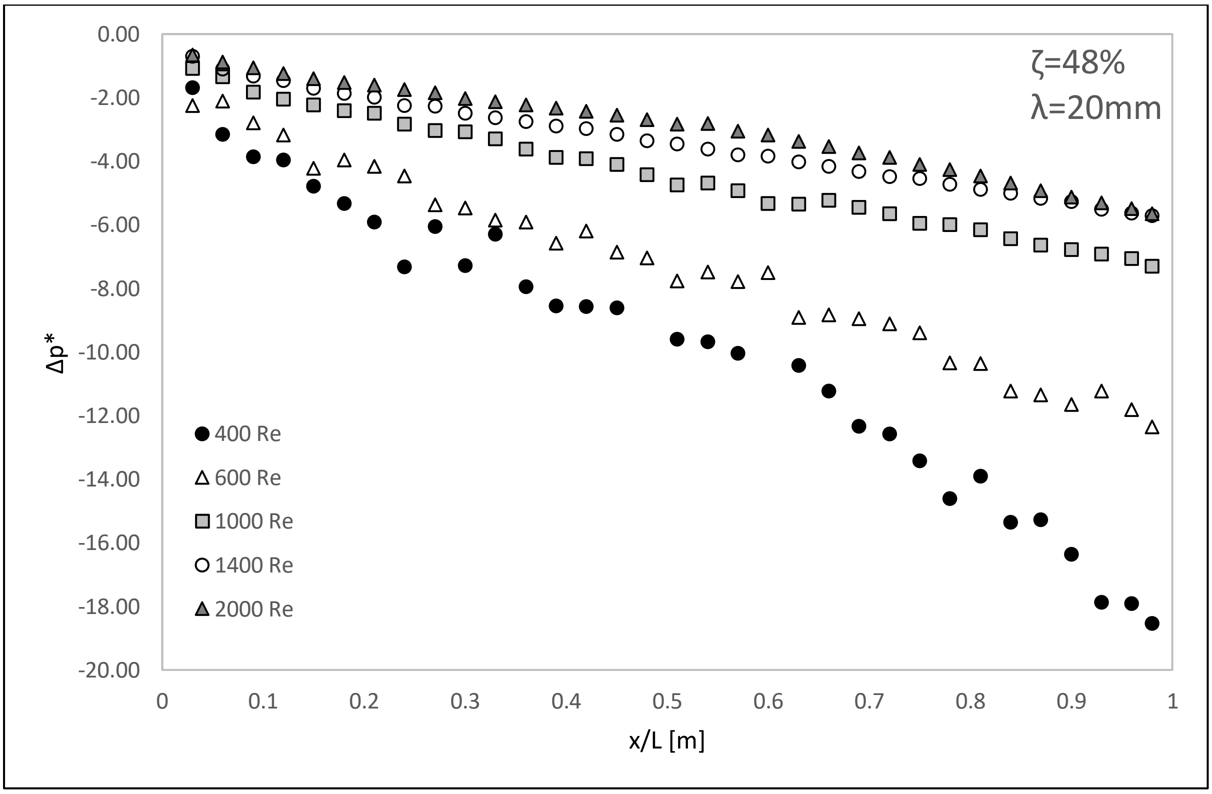

(a)

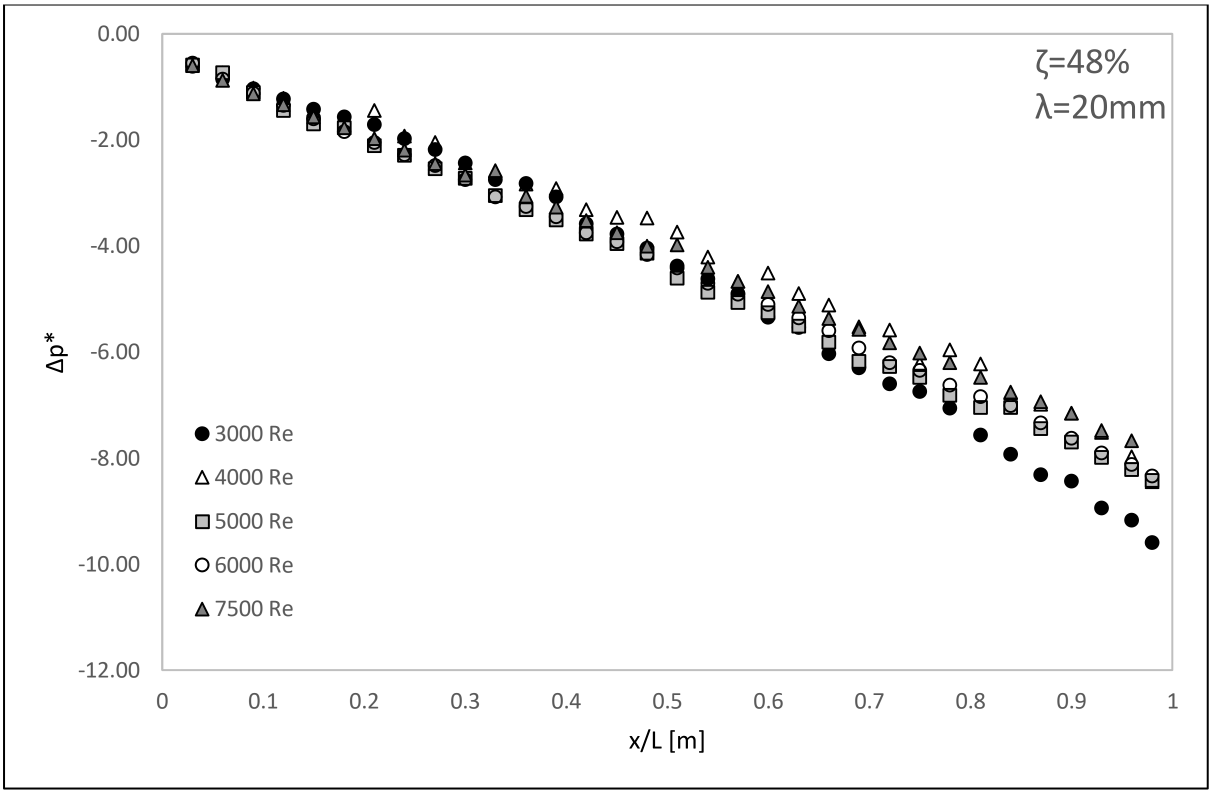
ζ=48%
λ=20mm
Δp*
0.00
-2.00
-4.00
-6.00
-8.00
-10.00
-12.00
0
0.1
0.2
0.3
0.4
0.5
0.6
0.7
0.8
0.9
1
x/L [m]
● 3000 Re
△ 4000 Re
▨ 5000 Re
○ 6000 Re
▲ 7500 Re

(b)

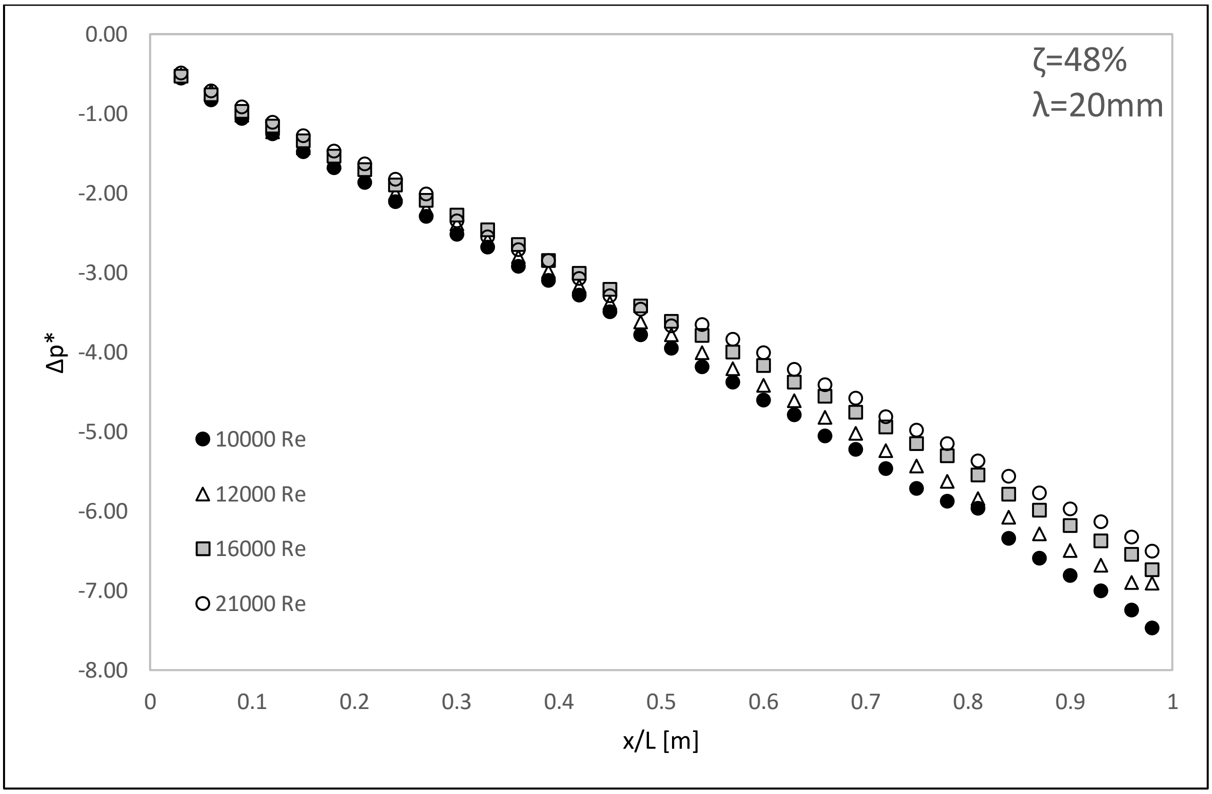
ζ=48%
λ=20mm
Δp*
0.00
-1.00
-2.00
-3.00
-4.00
-5.00
-6.00
-7.00
-8.00
0
0.1
0.2
0.3
0.4
0.5
0.6
0.7
0.8
0.9
1
x/L [m]
● 10000 Re
△ 12000 Re
▨ 16000 Re
○ 21000 Re

(c)

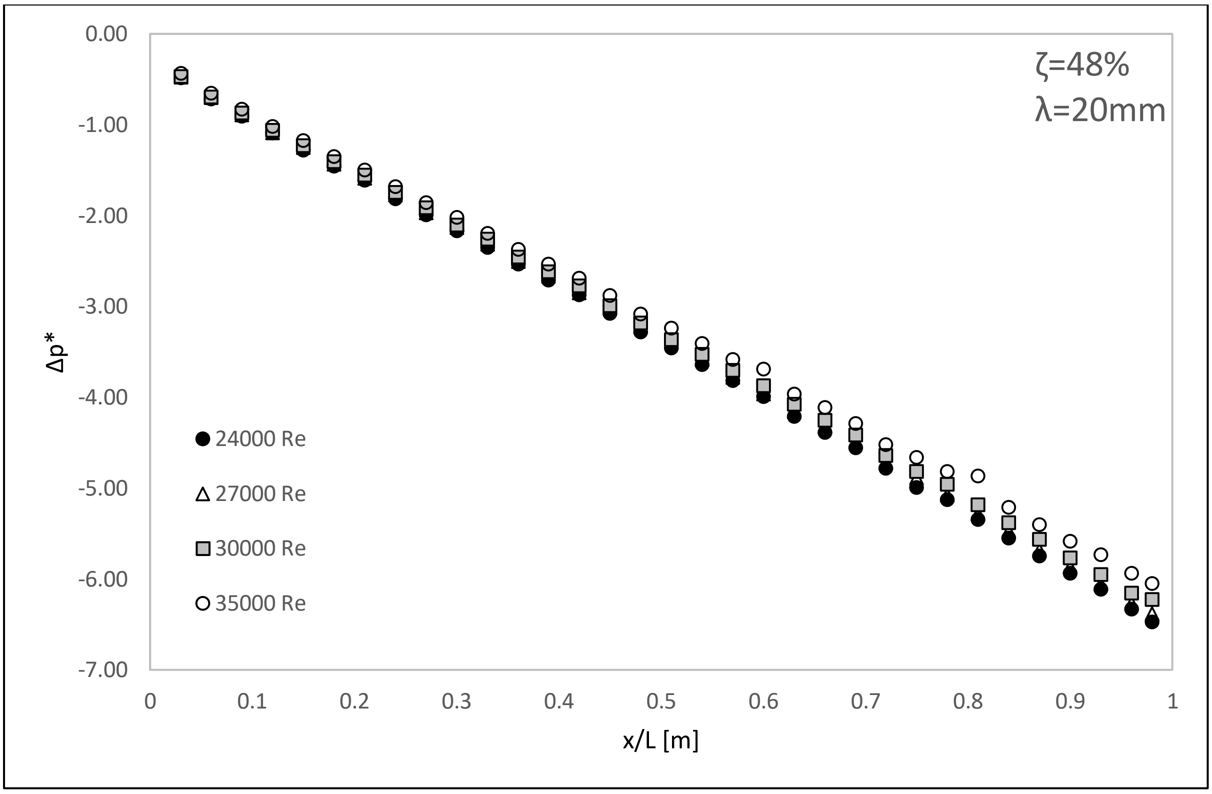

(d)

Figure C.29: Test section normalized pressure drop with insert 1.2 for Reynolds number range (a) 400 < Re < 2000, (b) 3000 < Re < 7500, (c) 10000 < Re < 21000 and (d) 24000 < Re < 35000

C.5. Mesh 2.1 (λ = 16 mm, ξ = 68 %)

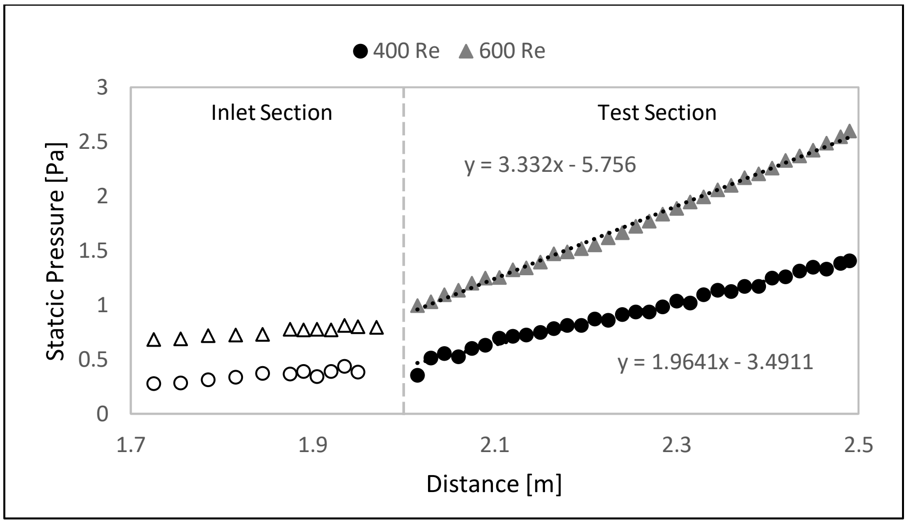

Figure C.30: Test Section Static Pressure for Insert 2.1 at Re = 400 and Re = 600

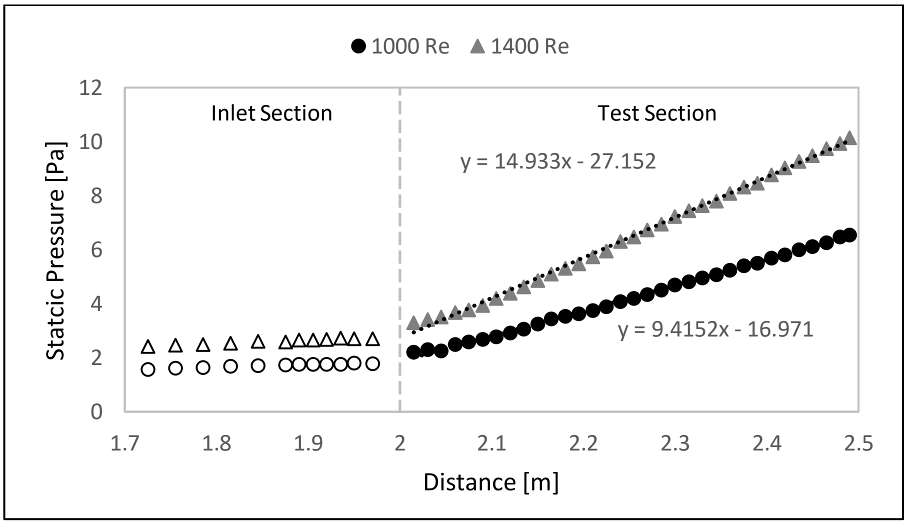

Figure C.31: Test Section Static Pressure for Insert 2.1 at Re = 1000 and Re = 1400

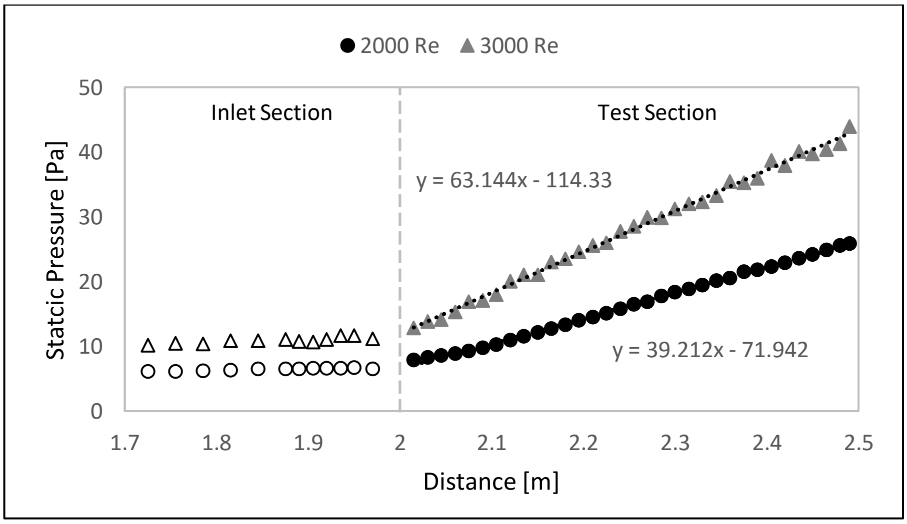

Figure C.32: Test Section Static Pressure for Insert 2.1 at Re = 2000 and Re = 3000

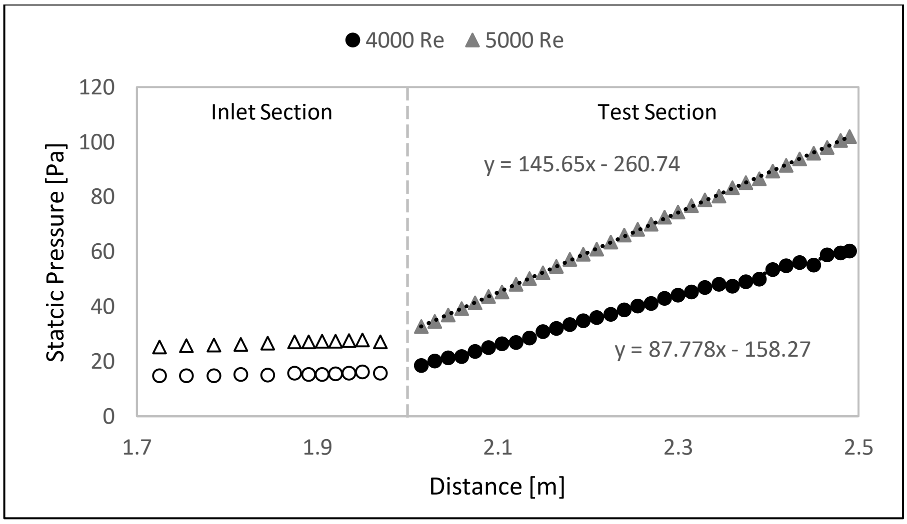

Figure C.33: Test Section Static Pressure for Insert 2.1 at Re = 4000 and Re = 5000

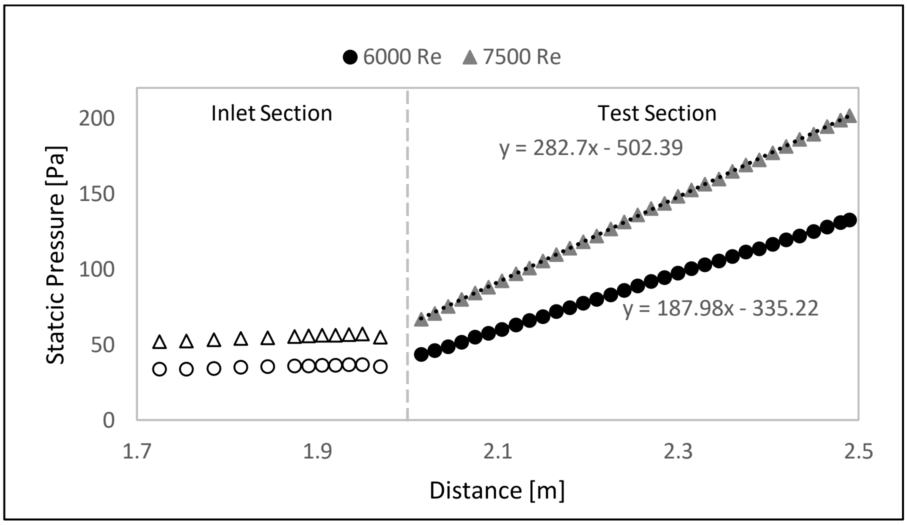

Figure C.34: Test Section Static Pressure for Insert 2.1 at Re = 6000 and Re = 7500

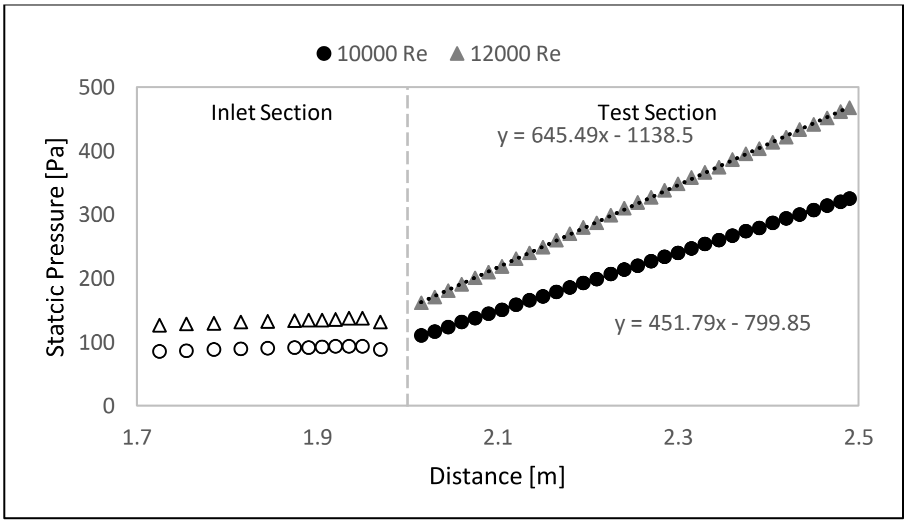

Figure C.35: Test Section Static Pressure for Insert 2.1 at Re = 10000 and Re = 12000

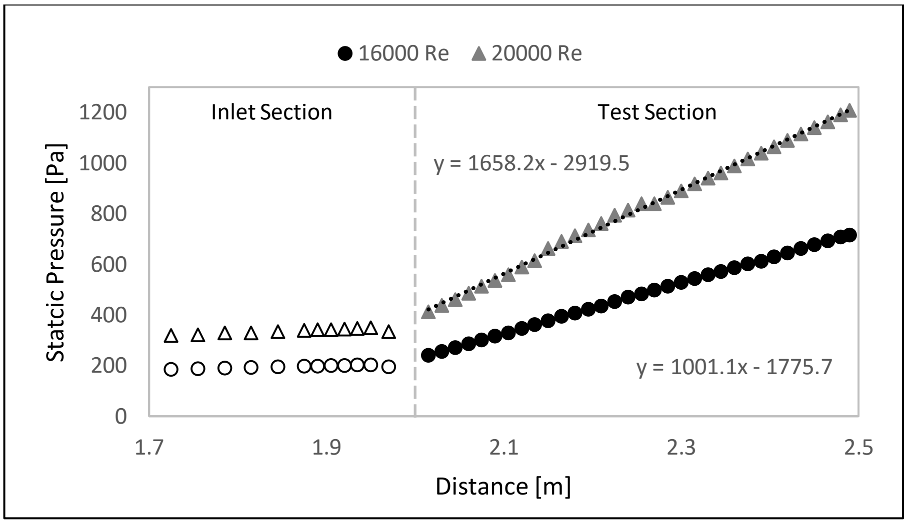

Figure C.36: Test Section Static Pressure for Insert 2.1 at Re = 16000 and Re = 20000

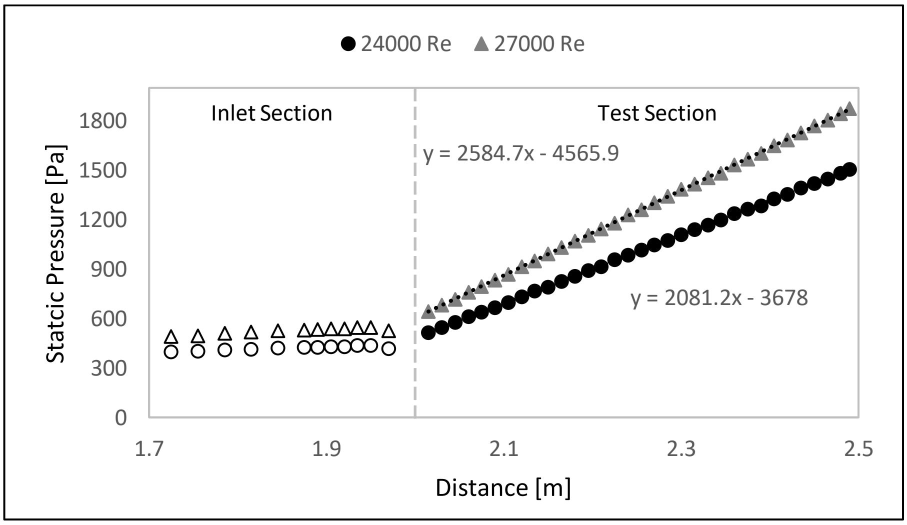

Figure C.37: Test Section Static Pressure for Insert 2.1 at Re = 24000 and Re = 27000

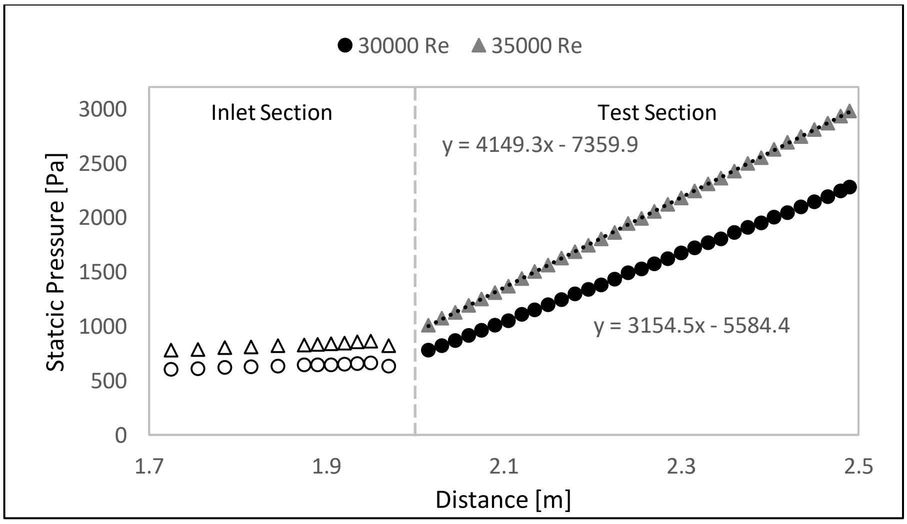

Figure C.38: Test Section Static Pressure for Insert 2.1 at Re = 30000 and Re = 35000

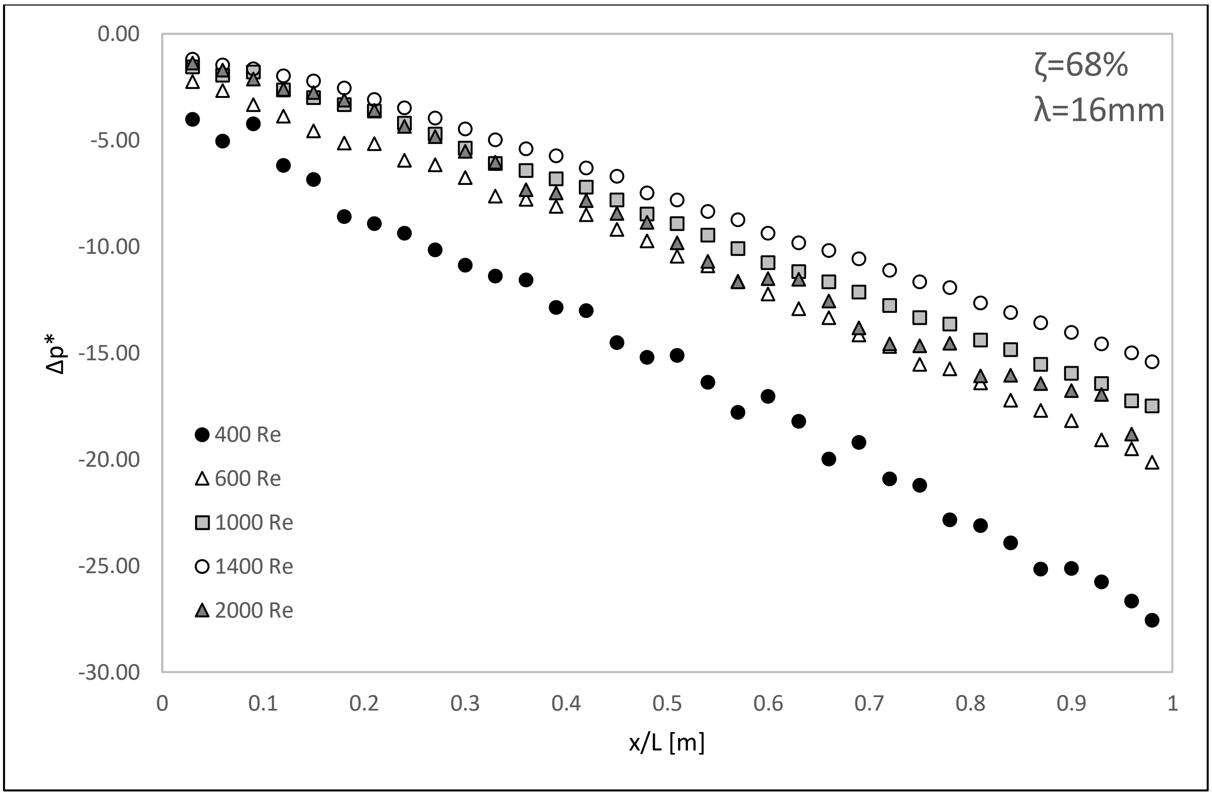
ζ=68%
λ=16mm
Δp*
0.00
-5.00
-10.00
-15.00
-20.00
-25.00
-30.00
0
0.1
0.2
0.3
0.4
0.5
0.6
0.7
0.8
0.9
1
x/L [m]
● 400 Re
△ 600 Re
▨ 1000 Re
○ 1400 Re
▲ 2000 Re

(a)

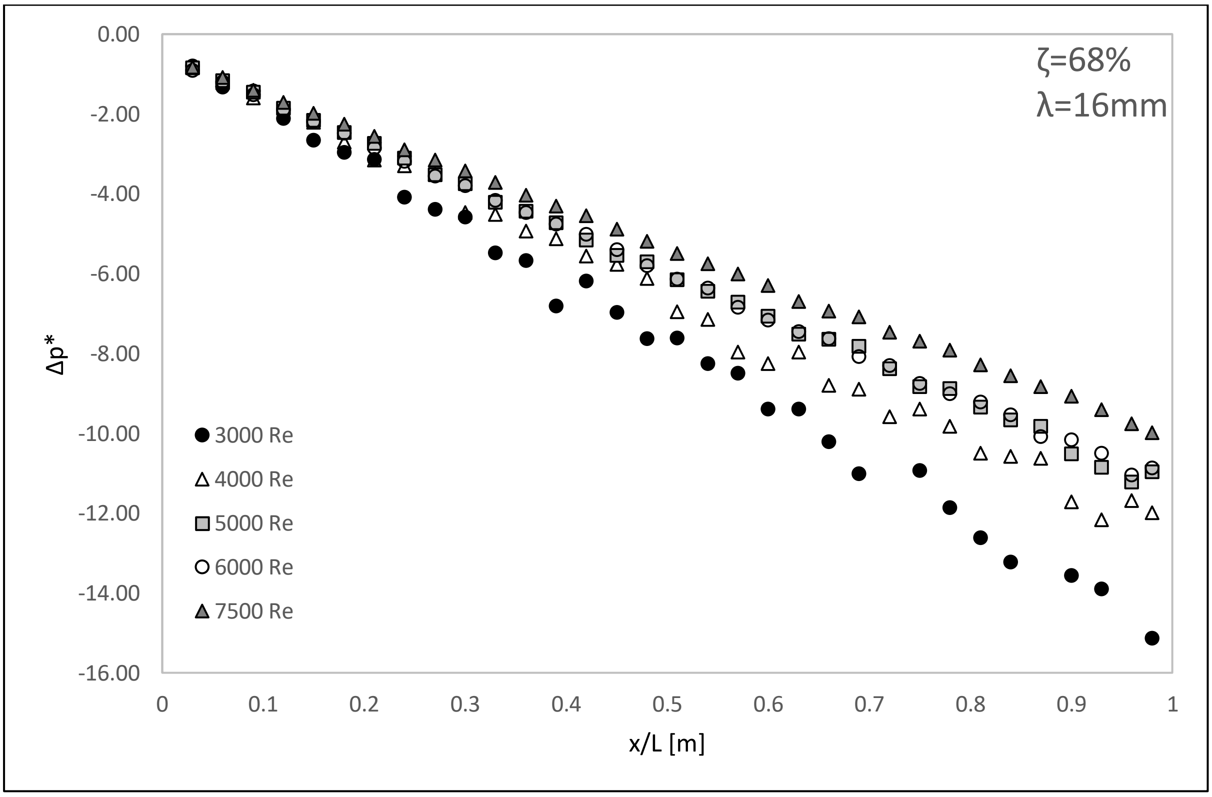
ζ=68%
λ=16mm
Δp*
0.00
-2.00
-4.00
-6.00
-8.00
-10.00
-12.00
-14.00
-16.00
0
0.1
0.2
0.3
0.4
0.5
0.6
0.7
0.8
0.9
1
x/L [m]
● 3000 Re
△ 4000 Re
▨ 5000 Re
○ 6000 Re
▲ 7500 Re

(b)

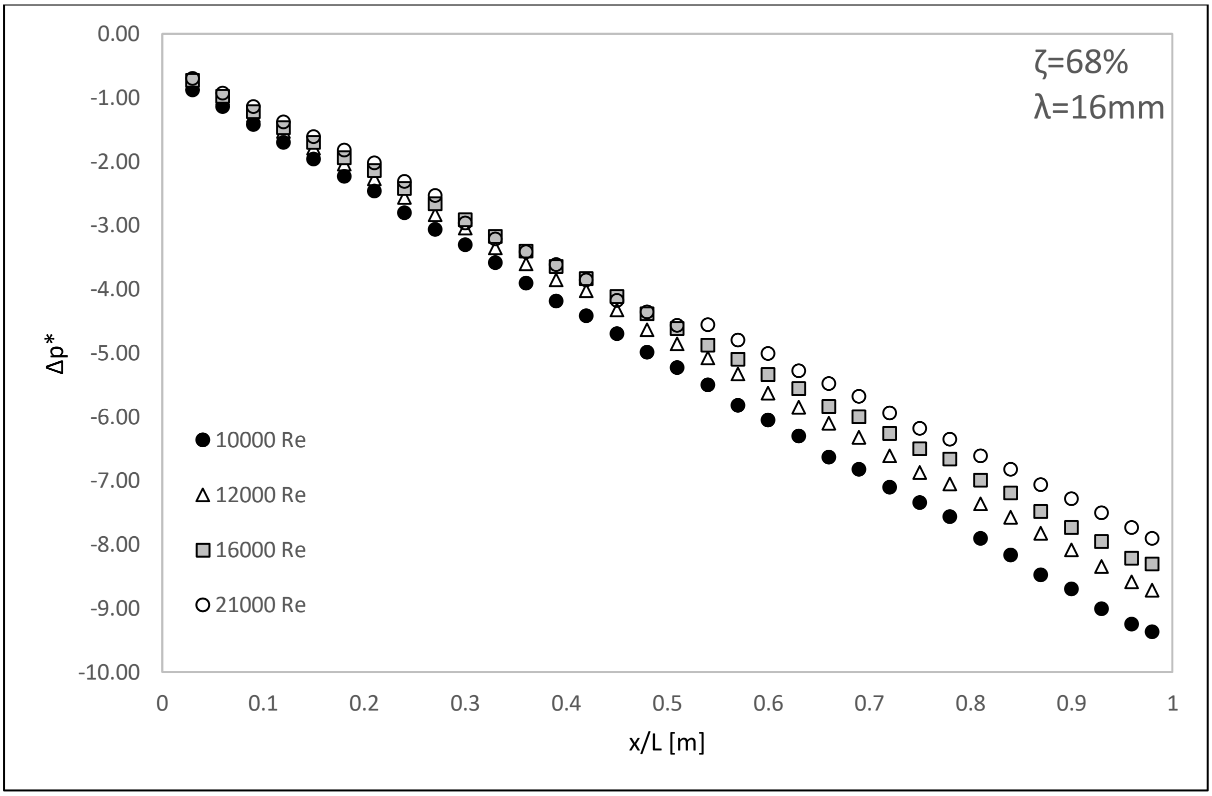

(c)

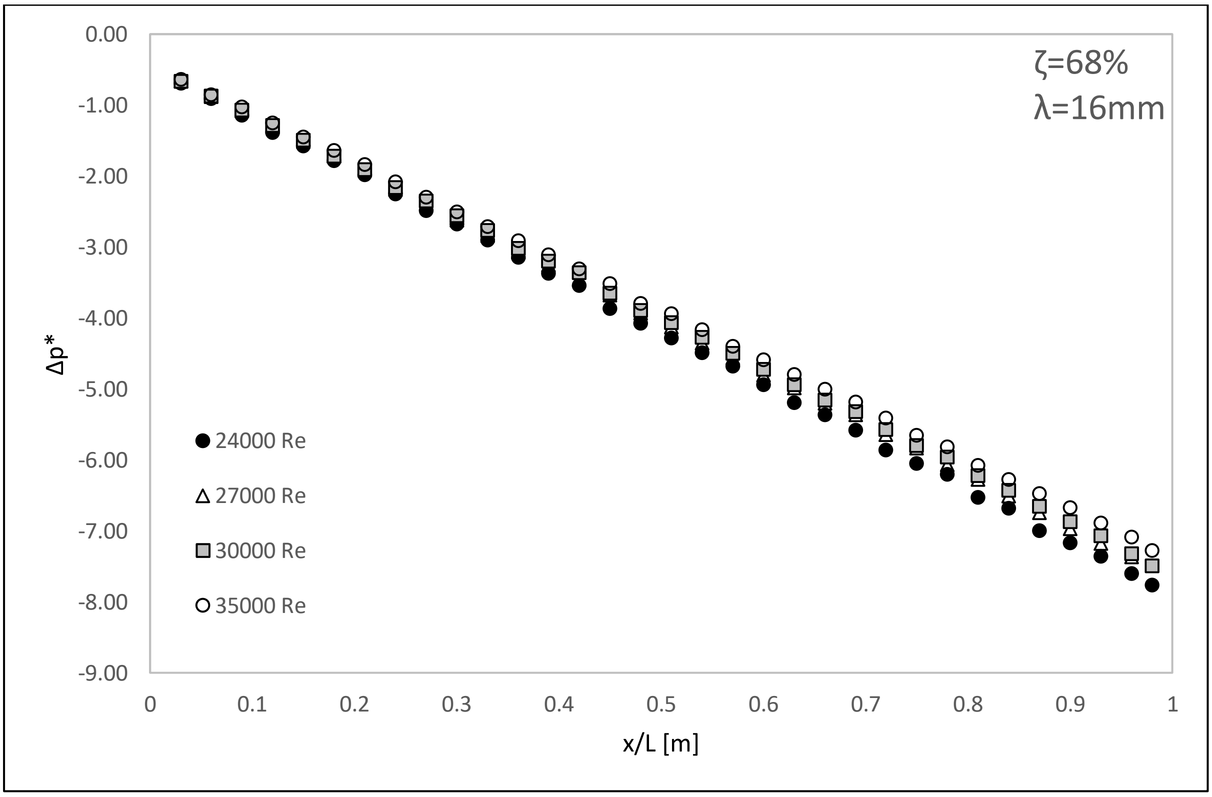

(d)

Figure C.39: Test section normalized pressure drop with insert 2.1 for Reynolds number range (a) 400 < Re < 2000, (b) 3000 < Re < 7500, (c) 10000 < Re < 21000 and (d) 24000 < Re < 35000

C.6. Mesh 2.2 (λ = 16 mm, ξ = 48 %)

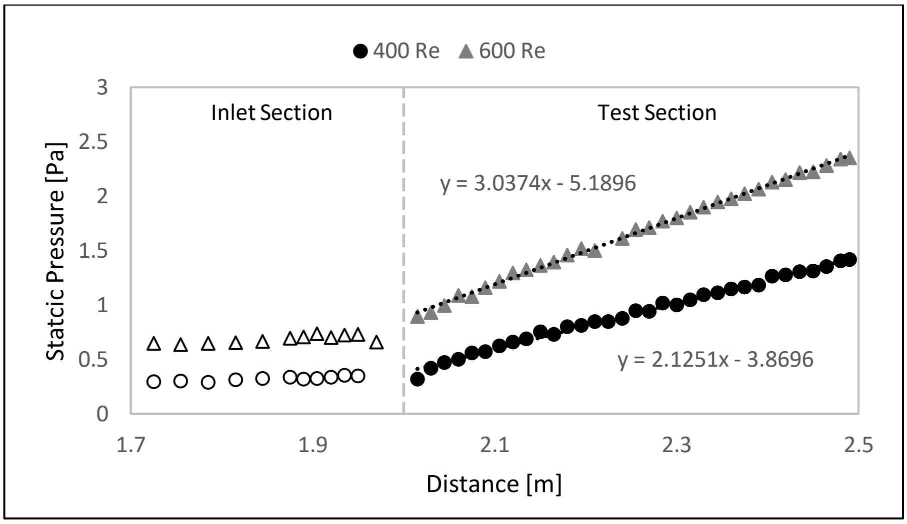

Figure C.40: Test Section Static Pressure for Insert 2.2 at Re = 400 and Re = 600

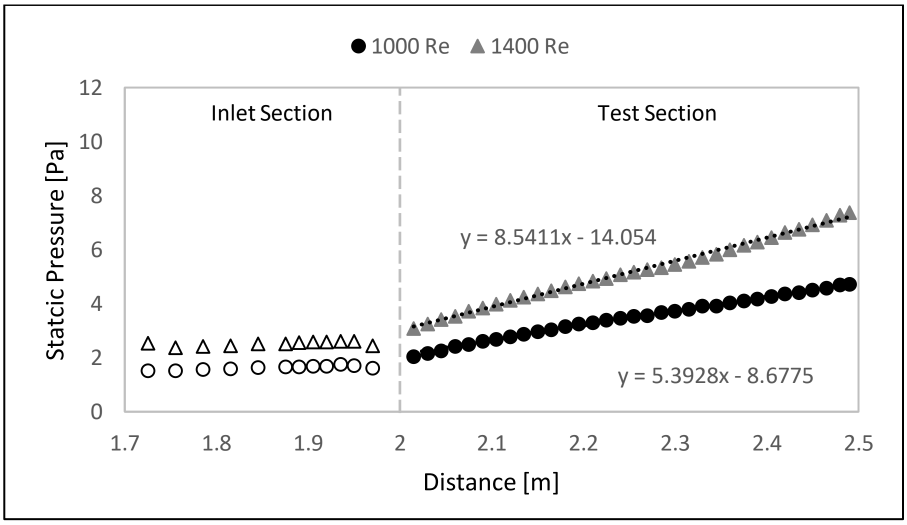

Figure C.41: Test Section Static Pressure for Insert 2.2 at Re = 1000 and Re = 1400

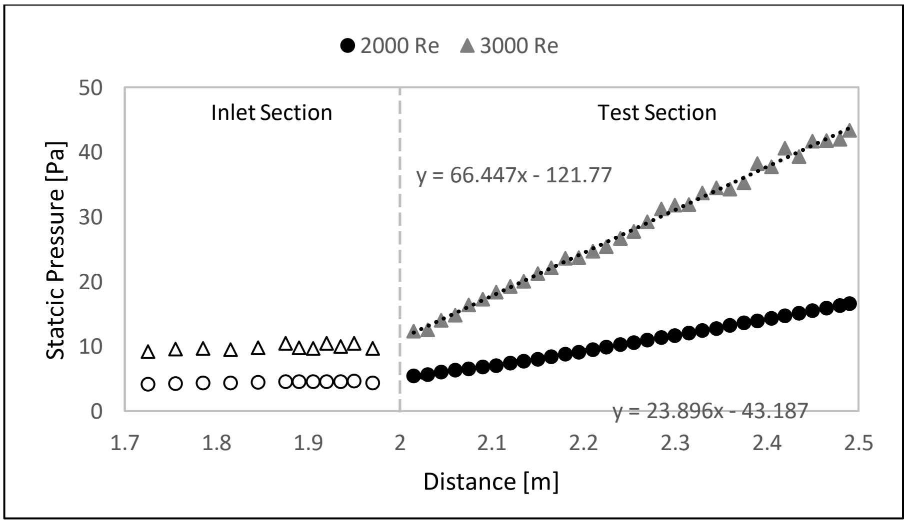

Figure C.42: Test Section Static Pressure for Insert 2.2 at Re = 2000 and Re = 3000

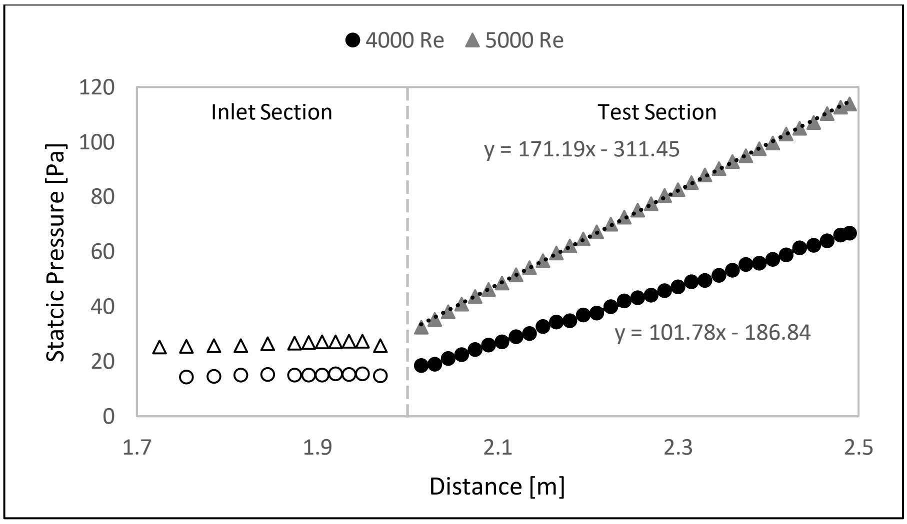

Figure C.43: Test Section Static Pressure for Insert 2.2 at Re = 4000 and Re = 5000

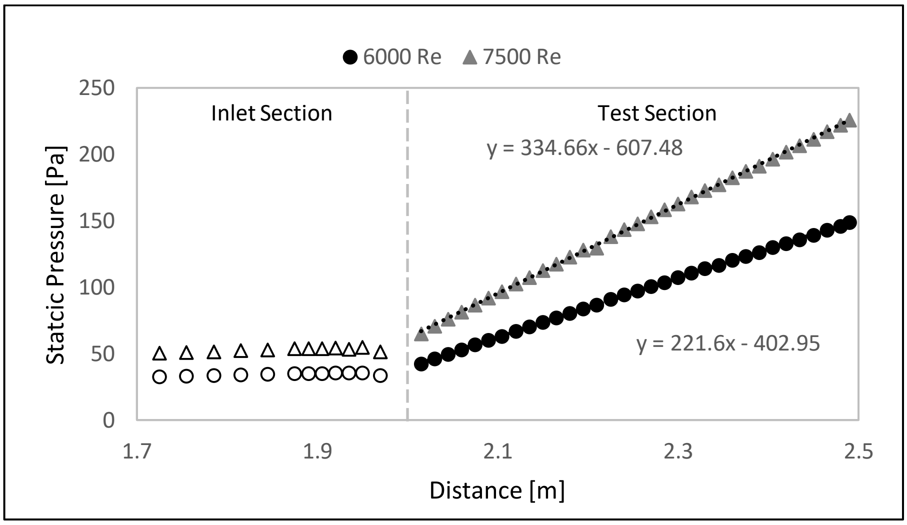

Figure C.44: Test Section Static Pressure for Insert 2.2 at Re = 6000 and Re = 7500

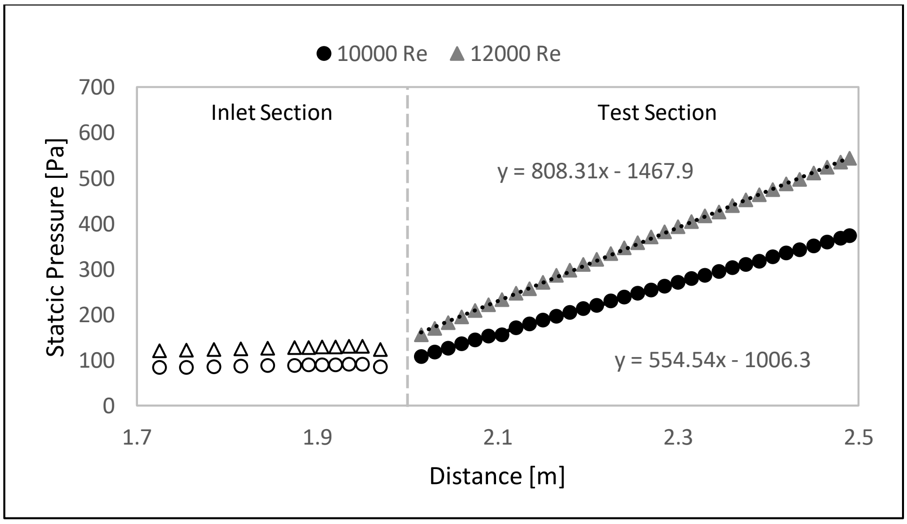

Figure C.45: Test Section Static Pressure for Insert 2.2 at Re = 10000 and Re = 1200

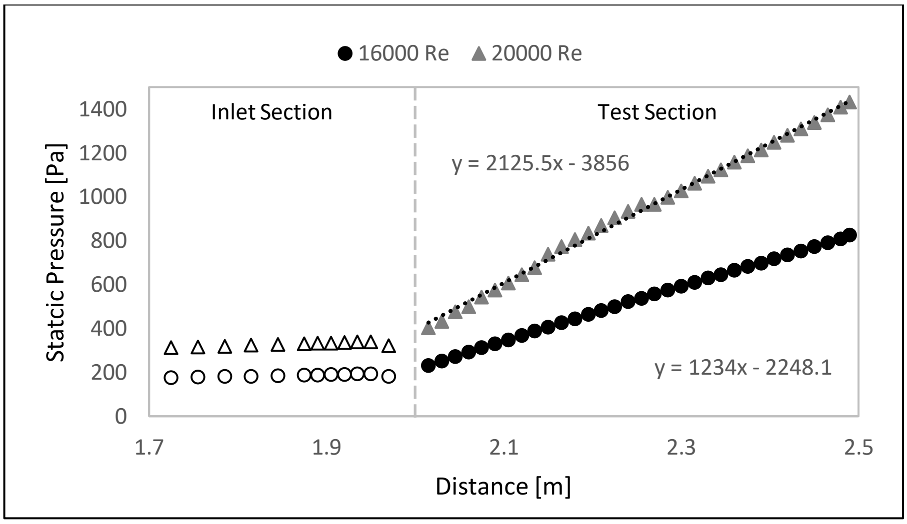

Figure C.46: Test Section Static Pressure for Insert 2.2 at Re = 16000 and Re = 20000

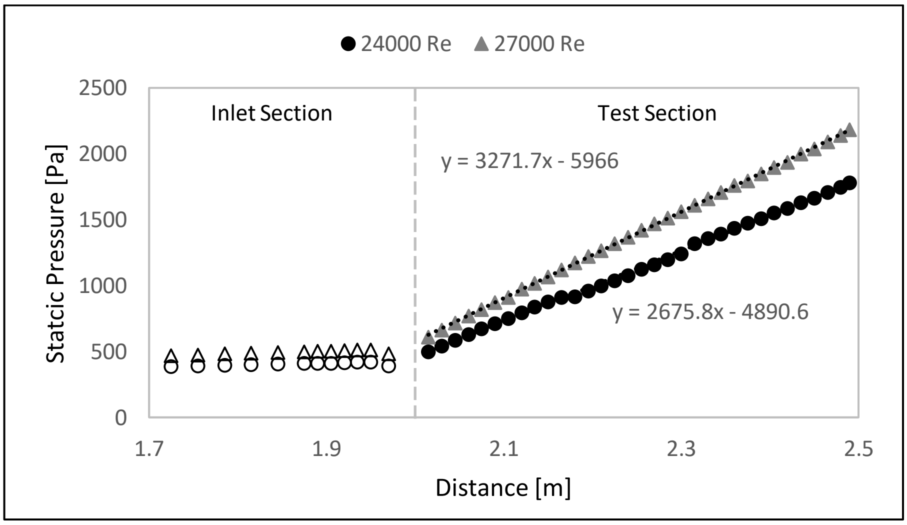

Figure C.47: Test Section Static Pressure for Insert 2.2 at Re = 24000 and Re = 27000

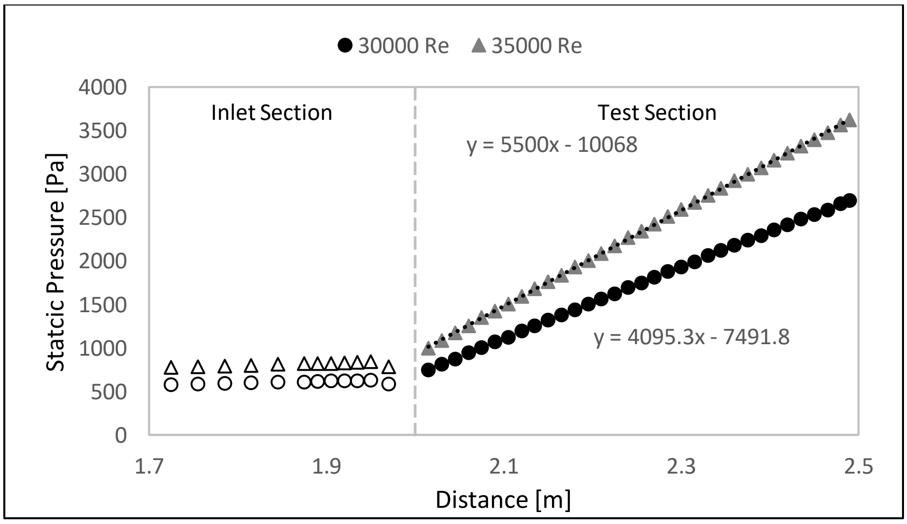

Figure C.48: Test Section Static Pressure for Insert 2.2 at Re = 30000 and Re = 35000

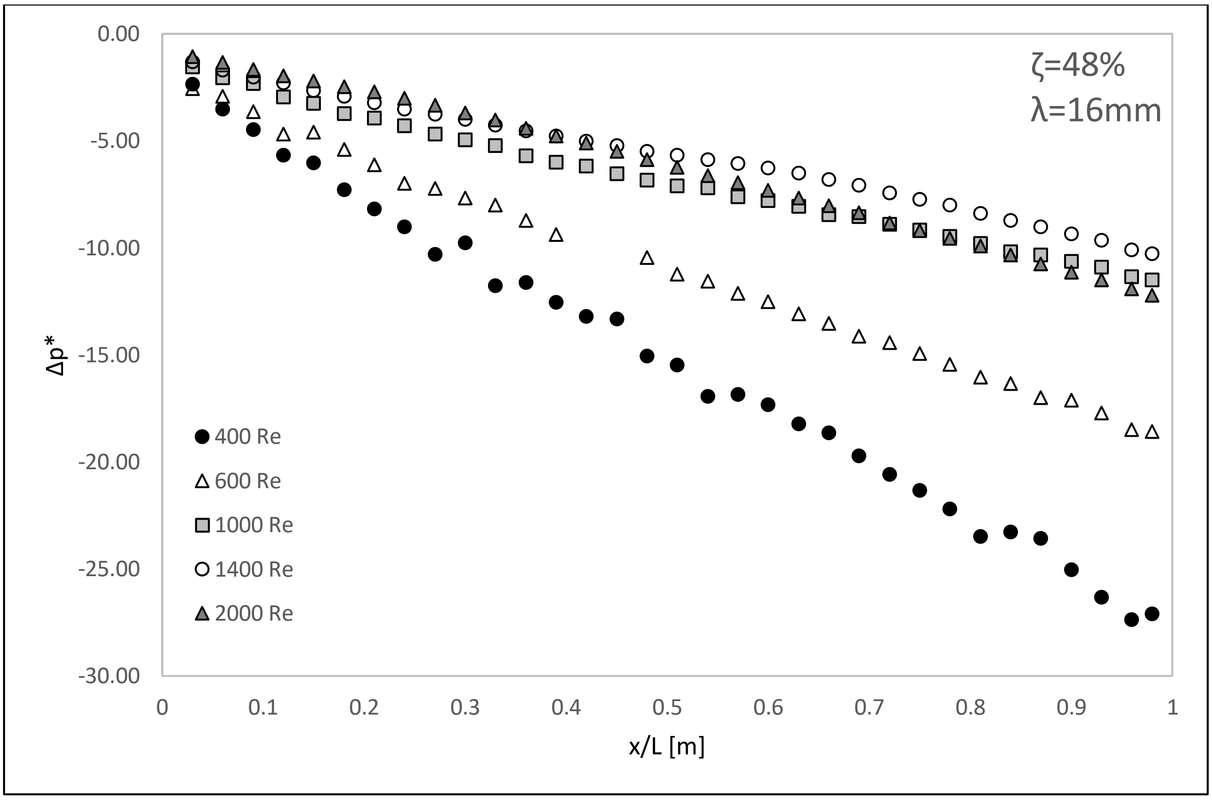
ζ=48%
λ=16mm
Δp*
0.00
-5.00
-10.00
-15.00
-20.00
-25.00
-30.00
0
0.1
0.2
0.3
0.4
0.5
0.6
0.7
0.8
0.9
1
x/L [m]
● 400 Re
△ 600 Re
▨ 1000 Re
○ 1400 Re
▲ 2000 Re

(a)

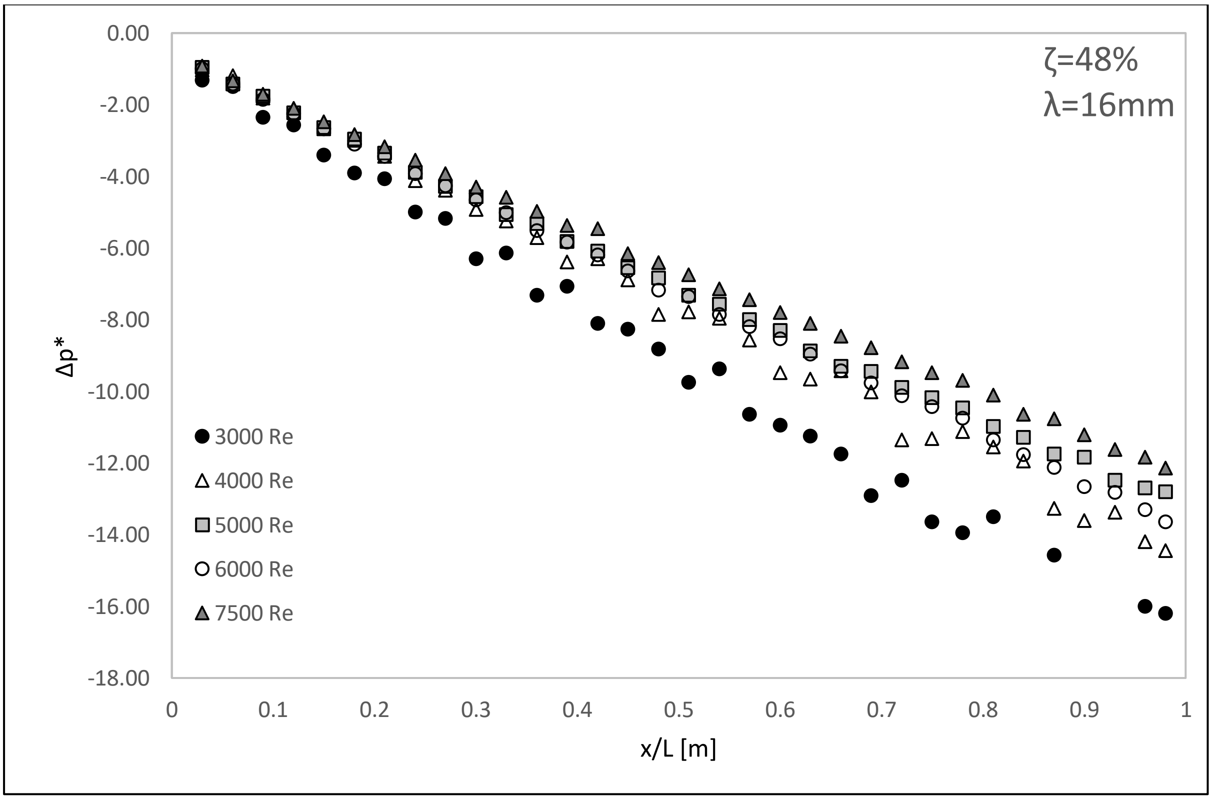
ζ=48%
λ=16mm
Δp*
0.00
-2.00
-4.00
-6.00
-8.00
-10.00
-12.00
-14.00
-16.00
-18.00
0
0.1
0.2
0.3
0.4
0.5
0.6
0.7
0.8
0.9
1
x/L [m]
● 3000 Re
△ 4000 Re
▨ 5000 Re
○ 6000 Re
▲ 7500 Re

(b)

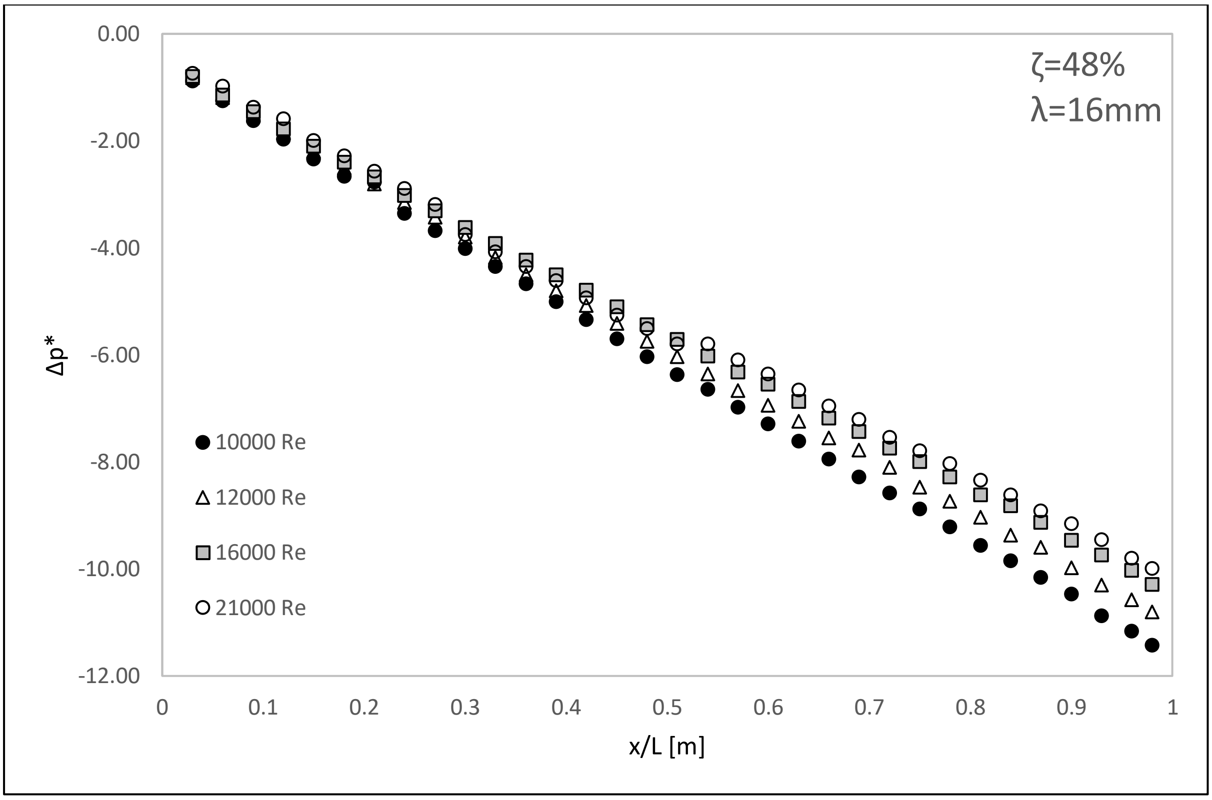

(c)

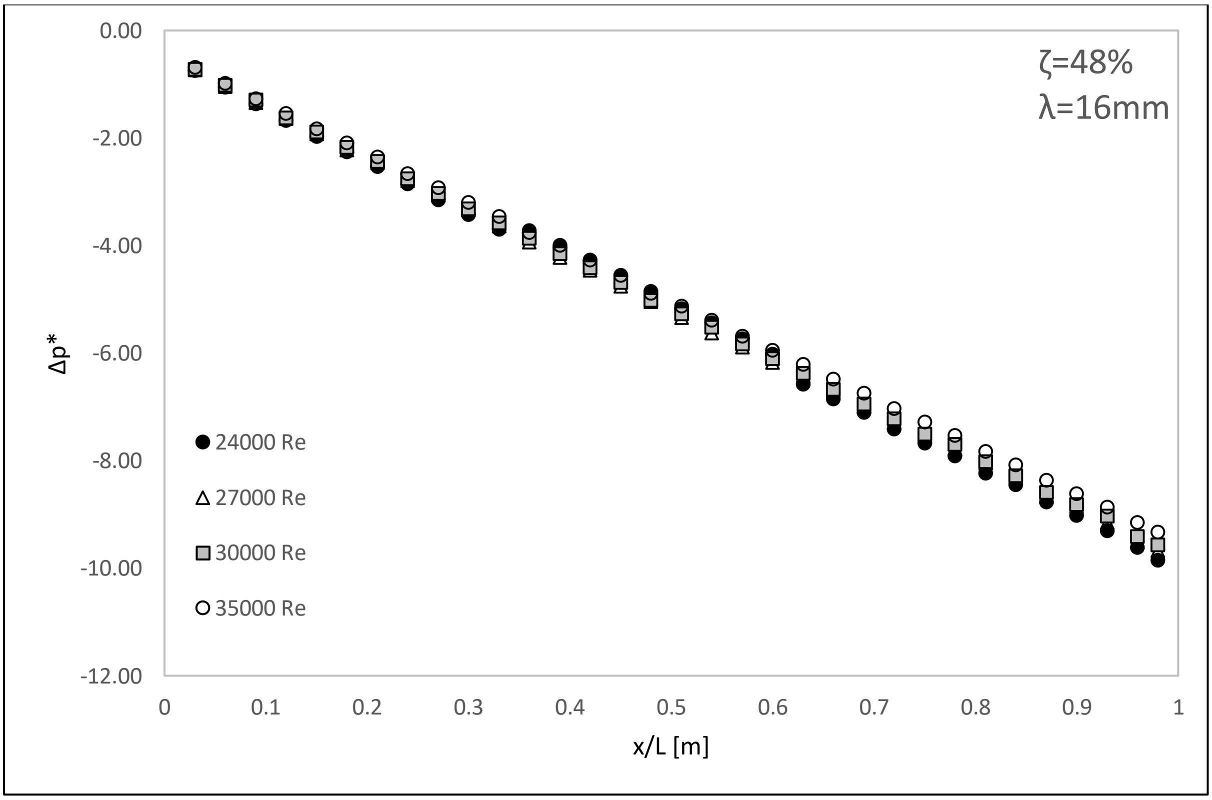

(d)

Figure C.49: Test section normalized pressure drop with insert 2.2 for Reynolds number range (a) 400 < Re < 2000, (b) 3000 < Re < 7500, (c) 10000 < Re < 21000 and (d) 24000 < Re < 35000

C.7. Mesh 3.1 (λ = 12 mm, ξ = 68 %)

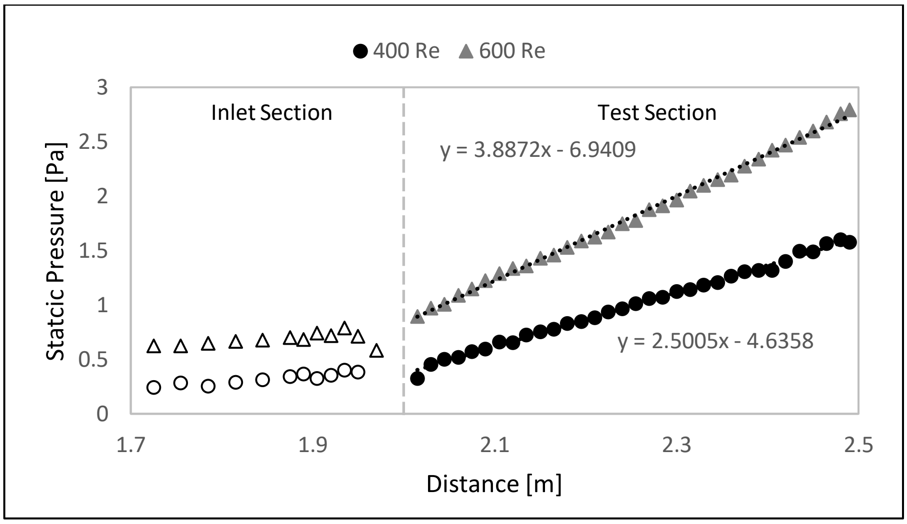

Figure C.50: Test Section Static Pressure for Insert 3.1 at Re = 400 and Re = 600

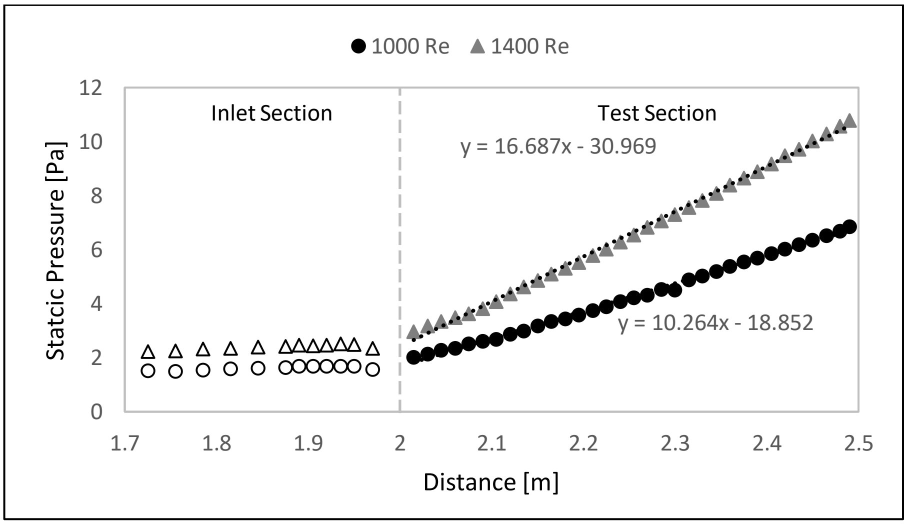

Figure C.51: Test Section Static Pressure for Insert 3.1 at Re = 1000 and Re = 1400

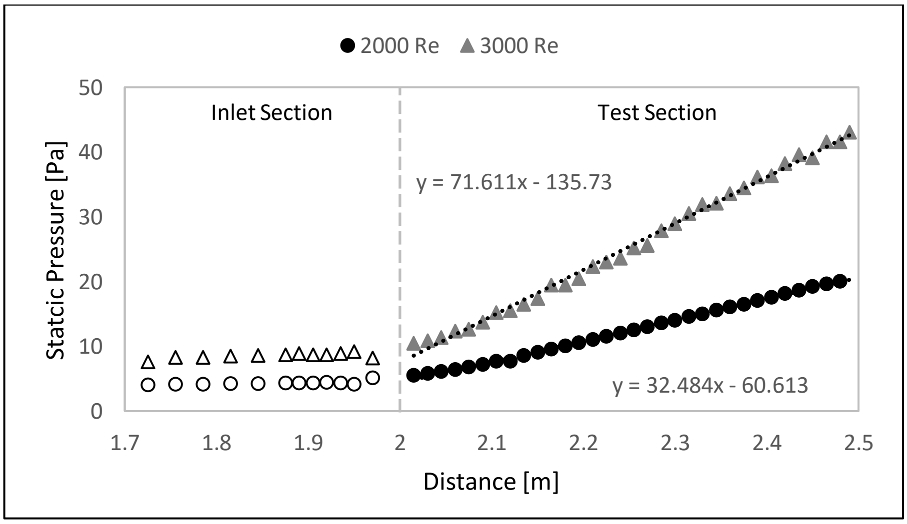

Figure C.52: Test Section Static Pressure for Insert 3.1 at Re = 2000 and Re = 3000

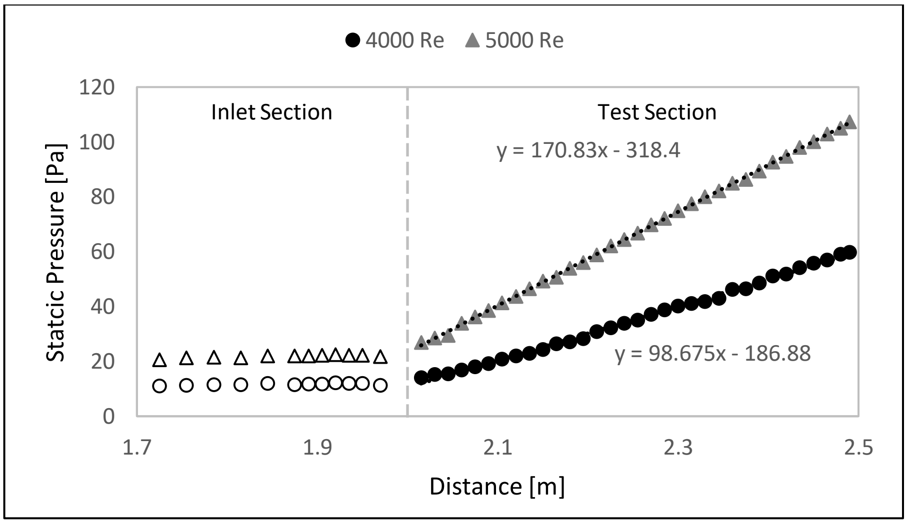

Figure C.53: Test Section Static Pressure for Insert 3.1 at Re = 4000 and Re = 5000

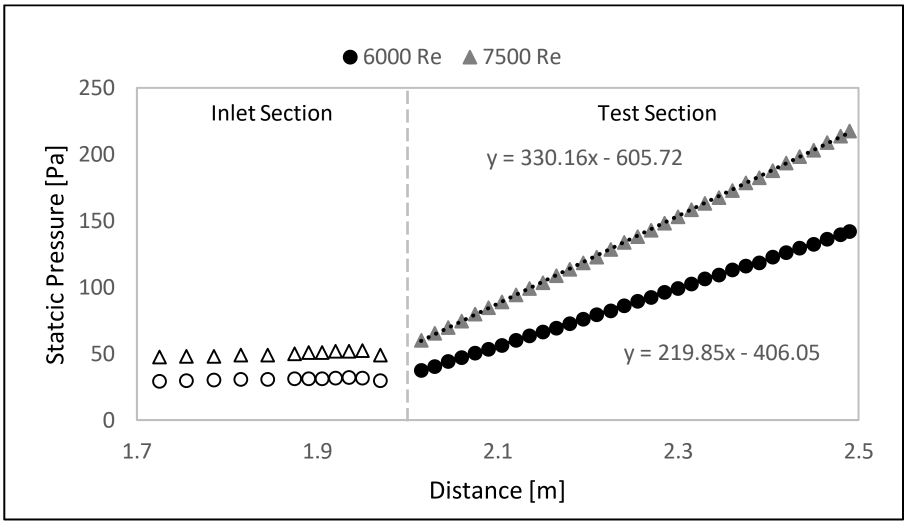

Figure C.54: Test Section Static Pressure for Insert 3.1 at Re = 6000 and Re = 7500

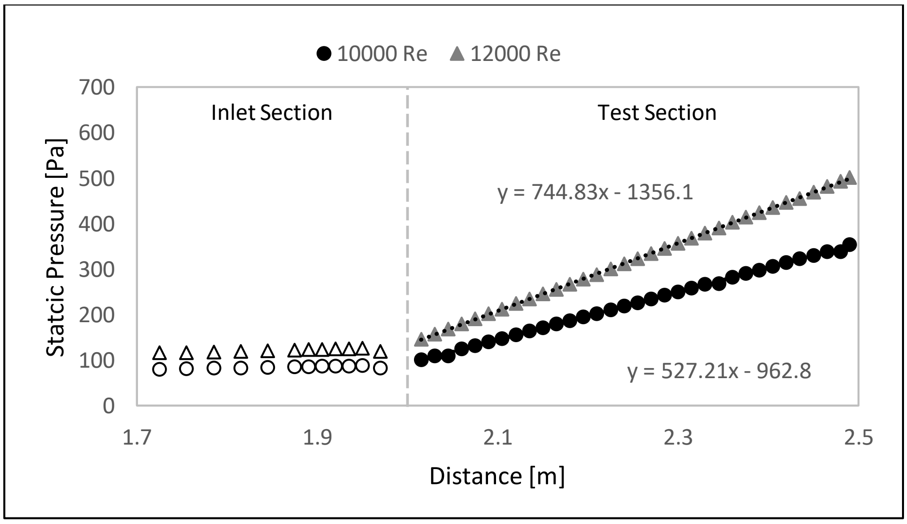

Figure C.55: Test Section Static Pressure for Insert 3.1 at Re = 10000 and Re = 12000

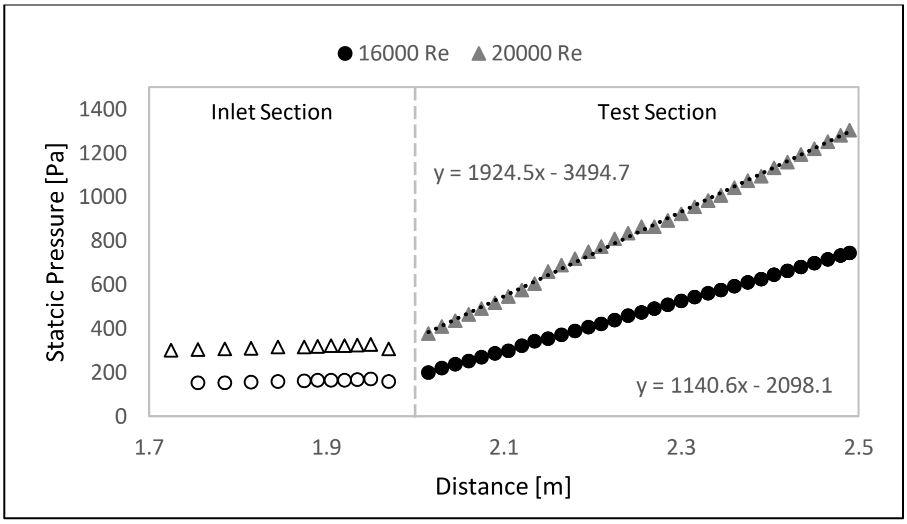

Figure C.56: Test Section Static Pressure for Insert 3.1 at Re = 16000 and Re = 20000

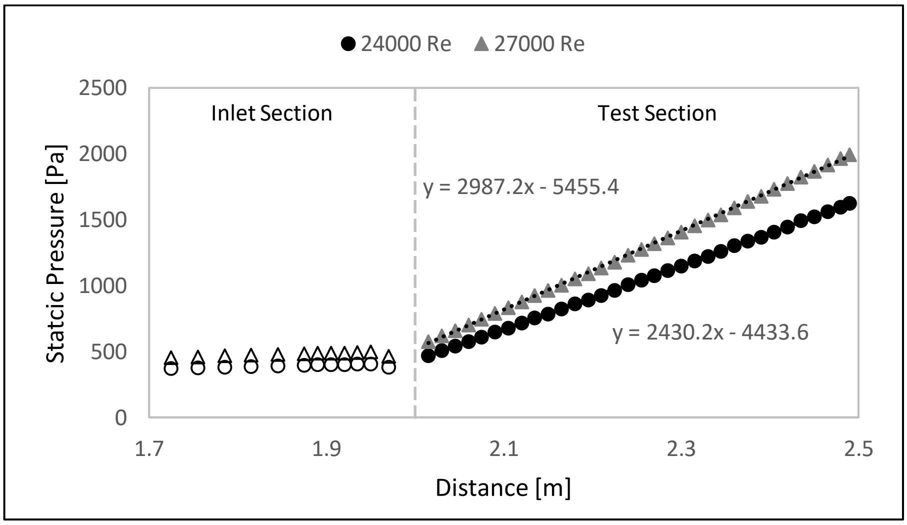

Figure C.57: Test Section Static Pressure for Insert 3.1 at Re = 24000 and Re = 27000

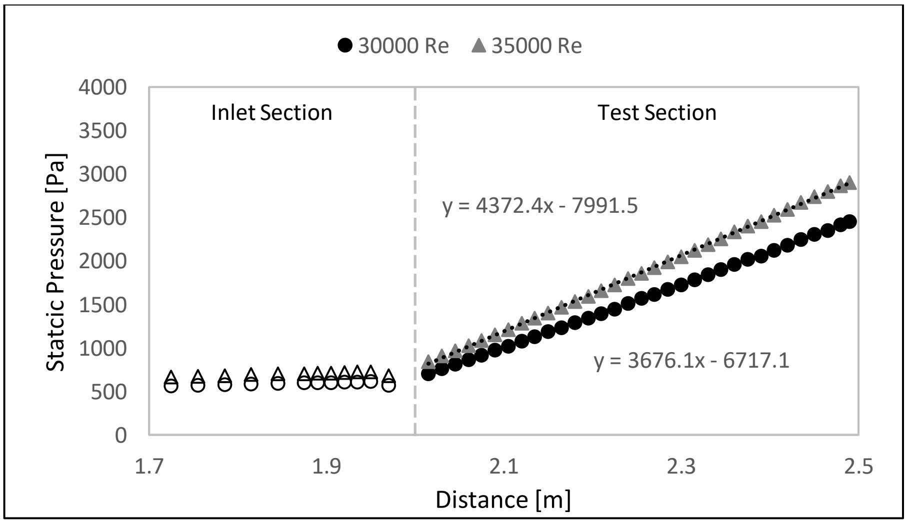

Figure C.58: Test Section Static Pressure for Insert 3.1 at Re = 30000 and Re = 35000

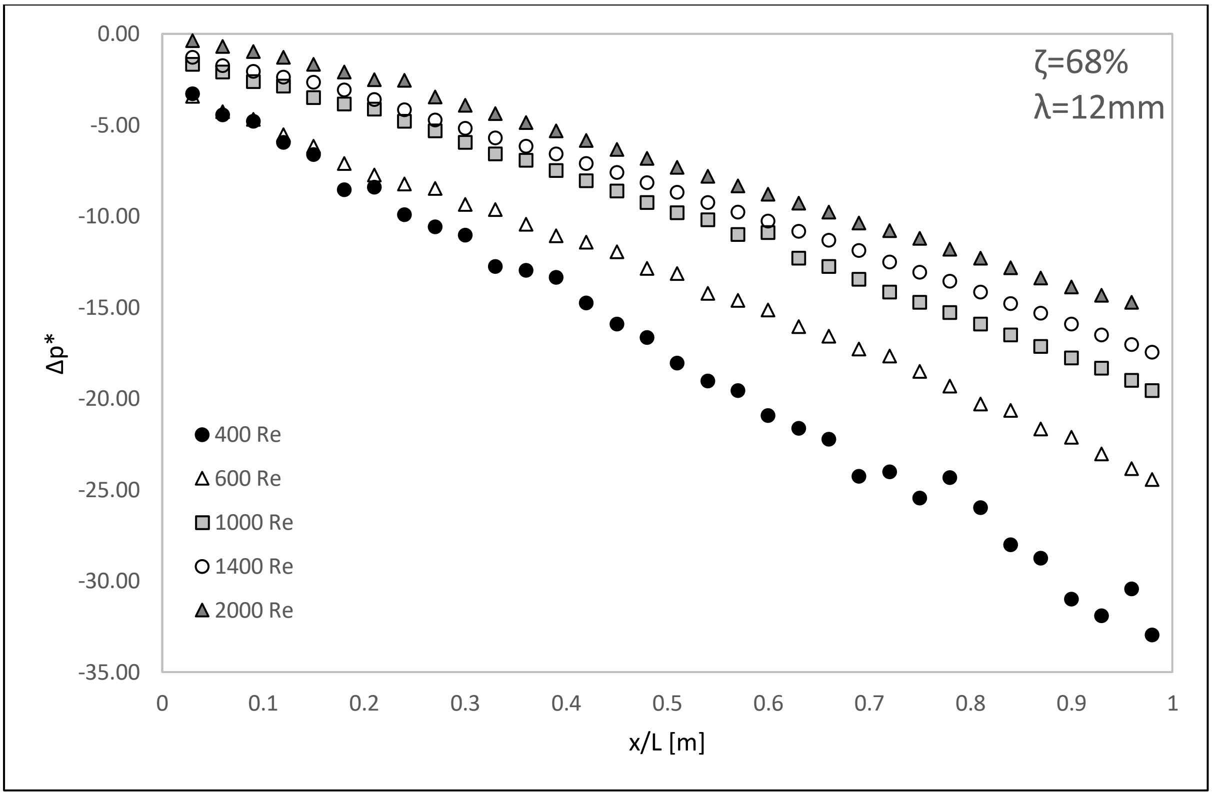
ζ=68%
λ=12mm
Δp*
0.00
-5.00
-10.00
-15.00
-20.00
-25.00
-30.00
-35.00
0
0.1
0.2
0.3
0.4
0.5
0.6
0.7
0.8
0.9
1
x/L [m]
● 400 Re
△ 600 Re
▨ 1000 Re
○ 1400 Re
▲ 2000 Re

(a)

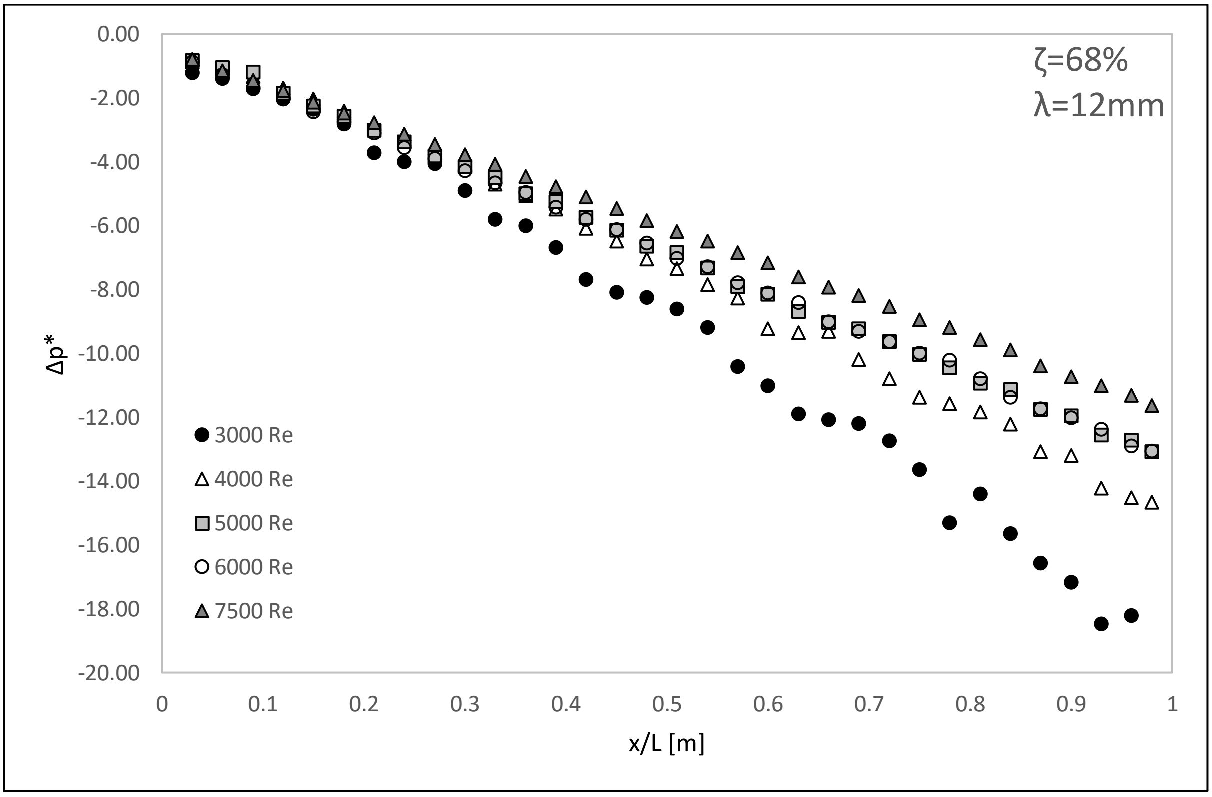
ζ=68%
λ=12mm
Δp*
0.00
-2.00
-4.00
-6.00
-8.00
-10.00
-12.00
-14.00
-16.00
-18.00
-20.00
0
0.1
0.2
0.3
0.4
0.5
0.6
0.7
0.8
0.9
1
x/L [m]
● 3000 Re
△ 4000 Re
▨ 5000 Re
○ 6000 Re
▲ 7500 Re

(b)

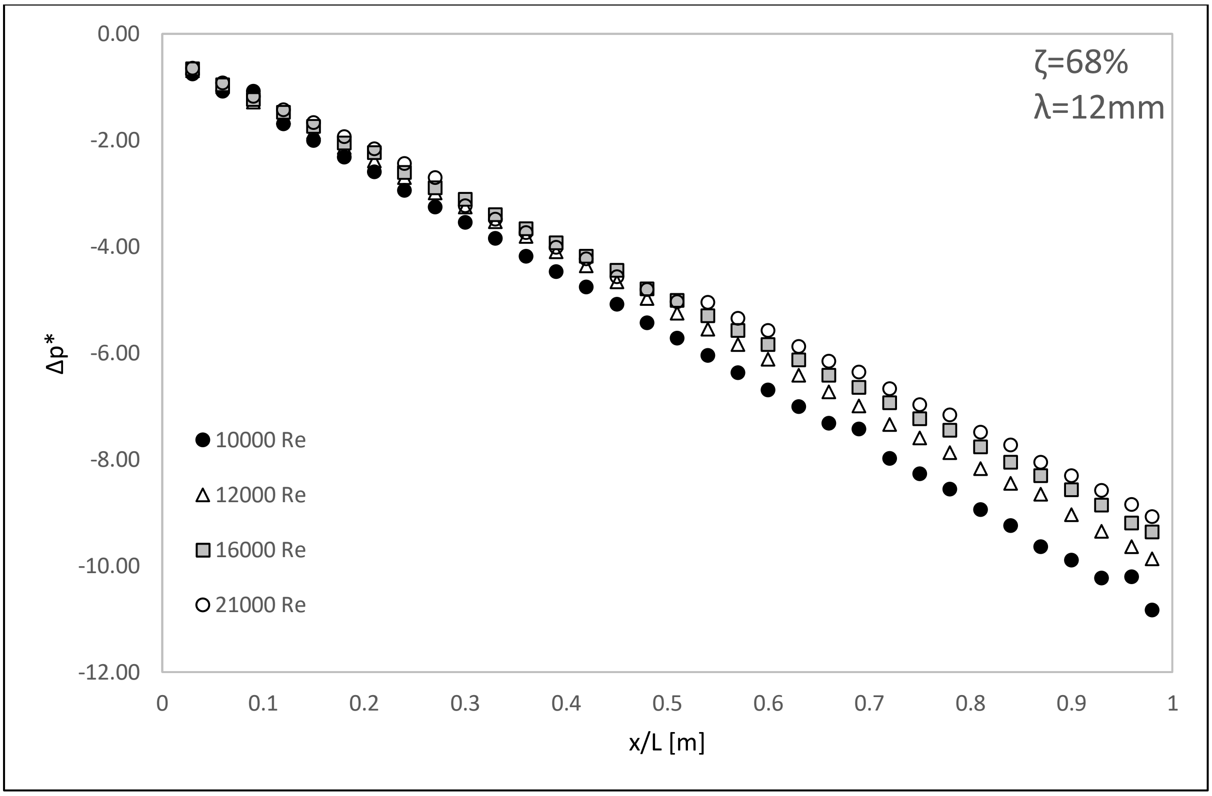

(c)

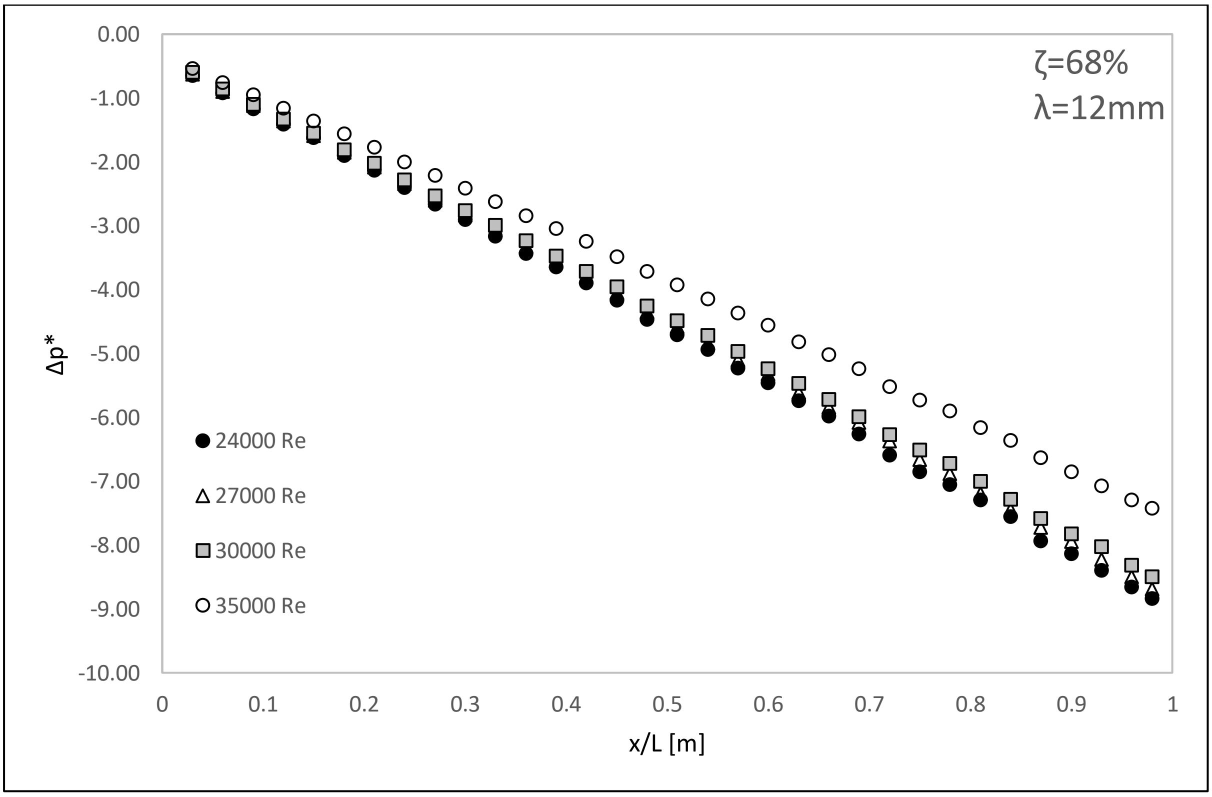

(d)

Figure C.59: Test section normalized pressure drop with insert 3.1 for Reynolds number range (a) 400 < Re < 2000, (b) 3000 < Re < 7500, (c) 10000 < Re < 21000 and (d) 24000 < Re < 35000

C.8. Mesh 3.2 (λ = 12 mm, ξ = 48 %)

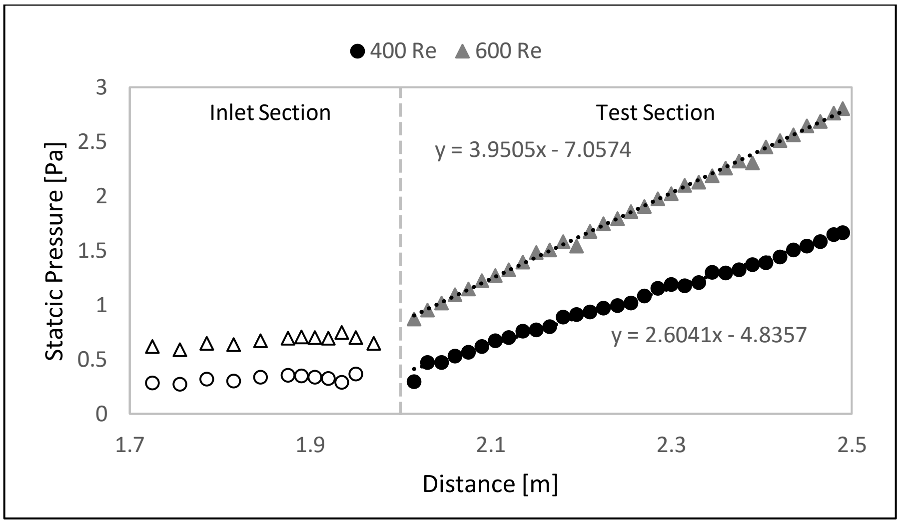

Figure C.60: Test Section Static Pressure for Insert 3.2 at Re = 400 and Re = 600

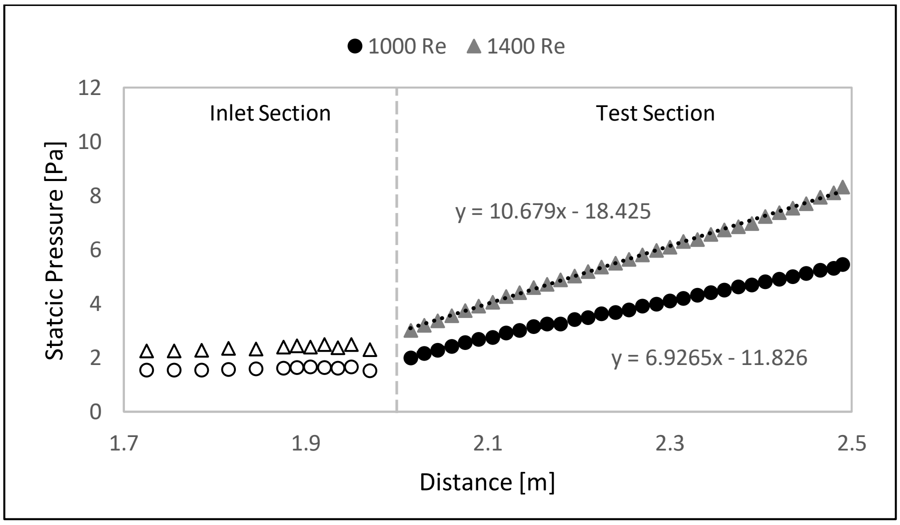

Figure C.61: Test Section Static Pressure for Insert 3.2 at Re = 1000 and Re = 1400

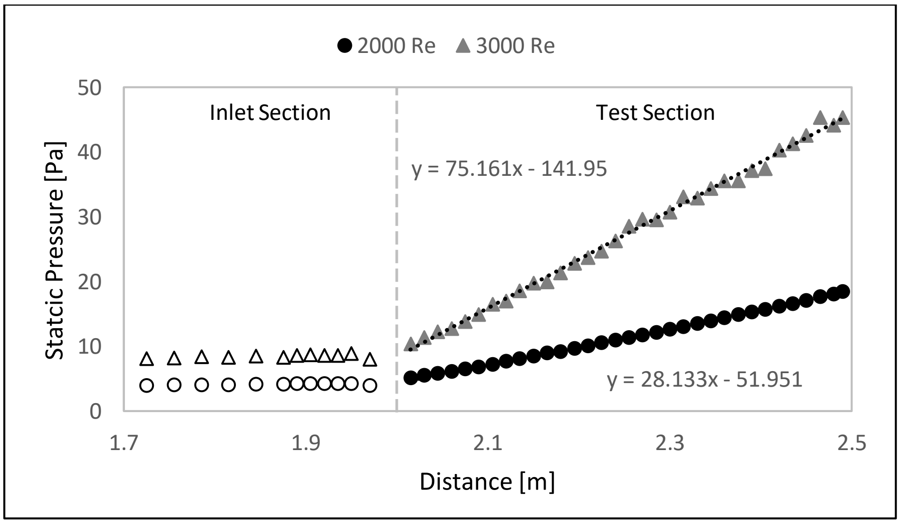

Figure C.62: Test Section Static Pressure for Insert 3.2 at Re = 2000 and Re = 3000

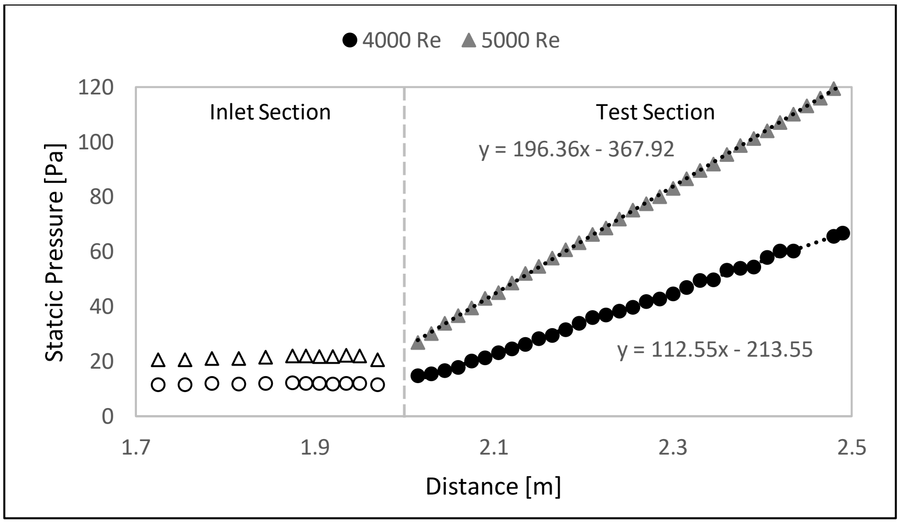

Figure C.63: Test Section Static Pressure for Insert 3.2 at Re = 4000 and Re = 5000

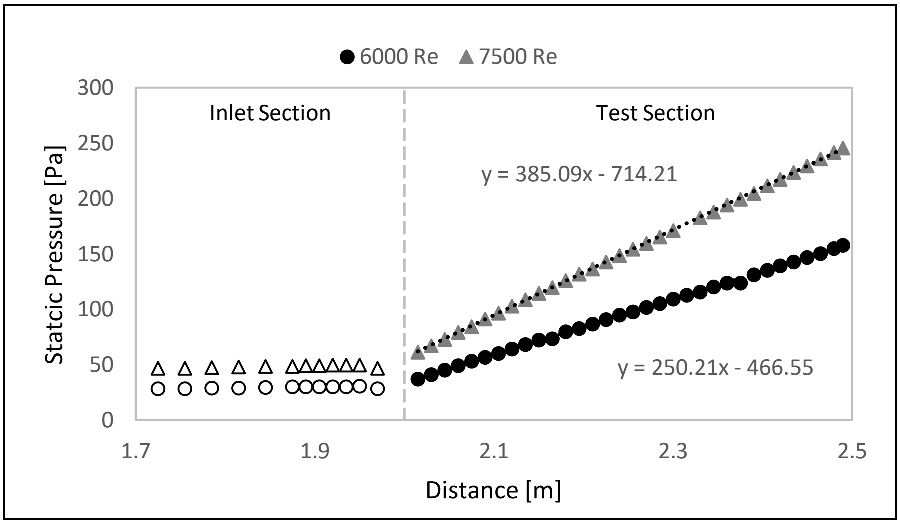

Figure C.64: Test Section Static Pressure for Insert 3.2 at Re = 6000 and Re = 7500

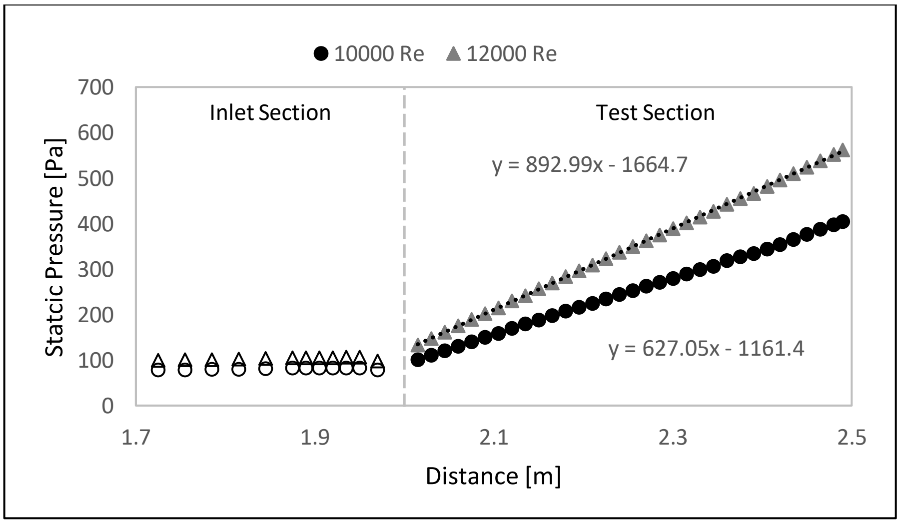

Figure C.65: Test Section Static Pressure for Insert 3.2 at Re = 10000 and Re = 12000

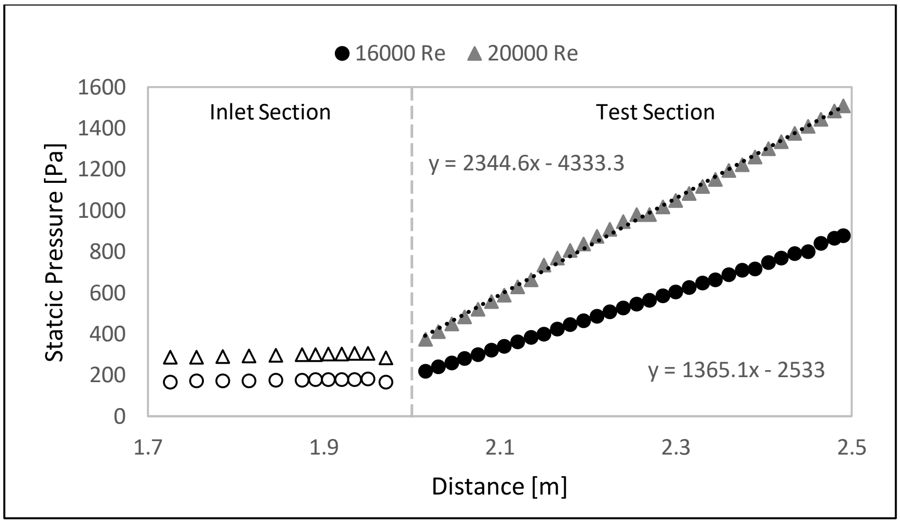

Figure C.66: Test Section Static Pressure for Insert 3.2 at Re = 16000 and Re = 20000

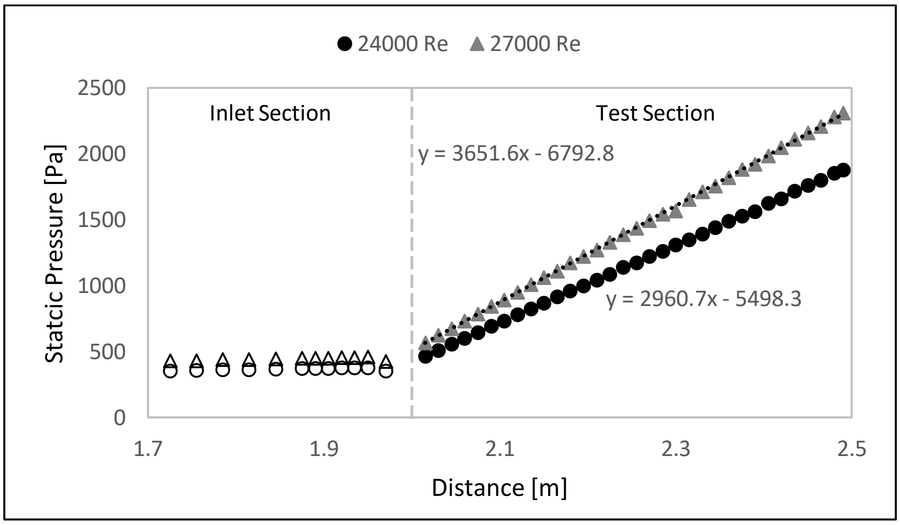

Figure C.67: Test Section Static Pressure for Insert 3.2 at Re = 24000 and Re = 27000

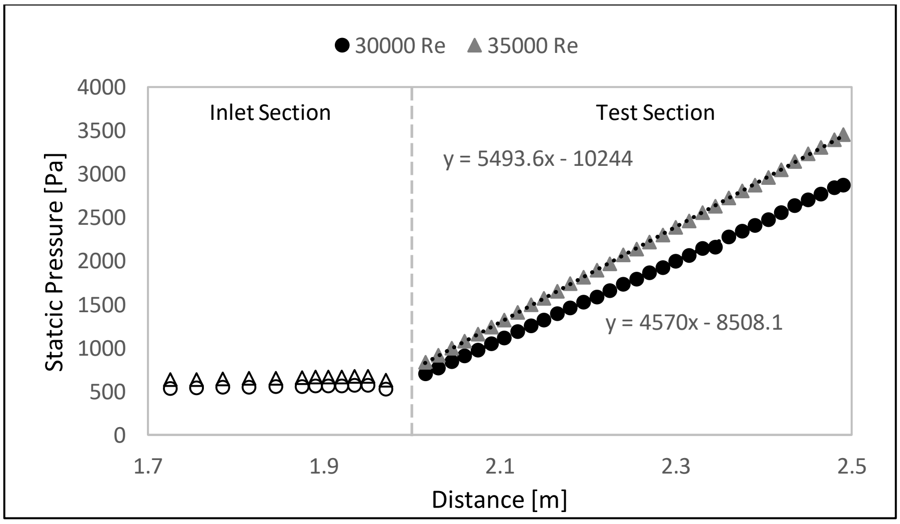

Figure C.68: Test Section Static Pressure for Insert 3.2 at Re = 30000 and Re = 35000

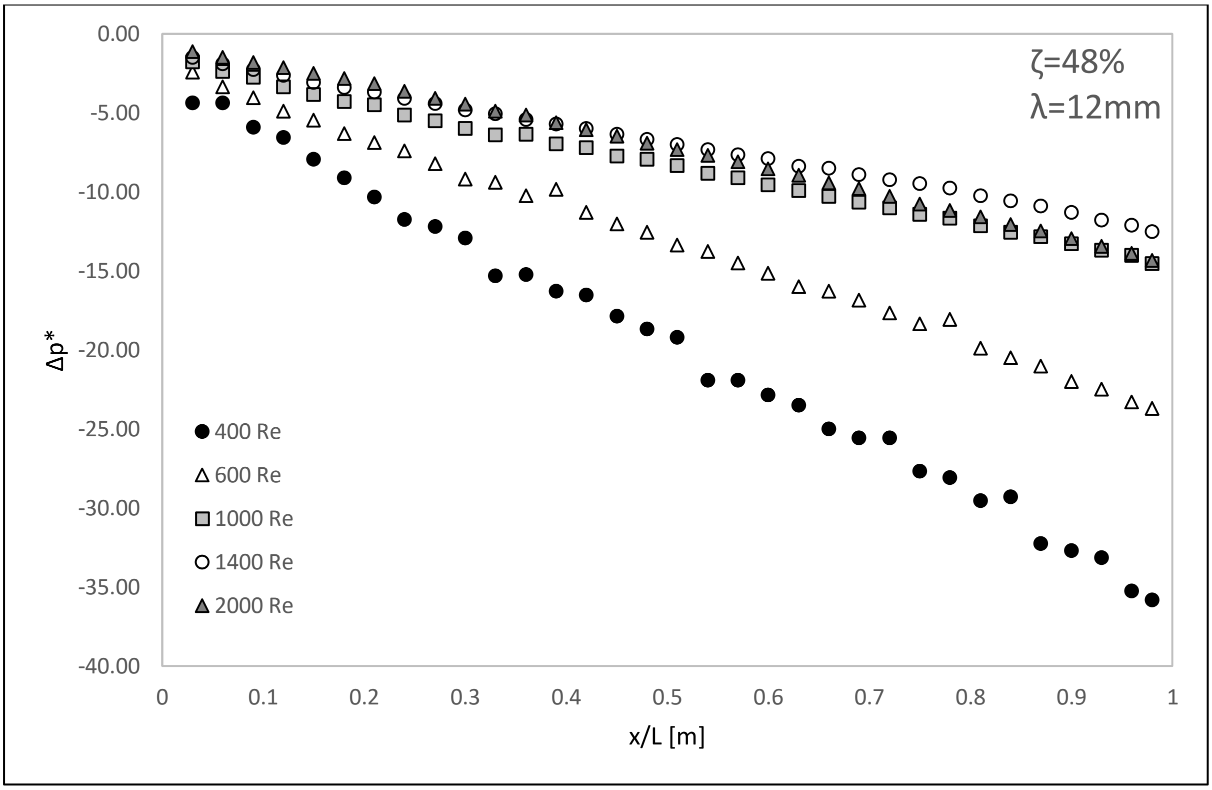
ζ=48%
λ=12mm
Δp*
0.00
-5.00
-10.00
-15.00
-20.00
-25.00
-30.00
-35.00
-40.00
0
0.1
0.2
0.3
0.4
0.5
0.6
0.7
0.8
0.9
1
x/L [m]
● 400 Re
△ 600 Re
▣ 1000 Re
○ 1400 Re
▲ 2000 Re

(a)

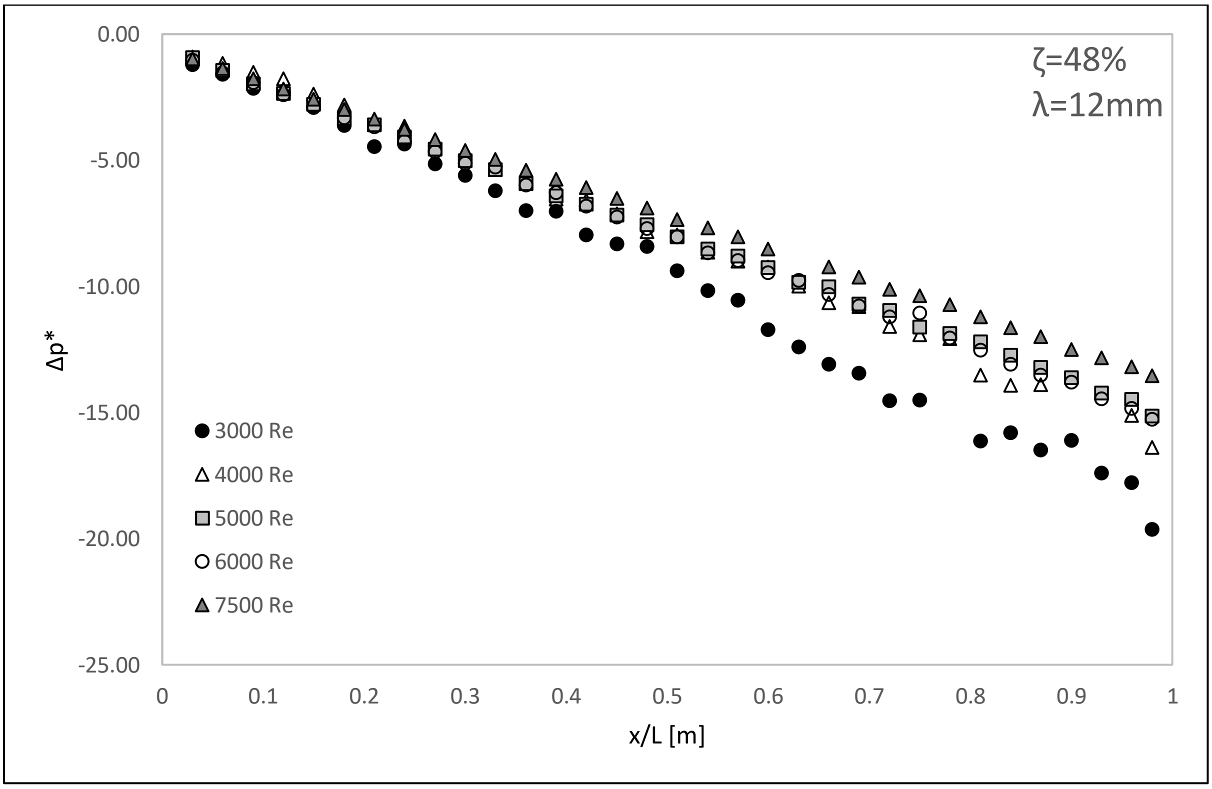
ζ=48%
λ=12mm
Δp*
0.00
-5.00
-10.00
-15.00
-20.00
-25.00
0
0.1
0.2
0.3
0.4
0.5
0.6
0.7
0.8
0.9
1
x/L [m]
● 3000 Re
△ 4000 Re
▣ 5000 Re
○ 6000 Re
▲ 7500 Re

(b)

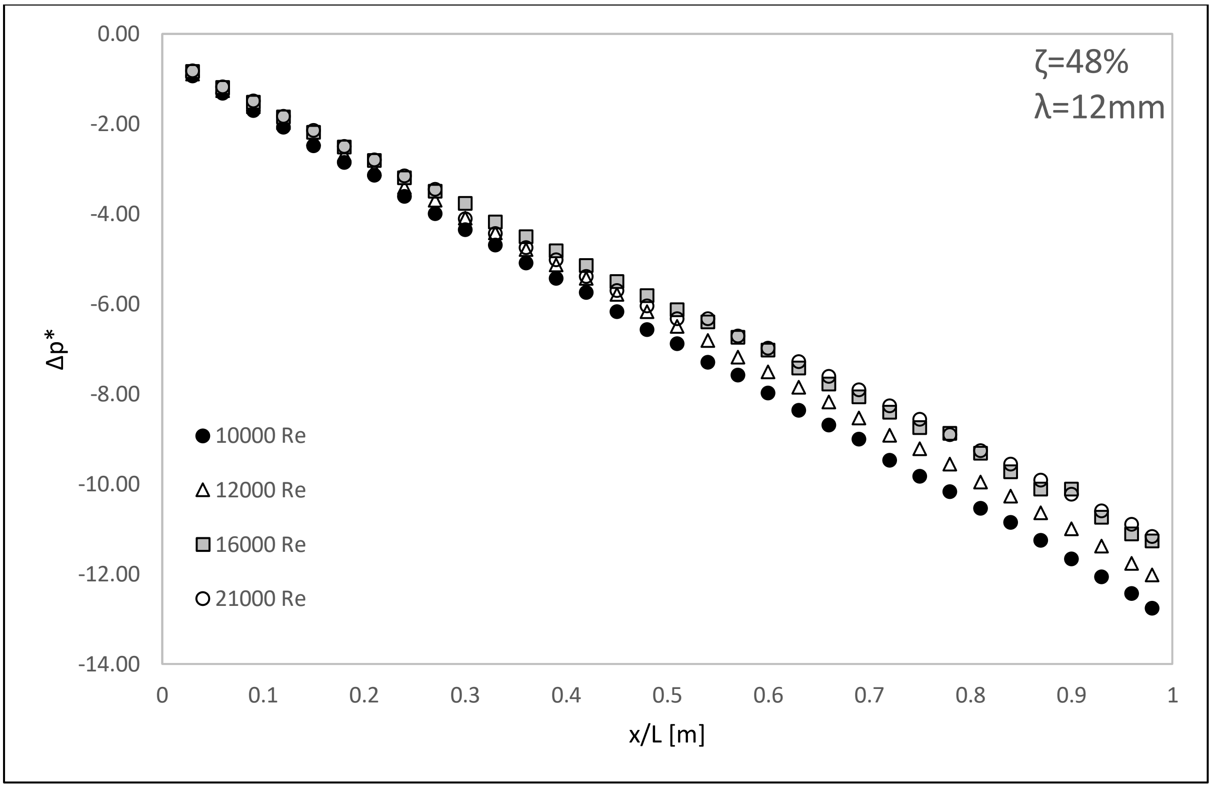

(c)

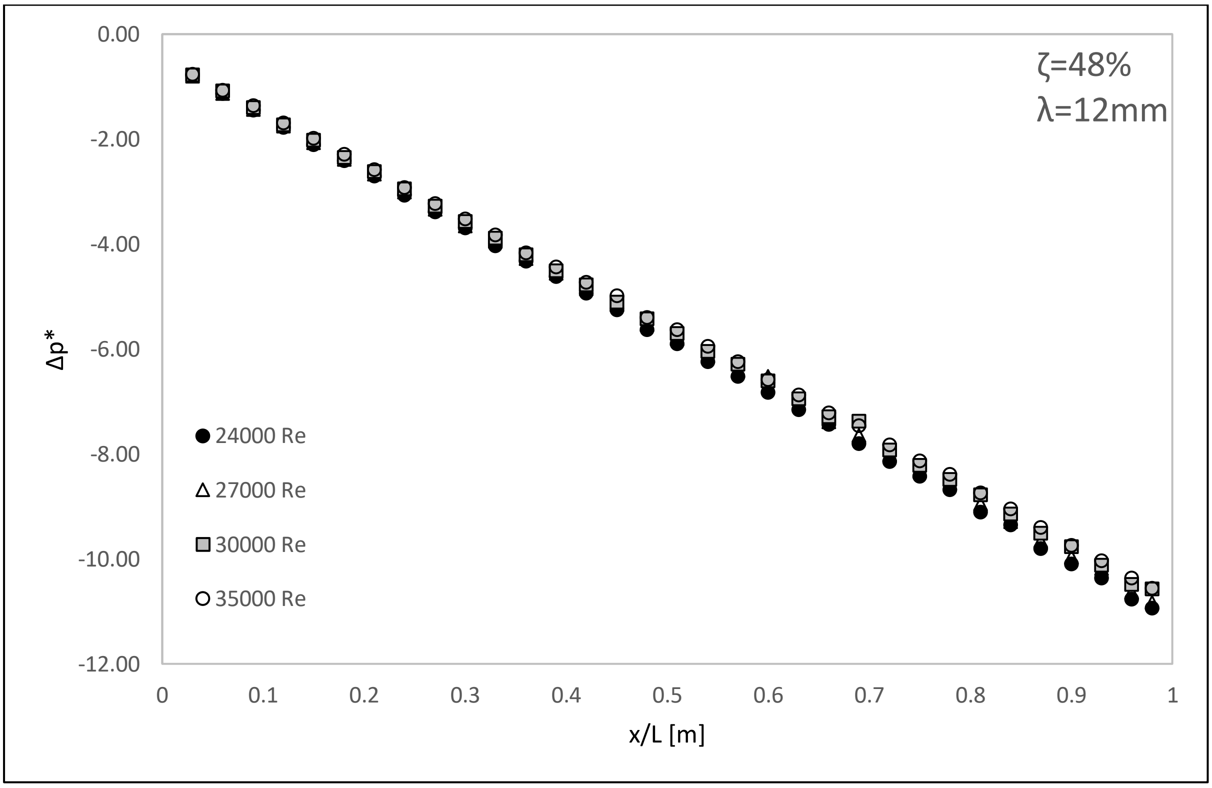

(d)

Figure C.69: Test section normalized pressure drop with insert 3.2 for Reynolds number range (a) 400 < Re < 2000, (b) 3000 < Re < 7500, (c) 10000 < Re < 21000 and (d) 24000 < Re < 35000

C.9. Effects of Porosity on f and f_0

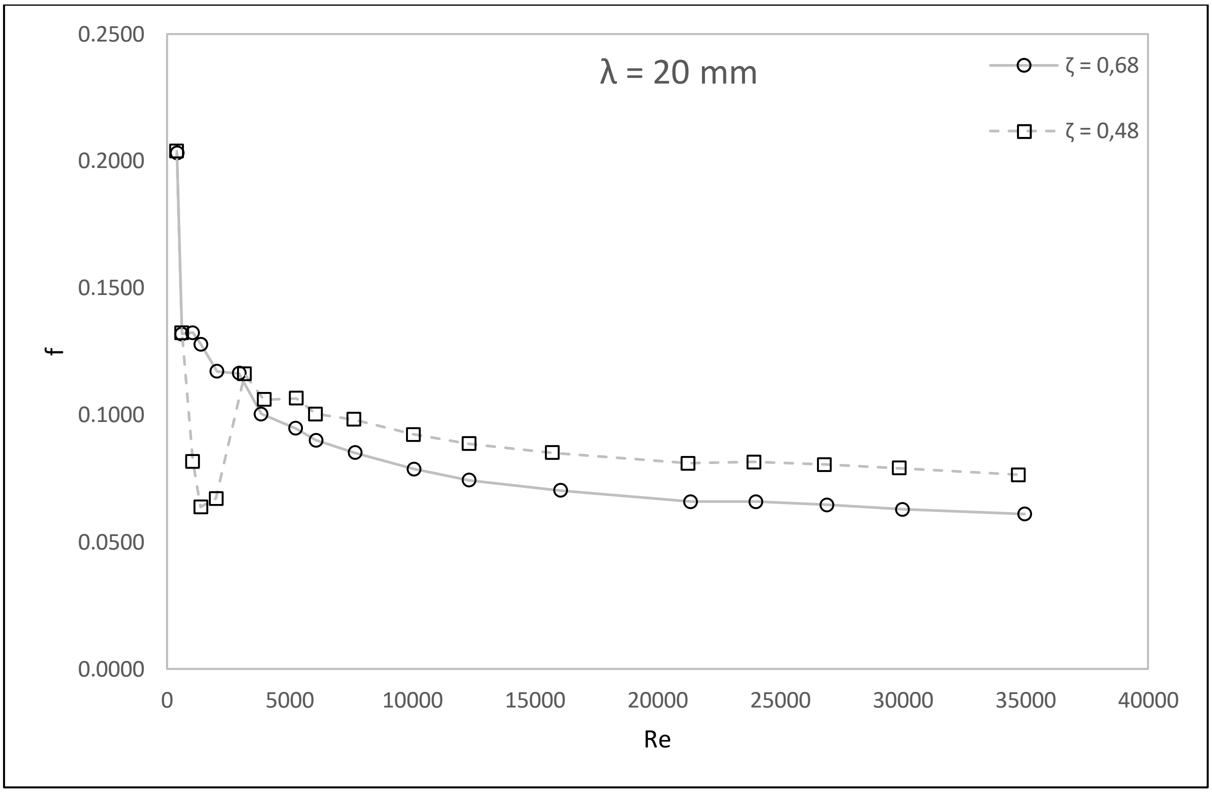

(a)

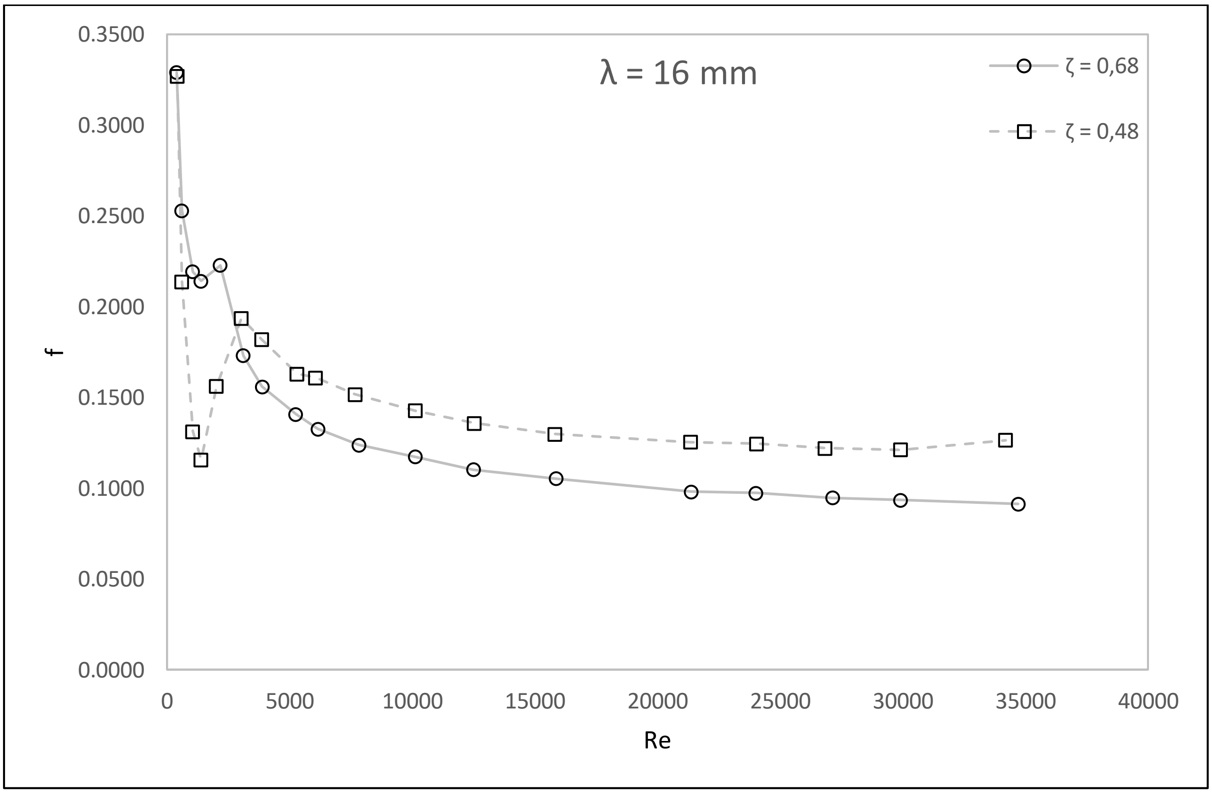

(b)

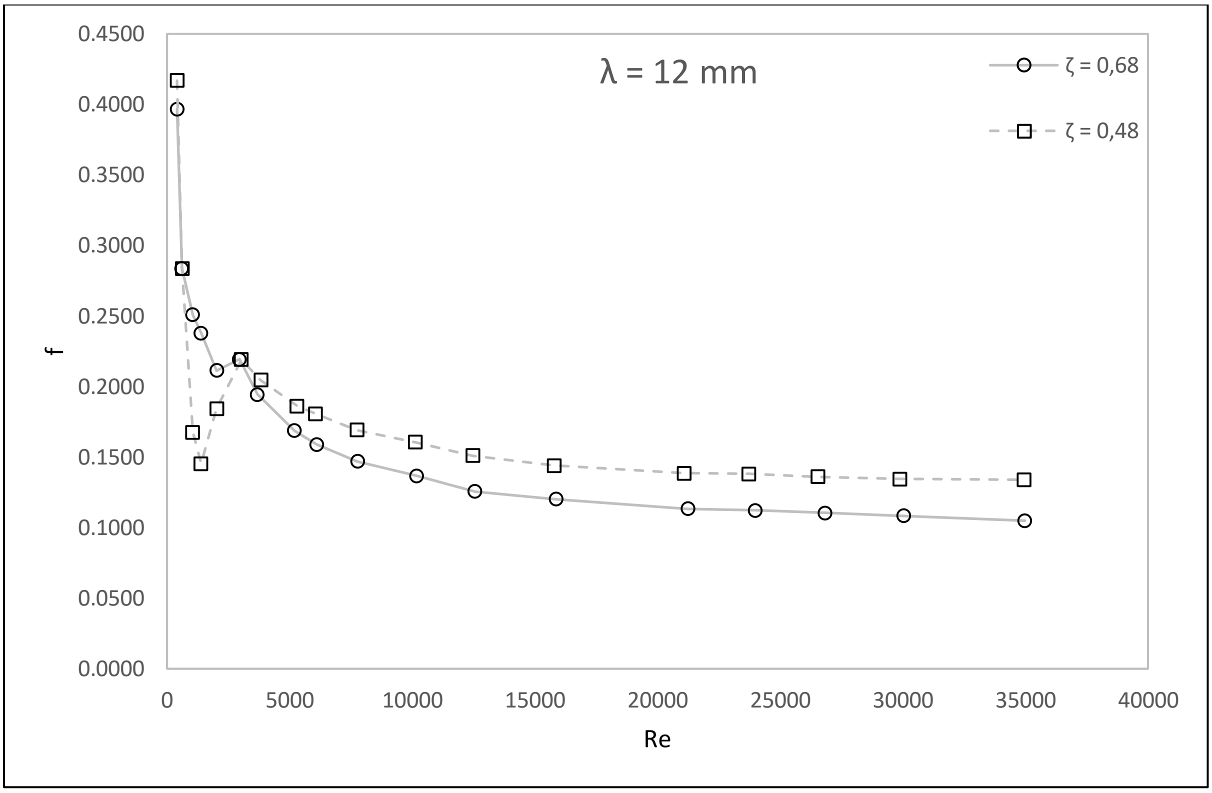

(c)

Figure C.70: Friction factor, f vs. Re for constant wavelength λ = (a) 20 mm, (b) 16 mm and (c) 12 mm

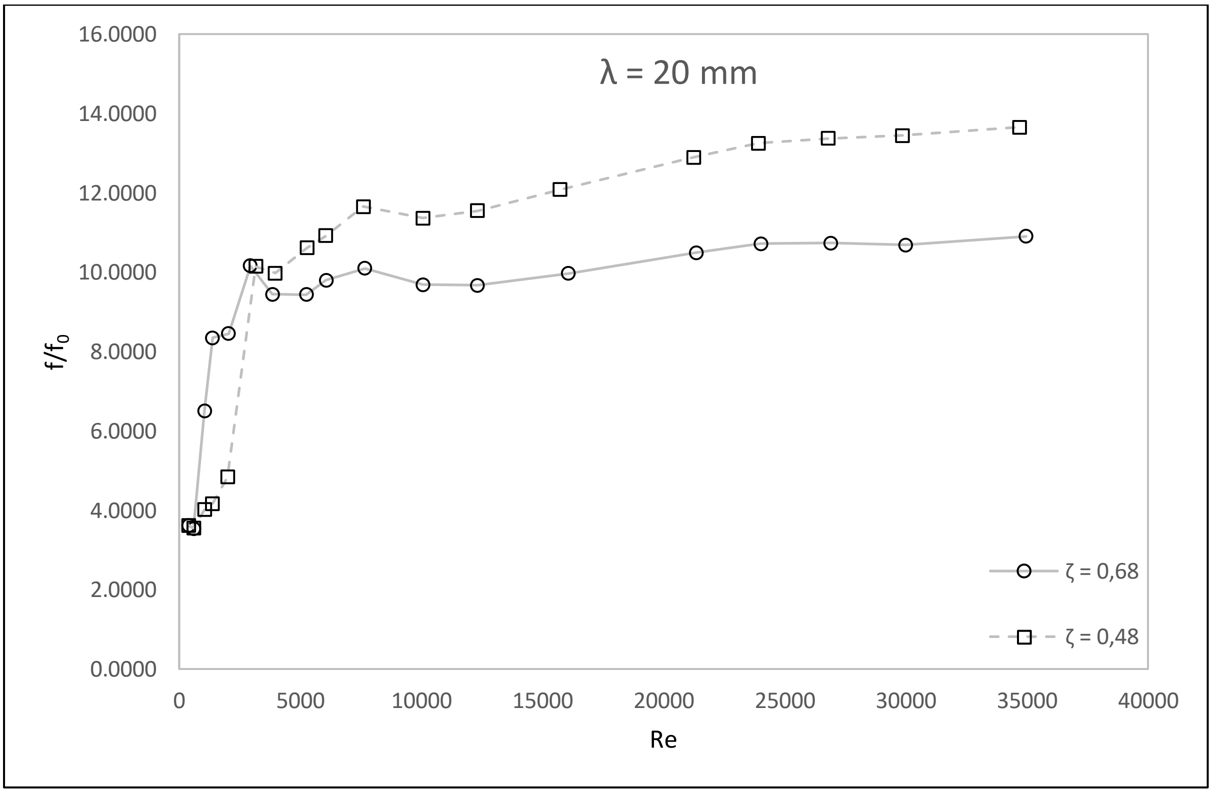

(a)

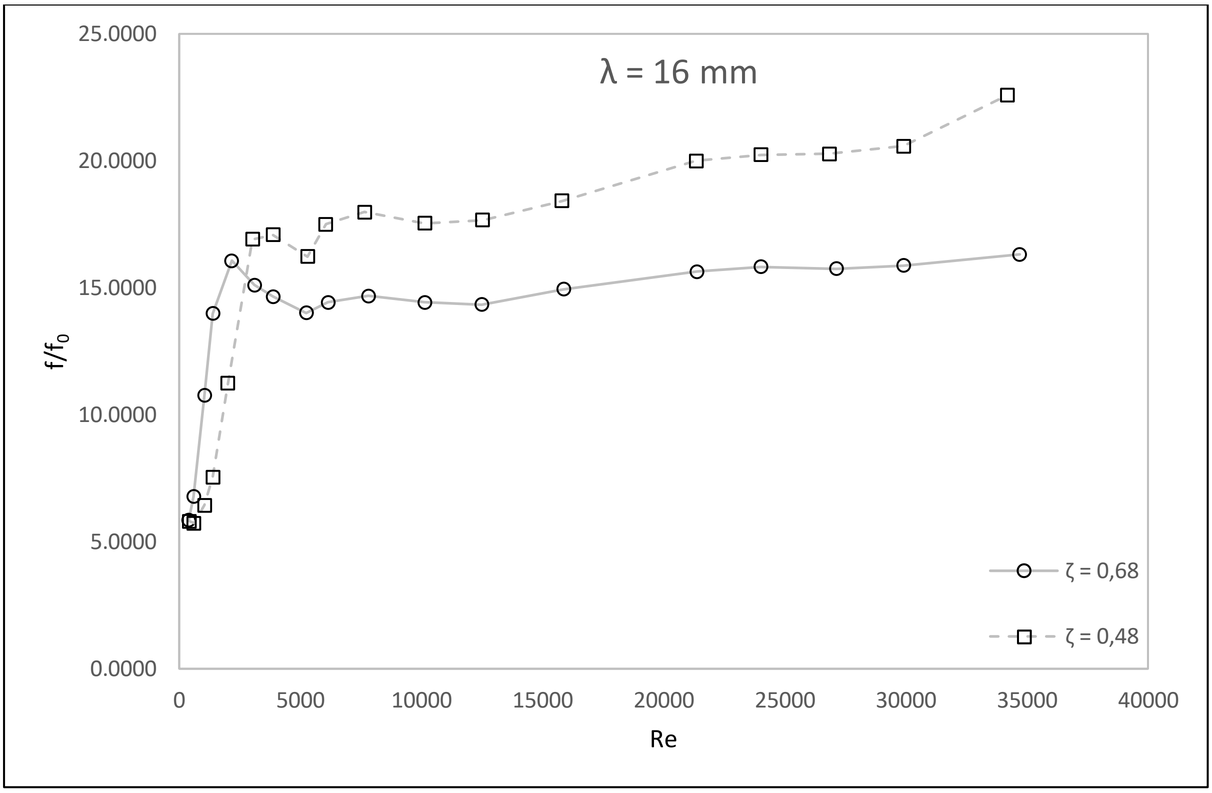

(b)

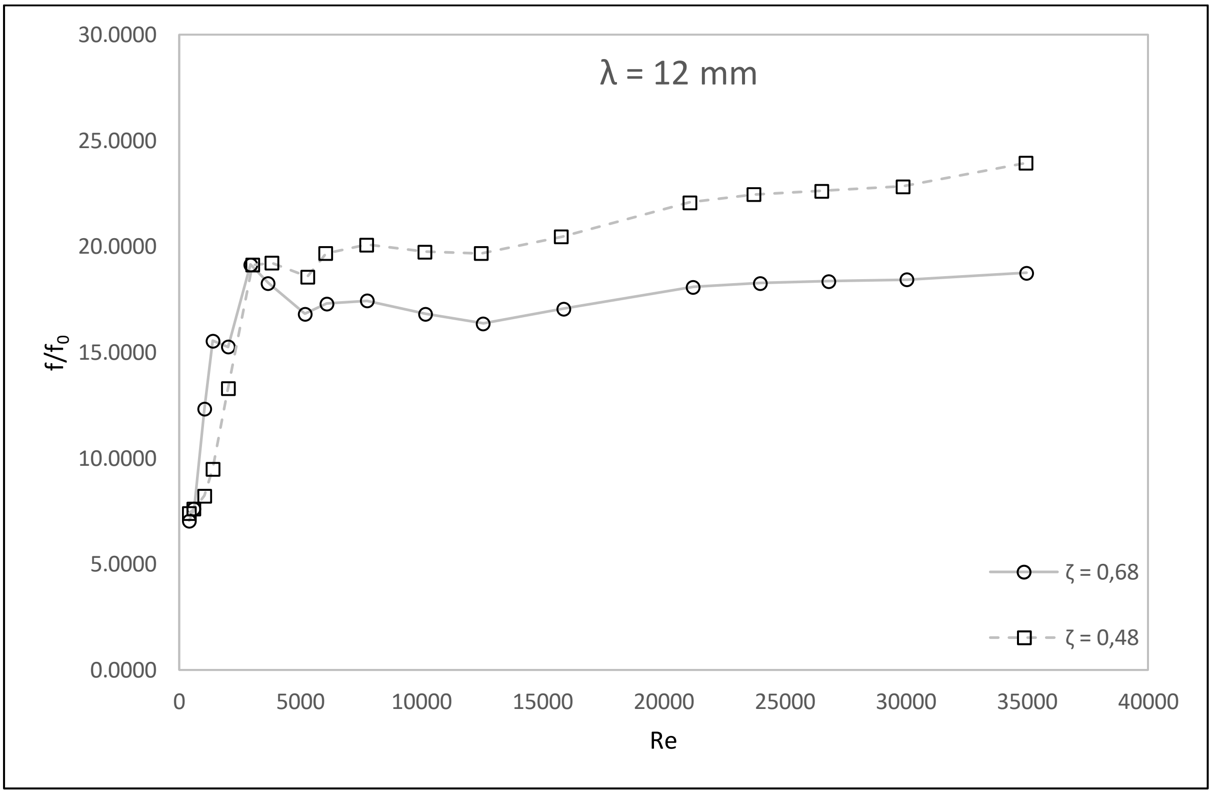

(c)

Figure C.71: Friction factor ratio, f/f_0 vs. Re for constant wavelength λ = (a): 20 mm, (b): 16 mm and (c): 12 mm

Appendix D: Two Wall Heat Transfer Data

D.1. Introduction

This appendix includes the test section wall temperature data used in determining the local Nusselt along the test section channel for the two wall heating experiments. Results are shown for each experiment conducted throughout the course of the research.

D.2. Baseline

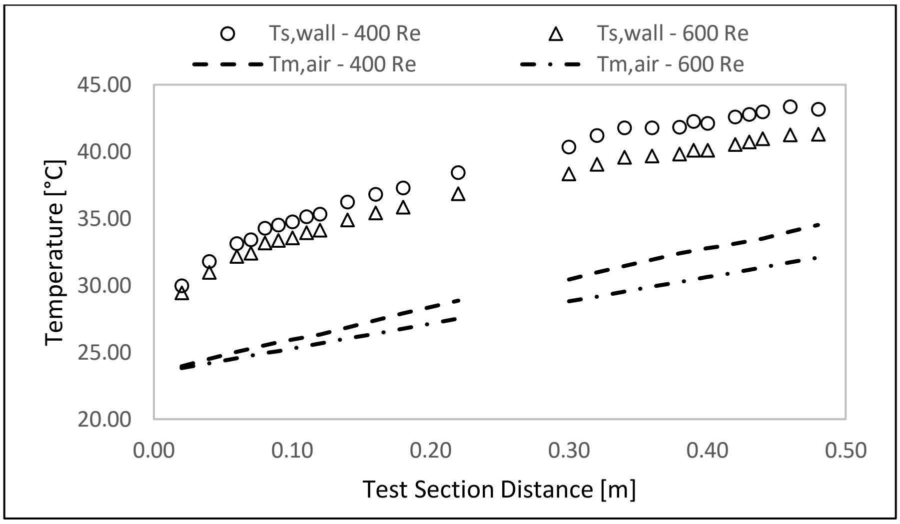

Figure D.1: Base Line Test Section Temperatures at Re = 400 and Re = 600

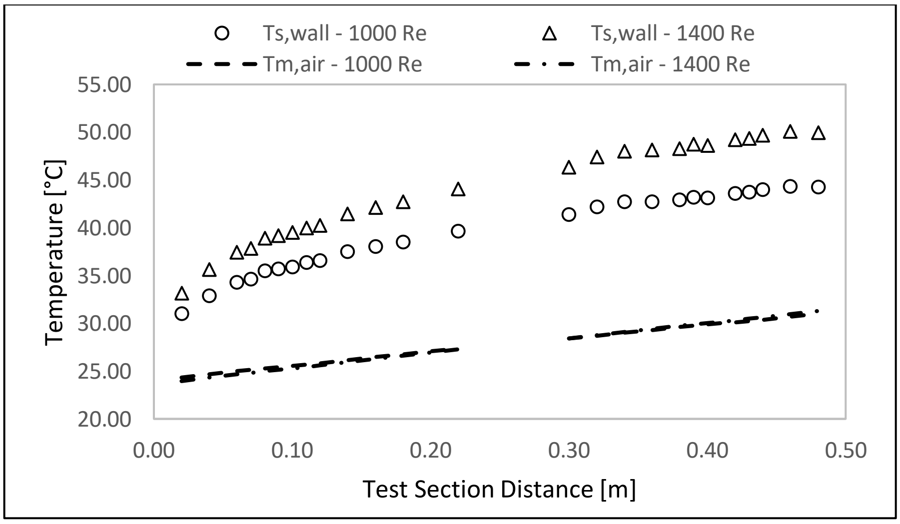

Figure D.2: Base Line Test Section Temperatures at Re = 1000 and Re = 1400

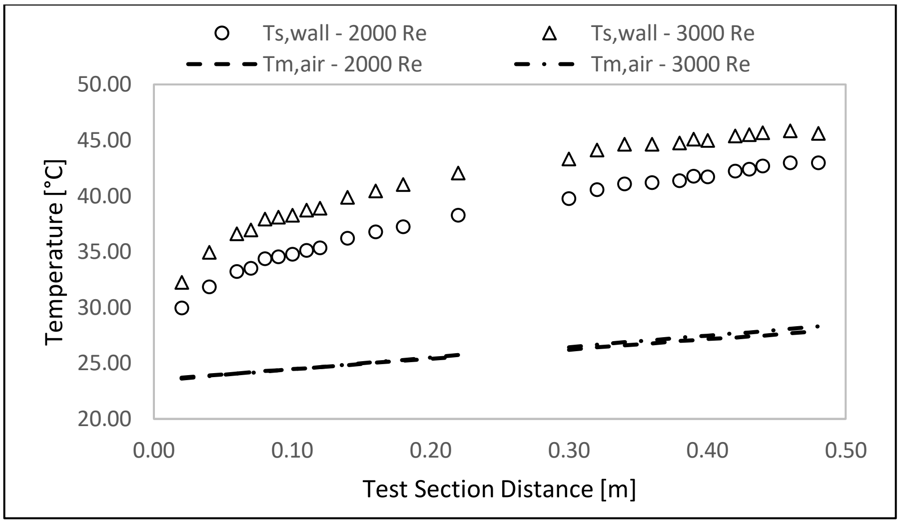

Figure D.3: Base Line Test Section Temperatures at Re = 2000 and Re = 3000

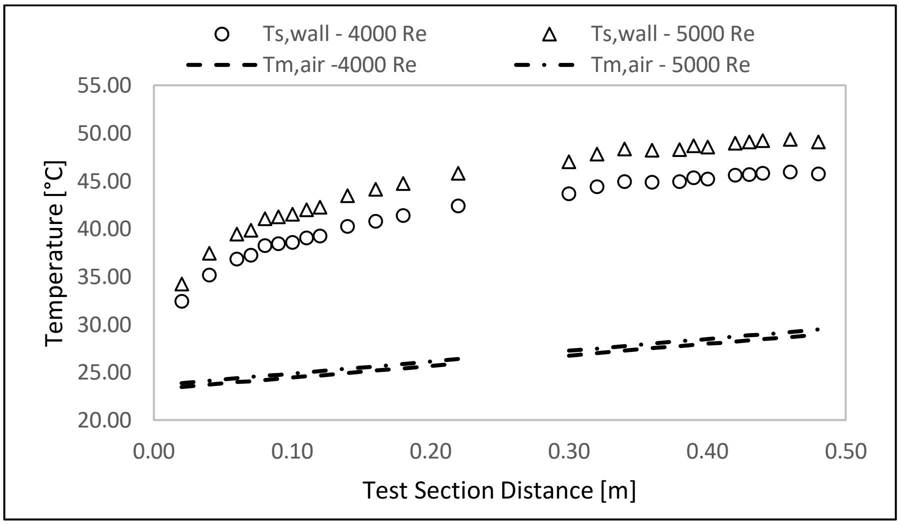

Figure D.4: Base Line Test Section Temperatures at Re = 4000 and Re = 5000

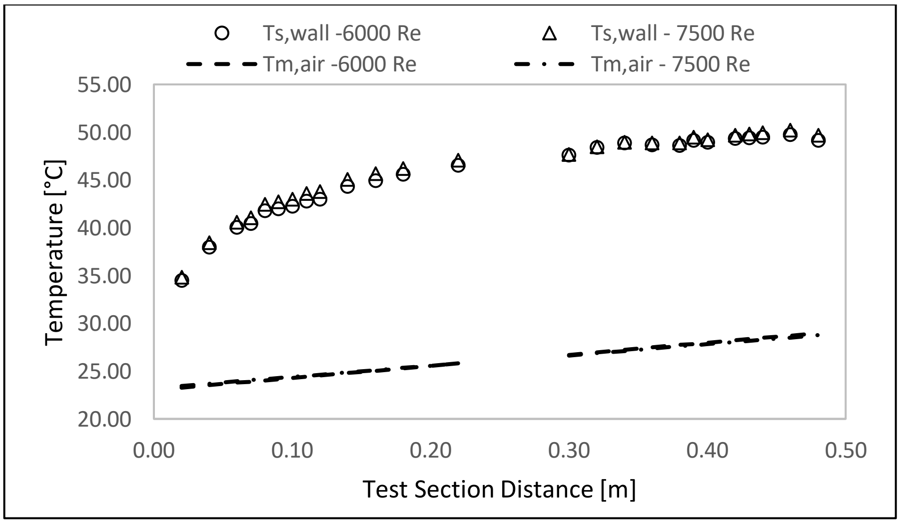

Figure D.5: Base Line Test Section Temperatures at Re = 6000 and Re = 7500

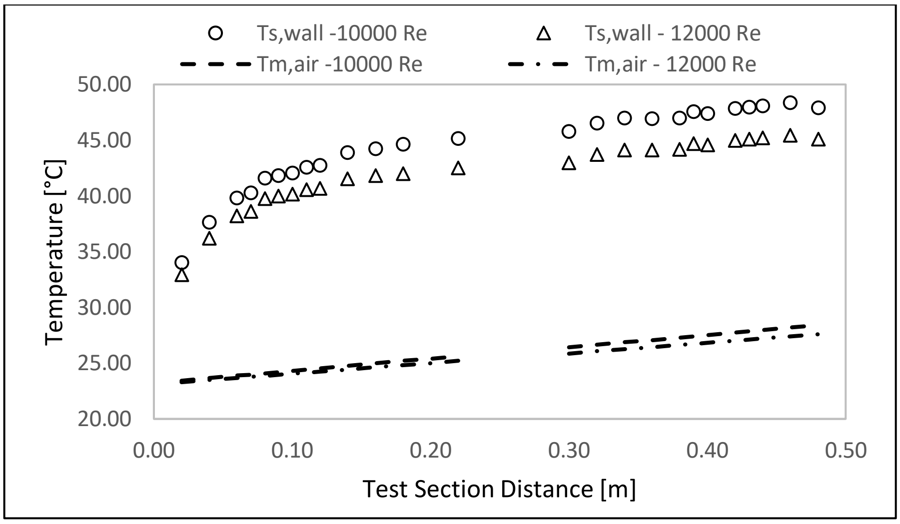

Figure D.6: Base Line Test Section Temperatures at Re = 10000 and Re = 12000

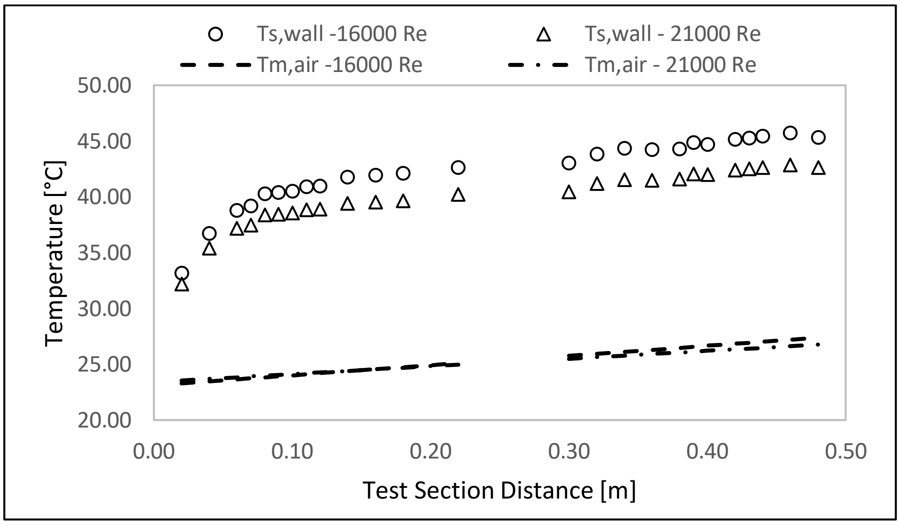

Figure D.7: Base Line Test Section Temperatures at Re = 16000 and Re = 21000

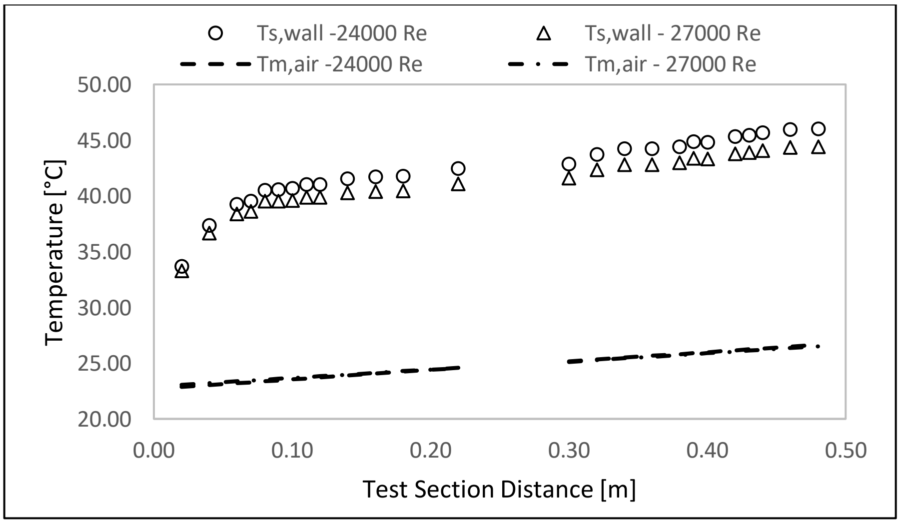

Figure D.8: Base Line Test Section Temperatures at Re = 24000 and Re = 27000

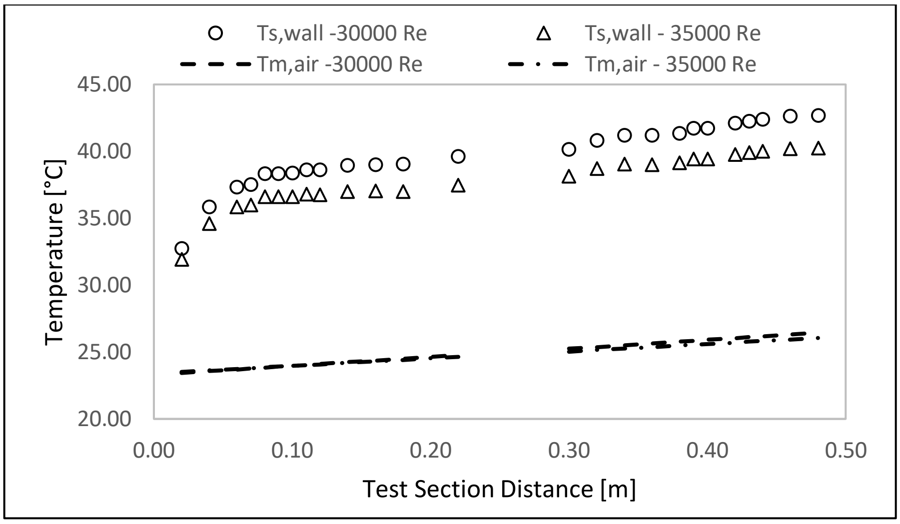

Figure D.9: Base Line Test Section Temperatures at Re = 30000 and Re = 35000

D.3. Mesh 1.1 (λ = 20 mm, ξ = 68 %)

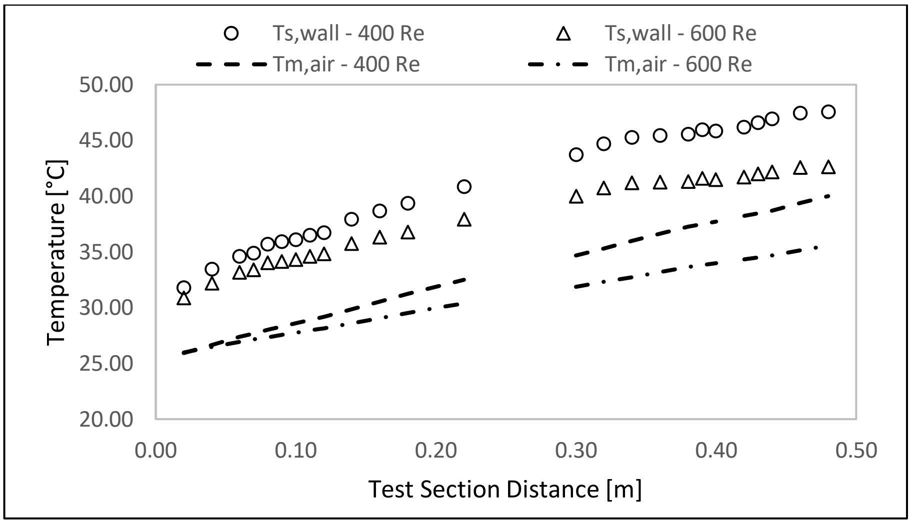

Figure D.10: Test Section Temperatures for Insert 1.1 at Re = 400 and Re = 600

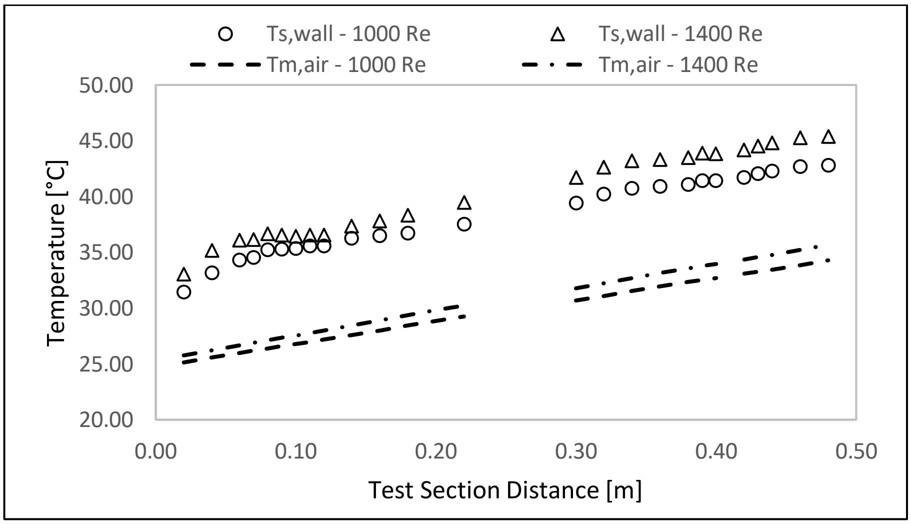

Figure D.11: Test Section Temperatures for Insert 1.1 at Re = 1000 and Re = 1400

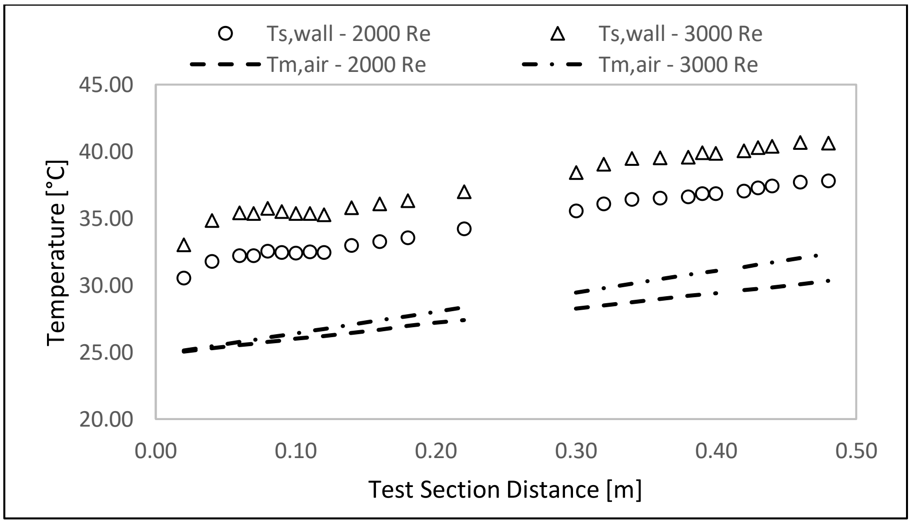

Figure D.12: Test Section Temperatures for Insert 1.1 at Re = 2000 and Re = 3000

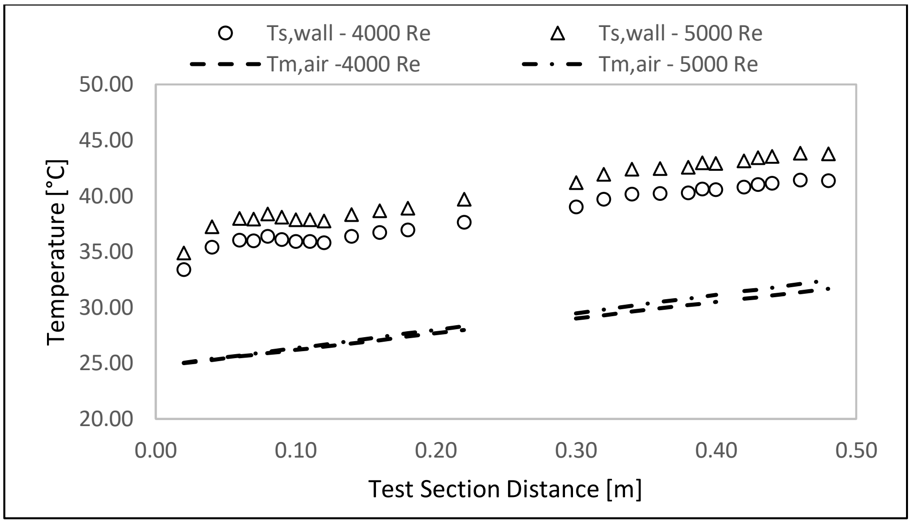

Figure D.13: Test Section Temperatures for Insert 1.1 at Re = 4000 and Re = 5000

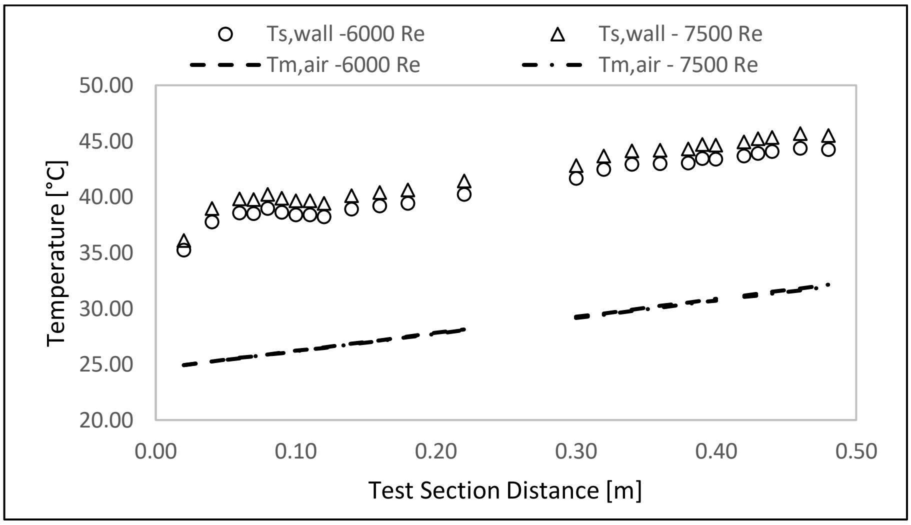

Figure D.14: Test Section Temperatures for Insert 1.1 at Re = 6000 and Re = 7500

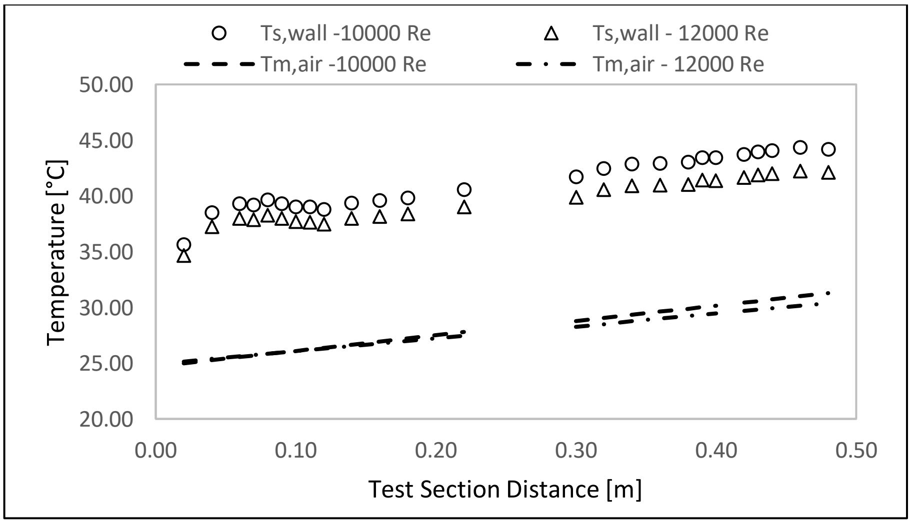

Figure D.15: Test Section Temperatures for Insert 1.1 at Re = 10000 and Re = 12000

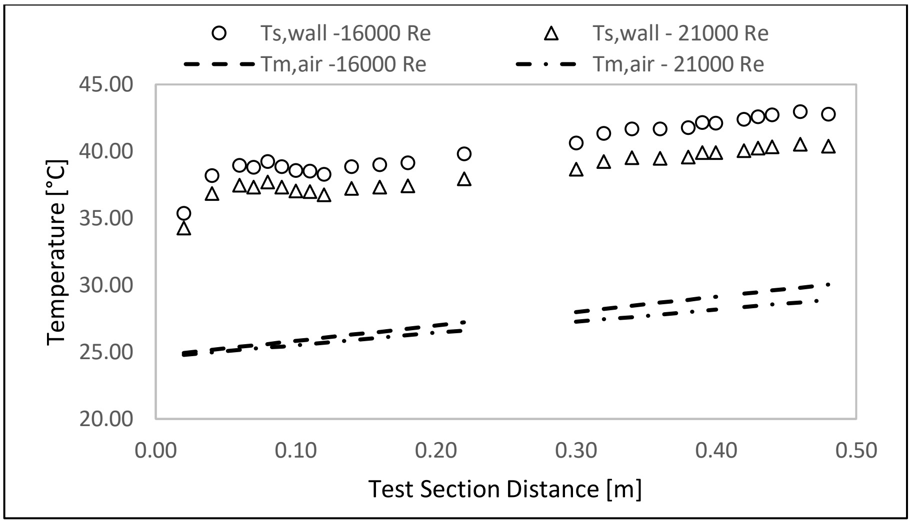

Figure D.16: Test Section Temperatures for Insert 1.1 at Re = 16000 and Re = 21000

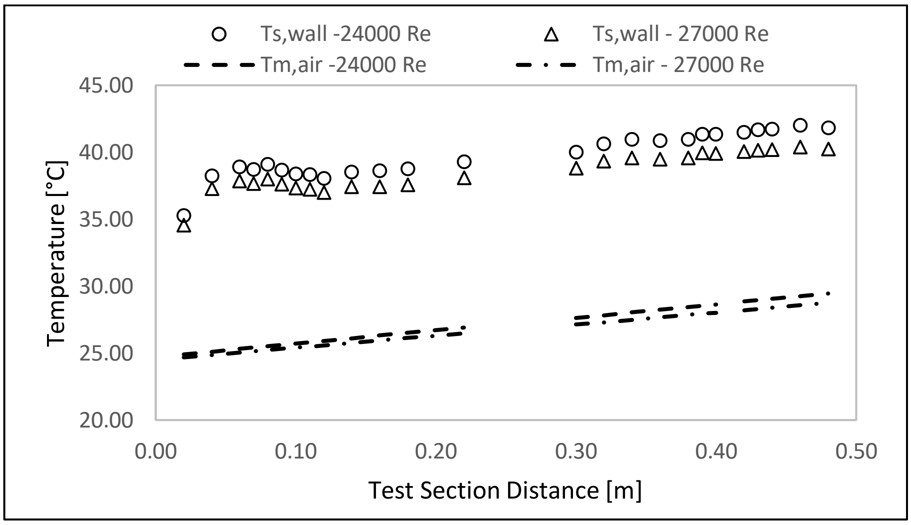

Figure D.17: Test Section Temperatures for Insert 1.1 at Re = 24000 and Re = 27000

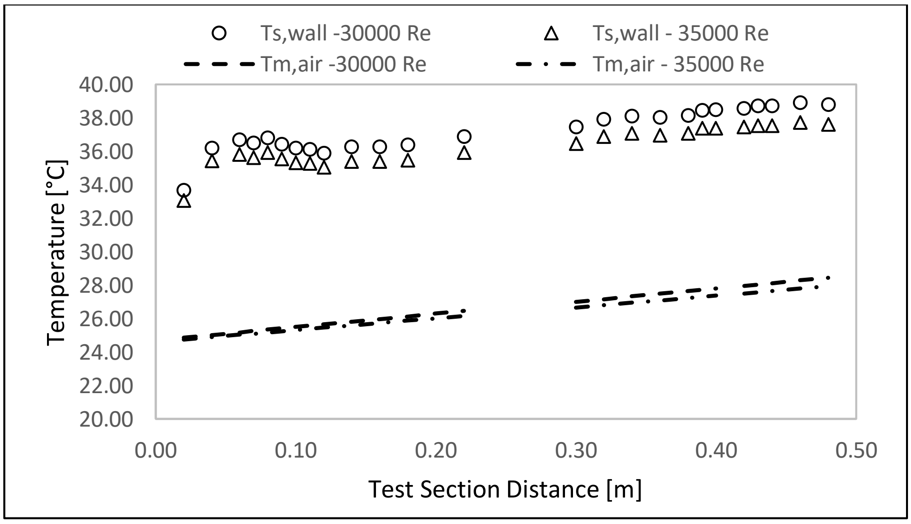

Figure D.18: Test Section Temperatures for Insert 1.1 at Re = 30000 and Re = 35000

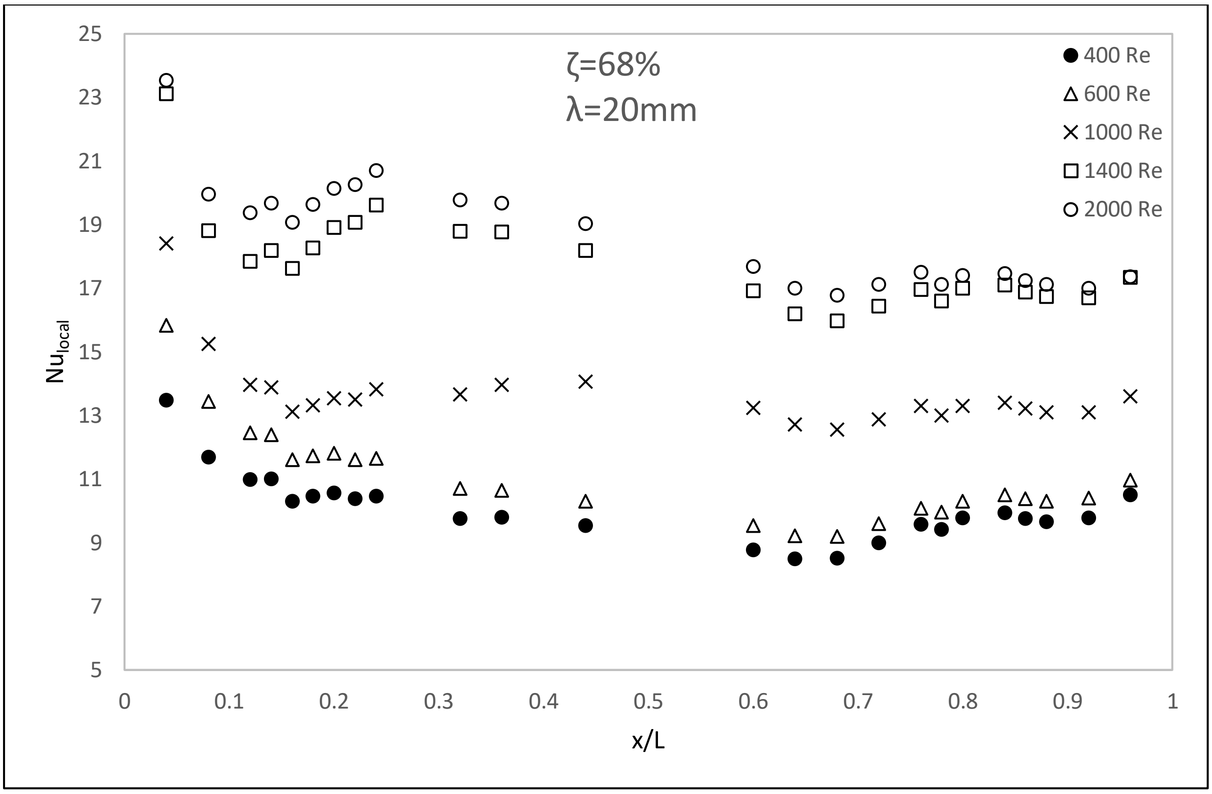
ζ=68%
λ=20mm
● 400 Re
△ 600 Re
× 1000 Re
□ 1400 Re
○ 2000 Re
Nu_local
x/L
25
23
21
19
17
15
13
11
9
7
5
0
0.1
0.2
0.3
0.4
0.5
0.6
0.7
0.8
0.9
1

(a)

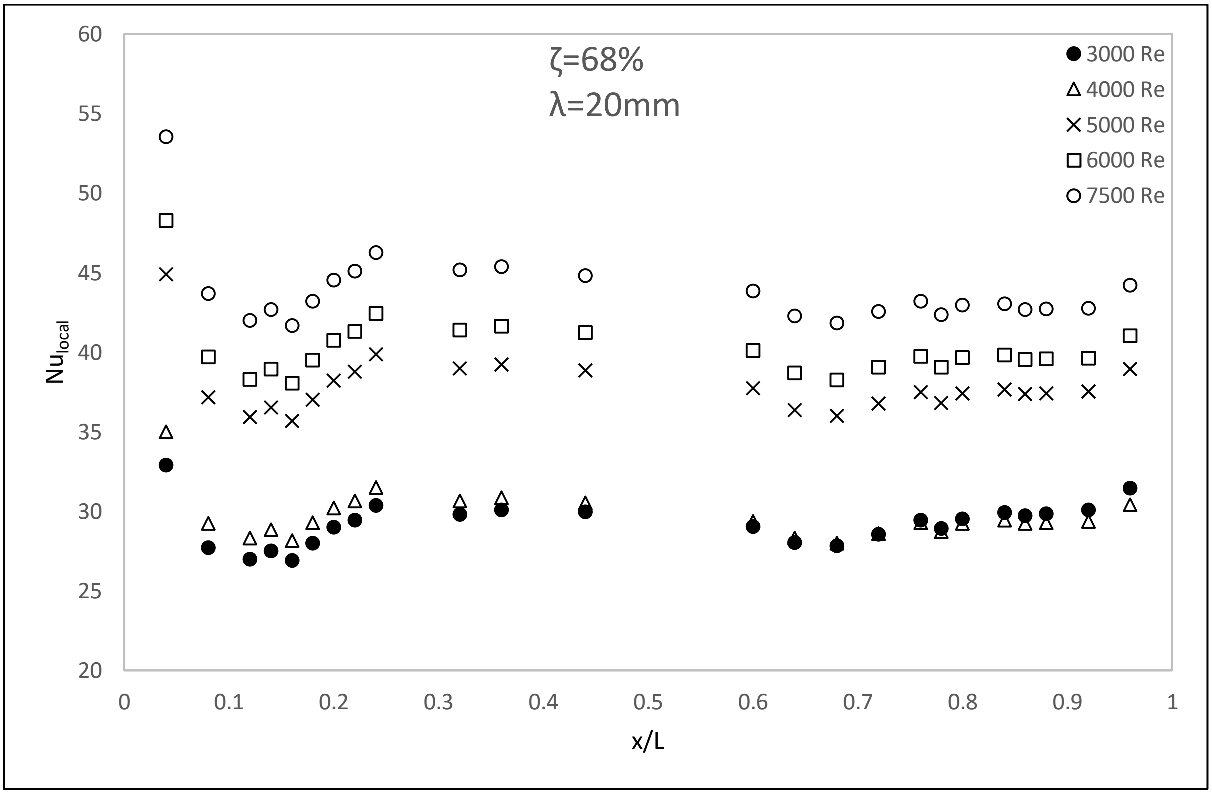
ζ=68%
λ=20mm
● 3000 Re
△ 4000 Re
× 5000 Re
□ 6000 Re
○ 7500 Re
Nu_local
x/L
60
55
50
45
40
35
30
25
20
0
0.1
0.2
0.3
0.4
0.5
0.6
0.7
0.8
0.9
1

(b)

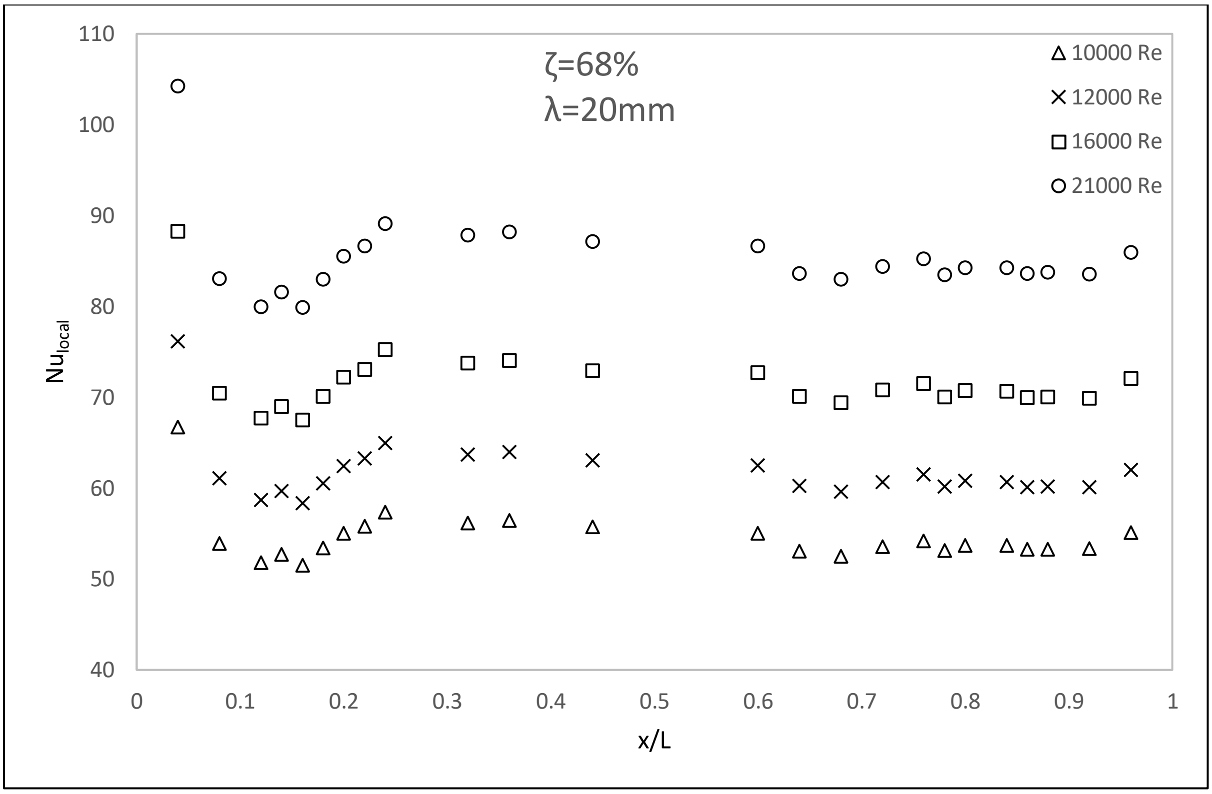

(c)

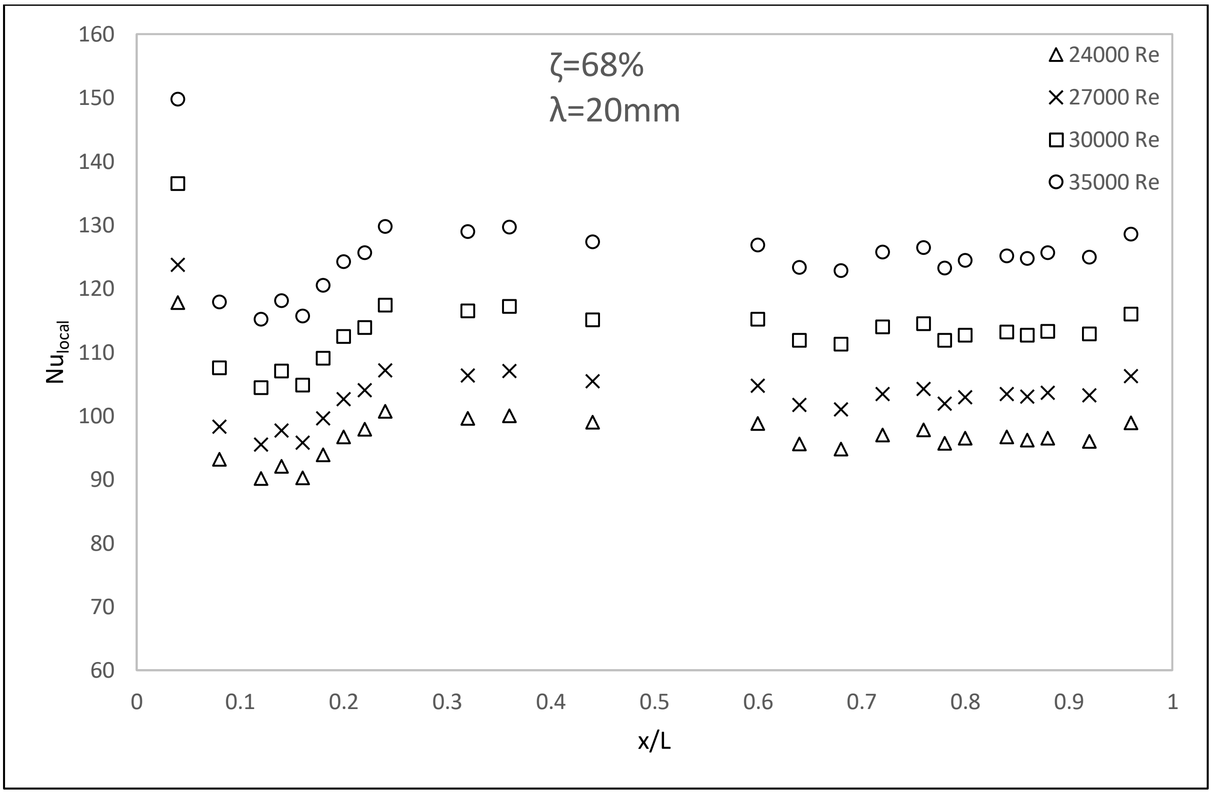

(d)

Figure D.19: Insert 1.1 ($\zeta = 68\%$, $\lambda = 20$ mm) test section centreline local Nusselt number with two walls heated for Reynolds number range: (a) $400 < Re < 2000$, (b) $3000 < Re < 7500$, (c) $10000 < Re < 21000$ and (d) $24000 < Re < 35000$

D.4. Mesh 1.2 (λ = 20 mm, ξ = 48 %)

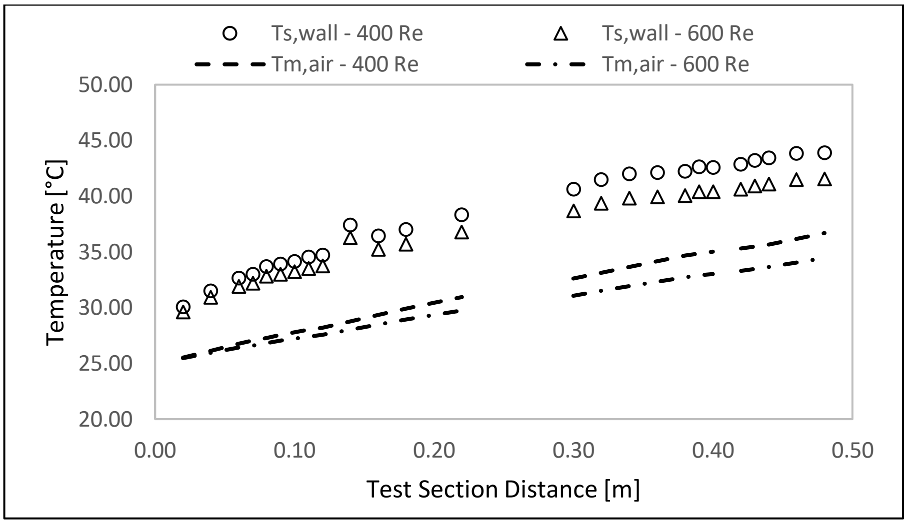

Figure D.20: Test Section Temperatures for Insert 1.2 at Re = 400 and Re = 600

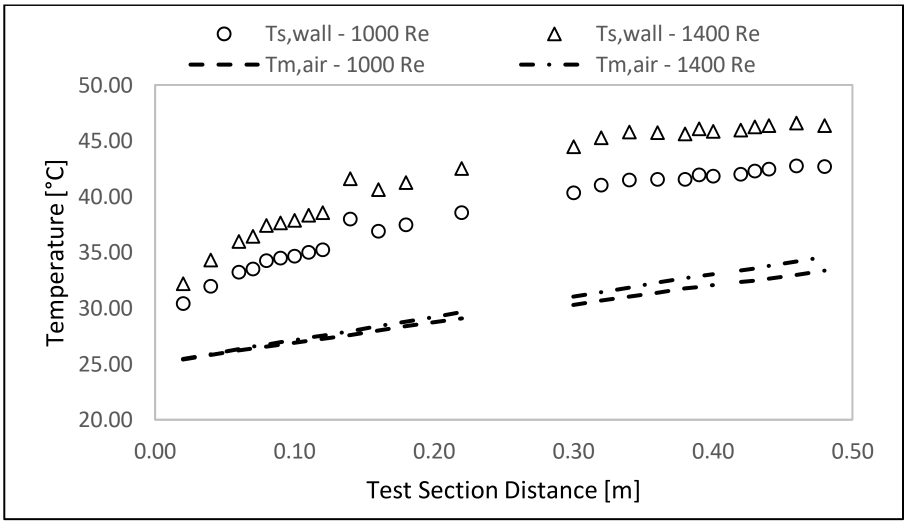

Figure D.21: Test Section Temperatures for Insert 1.2 at Re = 1000 and Re = 1400

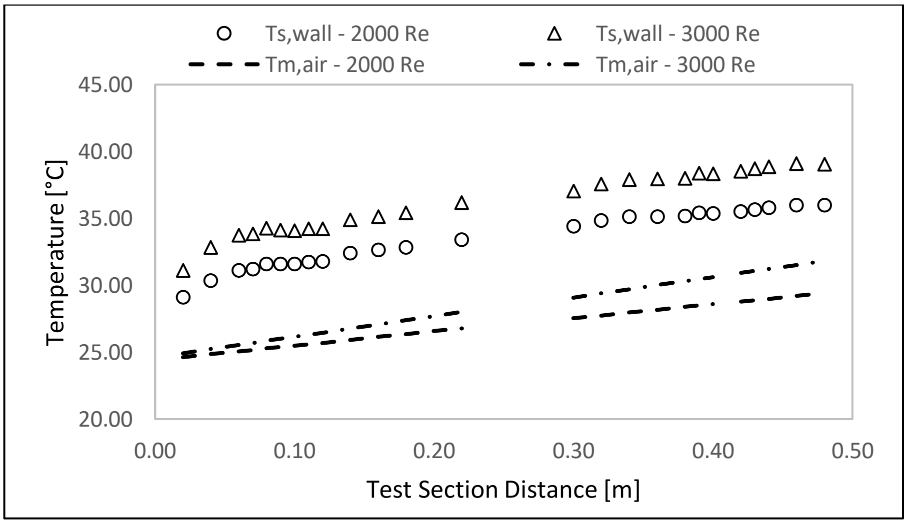

Figure D.22: Test Section Temperatures for Insert 1.2 at Re = 2000 and Re = 3000

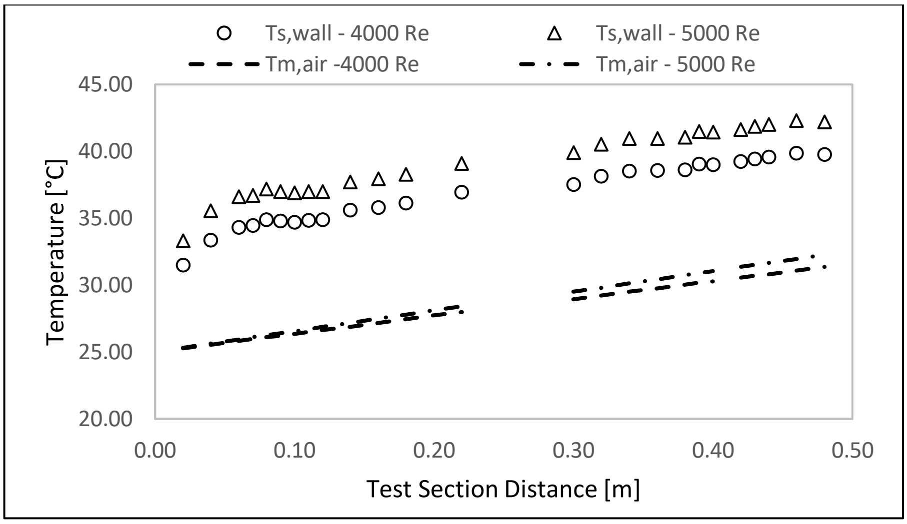

Figure D.23: Test Section Temperatures for Insert 1.2 at Re = 4000 and Re = 5000

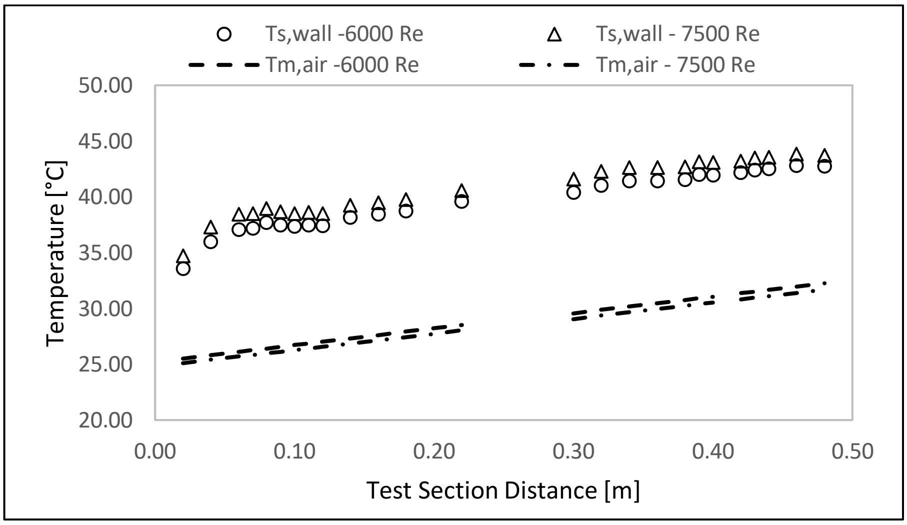

Figure D.24:Test Section Temperatures for Insert 1.2 at Re = 6000 and Re = 7500

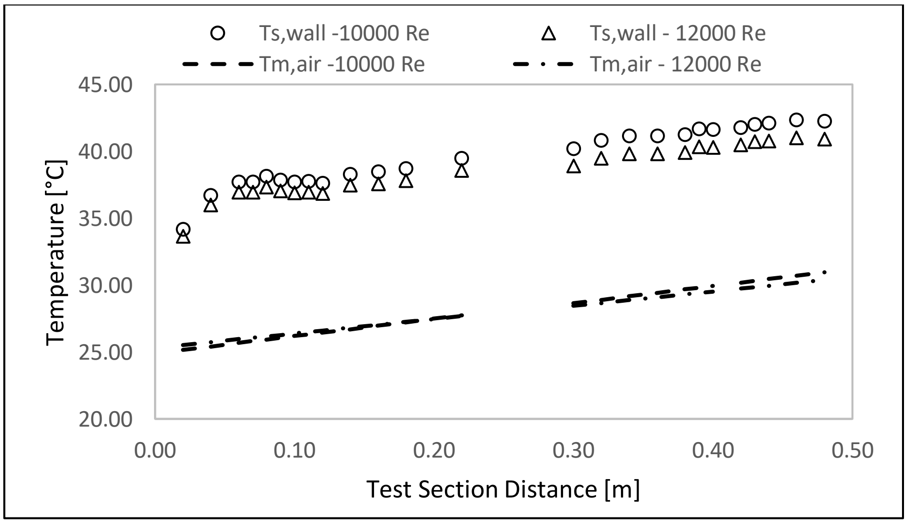

Figure D.25: Test Section Temperatures for Insert 1.2 at Re = 10000 and Re = 12000

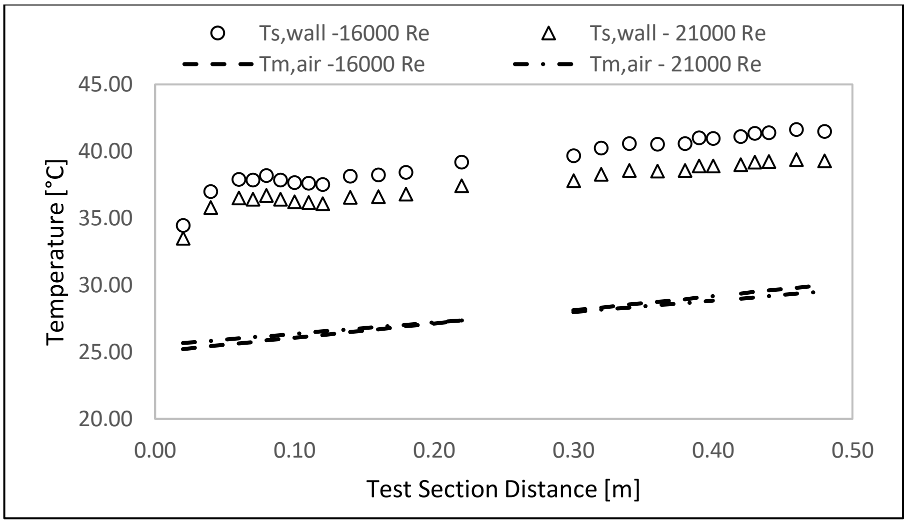

Figure D.26: Test Section Temperatures for Insert 1.2 at Re = 16000 and Re = 21000

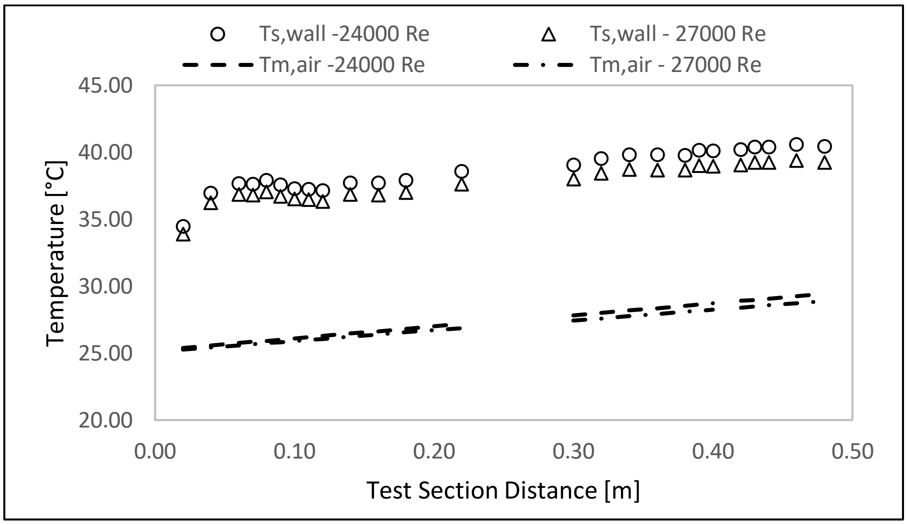

Figure D.27: Test Section Temperatures for Insert 1.2 at Re = 24000 and Re = 27000

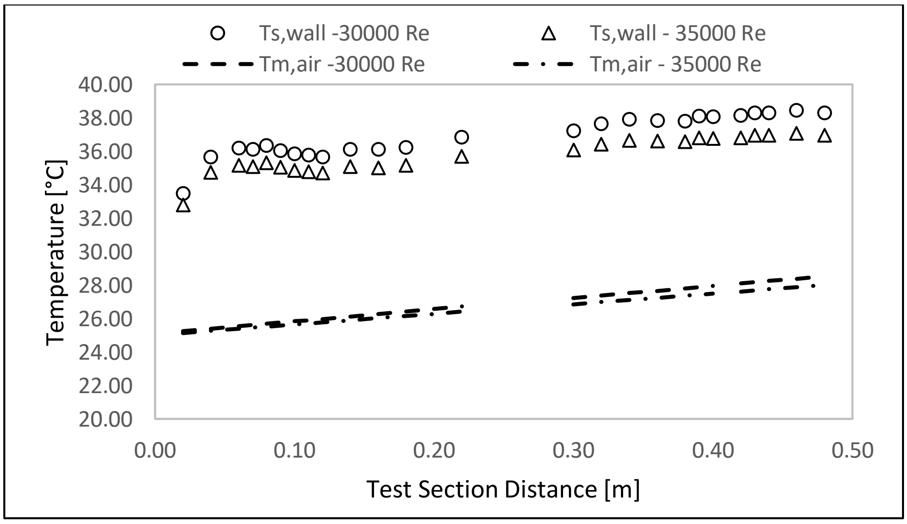

Figure D.28:Test Section Temperatures for Insert 1.2 at Re = 30000 and Re = 35000

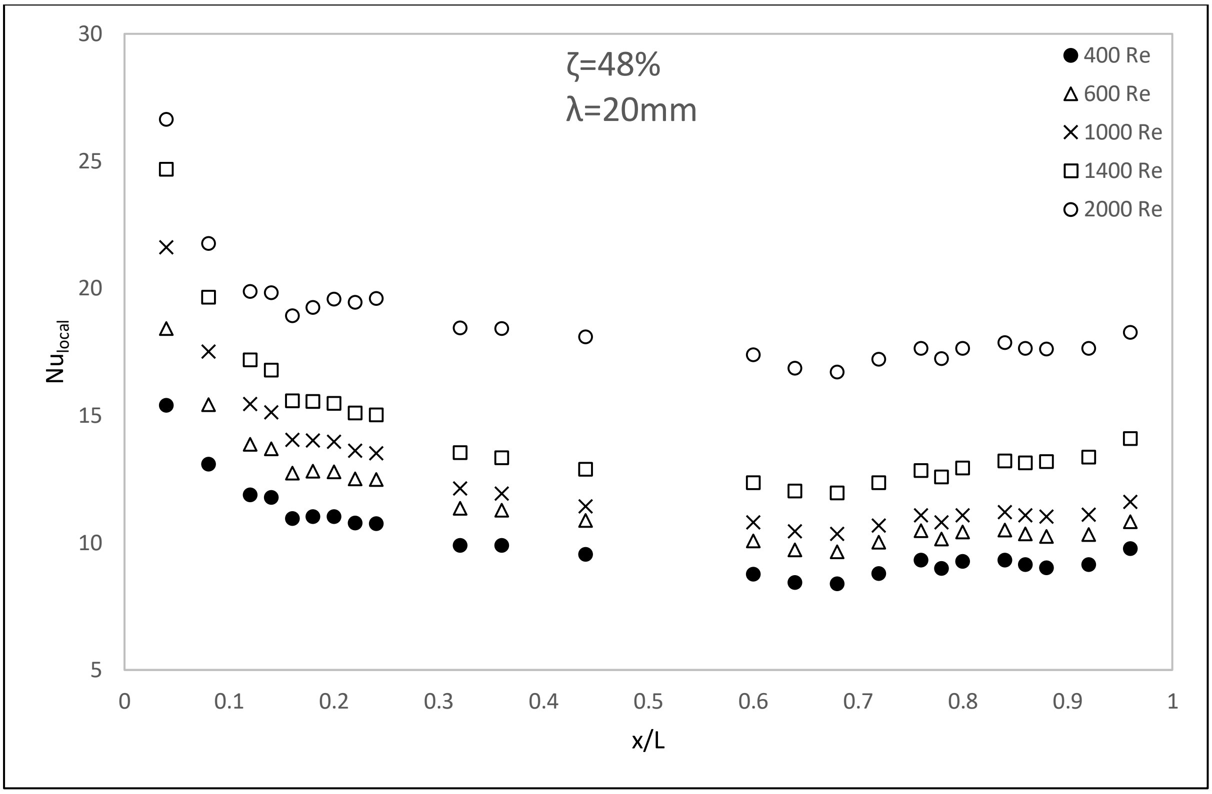
ζ=48%
λ=20mm
● 400 Re
△ 600 Re
× 1000 Re
□ 1400 Re
○ 2000 Re
Nu_{local}
x/L
30
25
20
15
10
5
0
0.1
0.2
0.3
0.4
0.5
0.6
0.7
0.8
0.9
1

(a)

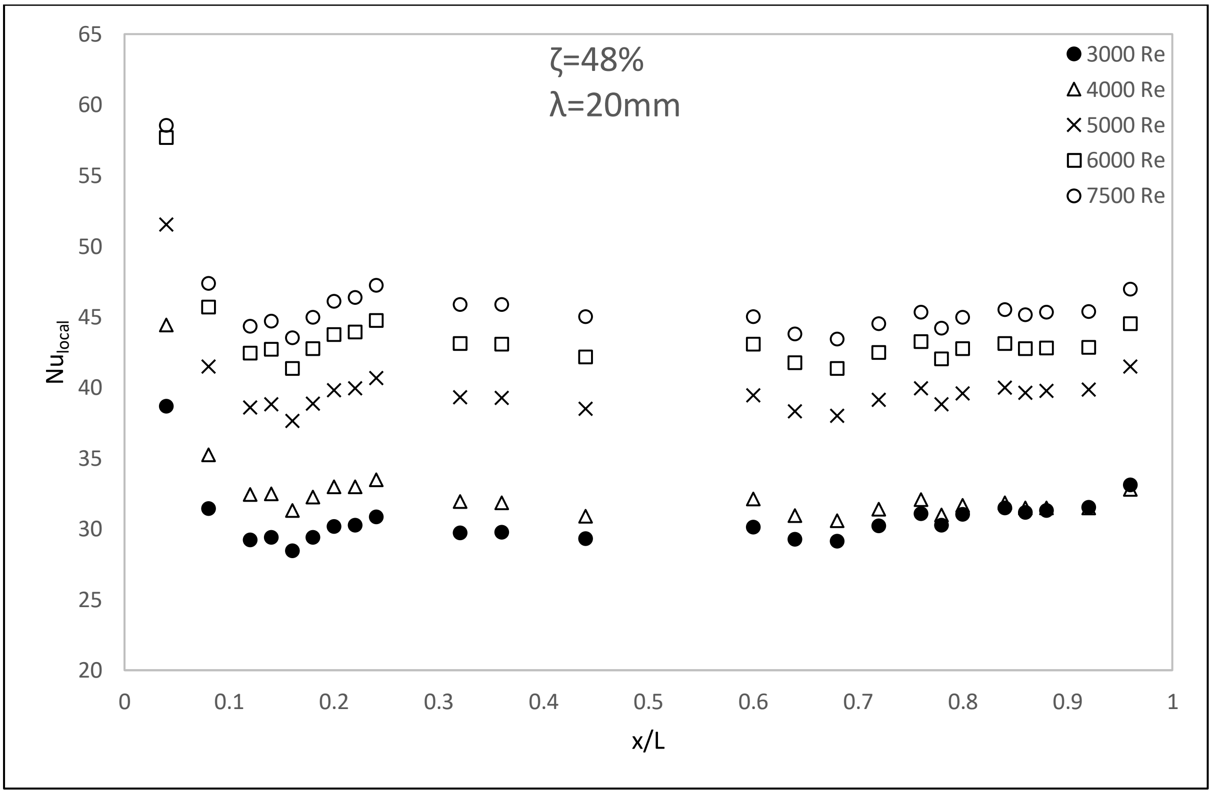
ζ=48%
λ=20mm
● 3000 Re
△ 4000 Re
× 5000 Re
□ 6000 Re
○ 7500 Re
Nu_{local}
x/L
65
60
55
50
45
40
35
30
25
20
0
0.1
0.2
0.3
0.4
0.5
0.6
0.7
0.8
0.9
1

(b)

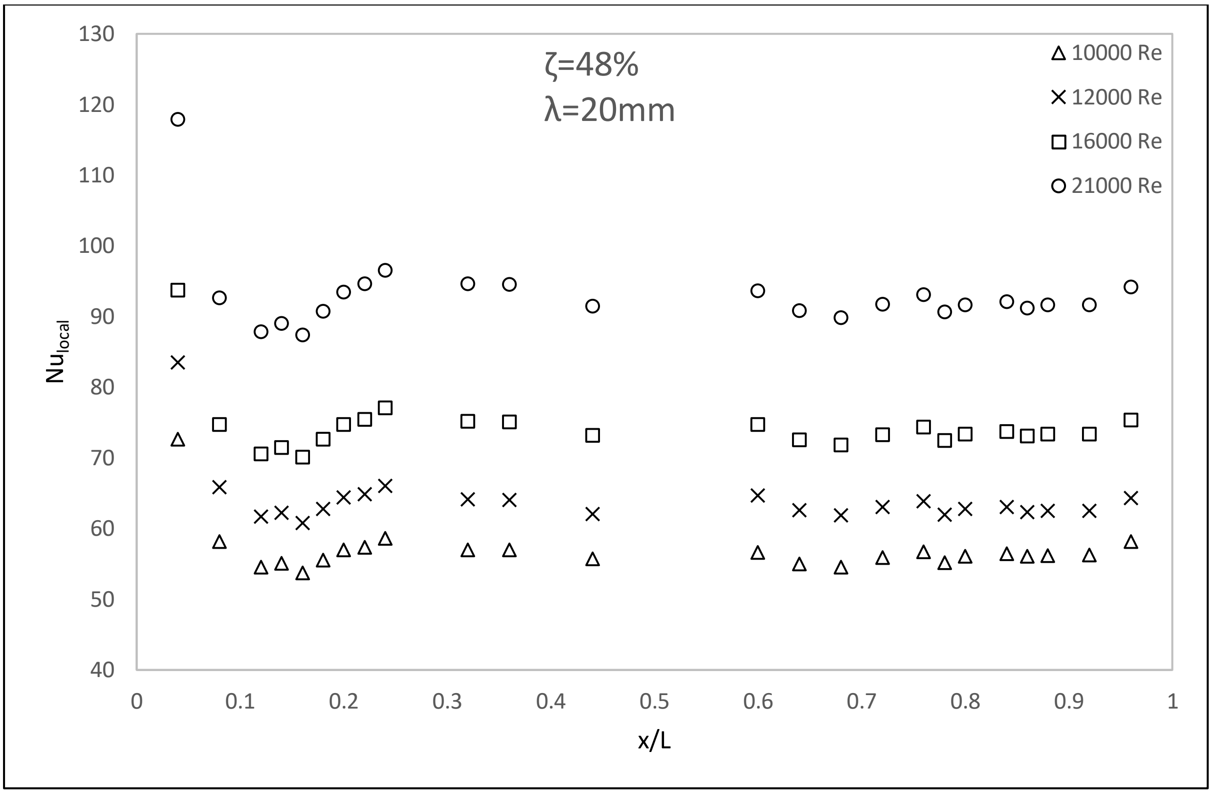

(c)

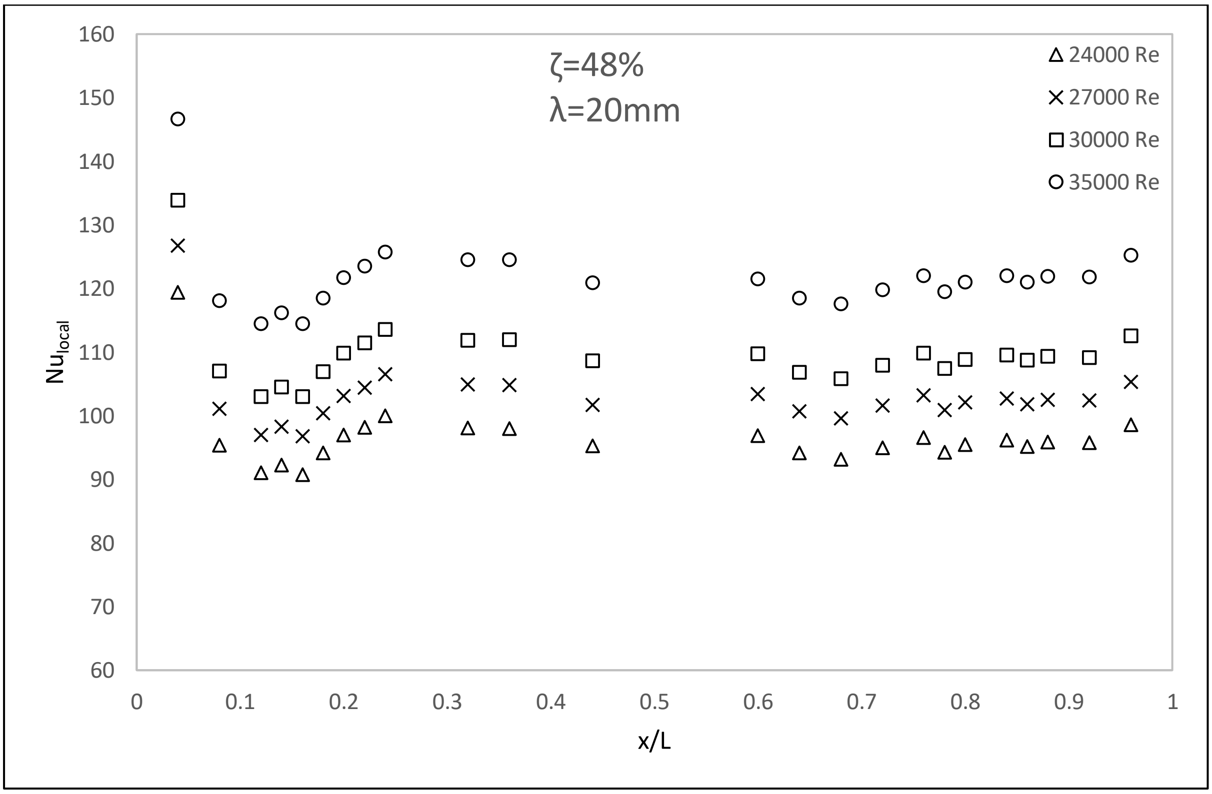

(d)

Figure D.29: Insert 1.2 (ζ = 48%, λ = 20 mm) test section centreline local Nusselt number with two walls heated for Reynolds number range: (a) 400 < Re < 2000, (b) 3000 < Re < 7500, (c) 10000 < Re < 21000 and (d) 24000 < Re < 35000

D.5. Mesh 2.1 (λ = 16 mm, ξ = 68 %)

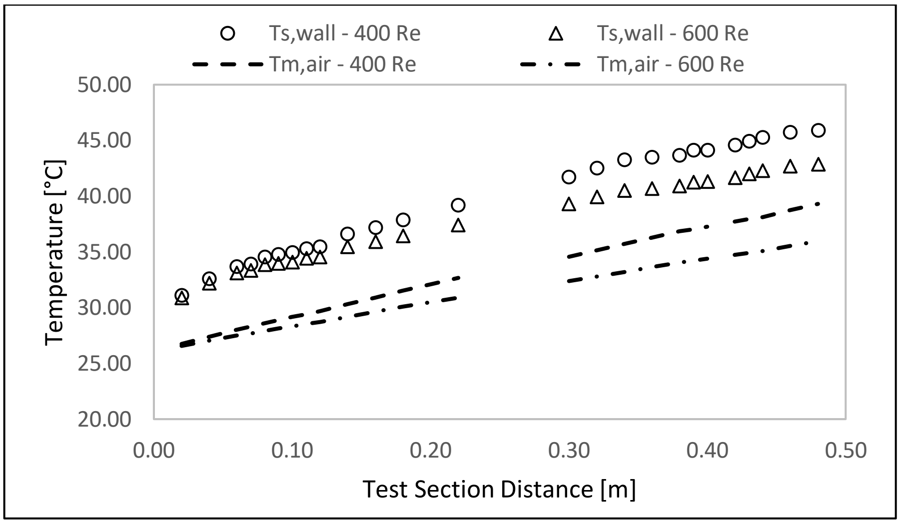

Figure D.30: Test Section Temperatures for Insert 2.1 at Re = 400 and Re = 600

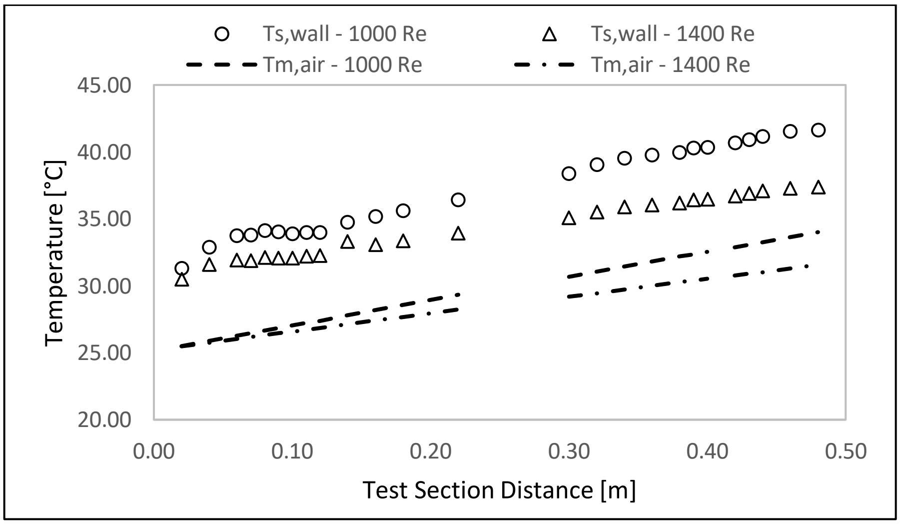

Figure D.31: Test Section Temperatures for Insert 2.1 at Re = 1000 and Re = 1400

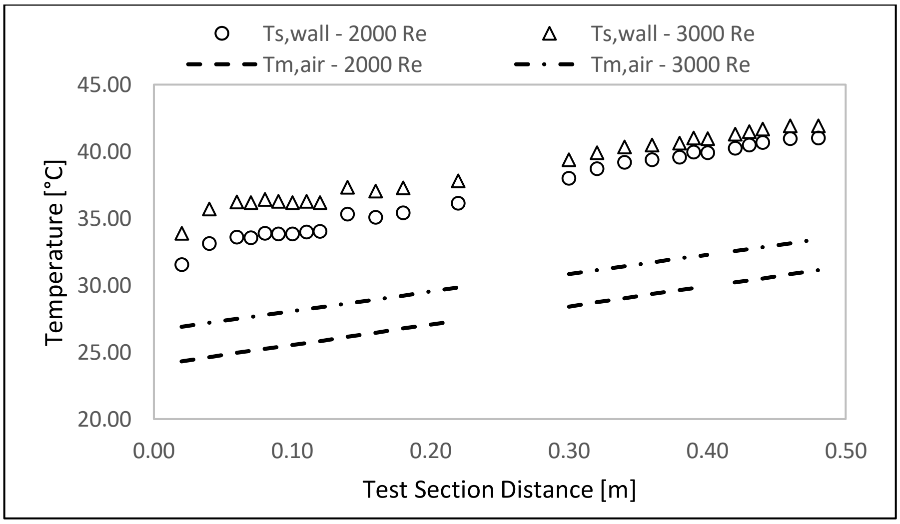

Figure D.32: Test Section Temperatures for Insert 2.1 at Re = 2000 and Re = 3000

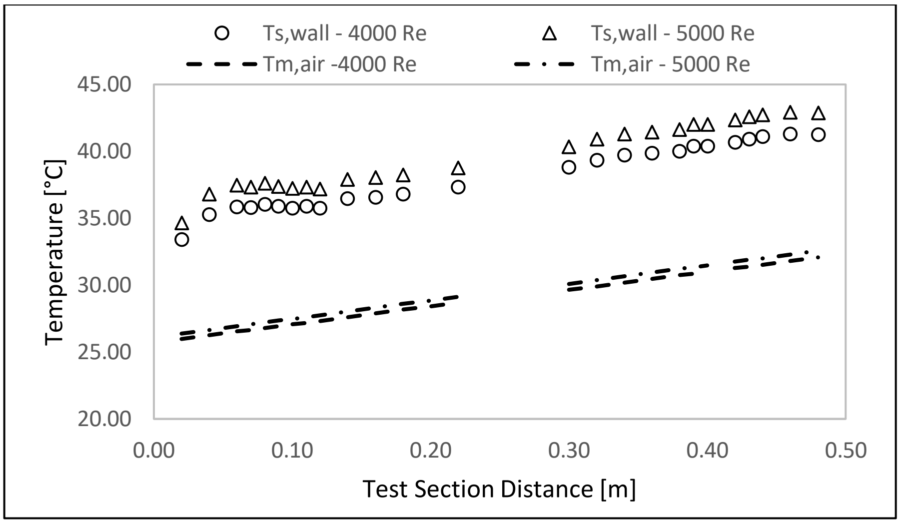

Figure D.33: Test Section Temperatures for Insert 2.1 at Re = 4000 and Re = 5000

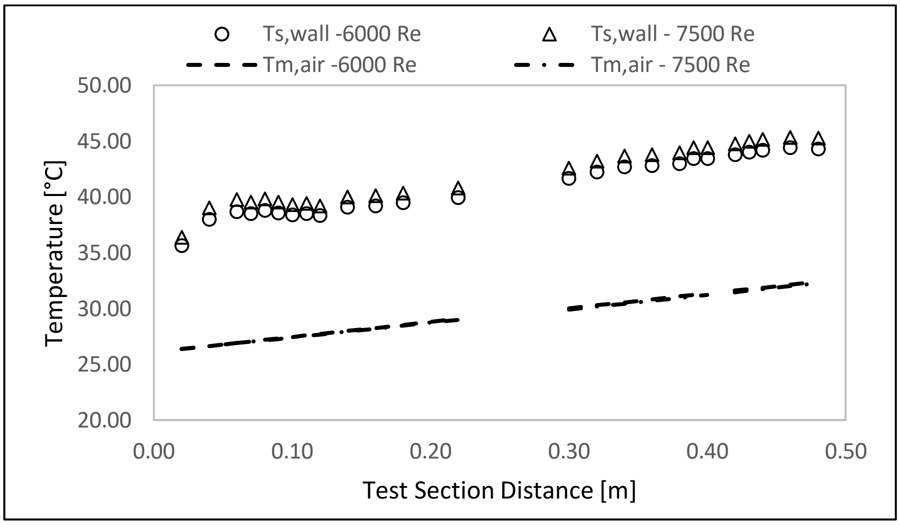

Figure D.34: Test Section Temperatures for Insert 2.1 at Re = 6000 and Re = 7500

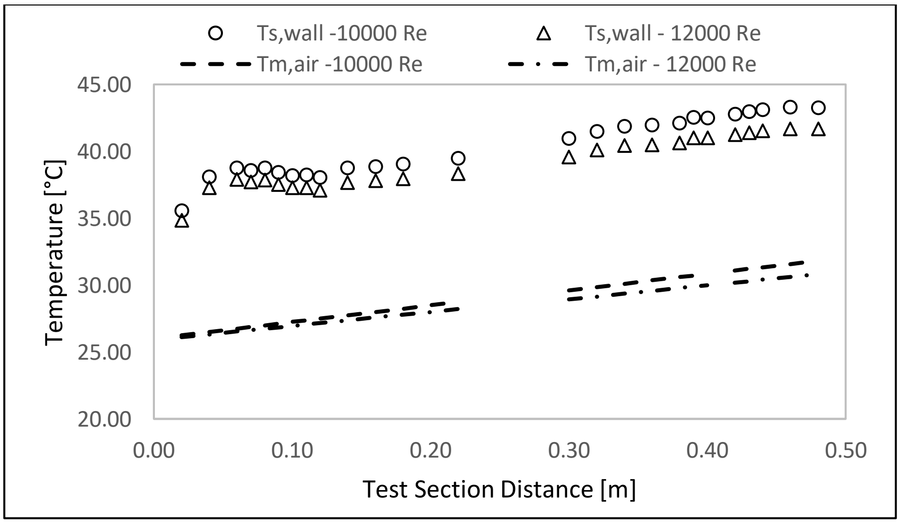

Figure D.35: Test Section Temperatures for Insert 2.1 at Re = 10000 and Re = 12000

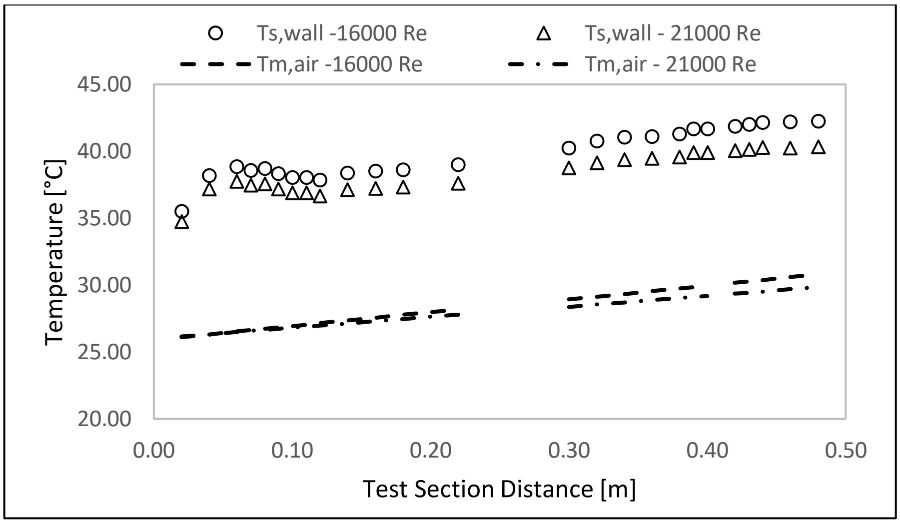

Figure D.36: Test Section Temperatures for Insert 2.1 at Re = 16000 and Re = 21000

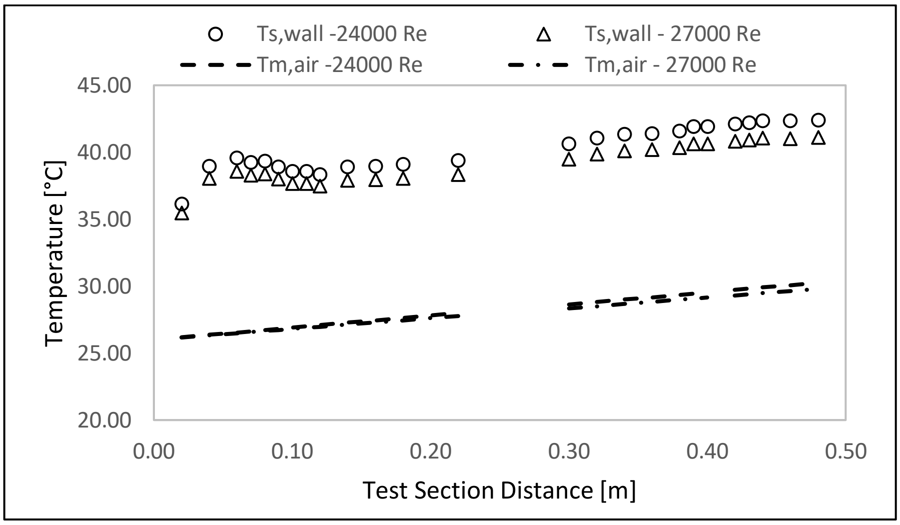

Figure D.37: Test Section Temperatures for Insert 2.1 at Re = 24000 and Re = 27000

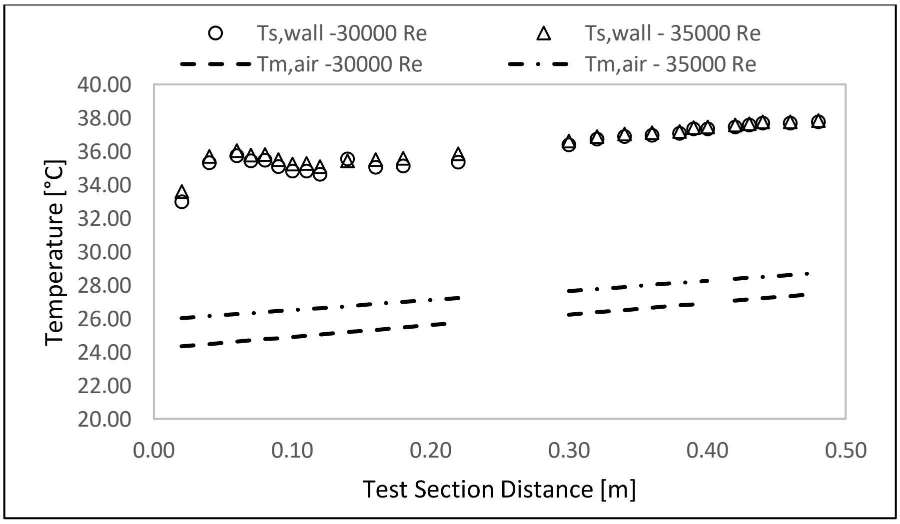

Figure D.38: Test Section Temperatures for Insert 2.1 at Re = 30000 and Re = 35000

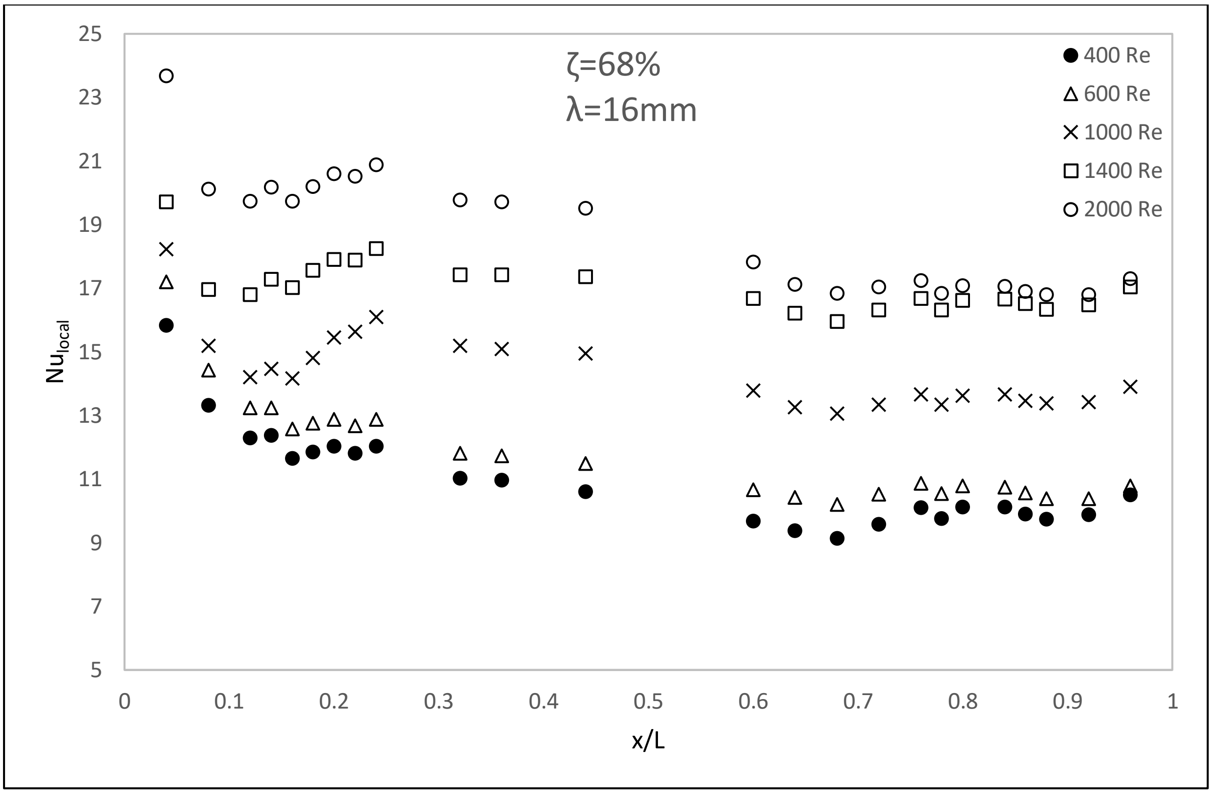
ζ=68%
λ=16mm
400 Re
600 Re
1000 Re
1400 Re
2000 Re
Nu_{local}
x/L
25
23
21
19
17
15
13
11
9
7
5
0
0.1
0.2
0.3
0.4
0.5
0.6
0.7
0.8
0.9
1

(a)

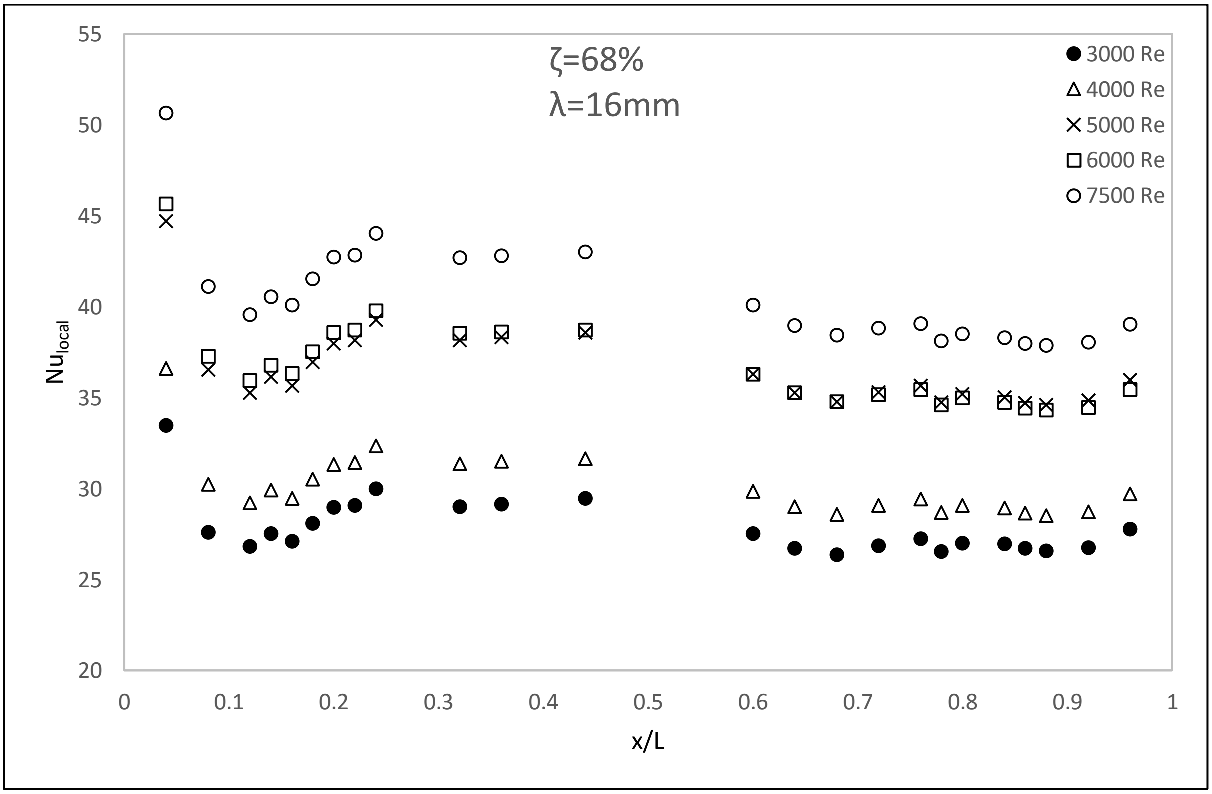
ζ=68%
λ=16mm
3000 Re
4000 Re
5000 Re
6000 Re
7500 Re
Nu_{local}
x/L
55
50
45
40
35
30
25
20
0
0.1
0.2
0.3
0.4
0.5
0.6
0.7
0.8
0.9
1

(b)

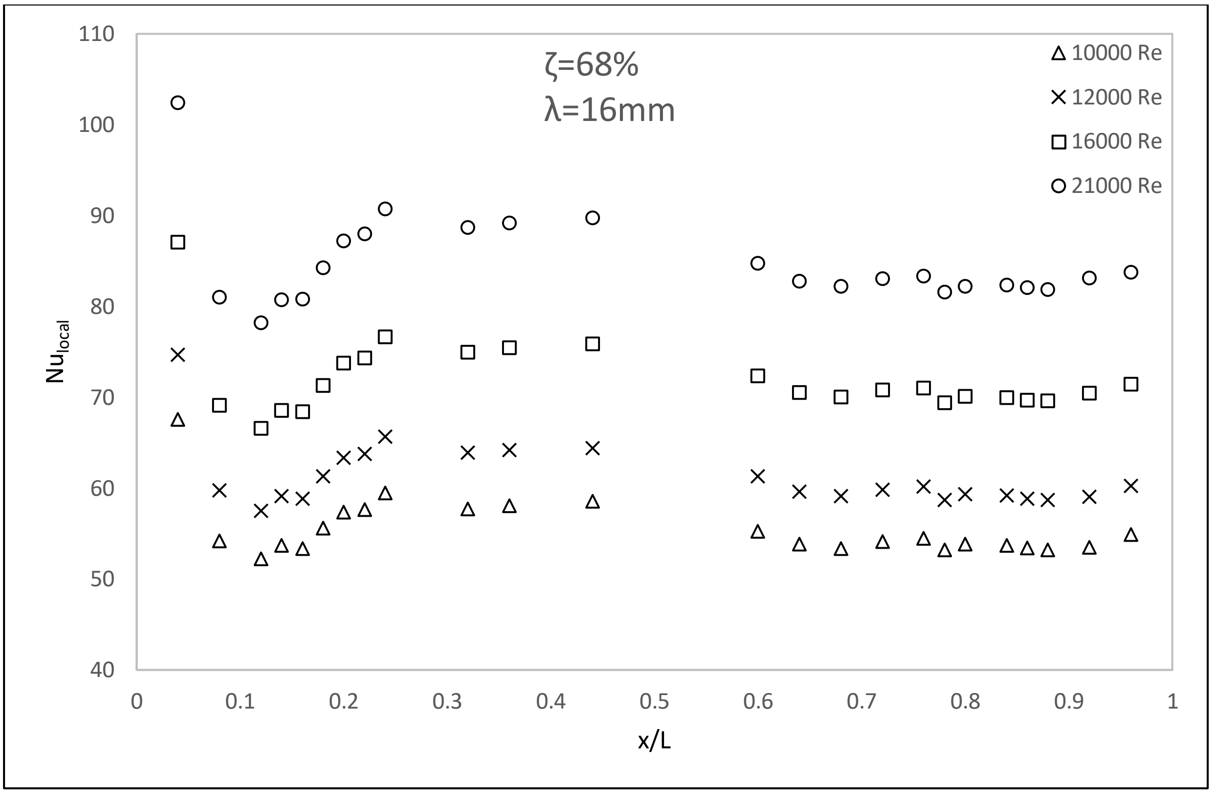

(c)

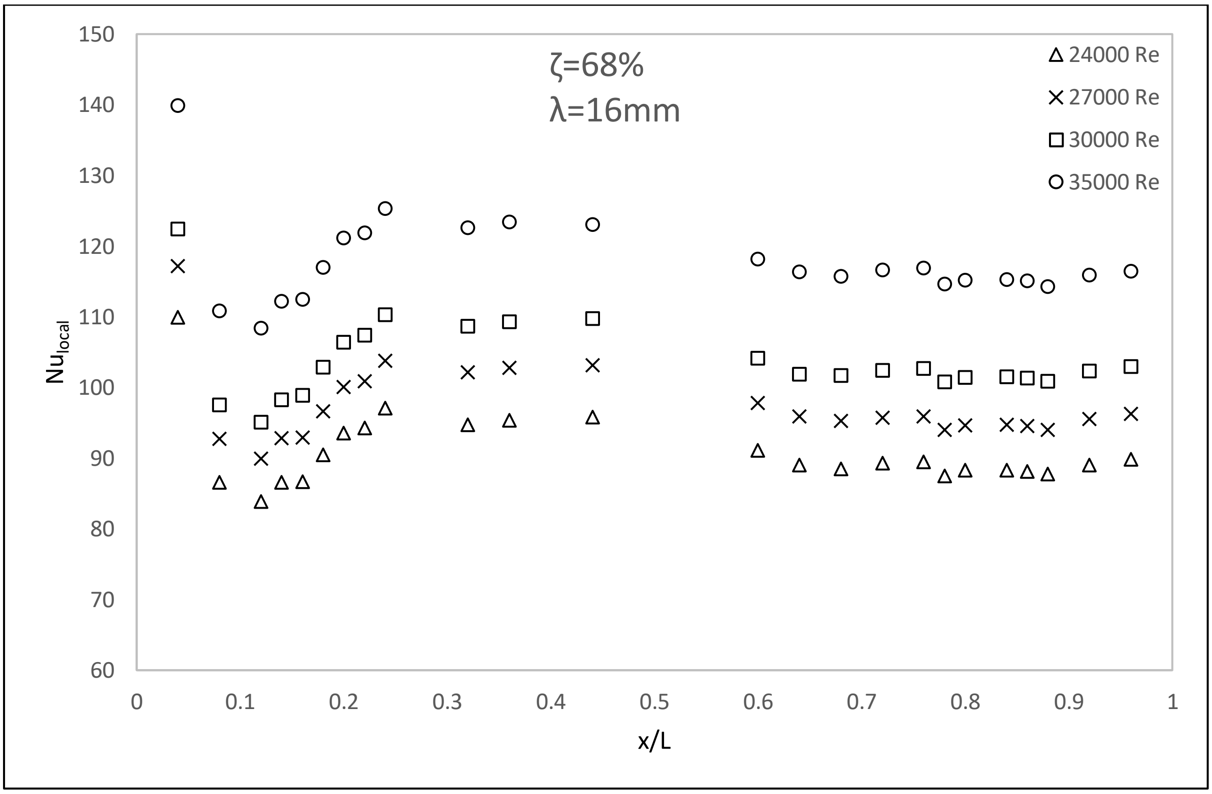

(d)

Figure D.39: Insert 2.1 (ζ = 68%, λ = 16 mm) test section centreline local Nusselt number with two walls heated for Reynolds number range: (a) 400 < Re < 2000, (b) 3000 < Re < 7500, (c) 10000 < Re < 21000 and (d) 24000 < Re < 35000

D.6. Mesh 2.2 (λ = 16 mm, ξ = 48 %)

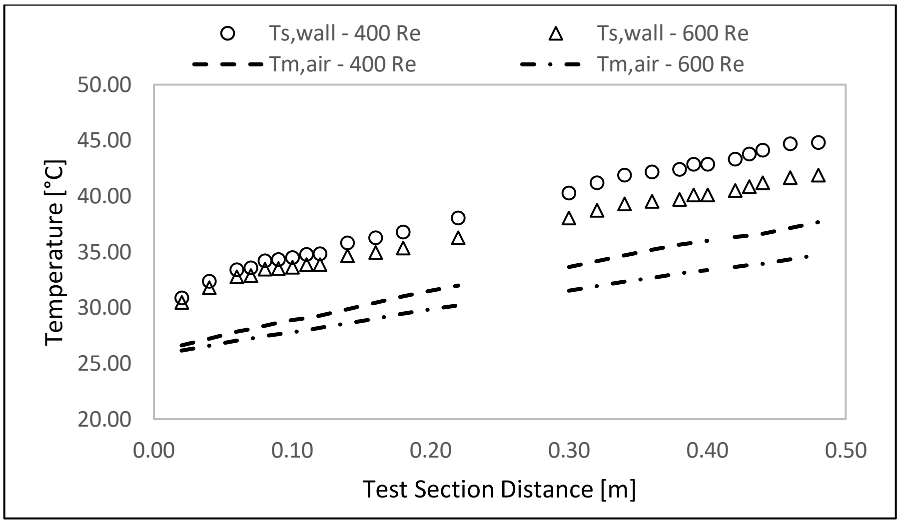

Figure D.40: Test Section Temperatures for Insert 2.2 at Re = 400 and Re = 600

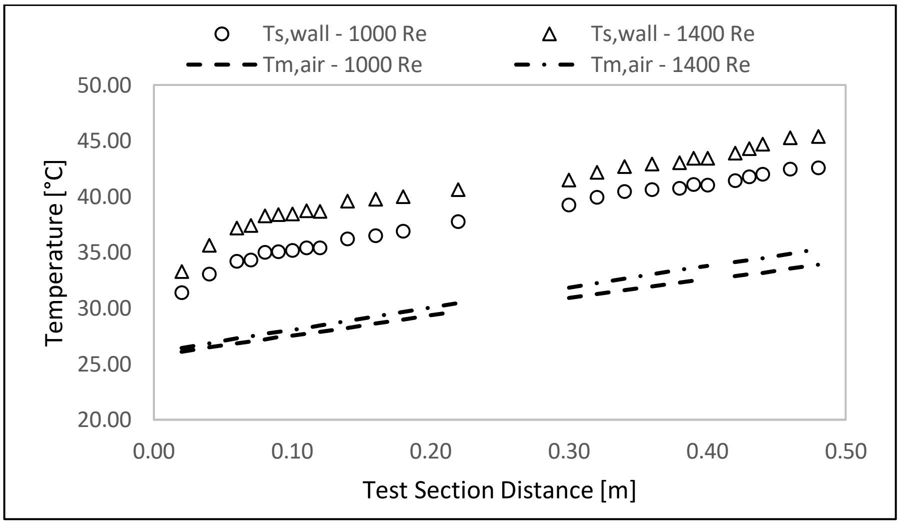

Figure D.41: Test Section Temperatures for Insert 2.2 at Re = 1000 and Re = 1400

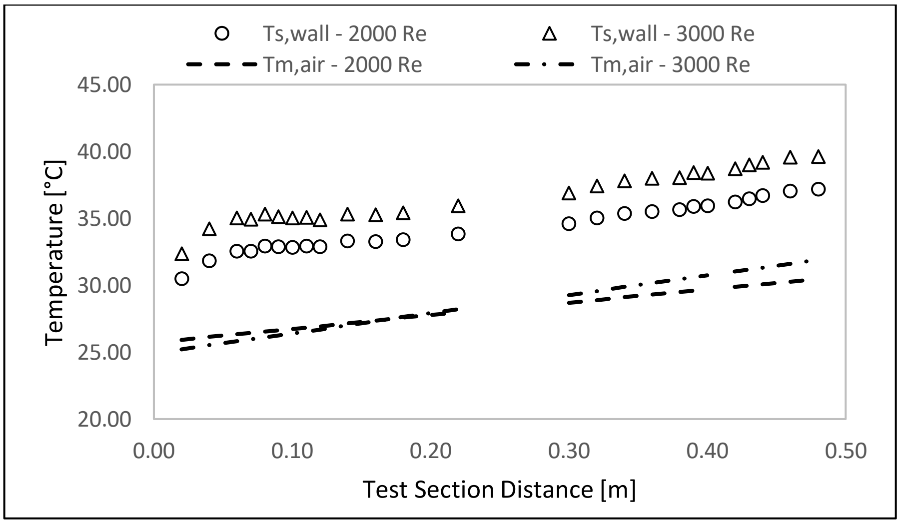

Figure D.42: Test Section Temperatures for Insert 2.2 at Re = 2000 and Re = 3000

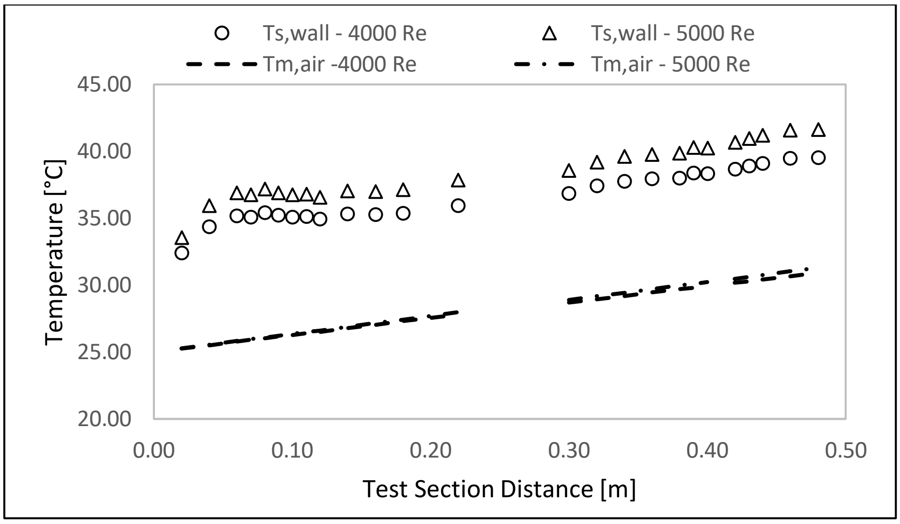

Figure D.43: Test Section Temperatures for Insert 2.2 at Re = 4000 and Re = 5000

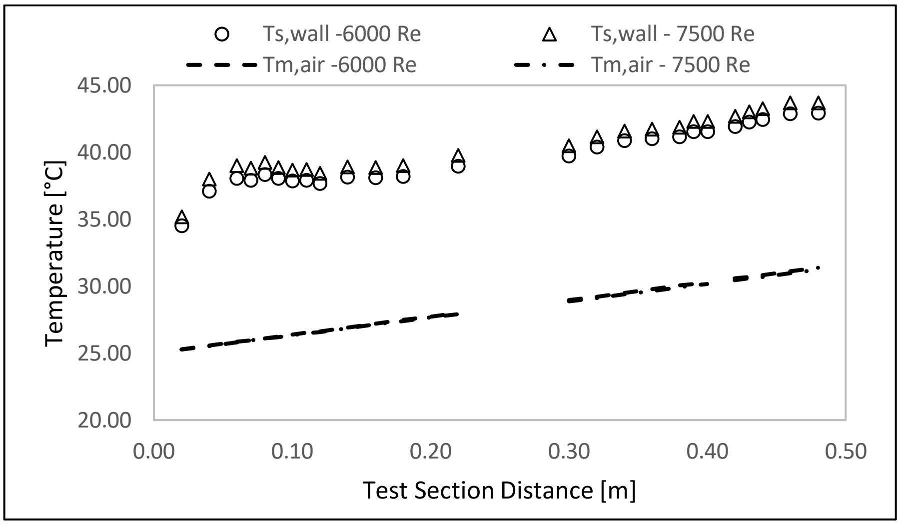

Figure D.44: Test Section Temperatures for Insert 2.2 at Re = 6000 and Re = 7500

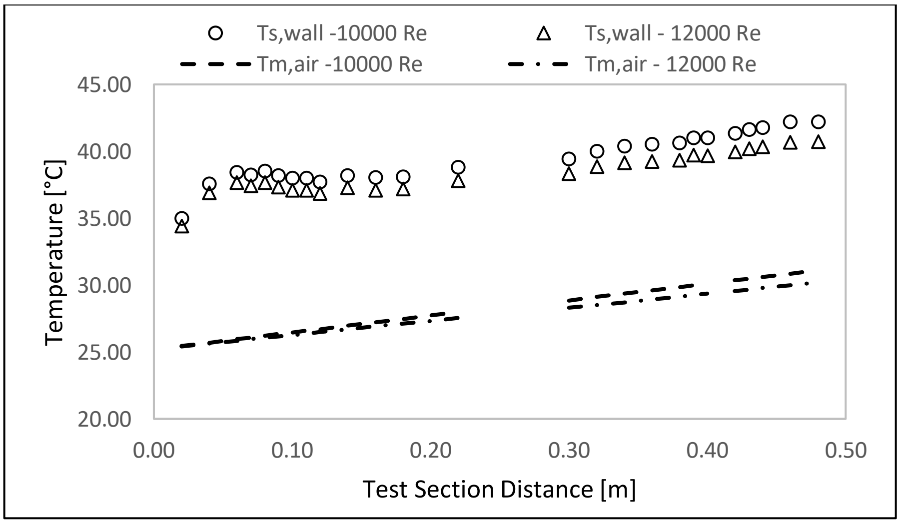

Figure D.45: Test Section Temperatures for Insert 2.2 at Re = 10000 and Re = 12000

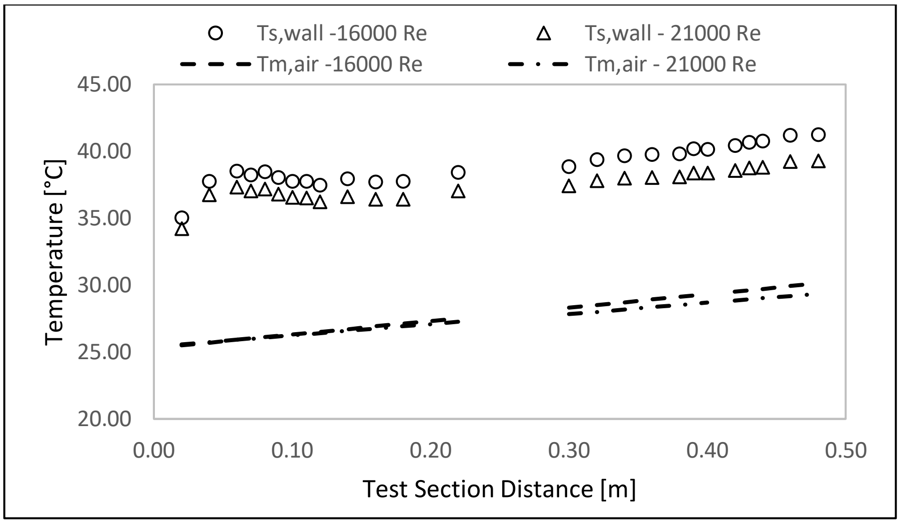

Figure D.46: Test Section Temperatures for Insert 2.2 at Re = 16000 and Re = 21000

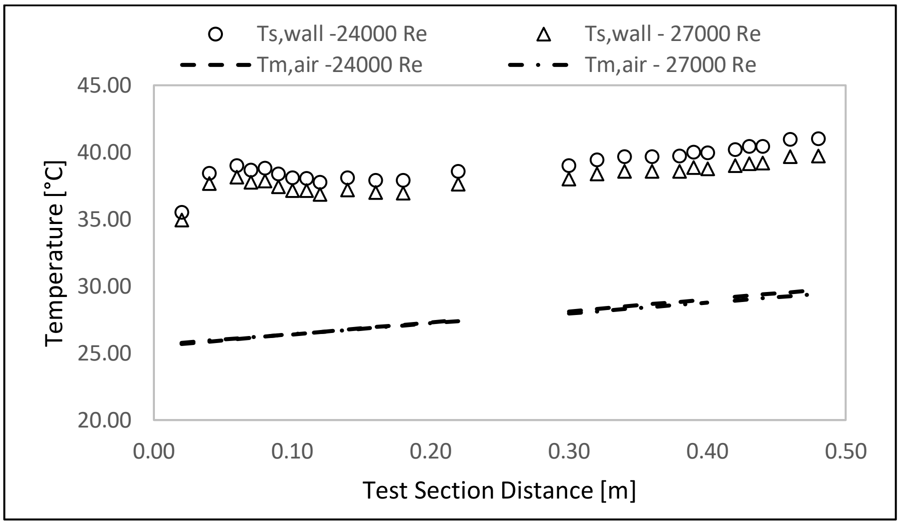

Figure D.47: Test Section Temperatures for Insert 2.2 at Re = 24000 and Re = 27000

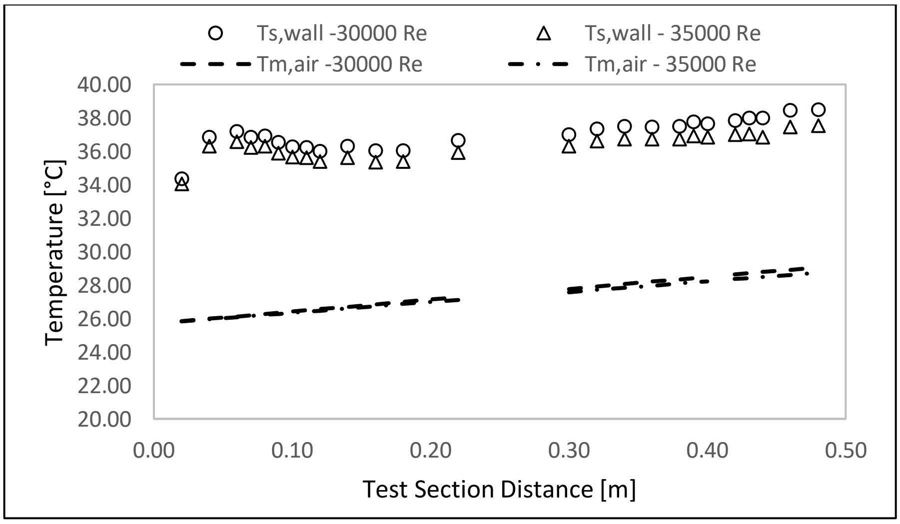

Figure D.48: Test Section Temperatures for Insert 2.2 at Re = 30000 and Re = 35000

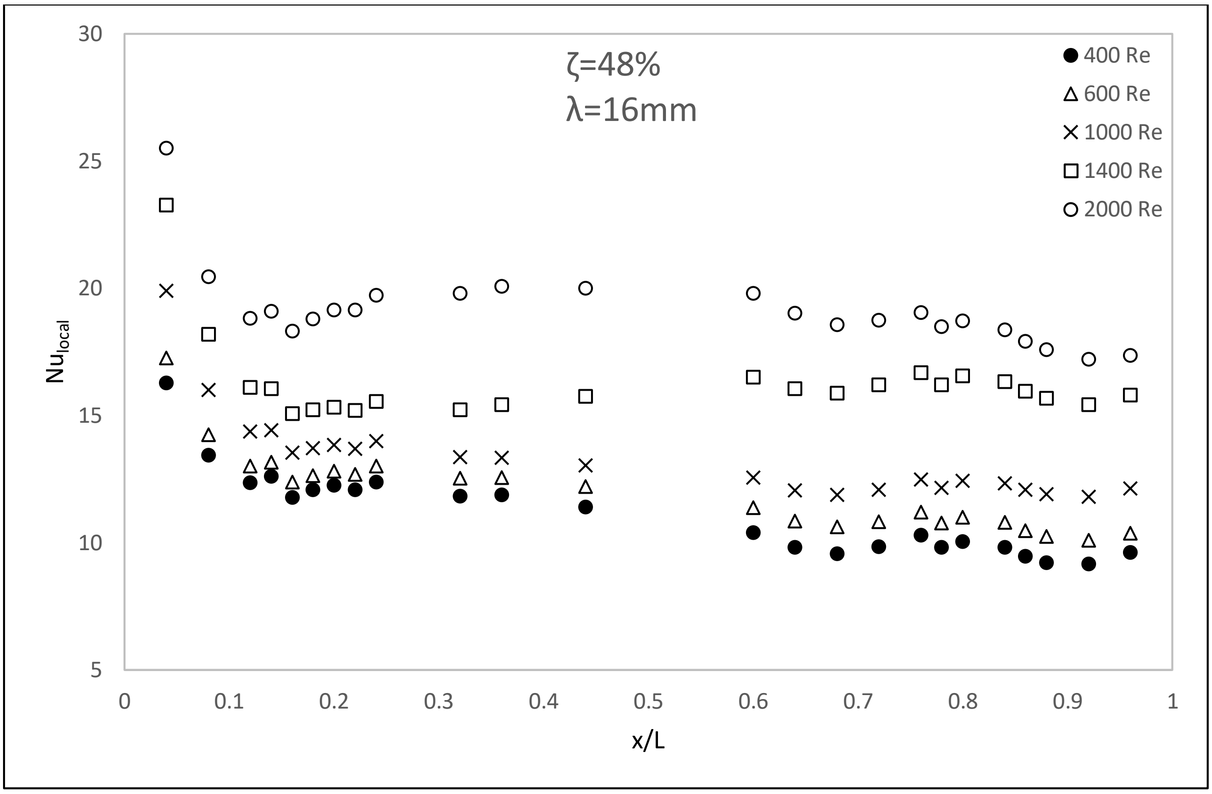
ζ=48%
λ=16mm
● 400 Re
△ 600 Re
× 1000 Re
□ 1400 Re
○ 2000 Re
Nu_{local}
x/L
30
25
20
15
10
5
0
0.1
0.2
0.3
0.4
0.5
0.6
0.7
0.8
0.9
1

(a)

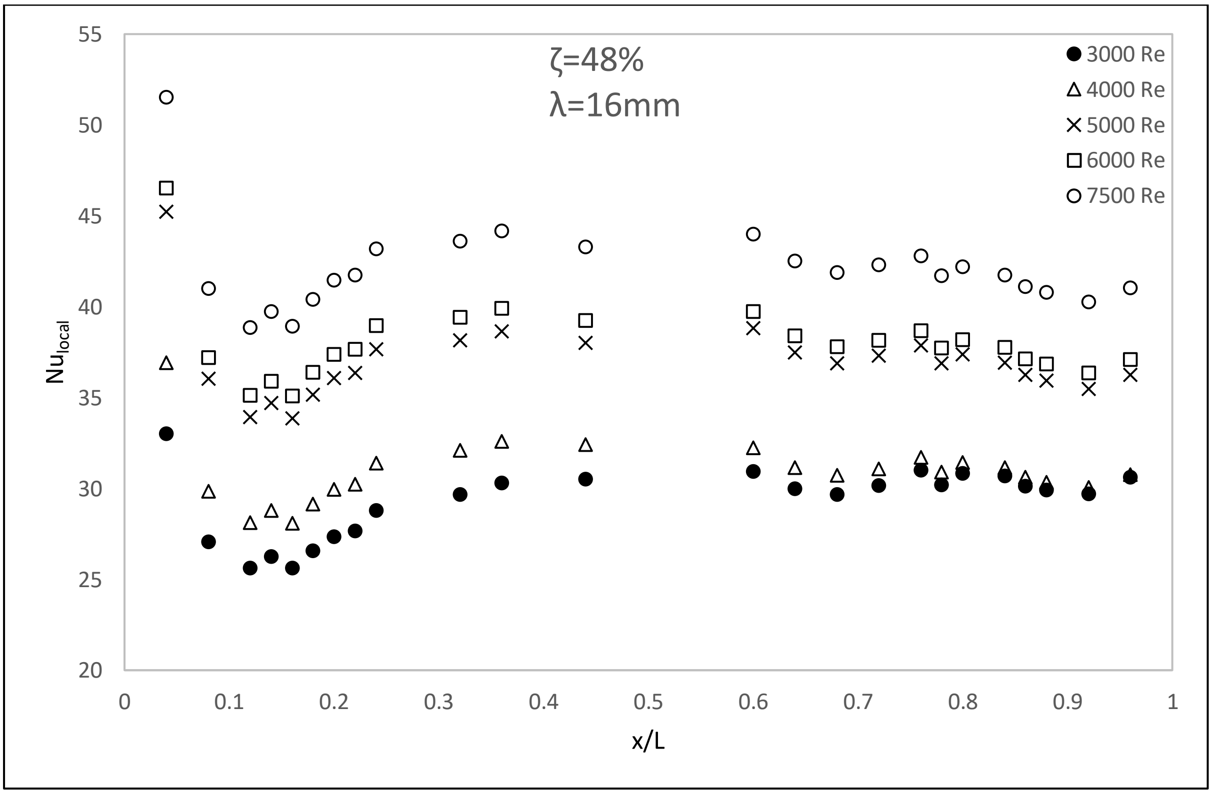
ζ=48%
λ=16mm
● 3000 Re
△ 4000 Re
× 5000 Re
□ 6000 Re
○ 7500 Re
Nu_{local}
x/L
55
50
45
40
35
30
25
20
0
0.1
0.2
0.3
0.4
0.5
0.6
0.7
0.8
0.9
1

(b)

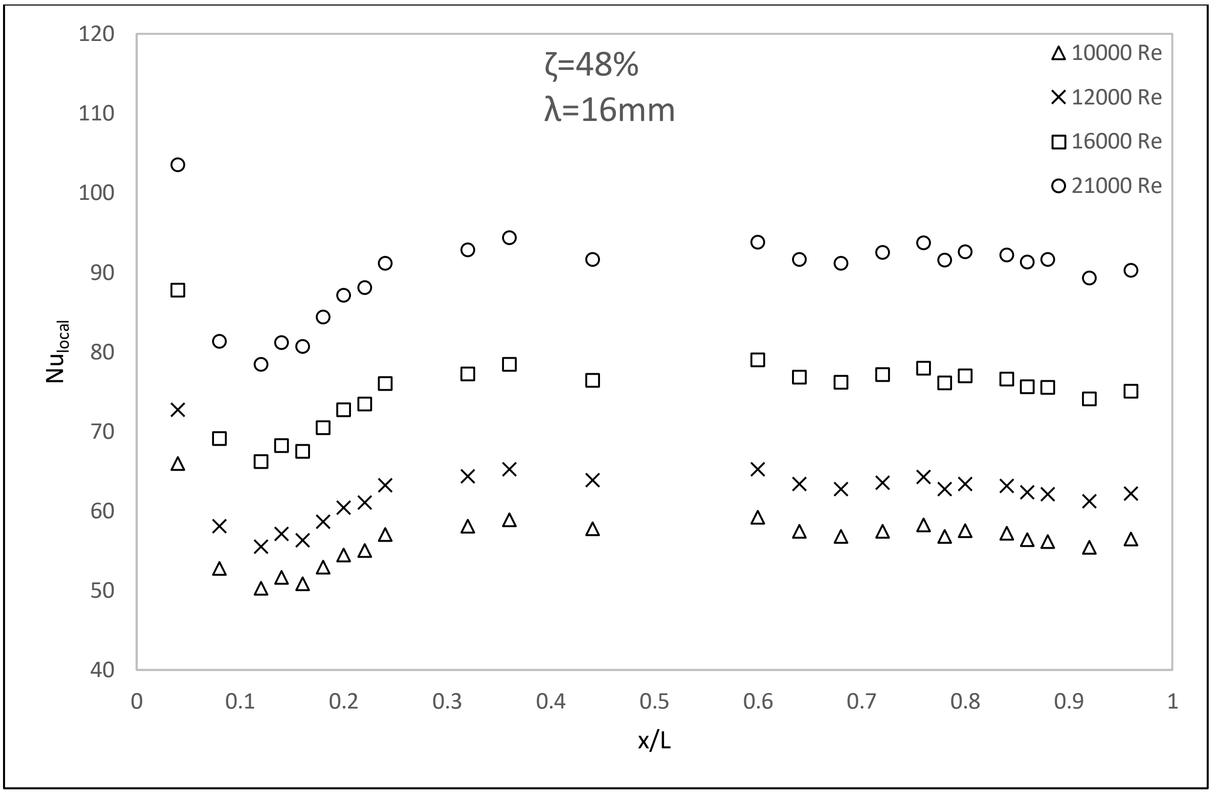

(c)

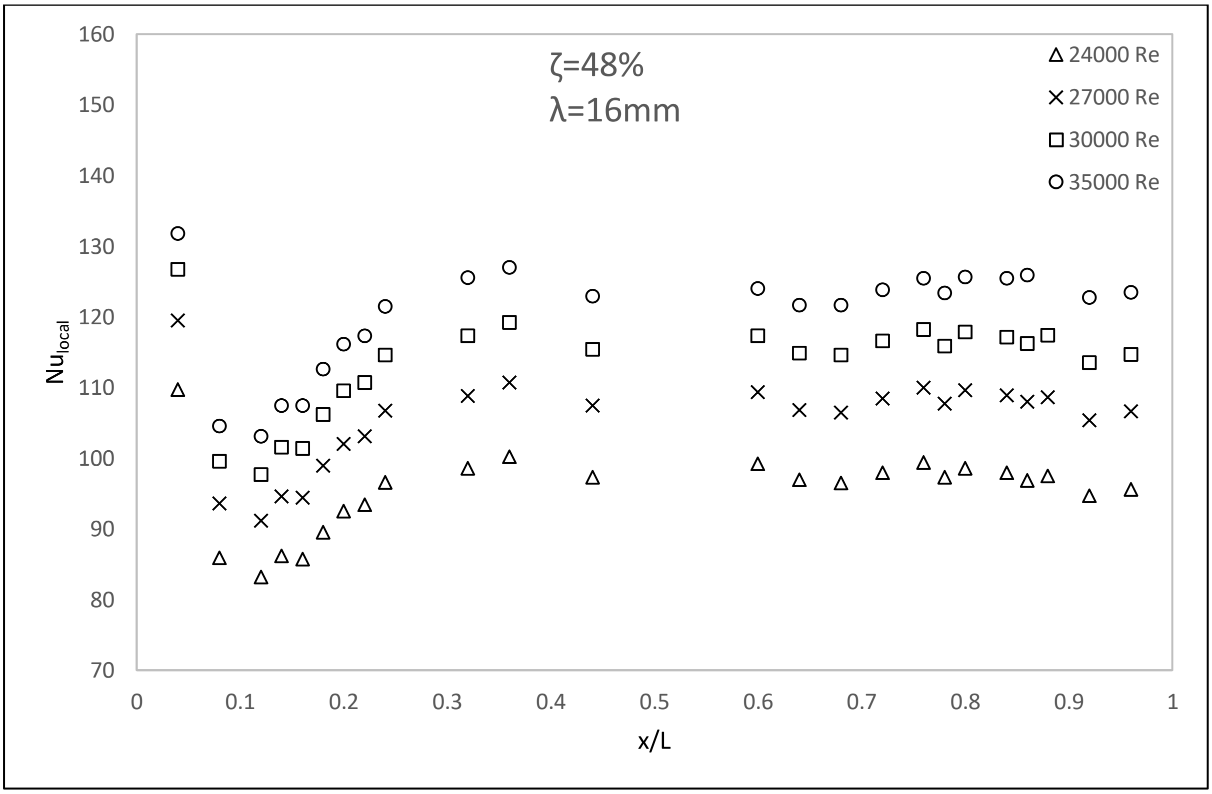

(d)

Figure D.49: Insert 2.2 (ζ = 48%, λ = 16 mm) test section centreline local Nusselt number with two walls heated for Reynolds number range: (a) 400 < Re < 2000, (b) 3000 < Re < 7500, (c) 10000 < Re < 21000 and (d) 24000 < Re < 35000

D.7. Mesh 3.1 (λ = 12 mm, ξ = 68 %)

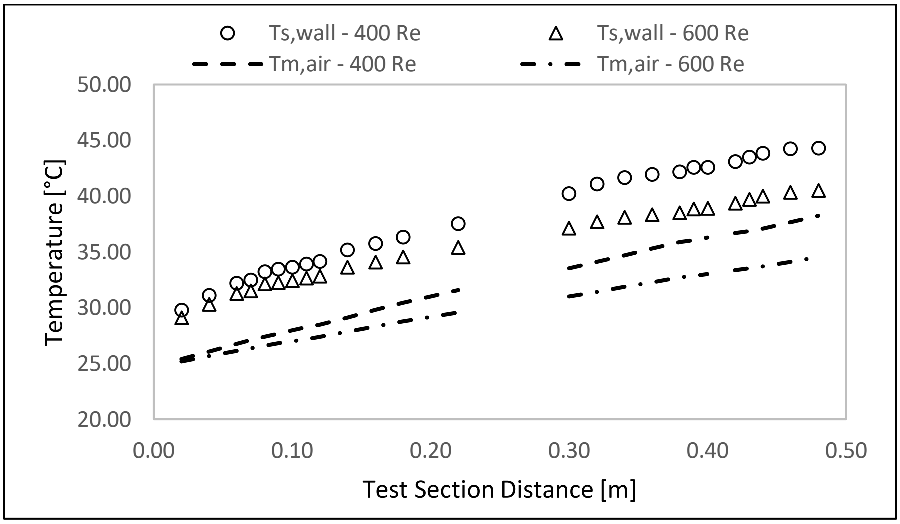

Figure D.50: Test Section Temperatures for Insert 3.1 at Re = 400 and Re = 600

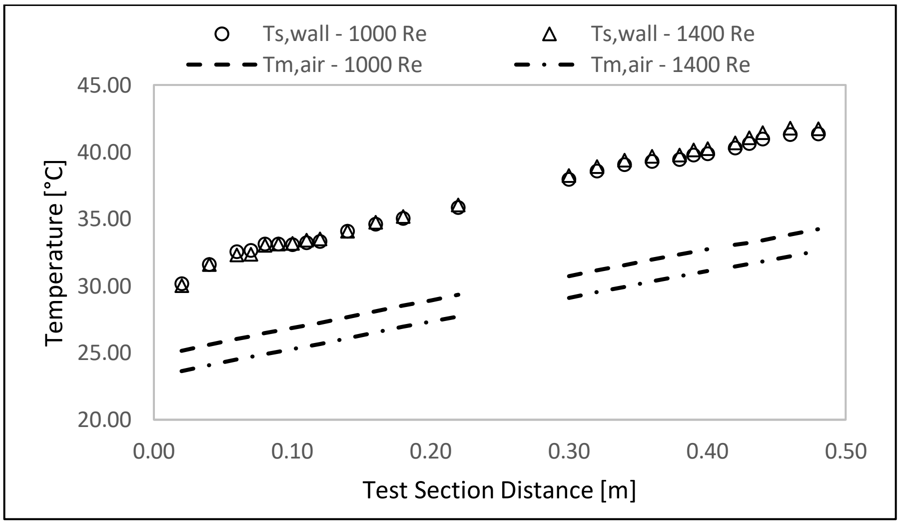

Figure D.51: Test Section Temperatures for Insert 3.1 at Re = 1000 and Re = 1400

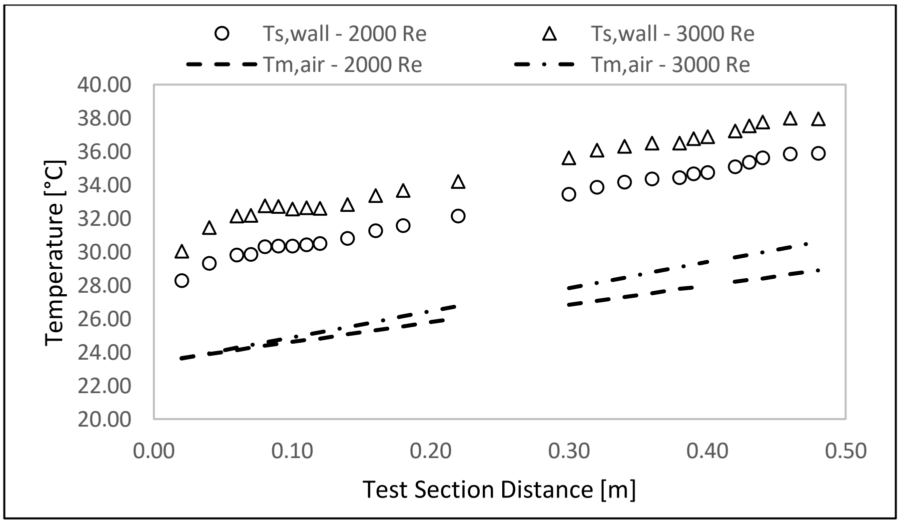

Figure D.52: Test Section Temperatures for Insert 3.1 at Re = 2000 and Re = 3000

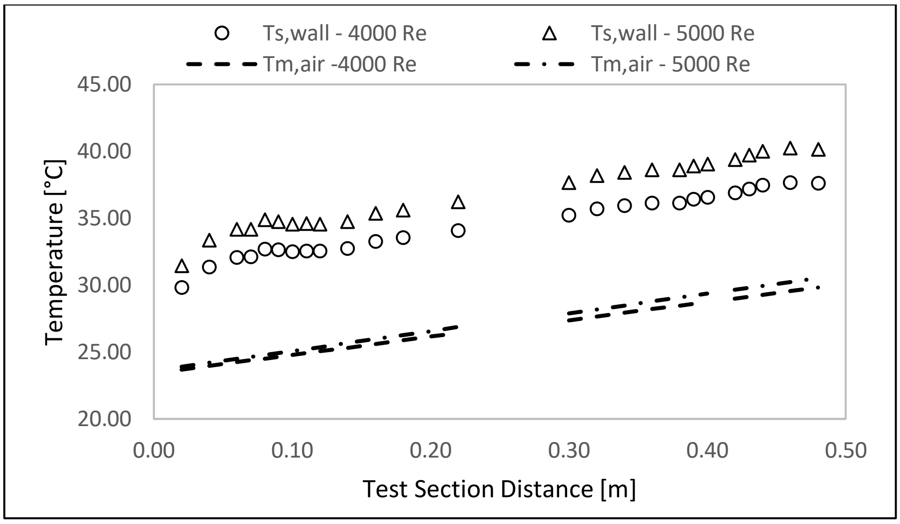

Figure D.53: Test Section Temperatures for Insert 3.1 at Re = 4000 and Re = 5000

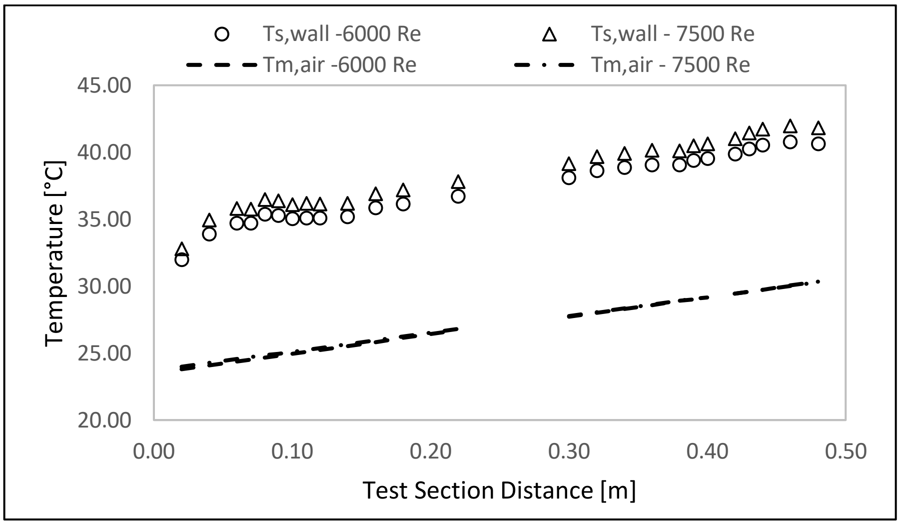

Figure D.54: Test Section Temperatures for Insert 3.1 at Re = 6000 and Re = 7500

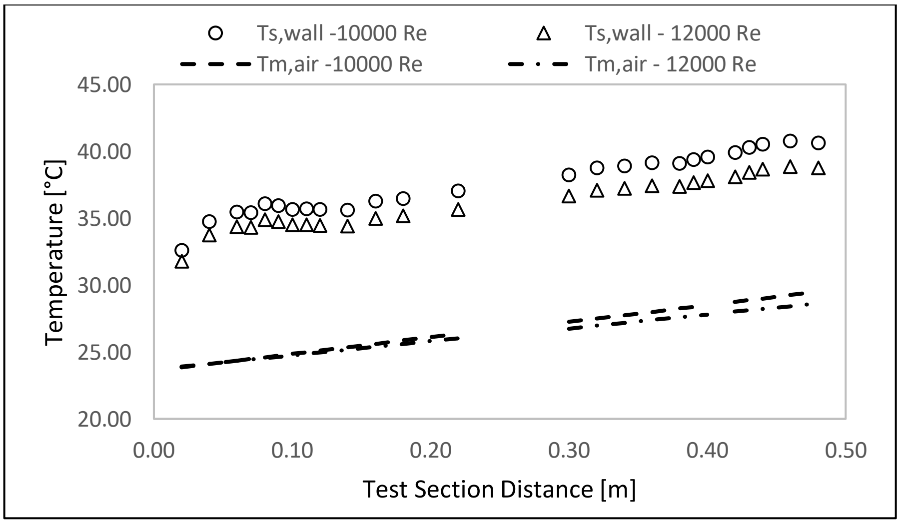

Figure D.55: Test Section Temperatures for Insert 3.1 at Re = 10000 and Re = 12000

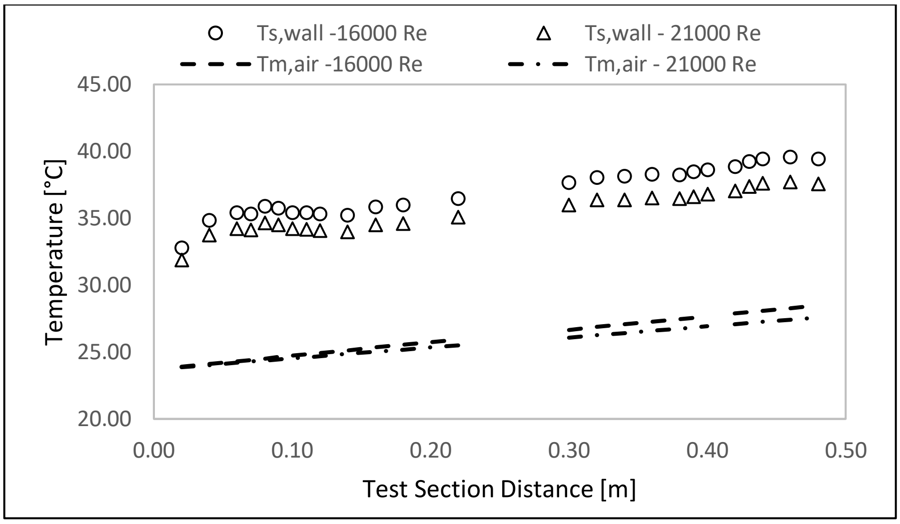

Figure D.56: Test Section Temperatures for Insert 3.1 at Re = 16000 and Re = 21000

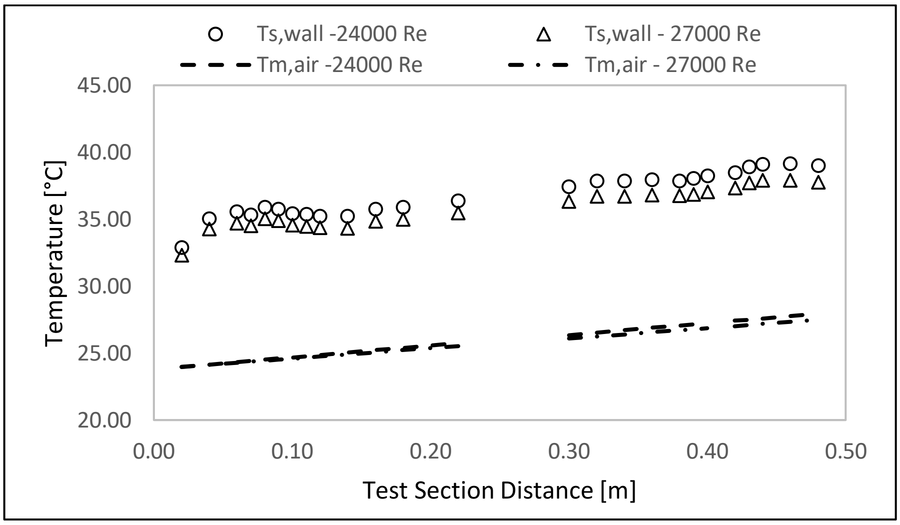

Figure D.57: Test Section Temperatures for Insert 3.1 at Re = 24000 and Re = 27000

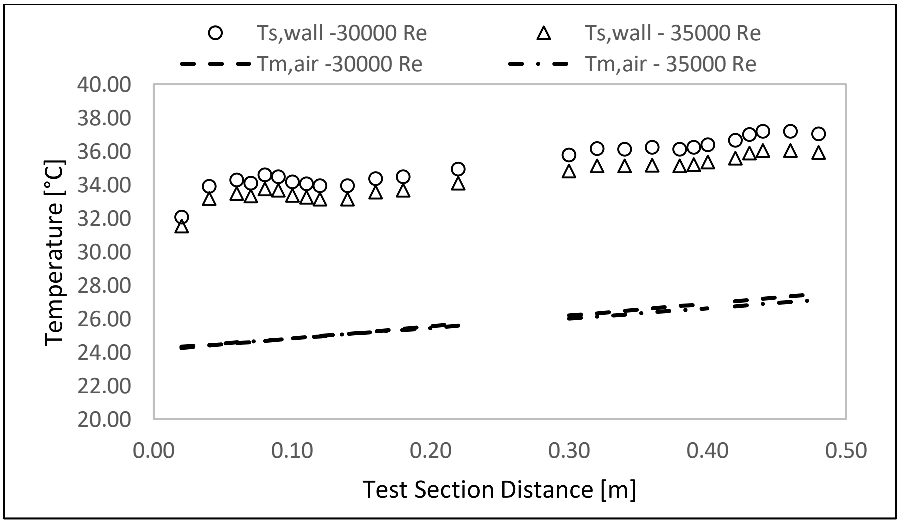

Figure D.58: Test Section Temperatures for Insert 3.1 at Re = 30000 and Re = 35000

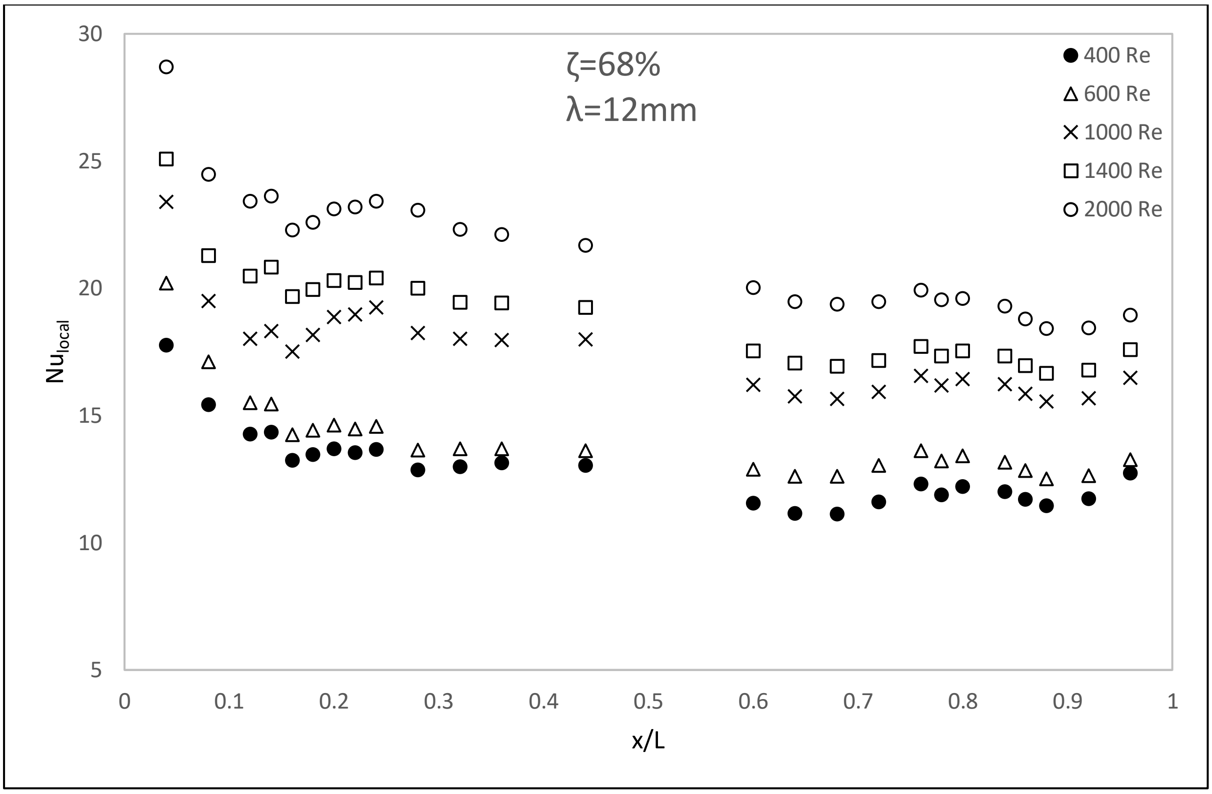
ζ=68%
λ=12mm
● 400 Re
△ 600 Re
× 1000 Re
□ 1400 Re
○ 2000 Re
Nu_{local}
x/L
30
25
20
15
10
5
0
0.1
0.2
0.3
0.4
0.5
0.6
0.7
0.8
0.9
1

(a)

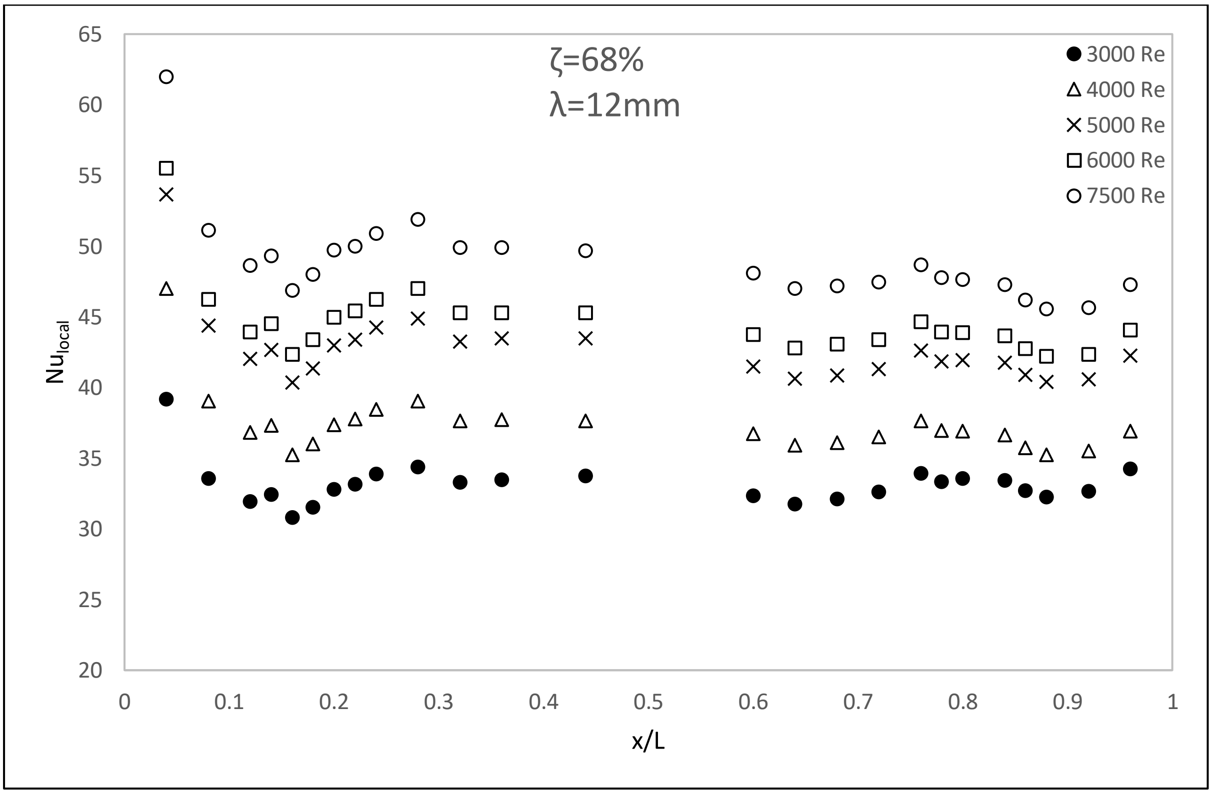
ζ=68%
λ=12mm
● 3000 Re
△ 4000 Re
× 5000 Re
□ 6000 Re
○ 7500 Re
Nu_{local}
x/L
65
60
55
50
45
40
35
30
25
20
0
0.1
0.2
0.3
0.4
0.5
0.6
0.7
0.8
0.9
1

(b)

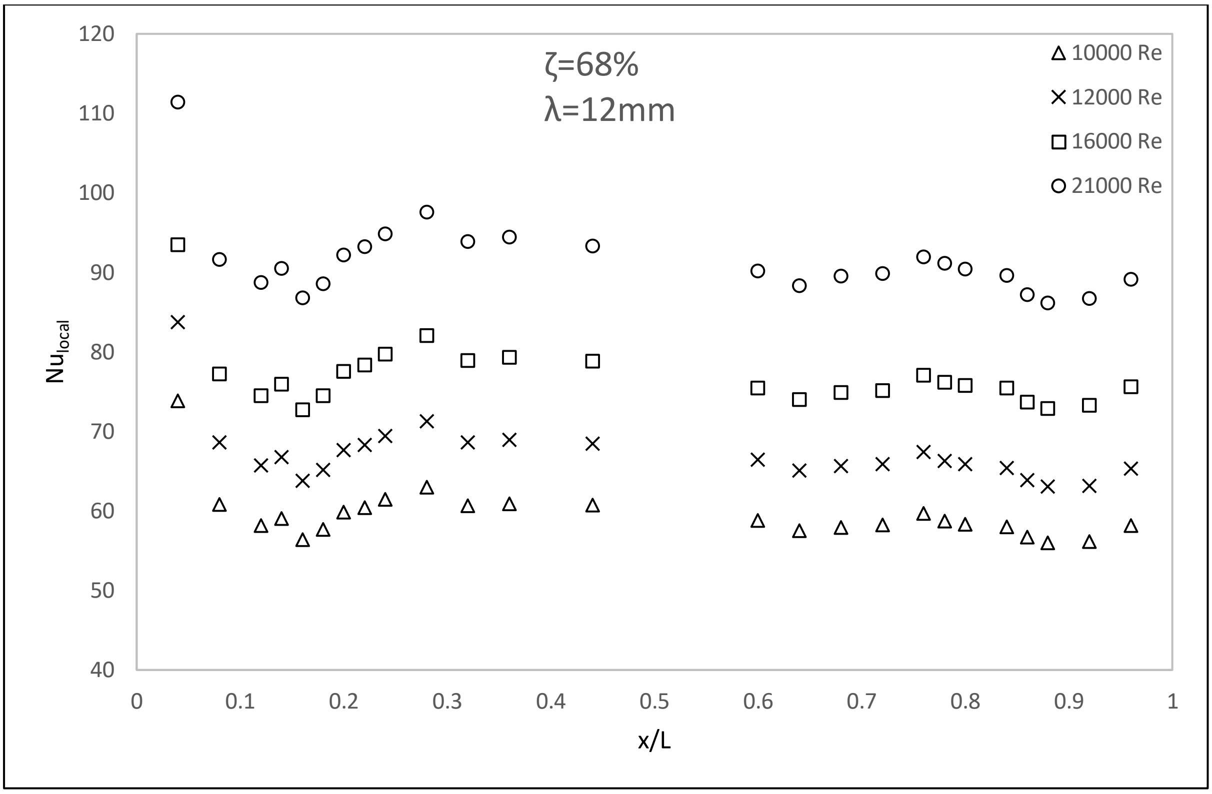

(c)

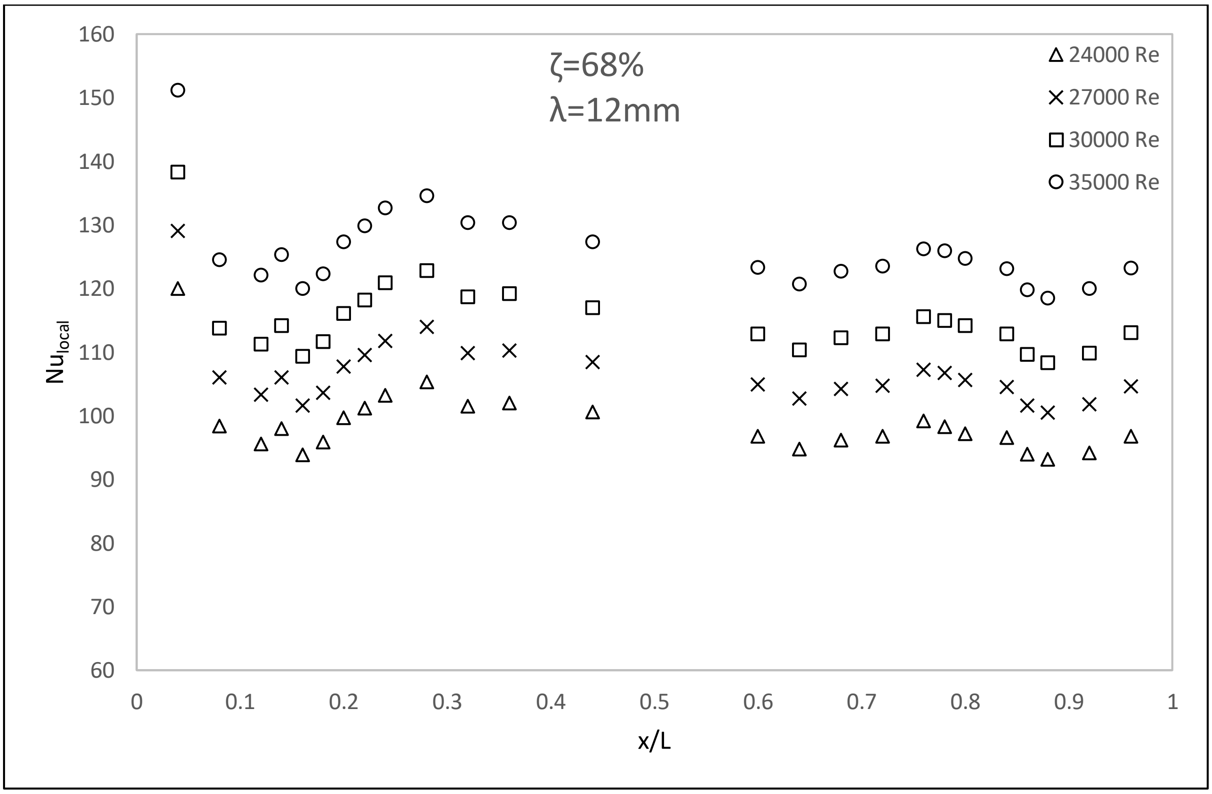

(d)

Figure D.59: Insert 3.1 (ζ = 68%, λ = 12 mm) test section centreline local Nusselt number with two walls heated for Reynolds number range: (a) 400 < Re < 2000, (b) 3000 < Re < 7500, (c) 10000 < Re < 21000 and (d) 24000 < Re < 35000

D.8. Mesh 3.2 (λ = 12 mm, ξ = 48 %)

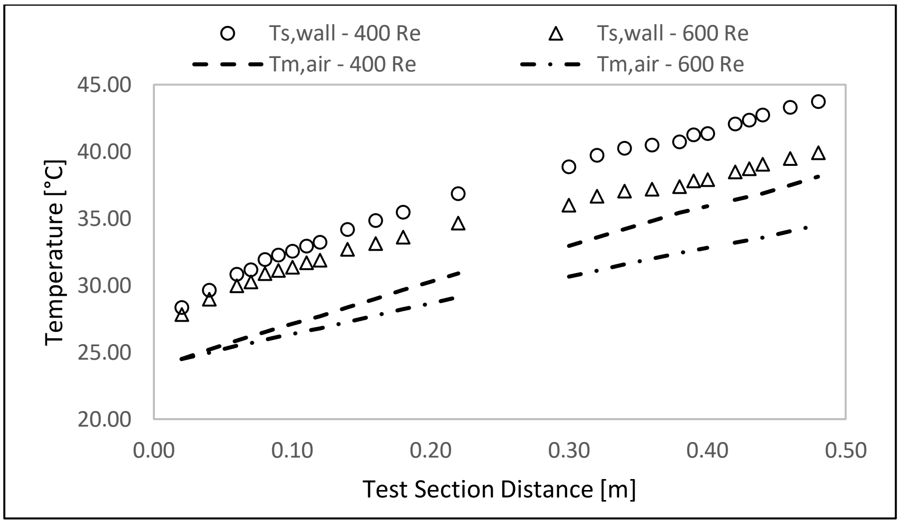

Figure D.60: Test Section Temperatures for Insert 3.2 at Re = 400 and Re = 600

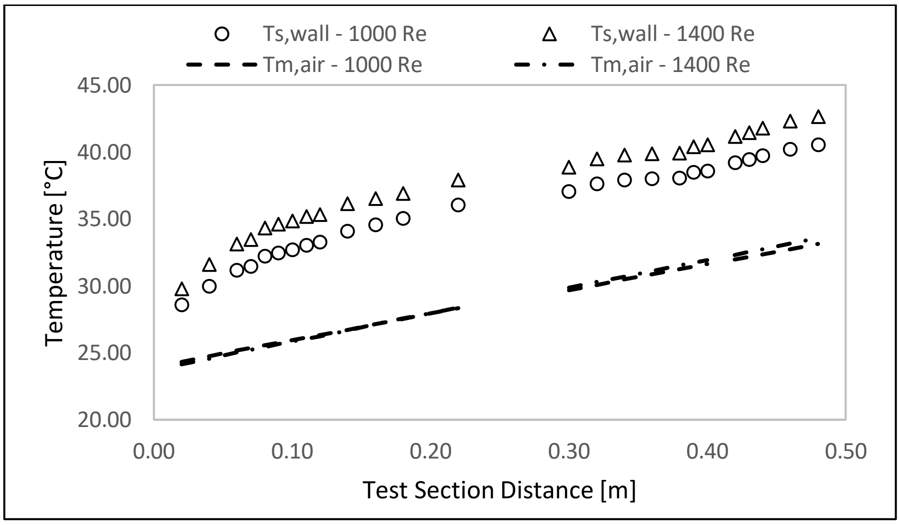

Figure D.61: Test Section Temperatures for Insert 3.2 at Re = 1000 and Re = 1400

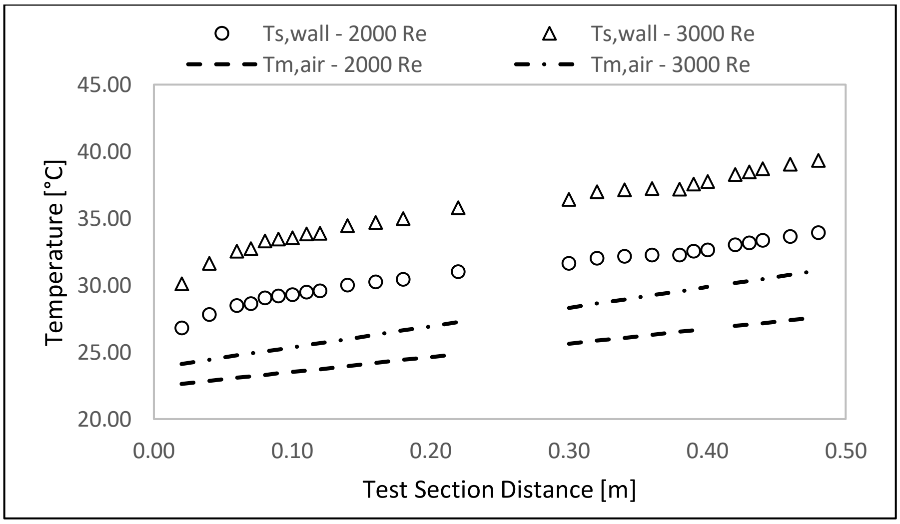

Figure D.62: Test Section Temperatures for Insert 3.2 at Re = 2000 and Re = 3000

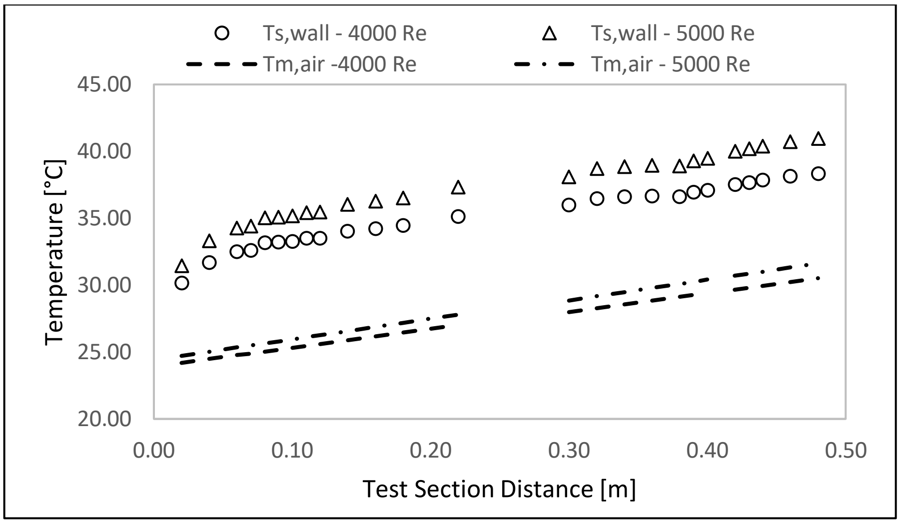

Figure D.63: Test Section Temperatures for Insert 3.2 at Re = 4000 and Re = 5000

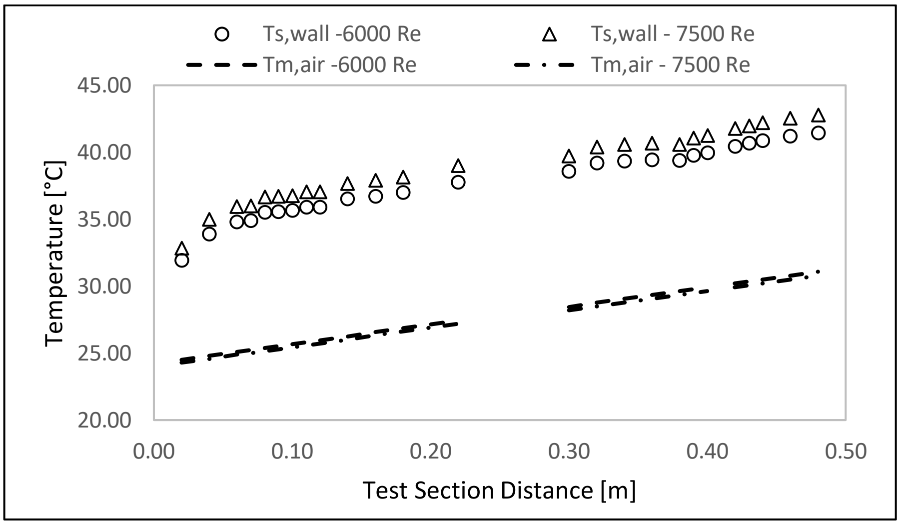

Figure D.64: Test Section Temperatures for Insert 3.2 at Re = 6000 and Re = 7500

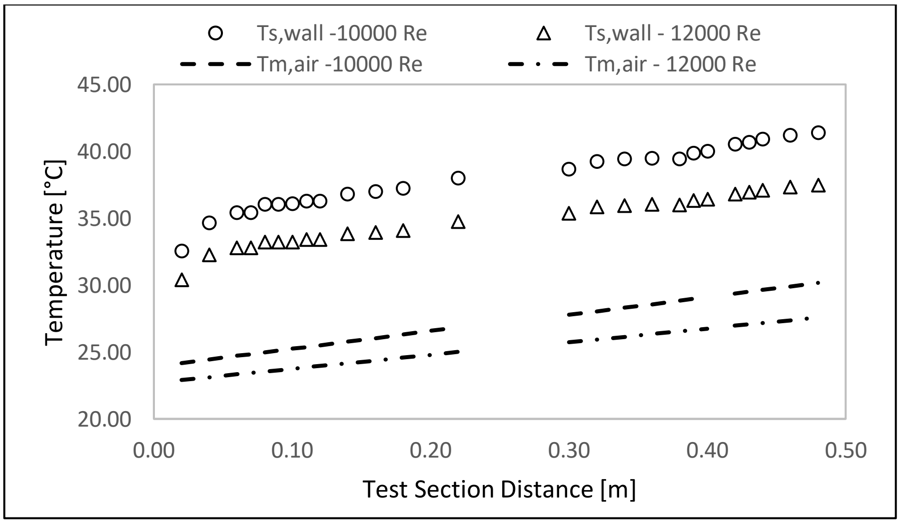

Figure D.65: Test Section Temperatures for Insert 3.2 at Re = 10000 and Re = 12000

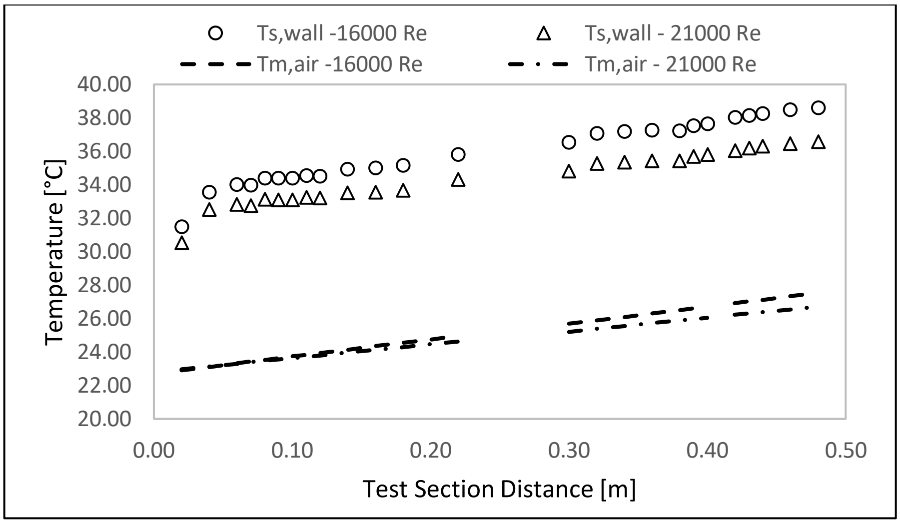

Figure D.66: Test Section Temperatures for Insert 3.2 at Re = 6000 and Re = 21000

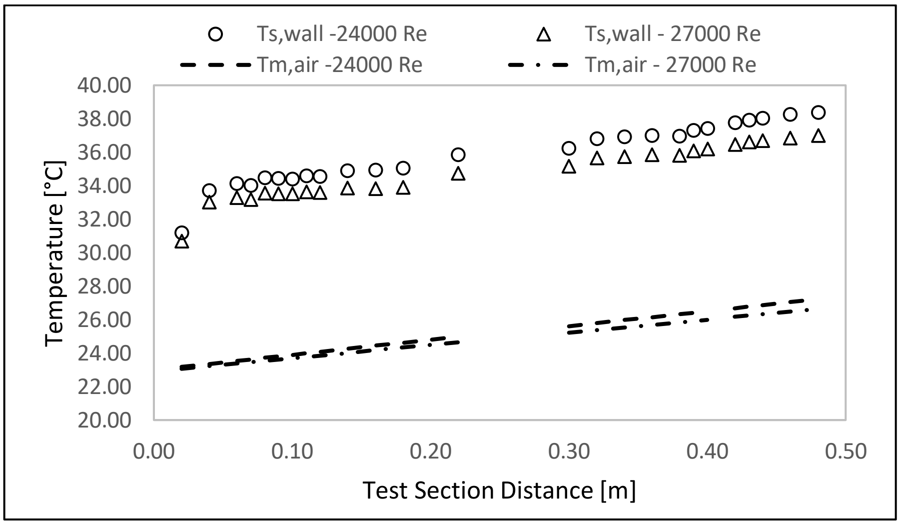

Figure D.67: Test Section Temperatures for Insert 3.2 at Re = 24000 and Re = 27000

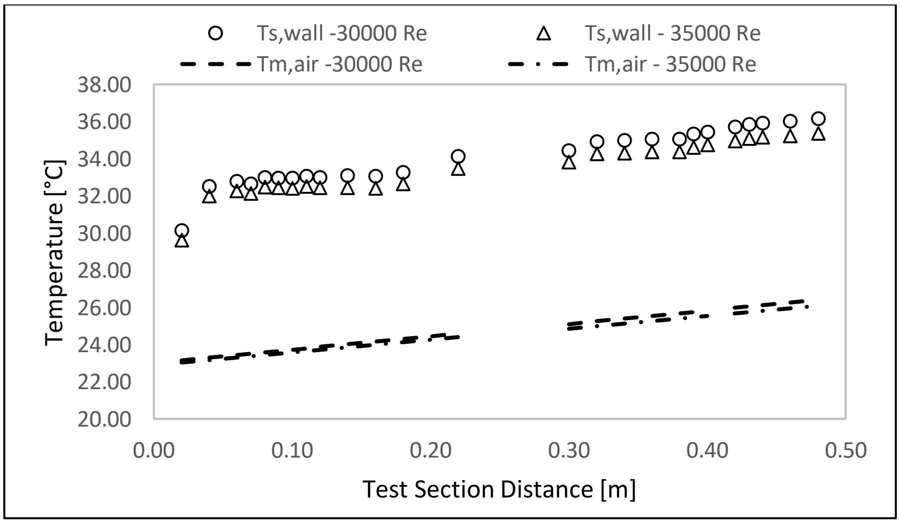

Figure D.68: Test Section Temperatures for Insert 3.2 at Re = 30000 and Re = 35000

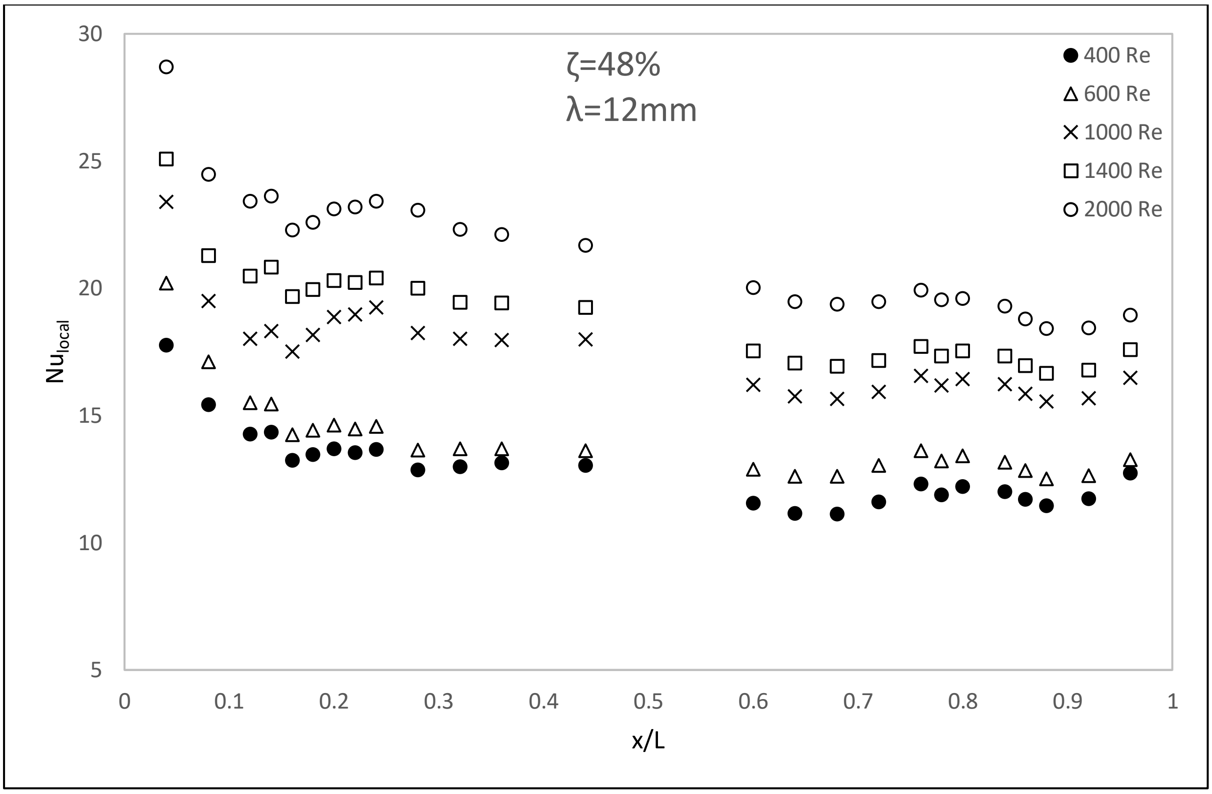
ζ=48%
λ=12mm
● 400 Re
△ 600 Re
× 1000 Re
□ 1400 Re
○ 2000 Re
Nu_{local}
x/L
30
25
20
15
10
5
0
0.1
0.2
0.3
0.4
0.5
0.6
0.7
0.8
0.9
1

(a)

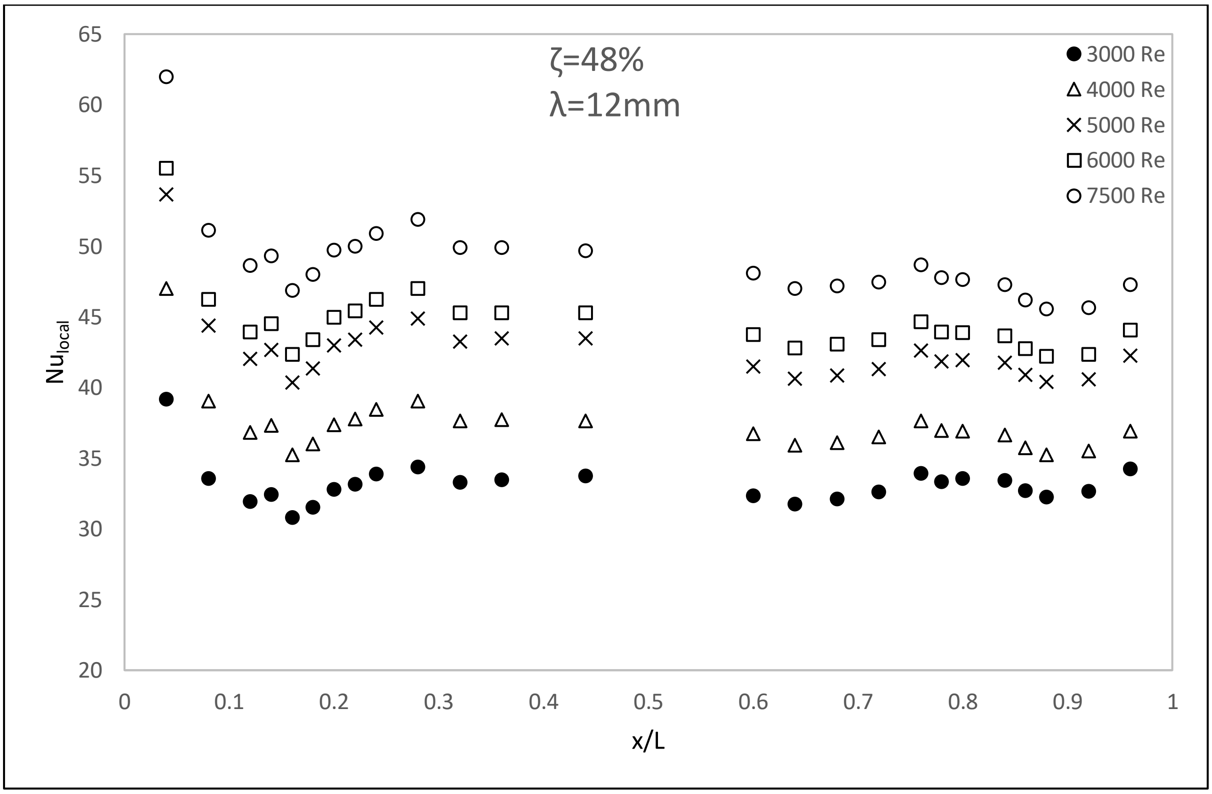
ζ=48%
λ=12mm
● 3000 Re
△ 4000 Re
× 5000 Re
□ 6000 Re
○ 7500 Re
Nu_{local}
x/L
65
60
55
50
45
40
35
30
25
20
0
0.1
0.2
0.3
0.4
0.5
0.6
0.7
0.8
0.9
1

(b)

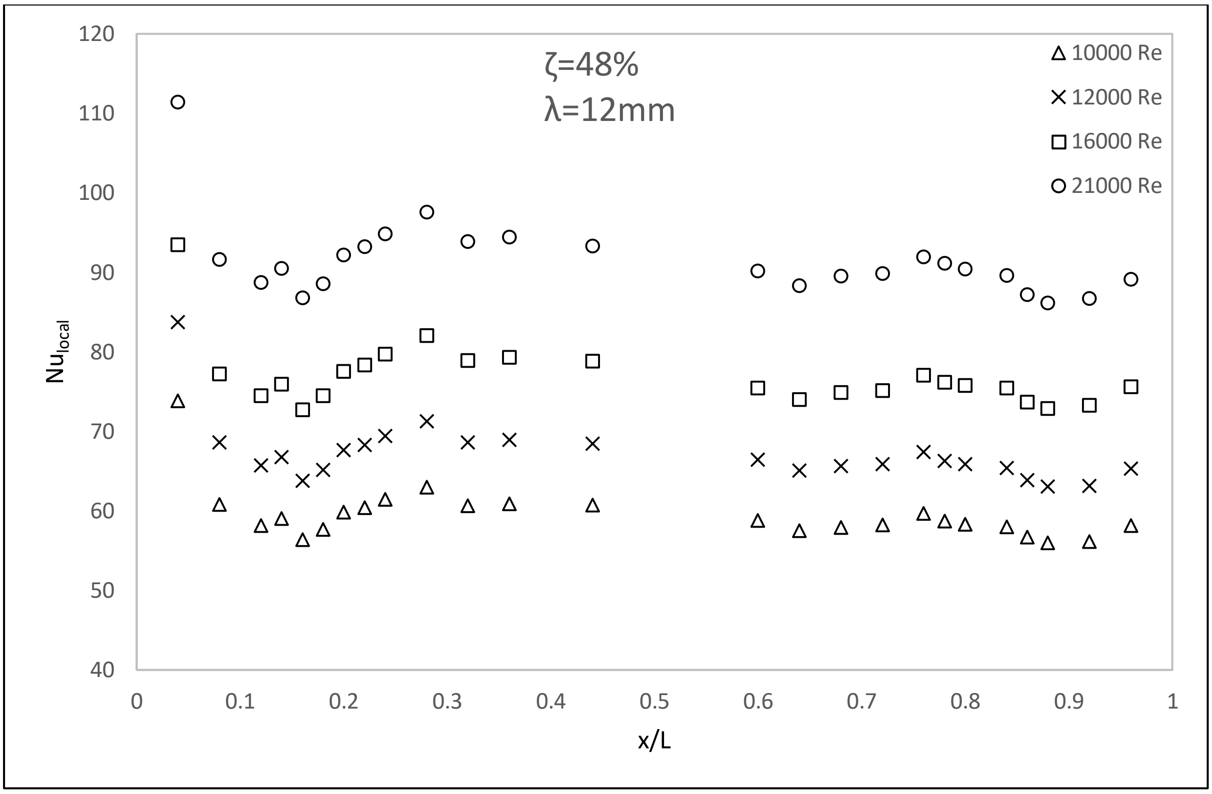

(c)

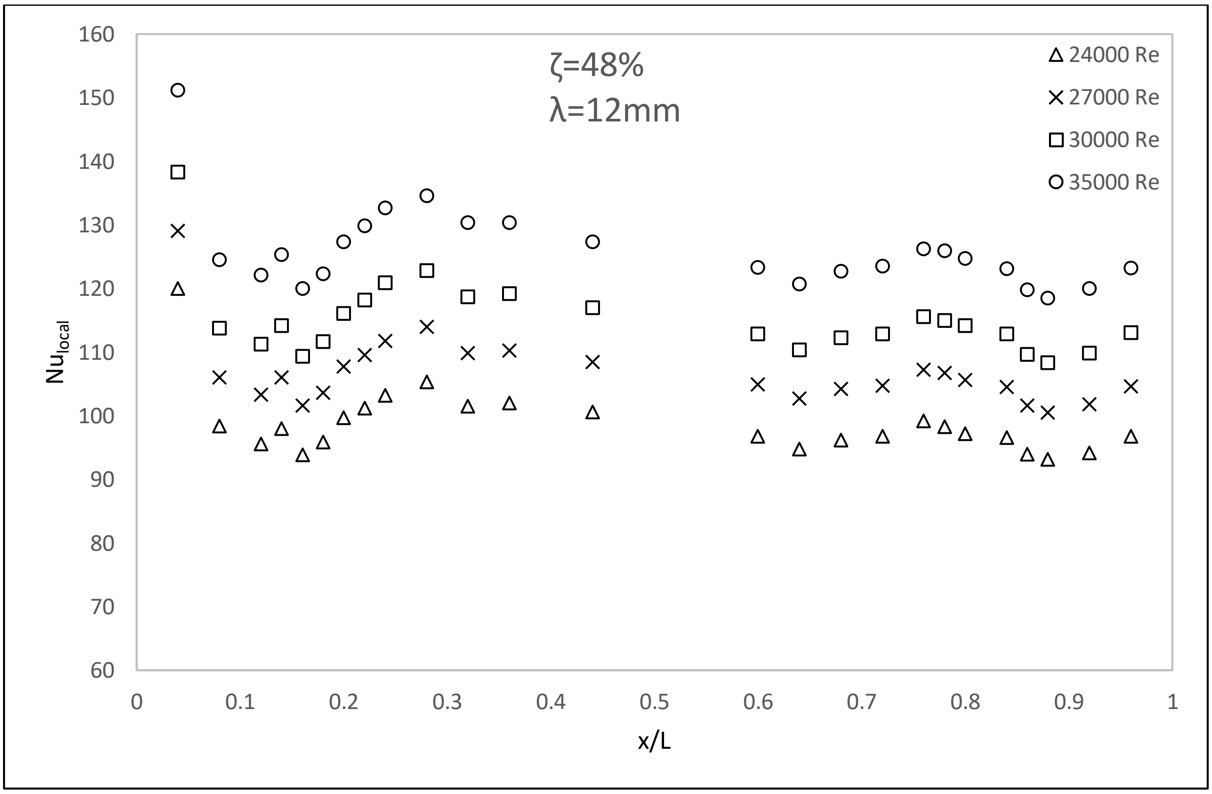

(d)

Figure D.69: Insert 3.2 (ζ = 48%, λ = 12 mm) test section centreline local Nusselt number with two walls heated for Reynolds number range: (a) 400 < Re < 2000, (b) 3000 < Re < 7500, (c) 10000 < Re < 21000 and (d) 24000 < Re < 35000

D.9. Effects of Porosity on Nu_{avg} and Nu/Nu_0

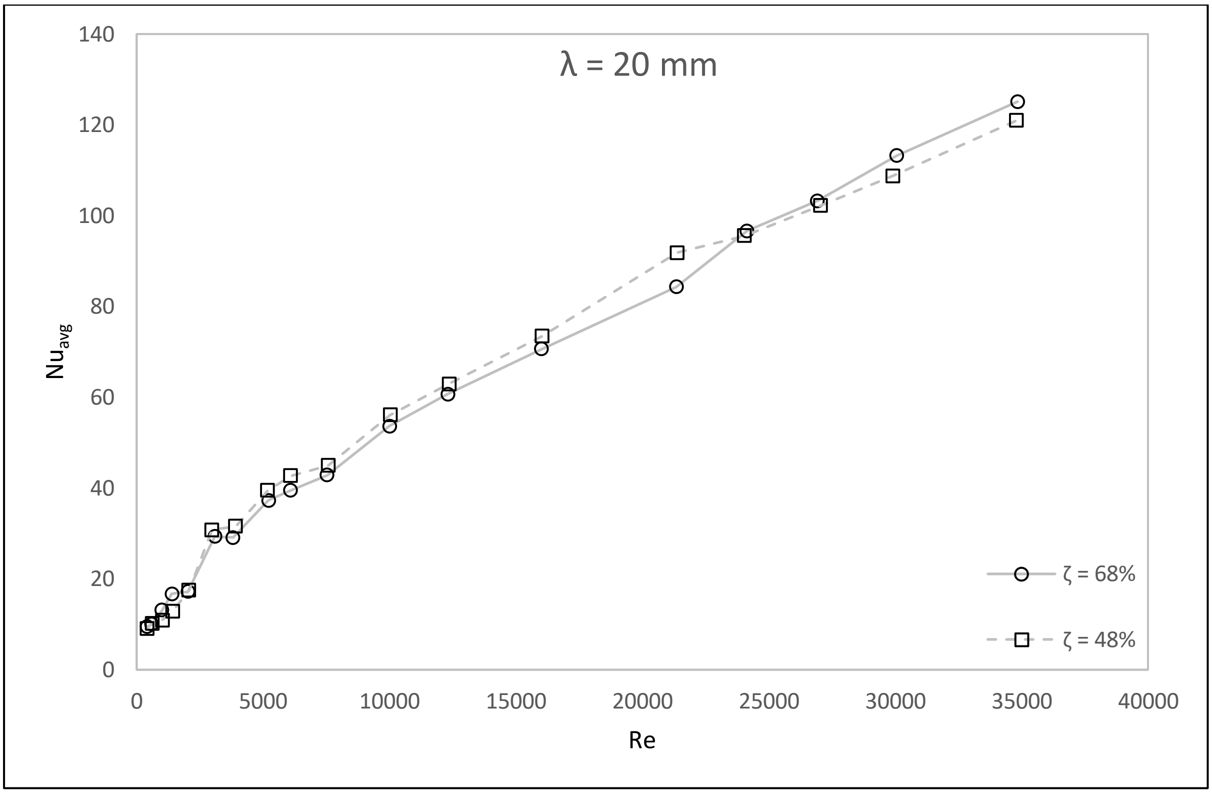

(a)

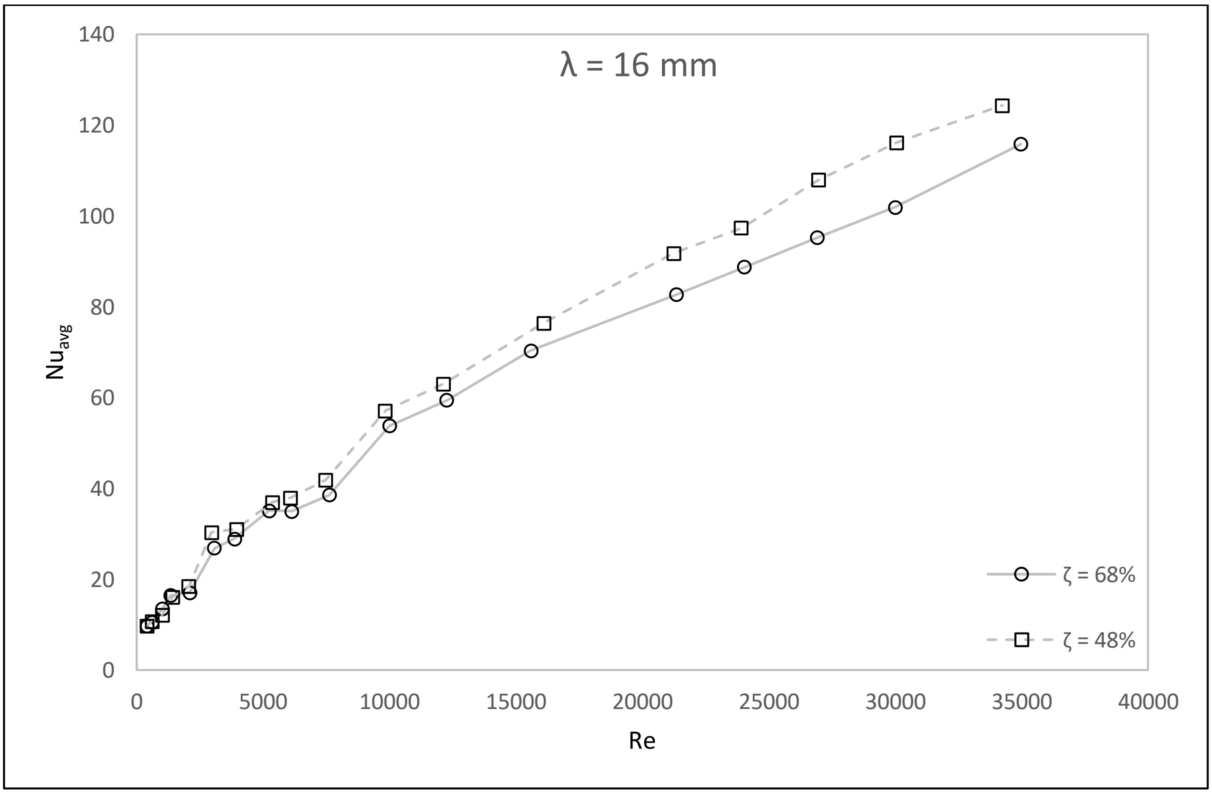

(b)

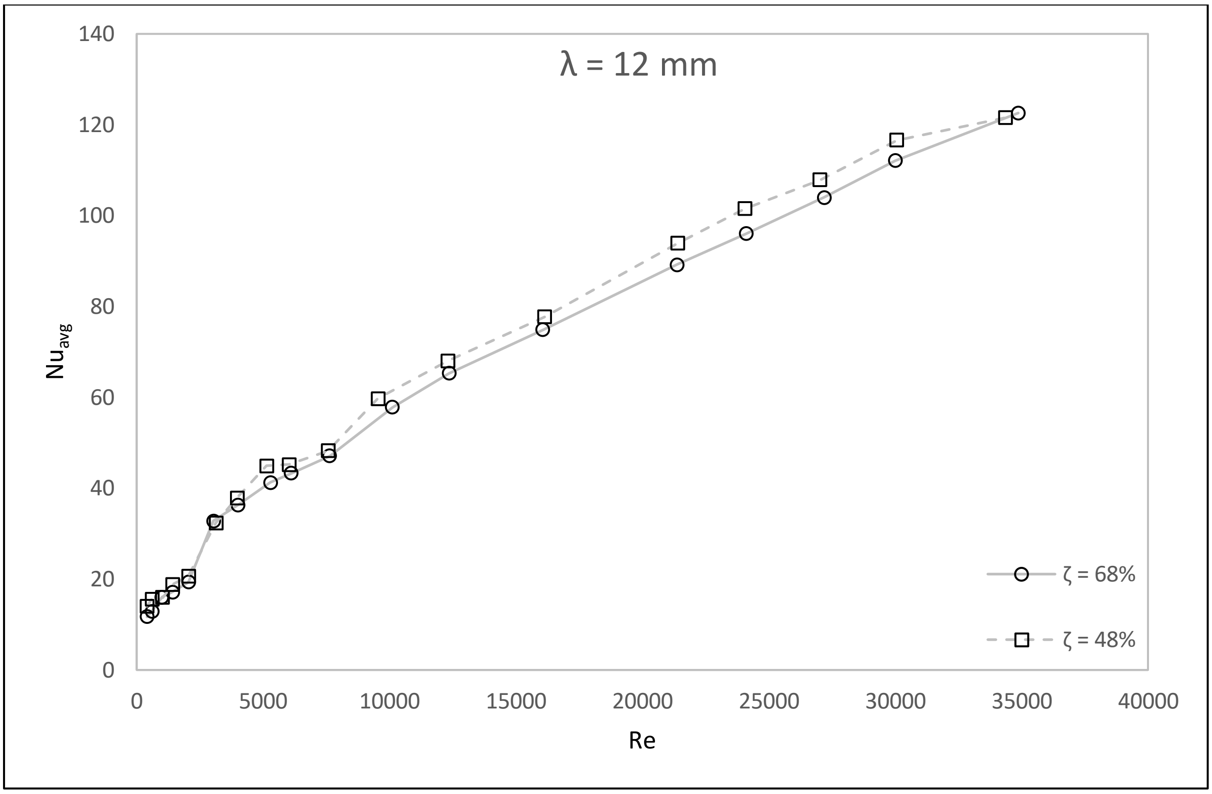

(c)

Figure D.70: Average Nusselt number, Nu$_{avg}$ vs. Re for constant wavelength λ = (a) 20 mm, (b) 16 mm and (c) 12 mm

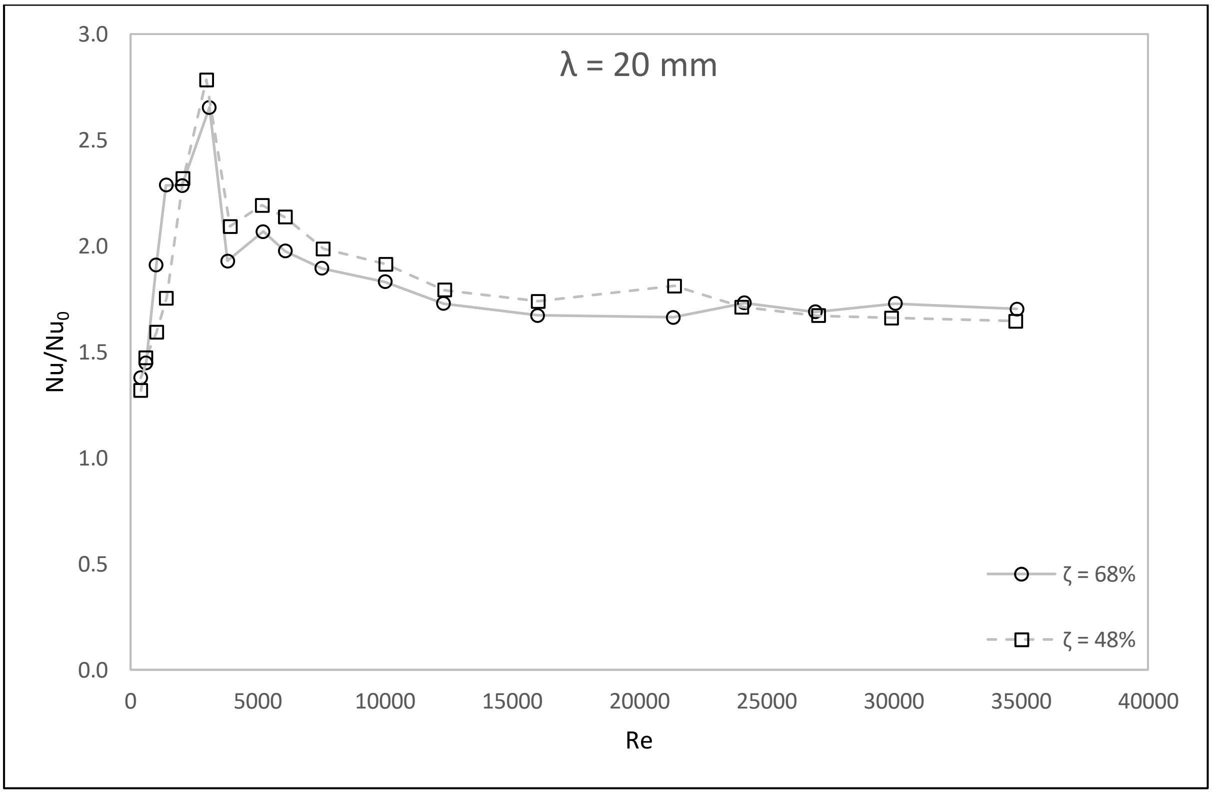

(a)

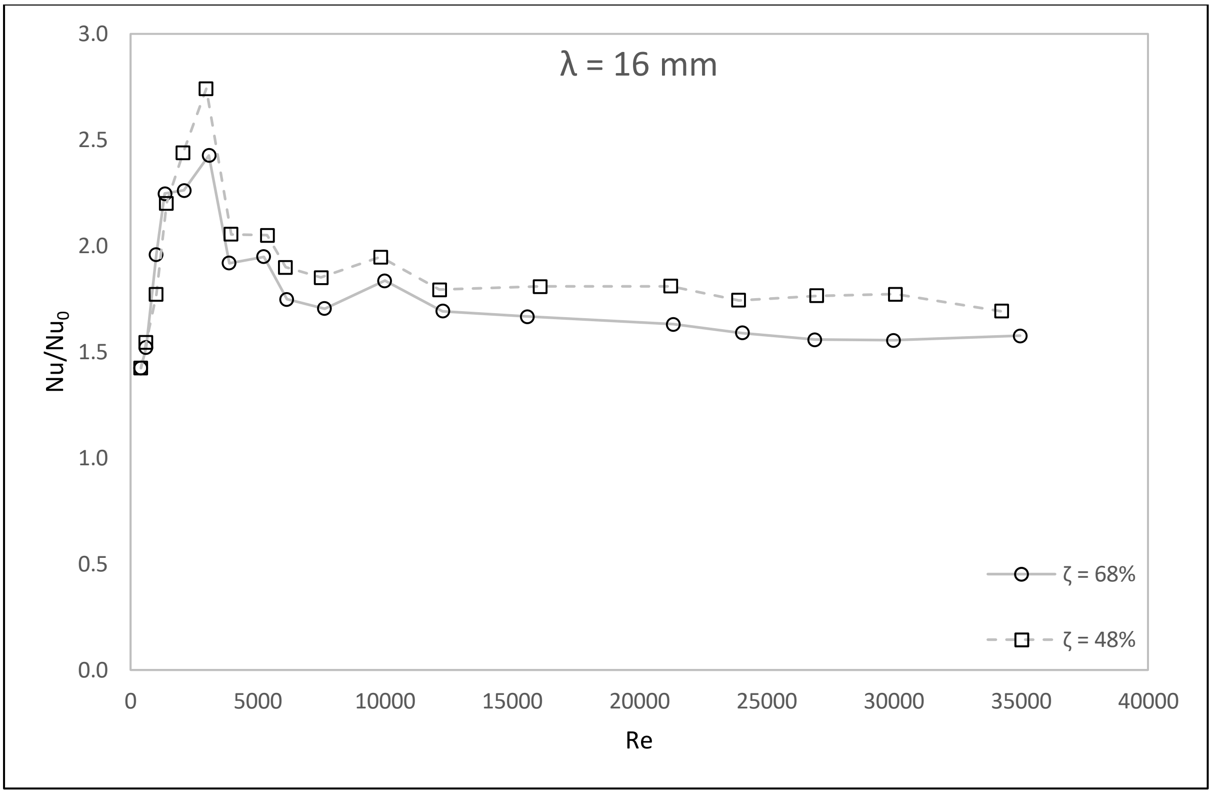

(b)

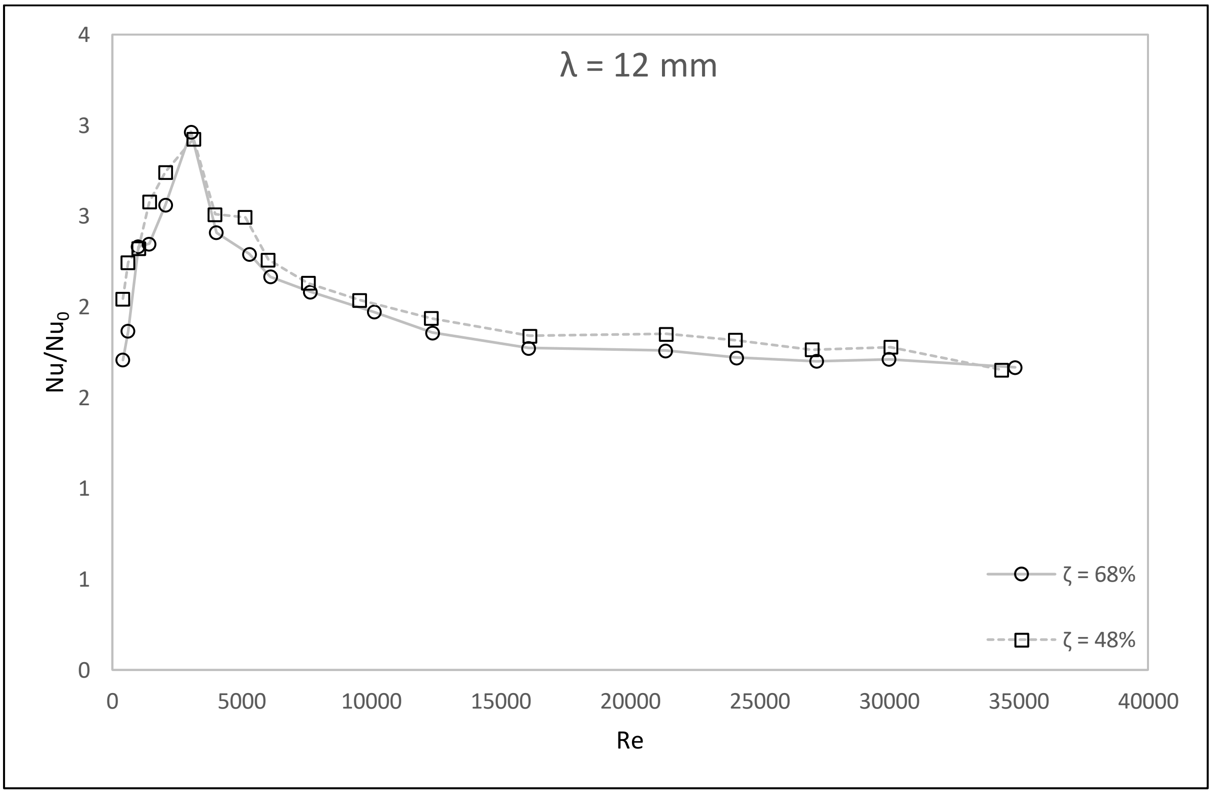

(c)

Figure D.71: Nusselt number ratio, Nu/Nu$_0$ vs. Re for constant wavelength λ = (a) 20 mm, (b) 16 mm and (c) 12 mm

D.10. Effects of Porosity on $(Nu/Nu_0)/(f/f_0)^{1/3}$

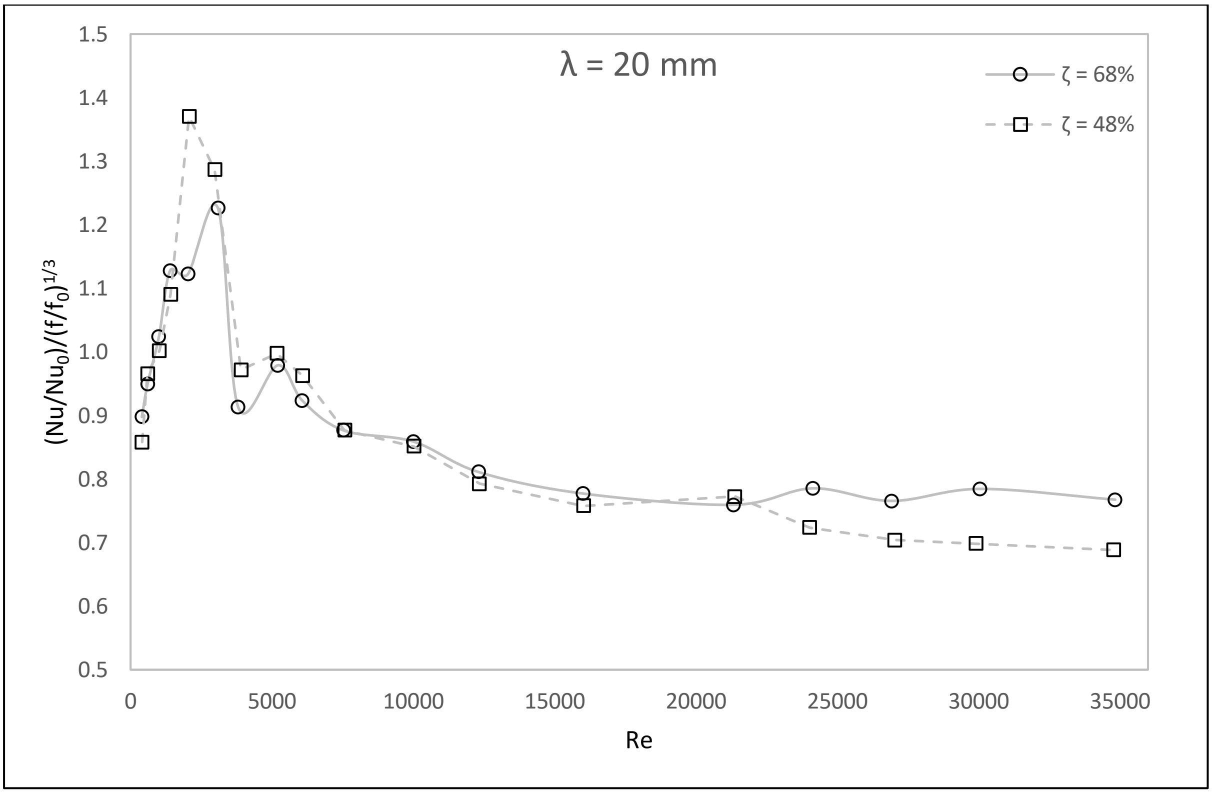

(a)

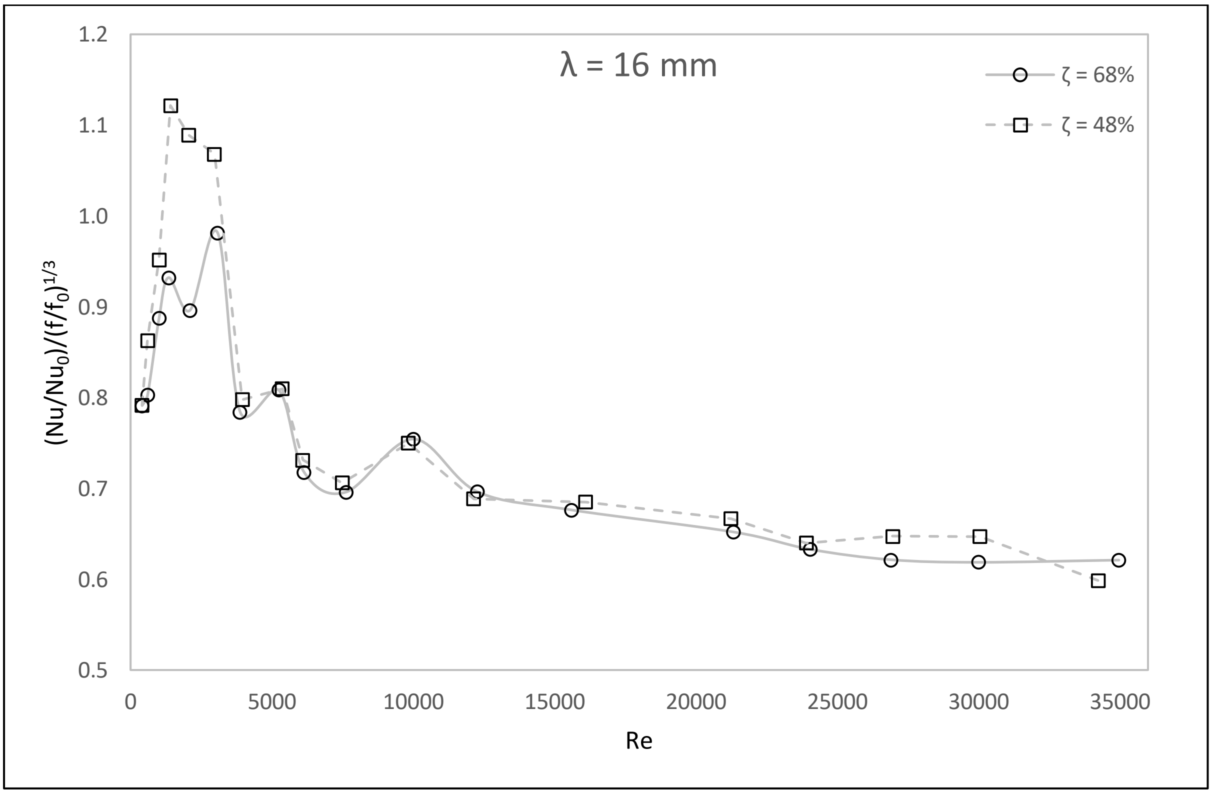

(b)

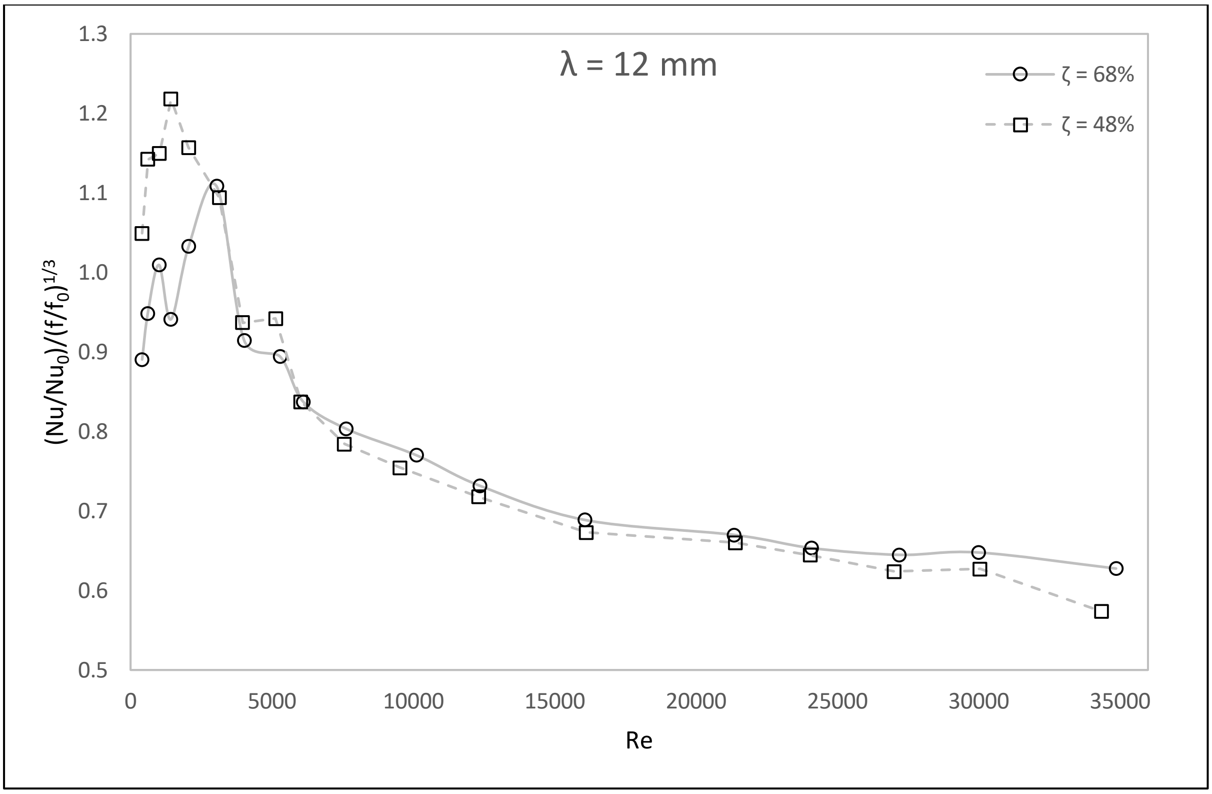

(c)

Figure D.72: Performance index, $(Nu/Nu_0)/(f/f_0)^{1/3}$ vs. Re for constant wavelength λ = (a) 20 mm, (b) 16 mm and (c) 12 mm

Appendix E: One Wall Heat Transfer Data

E.1. Introduction

This appendix includes the test section wall temperature data used in determining the local Nusselt along the test section channel for the one wall heating experiments. Results are shown for each experiment conducted throughout the course of the research.

E.2. Baseline

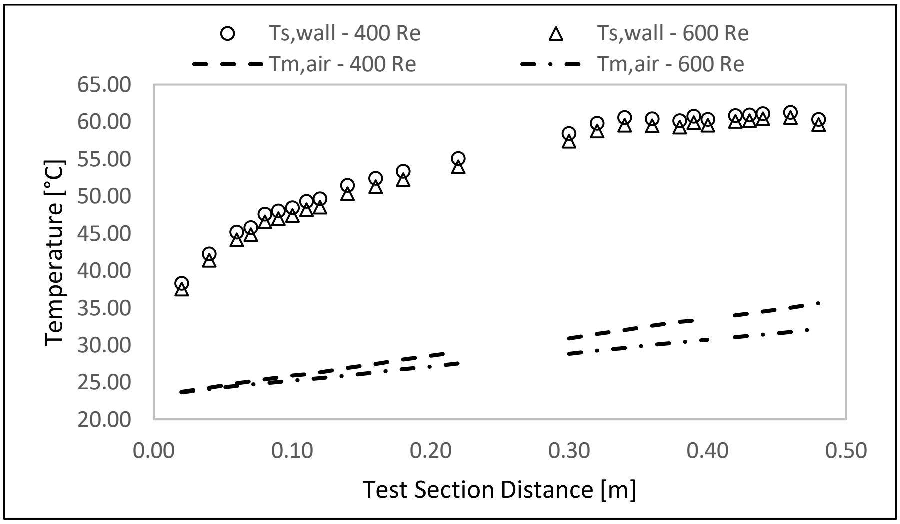

Figure E.1: Base Line Test Section Temperatures at Re = 400 and Re = 600

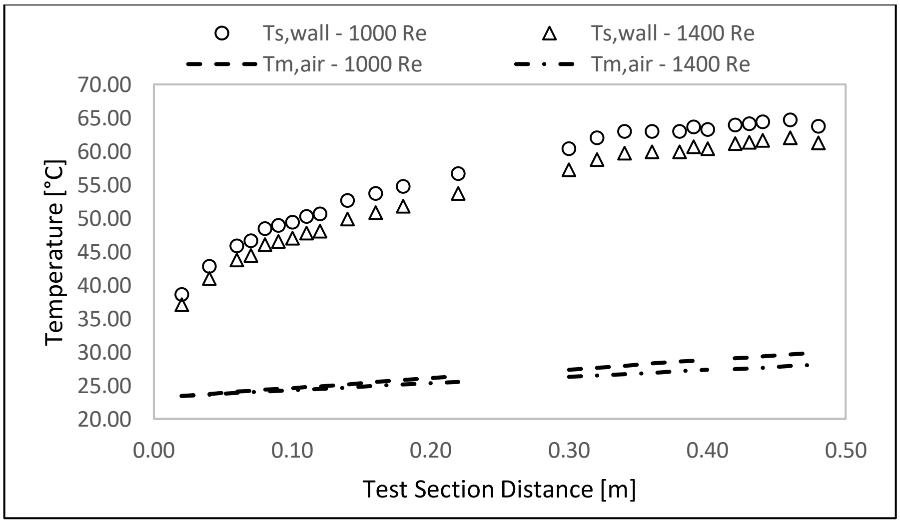

Figure E.2: Base Line Test Section Temperatures at Re = 1000 and Re = 1400

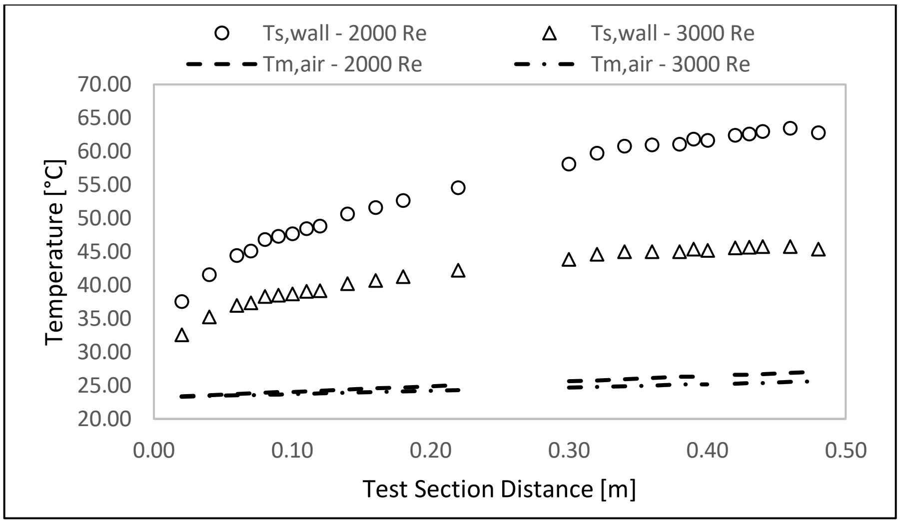

Figure E.3: Base Line Test Section Temperatures at Re = 2000 and Re = 3000

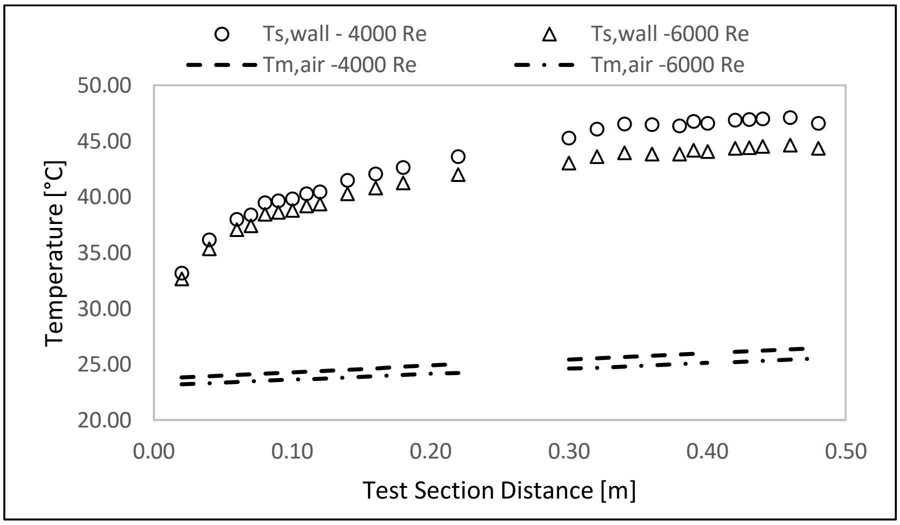

Figure E.4: Base Line Test Section Temperatures at Re = 4000 and Re = 6000

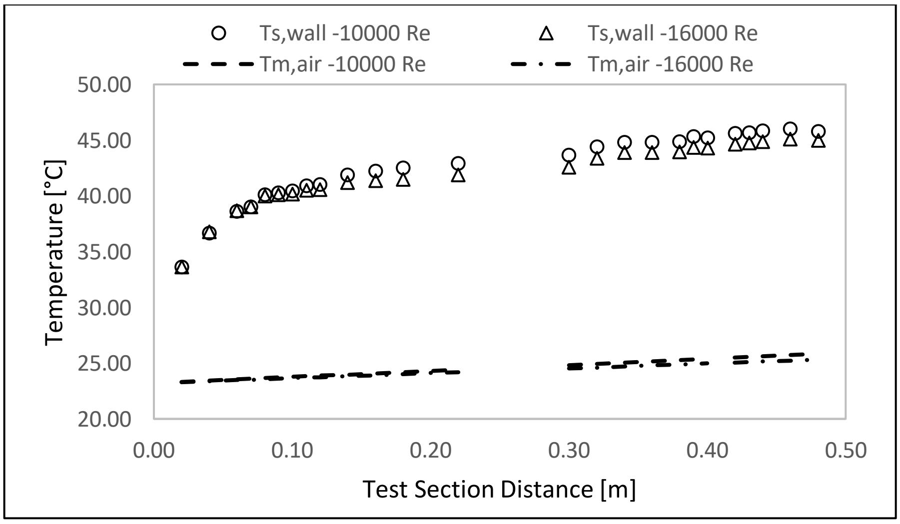

Figure E.5: Base Line Test Section Temperatures at Re = 10000 and Re = 16000

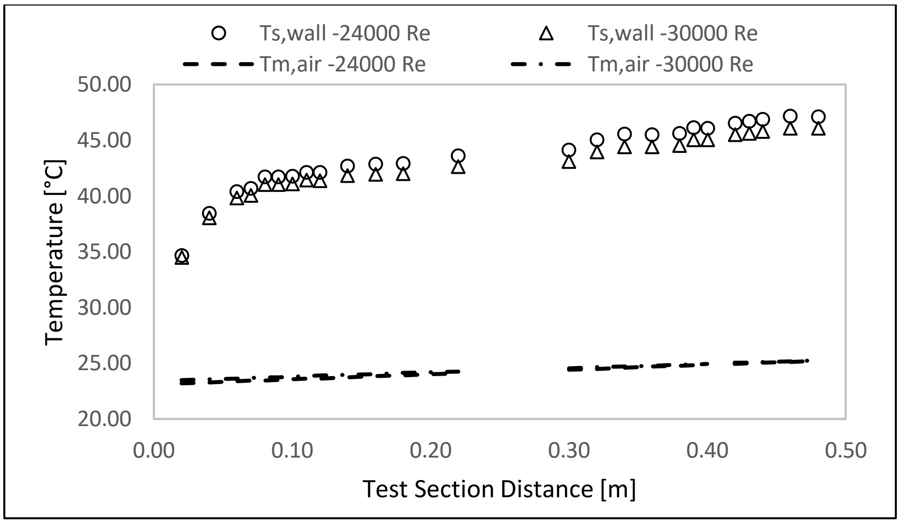

Figure E.6: Base Line Test Section Temperatures at Re = 24000 and Re = 30000

E.3. Mesh 1.1 (λ = 20 mm, ξ = 68 %)

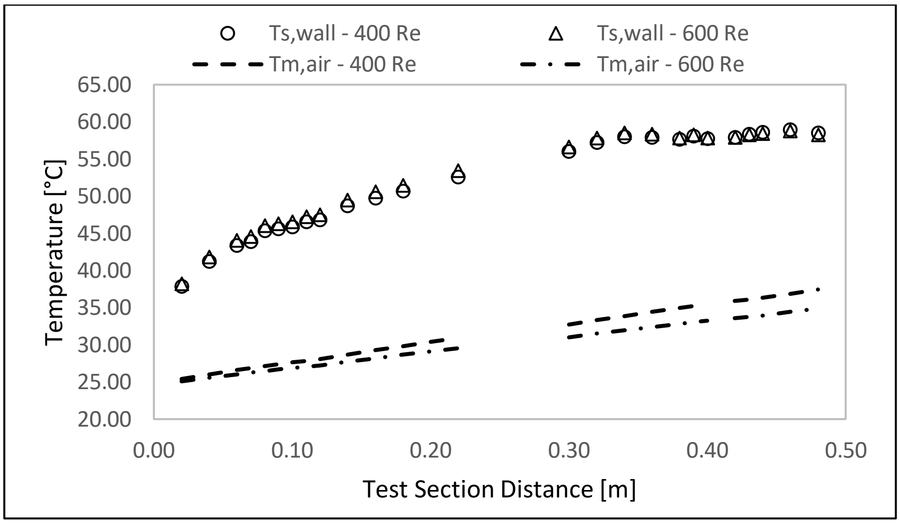

Figure E.7: Test Section Temperatures for Insert 1.1 at Re = 400 and Re = 600

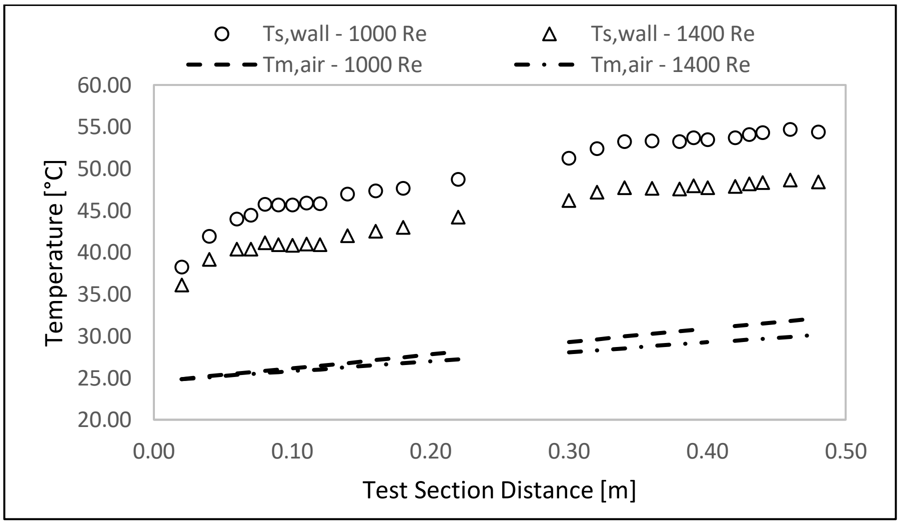

Figure E.8: Test Section Temperatures for Insert 1.1 at Re = 1000 and Re = 1400

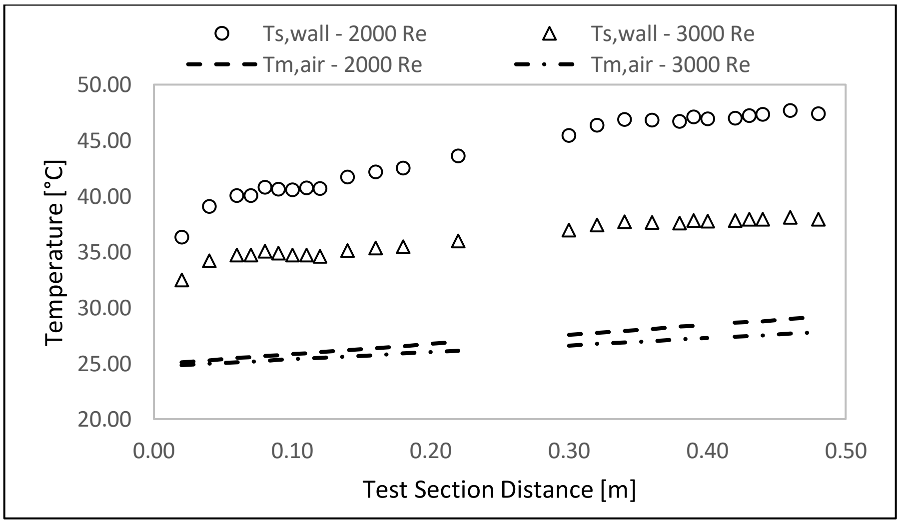

Figure E.9: Test Section Temperatures for Insert 1.1 at Re = 2000 and Re = 3000

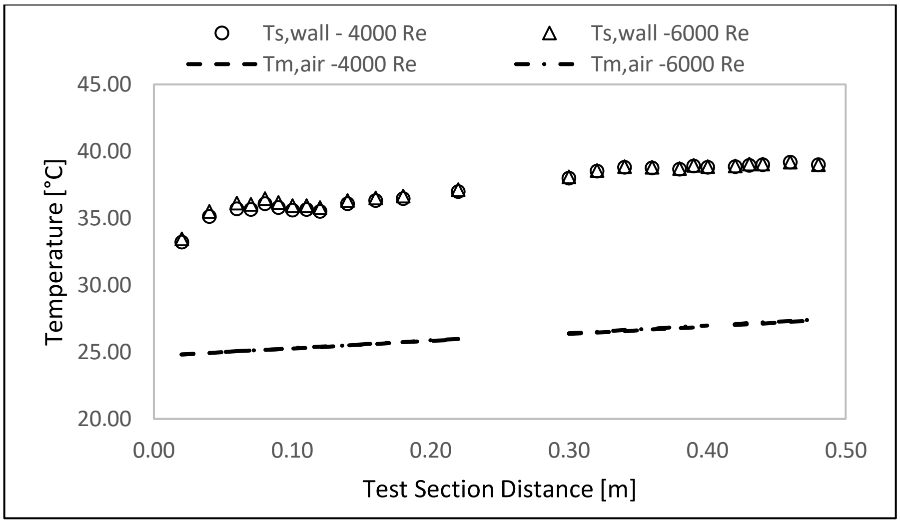

Figure E.10: Test Section Temperatures for Insert 1.1 at Re = 4000 and Re = 6000

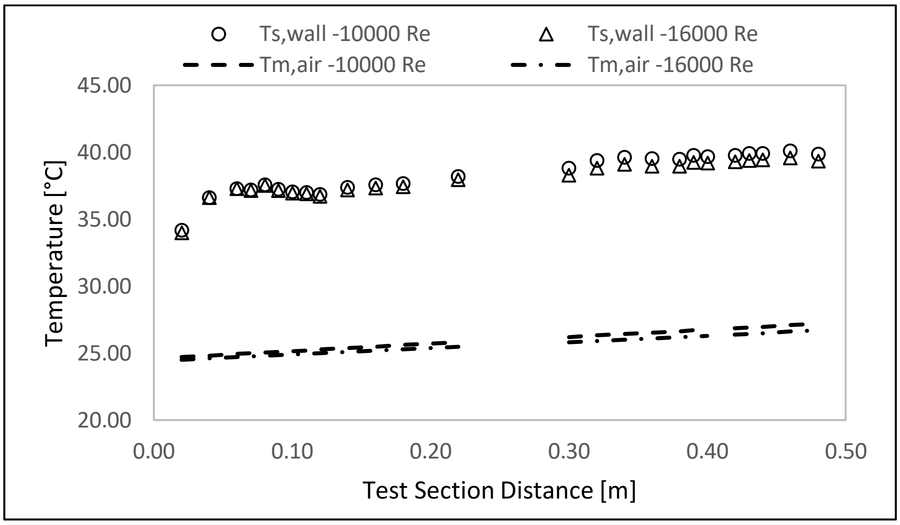

Figure E.11: Test Section Temperatures for Insert 1.1 at Re = 10000 and Re = 16000

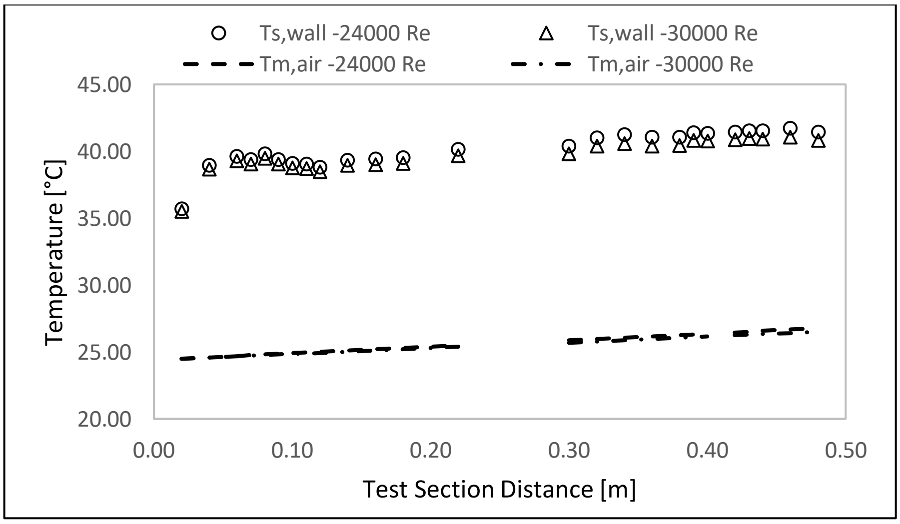

Figure E.12: Test Section Temperatures for Insert 1.1 at Re = 24000 and Re = 30000

E.4. Mesh 1.2 (λ = 20 mm, ξ = 48 %)

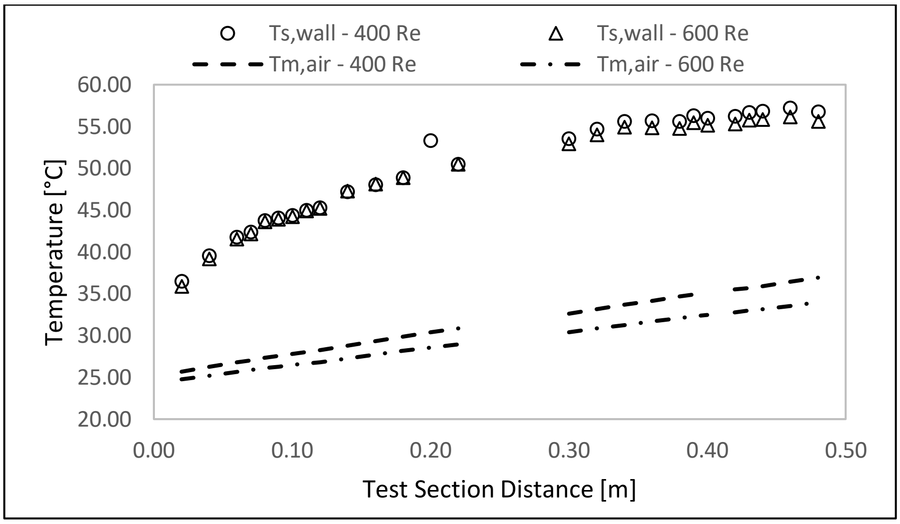

Figure E.13: Test Section Temperatures for Insert 1.2 at Re = 400 and Re = 600

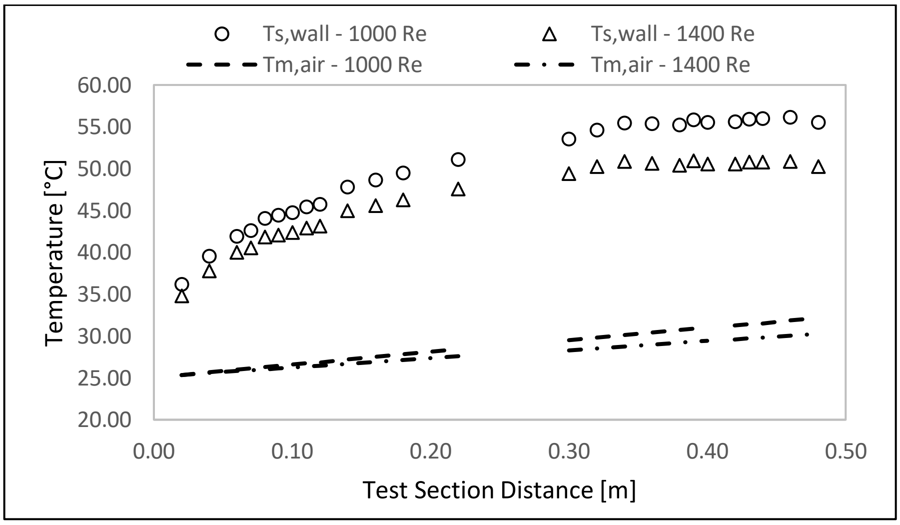

Figure E.14: Test Section Temperatures for Insert 1.2 at Re = 1000 and Re = 1400

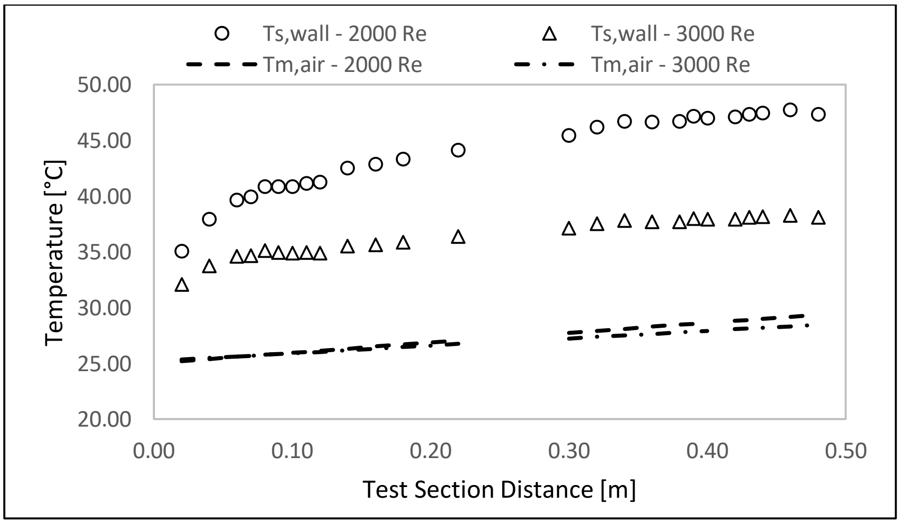

Figure E.15: Test Section Temperatures for Insert 1.2 at Re = 2000 and Re = 3000

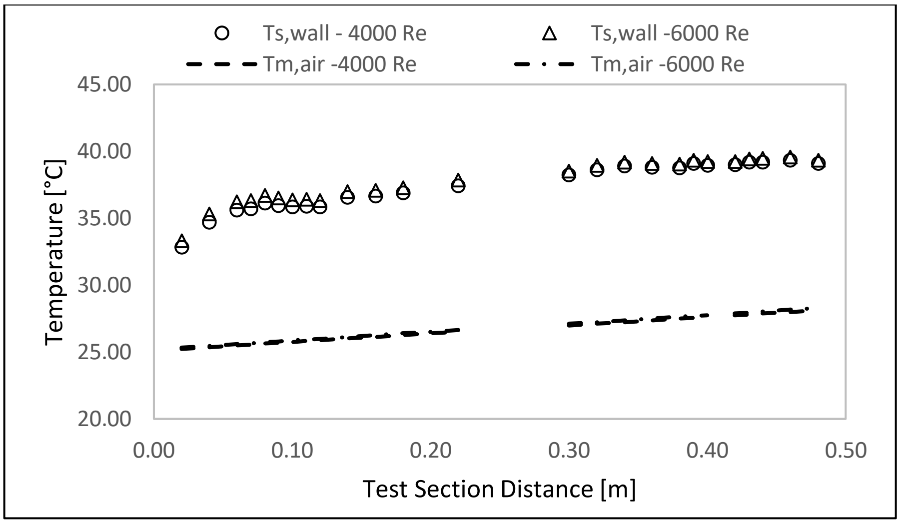

Figure E.16: Test Section Temperatures for Insert 1.2 at Re = 4000 and Re = 6000

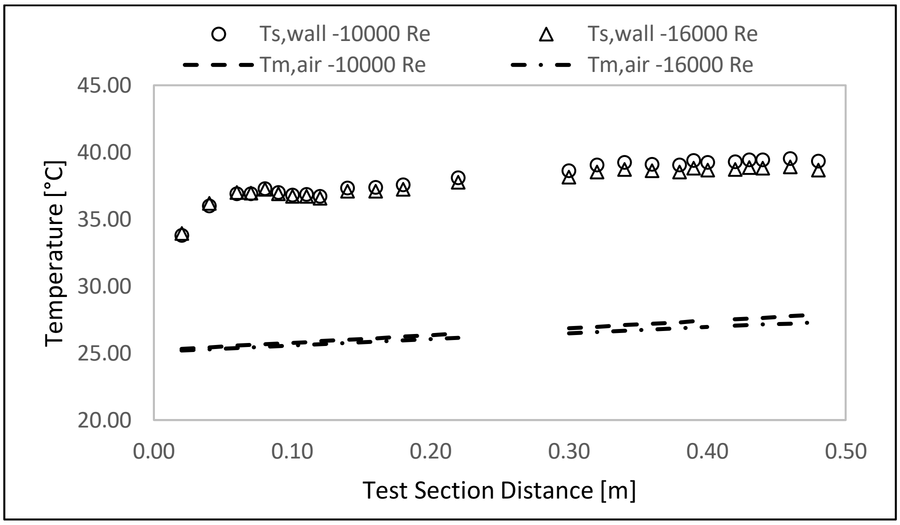

Figure E.17: Test Section Temperatures for Insert 1.2 at Re = 10000 and Re = 16000

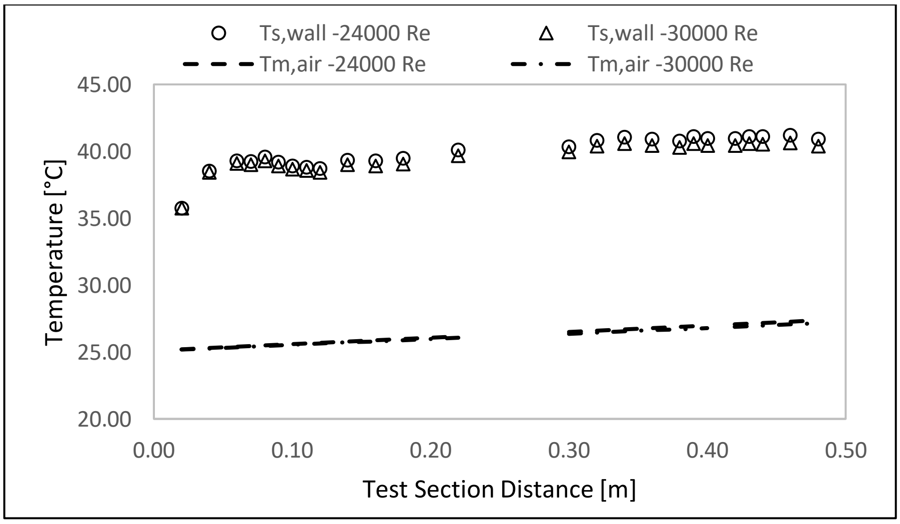

Figure E.18: Test Section Temperatures for Insert 1.2 at Re = 24000 and Re = 30000

E.5. Mesh 2.1 (λ = 16 mm, ξ = 68 %)

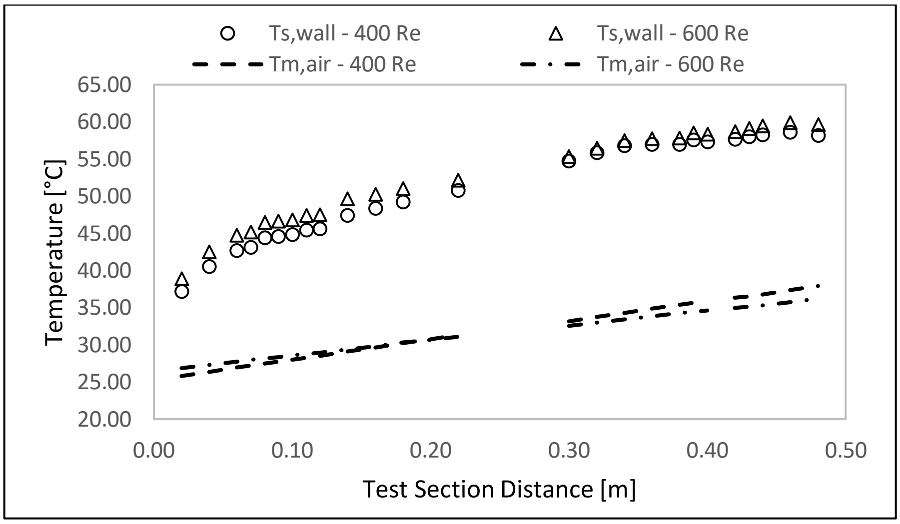

Figure E.19: Test Section Temperatures for Insert 2.1 at Re = 400 and Re = 600

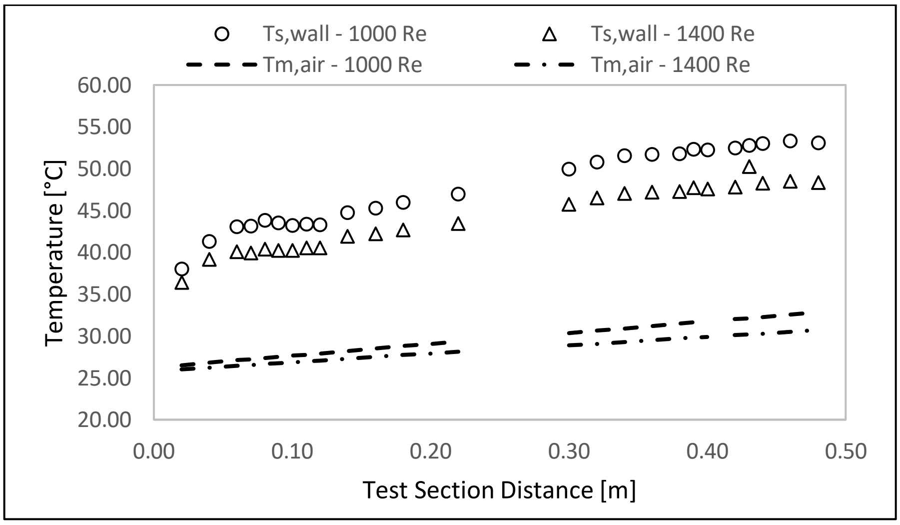

Figure E.20: Test Section Temperatures for Insert 2.1 at Re = 1000 and Re = 1400

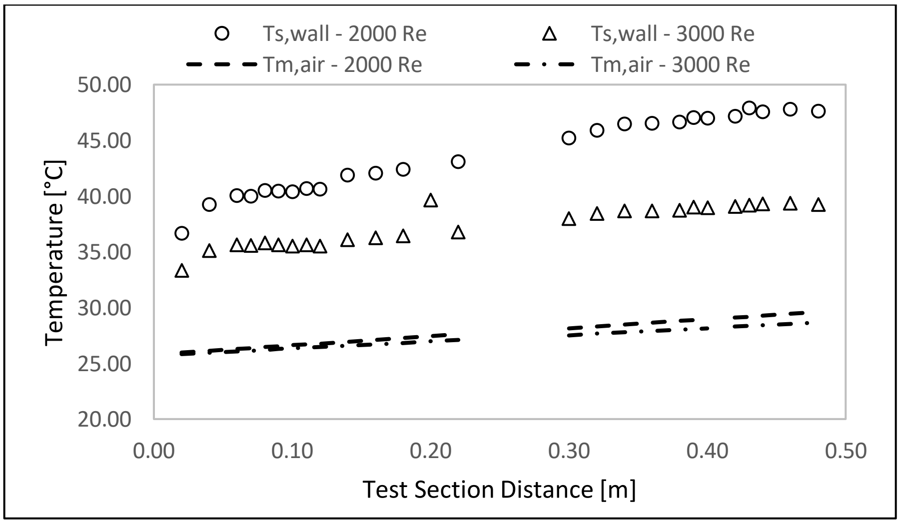

Figure E.21: Test Section Temperatures for Insert 2.1 at Re = 2000 and Re = 3000

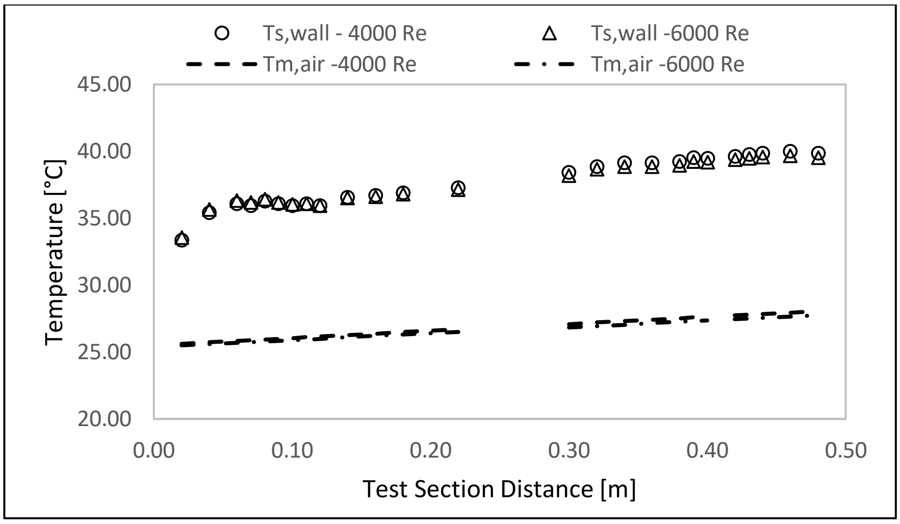

Figure E.22: Test Section Temperatures for Insert 2.1 at Re = 4000 and Re = 6000

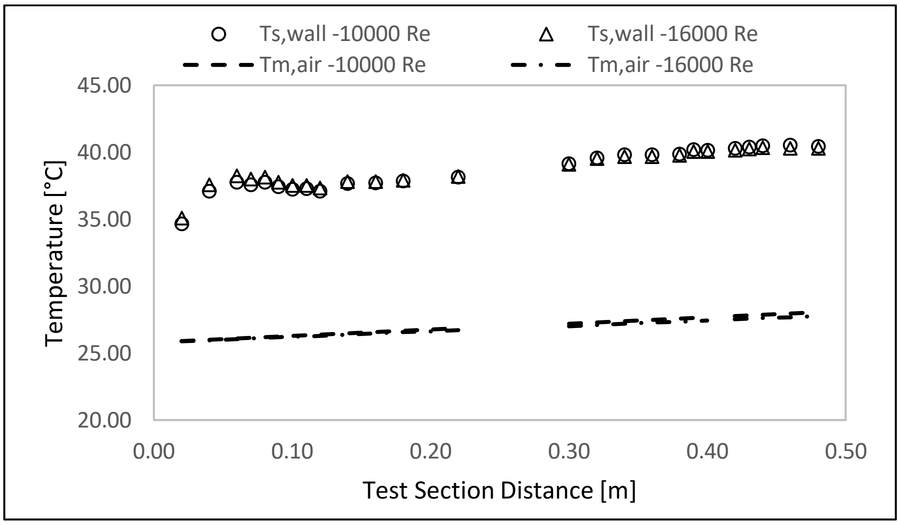

Figure E.23: Test Section Temperatures for Insert 2.1 at Re = 10000 and Re = 16000

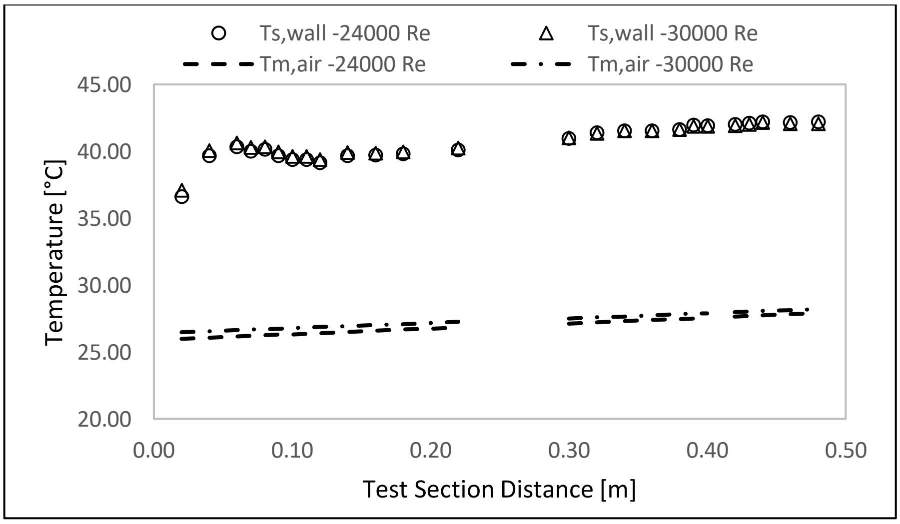

Figure E.24: Test Section Temperatures for Insert 2.1 at Re = 24000 and Re = 30000

E.6. Mesh 2.2 (λ = 16 mm, ξ = 48 %)

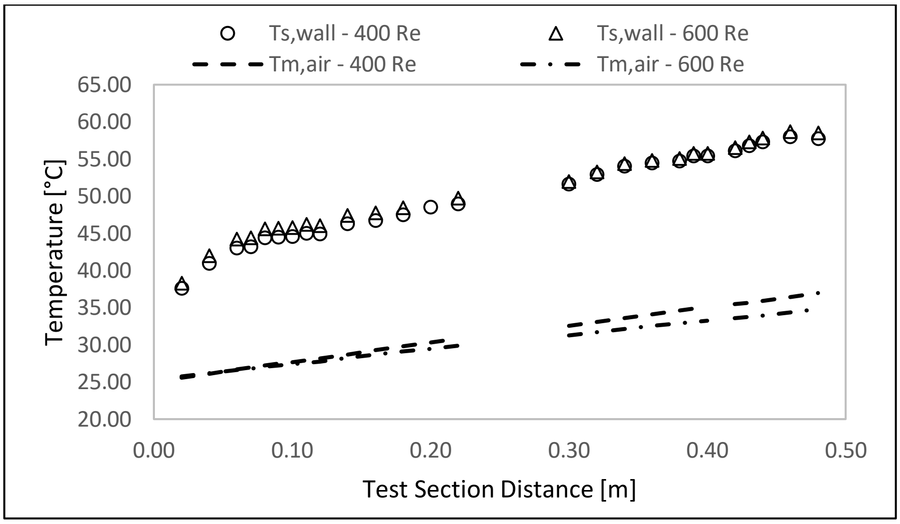

Figure E.25 Test Section Temperatures for Insert 2.2 at Re = 400 and Re = 600

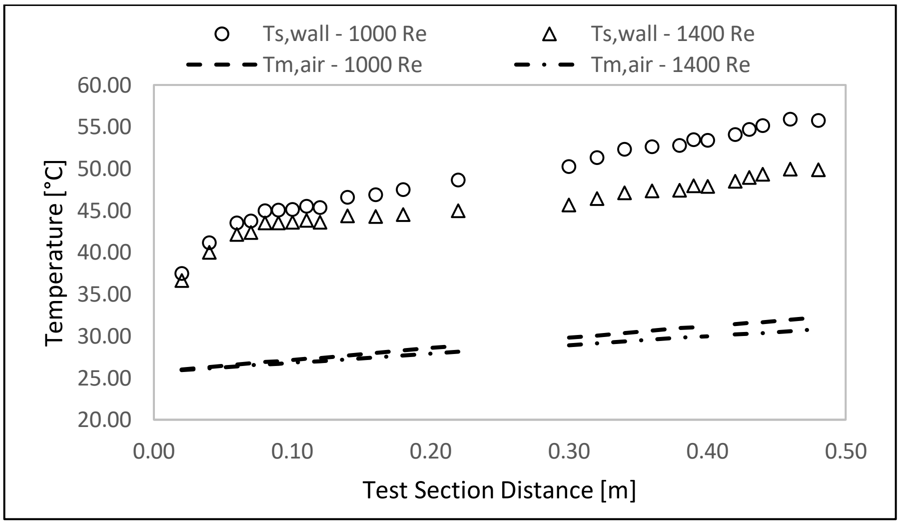

Figure E.26 Test Section Temperatures for Insert 2.2 at Re = 1000 and Re = 1400

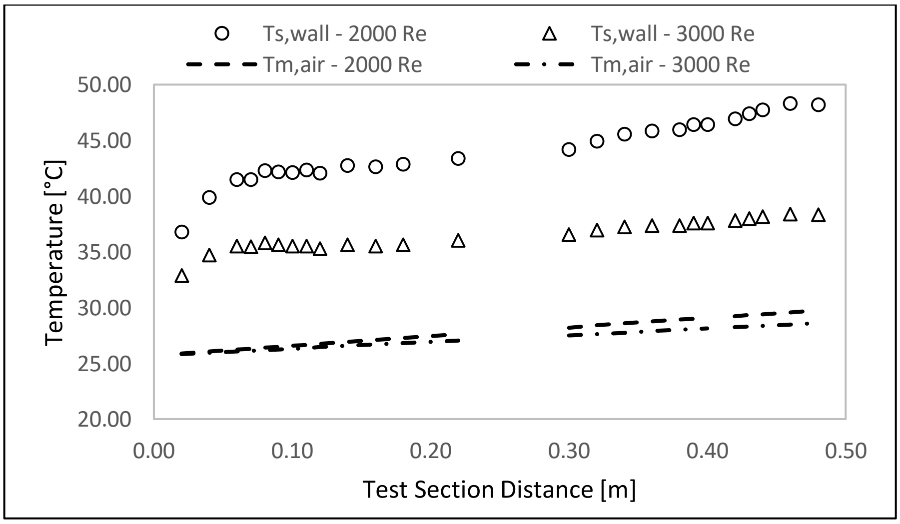

Figure E.27 Test Section Temperatures for Insert 2.2 at Re = 2000 and Re = 3000

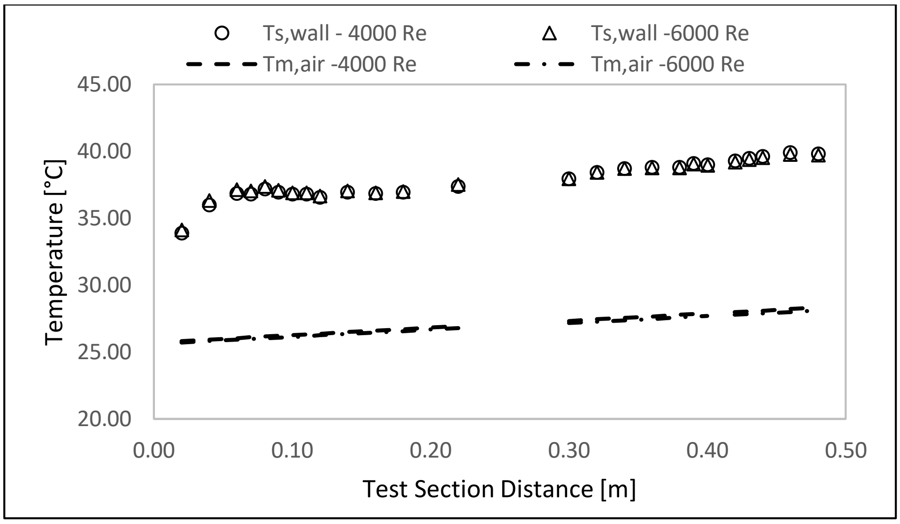

Figure E.28 Test Section Temperatures for Insert 2.2 at Re = 4000 and Re = 6000

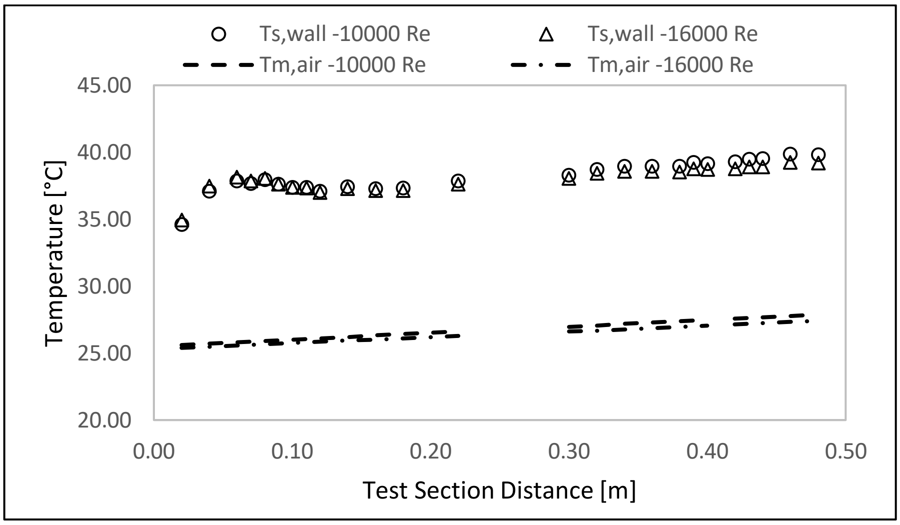

Figure E.29 Test Section Temperatures for Insert 2.2 at Re = 10000 and Re = 16000

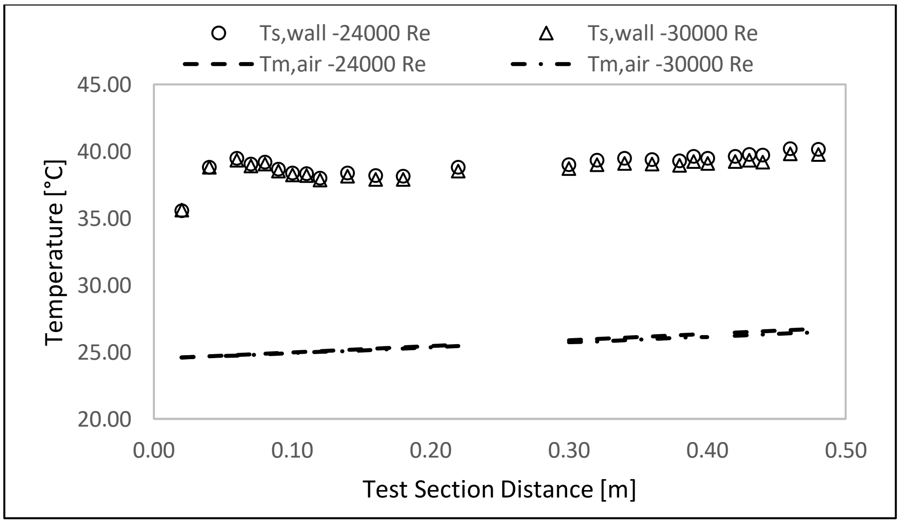

Figure E.30 Test Section Temperatures for Insert 2.2 at Re = 24000 and Re = 30000

E.7. Mesh 3.1 (λ = 12 mm, ξ = 68 %)

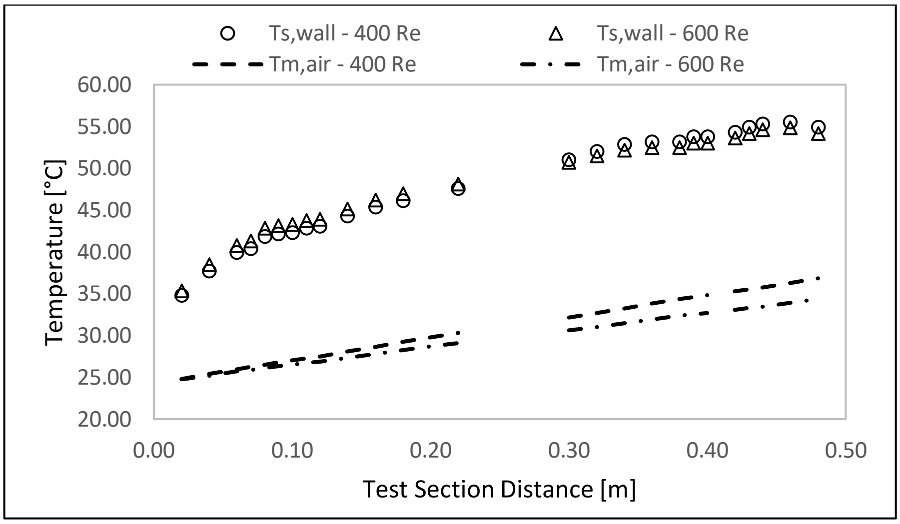

Figure E.31: Test Section Temperatures for Insert 3.1 at Re = 400 and Re = 600

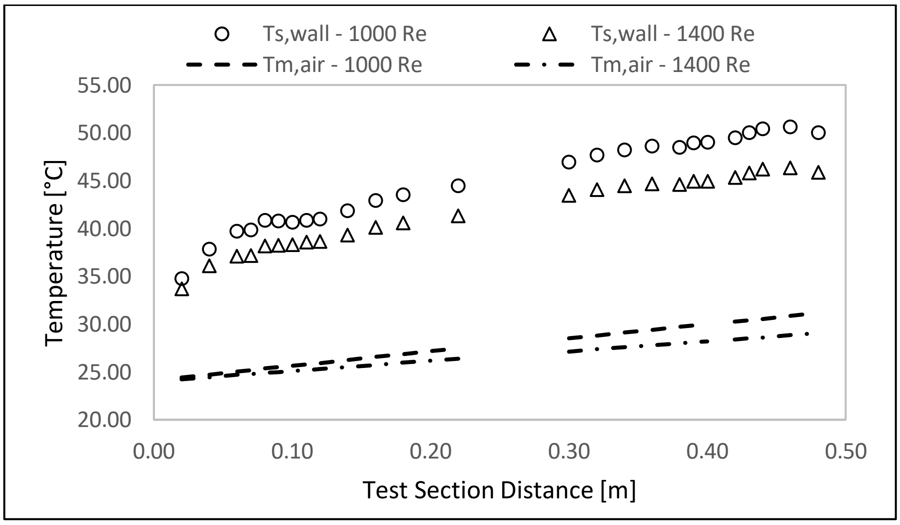

Figure E.32: Test Section Temperatures for Insert 3.1 at Re = 1000 and Re = 1400

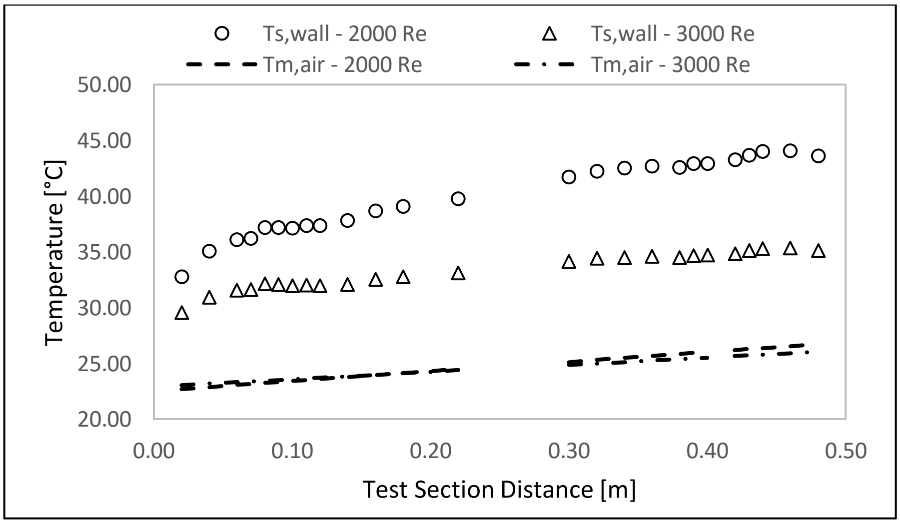

Figure E.33: Test Section Temperatures for Insert 3.1 at Re = 2000 and Re = 3000

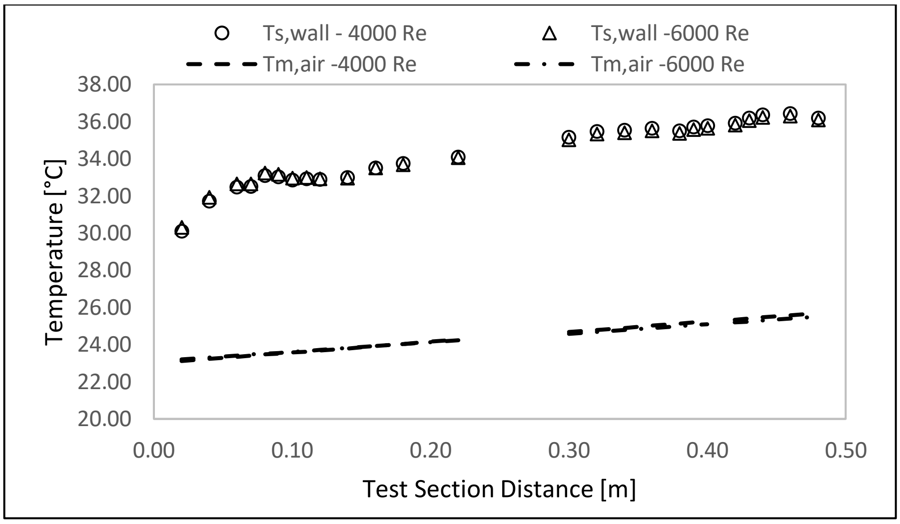

Figure E.34: Test Section Temperatures for Insert 3.1 at Re = 4000 and Re = 6000

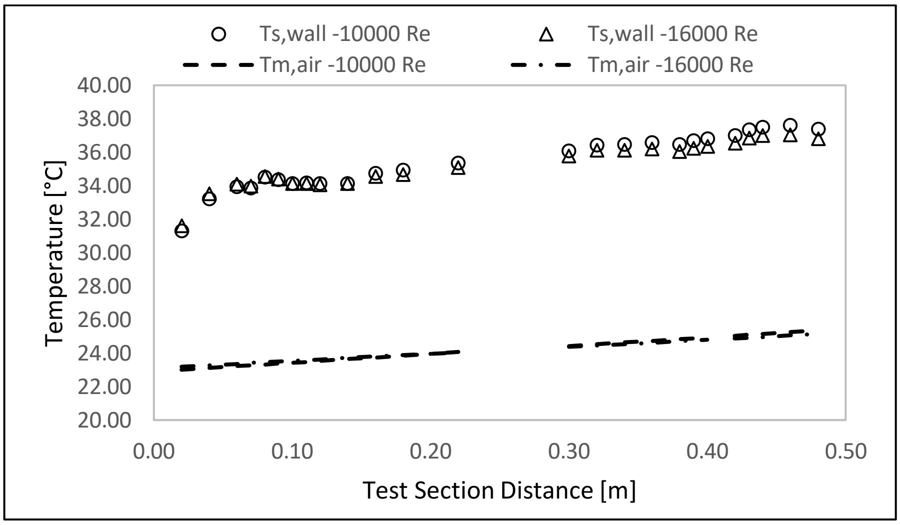

Figure E.35: Test Section Temperatures for Insert 3.1 at Re = 10000 and Re = 16000

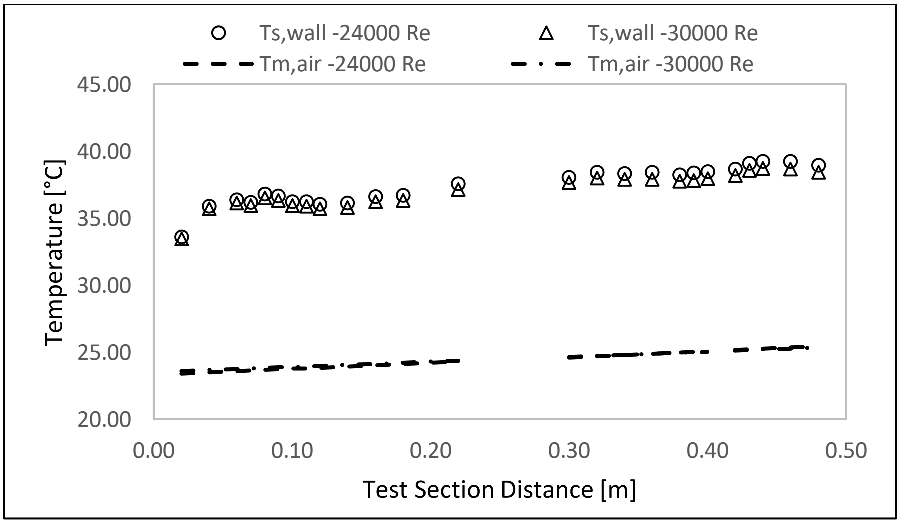

Figure E.36: Test Section Temperatures for Insert 3.1 at Re = 24000 and Re = 30000

E.8. Mesh 3.2 (λ = 12 mm, ξ = 48 %)

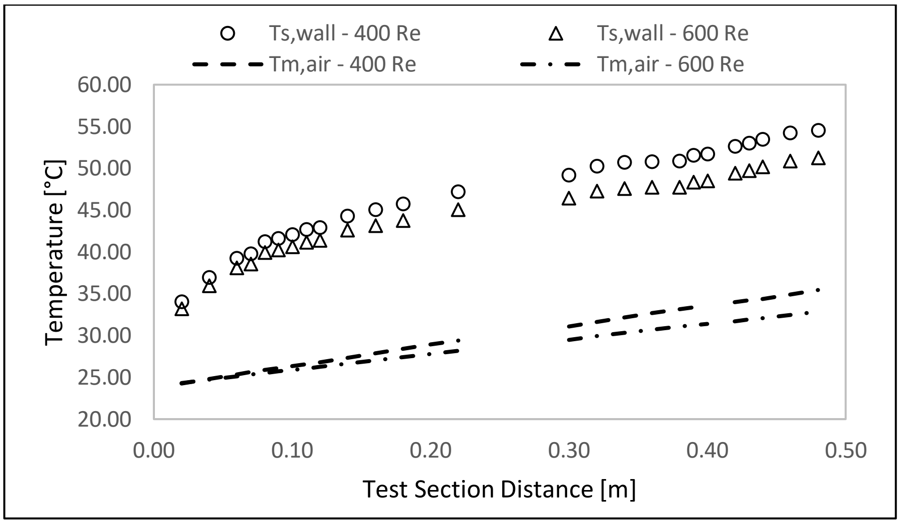

Figure E.37: Test Section Temperatures for Insert 3.2 at Re = 400 and Re = 600

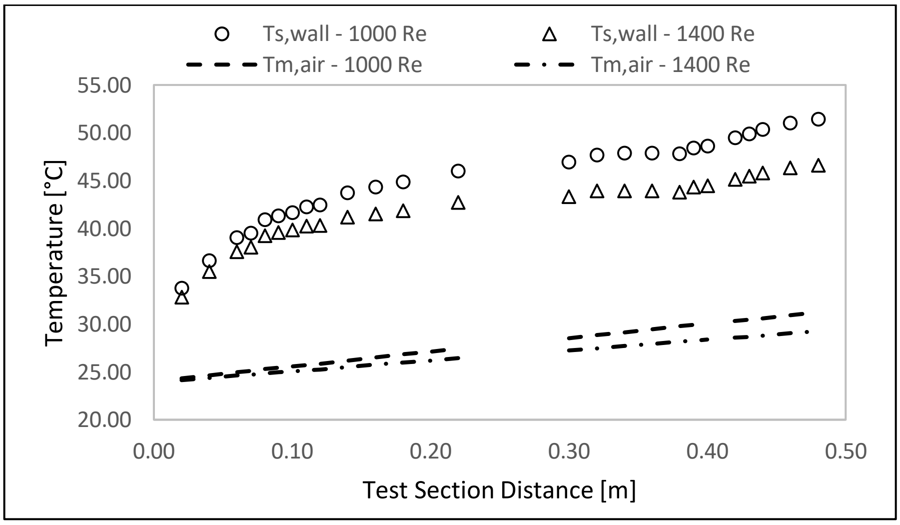

Figure E.38: Test Section Temperatures for Insert 3.2 at Re = 1000 and Re = 1400

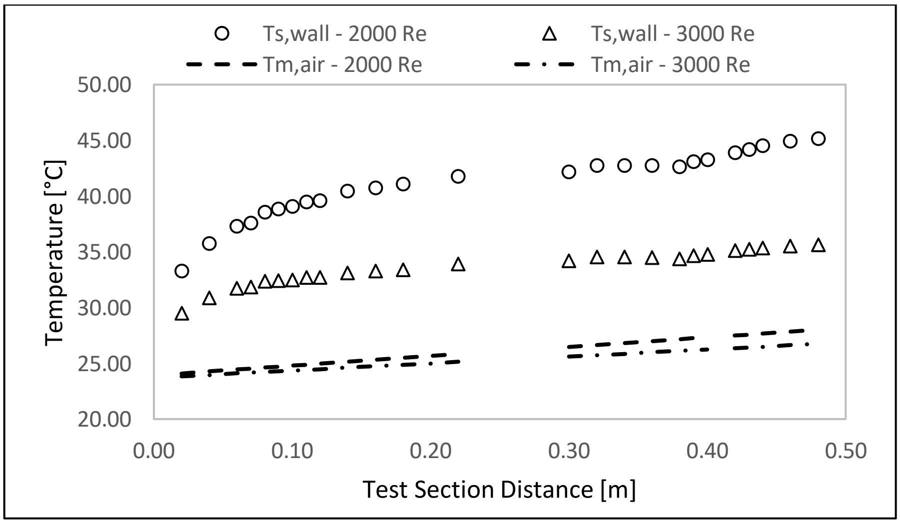

Figure E.39: Test Section Temperatures for Insert 3.2 at Re = 2000 and Re = 3000

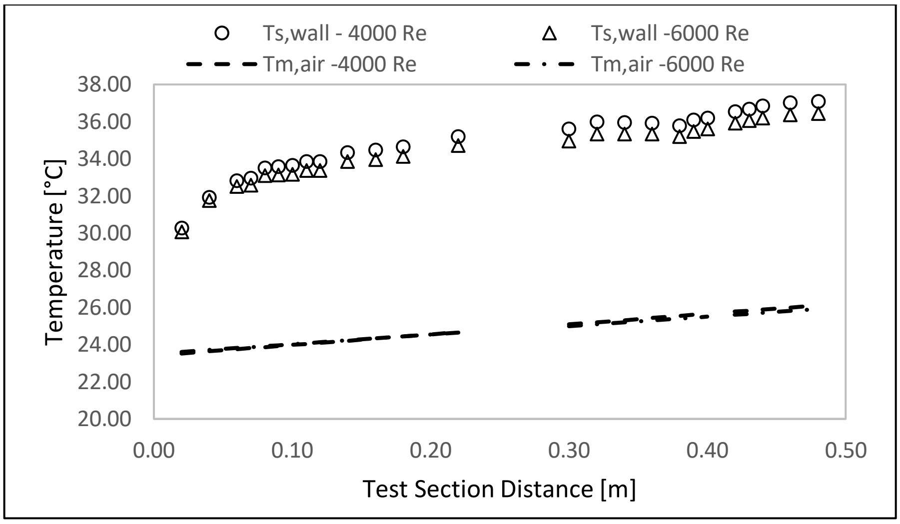

Figure E.40: Test Section Temperatures for Insert 3.2 at Re = 4000 and Re = 6000

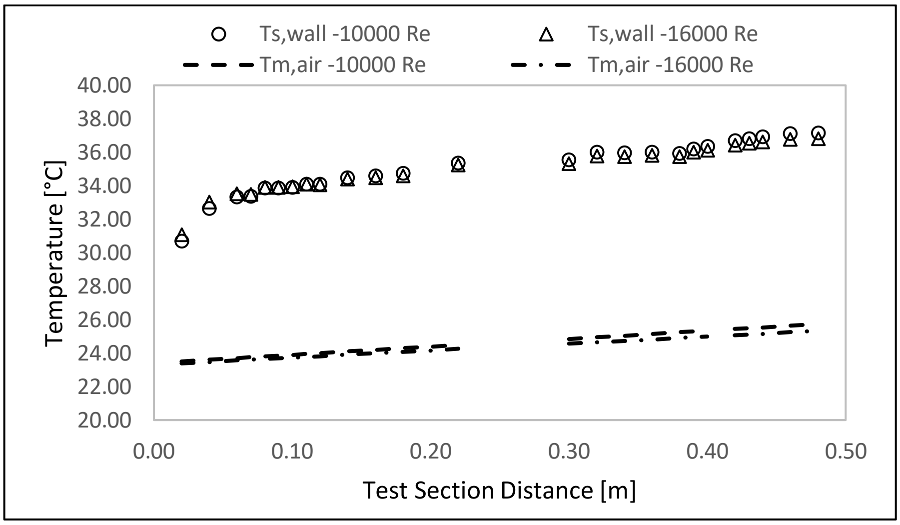

Figure E.41: Test Section Temperatures for Insert 3.2 at Re = 10000 and Re = 16000

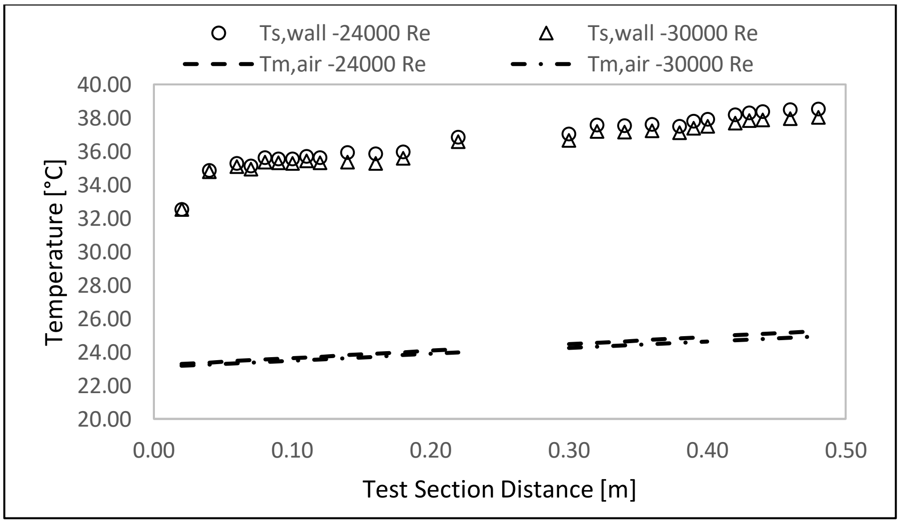

Figure E.42: Test Section Temperatures for Insert 3.2 at Re = 24000 and Re = 30000

E.9. Effects of Porosity on Nu_{avg} and Nu/Nu_0

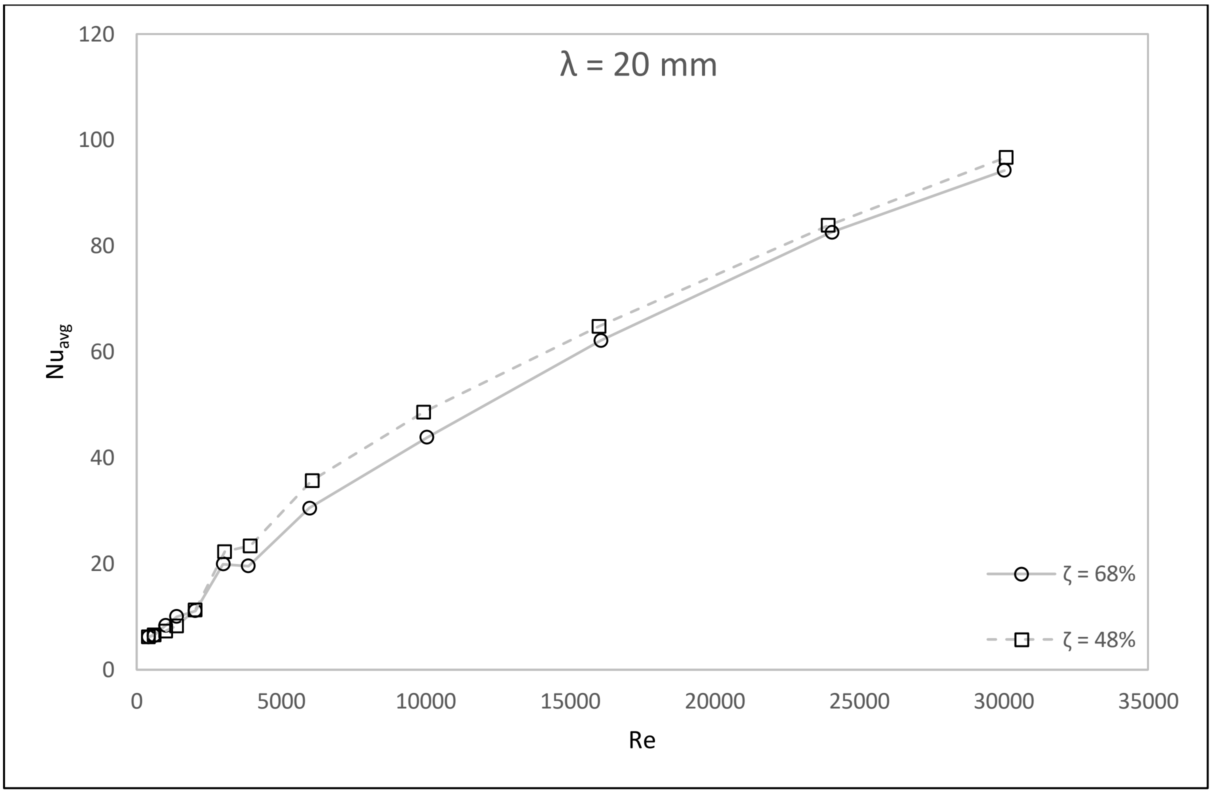

(a)

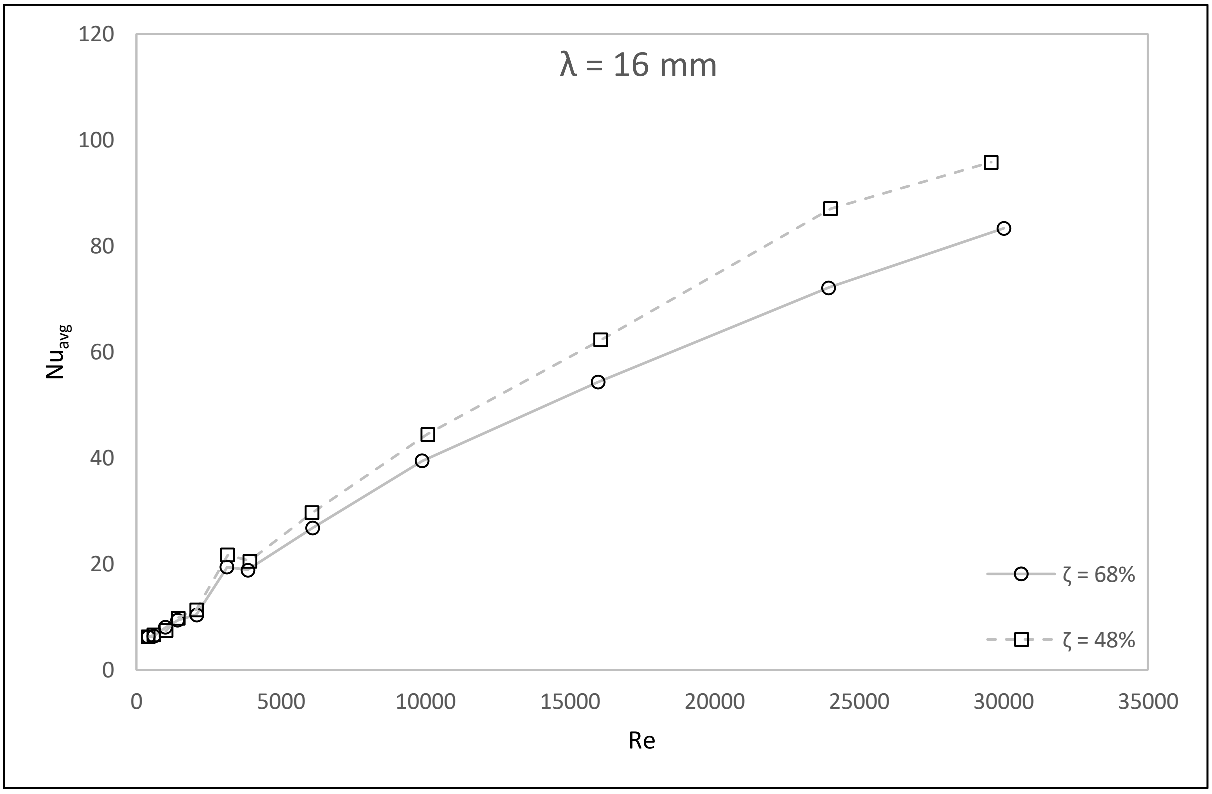

(b)

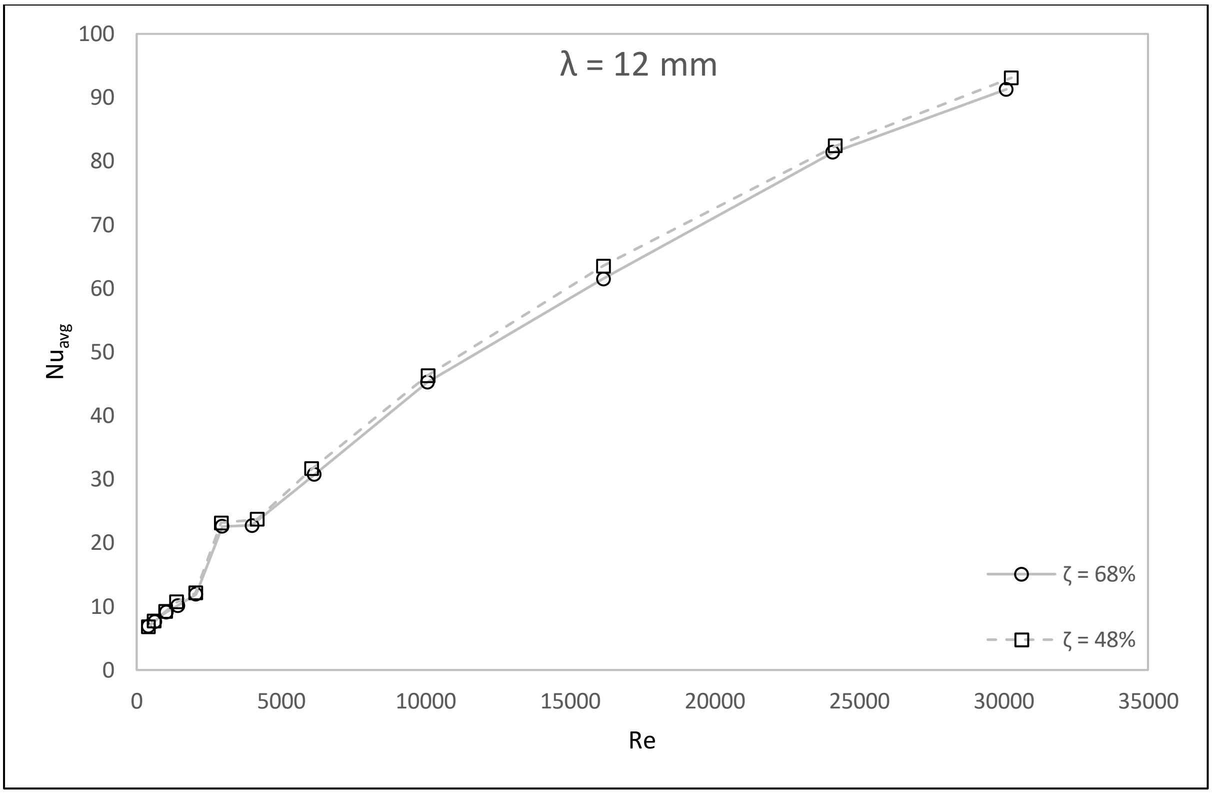

(c)

Figure E.43: Average Nusselt number, Nu_{avg} vs. Re for constant wavelength λ = (a) 20 mm, (b) 16 mm and (c) 12 mm

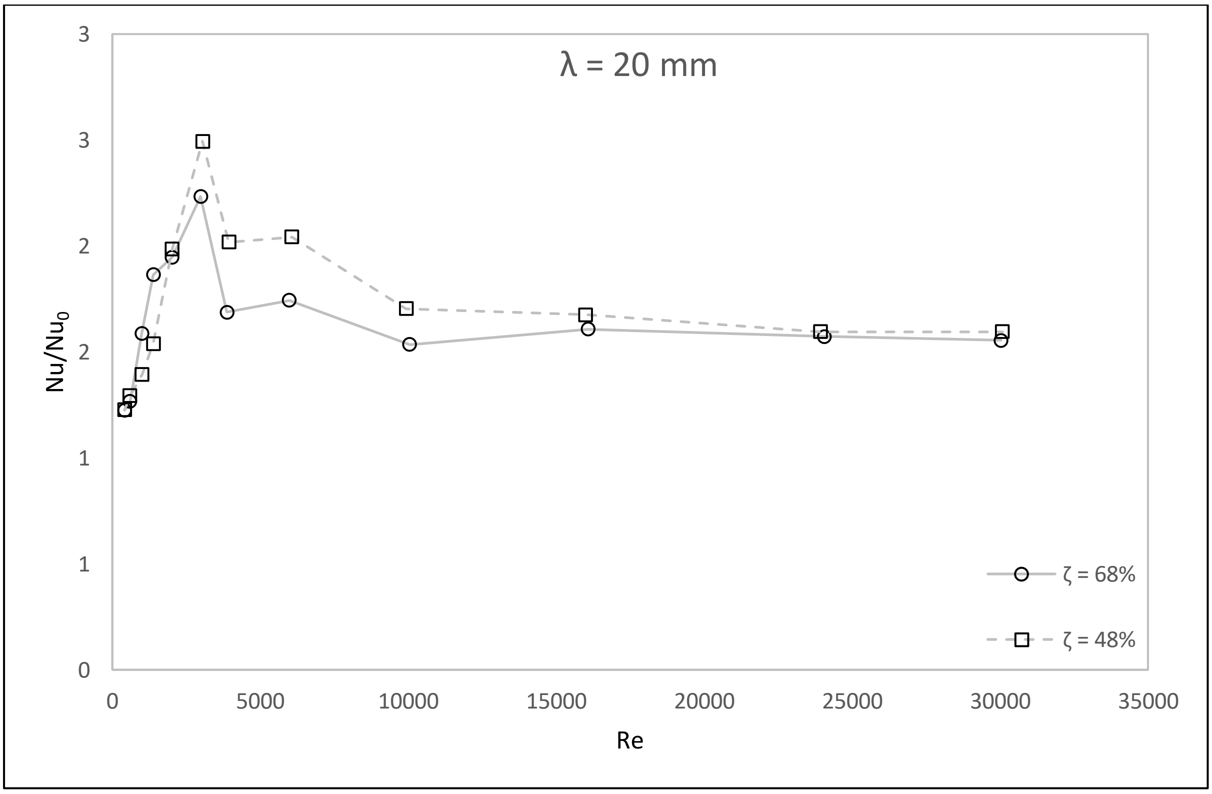

(a)

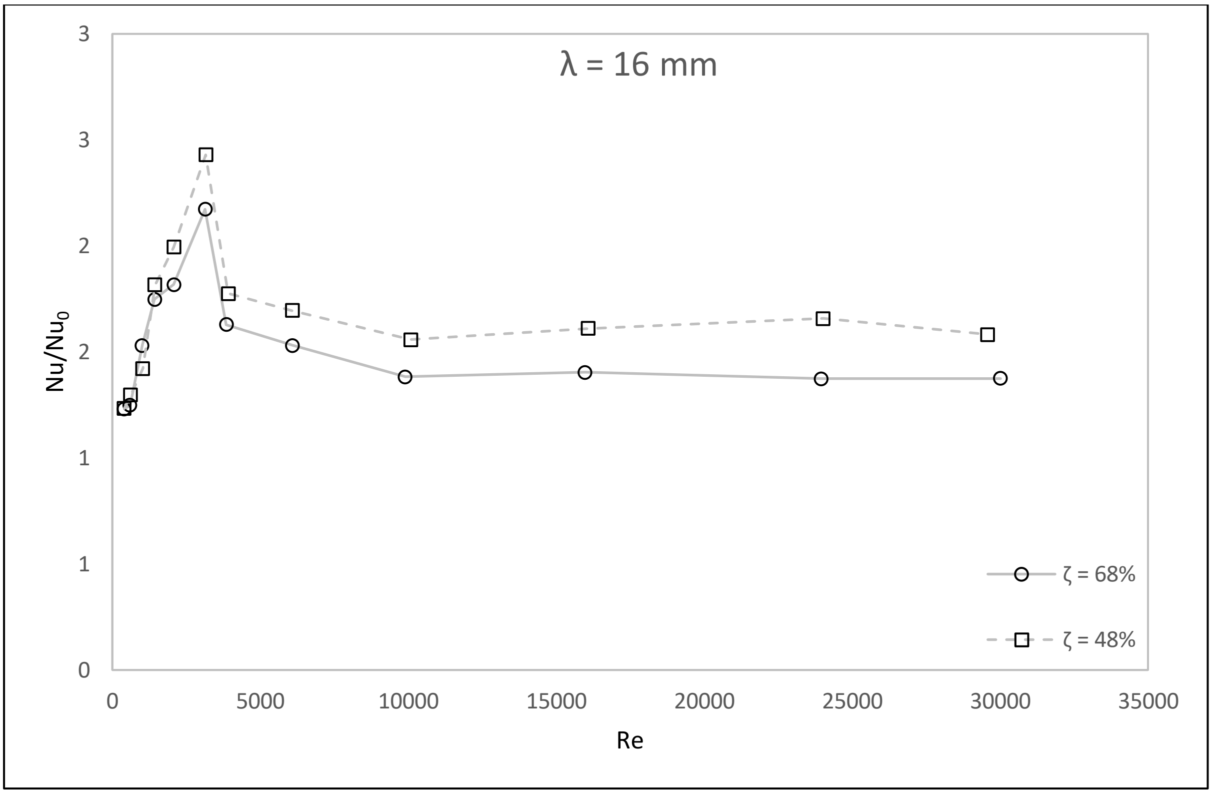

(b)

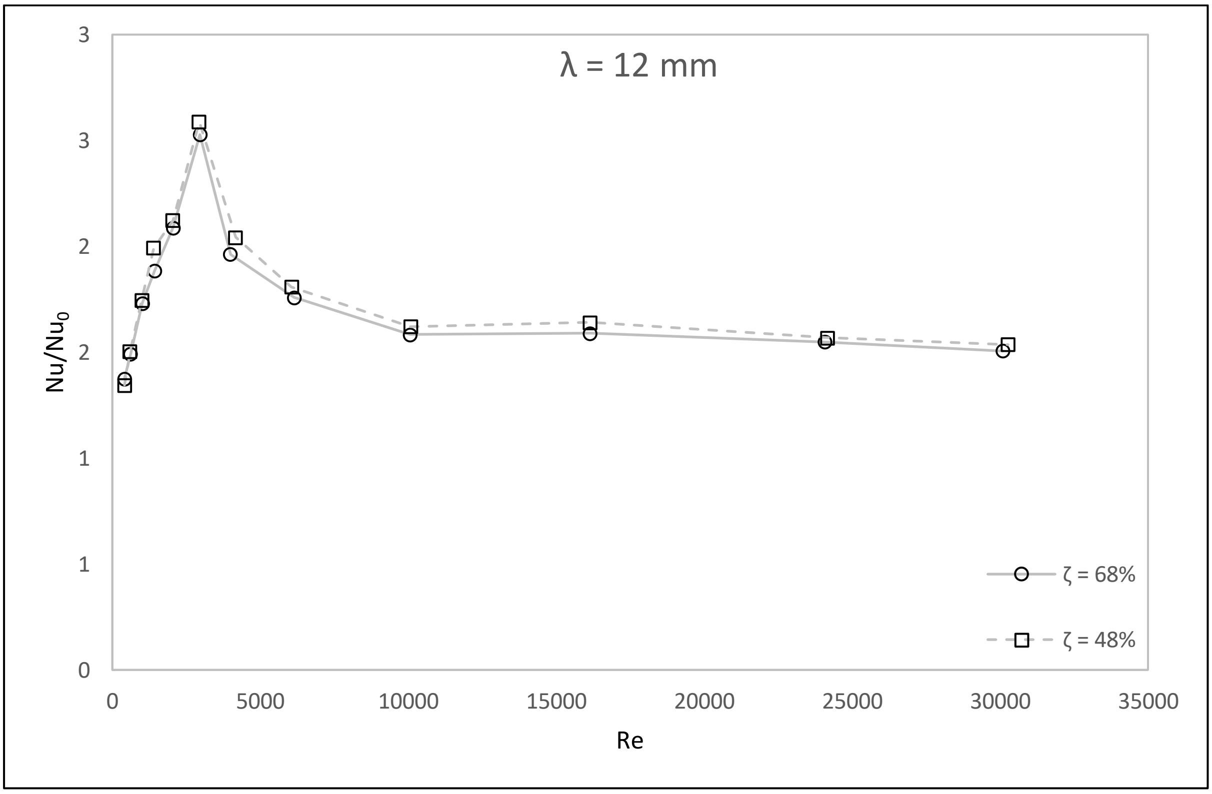

(c)

Figure E.44: Nusselt number ratio, Nu/Nu$_0$ vs. Re for constant wavelength λ = (a) 20 mm, (b) 16 mm and (c) 12 mm

E.10. Effects of Porosity on $(Nu/Nu_0)/(f/f_0)^{1/3}$

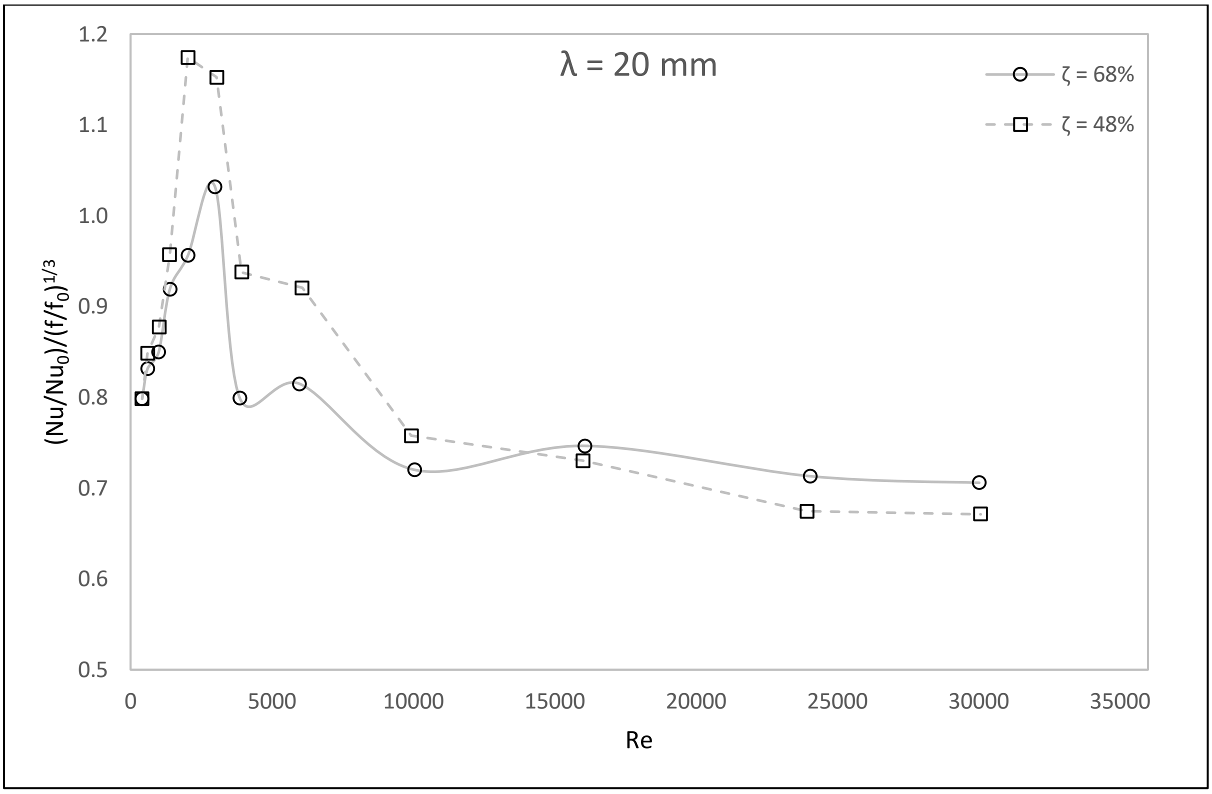

(a)

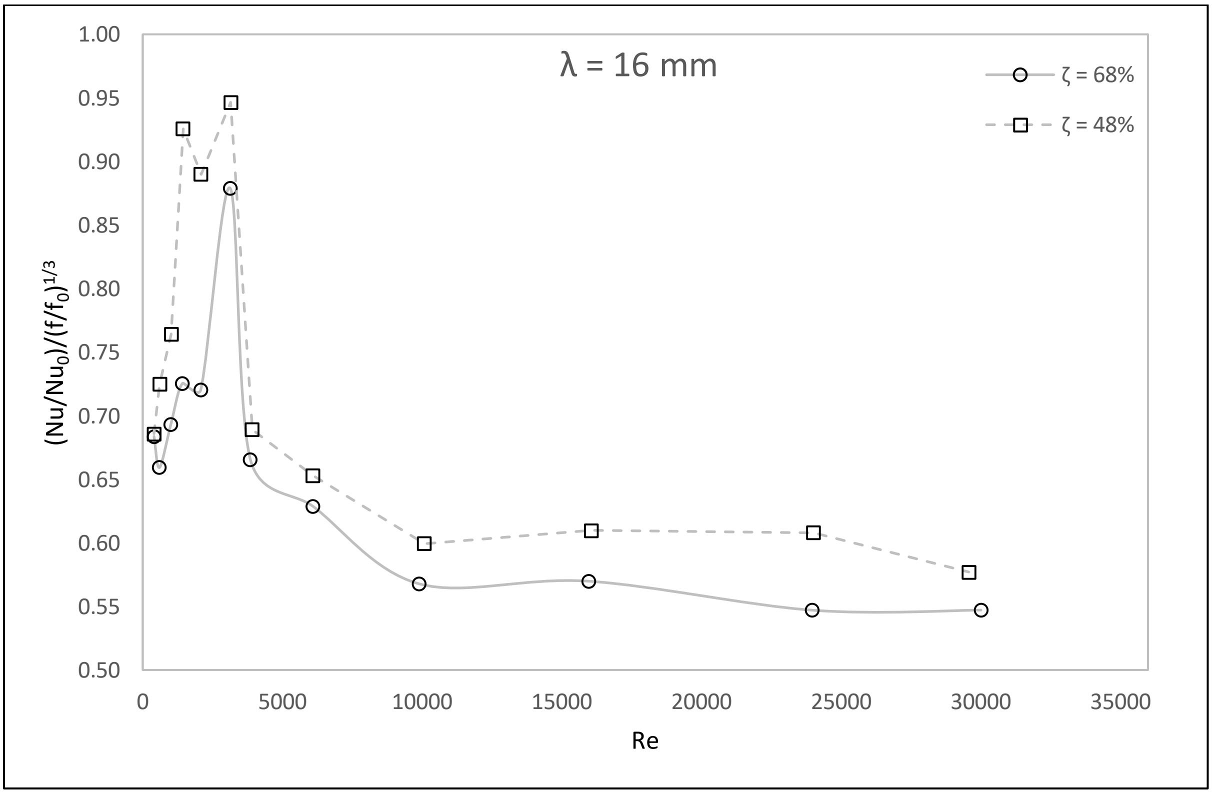

(b)

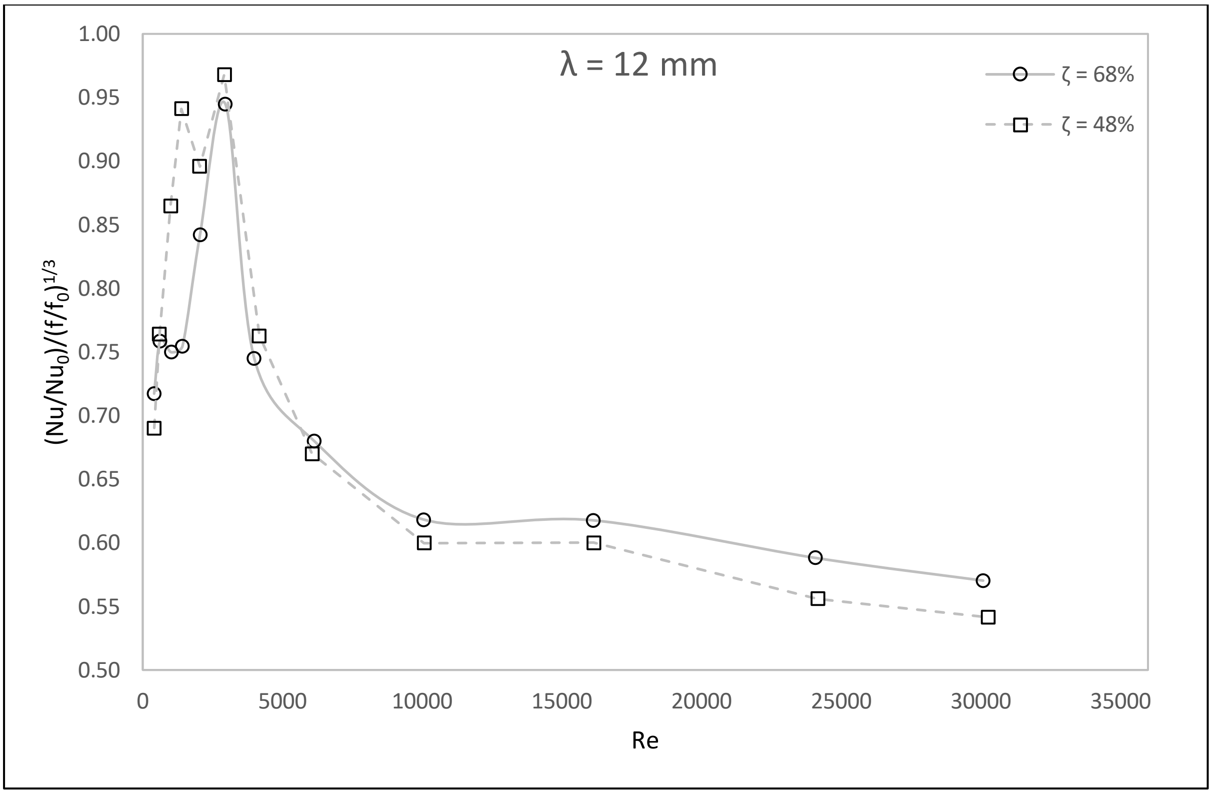

(c)

Figure E.45: Performance index, $(Nu/Nu_0)/(f/f_0)^{1/3}$ vs. Re for constant wavelength λ = (a) 20 mm, (b) 16 mm and (c) 12 mm

Appendix F: Nusselt Number – Friction Factor Correlations

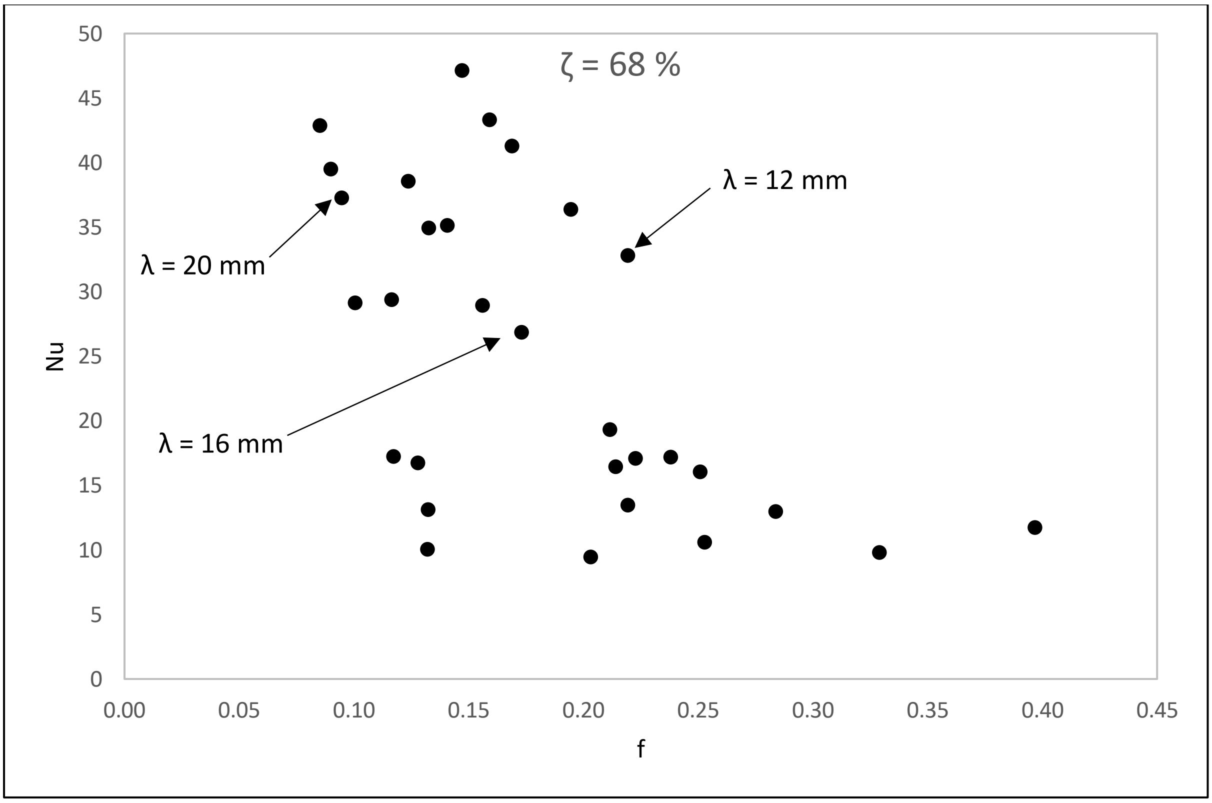

Figure F.1: Two wall heating Nu vs. f, ζ = 68 %, λ = (20 mm, 16 mm, 12 mm), 400 ≤ Re < 8000

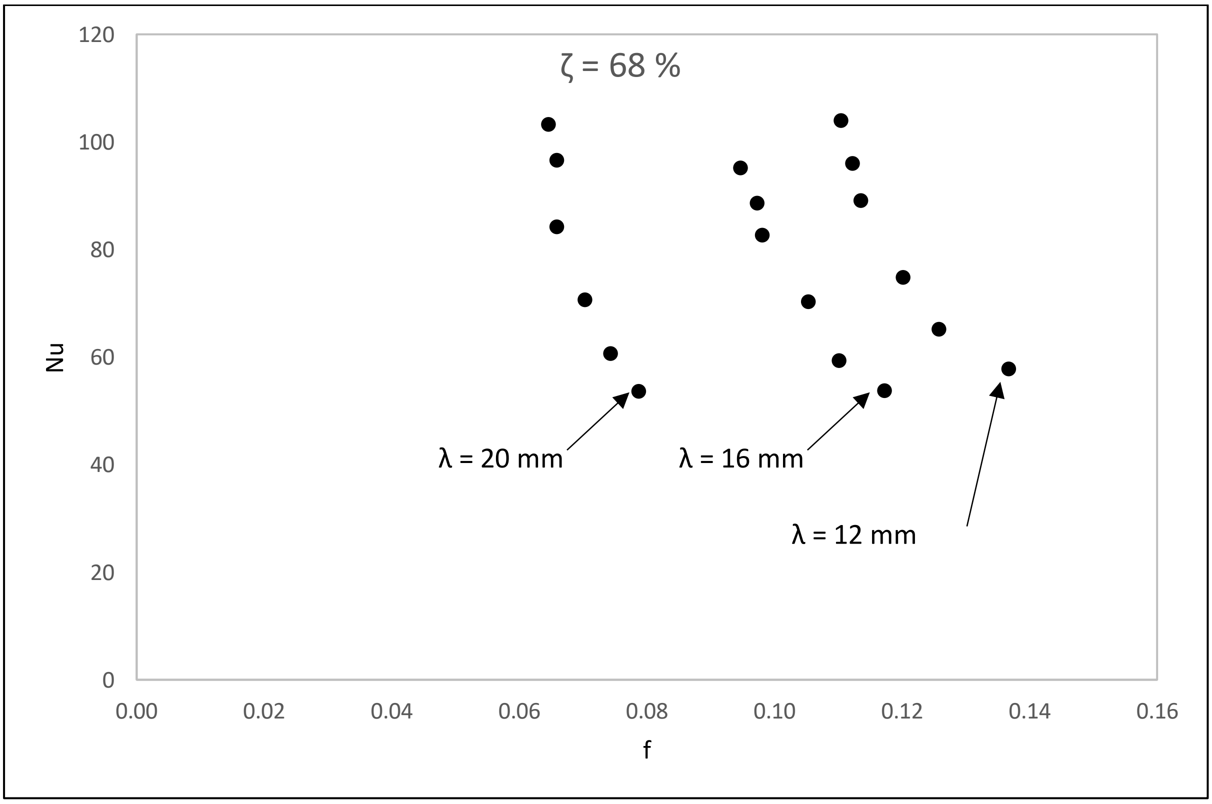

Figure F.2: Two wall heating Nu vs. f, ζ = 68 %, λ = (20 mm, 16 mm, 12 mm), 8000 ≤ Re < 28000

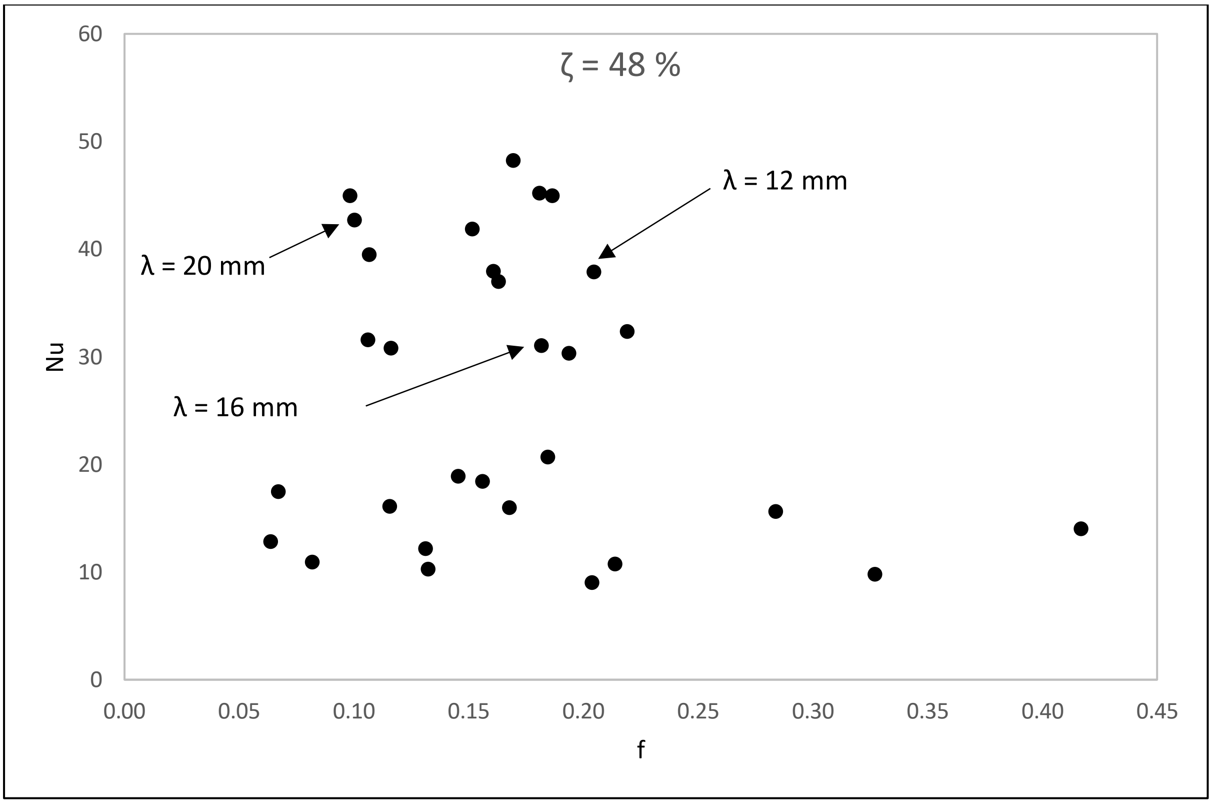

Figure F.3: Two wall heating Nu vs. f, ζ = 48 %, λ = (20 mm, 16 mm, 12 mm), 400 ≤ Re < 8000

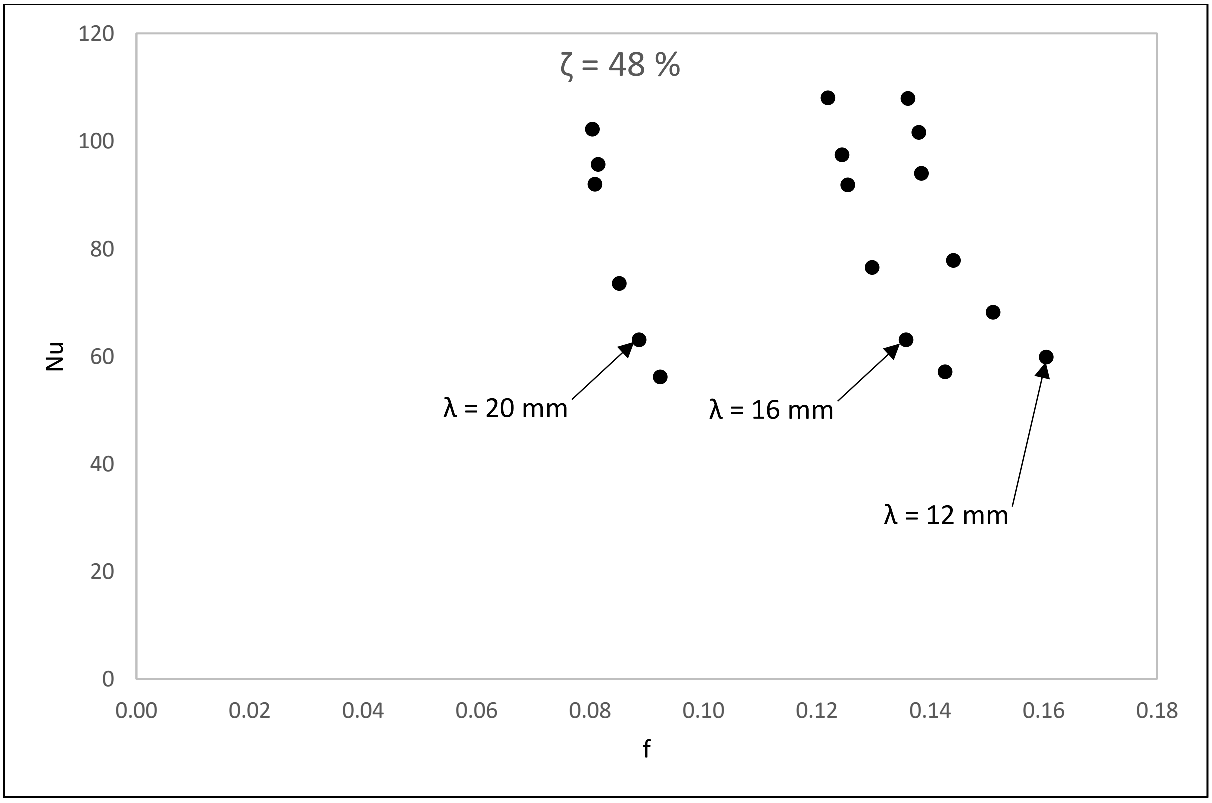

Figure F.4: Two wall heating Nu vs. f, ζ = 48 %, λ = (20 mm, 16 mm, 12 mm), 8000 ≤ Re < 28000

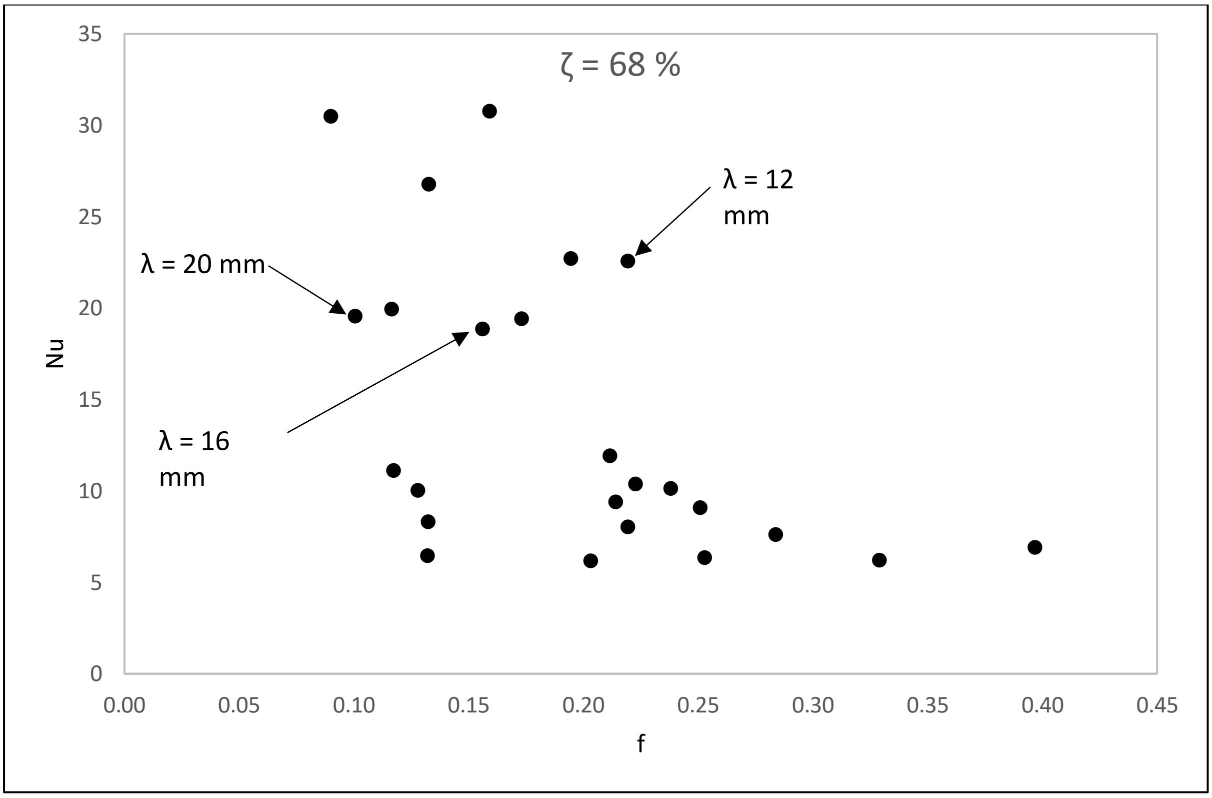

Figure F.5: One wall heating Nu vs. f, ζ = 68 %, λ = (20 mm, 16 mm, 12 mm), 400 ≤ Re < 8000

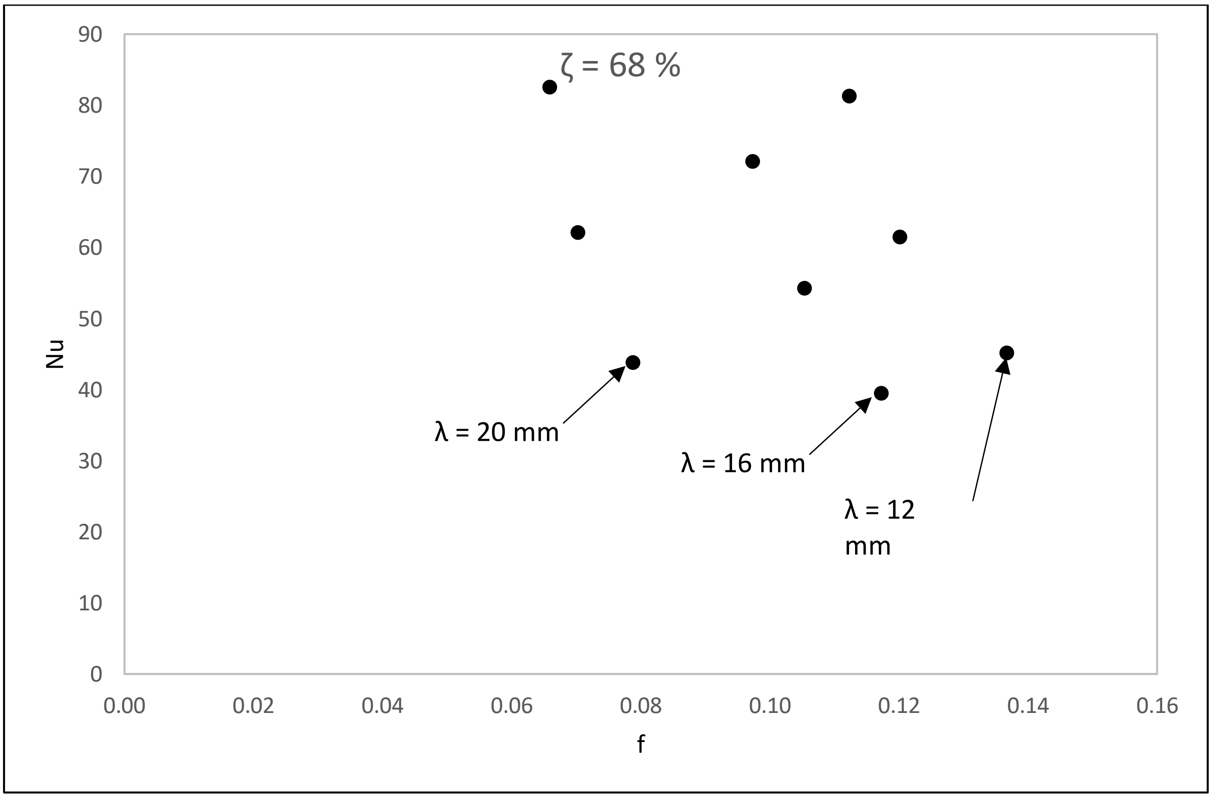

Figure F.6: One wall heating Nu vs. f, ζ = 68 %, λ = (20 mm, 16 mm, 12 mm), 8000 ≤ Re < 28000

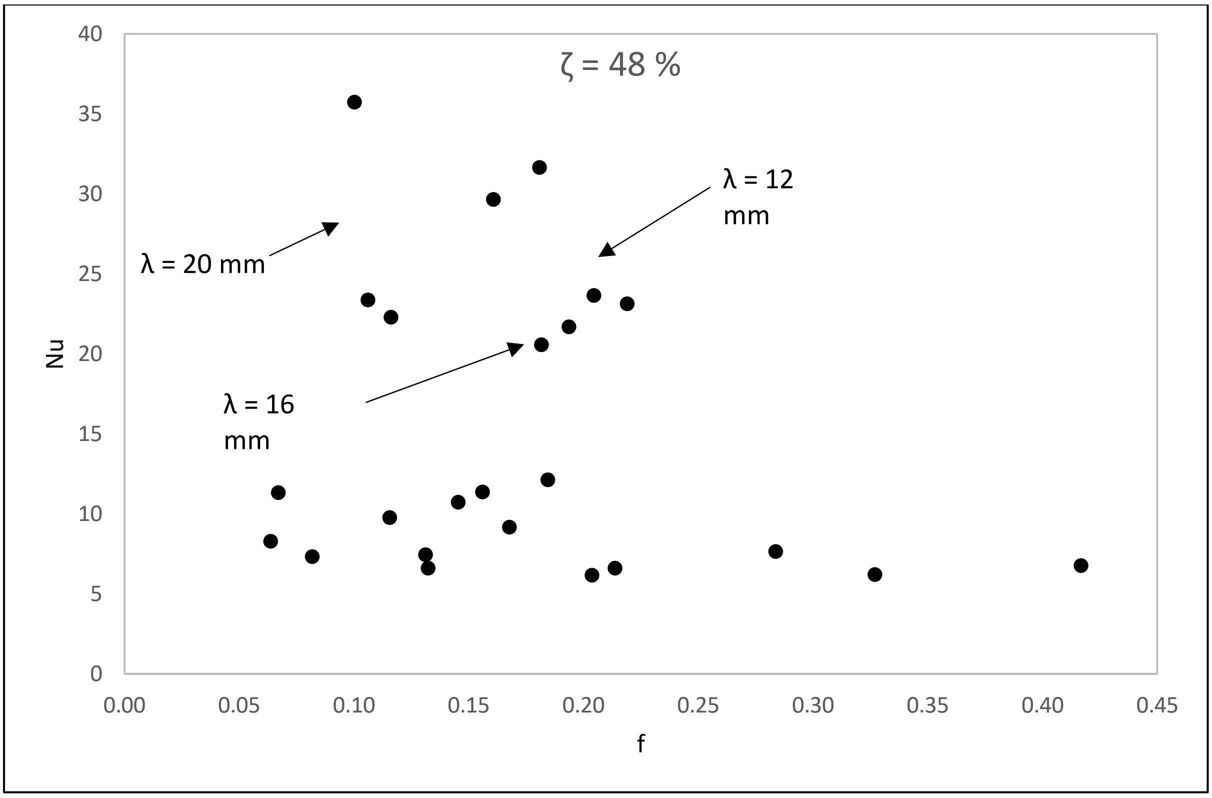

Figure F.7: One wall heating Nu vs. f, ζ = 48 %, λ = (20 mm, 16 mm, 12 mm), 400 ≤ Re < 8000

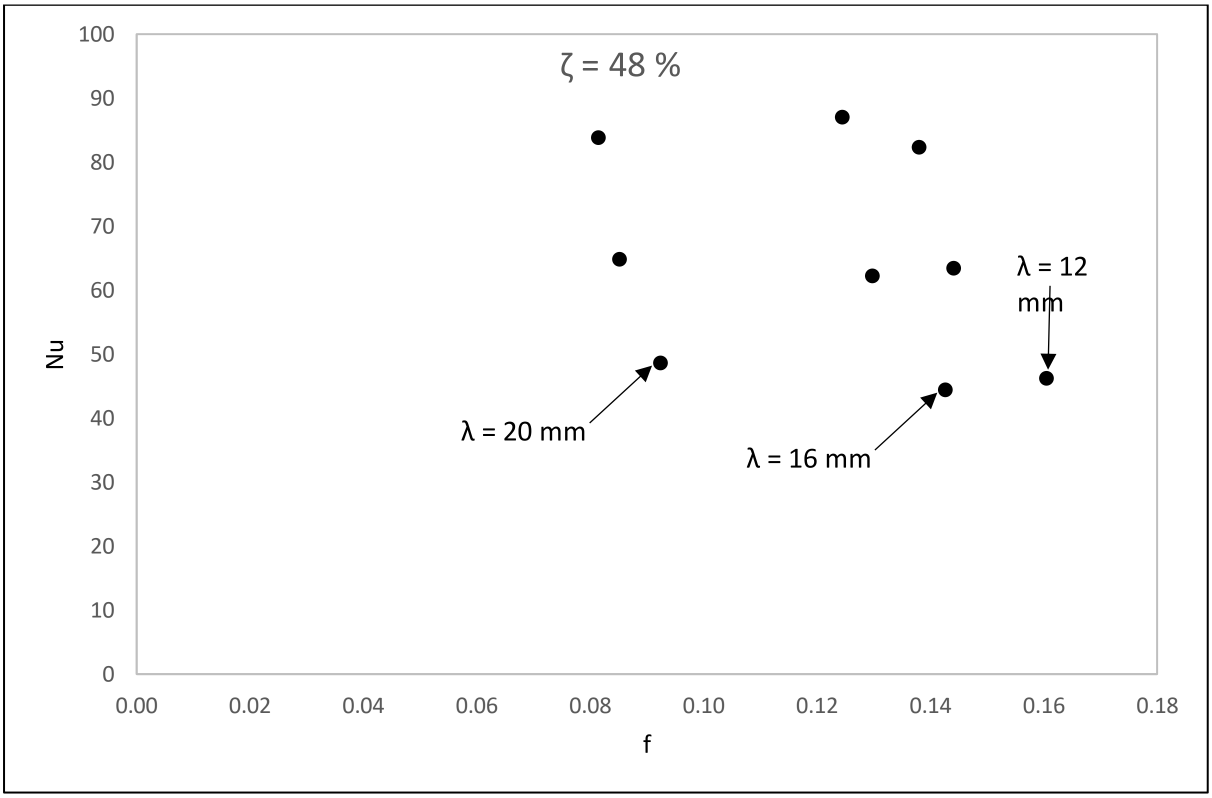

Figure F.8: One wall heating Nu vs. f, ζ = 48 %, λ = (20 mm, 16 mm, 12 mm), 8000 ≤ Re < 28000

Appendix G: % Difference of Nu/Nu_0 and f/f_0 Relative to the Porous Insert (ζ = 68 %, λ = 20 mm)

Table G.1: ΔNu % for two wall heating and Δf %

Re range	**λ [mm]**	**ζ [%]**	**$\Delta Nu\ \% = Nu_{(\lambda,\xi)} - Nu_{(20mm,68\%)}$**	**$\Delta f\ \% = f_{(\lambda,\xi)} - f_{(20mm,68\%)}$**
400 to 2000	12	48	13 % to 55 %	14 % to 115 %
	16		-7 % to 7 %	-10 % to 62 %
	20		-23 % to 2 %	-50 % to 0 %
3000 to 8000	12	48	10 % to 30 %	88 % to 104 %
	16		-4 % to 7 %	66 % to 81 %
	20		5 % to 8 %	0 % to 15 %
9000 to 28000	12	48	4 % to 12 %	103 % to 111 %
	16		1 % to 9 %	81 % to 91 %
	20		-1 % to 9 %	17 % to 25 %

Table G.2: ΔNu % for one wall heating

Re range	**λ [mm]**	**ζ [%]**	**$\Delta Nu\ \% = Nu_{(\lambda,\xi)} - Nu_{(20mm,68\%)}$**
400 to 2000	12	48	7 % to 19 %
	16		-10 % to 2 %
	20		-17 % to 2 %
3000 to 8000	12	48	4 % to 21 %
	16		-3 % to 9 %
	20		12 % to 20 %
9000 to 28000	12	48	0 % to 6 %
	16		0 % to 5 %
	20		2 % to 11 %

Appendix H: 1-D Heat Loss Calculations for the Porous Insert (ζ = 68 %, λ = 20 mm) at Re = 600

This appendix shows the 1-D heat loss calculations used to estimate the conductional heat loss through the broad side of the test section. Position 0 is the start of the test section, position 1 is 100 mm downstream of the start of the test section, position 2 is 200 mm downstream, position 3 is 300 mm downstream, position 4 is 400 mm downstream, and position 5 is end of the test section as by x0 to x4 in Table H. 1. Insulation 0 through to insulation 4 are thermocouple positioned between the two layers of insulation and perspex 0 through to Perspex 4 are thermocouples positions on the back of the perspex. Delta_T0 through to delta_T4 is the difference between the Perspex and the insulation thermocouples.

$$deltaT0 = perspex0 - insulation0$$

$$deltaT0 = 30.13 - 26.6 = 3.53\ °C$$

q_0 is the heat flux at position 0 through the first layer insulation. q_0 can be calculated using Fourier's law of heat conduction:

$$q0 = deltaT0 * \frac{k}{x}$$

$$q0 = 3.53 * \frac{0.037}{0.025} = 5.23\ W/m^2$$

q_1 through to q_4 are calculated in a similar manner and q5 is calculated via extrapolation. With q0 through to q5 known it possible to determine the thermal losses between thermocouple locations considering the area between these points. The thermal losses between location 0 and 1 are calculated as:

$$Q1 = 0.5 * (q0 + q1) * L * W$$

$$Q1 = 0.5 * (5.23 + 8.13) * 0.1 * 0.203 = 0.14\ W$$

Q2 through to Q5 are calculated in a similar manner. The total conductional heat loss through the one side of the test section can be calculated by the summation of Q0 to Q5:

$$QT = Q0 + Q1 + Q2 + Q3 + Q4 + Q5$$

$$QT = 0 + 0.14 + 0.19 + 0.24 + 0.29 + 0.31 = 1.17\ W$$

Table H.1: Typical heat loss table

Conduction Losses			
Position	**Temperature**	**Position**	**Heat Loss**
insultation 0	26,60	q_0	5,23
insultation 1	27,53	q_1	8,18
insultation 2	28,70	q_2	10,40
insultation 3	29,20	q_3	13,72
insultation 4	30,37	q_4	14,80
T_s @ x_0.02	30,63	q_5	15,87
perspex 0	30,13	Q_0	0,00
perspex 1	33,06	Q_1	0,14
perspex 2	35,73	Q_2	0,19
perspex 3	38,47	Q_3	0,24
perspex 4	40,37	Q_4	0,29
delta_T 0	3,53	Q_5	0,31
delta_T 1	5,53	Q_T	1,17
delta_T 2	7,03	x_0	0,00
delta_T 3	9,27	x_1	0,10
delta_T 4	10,00	x_2	0,20
		x_3	0,30
		x_4	0,40